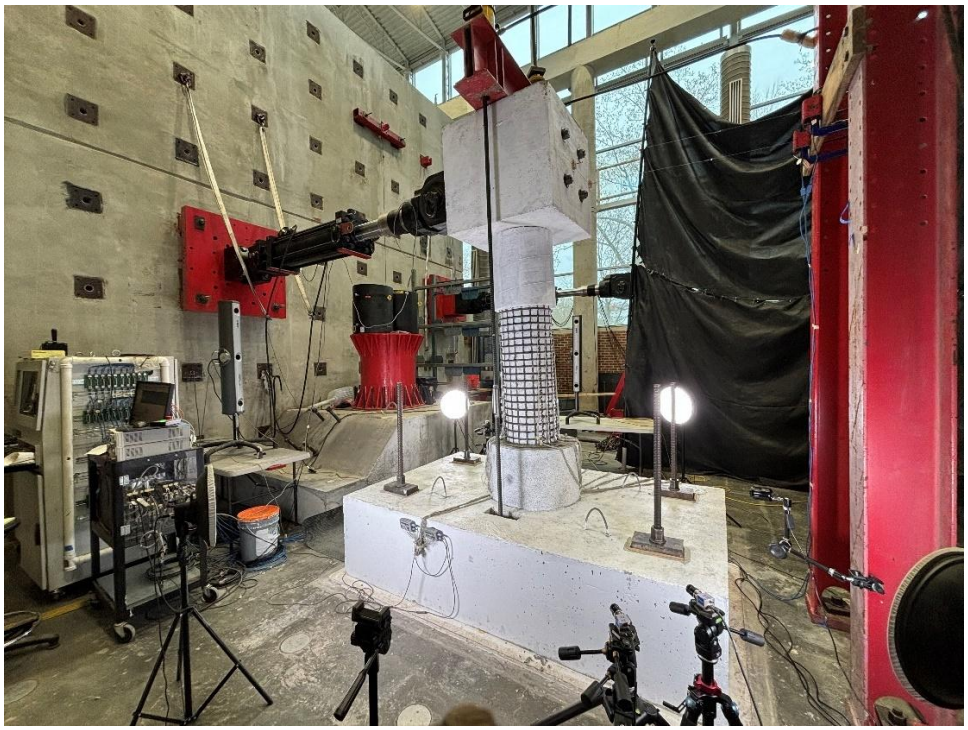
Research & Technology Transfer

External Pocket and Socket Connections for the Seismic Design of Alaska Bridges

FINAL REPORT



Prepared by:
Julio A. Samayoa, Ph.D.
Giorgio T. Proestos, Ph.D., Principal Investigator
Mervyn Kowalsky, Ph.D., Principal Investigator
Raleigh, North Carolina
Report # FHWA-AK-RD-4000(195)
December 19th, 2024

Prepared for:
Alaska Department of Transportation & Public Facilities Statewide Research Office
3132 Channel Drive
Juneau, AK 99801-7898

REPORT DOCUMENTATION PAGE

Form approved OMB No.

Public reporting for this collection of information is estimated to average 1 hour per response, including the time for reviewing instructions, searching existing data sources, gathering and maintaining the data needed, and completing and reviewing the collection of information. Send comments regarding this burden estimate or any other aspect of this collection of information, including suggestion for reducing this burden to Washington Headquarters Services, Directorate for Information Operations and Reports, 1215 Jefferson Davis Highway, Suite 1204, Arlington, VA 22202-4302, and to the Office of Management and Budget, Paperwork Reduction Project (0704-1833), Washington, DC 20503

1. AGENCY USE ONLY (LEAVE BLANK)	2. REPORT DATE	3. REPORT TYPE AND DATES COVERED
FHWA-AK-RD-4000(195)	December 19th, 2024	Final Report, January 2021 through December 2024

4. TITLE AND SUBTITLE
External Pocket and Socket Connections for the Seismic Design of Alaska Bridges

5. FUNDING NUMBERS
State # HFHWY00152
Federal #4000(195)

6. AUTHOR(S)
Julio A. Samayoa, Ph.D.
Giorgio T. Proestos, Ph.D., Principal investigator
Mervyn J. Kowalsky, Ph.D., Principal investigator

7. PERFORMING ORGANIZATION NAME(S) AND ADDRESS(ES)
Department of Civil, Construction, and Environmental Engineering
North Carolina State University
Raleigh, NC 27606

8. PERFORMING ORGANIZATION REPORT NUMBER
HFHWY00152

9. SPONSORING/MONITORING AGENCY NAME(S) AND ADDRESS(ES)
State of Alaska, Alaska Dept. of Transportation and Public Facilities
Research and Technology Transfer
3132 Channel Drive
Juneau, AK 99801-7898

10. SPONSORING/MONITORING AGENCY REPORT NUMBER
FHWA-AK-RD-4000(195)

11. SUPPLEMENTARY NOTES

12a. DISTRIBUTION / AVAILABILITY STATEMENT
No restrictions

12b. DISTRIBUTION CODE

13. ABSTRACT (Maximum 200 words)

This report investigates external socket connections, where a precast column is embedded in a preformed void outside a cap beam or foundation, with the gap filled with grout. Designing these connections poses challenges due to the lack of a mechanical model to relate design parameters to critical stresses. To address this, a strut-and-tie model (STM) was developed to analyze the impact of socket height on stress distribution. The model was validated through eight large-scale reverse cyclic tests on column-to-cap-beam connections, exploring various socket heights and structural systems, including RC and RCFST. The results highlighted that socket height is crucial for developing a full plastic hinge in the column and influences stress demands on the grout and socket walls. Analysis revealed that shorter socket heights require a higher shear capacity due to increased shear forces on the column. The proposed STM accurately predicted failure modes and critical stresses, offering a reliable tool for designing socket connections. Design equations and recommendations were developed to assist engineers in applying this connection type in seismic regions, ensuring both safety and efficiency.

14- KEYWORDS:
Accelerated Bridge Construction, Large-scale testing, External Socket Connection, Seismic Design of Bridges

15. NUMBER OF PAGES
438

16. PRICE CODE
N/A

17. SECURITY CLASSIFICATION OF REPORT	18. SECURITY CLASSIFICATION OF THIS PAGE	19. SECURITY CLASSIFICATION OF ABSTRACT	20. LIMITATION OF ABSTRACT
Unclassified	Unclassified	Unclassified	N/A

Notice

This document is disseminated under the sponsorship of the U.S. Department of Transportation in the interest of information exchange. The U.S. Government assumes no liability for the use of the information contained in this document. The U.S. Government does not endorse products or manufacturers. Trademarks or manufacturers' names appear in this report only because they are considered essential to the objective of the document.

Quality Assurance Statement

The Federal Highway Administration (FHWA) provides high-quality information to serve Government, industry, and the public in a manner that promotes public understanding. Standards and policies are used to ensure and maximize the quality, objectivity, utility, and integrity of its information. FHWA periodically reviews quality issues and adjusts its programs and processes to ensure continuous quality improvement.

Author's Disclaimer

Opinions and conclusions expressed or implied in the report are those of the author. They are not necessarily those of the Alaska DOT&PF or funding agencies.

METRIC (SI*) CONVERSION FACTORS

APPROXIMATE CONVERSIONS TO SI UNITS

Symbol	When You Know	Multiply By	To Find	Symbol
		LENGTH		
in	inches	25.4		mm
ft	feet	0.3048		m
yd	yards	0.914		m
mi	Miles (statute)	1.61		km
		AREA		
in^2	square inches	645.2	millimeters squared	cm^2
ft^2	square feet	0.0929	meters squared	m^2
yd^2	square yards	0.836	meters squared	m^2
mi^2	square miles	2.59	kilometers squared	km^2
ac	acres	0.4046	hectares	ha
		MASS (weight)		
oz	Ounces (avdp)	28.35	grams	g
lb	Pounds (avdp)	0.454	kilograms	kg
T	Short tons (2000 lb)	0.907	megagrams	mg
		VOLUME		
fl oz	fluid ounces (US)	29.57	milliliters	mL
gal	Gallons (liq)	3.785	liters	liters
ft^3	cubic feet	0.0283	meters cubed	m^3
yd^3	cubic yards	0.765	meters cubed	m^3

Note: Volumes greater than 1000 L shall be shown in m^3

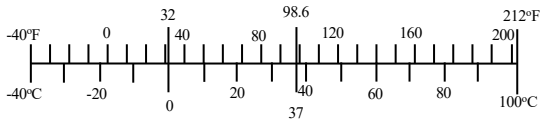
		TEMPERATURE (exact)		
ºF	Fahrenheit temperature	5/9 (ºF-32)	Celsius temperature	ºC
		ILLUMINATION		
fc	Foot-candles	10.76	lux	lx
fl	foot-lamberts	3.426	candela/m^2	cd/cm^2
		FORCE and PRESSURE or STRESS		
lbf	pound-force	4.45	newtons	N
psi	pound-force per square inch	6.89	kilopascals	kPa

These factors conform to the requirement of FHWA Order 5190.1A *SI is the symbol for the International System of Measurements

APPROXIMATE CONVERSIONS FROM SI UNITS

Symbol	When You Know	Multiply By	To Find	Symbol
		LENGTH		
mm	millimeters	0.039	inches	in
m	meters	3.28	feet	ft
m	meters	1.09	yards	yd
km	kilometers	0.621	Miles (statute)	mi
		AREA		
mm^2	millimeters squared	0.0016	square inches	in^2
m^2	meters squared	10.764	square feet	ft^2
km^2	kilometers squared	0.39	square miles	mi^2
ha	hectares (10,000 m^2)	2.471	acres	ac
		MASS (weight)		
g	grams	0.0353		oz
kg	kilograms	2.205		lb
mg	megagrams (1000 kg)	1.103	short tons	T
		VOLUME		
mL	milliliters	0.034	fluid ounces (US)	fl oz
liters	liters	0.264	Gallons (liq)	gal
m^3	meters cubed	35.315	cubic feet	ft^3
m^3	meters cubed	1.308	cubic yards	yd^3

		TEMPERATURE (exact)		
ºC	Celsius temperature	9/5 ºC+32	Fahrenheit temperature	ºF
		ILLUMINATION		
lx	lux	0.0929	foot-candles	fc
cd/cm^2	candela/m^2	0.2919	foot-lamberts	fl
		FORCE and PRESSURE or STRESS		
N	newtons	0.225	pound-force	lbf
kPa	kilopascals	0.145	pound-force per square inch	psi





NC STATE UNIVERSITY

Constructed Facilities Laboratory
Department of Civil, Construction, and Environmental Engineering

Research Report
No. RD-24-03

EXTERNAL POCKET AND SOCKET CONNECTIONS FOR THE SEISMIC DESIGN OF ALASKA BRIDGES

Prepared by:

Julio A. Samayoa, Ph.D.
Giorgio T. Proestos, Ph.D., Principal Investigator
Mervyn Kowalsky, Ph.D., Principal Investigator

Prepared for:

Alaska Department of Transportation and Public Facilities (AKDOT&PF)

Constructed Facilities Laboratory
NC STATE UNIVERSITY

December 19th, 2024

Constructed Facilities Laboratory
2414 Campus Shore Drive
North Carolina State University
Raleigh, NC 27695-7533
Tel: (919) 513-1733
Fax: (919) 513-1765
Email: cfl@ncsu.edu
Web Site: www.cfl.ncsu.edu

EXTERNAL POCKET AND SOCKET CONNECTIONS FOR THE SEISMIC DESIGN OF ALASKA BRIDGES

Final Report

December 19th, 2024

The research described in this report is supported by the Alaska Department of Transportation and Public Facilities. Their support is gratefully acknowledged. The conclusions are those of the authors alone and should not be construed as to imply endorsement by AKDOT&PF.

TABLE OF CONTENTS

LIST OF TABLES vi
LIST OF FIGURES viii
ABBREVIATIONS xxx
LIST OF SYMBOLS xxxi
ACKNOWLEDGMENTS xxxii
EXECUTIVE SUMMARY xxxiii
1. Chapter 1: Introduction 1
1.1. Research Need 2
1.2. Research Scope and Objectives 3
1.3. Report Layout 4
2. Chapter 2: Literature Review 5
2.1. Socket height 6
2.2. Gap size, shape, and filling materials 14
2.3. Shear mechanism between adjoining elements 18
2.4. Analytical Models for Socket Connections 25
2.5. Discussion and knowledge gaps 28
3. Chapter 3: Experimental Program 29
3.1. Column Test Matrix 29
3.2. Column Test Details 30
3.3. Construction Process 38
3.3.1. Footing and external socket 41
3.3.2. RC column and cap-beam 50
3.3.3. RCFST column and cap-beam 61
3.3.4. RC column repair 67
3.3.5. Integrating Column into external socket 70
3.4. Material tests for column and connection components 75
3.5. Experimental Test Setup 83
3.5.1. Loading Protocol 85

3.5.2. Instrumentation 87
4. Chapter 4: Global Response and Experimental Observations 91
4.1. Specimen SJS1 93
4.1.1. Loading Protocol of SJS1 94
4.1.2. Global Response of SJS1 95
4.1.3. Damage progression of SJS1 97
4.2. Specimen SJS-2 104
4.2.1. Loading Protocol of SJS2 105
4.2.2. Global Response of SJS2 106
4.2.3. Damage progression of SJS2 108
4.3. Specimen SJS-3 116
4.3.1. Loading Protocol of SJS 3 117
4.3.2. Global Response of SJS 3 118
4.3.3. Damage progression of SJS 3 120
4.4. Specimen SJS-4 128
4.4.1. Loading Protocol of SJS 4 129
4.4.2. Global Response of SJS 4 130
4.4.3. Damage progression of SJS 4 132
4.5. Specimen SJS-5 142
4.5.1. Loading Protocol of SJS 5 143
4.5.2. Global Response of SJS 5 144
4.5.3. Damage progression of SJS 5 146
4.6. Specimen SJS-6 155
4.6.1. Loading Protocol of SJS 6 156
4.6.2. Global Response of SJS 6 157
4.6.3. Damage progression of SJS 6 159
4.7. Specimen SJS-7 167

4.7.1. Loading Protocol of SJS 7 168
4.7.2. Global Response of SJS 7 169
4.7.3. Damage progression of SJS 7 171
4.8. Specimen SJS-8 180
4.8.1. Loading Protocol of SJS 8 181
4.8.2. Global Response of SJS 8 182
4.8.3. Damage progression of SJS 8 184
4.9. Observed Failure modes for experimental tests 194
5. Chapter 5: Analysis of Experimental Results 199
5.1. Methodology for data analysis 199
5.1.1. Axial strain analysis 199
5.1.2. Energy dissipation and hysteretic damping 202
5.1.3. Displacement components 205
5.2. Experimental Results for Specimen SJS-1 218
5.2.1. Axial strain analysis for SJS-1 218
5.2.2. Energy dissipation and hysteretic damping for SJS-1 226
5.2.3. Displacement components for SJS-1 227
5.2.4. Summary of Results for SJS-1 234
5.3. Experimental Results for Specimen SJS-2 235
5.3.1. Axial strain analysis for SJS-2 235
5.3.2. Energy dissipation and hysteretic damping for SJS-2 243
5.3.3. Displacement components for SJS-2 245
5.3.4. Summary of Results for SJS-2 252
5.4. Experimental Results for Specimen SJS-3 253
5.4.1. Axial strain analysis for SJS-3 253
5.4.2. Energy dissipation and hysteretic damping for SJS-3 260
5.4.3. Displacement components for SJS-3 262

5.4.4. Summary of Results for SJS-3 269
5.5. Experimental Results for Specimen SJS-4 270
5.5.1. Axial strain analysis for SJS-4 270
5.5.2. Energy dissipation and hysteretic damping for SJS-4 277
5.5.3. Displacement components for SJS-4 279
5.5.4. Summary of Results for SJS-4 286
5.6. Experimental Results for Specimen SJS-5 287
5.6.1. Axial strain analysis for SJS-5 287
5.6.2. Energy dissipation and hysteretic damping for SJS-5 294
5.6.3. Displacement components 296
5.6.4. Summary of Results for SJS-5 303
5.7. Experimental Results for Specimen SJS-6 304
5.7.1. Axial strain analysis for SJS-6 304
5.7.2. Energy dissipation and hysteretic damping for SJS-6 310
5.7.3. Displacement components for SJS-6 312
5.7.4. Discussion of Results for SJS-6 319
5.8. Experimental Results for Specimen SJS-7 320
5.8.1. Axial strain analysis for SJS-7 320
5.8.2. Energy dissipation and hysteretic damping for SJS-7 328
5.8.3. Socket rotation and RCFST gap opening for SJS-7 330
5.8.4. Summary of Results for SJS-7 332
5.9. Experimental Results of Specimen SJS-8 332
5.9.1. Axial strain analysis for SJS-8 333
5.9.2. Energy dissipation and hysteretic damping for SJS-8 341
5.9.3. Socket rotation and RCFST gap opening for SJS-8 343
5.9.4. Summary of Results for SJS-8 345

6. Chapter 6: Analytical model 346
6.1. Strut and Tie Model 347
6.2. Analytical Model Outputs 357
6.3. Comparison with Experimental Results 365
7. Chapter 7: Design of External Socket Connections 373
7.1. Design Equations and Recommendations 373
7.2. Design Example 377
8. Chapter 8: Conclusions and Future Work 382
8.1. Experimental Program 382
8.2. Analytical Model 383
8.3. Future Work 385
REFERENCES 387
APPENDIX 390

LIST OF TABLES

Table 2-1. Summary of available test data evaluating socket height for socket connections..... 12

Table 2-2. Summary of available test data for gap size, shape, and filling material for socket connections 17

Table 3-1. Column test matrix 29

Table 3-2. Casting dates of structural components 75

Table 3-3. Test Day concrete compression strength of footing and cap beam 76

Table 3-4. Test Day concrete compression strength of columns 76

Table 3-5. Test Day concrete compression strength of the repaired portion of columns 77

Table 3-6. Test Day concrete compression strength of external socket wall..... 77

Table 3-7. Test Day grout compression strength 78

Table 3-8. Tension test parameters 83

Table 4-1. Summary of global response of test SJS1 to SJS8 92

Table 4-2. Summary of SJS1 parameters..... 93

Table 4-3. Displacement ductility of SJS 1 94

Table 4-4. Summary of SJS2 parameters..... 104

Table 4-5. Displacement ductility of SJS 2 105

Table 4-6. Summary of SJS3 parameters..... 116

Table 4-7. Displacement ductility of SJS 3 117

Table 4-8. Summary of SJS4 parameters..... 128

Table 4-9. Displacement ductility of SJS 4 129

Table 4-10. Summary of SJS5 parameters..... 142

Table 4-11. Displacement ductility of SJS 5 143

Table 4-12. Summary of SJS6 parameters 155

Table 4-13. Loading history for the single cycles of SJS 6 156

Table 4-14. Displacement ductility of SJS 6 157

Table 4-15. Summary of SJS7 parameters 167

Table 4-16. Displacement ductility of SJS 7 169

Table 4-17. Summary of SJS8 parameters 180

Table 4-18. Displacement ductility of SJS 7 182

Table 5-1. Displacement components for pushing cycles for SJS 1 232

Table 5-2. Displacement components for pulling cycles for SJS 1 233

Table 5-3. Displacement components for pushing cycles for SJS 2 250

Table 5-4. Displacement components for pulling cycles for SJS 2 250

Table 5-5. Displacement components for pushing cycles for SJS 3 267

Table 5-6. Displacement components for pulling cycles for SJS 3 267

Table 5-7. Displacement components for pushing cycles for SJS 4 284

Table 5-8. Displacement components for pulling cycles for SJS 4 284

Table 5-9. Displacement components for pushing cycles for SJS 5 301

Table 5-10. Displacement components for pulling cycles for SJS 5 301

Table 5-11. Displacement components for pushing cycles for SJS 6 317

Table 5-12. Displacement components for pulling cycles for SJS 6 317

Table 6-1. STM results for the different components of the external socket connection with different socket heights 364

Table 7-1. Design parameters for external socket connection 380

LIST OF FIGURES

Figure 1-1. Socket connection between column and cap beam [2] 1

Figure 1-2. External socket connection 3

Figure 2-1. Socket connection. (a) Internal connection, (b) External connection 5

Figure 2-2. Socket height. (a) Internal connection, (b) External connection..... 6

Figure 2-3. Specimen response at 4.2% drift ratio (μ8) – CPFD [3]..... 7

Figure 2-4. Lateral force-displacement – CPFD [3] 8

Figure 2-5. Base moment - drift response for the three specimens [13]..... 8

Figure 2-6. Lateral force-drift response of the column with a 1.2 Dc socket height [4] 9

Figure 2-7. Damage on the column with a 1.2 Dc socket height at a 10% drift ratio [4]..... 10

Figure 2-8. Lateral force-displacement response. a) CIP specimen, b) Socket connection [14].. 10

Figure 2-9. Force-displacement hysteretic response. a-c) Socket connections, d) CIP [16] 11

Figure 2-10. Accumulated energy dissipation for specimens [16] 12

Figure 2-11. Gap between adjoining elements. a) Internal connection, b) External connection.. 14

Figure 2-12. Octagonal shape for a socket connection [5] 15

Figure 2-13. Cap beam with square socket connection [6]..... 16

Figure 2-14. Foundation with a square socket connection [16]..... 17

Figure 2-15. Test configuration for uniaxial compression test in socket connection [19] 19

Figure 2-16. Different surface preparation for embedded elements [19] 20

Figure 2-17. Column-to-grout interface displacements with different surface preparations [19] 21

Figure 2-18. Test setup for lateral load and constant axial load [3] 21

Figure 2-19. Test setup for external socket connection [10] 22

Figure 2-20. Bending moment versus strain of longitudinal bars of the column, with socket height of 2.0 Dc [10] 23

Figure 2-21. Bending moment versus strain of longitudinal bars of the column, with socket height of 1.6 Dc [10] 23

Figure 2-22. Socket connection with a threaded rod for enhancing the transfer of forces [4] 24

Figure 2-23. Shear keys on the socket connection surfaces [16] 24

Figure 2-24. Strain profile of longitudinal reinforcement. (a) With a shear key, (b) Smooth surfaces [16] 25

Figure 2-25. Force transfer model for socket connections [20] 26

Figure 2-26. Analytical model of the column inside a socket connection. [10] 27

Figure 3-1. Column reinforcement for SJS1 to SJS4 - plan view 31

Figure 3-2. Column reinforcement for SJS1 to SJS4 - elevation view 31

Figure 3-3. External socket reinforcement for SJS1 to SJS4 - plan view 32

Figure 3-4. External socket reinforcement for SJS1 to SJS4 - elevation view 32

Figure 3-5. Column reinforcement for SJS5 and SJS6 - plan view 33

Figure 3-6. Column reinforcement for SJS5 and SJS6 - elevation view 33

Figure 3-7. Column reinforcement for SJS7 and SJS8 (inside socket connection) - plan view ... 34

Figure 3-8. Column reinforcement for SJS7 and SJS8 (outside socket connection) - plan view . 34

Figure 3-9. Column reinforcement for SJS7 and SJS8 - elevation view 35

Figure 3-10. External socket reinforcement for SJS5 to SJS8 - plan view 36

Figure 3-11. External socket reinforcement for SJS5 to SJS8 - elevation view 36

Figure 3-12. Footing dimensions - plan view 37

Figure 3-13. Footing reinforcement - plan view 37

Figure 3-14. Footing reinforcement – front view 38

Figure 3-15. Footing reinforcement - side view 38

Figure 3-16. Construction sequence for footing and external socket 39
Figure 3-17. Construction sequence for RC column and cap-beam 39
Figure 3-18. Construction sequence for RCFST column and cap-beam 40
Figure 3-19. Construction sequence for RC column repair 40
Figure 3-20. Formwork assembly for the footing 41
Figure 3-21. Z-bars and U-bars tied together 42
Figure 3-22. Placement of PVC pipes and foam block-outs 42
Figure 3-23. Placement of Z-bars and U-bars for the footing 43
Figure 3-24. Placement of J-hooks near the PVC pipes 43
Figure 3-25. Placement of longitudinal reinforcement of the external socket wall 44
Figure 3-26. Placement of J-hooks around the external socket reinforcement 44
Figure 3-27. Formwork and reinforcing steel ready for casting 45
Figure 3-28. Footing surface after casting 46
Figure 3-29. Footing concrete after removing the formwork 46
Figure 3-30. External steel sleeve with mill scale removed 47
Figure 3-31. Placement of steel sleeves for external socket connection 47
Figure 3-32. Placement of silicon on the internal socket sleeve 48
Figure 3-33. Placement of silicone on the external socket sleeve 48
Figure 3-34. External socket wall after casting 49
Figure 3-35. Final coating of external socket sleeve 49
Figure 3-36. Speckle pattern on external socket sleeve 50
Figure 3-37. Setup for building the steel cage of the RC column 51
Figure 3-38. Wood spacer for transverse steel of the RC column 51

Figure 3-39. Internal wood template for the longitudinal steel of the RC column 52

Figure 3-40. Transverse reinforcement tied to the longitudinal reinforcement of the RC column 53

Figure 3-41. Cap beam formwork 53

Figure 3-42. Cap beam reinforcement and steel cage of the RC column 54

Figure 3-43. Cap beam reinforcement inside the formwork 55

Figure 3-44. Cap beam formwork and steel reinforcement for RC column ready to cast 56

Figure 3-45. Cap beam after removing the formwork 57

Figure 3-46. Foam block-outs attached to the longitudinal and transverse reinforcement 57

Figure 3-47. Foam block-out along the plastic hinge region of the RC column 58

Figure 3-48. Sonotube placed around the longitudinal reinforcement of the RC column 58

Figure 3-49. Concrete column after casting 59

Figure 3-50. Concrete column after removing the Sonotube 59

Figure 3-51. Concrete column after removing the block-outs 60

Figure 3-52. Concrete column after cleaning the reinforcing bars 60

Figure 3-53. Setup for building the steel cage of the RCFST column 61

Figure 3-54. Cap beam reinforcement and steel cage of the RCFST column 62

Figure 3-55. Cap beam formwork and steel reinforcement for RCFST column ready to cast 63

Figure 3-56. Cap beam of the RCFST after removing the formwork 63

Figure 3-57. Circular steel tube (3/8″) without mill scale at the expected plastic hinge region 64

Figure 3-58. Circular steel tube (1/8″) without mill scale at the expected plastic hinge region 64

Figure 3-59. Steel tubes placed around the longitudinal reinforcement of the RCFST column 65

Figure 3-60. Casting of RCFST column 66

Figure 3-61. Speckle pattern on circular steel tubes for RCFST column 67

Figure 3-62. Removing damaged concrete for repair 68
Figure 3-63. Repaired area without loose material 69
Figure 3-64. Casting of the repaired RC column 69
Figure 3-65. Repaired RC column 70
Figure 3-66. Positioning the column horizontally 71
Figure 3-67. Lifting the column in a vertical position 72
Figure 3-68. Inserting the column in the external socket connection 73
Figure 3-69. Leveling the column in the external socket 73
Figure 3-70. Casting the grout to fill the gap between structural elements 74
Figure 3-71. Column and external socket connection after filling the gap with grout 74
Figure 3-72. Instrumented reinforcing bar with Optotrak LED markers 80
Figure 3-73. Instrumented coupon steel with strain gage 81
Figure 3-74. Stress-strain curves for reinforcing steel bars used in SJS 1 to SJS 8 81
Figure 3-75. Stress-strain curves for steel sleeves used in SJS 1 to SJS 8 82
Figure 3-76. Stress-strain curves for steel tubes used in SJS 7 and SJS 8 82
Figure 3-77. Experimental test setup – lateral view 84
Figure 3-78. Experimental test setup – actual test setup 84
Figure 3-79. Loading scheme of the large-scale column test 85
Figure 3-80. Example of loading protocol for the experimental program 86
Figure 3-81. Force-displacement response of SJS 1 87
Figure 3-82. Actual location of string potentiometers 88
Figure 3-83. Typical layout of strain gages for external socket longitudinal bars 88
Figure 3-84. Distribution of LED markers on the south face of the column 89

Figure 3-85. View of DIC cameras for an external socket sleeve 90

Figure 3-86. Test setup and instrumentation..... 90

Figure 4-1. Label of longitudinal reinforcing bar. a) For SJS 1 to SJS 4. b) For SJS 5 y SJS6 ... 91

Figure 4-2. Displacement history of SJS1 95

Figure 4-3. Moment-displacement response of SJS 1 96

Figure 4-4. SJS 1 experimental envelopes compared to an RC column prediction..... 96

Figure 4-5. Cracks at external socket connection at half of the first yield displacement 97

Figure 4-6. Gap between the steel sleeve and concrete on south face of the socket at ductility one 98

Figure 4-7. Crack pattern on south surface at last cycle of ductility one..... 98

Figure 4-8. The crack pattern on the south surface at last cycle of ductility two 99

Figure 4-9. Damage of the specimen on the south surface at ductility three..... 100

Figure 4-10. Buckling of longitudinal bars on north surface at ductility four..... 101

Figure 4-11. Fracture of longitudinal bars on the north surface at ductility four 101

Figure 4-12. Buckled bars on the north surface of the column at ductility five 102

Figure 4-13. Damage on the footing and the external socket 102

Figure 4-14. Spread of damage on the column at the north face 103

Figure 4-15. Displacement history of SJS 2 106

Figure 4-16. Moment-displacement response of SJS 2 107

Figure 4-17. SJS 2 experimental envelopes compared to an RC column prediction..... 107

Figure 4-18. Cracks at external socket connection at half of the first yield displacement 108

Figure 4-19. Gap between the steel sleeve and concrete on the south surface of the socket at ductility one 109

Figure 4-20. Uplift of the column at three-quarters of the first yielding..... 109

Figure 4-21. Crack pattern on the south surface at the first yielding 110
Figure 4-22. Gaps at the external socket connection at the first cycle of ductility one 111
Figure 4-23. Uplift of steel sleeve and concrete column at the first cycle of ductility one 111
Figure 4-24. Damage of the socket connection at the third cycle of ductility one 112
Figure 4-25. Damage of the specimen on the north surface at ductility one and a half 113
Figure 4-26. Uplift on the south surface of the column at ductility two 114
Figure 4-27. Damage of the column inside the external socket connection 115
Figure 4-28. Damaged surface of the column inside the external socket connection 115
Figure 4-29. Displacement history of SJS 3 118
Figure 4-30. Moment-displacement response of SJS 3 119
Figure 4-31. SJS 3 experimental envelopes compared to an RC column prediction 119
Figure 4-32. Cracks in external socket connection at half of the first yield displacement 120
Figure 4-33. Gap between the steel sleeve and grout on the south surface at ductility one 121
Figure 4-34. Uplift of the column at the last cycle of ductility one 121
Figure 4-35. Crack pattern on the south surface at the last cycle of ductility one 122
Figure 4-36. Gaps at the external socket connection at the last cycle of ductility one and a half 123
Figure 4-37. Damage of the column and uplift of grout at the last cycle of ductility one and a half 123
Figure 4-38. Damage of the socket connection at the third cycle of ductility two 124
Figure 4-39. Damage of the specimen on the south surface at ductility three 125
Figure 4-40. Displaced column at the third cycle of ductility three 126
Figure 4-41. Damage of the column inside the external socket connection 127
Figure 4-42. Damaged surface of the column inside the external socket connection 127

Figure 4-43. Displacement history of SJS 4 130

Figure 4-44. Moment-displacement response of SJS 4 131

Figure 4-45. SJS 4 experimental envelopes compared to an RC column prediction..... 132

Figure 4-46. Damage on the column and socket wall at the start of SJS 4..... 133

Figure 4-47. Gap between the steel sleeve and grout on the south surface at ductility one 133

Figure 4-48. Uplift of the column at the last cycle of ductility one..... 134

Figure 4-49. Crack pattern on the south surface at the last cycle of ductility one..... 135

Figure 4-50. Gaps at the external socket connection at the last cycle of ductility one and a half 136

Figure 4-51. Damage of the column and uplift of grout at the last cycle of ductility one and a half 136

Figure 4-52. Damage of the socket connection at the third cycle of ductility two 137

Figure 4-53. Gaps at the external socket connection at the last cycle of ductility three..... 138

Figure 4-54. Damage of the socket connection at the third cycle of ductility three 138

Figure 4-55. Damage of the specimen on the south surface at ductility four 139

Figure 4-56. Displaced column at the third cycle of ductility four..... 140

Figure 4-57. Damage of the column inside the external socket connection 141

Figure 4-58. Damaged surface of the column inside the external socket connection..... 141

Figure 4-59. Displacement history of SJS 5 144

Figure 4-60. Moment-displacement response of SJS 5 145

Figure 4-61. SJS 5 experimental envelopes compared to an RC column prediction..... 146

Figure 4-62. Initial cracks on the column and socket wall at the start of SJS 5 147

Figure 4-63. Gap between the steel sleeve and grout on the south surface at ductility one 147

Figure 4-64. Crack pattern on the south surface at the last cycle of ductility one..... 148

Figure 4-65. Damage of the column at the last cycle of ductility one and a half 149

Figure 4-66. Damage of the socket connection at the third cycle of ductility two 150

Figure 4-67. Splitting and uplifting of grout at the last cycle of ductility three 150

Figure 4-68. Damage of column and the socket connection at the third cycle of ductility three 151

Figure 4-69. Damage of the specimen on the south surface at ductility four 152

Figure 4-70. Displaced column at the first cycle of ductility four 153

Figure 4-71. Damage to the column inside the external socket connection 154

Figure 4-72. Displacement history of SJS 6 157

Figure 4-73. Moment-displacement response of SJS 6 158

Figure 4-74. SJS 6 experimental envelopes compared to an RC column prediction 159

Figure 4-75. Initial damage on the column and socket wall at the start of the SJS6 160

Figure 4-76. Uplift of grout on the south surface at the last cycle of ductility two 160

Figure 4-77. Damage of the socket connection at the third cycle of ductility three 161

Figure 4-78. Damage of column and the grout on the south side at the first cycle of ductility four 162

Figure 4-79. Damage of the column and the socket connection on the north side at the second cycle of ductility four 162

Figure 4-80. Damage of the column and the socket connection on the south side at the second cycle of ductility four 163

Figure 4-81. Damage of the column and the socket connection on the north side at the last positive cycle of ductility four 163

Figure 4-82. Damage of the column and the socket connection on the north side at the last negative cycle of ductility four 164

Figure 4-83. Damage of the column and the socket connection on the south side at the last negative cycle of ductility four 164

Figure 4-84. Damage on the footing and the external socket connection at the end of the experimental test for SJS-6 165

Figure 4-85. Spread of damage on the column at the south face at the end of the experimental test for SJS-6..... 166

Figure 4-86. Displacement history of SJS 7 169

Figure 4-87. Moment-displacement response of SJS 7 170

Figure 4-88. SJS 7 experimental envelopes compared to an RC column prediction..... 171

Figure 4-89. Initial cracks on the socket wall at the start of SJS 7 172

Figure 4-90. Radial cracks on the socket wall at the last cycle of ductility one..... 172

Figure 4-91. Crack pattern on the south surface at the last cycle of ductility one..... 173

Figure 4-92. Damage of the column and socket connection at the last cycle of ductility two ... 174

Figure 4-93. Damage of the column and socket connection at the last cycle of ductility three . 174

Figure 4-94. Damage of the column and socket connection at the last cycle of ductility four... 175

Figure 4-95. Damage of the column and the socket connection at the last cycle of ductility five 176

Figure 4-96. Damage of the column and the socket connection at the last cycle of ductility six176

Figure 4-97. Displaced column at the last cycle of ductility six..... 177

Figure 4-98. Damage to the grout inside the external socket connection..... 178

Figure 4-99. Damage to the north face of the column inside the external socket connection 179

Figure 4-100. Damage to the west face of the column inside the external socket connection ... 179

Figure 4-101. Displacement history of SJS 8 182

Figure 4-102. Moment-displacement response of SJS 8 183

Figure 4-103. SJS 8 experimental envelopes compared to an RC column prediction..... 184

Figure 4-104. Socket wall at the start of SJS 8 185

Figure 4-105. Radial cracks on the socket wall at yield displacement 185

Figure 4-106. Gap between steel tubes at the last cycle of ductility one 186
Figure 4-107. Damage of the column and the connection at the last cycle of ductility two..... 187
Figure 4-108. Damage of the column and the connection at the last cycle of ductility three..... 187
Figure 4-109. Damage of the column and the connection at the last cycle of ductility four 188
Figure 4-110. Damage of the column and the connection at the last cycle of ductility five 189
Figure 4-111. Damage of the column and the connection at the last cycle of ductility six 189
Figure 4-112. Damage of column at the ductility seven 190
Figure 4-113. Displaced column at ductility seven 191
Figure 4-114. Damage to the grout inside the external socket connection 192
Figure 4-115. Damage to the socket wall of the external socket connection 193
Figure 4-116. Damage to the column inside the external socket connection 193
Figure 4-117. Failure mechanisms for the experimental program 194
Figure 4-118. Envelopes of experimental tests exhibiting bar fracture 195
Figure 4-119. Envelopes of experimental tests exhibiting grout crushing 196
Figure 4-120. Envelopes of experimental tests exhibiting bar fracture 197
Figure 4-121. Moment-displacement curves for all eight experimental tests 198
Figure 5-1. Example of strain profile up to first yield cycle 201
Figure 5-2. Example of strain profile for post-yield cycles 201
Figure 5-3. Example of strain vs displacement history 202
Figure 5-4. Example of force-displacement loop area for dissipated energy 203
Figure 5-5. Example of energy dissipation plot 203
Figure 5-6. Example of Area 1 and Area 2 for Jacobsen hysteretic damping 204
Figure 5-7. Example of hysteretic damping plot 205

Figure 5-8. Displacements from curvature distribution [24] 206

Figure 5-9. Strain profile for a cross-section in the loading direction 206

Figure 5-10. Example for curvature calculation 207

Figure 5-11. Example of linear interpolation in curvature profile 208

Figure 5-12. Example of curvature profile for cycles up to first yield 209

Figure 5-13. Example of curvature profile for post-yield cycles 209

Figure 5-14. Example of curvature distribution along the height of the column 210

Figure 5-15. Example of rotation of the column at the socket interface 211

Figure 5-16. LED grid position for shear strain calculation 212

Figure 5-17. Example of strains measured on a grid 213

Figure 5-18.Example of a best fit of the Mohr circle 214

Figure 5-19. Example of shear strain distribution along the measured height of the column 215

Figure 5-20. Example of area of interest for DIC analysis 216

Figure 5-21. Example of socket rotation throughout the test 216

Figure 5-22. Example of displacement components for post-yield cycles 217

Figure 5-23. Strain profile up to first yield cycle for SJS1on the north side of the column 219

Figure 5-24. Strain profile for post-yield cycles for SJS1 on the north side of the column 219

Figure 5-25. Strain profile up to first yield cycle for SJS1on the south side of the column 220

Figure 5-26. Strain profile for post-yield cycles for SJS1 on the south side of the column 220

Figure 5-27. Strain vs displacement history for N6 of SJS1 221

Figure 5-28. Strain vs displacement history for S6 of SJS1 222

Figure 5-29. Strain vs displacement history for the extreme bar of socket wall reinforcement at the north side of SJS1 222

Figure 5-30. Strain vs displacement history for the extreme bar of socket wall reinforcement at the north side of SJS1 223

Figure 5-31. Horizontal strain history of external socket sleeve at the north side of SJS1 224

Figure 5-32. Vertical strain history of external socket sleeve at the north side of SJS1 224

Figure 5-33. Horizontal strain history of external socket sleeve at the south side of SJS1 225

Figure 5-34. Vertical strain history of external socket sleeve at the south side of SJS1 225

Figure 5-35. Energy dissipation plot for SJS1 226

Figure 5-36. Hysteretic damping plot for SJS1 227

Figure 5-37. Curvature profile of the column up to the first yield cycle for SJS1 228

Figure 5-38. Curvature profile of the column for post-yield cycles for SJS1..... 228

Figure 5-39. Rotation of the column for pushing cycles at the socket interface of SJS1 229

Figure 5-40. Rotation of the column for pulling cycles at the socket interface of SJS1 229

Figure 5-41. Shear strain distribution of the column for pushing cycles for SJS1 230

Figure 5-42. Shear strain distribution of the column for pulling cycles for SJS1 231

Figure 5-43. Socket rotation at the north side of SJS1 231

Figure 5-44. Socket rotation at the south side of SJS1 232

Figure 5-45. Displacement components for pushing cycles for SJS1 233

Figure 5-46. Displacement components for pulling cycles for SJS1..... 234

Figure 5-47. Strain profile up to first yield cycle for SJS2 on the north side of the column..... 236

Figure 5-48. Strain profile for post-yield cycles for SJS2 on the north side of the column 237

Figure 5-49. Strain profile up to first yield cycle for SJS2 on the south side of the column..... 237

Figure 5-50. Strain profile for post-yield cycles for SJS2 on the south side of the column..... 238

Figure 5-51. Strain vs displacement history for N6 of SJS2..... 239

Figure 5-52. Strain vs displacement history for S6 of SJS2 239

Figure 5-53. Strain vs displacement history for the extreme bar of socket wall reinforcement at the north side of SJS2 240

Figure 5-54. Strain vs displacement history for the extreme bar of socket wall reinforcement at the north side of SJS2 240

Figure 5-55. Horizontal strain history of external socket sleeve at the north side of SJS2 241

Figure 5-56. Vertical strain history of external socket sleeve at the north side of SJS2 242

Figure 5-57. Horizontal strain history of external socket sleeve at the south side of SJS2 242

Figure 5-58. Vertical strain history of external socket sleeve at the south side of SJS2 243

Figure 5-59. Energy dissipation plot for SJS2 244

Figure 5-60. Hysteretic damping plot for SJS2 244

Figure 5-61. Curvature profile of the column up to the first yield cycle for SJS2 245

Figure 5-62. Curvature profile of the column for post-yield cycles for SJS2..... 246

Figure 5-63. Rotation of the column for pushing cycles at the socket interface of SJS2 247

Figure 5-64. Rotation of the column for pulling cycles at the socket interface of SJS2 247

Figure 5-65. Shear strain distribution of the column for pushing cycles for SJS2 248

Figure 5-66. Shear strain distribution of the column for pulling cycles for SJS2 248

Figure 5-67. Socket rotation at the north side of SJS2 249

Figure 5-68. Socket rotation at the south side of SJS2 249

Figure 5-69. Displacement components for pushing cycles for SJS2 251

Figure 5-70. Displacement components for pulling cycles for SJS2..... 251

Figure 5-71. Strain profile up to first yield cycle for SJS3 on the north side of the column..... 254

Figure 5-72. Strain profile for post-yield cycles for SJS3 on the north side of the column 254

Figure 5-73. Strain profile up to first yield cycle for SJS3 on the south side of the column..... 255

Figure 5-74. Strain profile for post-yield cycles for SJS3 on the south side of the column 255

Figure 5-75. Strain vs displacement history for N6 of SJS3 256

Figure 5-76. Strain vs displacement history for S6 of SJS3 256

Figure 5-77. Strain vs displacement history for the extreme bar of socket wall reinforcement at the north side of SJS3 257

Figure 5-78. Strain vs displacement history for the extreme bar of socket wall reinforcement at the north side of SJS3 258

Figure 5-79. Horizontal strain history of external socket sleeve at the north side of SJS3 258

Figure 5-80. Vertical strain history of external socket sleeve at the north side of SJS3 259

Figure 5-81. Horizontal strain history of external socket sleeve at the south side of SJS3 259

Figure 5-82. Vertical strain history of external socket sleeve at the south side of SJS3 260

Figure 5-83. Energy dissipation plot for SJS3 261

Figure 5-84. Hysteretic damping plot for SJS3 261

Figure 5-85. Curvature profile of the column up to the first yield cycle for SJS3 262

Figure 5-86. Curvature profile of the column for post-yield cycles for SJS3..... 263

Figure 5-87. Rotation of the column for pushing cycles at the socket interface of SJS3 263

Figure 5-88. Rotation of the column for pulling cycles at the socket interface of SJS3 264

Figure 5-89. Shear strain distribution of the column for pushing cycles for SJS3 265

Figure 5-90. Shear strain distribution of the column for pulling cycles for SJS3 265

Figure 5-91. Socket rotation at the north side of SJS3 266

Figure 5-92. Socket rotation at the south side of SJS3 266

Figure 5-93. Displacement components for pushing cycles for SJS3 268

Figure 5-94. Displacement components for pulling cycles for SJS3..... 268

Figure 5-95. Strain profile up to first yield cycle for SJS4 on the north side of the column..... 271

Figure 5-96. Strain profile for post-yield cycles for SJS4 on the north side of the column 271

TyFHWA-AR-RD-4000(195)pe text here

Figure 5-97. Strain profile up to first yield cycle for SJS4 on the south side of the column..... 272

Figure 5-98. Strain profile for post-yield cycles for SJS4 on the south side of the column..... 272

Figure 5-99. Strain vs displacement history for N6 of SJS4..... 273

Figure 5-100. Strain vs displacement history for S6 of SJS4 273

Figure 5-101. Strain vs displacement history for the extreme bar of socket wall reinforcement at the north side of SJS4 274

Figure 5-102. Strain vs displacement history for the extreme bar of socket wall reinforcement at the north side of SJS4 275

Figure 5-103. Horizontal strain history of external socket sleeve at the north side of SJS4 275

Figure 5-104. Vertical strain history of external socket sleeve at the north side of SJS4 276

Figure 5-105. Horizontal strain history of external socket sleeve at the south side of SJS4..... 276

Figure 5-106. Vertical strain history of external socket sleeve at the south side of SJS4 277

Figure 5-107. Energy dissipation plot for SJS4..... 278

Figure 5-108. Hysteretic damping plot for SJS4 278

Figure 5-109. Curvature profile of the column up to the first yield cycle for SJS4 279

Figure 5-110. Curvature profile of the column for post-yield cycles for SJS4..... 280

Figure 5-111. Rotation of the column for pushing cycles at the socket interface of SJS4..... 280

Figure 5-112. Rotation of the column for pulling cycles at the socket interface of SJS4 281

Figure 5-113. Shear strain distribution of the column for pushing cycles for SJS4..... 282

Figure 5-114. Shear strain distribution of the column for pulling cycles for SJS4 282

Figure 5-115. Socket rotation at the north side of SJS4 283

Figure 5-116. Socket rotation at the south side of SJS4 283

Figure 5-117. Displacement components for pushing cycles for SJS4 285

Figure 5-118. Displacement components for pulling cycles for SJS4..... 285

Figure 5-119. Strain profile up to first yield cycle for SJS5 on the north side of the column 288

Figure 5-120. Strain profile for post-yield cycles for SJS5 on the north side of the column 288

Figure 5-121. Strain profile up to first yield cycle for SJS5 on the south side of the column 289

Figure 5-122. Strain profile for post-yield cycles for SJS5 on the south side of the column 289

Figure 5-123. Strain vs displacement history for N5 of SJS5 290

Figure 5-124. Strain vs displacement history for S5 of SJS5 290

Figure 5-125. Strain vs displacement history for the extreme bar of socket wall reinforcement at the north side of SJS5 291

Figure 5-126. Strain vs displacement history for the extreme bar of socket wall reinforcement at the north side of SJS5 292

Figure 5-127. Horizontal strain history of external socket sleeve at the north side of SJS5 292

Figure 5-128. Vertical strain history of external socket sleeve at the north side of SJS5 293

Figure 5-129. Horizontal strain history of external socket sleeve at the south side of SJS5 293

Figure 5-130. Vertical strain history of external socket sleeve at the south side of SJS5 294

Figure 5-131. Energy dissipation plot for SJS5 295

Figure 5-132. Hysteretic damping plot for SJS5 295

Figure 5-133. Curvature profile of the column up to the first yield cycle for SJS5 296

Figure 5-134. Curvature profile of the column for post-yield cycles for SJS5 297

Figure 5-135. Rotation of the column for pushing cycles at the socket interface of SJS5 297

Figure 5-136. Rotation of the column for pulling cycles at the socket interface of SJS5 298

Figure 5-137. Shear strain distribution of the column for pushing cycles for SJS5 299

Figure 5-138. Shear strain distribution of the column for pulling cycles for SJS5 299

Figure 5-139. Socket rotation at the north side of SJS5 300

Figure 5-140. Socket rotation at the south side of SJS5 300

Figure 5-141. Displacement components for pushing cycles for SJS5 302
Figure 5-142. Displacement components for pulling cycles for SJS5 302
Figure 5-143. Strain profile up to first yield cycle for SJS6 on the north side of the column 305
Figure 5-144. Strain profile for post-yield cycles for SJS6 on the north side of the column 306
Figure 5-145. Strain profile up to first yield cycle for SJS6 on the south side of the column 306
Figure 5-146. Strain profile for post-yield cycles for SJS6 on the south side of the column 307
Figure 5-147. Strain vs displacement history for N5 of SJS6 307
Figure 5-148. Strain vs displacement history for S5 of SJS6 308
Figure 5-149. Horizontal strain history of external socket sleeve at the north side of SJS6 308
Figure 5-150. Vertical strain history of external socket sleeve at the north side of SJS6 309
Figure 5-151. Horizontal strain history of external socket sleeve at the south side of SJS6 309
Figure 5-152. Vertical strain history of external socket sleeve at the south side of SJS6 310
Figure 5-153. Energy dissipation plot for SJS6 311
Figure 5-154. Hysteretic damping plot for SJS6 311
Figure 5-155. Curvature profile of the column up to the first yield cycle for SJS6 312
Figure 5-156. Curvature profile of the column for post-yield cycles for SJS6 313
Figure 5-157. Rotation of the column for pushing cycles at the socket interface of SJS6 313
Figure 5-158. Rotation of the column for pulling cycles at the socket interface of SJS6 314
Figure 5-159. Shear strain distribution of the column for pushing cycles for SJS6 315
Figure 5-160. Shear strain distribution of the column for pulling cycles for SJS6 315
Figure 5-161. Socket rotation at the north side of SJS6 316
Figure 5-162. Socket rotation at the south side of SJS6 316
Figure 5-163. Displacement components for pushing cycles for SJS6 318

Figure 5-164. Displacement components for pulling cycles for SJS6 318

Figure 5-165. Strain vs displacement history for the extreme bar of socket wall reinforcement at the north side of SJS7 321

Figure 5-166. Strain vs displacement history for the extreme bar of socket wall reinforcement at the north side of SJS7 321

Figure 5-167. Horizontal strain history of external socket sleeve at the north side of SJS7 322

Figure 5-168. Vertical strain history of external socket sleeve at the north side of SJS7 322

Figure 5-169. Horizontal strain history of external socket sleeve at the south side of SJS7 323

Figure 5-170. Vertical strain history of external socket sleeve at the south side of SJS7 323

Figure 5-171. Horizontal strain history of RCFST column at the north side of SJS7 324

Figure 5-172. Vertical strain history of RCFST column at the north side of SJS7 325

Figure 5-173. Horizontal strain history of RCFST column at the south side of SJS7 325

Figure 5-174. Vertical strain history of RCFST column at the south side of SJS7 326

Figure 5-175. Horizontal strain history of steel tube at the socket interface at the north side of SJS7 326

Figure 5-176. Vertical strain history of steel tube at the socket interface at the north side of SJS7 327

Figure 5-177. Horizontal strain history of steel tube at the socket interface at the south side of SJS7 327

Figure 5-178. Vertical strain history of steel tube at the socket interface at the south side of SJS7 328

Figure 5-179. Energy dissipation plot for SJS7 329

Figure 5-180. Hysteretic damping plot for SJS7 329

Figure 5-181. Socket rotation at the north side of SJS7 330

Figure 5-182. Socket rotation at the south side of SJS7 331

Figure 5-183. Opening of the gap between steel tubes at the north face of SJS7 331

Figure 5-184. Strain vs displacement history for the extreme bar of socket wall reinforcement at the north side of SJS8 334

Figure 5-185. Strain vs displacement history for the extreme bar of socket wall reinforcement at the north side of SJS8 334

Figure 5-186. Horizontal strain history of external socket sleeve at the north side of SJS8 335

Figure 5-187. Vertical strain history of external socket sleeve at the north side of SJS8 335

Figure 5-188. Horizontal strain history of external socket sleeve at the south side of SJS8 336

Figure 5-189. Vertical strain history of external socket sleeve at the south side of SJS8 336

Figure 5-190. Horizontal strain history of RCFST column at the north side of SJS8 337

Figure 5-191 Vertical strain history of RCFST column at the north side of SJS8 338

Figure 5-192. Horizontal strain history of RCFST column at the south side of SJS8 338

Figure 5-193. Vertical strain history of RCFST column at the south side of SJS8 339

Figure 5-194 Horizontal strain history of steel tube at the socket interface at the north side of SJS8..... 339

Figure 5-195. Vertical strain history of steel tube at the socket interface at the north side of SJS8 340

Figure 5-196. Horizontal strain history of steel tube at the socket interface at the south side of SJS8..... 340

Figure 5-197. Vertical strain history of steel tube at the socket interface at the south side of SJS8 341

Figure 5-198. Energy dissipation plot for SJS8 342

Figure 5-199. Hysteretic damping plot for SJS8 342

Figure 5-200. Socket rotation at the north side of SJS8 343

Figure 5-201. Socket rotation at the south side of SJS8 344

Figure 5-202. Opening of the gap between steel tubes at the north face of SJS8..... 344

Figure 6-1. D-regions (shaded areas) due to geometrical discontinuities [27] 346

Figure 6-2. STM for the column 347
Figure 6-3. STM for external socket / Tension field 348
Figure 6-4. STM for external socket / Compression field 348
Figure 6-5. Compression zone at the top of the external socket of SJS8..... 349
Figure 6-6. Compression zone at the bottom of the external socket of SJS7 350
Figure 6-7. Location of the strut for the STM of the column 351
Figure 6-8. Location of the tie for the STM of the column 352
Figure 6-9. Location of strut, tie, and reaction forces of the analytical model for the column .. 352
Figure 6-10. Considered compression contact length between grout and column 353
Figure 6-11. Width of the incline strut of the column inside the socket..... 354
Figure 6-12. Width of the inclined strut of the external socket wall 354
Figure 6-13. Width of the inclined tie of the external socket sleeves..... 355
Figure 6-14. Width of the horizontal tie of the external socket sleeve 355
Figure 6-15. First cracks on external socket wall for SJS2..... 356
Figure 6-16. Compression area and reinforcing bar area for the external socket wall 357
Figure 6-17. Example of STM results of tensile stress on longitudinal steel of the column 358
Figure 6-18. Example of STM results of diagonal compressive stress on the precast column .. 359
Figure 6-19. Example of STM results of shear forces on the precast column within the socket 359
Figure 6-20. Example of STM results of vertical compressive stress on the precast column 360
Figure 6-21. Example of STM results of compressive stress within the grout..... 361
Figure 6-22. Example of STM results of tensile stress on longitudinal steel of the socket wall 361
Figure 6-23. Example of STM results of horizontal tensile stress on the socket sleeves 362
Figure 6-24. Example of STM results of diagonal compressive stress on the socket wall..... 363

Figure 6-25. Example of STM results of diagonal tensile stress on the socket sleeves 363

Figure 6-26. Example of STM results of vertical compressive stress on the socket wall 364

Figure 6-27. Demand-capacity vs. Applied moment for SJS1 366

Figure 6-28. Demand-capacity vs. Applied moment for SJS2 367

Figure 6-29. Demand-capacity vs. Applied moment for SJS3 367

Figure 6-30. Demand-capacity vs. Applied moment for SJS4 368

Figure 6-31. Demand-capacity vs. Applied moment for SJS5 369

Figure 6-32. Demand-capacity vs. Applied moment for SJS6 370

Figure 6-33. Demand-capacity vs. Applied moment for SJS7 371

Figure 6-34. Demand-capacity vs. Applied moment for SJS8 371

Figure 6-35. Prediction-failure ratio of the STM for the eight experimental tests 372

Figure 7-1. Lateral view of the designed external socket connection example 381

Figure 7-2. Plan view of the designed external socket connection example 381

ABBREVIATIONS

ABC	Accelerated Bridge Construction
ALR	Axial Load Ratio
ASTM	American Standard of Testing Materials
CFL	Constructed Facilities Laboratory
CIP	Cast in Place
DIC	Digital Image Correlation
G	Grade of steel
NCHRP	National Cooperative Highway Research Program
NCSU	North Carolina State University
O.C	On Center
RC	Reinforced Concrete
RCFST	Reinforced Concrete Filled Steel Tube
STM	Strut and Tie Model
UHPC	Ultra-High-Performance Concrete
UTM	Universal Testing Machine

LIST OF SYMBOLS

A_{sp}	Transverse area of spiral
e	Thickness
Dc	Column Diameter
f'_c	Concrete compressive strength
f'_{cd}	Design concrete compressive strength
f'_{cg}	Grout compressive strength (Cylinder)
f'_{cgd}	Design grout compressive strength (Cylinder)
f_y	Yield stress
f_{yd}	Design yield stress
Hs	Socket Height
L_o	Initial gauge length
M_n	Nominal moment capacity
M_{ne}	Nominal moment capacity using expected properties
M'_y	First yield moment
P	Axial force
Δ_y'	First yield displacement
ε_c	Axial compression strain
ε_t	Axial tension strain
μ	Ductility
ξ_{hyst}	Hysteretic damping
ρl	Longitudinal steel ratio
ρs	Transverse volumetric steel ratio
φ	Reduction factor
ϕ	Curvature
χ	Ratio between socket height and diameter of the column

ACKNOWLEDGMENTS

The research reported herein was performed by the Constructed Facilities Laboratory, Department of Civil, Construction, and Environmental Engineering, North Carolina State University.

Mervyn J. Kowalsky, Christopher W. Clark, Distinguished Professor of Civil, Construction, and Environmental Engineering, North Carolina State University, and Giorgio T. Proestos, Assistant Professor of Civil, Construction, and Environmental Engineering, North Carolina State University, were the principal investigators. The other author of this report is Julio A. Samayoa, a former Research Assistant at North Carolina State University, now a Postdoctoral Research Scholar of Civil, Construction, and Environmental Engineering at North Carolina State University.

The support from Faculty, students, and technical staff at the Constructed Facilities Laboratory at North Carolina State University was very much appreciated.

EXECUTIVE SUMMARY

This research addresses the challenges associated with designing external socket connections used in Accelerated Bridge Construction (ABC) within seismic regions. These connections involve embedding a precast column into a preformed void in a cap beam or foundation, with the gap between the elements filled with grout. The primary objective of this study was to develop a robust design methodology and a mechanical model capable of relating key design parameters, such as socket height, to critical stresses within the connection and adjoining structural members.

A strut-and-tie model (STM) was developed to evaluate the influence of socket height on stress distribution within the connection and adjoining structural members. The STM provides detailed insights into stress on the connection's different components, including the column's longitudinal reinforcing steel, the reinforcement of the external socket wall, the concrete of the external socket wall, and the grout used to fill the gap. The model is based on equilibrium principles and incorporates the effects of compression and tension forces acting throughout the connection.

Eight large-scale reverse cyclic tests were conducted on column-to-cap-beam connections to validate the proposed STM. These tests varied socket heights and structural configurations, considering both Reinforced Concrete (RC) and Reinforced Concrete Filled Steel Tube (RCFST) systems. The experimental setup applied lateral loads at the top of the column, and an axial load was maintained constant throughout the experimental test. Data was collected using advanced instrumentation, including the Optotrak system, Digital Image Correlation (DIC), and string potentiometers during the test. This data was subsequently used to calculate moment-displacement relationships, axial and shear strain profiles, energy dissipation, and displacement components and to identify different failure mechanisms for external socket connections.

The experimental results provided essential insights into the behavior of external socket connections under seismic loads: 1) Socket height emerged as a critical design variable. Shorter socket heights were shown to require higher grout strengths and greater shear capacity to prevent

failure, as they increase the stress demands on the grout and shear forces acting on the embedded portion of the column. 2) For columns to develop a full plastic hinge above the socket interface, socket height must be carefully optimized. The tests confirmed that well-designed sockets could achieve this behavior, with plastic strains confined to the column and preventing damage to the foundation or cap beam. 3) The experiments also revealed enhanced energy dissipation compared to traditional cast-in-place (CIP) columns. The external socket connections demonstrated higher elastic damping, which can be attributed to early cracking in the grout and socket walls. 4) Displacement components were dominated by strain penetration and rocking, accounting for more than 65% of total displacements, particularly for shorter sockets. This behavior differed from that of CIP columns, where strain penetration and rocking account for around 35% of the total displacements.

The developed STM successfully correlated socket height with the applied moment and critical stresses. It predicted stress distributions in the connection components with high accuracy, typically within a conservative error margin of less than 10% compared to experimental results. The STM highlighted the significance of shear and compressive forces, demonstrating that critical stresses in the grout and external socket wall increased with shorter socket heights. The model also identified potential failure modes, such as grout crushing, column shear failure, or the column's flexural failure above the external connection.

Using the STM, design equations were derived so that practitioners could calculate the necessary socket height and material strength requirements. The equations consider factors like grout strength, column diameter, and the required shear capacity to ensure safety. Recommendations include using reduction factors for material strength and providing a safety margin in the design process. This research provides a comprehensive understanding of the seismic behavior of external socket connections and presents a validated analytical model to guide design. The findings emphasize the critical role of socket height and the need for higher material strengths with shorter socket heights. The developed methodology enhances the safety and performance of ABC in seismic regions, offering practical tools and guidelines for bridge engineers.

Chapter 1: Introduction

The design and construction of bridges using innovative technologies and practices in the United States is increasing. One emerging technique that has gained popularity in recent years is Accelerated Bridge Construction (ABC). According to the Federal Highway Administration [1], ABC enhances site constructability, reduces total project delivery time, improves material quality and product durability, and increases work-zone safety for the traveling public and contractor personnel. Additionally, ABC offers benefits such as minimized impacts on traffic patterns, reduced on-site construction time, fewer weather-related delays, and diminished environmental impacts. ABC employs various methods (e.g., grouted connections, bar coupler connections, socket connections) to improve bridge construction, often involving prefabricated elements like foundations, cap beams, and columns. An important aspect of ABC component design is the connection of these elements, particularly in regions subjected to significant seismicity.

This report focuses on socket connections. In this type of connection, a precast column is embedded into a voided opening within elements such as a cap beam or foundation. The components are bonded using cast-in-place concrete or grout without the need for additional reinforcement. The connection primarily relies on 'socket' action rather than conventional bonding with reinforcement and concrete. Figure 1-1 illustrates a socket connection.

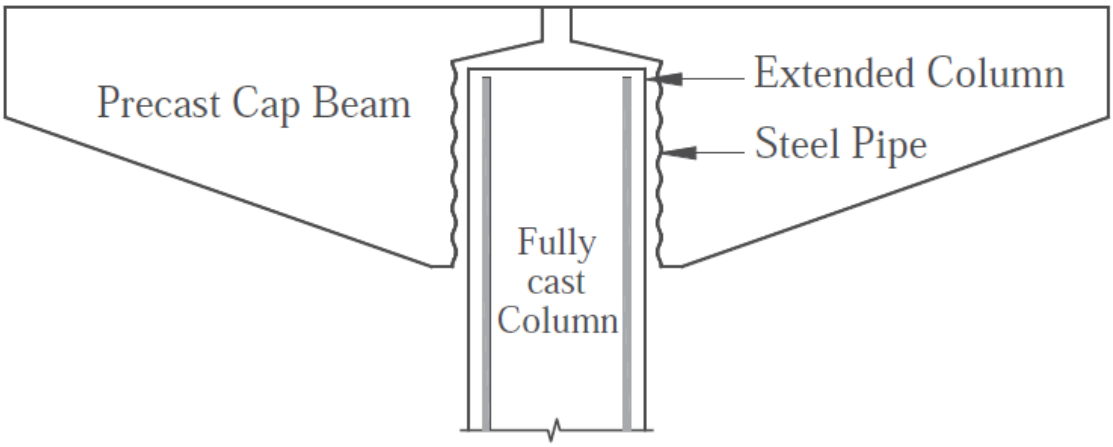


Figure 1-1. Socket connection between column and cap beam [2]

Socket connections can be either internal or external to the joint. However, the National Academies of Sciences, Engineering, and Medicine [2] indicated that multiple experimental studies had been conducted on internal connections. On the other hand, as noted in Chapter 2 of this report, there have been limited analytical and experimental studies for external socket connections.

1.1. Research Need

External sockets provide several advantages over internal sockets, such as (1) Simplified adjoining member construction as there is less steel congestion and (2) Reduced plastic strain demands from the column into the adjoining member since the interface between the adjoining member and the column is connected with a socket that is designed to remain elastic. However, accurate assessment and design of external socket connections require determining various design parameters, such as the required socket height (Hs), the thickness of the external socket wall, and grout strength. While internal socket connections have been proposed in the past, no mechanical model has been proposed to define the demands on the different components of a socket connection. Furthermore, internal sockets benefit from the surrounding footing or cap beam to develop a force transfer mechanism. In contrast, Figure 1-2 shows that the thickness of the socket wall limits the force transfer mechanism of an external socket connection.

The socket height must be sufficiently large to allow the development of the full plastic moment of the column. The typical approach used to define the socket height is to consider a fraction of the column diameter (Dc), thus normalizing the definition of this design variable. Several researchers [3], [4], [5], [6] have studied the response of internal socket connections considering different socket heights ranging between 1.0 Dc to 1.5 Dc. These researchers indicated that the socket height was sufficient to develop the plastic hinge in the column just outside the cap beam or foundation, maintaining structural integrity during the test. While some experimental work has been conducted, there is limited understanding of the fundamental behavior of socket connections, resulting in little guidance for their design.

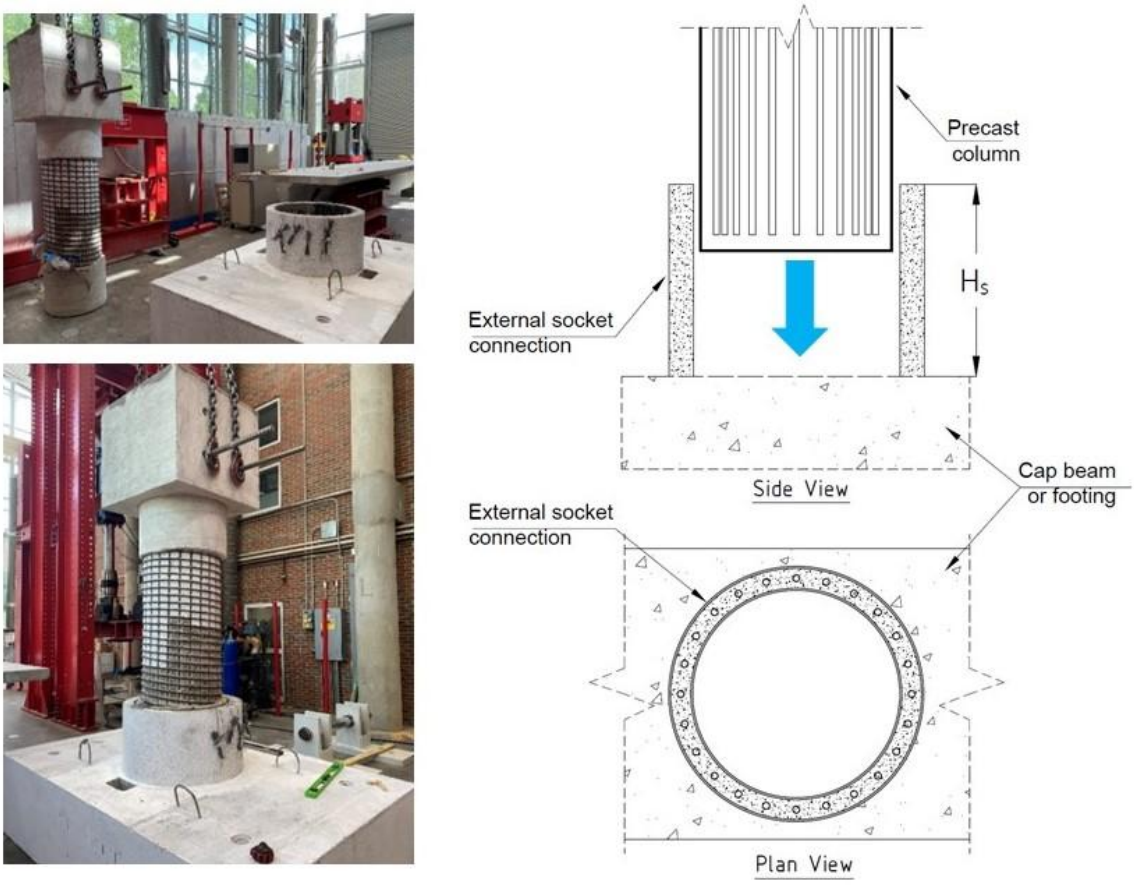


Figure 1-2. External socket connection

1.2. Research Scope and Objectives

This research aims to understand the fundamental behavior of external socket connections comprehensively. The research focused on investigating the influence of different design parameters (e.g., column type, socket heights, grout strength, external wall thickness) on the behavior of these connections and their corresponding structural components. The research intends to develop a robust design methodology applicable to various scenarios for the different structural components of the connection.

A key aspect of this research is introducing a strut-and-tie model (STM) that illustrates the impact of socket height on stresses within the connection. This model is used to analyze and design the different components of the external socket connection. The proposed analytical model was applied to design eight large-scale specimens of a column-to-cap beam connection.

The research involved large-scale specimens comprising six Reinforced Concrete (RC) columns and two Reinforced Concrete Steel Tube (RCFST) columns. These specimens varied in socket height and incorporated the connection details derived from the proposed STM. Advanced non-contact instrumentation techniques, including digital image correlation and an optical measurement system, were employed to establish strain demands within the external socket and the adjacent structural member. The data obtained from these techniques validated the proposed STM and investigated key variables, such as displacement response, damping, and degradation rate, essential for characterizing the seismic behavior of the external socket connection.

By analyzing the outputs of the proposed STM and the results from the large-scale tests, this research aims to identify the feasible boundaries of external socket connections and determine the various failure modes associated with this type of connection. This comprehensive analysis will significantly enhance our understanding of the seismic behavior of the connection and provide a clear relationship between socket height and the stresses within the connection.

1.3. Report Layout

This report is structured to address the research objectives systematically. Chapter 1 introduces the study, highlighting the research need, scope, and objectives. Chapter 2 provides a comprehensive literature review, summarizing key parameters influencing socket connection design and performance, as well as existing analytical models. Chapter 3 details the experimental setup, describing test details, construction process, and instrumentation. Chapter 4 describes the global response of the eight large-scale tests and provides observations on damage progression, while Chapter 5 presents the data analysis and experimental results. Chapter 6 introduces the strut-and-tie model and compares it with experimental results. Chapter 7 offers design recommendations for external socket connections, including design equations and an applied example for engineers. Finally, Chapter 8 concludes the report with a summary of the findings of the experimental program and analytical model and outlines future work, including potential publications and further research directions.

Chapter 2: Literature Review

Despite the extensive study dedicated to ABC, there is limited information on design criteria for connections between columns and adjoining members (*i.e.,* pockets and sockets) and even less information for external socket connections, which is the primary focus of this research. Figure 2-1 depicts an example of internal and external socket connections.

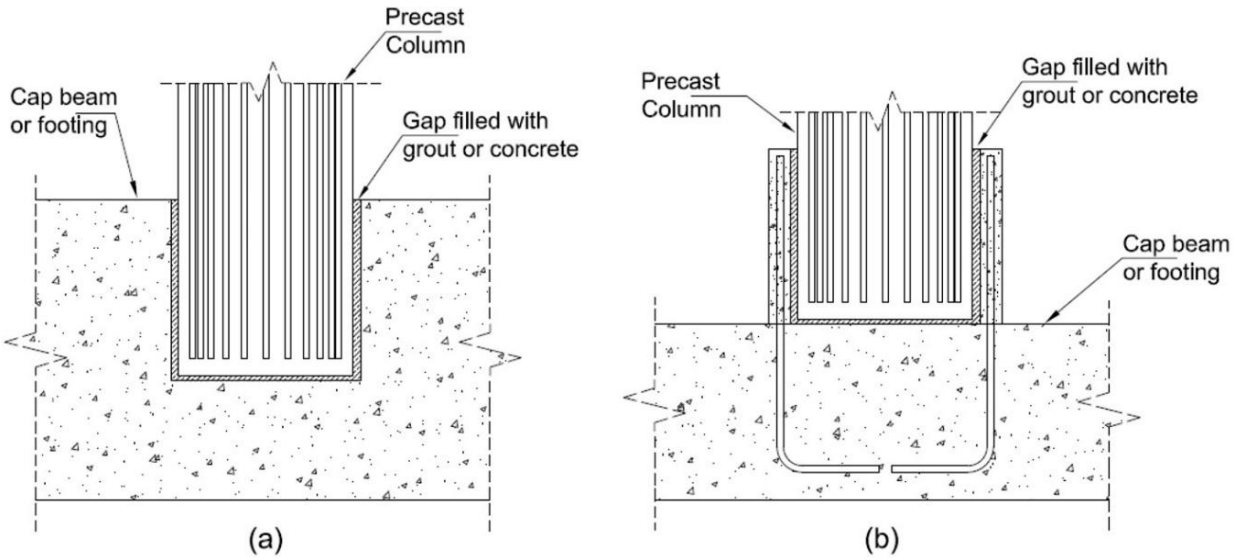


Figure 2-1. Socket connection. (a) Internal connection, (b) External connection

Socket connections have been employed in steel structures and have performed well, including when subjected to seismic conditions [7]. Previous studies have indicated that socket connections in reinforced concrete structures may be a promising ABC alternative in moderate and high seismic zones [3], [8]. Prior studies have demonstrated that if the connections are designed appropriately, they exhibit good seismic performance and can achieve the performance of cast-in-place (CIP) connections [2], [3], [8], [9]. Good seismic behavior ensures the plastic hinge develops in the columns, keeping the cap beams or foundations elastic. The National Academies of Sciences [2], [8] noted that multiple experimental studies have been conducted, but there have been limited analytical studies, especially for external socket connections. The following sections summarize the key parameters that influence the design and performance of socket connections.

2.1. Socket height

The socket height is defined as the length of the void into which a structural element, such as a column, is inserted within the internal or external socket (see Figure 2-2). The NCHRP report [2] indicated that socket height significantly influences socket connection performance.

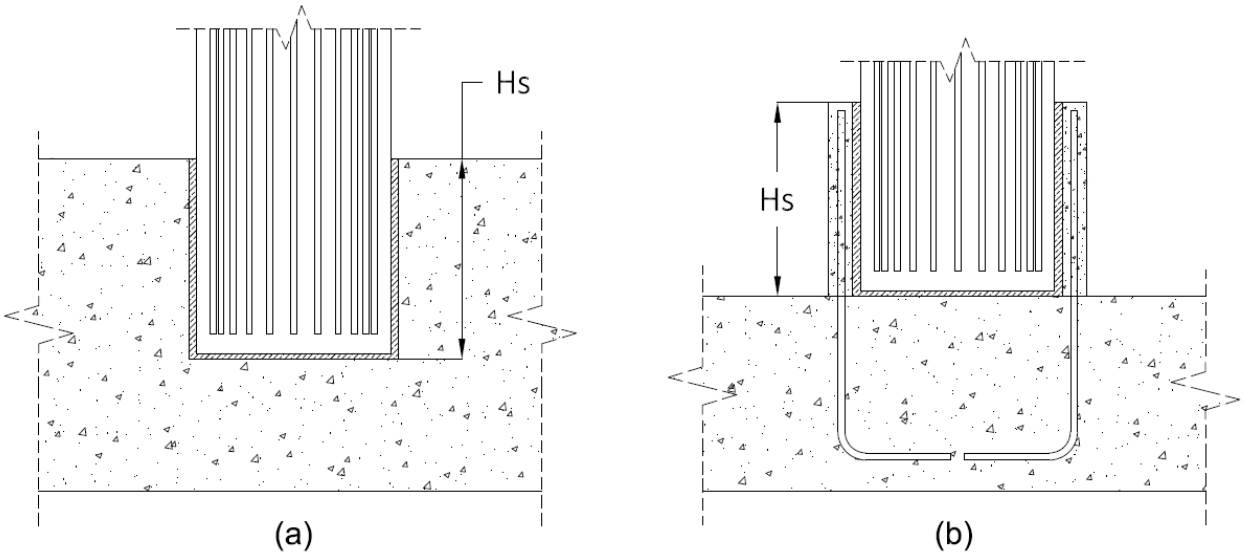


Figure 2-2. Socket height. (a) Internal connection, (b) External connection

The socket height is a design variable that influences the performance of socket connections and is particularly important to ensure that the full plastic moment can be developed in the column at the interface with the connection. As a result, numerous studies have examined this design parameter [3], [4], [10], [11], [12]. The approach commonly used to define the socket height is to consider a fraction of the column width, thus normalizing the definition of this parameter. Previous studies have investigated the response of various embedment length to column diameter (Dc) ratios, ranging between 1.0 Dc and 1.5 Dc.

Restrepo *et al.* [3] tested two 0.42-scale columns that utilized pocket connections with a cap beam. The columns were subjected to quasi-static reverse cyclic loads and were tested until failure. These columns were detailed to exhibit high and low ductility and were labeled CPFD and CPLD, respectively. The dimension for the socket height was 1.2 Dc for both specimens. Figure 2-3 shows the plastic hinge formed near the cap beam and governed the response of the structural

member. Since the plastic hinge formed in the column, the performance of the pocket connection was considered sufficient and at least as good as the cast-in-place (CIP) member.

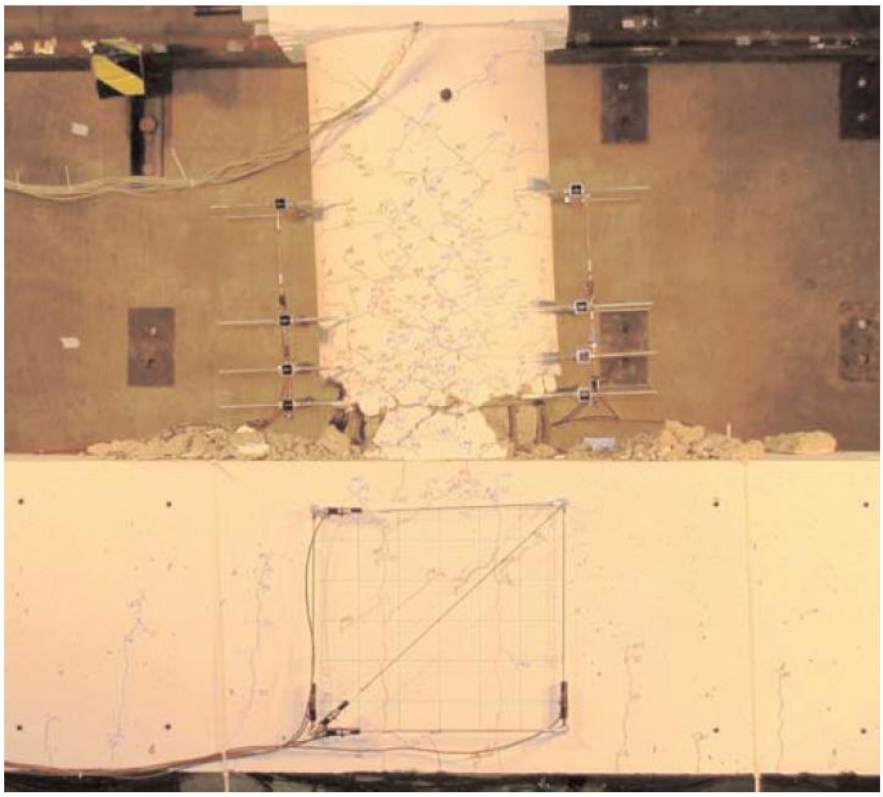


Figure 2-3. Specimen response at 4.2% drift ratio (μ8) – CPFD [3]

Furthermore, the CPFD specimen achieved a drift of 3.3% (nominal displacement ductility of 6, with minimal loss of strength), as shown in Figure 2-4. The strength loss was almost 20% at 4.3% drift. A model of the CIP companion specimen also gave good predictions (through a drift of 3.3%) for the load-displacement response of the column with the pocket connection.

Haraldsson *et al.* [13] evaluated the seismic performance of three socket connections considering different values of socket height. The first two specimens had socket height values equal to 1.1 Dc. The damage from the lateral load appears on the structural element and not the foundation. The third specimen was tested with 0.5 Dc, and while it experienced additional damage in the connection, the behavior was very similar to the companion specimens with larger socket heights. Figure 2-5 shows the lateral behavior of the three specimens.

Mehrsoroush, A., & Saiidi, M. S. [4] performed a column and cap beam assembly test utilizing a socket connection with a socket height of 1.2 Dc. The assembly performed as well as the CIP companion specimen. Figure 2-6 presents the force-drift response of the column with the socket connection. Figure 2-7 shows the plastic hinge appearing below the cap beam. The cap beam did not present any damage other than minor spalling of the grout at the edges of the structural element.

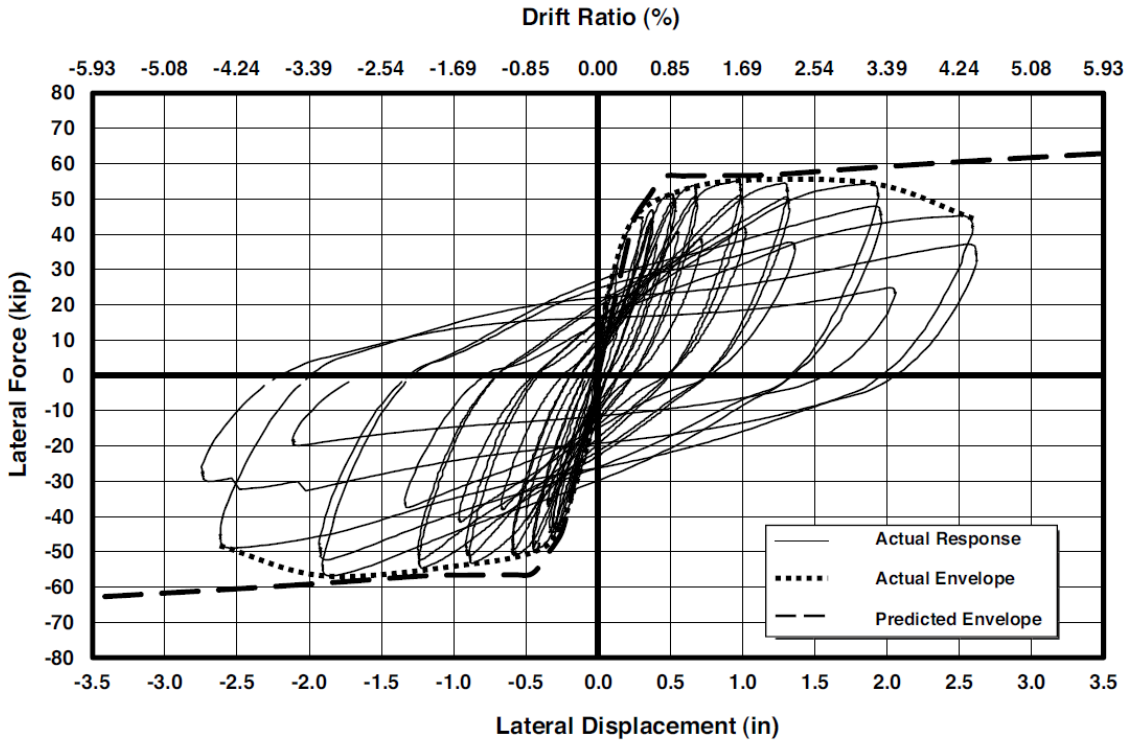


Figure 2-4. Lateral force-displacement – CPFD [3]

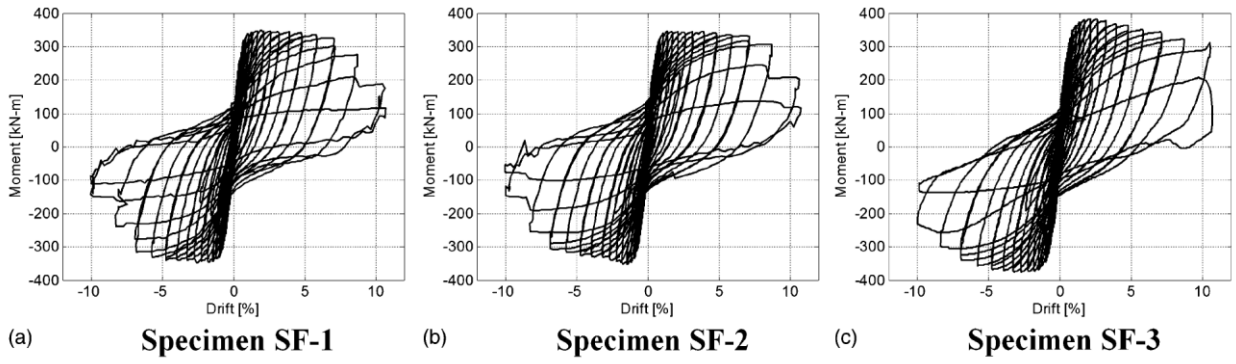


Figure 2-5. Base moment - drift response for the three specimens [13]

Motaref *et al.* [5] tested socket connections with embedment lengths of 1.5 Dc. This study found that the plastic hinge occurs in the structural element, preventing any inelasticity in the cap beam or foundations. Mohebbi *et al.* [6] also tested a socket connection using 1.0 Dc for the embedment length. The study indicated that the socket height was sufficient to develop the plastic hinge in the structural member just below the cap beam, maintaining structural integrity during the test with a 5% drift ratio. A 15% strength loss was reported at 9% drift, leading to a nominal displacement ductility of twelve.

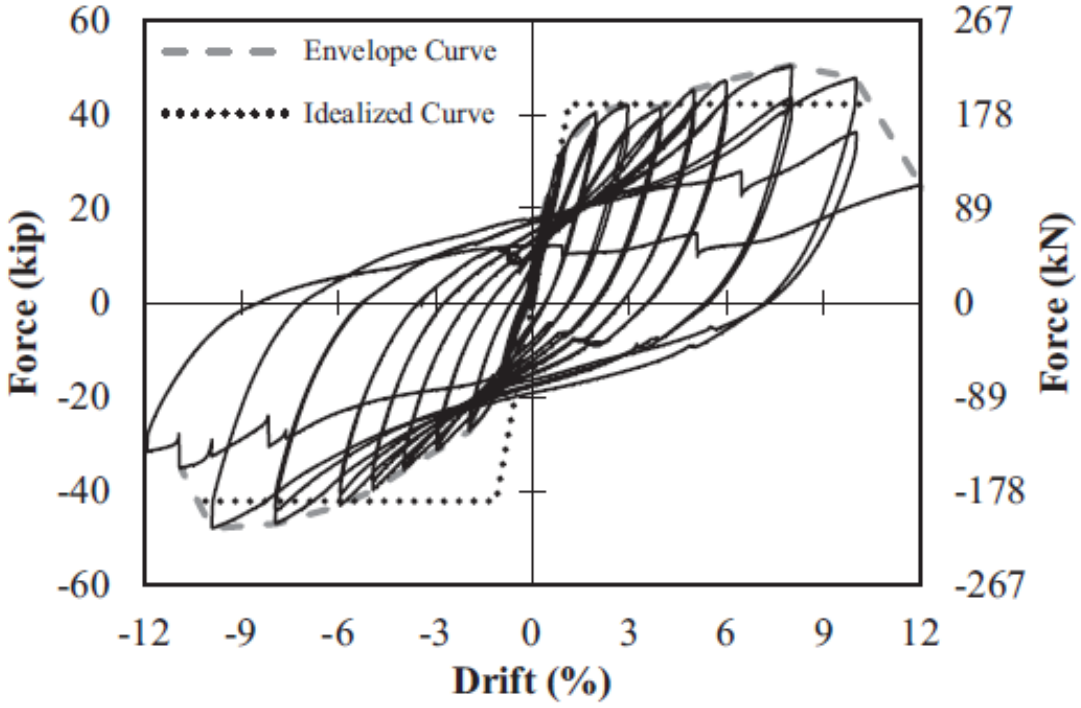


Figure 2-6. Lateral force-drift response of the column with a 1.2 Dc socket height [4]

Wang *et al.* [14] performed two tests; the first was a CIP to compare with the test results of the second specimen which had a socket connection. The socket height examined was 1.13 Dc. As can be seen in Figure 2-8, the specimens with ABC connections presented similar hysteretic behavior compared with the CIP reference test. The specimen utilizing the socket connection did not present any damage in the footing. For further comparison, the study divided the seismic performance into five phases as proposed by Hose *et al.* [15] (1) cracking, (2) yielding, (3) initiation of a local mechanism, (4) full development of a local mechanism, and (5) strength degradation.



Figure 2-7. Damage on the column with a 1.2 Dc socket height at a 10% drift ratio [4]

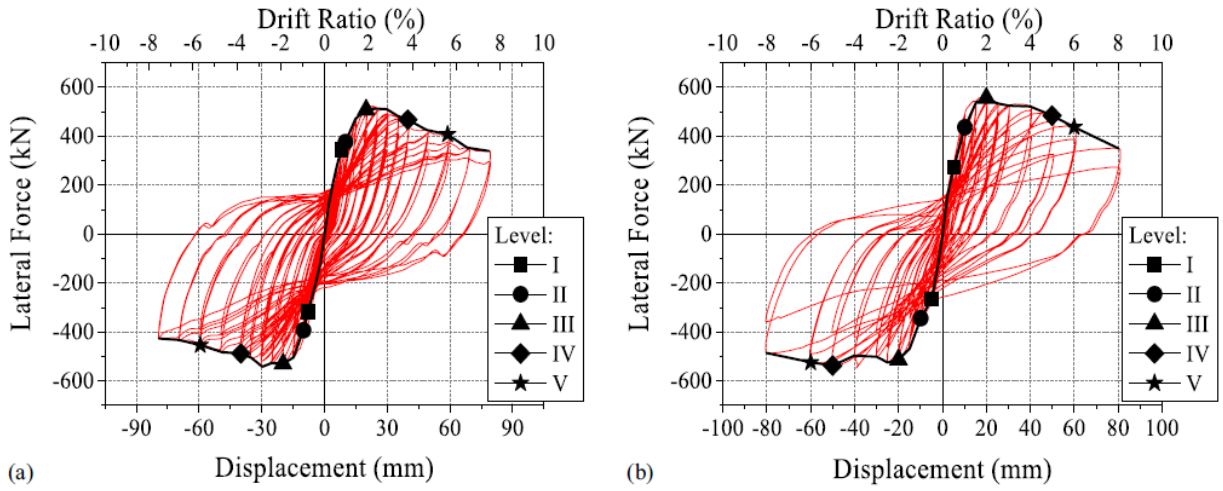


Figure 2-8. Lateral force-displacement response. a) CIP specimen, b) Socket connection [14]

Zhang *et al.* [16] tested three column-foundation specimens using socket connections in reinforced concrete elements and one CIP reference experiment. The socket height for the first two specimens was 0.8 Dc, while the third specimen used 1.0 Dc. It was reported that the damage evolution, failure modes, and hysteretic responses of the precast bridge column were similar to those of the CIP bridge column, as can be observed in Figure 2-9.

To describe the damage evolution, the authors [16] categorized the test into five phases: (1) flexural cracking, (2) yielding of the longitudinal reinforcement bars, (3) spalling of concrete cover, (4) buckling of the longitudinal reinforcement bars, and (5) rupture of the longitudinal reinforcement bars. The final failure mode of all specimens was buckling of the longitudinal reinforcement bars followed by rupturing. Visible cracks were not identified in the footing after the tests were completed. Additionally, as shown in Figure 2-10, the energy dissipated by all the specimens was similar. Thus, the study concluded that having a socket height of 0.8 Dc is sufficient to ensure the ABC connection performed as well as the CIP companion specimen.

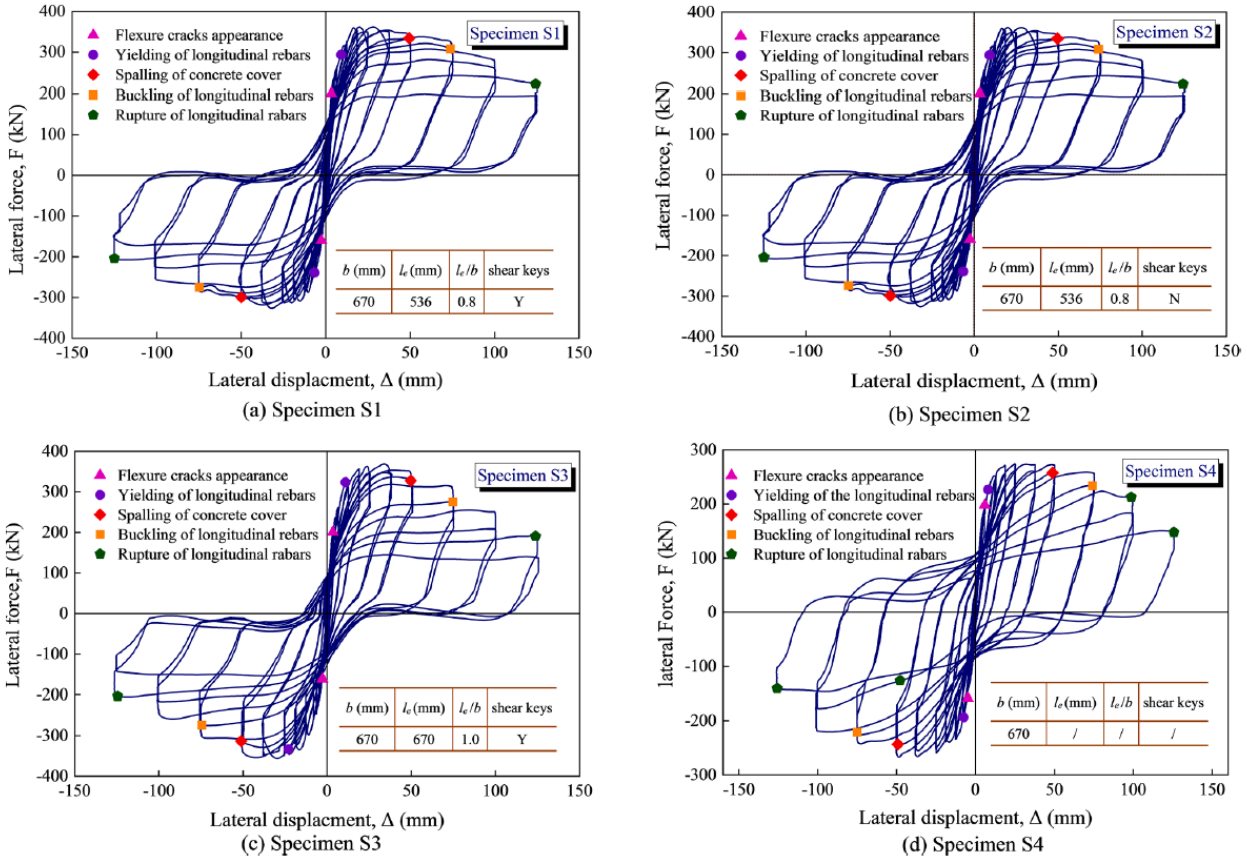


Figure 2-9. Force-displacement hysteretic response. a-c) Socket connections, d) CIP [16]

Although not explicitly mentioned above, nearly all of the tests conducted show some gradual reduction in strength with increasing ductility that appears to be more substantial than conventional detailing. This is especially evident for socket connections (see Figure 2-9, for example).

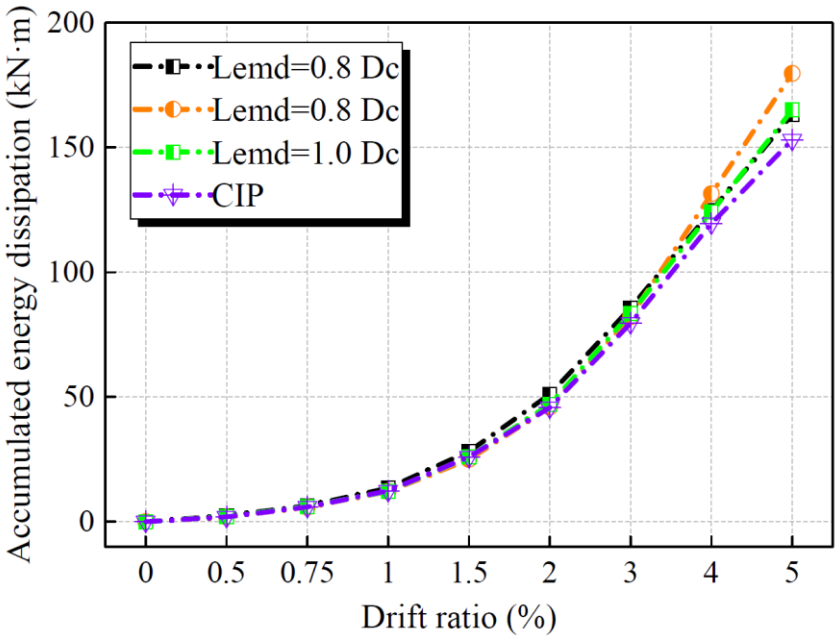


Figure 2-10. Accumulated energy dissipation for specimens [16]

A summary of the information collected for the socket height variable is provided in Table 2-1. Included in Table 2-1, is an overview of the connection performance presented in the NCHRP report [2].

Table 2-1. Summary of available test data evaluating socket height for socket connections

Author	Type of connection	Socket height	Connection performance
Restrepo *et al.* [3]	Internal pocket	1.2 Dc	Plastic hinging of the column near the cap beam. The connection performed as well as the CIP companion specimen
Haraldsson *et al.* [12]	Internal socket	1.1 Dc	The damage from lateral load appears on the structural element, and the foundation was without any considerable damage
Haraldsson *et al.* [12]	Internal socket	0.5 Dc	Experienced damage in connection, but the lateral behavior was identical to companion specimens with larger socket height

Table 2-1. Summary of available test data evaluating socket height for socket connections (continued)

Author	Type of connection	Socket height	Connection performance
Mehrsoroush, A., & Saiidi, M. S. [4]	Internal socket	1.2 Dc	The plastic hinge developed in the structural element, and the cap beam did not exhibit any damage
Motaref *et al.* [5]	Internal socket	1.5 Dc	A plastic hinge occurred in the structural element, and the cap beam or foundation remained elastic
Mohebbi *et al.* [6]	Internal socket	1.0 Dc	Development of the plastic hinge in the structural member just below the cap beam
Wang *et al.* [14]	Internal socket	1.13 Dc	Similar hysterical behavior compared with the CIP reference test. No damage was reported on the footing
Zhang *et al.* [16]	Internal socket	0.8 Dc and 1.0 Dc	The damage evolution, failure modes, and hysteretic response of the precast bridge column were equivalent to the CIP bridge column
Kavianipour and Saiidi [17]	Internal socket	1.5 Dc	Socket connections exhibited a significant drift ratio capacity with no apparent damage to the connection
Thonstad *et al.* [18]	Internal socket	1.8 Dc	Many column longitudinal bars fractured, which indicates that bars were fully anchored in the pocket connections
Canha *et al.* [10]	External socket	2.0 Dc and 1.6 Dc	Damage occurred outside of the embedment region. Both tests exhibited similar behavior

2.2. Gap size, shape, and filling materials

Given that a socket connection requires at least one precast element, there is always a space between the adjoining elements, which will be filled with cast-in-place material. Figure 2-11 illustrates the gap between adjoining elements for socket connections. The filling material, such as grout or cast-in-place concrete, is intended to join the two members so they act as a single unit. The gap size, shape, and filling material used within the connection help ensure that a moment connection develops and allows for element tolerances that may be needed during field installation.

Culmo, M. P. [9] describes how the distance between the connecting elements should be determined based on the maximum specified element tolerance. Specifically, Culmo suggests that the space between elements should be approximately one inch but may increase depending on the size of the elements being connected. The study described that the purpose of the grout is to contribute to the transfer of forces between the adjoining elements.

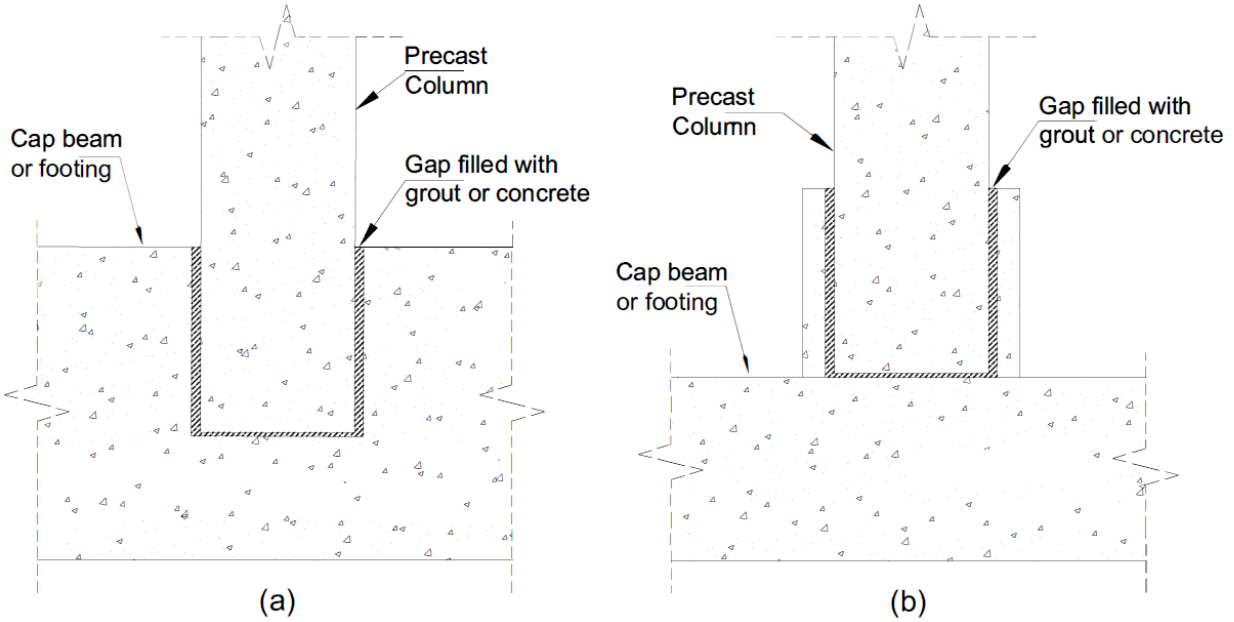


Figure 2-11. Gap between adjoining elements. a) Internal connection, b) External connection

Additionally, Restrepo *et al.* [3] recommended that the gap size for the socket connection should be limited to 3 inches. To ensure the grout is not the weak link in the connection, the filling material should have a compressive strength of at least 500 psi higher than the adjoining members.

It was also recommended that for socket connections, the clear spacing between the reinforcing bars and the formed surfaces of the socket should be at least three times the aggregate maximum size to ensure adequate concrete flow.

Motaref *et al.* [5] considered using an octagonal shape for the internal socket with a gap size of 1.5 inches between the circular column and socket, as shown in Figure 2-12. The gap was filled with high-strength grout with a compressive strength of 7,000 psi. No damage was found in the foundation when the column was subjected to lateral loads.

Mehrsoroush, A., & Saiidi, M. S. [4] used a gap size of 2 inches and high-strength non-shrinkage grout as the filling material in their circular socket connection. The test exhibited minor spalling of the grout near the edges of the interface between the column and foundation when the plastic moment was reached in the column.



Figure 2-12. Octagonal shape for a socket connection [5]

Mohebbi *et al.* [6] evaluated a square socket connection using high-strength non-shrinkage grout as the filling material with a compression strength of 8,600 psi and a gap size of 1 inch. No damage was reported in the socket connection after achieving a drift ratio of 9.6%. Figure 2-13 shows the square pocket connection.



Figure 2-13. Cap beam with square socket connection [6]

Wang *et al.* [14] performed two tests on ABC connections. The first test was a square socket connection with a gap size of 0.8 inches, and the filling material was a high-strength grout of 10,100 psi. The compressive strength of the CIP concrete was 5,000 psi. The second test was a circular pocket connection where concrete with a compression strength of 9,000 psi was used instead of high-strength grout. At the final stage of the test, it was reported that the column exhibited concrete crushing and buckling of longitudinal bars. Still, the ABC connections and cap beam or foundation experienced almost no damage.

Zhang *et al.* [16] used ultra-high-performance concrete (UHPC) with a compressive strength of 17,400 psi as the filling material for an internal socket connection. The test examined a square shape for the internal socket and a 1.2 inches gap size between the precast members (see Figure 2-14). After the test, the foundation had no visible cracks or damage for any of the specimens. However, the column had some bar fractures near the foundation. It was reported that the damage evolution and failure modes of the socket connection utilizing UHPC as filling material were similar to that of the CIP connections.



Figure 2-14. Foundation with a square socket connection [16]

A summary of the information collected for the gap size, shape, and filling material is provided in Table 2-2. Included in Table 2-2 is an overview of the connection performance presented in the NCHRP report [2].

Table 2-2. Summary of available test data for gap size, shape, and filling material for socket connections

Author	Type of connection	Shape of connection	Gap size	Filling material	Connection performance
Restrepo *et al.* [3]	Internal pocket	Circular	Less than 3″	Conventional concrete with at least 500 psi higher strength than adjoining members	The failure was due to buckling and fracture of two-column reinforcing bars. The connection did not lose anchorage
Motaref *et al.* [5]	Internal pocket	Octagonal	1.5″	High-strength grout (7,000 psi)	No damage to the foundation
Mehrsoroush, A., & Saiidi, M. S. [4]	Internal socket	Circular	2.0″	High-strength non-shrinkage grout (7,710 psi)	Minor spalling of the grout near the edges of the socket

Table 2-2. Summary of available test data for gap size, shape, and filling material for socket connections (continued)

Author	Type of connection	Shape of connection	Gap size	Filling material	Connection performance
Mohebbi *et al.* [6]	Internal socket	Square	1.0″	High-strength non-shrinkage grout (8,600 psi)	No damage was reported in the socket connection after achieving a drift ratio of 9.6%
Wang *et al.* [14]	Internal socket	Square	0.8″	High-strength grout (10,100 psi)	The column had concrete crushing and buckling of longitudinal bars. No damage to the ABC connections
Zhang *et al.* [16]	Internal socket	Square	1.2″	UHPC (17,400 psi)	A similar response to companion CIP connection tests
Canha *et al.* [10]	External socket	Square	2.0″	Conventional concrete (7,800 psi)	Yielding of column reinforcement outside of the socket connection

2.3. Shear mechanism between adjoining elements

An important consideration when examining the seismic behavior of a socket connection is the development of shear forces at the interface of the adjoining members and how these internal forces influence the socket height or the choice of filling material. Furthermore, experimental studies [3], [4], [10], [16], [19] have been performed to understand this shear transfer mechanism and the variables that may influence the performance of the socket connection. Uniaxial tests are beneficial for identifying friction forces developed at the interface of adjoining members. Tests with lateral load and constant axial force at the top of the column simulate the moment, axial force, and shear force the connection will experience in real-world conditions.

Socket connections are subjected to complex stresses, including combinations of shear forces, axial loads, and bending moments. Uniaxial tests isolate the axial load and help better understand the connection performance under simplified conditions. This facilitates the study of the fundamental bond characteristics of socket connections. A precise knowledge of this behavior provides a basis for understanding a more complicated arrangement of loads for socket connections.

Cheng, Z., & Sritharan, S. [19] conducted a uniaxial compression force test in a socket connection. Figure 2-15 shows the test configuration. The authors indicated that some parameters significantly influence the seismic behavior of the socket connection, especially for the shear transfer mechanisms. These parameters included surface preparation along the socket height for the socket walls and the precast structural element, gap size, and the filling material strength.

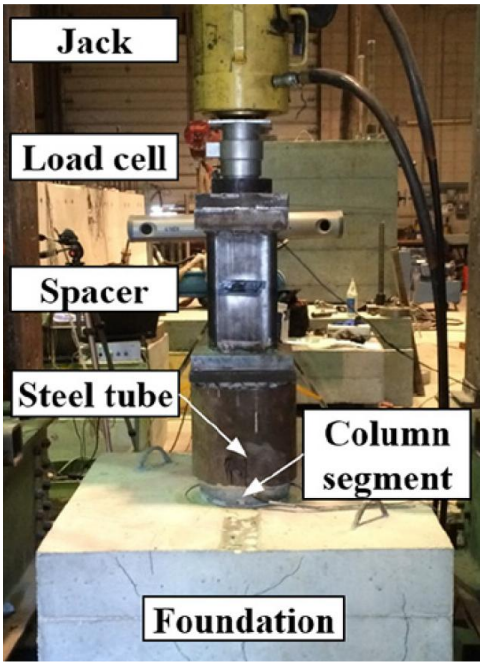


Figure 2-15. Test configuration for uniaxial compression test in socket connection [19]

Cheng, Z., & Sritharan, S. [19] also indicated that the variable that controls the bond strength in the socket is the surface preparation of the precast structural element. Thus, having a smooth surface will deliver a lower bond strength increasing the likelihood of sliding between the adjoining elements. Specifically, this study considered four different surface preparations for the precast structural element, such as 13 mm fluted fin (F1G1M), 19 mm fluted fin (F2G1M),

Exposed aggregate (EG1M), and Smooth (SG1C). Figure 2-16 depict the different surface preparations.

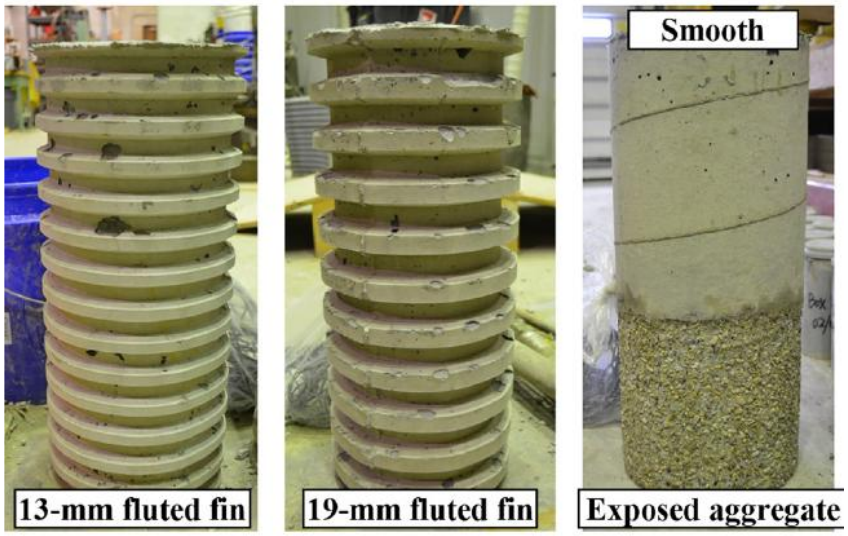


Figure 2-16. Different surface preparation for embedded elements [19]

Figure 2-17 demonstrates that surface preparation influences the behavior of the connection because roughness is necessary to develop bond strength between the filling material and the precast element.

In their experiments, several researchers, such as Restrepo et al.[3], have considered a lateral load and constant axial ratio to examine the external actions that act on a socket connection in seismic conditions. Figure 2-18 shows the test setup of the socket connection, considering a 16-gage corrugated steel pipe to form the socket and to help as hoop reinforcement.

Restrepo *et al.* [3] found that the reinforcement bars inside the socket had only minor bar slips, indicating that the column bars were well anchored. Additionally, the stirrups placed within the connection reached a maximum of 25% yielding, and the strains developed on the corrugated steel pipe reached a maximum value of 37% yield at the mid-height of the socket. A supplementary hoop on the connection at each end of the steel pipe was included to avoid unraveling; this reinforcement reached 52% yield, indicating its contribution to the joint performance.

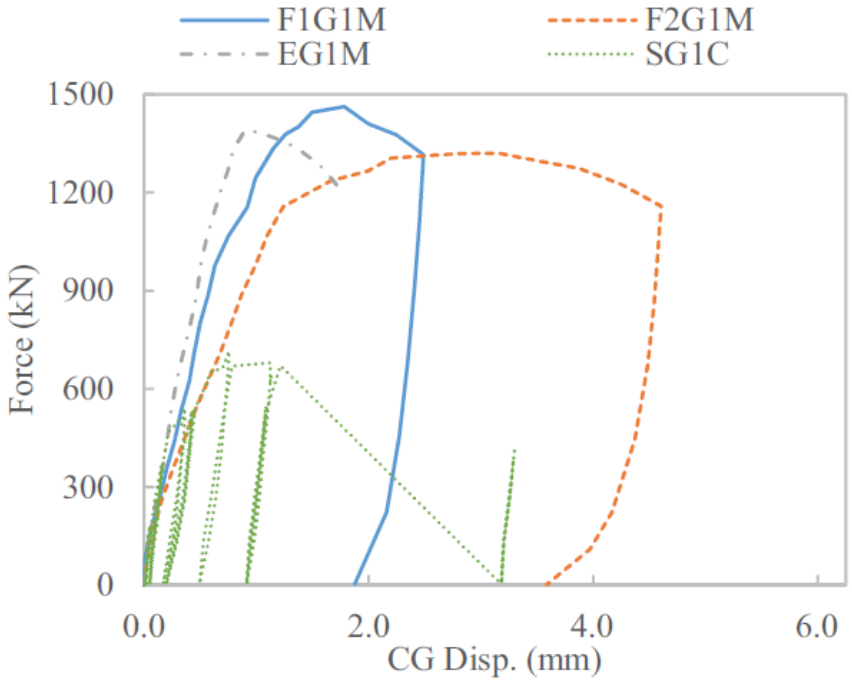


Figure 2-17. Column-to-grout interface displacements with different surface preparations [19]

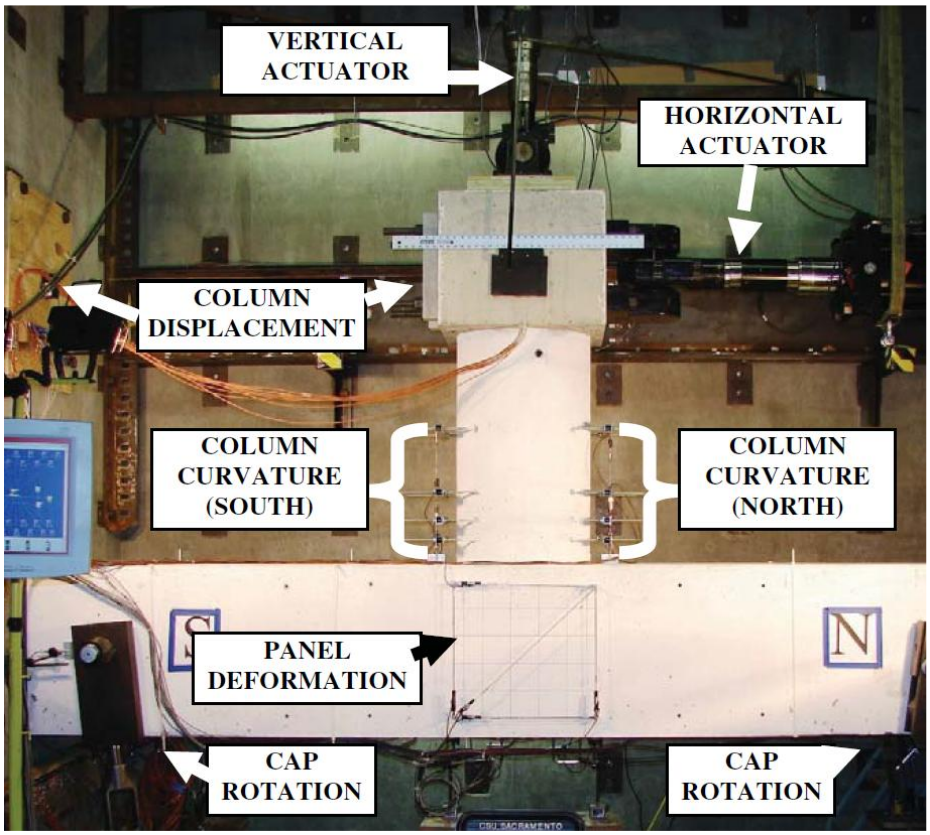


Figure 2-18. Test setup for lateral load and constant axial load [3]

Canha *et al.* [10] tested an external socket connection considering smooth interfaces between the structural and socket elements. The test setup was arranged to transmit only axial forces and bending moment and was achieved by applying an axial force with an eccentricity, as shown in Figure 2-19.

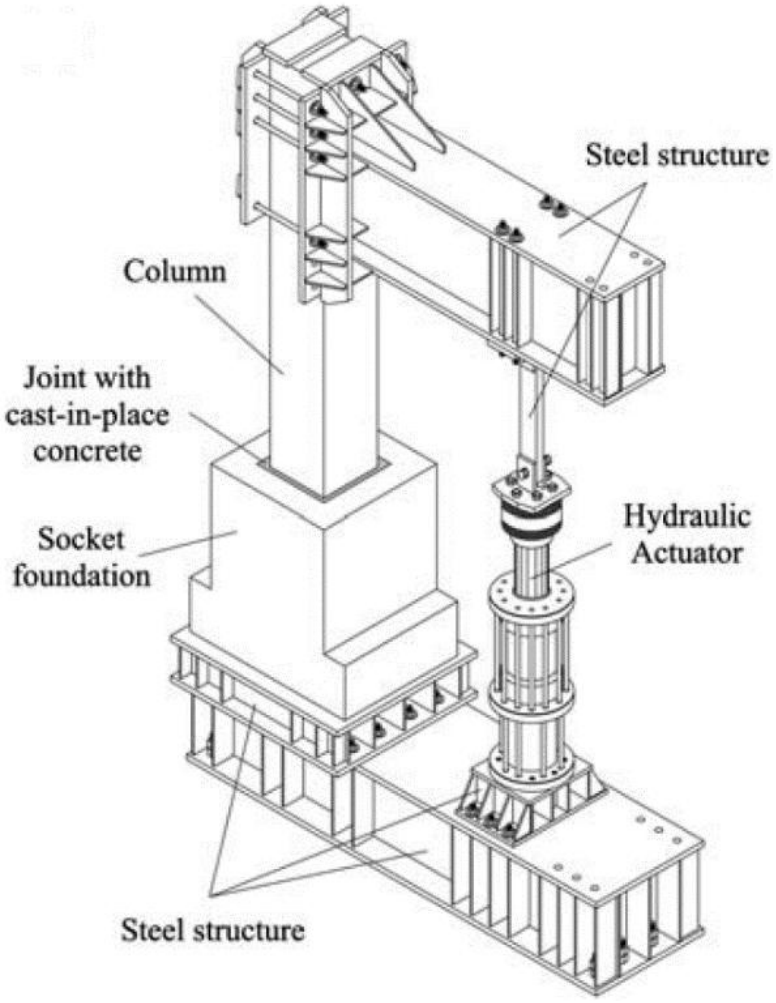


Figure 2-19. Test setup for external socket connection [10]

The bending moment and the strains developed at the reinforcement bars on the tension side of the precast column inserted on the socket connection are shown in Figure 2-20 and Figure 2-21. Strains increase from the bottom of the column to the upper part of the socket connection, indicating the transfer of forces from the column to the socket. In the test with a socket height of 1.6 Dc, the longitudinal bars experienced a slip in tension at the bottom of the socket. Strain patterns in both specimens were observed to be similar.

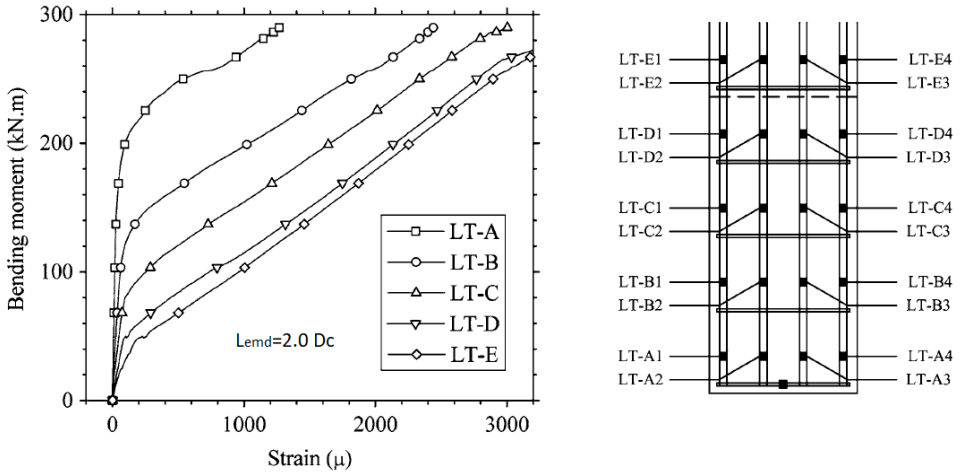


Figure 2-20. Bending moment versus strain of longitudinal bars of the column, with socket height of 2.0 Dc [10]

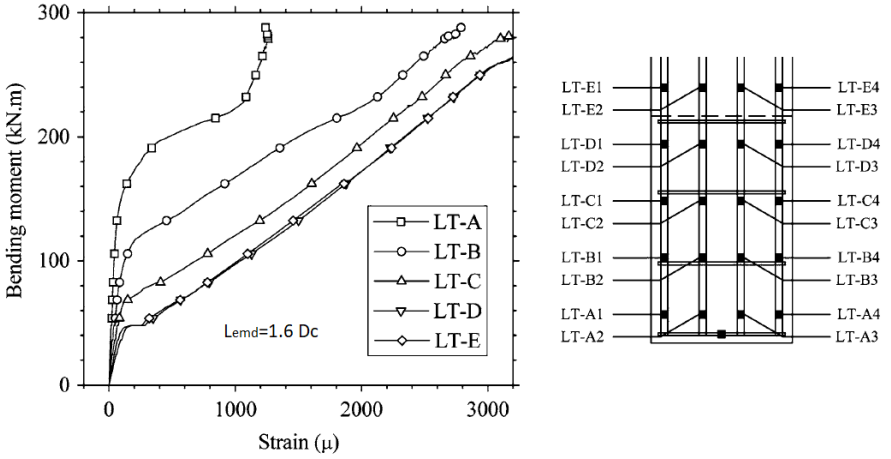


Figure 2-21. Bending moment versus strain of longitudinal bars of the column, with socket height of 1.6 Dc [10]

Mehrsoroush, A., & Saiidi, M. S. [4] performed a quasi-static reverse cyclic test on a socket connection to investigate the influence of additional reinforcement on the shear transfer between adjoining precast elements. Hence, a threaded rod was embedded in the connection. Figure 2-22 shows how the threaded rod was placed inside the top of the column passing through the cap beam. The maximum strains measured in the threaded rod were much less than the yielding strain, indicating that the forces were mainly transferred by shear mechanisms between the column and the cap beam at the socket interface.

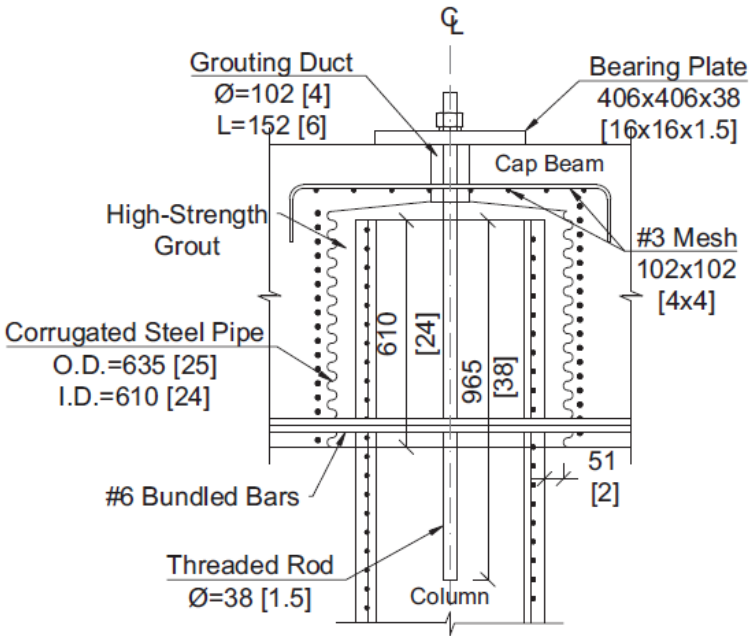


Figure 2-22. Socket connection with a threaded rod for enhancing the transfer of forces [4]

Zhang *et al.* [16] tested a socket connection considering a tooth on both surfaces between the columns and the socket wall to act as a shear key, shown in Figure 2-23. In addition, a specimen without shear keys was tested to compare the behavior of both scenarios. The strains on the longitudinal bars were measured at different lateral displacement levels, as shown in Figure 2-24. The strains are lower at the bottom of the column inside the socket connection, and the maximum strain values are near the socket connection interface.

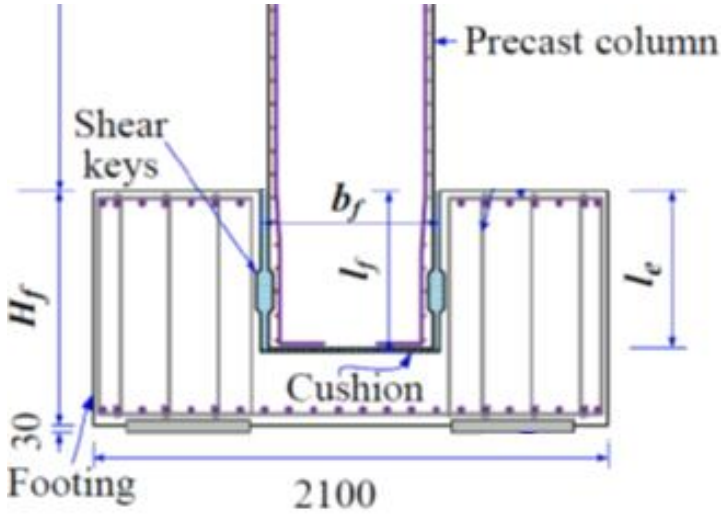


Figure 2-23. Shear keys on the socket connection surfaces [16]

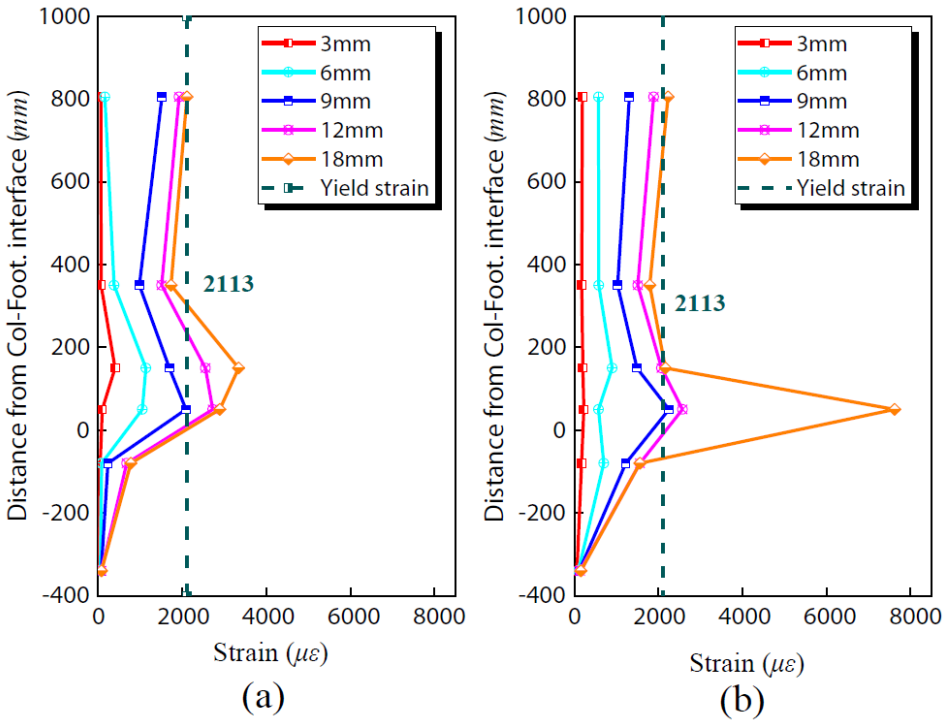


Figure 2-24. Strain profile of longitudinal reinforcement. (a) With a shear key, (b) Smooth surfaces [16]

It was determined that the shear keys provide greater load transfer, which helps to reduce the strain on the longitudinal reinforcement of the column near the interface with the socket. The members tested with shear keys also reduced the strain penetration length inside the socket connection. Zhang *et al.* [16] indicated the shear key's importance in reducing the longitudinal bar strain penetration inside the socket connection. While there were observed benefits using shear keys, the global behavior of the connection was similar for both specimens.

2.4. Analytical Models for Socket Connections

The researchers mentioned earlier in this chapter have been working to understand the behavior of socket connections by studying parameters such as socket height, material properties, and shear mechanisms through experimental programs. However, only a few proposed analytical models can predict the transfer of forces and stresses acting on socket connections and their components. Furthermore, no existing analytical model comprehensively relates the forces acting

on different components and the impact of these forces on the various variables such as required grout, required concrete strength, or socket height.

The analytical model proposed by Osanai *et al.* [20], shown in Figure 2-25, is a significant contribution to understanding socket connections. This model, based on the equilibrium of forces, has been verified through experimental tests. Applying axial and lateral forces at the top of the columns generates shear and moment forces on the foundations, leading to internal friction forces and horizontal reactions.

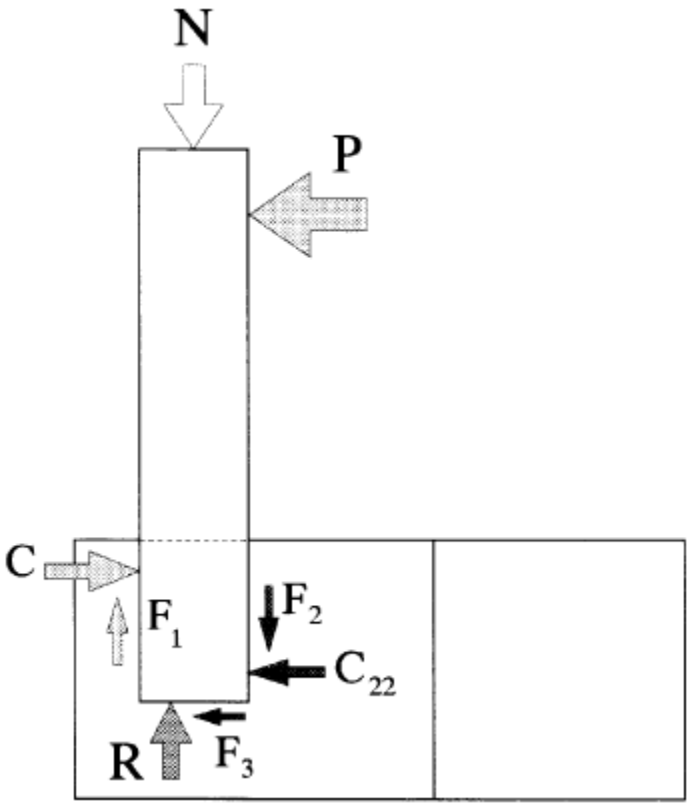


Figure 2-25. Force transfer model for socket connections [20]

Osanai *et al.* [20] observed that the load-strain curves for the foundation reinforcement closely match the predicted values near the ultimate load when friction coefficients between 0.5 and 1.0 are used. Specimens with embedment depths of 1.5 Dc and 1.25 Dc, provided with shear keys, yielded results comparable to calculations with a friction coefficient of 1.0. Similarly, specimens with an embedment depth of 1.0 Dc with shear keys produced results similar to those

with a friction coefficient of 0.5. In conclusion, the model accurately predicted the forces acting on the footing and columns, leading to a conservative reinforcement design for the structural elements.

Canha *et al.* [10] have proposed an analytical model for the portion of the column embedded in the socket connection, as shown in Figure 2-26. This model, which is based on the results of two experimental tests with socket heights of 1.6 h and 2.0 h for a square column, has practical implications. It represents the behavior of the base of a precast column in socket foundation connections with smooth interfaces, providing a safe estimate of the transverse reinforcement required for these connections.

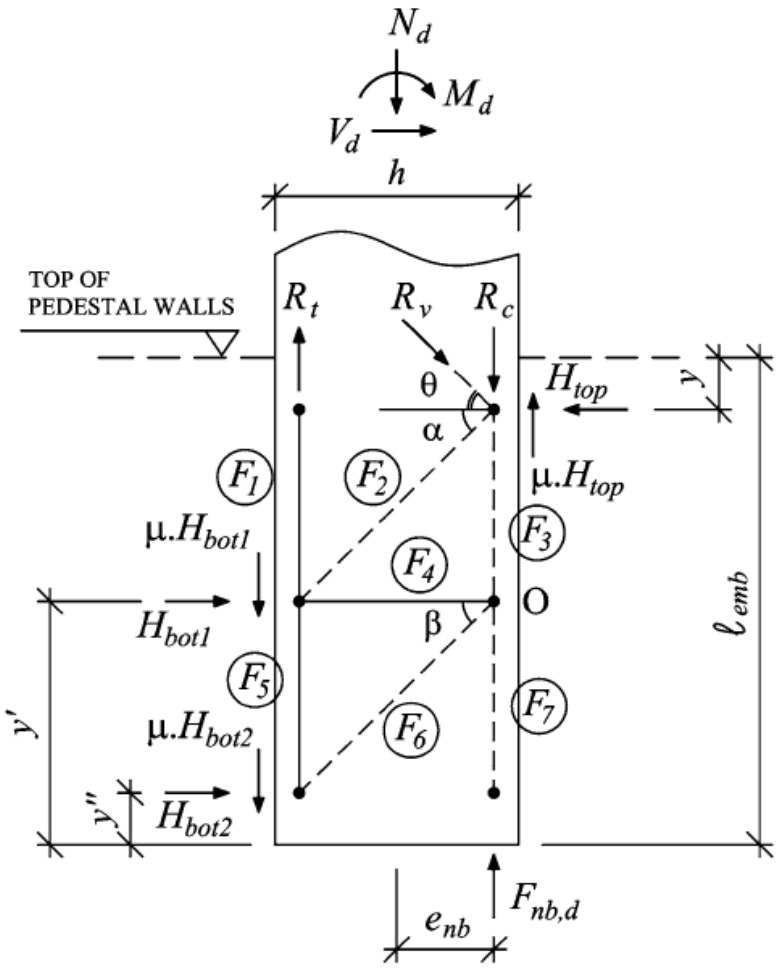


Figure 2-26. Analytical model of the column inside a socket connection. [10]

2.5. Discussion and knowledge gaps

While previous studies have explored the use of different socket heights for socket connections, there is no consensus on how this variable should be designed. Additionally, comparing socket heights across different studies can be challenging since multiple variables often change, and it cannot be easy to attribute performance differences to a single variable.

The studies in this chapter considered different filling material types, demonstrating that materials with higher compressive strength than precast elements can protect the socket. However, there is no information on determining the required filling material strength to have a similar behavior compared to the CIP structures while varying the socket heights. While different shapes and gap sizes for socket connections have been examined, there is no direct relationship between these design parameters and the global response of the structure.

Examining different approaches to enhance the transfer of forces from the structural element to the adjoining member leads to reduced strains on the column reinforcement inside the socket. However, the global behavior remains similar to an interface without additional shear transfer mechanisms such as shear keys. Additionally, there has been little effort to quantify the load transfer mechanisms to delineate what proportion of the load is transferred through contact stresses (socket action) or shear stresses at the column-connection interface.

Despite the existence of different analytical models to predict the forces acting on the column and the socket connection, no model currently relates different variables of the connection. For example, there is no model that describes how varying socket heights impact the required grout strength needed to develop the plastic hinge outside the connection.

Chapter 3: Experimental Program

This chapter discusses the experimental program, which consisted of eight large-scale tests on external socket connections. The program included six tests on circular reinforced concrete (RC) columns and two tests on circular reinforced concrete-filled steel tube (RCFST) columns. The experiments were conducted at the Constructed Facilities Laboratory (CFL) at North Carolina State University (NCSU). This chapter outlines the experimental details of the columns and external socket connections, including specimen construction and the instrumentation used for data analysis in each test.

3.1. Column Test Matrix

The experimental program utilizes large-scale specimens comprising six RC columns and two RCFST columns. These specimens are at a ½ scale, with column detailing representative of common bridge construction practices. An analytical model, presented in Chapter 5, was used to design the eight specimens, focusing on investigating the influence of different design parameters, such as socket height and the concrete strength of the column portion inside the socket connection. Table 1-1 outlines the key design parameters considered for the eight columns of this experimental program.

Table 3-1. Column test matrix

Test number	Diameter (in)	Socket height (in)	Concrete strength of the column inside the socket (ksi)	Longitudinal steel	Transverse steel (spirals)
SJS 1 (RC)	24	24 (1.0 Dc)	6.0	24 #6 (ρl=2.34%)	#3 @ 2″ (ρs =1.04%)
SJS 2 (RC)	24	18 (0.75 Dc)	6.0	24 #6 (ρl=2.34%)	#3 @ 2″ (ρs =1.04%)
SJS 3 (RC)	24	20.4 (0.85 Dc)	8.3	24 #6 (ρl=2.34%)	#3 @ 2″ (ρs =1.04%)

Table 3-1. Column test matrix (continued)

Test number	Diameter (in)	Socket height (in)	Concrete strength of the column inside the socket (ksi)	Longitudinal steel	Transverse steel (spirals)
SJS 4 (RC)	24	20.4 (0.85 Dc)	8.6	24 #6 (ρl=2.34%)	#3 @ 2″ (ρs =1.04%)
SJS 5 (RC)	18	15.3 (0.85 Dc)	6.7	20 #5 (ρl=2.40%)	#3 @ 2″ (ρs =1.30%)
SJS 6 (RC)	18	15.3 (0.85 Dc)	9.2	20 #5 (ρl=2.40%)	#3 @ 2″ (ρs =1.30%)
SJS 7 (RCFST)	18	15.3 (0.85 Dc)	5.6	20 #5 (ρl=2.40%)	no spirals
SJS 8 (RCFST)	18	22 (1.22 Dc)	7.0	20 #5 (ρl=2.40%)	no spirals

3.2. Column Test Details

The specimens SJS 1 to SJS 4 had a clear height of 7’-6″ and a diameter of 24″, resulting in a height-to-diameter aspect ratio of 3.62, with a concrete cover of 1″. The columns were reinforced with 24 Grade 60–A706 #6 longitudinal bars (ρl = 2.34%), and the transverse steel consisted of #3 spirals spaced at 2.0″ intervals (ρs = 1.04%). Figure 3-1 and Figure 3-2 show the plan and elevation views of the column reinforcement, respectively.

The longitudinal reinforcement of the external socket for specimens SJS 1 to SJS 4 consisted of 24 Grade 80-A706 #7 bars. Steel sleeves-A36, 1/4″ thick, were used to enclose the concrete, and the socket wall thickness was 3 inches. Figure 3-3 and Figure 3-4 show the reinforcement plan of the external socket wall. The external socket height varied, as shown in Table 3-1.

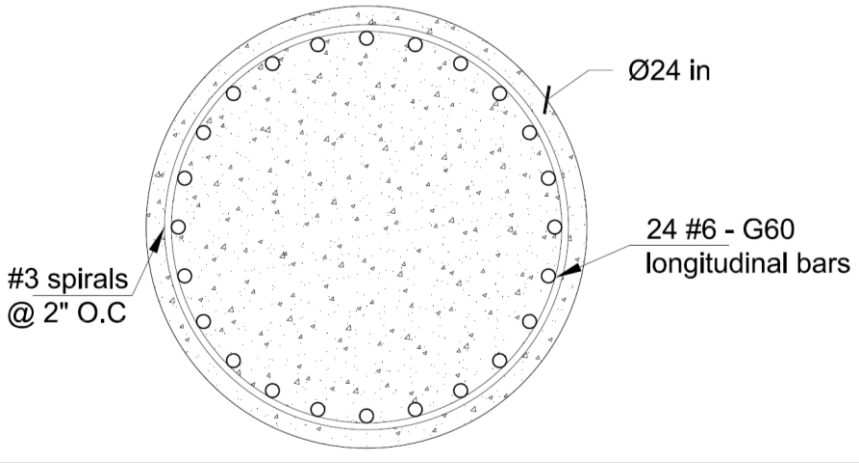


Figure 3-1. Column reinforcement for SJS1 to SJS4 - plan view

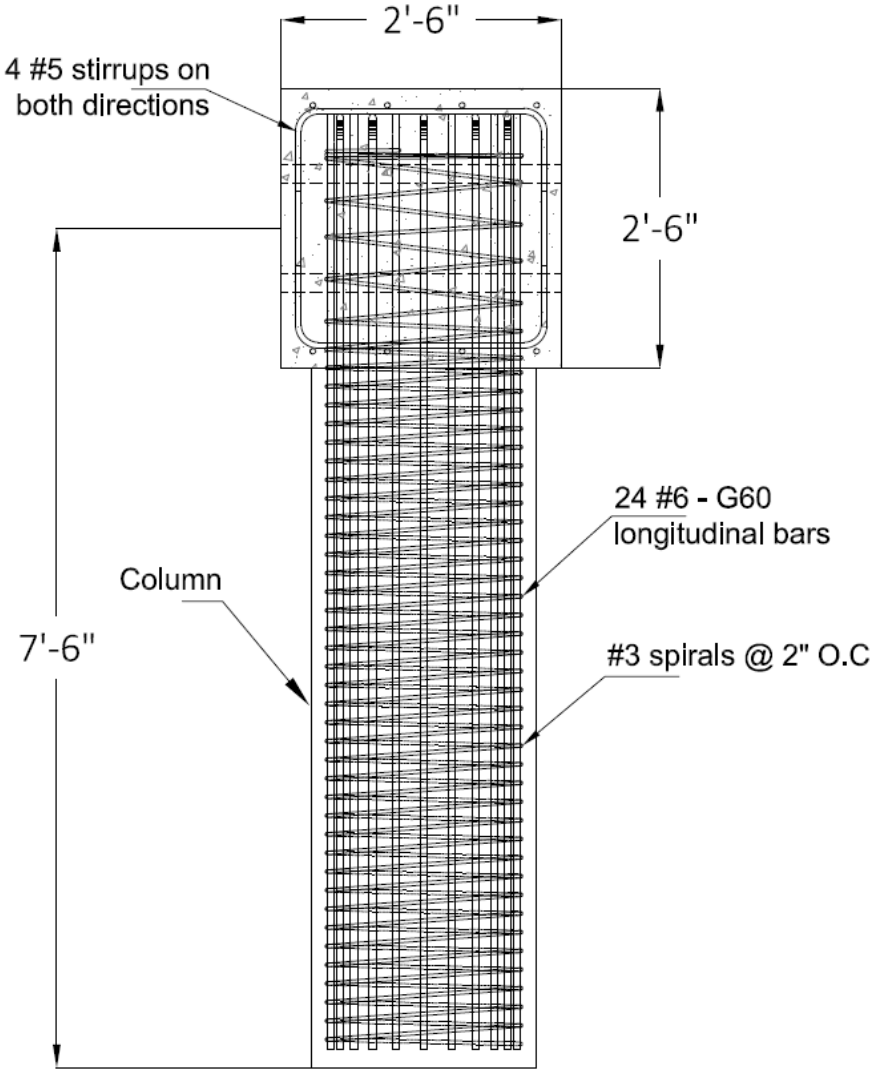


Figure 3-2. Column reinforcement for SJS1 to SJS4 - elevation view

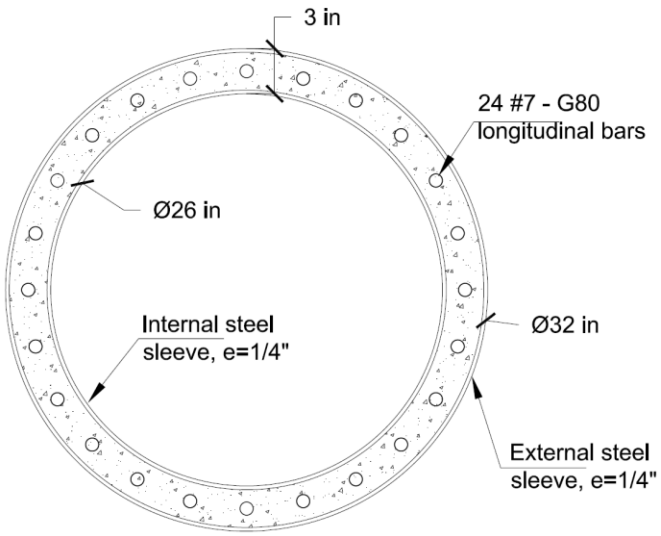


Figure 3-3. External socket reinforcement for SJS1 to SJS4 - plan view

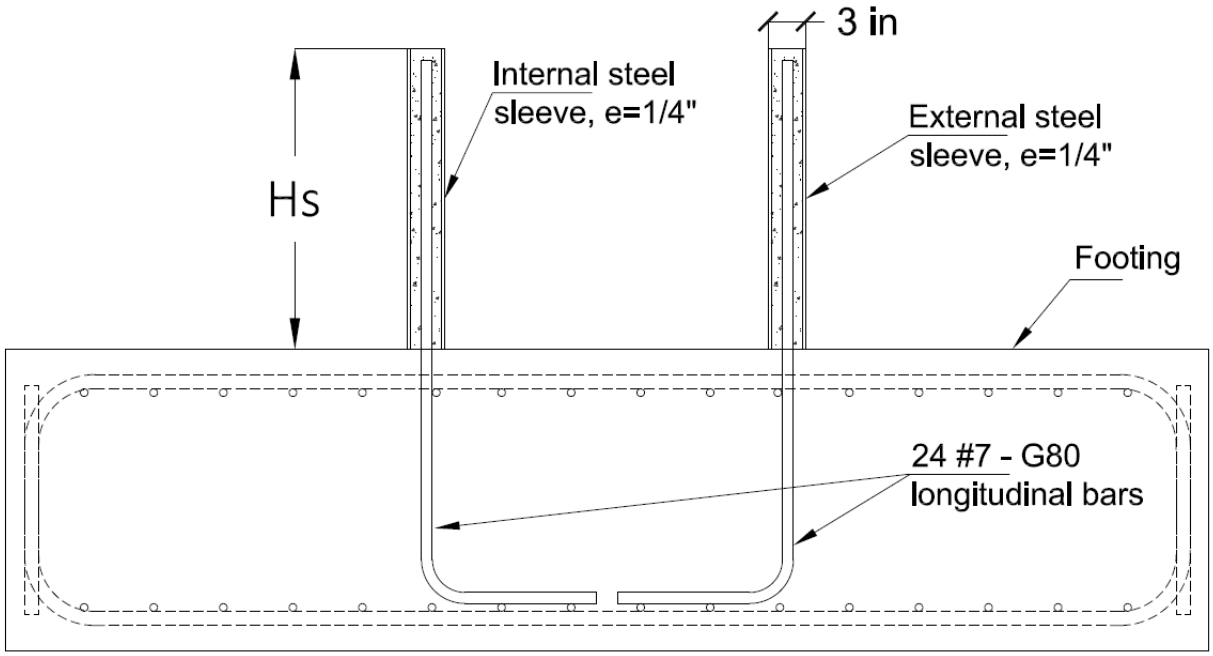


Figure 3-4. External socket reinforcement for SJS1 to SJS4 - elevation view

The specimens SJS 5 and SJS 6 had a clear height of 7'-6″ and a diameter of 18″, resulting in a height-to-diameter aspect ratio of 5.0, with a concrete cover of 1″. The columns were reinforced with 20 Grade 60-A706 #5 longitudinal bars ($\rho l = 2.4\%$). The transverse steel consisted of #3 spirals spaced at 2.0″ intervals ($\rho s = 1.3\%$). Figure 3-5 and Figure 3-6 show the plan and elevation views of the column reinforcement, respectively.

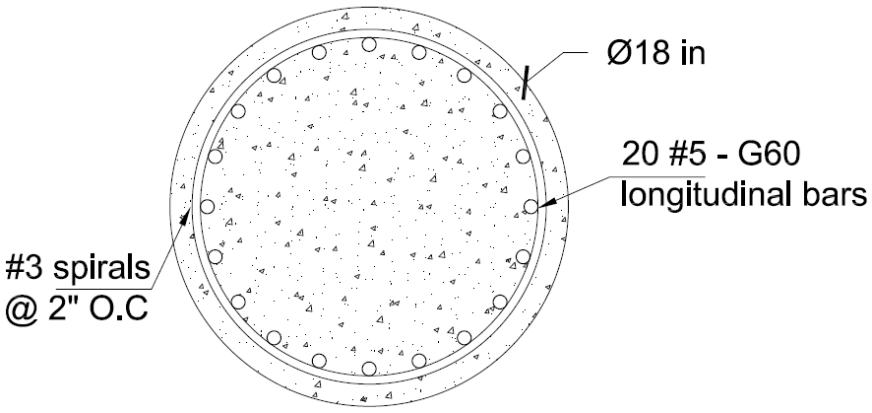


Figure 3-5. Column reinforcement for SJS5 and SJS6 - plan view

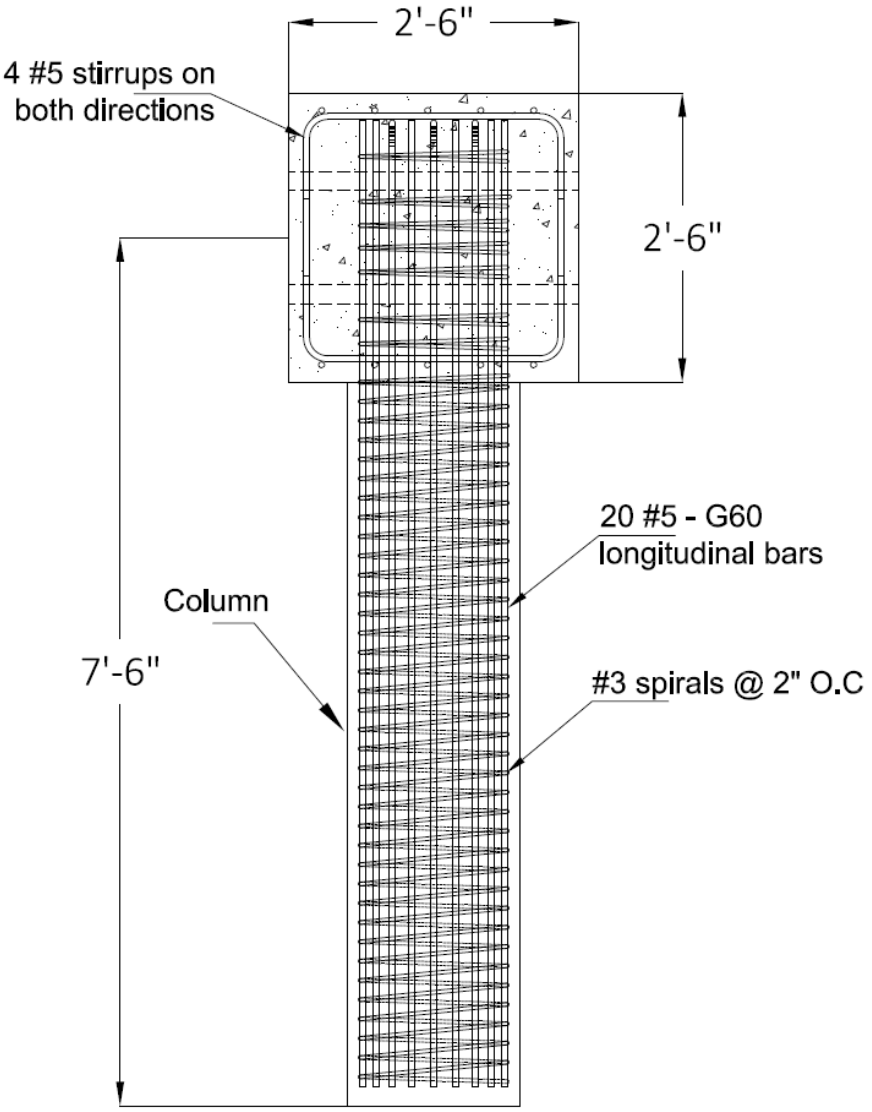


Figure 3-6. Column reinforcement for SJS5 and SJS6 - elevation view

The specimens SJS 7 and SJS 8 had a clear height of 7'-6″ and a diameter of 18″, resulting in a height-to-diameter aspect ratio of 5.0. The columns were reinforced with 20 Grade 60-A706 #5 longitudinal bars (ρl = 2.4%) and an external steel tube to confine the concrete, resulting in an RCFST column. The clear distance between the longitudinal reinforcing steel and the inner surface of the steel tube was 1″. The RCSFT has two cross-sections with varying steel thicknesses. The portion of the column inside the external connection has a reduced steel thickness to minimize the forces transmitted to the external socket. Figure 3-7 and Figure 3-8 show the plan view of the RCFST column inside and outside of the external socket connection, and Figure 3-9 shows the elevation view of the RCFST column reinforcement.

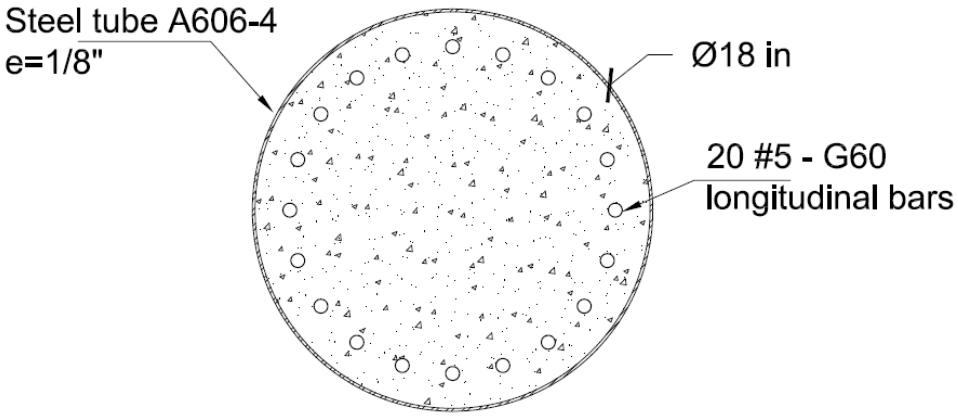


Figure 3-7. Column reinforcement for SJS7 and SJS8 (inside socket connection) - plan view

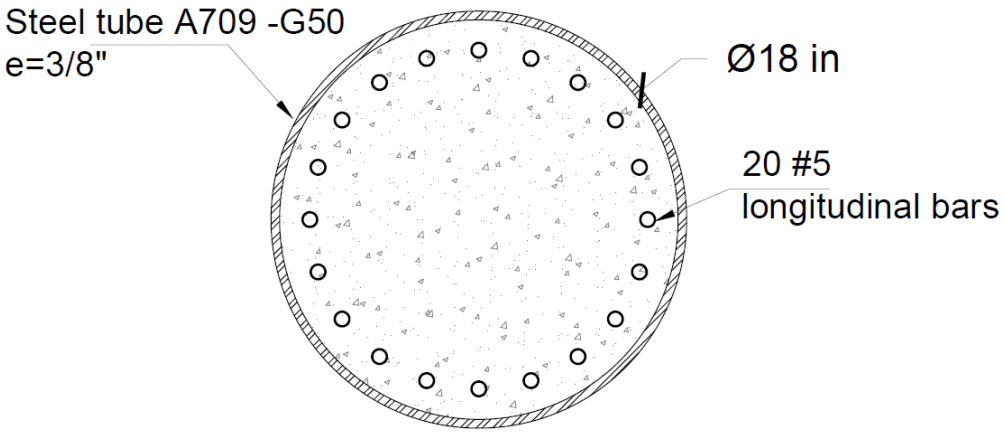


Figure 3-8. Column reinforcement for SJS7 and SJS8 (outside socket connection) - plan view

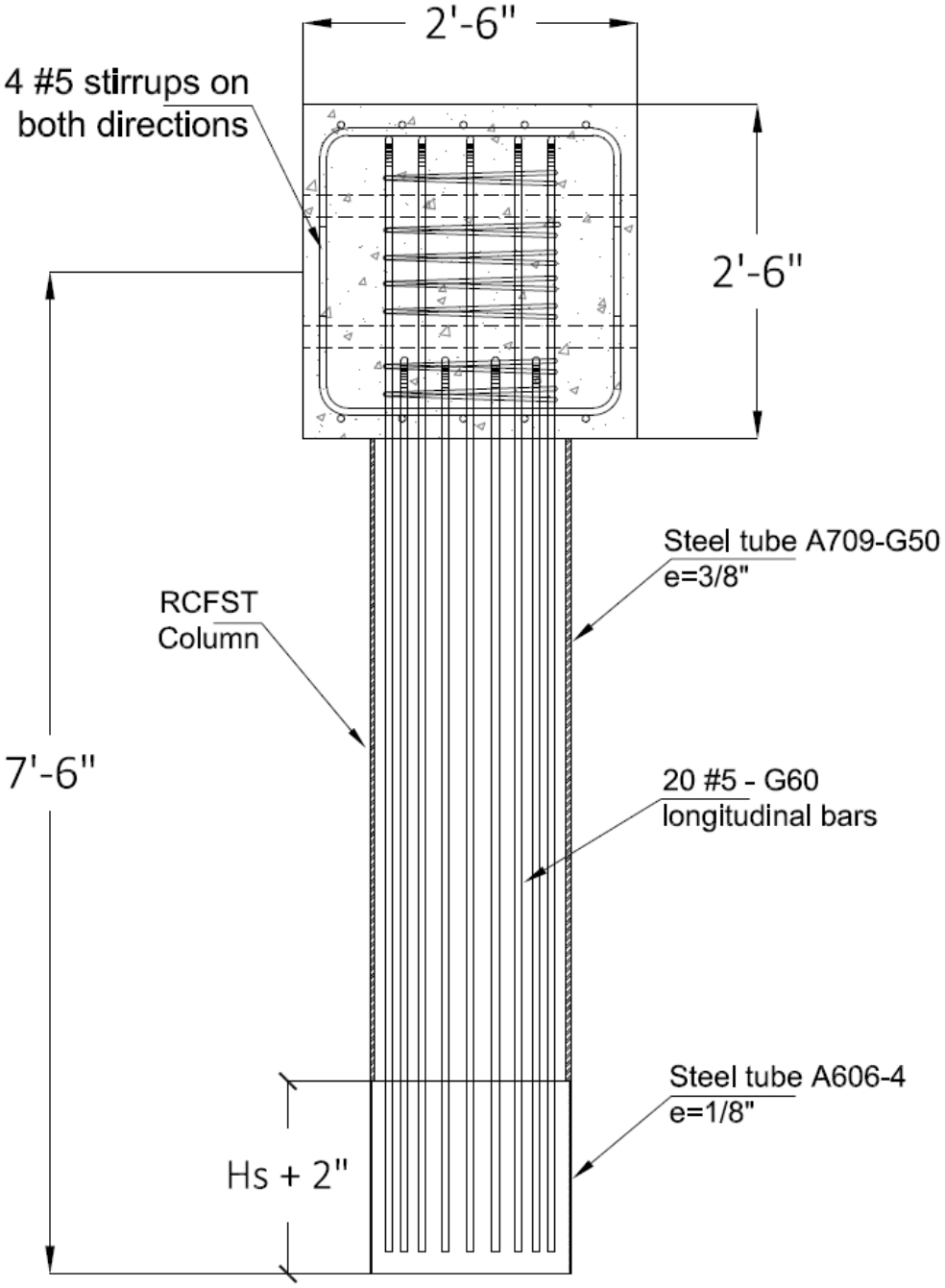


Figure 3-9. Column reinforcement for SJS7 and SJS8 - elevation view

The longitudinal reinforcement of the external socket for specimens SJS 5 to SJS 8 consisted of 20 Grade 80-A706 #6 bars. Steel sleeves-A36, 1/4″ thick, were used to enclose the concrete, and the socket wall thickness was 3-1/4 inches. Figure 3-10 and Figure 3-11 show the reinforcement plan of the external socket wall. The external socket height varied, as shown in Table 3-1.

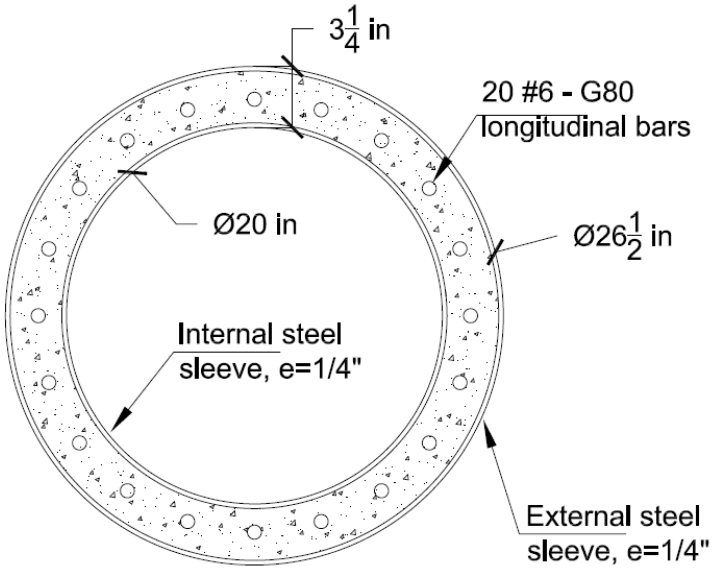


Figure 3-10. External socket reinforcement for SJS5 to SJS8 - plan view

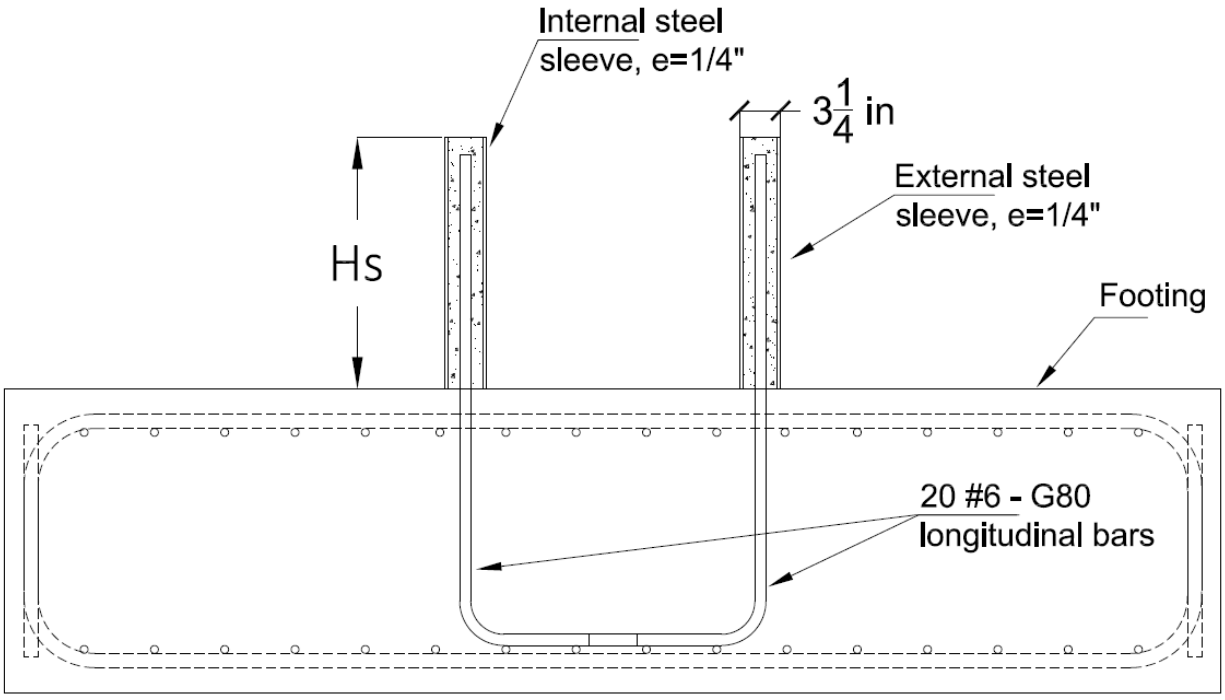


Figure 3-11. External socket reinforcement for SJS5 to SJS8 - elevation view

The footing and cap beam were designed as capacity-protected components, and the same detailing was used throughout all the specimens. Figure 3-12 shows the footing dimensions while Figure 3-13, Figure 3-14, and Figure 3-15 show the plan and lateral views of the footing reinforcement, respectively.

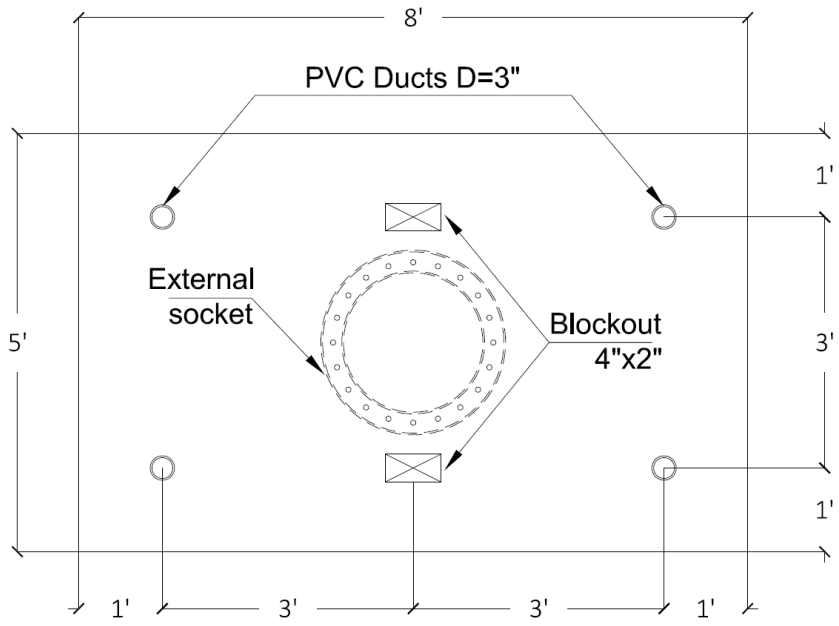


Figure 3-12. Footing dimensions - plan view

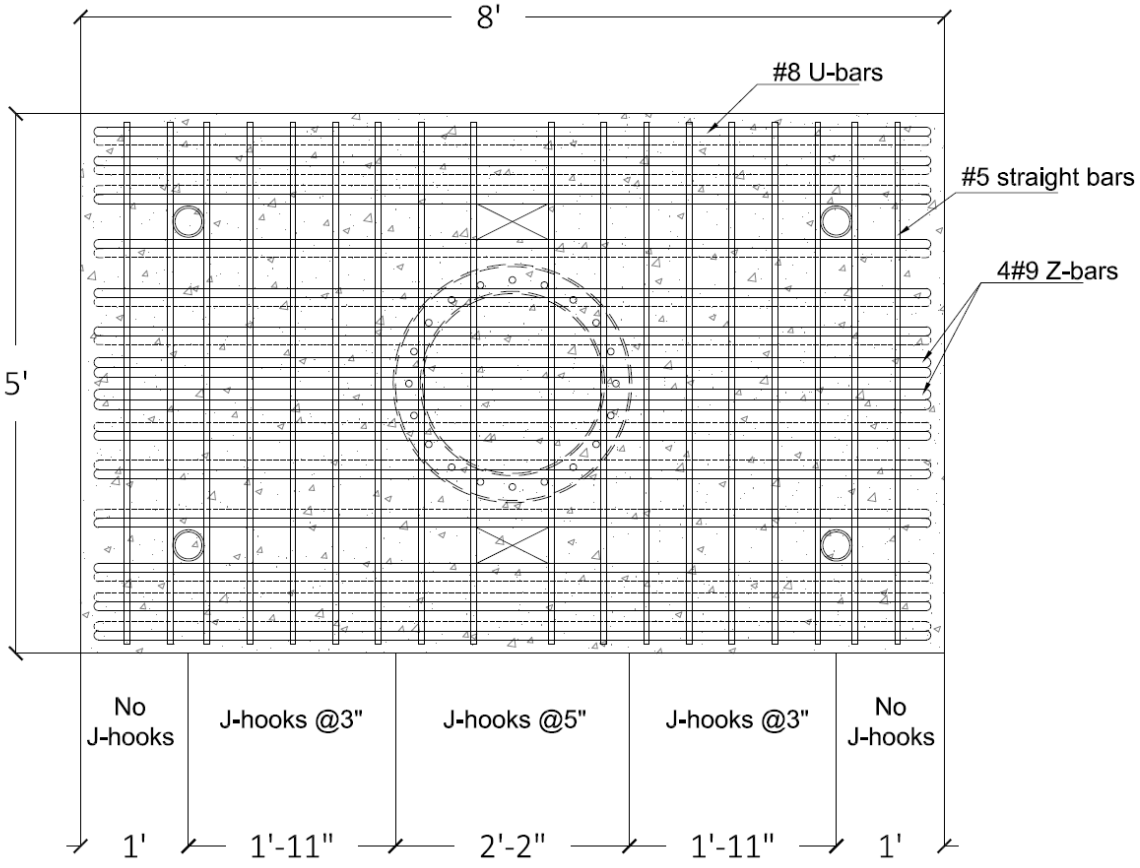


Figure 3-13. Footing reinforcement - plan view

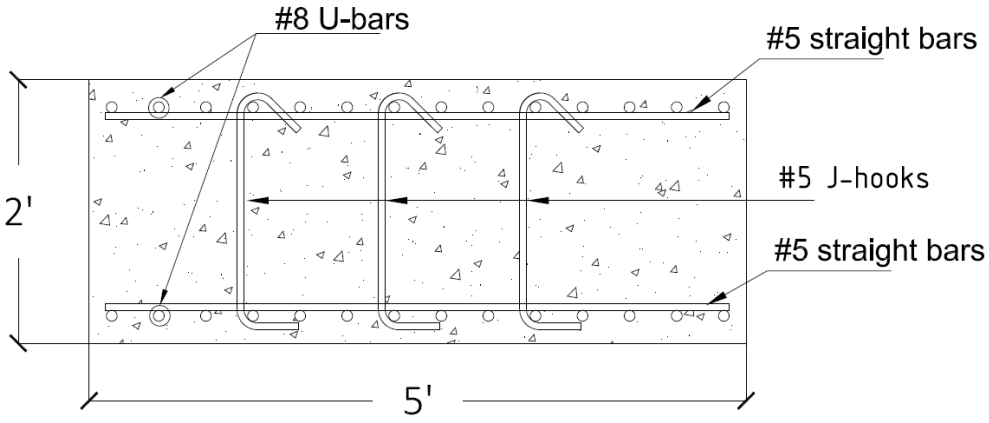


Figure 3-14. Footing reinforcement – front view

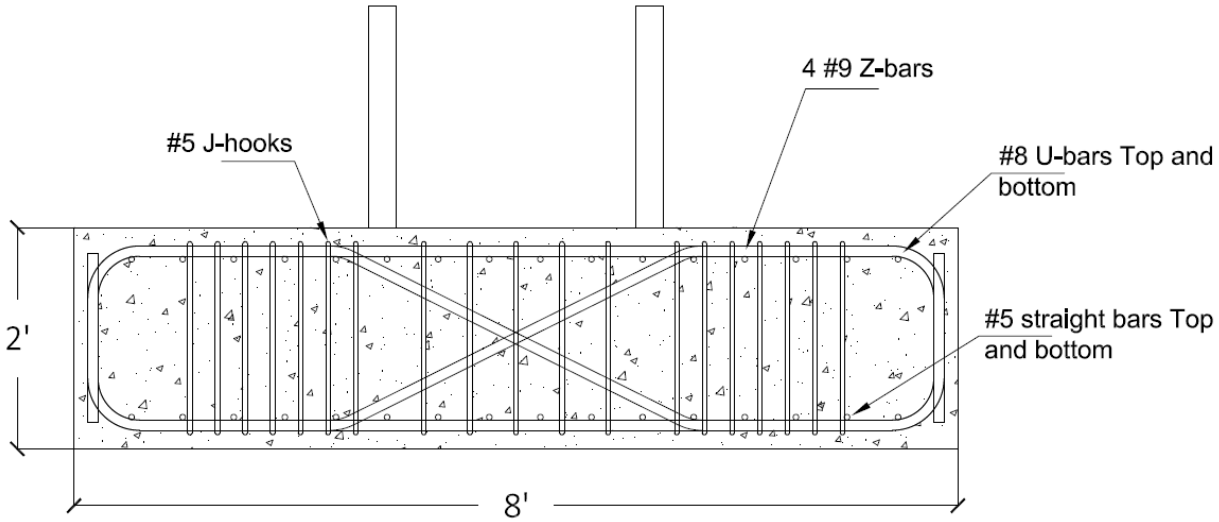


Figure 3-15. Footing reinforcement - side view

3.3. Construction Process

This section describes the construction process for the footings, external socket wall, RC columns, and RCFST columns. Notably, SJS 2, SJS 3, and SJS 5 did not sustain significant damage (as explained in Chapter 4), allowing for the repair of the column portions inside the sockets, which led to the tests SJS 3, SJS 4, and SJS 6, respectively. Schematics of the construction processes are provided: Figure 3-16 for the footing and external socket, Figure 3-17 for the RC column and cap-beam, Figure 3-18 for the RCFST column and cap-beam, and Figure 3-19 for the repair process.

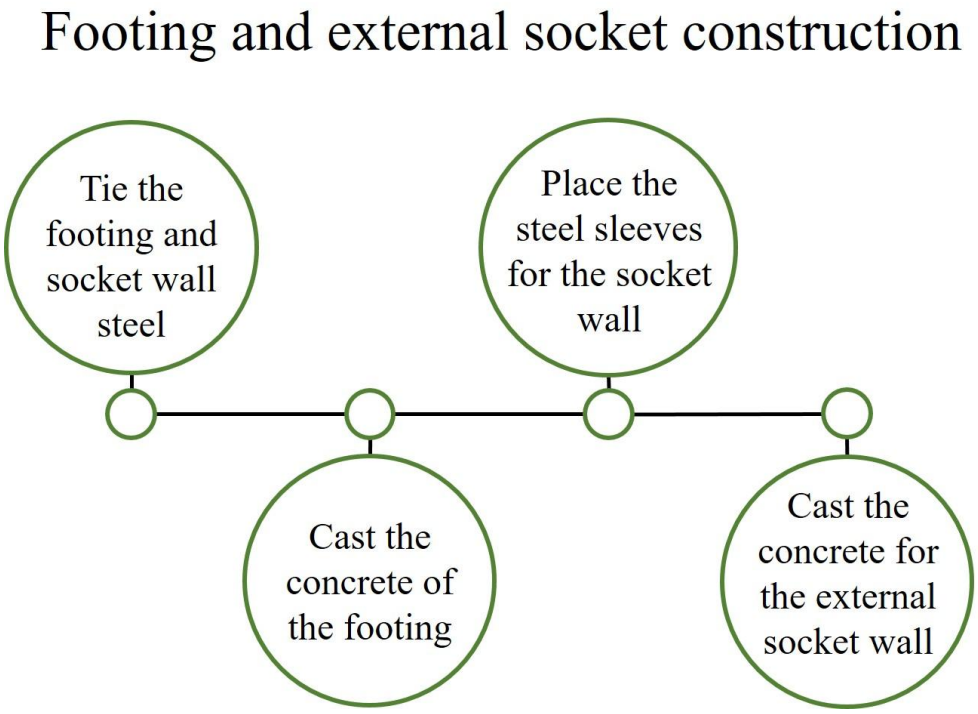


Figure 3-16. Construction sequence for footing and external socket

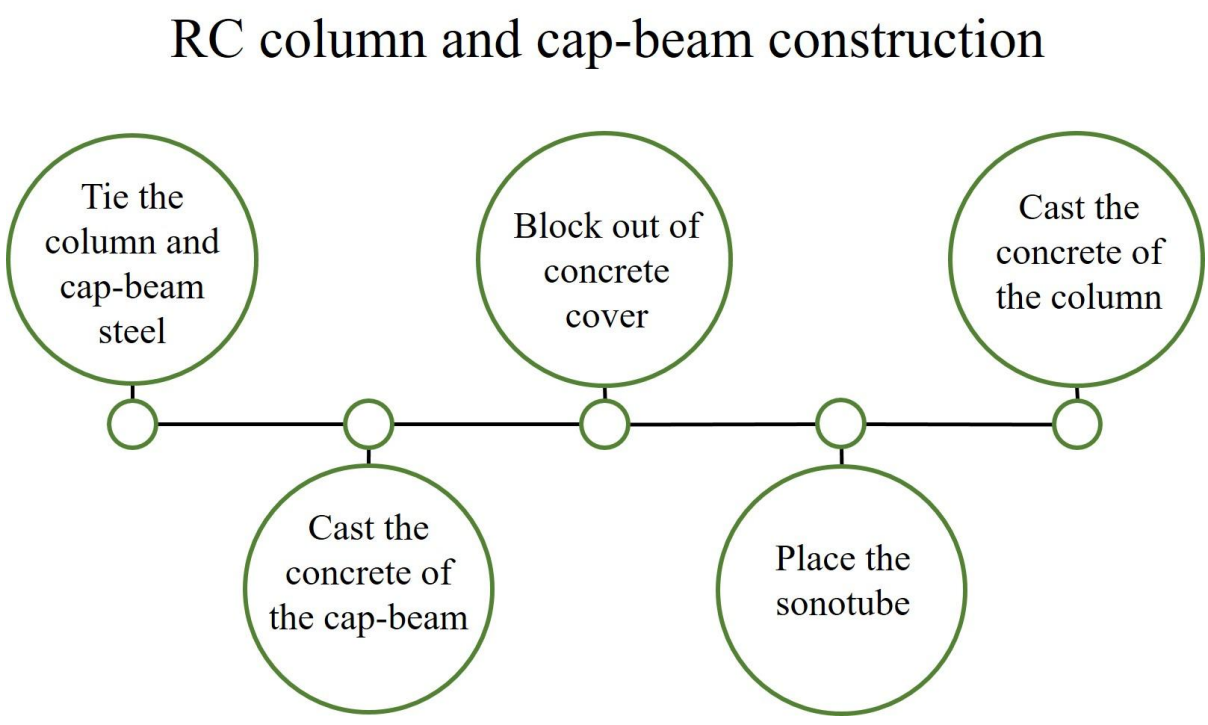


Figure 3-17. Construction sequence for RC column and cap-beam

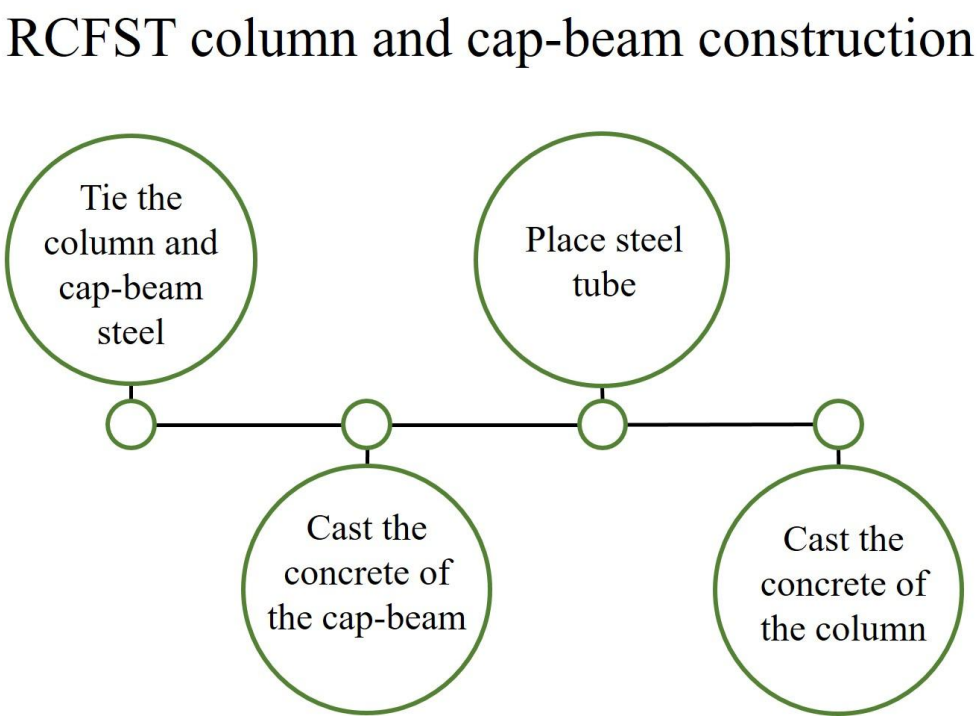


Figure 3-18. Construction sequence for RCFST column and cap-beam

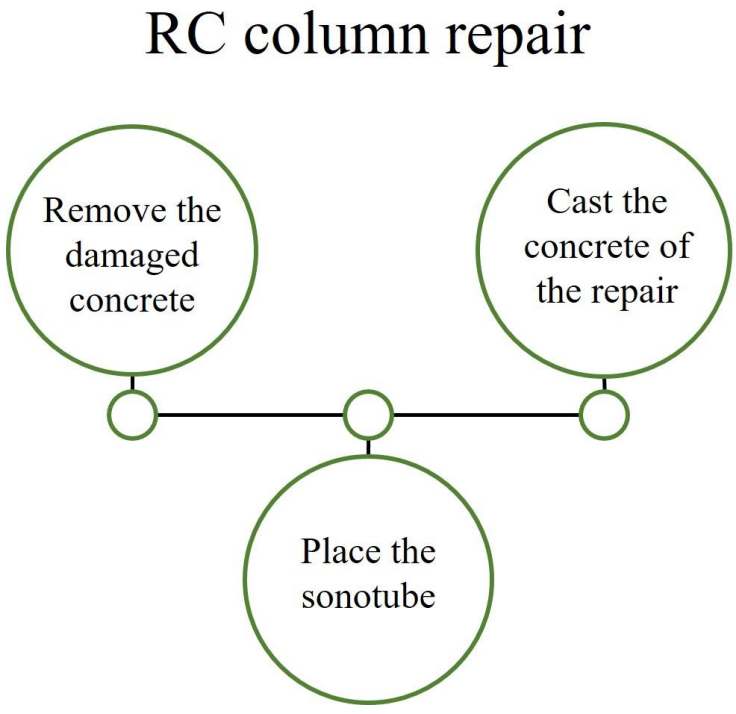


Figure 3-19. Construction sequence for RC column repair

3.3.1. Footing and external socket

To start the footing construction process, a steel formwork was assembled with one wall left open to facilitate the placement of the footing reinforcement, as shown in Figure 3-20. Four PVC pipes of 3 inches and a 4″x10″ foam block were placed in the formwork to allocate post-tension bars and axial load bars, respectively. The longitudinal Z-bars and U-bars were tied together before being placed in the formwork (see Figure 3-21) and set on 1.5-inch slab bolsters, with temporary bars at the top to maintain the correct position of the reinforcement, as shown in Figure 3-22.

Next, the rest of the longitudinal steel and the bottom layer of the transverse steel were placed in the formwork, as shown in Figure 3-23. Afterward, the top layer of transverse steel was added, and J-hooks were positioned near the pipes (see Figure 3-24). The longitudinal steel for the external socket was placed using a wooden template, as shown in Figure 3-25, and the remaining J-hooks were positioned around the external socket reinforcement, as shown in Figure 3-26.



Figure 3-20. Formwork assembly for the footing



Figure 3-21. Z-bars and U-bars tied together



Figure 3-22. Placement of PVC pipes and foam block-outs



Figure 3-23. Placement of Z-bars and U-bars for the footing



Figure 3-24. Placement of J-hooks near the PVC pipes



Figure 3-25. Placement of longitudinal reinforcement of the external socket wall



Figure 3-26. Placement of J-hooks around the external socket reinforcement

Finally, the remaining formwork wall was added, and the footing was ready for casting. Figure 3-27 shows the footing ready to be cast with the reinforcement for the external socket connection. Figure 3-28 and Figure 3-29 show the footing after casting and after removing the formwork.



Figure 3-27. Formwork and reinforcing steel ready for casting

The next step was removing the mill scale from the external sleeve for instrumentation. The cleaned sleeve can be seen in Figure 3-30. Then, the two sleeves were placed around the external reinforcement of the socket, as shown in Figure 3-31. As shown in Figure 3-32 and Figure 3-33, the external sleeve was painted with primer, and silicone was applied at the bottom of both sleeves to prevent concrete leakage during casting.



Figure 3-28. Footing surface after casting



Figure 3-29. Footing concrete after removing the formwork



Figure 3-30. External steel sleeve with mill scale removed



Figure 3-31. Placement of steel sleeves for external socket connection



Figure 3-32. Placement of silicon on the internal socket sleeve



Figure 3-33. Placement of silicone on the external socket sleeve

After the silicone dried, the external sleeve was wrapped in plastic to facilitate cleaning after casting. Figure 3-34 shows the external socket wall after casting. Finally, the external sleeve was cleaned, and a final coat of paint was given (see Figure 3-35). Additionally, it was speckled for Digital Image correlation (DIC), as shown in Figure 3-36.



Figure 3-34. External socket wall after casting



Figure 3-35. Final coating of external socket sleeve



Figure 3-36. Speckle pattern on external socket sleeve

3.3.2. RC column and cap-beam

The longitudinal bars of the RC column were placed through a continuous spiral and tied to two wooden exterior supports in a circular configuration, as shown in Figure 3-37. As shown in Figure 3-38, wooden spacers were used to maintain a clear spacing of 1.625 inches for the transverse reinforcement, and interior circular wooden supports were used at two locations to ensure the column circular shape remained consistent throughout its height, as can be noticed in Figure 3-39. The spirals were then tied to the longitudinal steel at a uniform spacing of 2 inches from center to center. Each spiral and longitudinal bar intersection was tied diagonally to prevent slipping, as can be noticed in Figure 3-40.



Figure 3-37. Setup for building the steel cage of the RC column



Figure 3-38. Wood spacer for transverse steel of the RC column



Figure 3-39. Internal wood template for the longitudinal steel of the RC column

Next, the formwork for the cap beam was constructed using 2x4 wood and 3/4″ plywood, as shown in Figure 3-41. Holes were drilled in the cap beam box for 2-inch diameter horizontal PVC pipes used for the actuator connection. Care was taken to ensure the cap beam was square and level.



Figure 3-40. Transverse reinforcement tied to the longitudinal reinforcement of the RC column



Figure 3-41. Cap beam formwork

Once the cap-beam formwork was ready, the longitudinal steel cage was removed from the wooden templates. The reinforcing steel cage for the cap beam was then tied to the column steel (see Figure 3-42) and was located inside the cap-beam formwork. The PVC pipes were inserted, and the cap-beam formwork was closed in preparation for casting. Figure 3-43 shows the PVC pipes and the steel of the cap beam inside the formwork. The column reinforcement and cap beam formwork were moved to a flat casting slab for the casting process, as shown in Figure 3-44, where it can be noticed that the column was leveled using straps attached to the formwork. A photo of the cap beam after removing the formwork is shown in Figure 3-45.

For instrumentation purposes, foam strips were tied to the transverse and longitudinal bars to block the concrete cover at the expected location of the plastic hinge on the column. The foam was wrapped in plastic to ensure easy removal of the concrete paste after casting. Figure 3-46 and Figure 3-47 show the block-outs on the column. As shown in Figure 3-48, a Sonotube (heavy-duty cardboard formwork) was placed around the reinforcing steel to give the circular shape to the column.



Figure 3-42. Cap beam reinforcement and steel cage of the RC column



Figure 3-43. Cap beam reinforcement inside the formwork

With the Sonotube in place, the final step was casting the column. Figure 3-49 shows the column after casting, and Figure 3-50 shows the columns after removing the Sonotube.

Figure 3-51 shows the column after the block-outs were removed. The exposed reinforcing steel bars were cleaned with a wire brush to remove the excess cement paste, as shown in Figure 3-52. After cleaning the reinforcement, the column was ready to be inserted into the external socket connection.



Figure 3-44. Cap beam formwork and steel reinforcement for RC column ready to cast



Figure 3-45. Cap beam after removing the formwork



Figure 3-46. Foam block-outs attached to the longitudinal and transverse reinforcement



Figure 3-47. Foam block-out along the plastic hinge region of the RC column



Figure 3-48. Sonotube placed around the longitudinal reinforcement of the RC column



Figure 3-49. Concrete column after casting



Figure 3-50. Concrete column after removing the Sonotube



Figure 3-51. Concrete column after removing the block-outs



Figure 3-52. Concrete column after cleaning the reinforcing bars

3.3.3. RCFST column and cap-beam

The longitudinal bars of the RCFST column were tied to two wooden exterior supports in a circular configuration, with interior circular wooden supports used at two locations to ensure the column circular shape remained consistent throughout its height, as shown in Figure 3-53. Circular hoops were placed along the column height to maintain the longitudinal steel position until the cap beam was cast. The reinforcing steel cage for the cap beam was then tied to the column longitudinal steel. Figure 3-54 shows the cap beam reinforcement tied to the column reinforcing steel.



Figure 3-53. Setup for building the steel cage of the RCFST column



Figure 3-54. Cap beam reinforcement and steel cage of the RCFST column

The formwork for the cap beam followed the same procedure as that used for the RC column (see Figure 3-41 and Figure 3-43). Once the cap-beam formwork was ready, the longitudinal steel cage was removed from the wooden templates and placed inside the formwork. Straps were used to level and stabilize the column before casting. Figure 3-55 shows the column and cap beam ready to be moved to a flat slab for casting. A photo of the cap beam after removing the formwork is shown in Figure 3-56.

The mill scale at the expected plastic hinge region was removed from the two circular steel tubes for instrumentation purposes. Figure 3-57 and Figure 3-58 show the cleaned steel tubes for the 3/8″ thickness and 1/8″ thickness, respectively.



Figure 3-55. Cap beam formwork and steel reinforcement for RCFST column ready to cast



Figure 3-56. Cap beam of the RCFST after removing the formwork

The steel tubes were placed around the column longitudinal reinforcing steel, as seen in Figure 3-59. Silicone was applied where the steel tube touched the cap beam to avoid leakage during casting, and duct tape was used to seal the interface between the two steel tubes for easy removal after casting. Figure 3-60 shows the casting of the RCFST column.



Figure 3-57. Circular steel tube (3/8″) without mill scale at the expected plastic hinge region



Figure 3-58. Circular steel tube (1/8″) without mill scale at the expected plastic hinge region



Figure 3-59. Steel tubes placed around the longitudinal reinforcement of the RCFST column



Figure 3-60. Casting of RCFST column

After casting, a final coat of paint was applied to the portion of the column where the plastic hinge is expected, and then a speckle pattern for DIC was added, as shown in Figure 3-61.



Figure 3-61. Speckle pattern on circular steel tubes for RCFST column

3.3.4. RC column repair

After each experimental test, the column and external socket connection were examined for damage. For specimens SJS 2, SJS 3, and SJS 5, the damage was concentrated on the portion of the column inside the external socket connection. However, the column above the connection interface remained elastic, with only minor cracks in the concrete column. Therefore, it was

decided to repair only the damaged portion of the column, using higher concrete strength as suggested by the analytical model (discussed in Chapter 6) to ensure failure occurs above the external socket connection interface.

Initially, any damaged concrete was carefully removed with a chipping hammer until the remaining concrete was solid. Figure 3-62 shows the process of removing the loose concrete, and Figure 3-63 shows the column after the loose material was removed.



Figure 3-62. Removing damaged concrete for repair

After cleaning the column, it was placed vertically, and a Sonotube was positioned around the repair area. Silicone was applied at the interface with the concrete column to prevent leakage during the casting of the repaired portion. Figure 3-64 shows the casting of the repaired portion of the column, and Figure 3-65 shows the repaired column after removing the Sonotube.



Figure 3-63. Repaired area without loose material



Figure 3-64. Casting of the repaired RC column



Figure 3-65. Repaired RC column

3.3.5. Integrating Column into external socket

An overhead crane was employed to insert the column into the external socket connection. The crane brought the column to a horizontal position, as seen in Figure 3-66. The next step involved placing hooks on the cap beam to lift the column vertically, as Figure 3-67 shows.



Figure 3-66. Positioning the column horizontally

The crane was then used to align the column with the socket and slowly lowered into place. Figure 3-68 illustrates the column positioned inside the external socket connection, and Figure 3-69 shows the leveling of the column once it was inserted into the connection.

After the column was inserted into the socket, grout was used to fill the gap between the column and the external socket walls. The gap was filled carefully to ensure uniform distribution of the material around the connection. Figure 3-70 shows the casting of the grout around the column within the socket while Figure 3-71 depicts the column and external socket connection after the grout has filled the gap between both structural elements.



Figure 3-67. Lifting the column in a vertical position

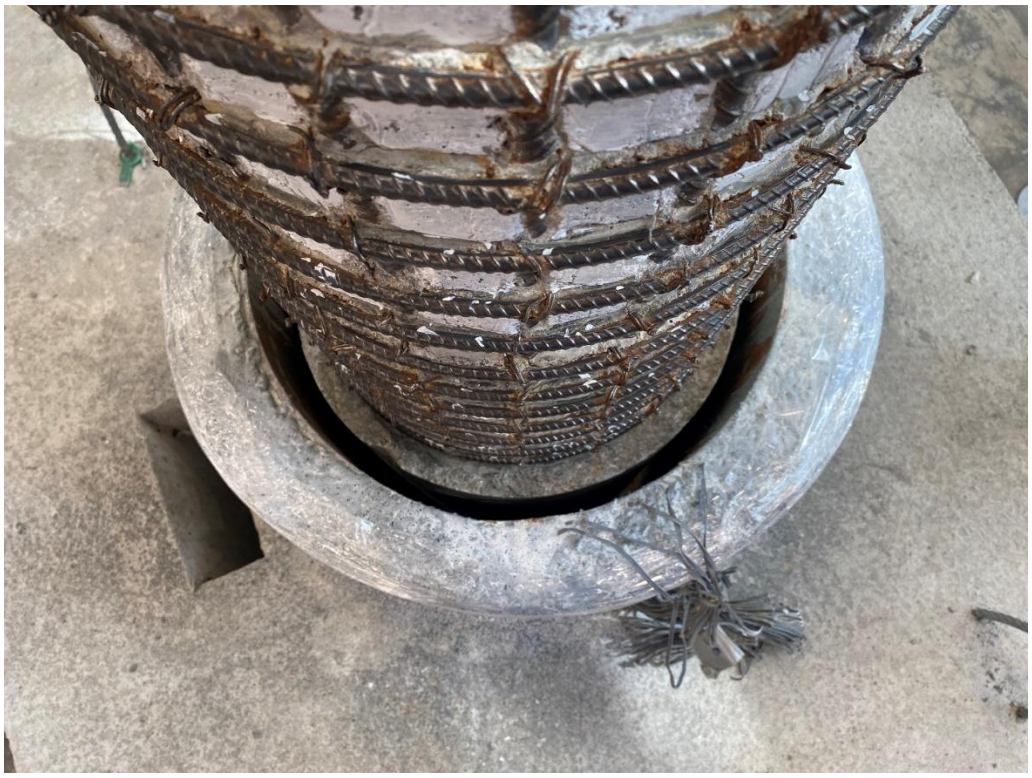


Figure 3-68. Inserting the column in the external socket connection

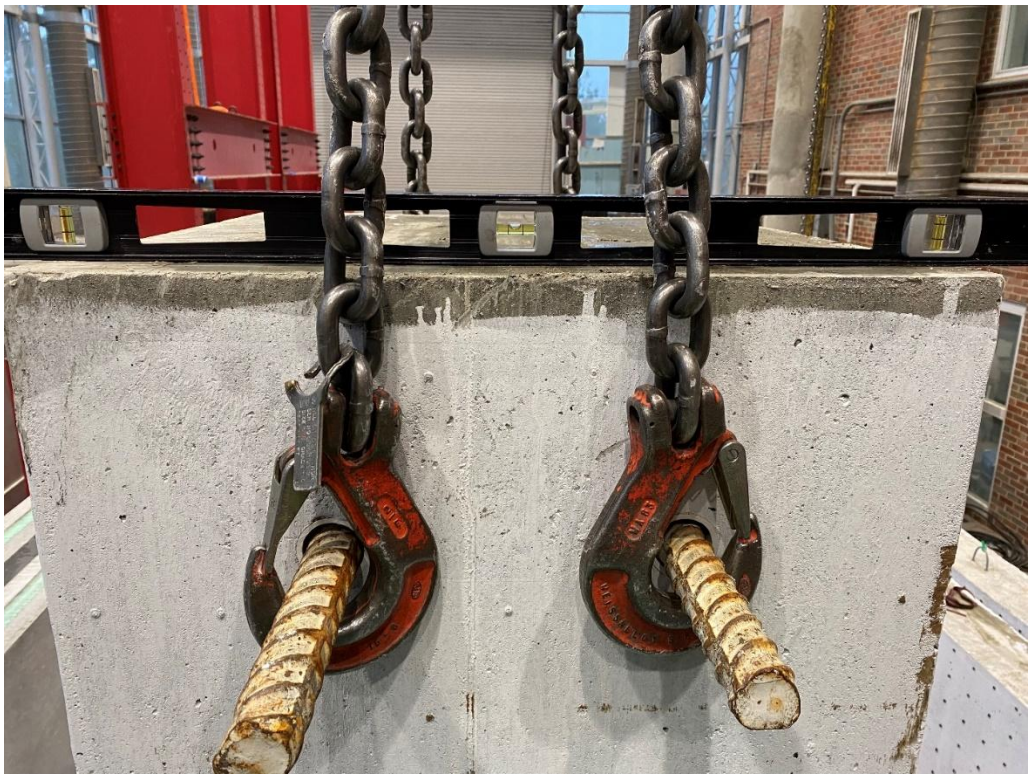


Figure 3-69. Leveling the column in the external socket



Figure 3-70. Casting the grout to fill the gap between structural elements



Figure 3-71. Column and external socket connection after filling the gap with grout

3.4. Material tests for column and connection components

Material tests were conducted on the concrete, grout, and steel used in each specimen to assess mechanical properties, including concrete strength, grout strength, and the stress-strain characteristics of the different types of steel utilized in the experimental program.

Concrete and grout compression tests were performed on 4″x8″ cylinders in accordance with ASTM C39 [21]. We used ASTM C39 for testing the grout material because, in most cases, coarse aggregate was included in the grout mix, making ASTM C39 a more appropriate standard for evaluating its compressive strength. As summarized in Table 3-2, concrete casting dates for each specimen are provided for the footings, cap beams, columns, repaired columns, external socket walls, and grout. On the test day, material test cylinders corresponding to each structural component were tested. These cylinders were stored under the same environmental conditions as the specimens to ensure consistency. The test day strengths for footing and cap beams, columns, repaired columns, external socket wall, and grout are provided in Table 3-3, Table 3-4, Table 3-5, Table 3-6, and Table 3-7, respectively.

Table 3-2. Casting dates of structural components

Specimen	Footing and cap beam	Column	Repaired column (inside socket connection)	Socket wall	Grout
SJS 1	21-Jun-2021	8-Oct-2021	N/A	31-Aug-2021	22-Dec-2021
SJS 2			N/A	27-Apr-2022	4-May-2022
SJS 3			3-Aug-2022	3-Aug-2022	14-Sep-2022
SJS 4			25-Jan-2023	3-Aug-2022	9-Mar-2023
SJS 5	12-Jan-2023	31-Mar-2023	N/A	15-Sep-2023	9-Oct-2023
SJS 6			30-Nov-2023	15-Sep-2023	15-Dec-2023
SJS 7	9-Aug-2023	28-Aug-2023	N/A	10-Oct-2023	8-Nov-2023
SJS 8		6-Apr-2024	N/A	23-Apr-2024	1-May-2024

Table 3-3. Test Day concrete compression strength of footing and cap beam

Structural component	Cylinder	Concrete *f'c* (ksi)
Footing and cap beam (SJS 1 to SJS 4)	1	5.46
	2	5.67
	3	5.69
	average	**5.61**
Footing and cap beam (SJS 5 and SJS 6)	1	4.22
	2	4.23
	3	4.33
	average	**4.26**
Footing and cap beam (SJS 7 and SJS 8)	1	6.16
	2	6.21
	3	6.28
	average	**6.22**

Table 3-4. Test Day concrete compression strength of columns

Structural component	Cylinder	Concrete *f'c* (ksi)
RC column (SJS 1 to SJS 4)	1	6.32
	2	5.87
	3	5.93
	average	**6.04**
RC column (SJS 5 and SJS 6)	1	6.69
	2	7.04
	3	6.61
	average	**6.78**
RCFST column (SJS 7)	1	5.53
	2	5.71
	3	5.53
	average	**5.59**

Table 3-4. Test Day concrete compression strength of columns (continued)

Structural component	Cylinder	Concrete *f'c* (ksi)
RCFST Column (SJS 8)	1	6.72
	2	7.30
	3	6.98
	average	**7.00**

Table 3-5. Test Day concrete compression strength of the repaired portion of columns

Structural component	Cylinder	Concrete *f'c* (ksi)
Repaired portion of columns (SJS 3)	1	10.07
	2	9.89
	3	9.99
	average	**9.98**
Repaired portion of columns (SJS 4)	1	8.26
	2	8.50
	3	8.03
	average	**8.27**
Repaired portion of columns (SJS 6)	1	8.00
	2	11.18
	3	8.39
	average	**9.19**

Table 3-6. Test Day concrete compression strength of external socket wall

Structural component	Cylinder	Concrete *f'c* (ksi)
Socket wall (SJS 1)	1	12.97
	2	12.93
	3	12.89
	average	**12.93**

Table 3-6. Test Day concrete compression strength of external socket wall (continued)

Structural component	Cylinder	Concrete *f'c* (ksi)
Socket wall (SJS 2)	1	10.39
	2	8.90
	3	9.25
	average	**9.51**
Socket wall (SJS 3 and SJS 4)	1	12.64
	2	11.71
	3	11.98
	average	**12.11**
Socket wall (SJS 5 and SJS 6)	1	14.55
	2	12.66
	3	14.76
	average	**13.99**
Socket wall (SJS 7)	1	11.45
	2	11.49
	3	10.91
	average	**11.28**
Socket wall (SJS 8)	1	13.86
	2	13.39
	3	14.91
	average	**14.05**

Table 3-7. Test Day grout compression strength

Structural component	Cylinder	Grout *f'cg* (ksi)
Grout (SJS 1)	1	7.75
	2	8.27
	3	7.64
	average	**7.89**

Table 3-7. Test Day grout compression strength (continued)

Structural component	Cylinder	Grout *f'cg* (ksi)
Grout (SJS 2)	1	6.98
	2	6.19
	3	6.44
	average	**6.53**
Grout (SJS 3)	1	9.36
	2	8.96
	3	9.06
	average	**9.13**
Grout (SJS 4)	1	9.55
	2	9.66
	3	9.93
	average	**9.71**
Grout (SJS 5)	1	10.01
	2	10.33
	3	10.65
	average	**10.33**
Grout (SJS 6)	1	10.10
	2	9.93
	3	9.93
	average	**9.99**
Grout (SJS 7)	1	9.05
	2	9.08
	3	9.06
	average	**9.06**
Grout (SJS 8)	1	5.90
	2	5.97
	3	5.59
	average	**5.82**

Tension tests were performed to quantify the stress-strain properties of the reinforcing steel used in the construction of the columns, footings, and external sockets. These tests were conducted in accordance with ASTM A370 [22]. For reinforcing bars, stress-strain curves were obtained using Optotrak LED markers, as shown in Figure 3-72, while strain gauges were used for the sleeves and tubes, as shown in Figure 3-73.



Figure 3-72. Instrumented reinforcing bar with Optotrak LED markers

Figure 3-74, Figure 3-75, and Figure 3-76 illustrate the stress-strain responses of the steel used for concrete reinforcement, the socket wall's external and internal sleeves, and the RCFST column's steel tube that goes inside the connection, respectively. Table 3-8 summarizes the tension test parameters for the various components of the specimens. The yield strain of the steel was determined at the transition point where the linear portion of the stress-strain curve ends, and the non-linear portion begins.



Figure 3-73. Instrumented coupon steel with strain gage

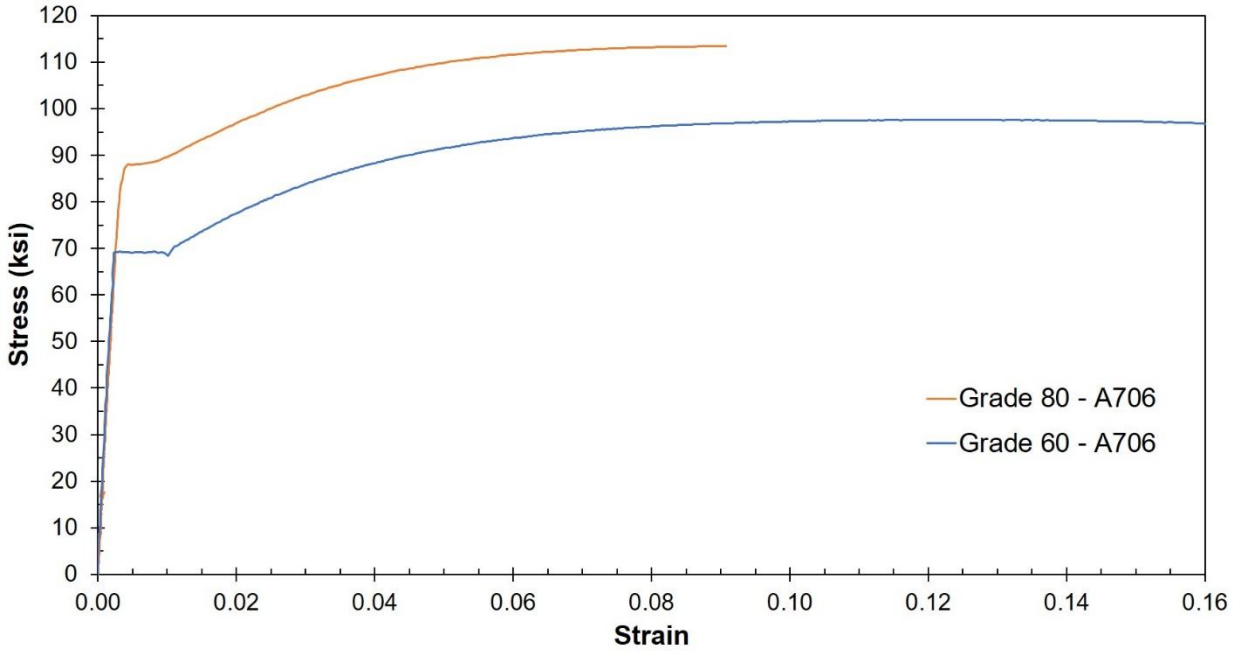


Figure 3-74. Stress-strain curves for reinforcing steel bars used in SJS 1 to SJS 8

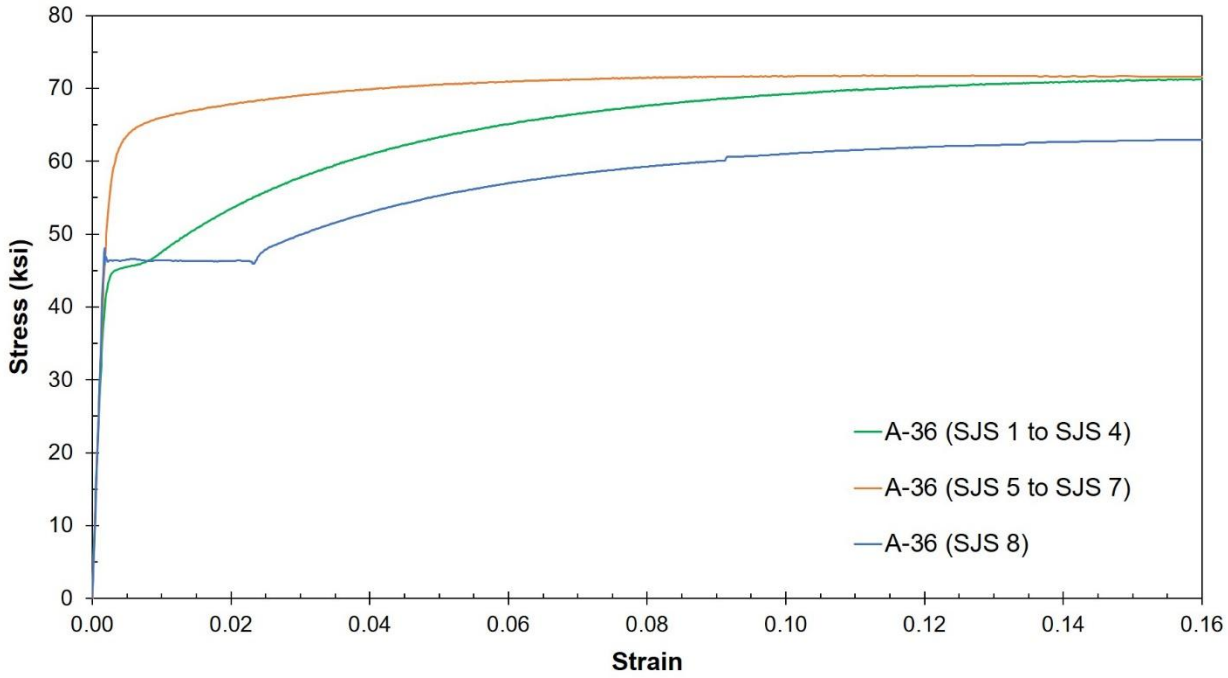


Figure 3-75. Stress-strain curves for steel sleeves used in SJS 1 to SJS 8

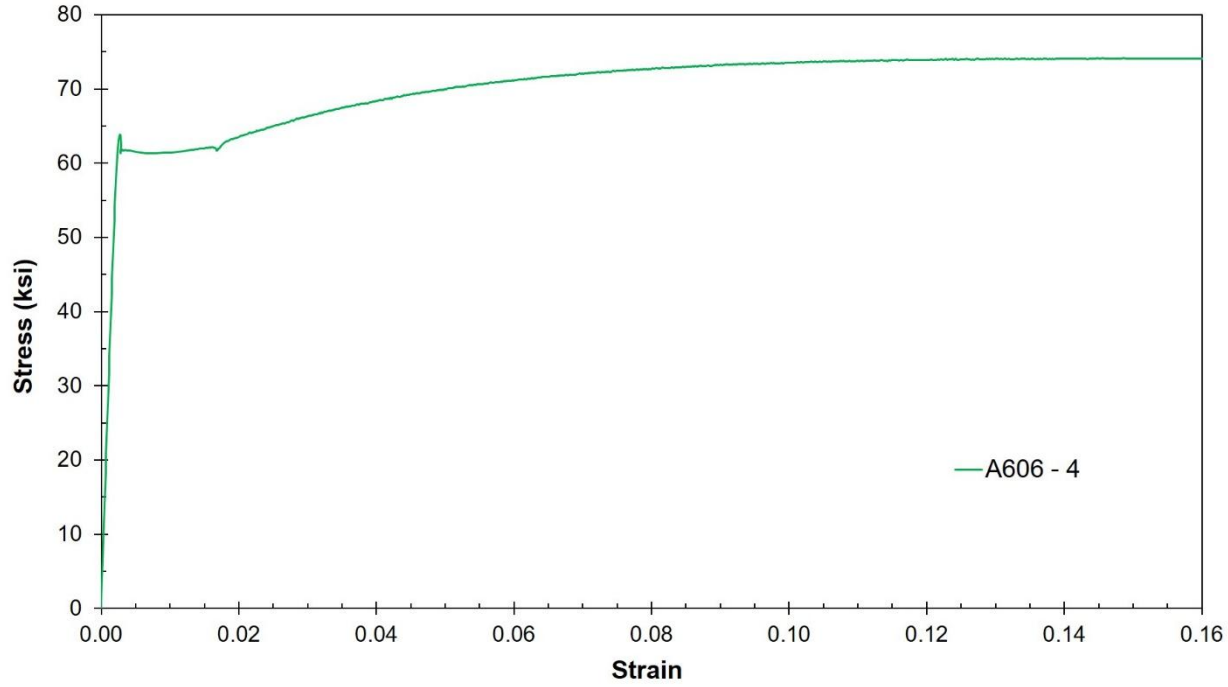


Figure 3-76. Stress-strain curves for steel tubes used in SJS 7 and SJS 8

Table 3-8. Tension test parameters

Steel	Yield stress (ksi)	Yield strain (%)	Maximum stress (ksi)	Strain at maximum stress (%)
Longitudinal steel of the column and footing (Grade 60 - A706)	68.4	0.23	97.6	12.6
Longitudinal steel of the socket (Grade 80 - A706)	86.5	0.37	113.4	9.07
Steel of socket sleeve for SJS 1 to SJS 4 (A-36)	42.6	0.21	71.3	17.6
Steel of socket sleeve for SJS 5 to SJS 7 (A-36)	55.0	0.24	71.2	11.5
Steel of socket sleeve for SJS8 (A-36)	46.6	0.18	63.1	20.1
Steel tube inside the external connection (A606-4)	60.6	0.23	74.0	15.7
Steel tube outside the external connection (A709-G50)	56.8	---	80.3	23.4

3.5. Experimental Test Setup

The large-scale specimens were subjected to lateral loading using a 220-kip hydraulic actuator with a 40-inch stroke, anchored to a strong wall via a steel plate. The specimen was positioned at mid-stroke. To apply an axial load ratio of 5% to the column, two 100-kip hydraulic jacks were used, interconnected with a third jack in a Universal Testing Machine (UTM) to maintain a constant axial load. The UTM automatically compensated for any pressure variations, ensuring consistent load application throughout the test. Gypsum cement was cast between the footing and the strong floor to optimize surface contact and increase friction. Additionally, the foundation was post-tensioned to the strong floor using four 1-3/8″ bars, each stressed to 100 kips. Figure 3-77 and Figure 3-78 illustrate the experimental test setup.

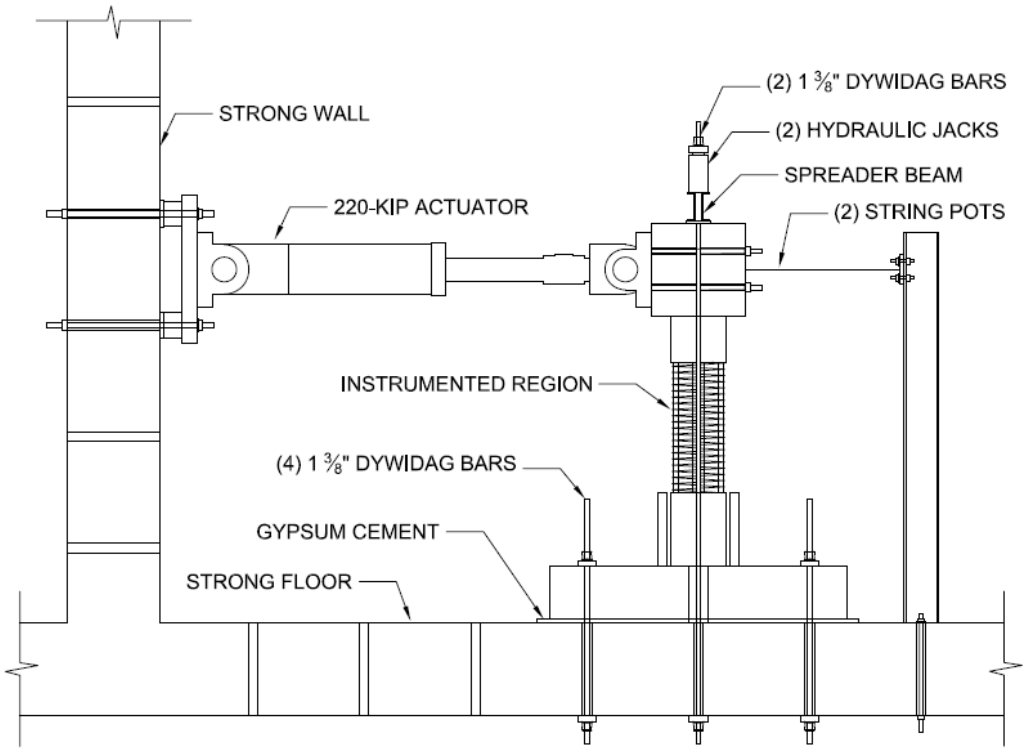


Figure 3-77. Experimental test setup – lateral view



Figure 3-78. Experimental test setup – actual test setup

3.5.1. Loading Protocol

During the experiments, the specimens were subjected to a reverse cyclic unidirectional quasi-static load applied at the top of the column, as illustrated in Figure 3-79. Positive force and displacement values indicate an applied force pushing the column north, while negative values signify forces pulling the column south.

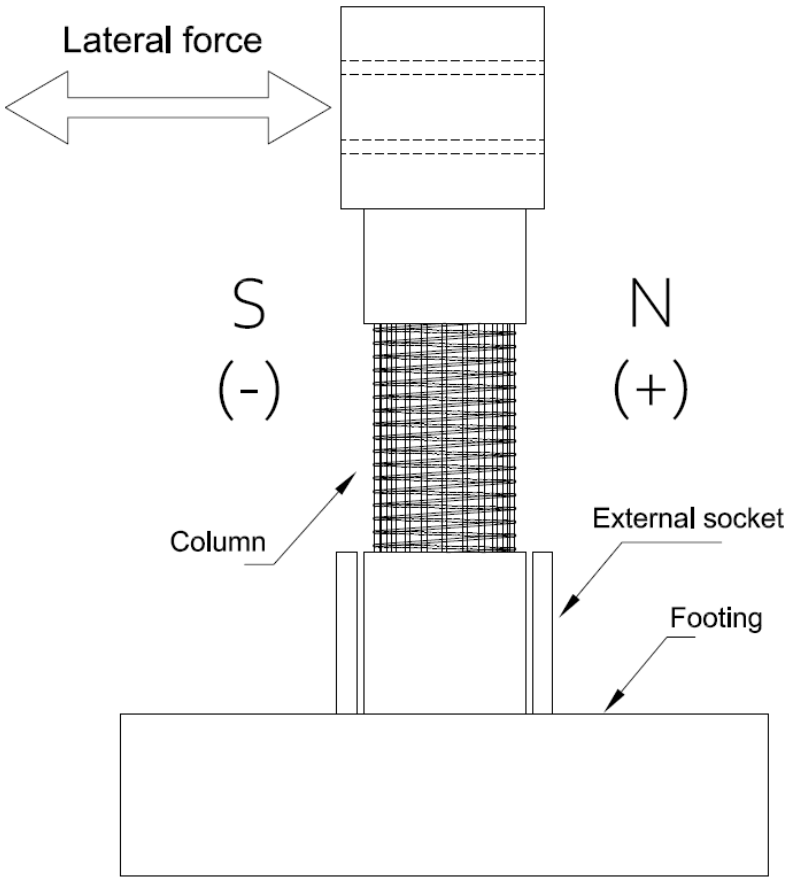


Figure 3-79. Loading scheme of the large-scale column test

The loading protocol for the eight large-scale tests included a single cycle at quarter, half, three-quarters, and yield displacement. Beyond the first yield, the protocol involved three cycles at increasing increments of displacement ductility. The displacement ductility of one is determined by extrapolating the experimentally measured first yield displacement to the nominal moment capacity of the cross-section, as expressed in Equation 3-1. To calculate any displacement at any

given ductility level ″n″, the displacement at ductility one is multiplied by the desired ductility ″n″ as described in Equation 3-2. For instance, the displacement at ductility three is obtained by multiplying the displacement at ductility one by three. This method provides a consistent reference point for assessing the column inelastic behavior and is a standard approach used in both research and engineering practice.

Equation 3-1 $$\mu_1 = \frac{M_N}{M'_y}\Delta'_y$$

Equation 3-2 $$\mu_n = n * \mu_1$$

Displacement ductility is crucial for identifying the inelastic response of the structural element, which is important for understanding its ability to displace without significant strength degradation during a seismic event. Figure 3-80 provides an example of a loading protocol for the experimental program.

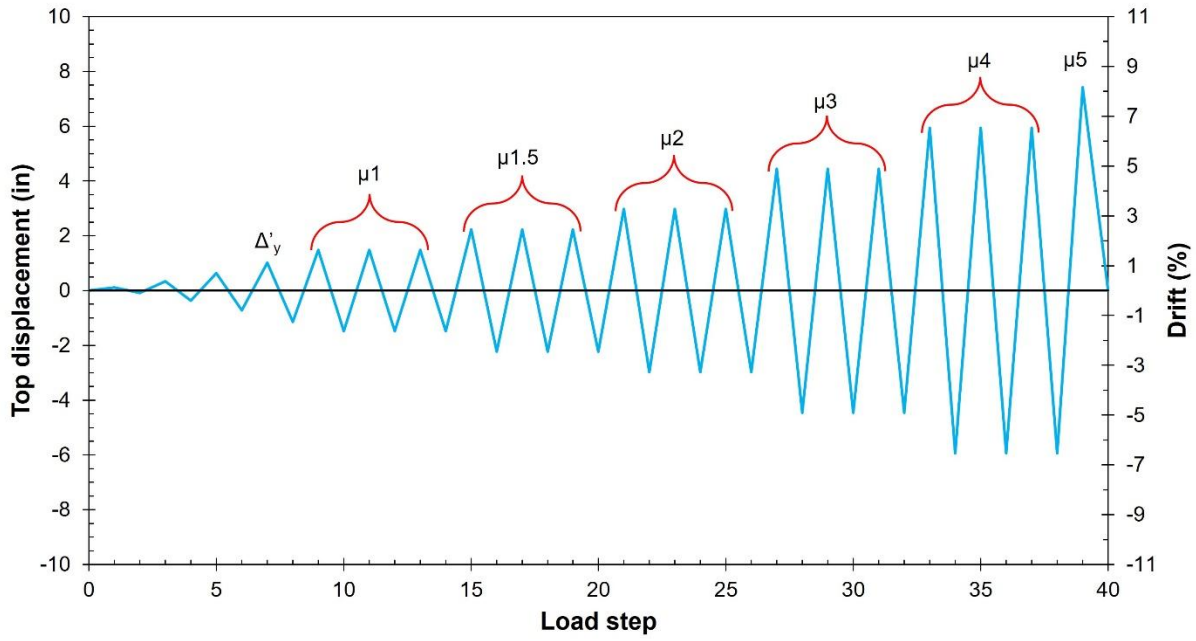


Figure 3-80. Example of loading protocol for the experimental program

The experimental tests were conducted until the recorded force dropped by approximately 40% from the maximum value observed during the experiment. Figure 3-81 illustrates a force-displacement response, where the force degradation and subsequent force drop can be observed.

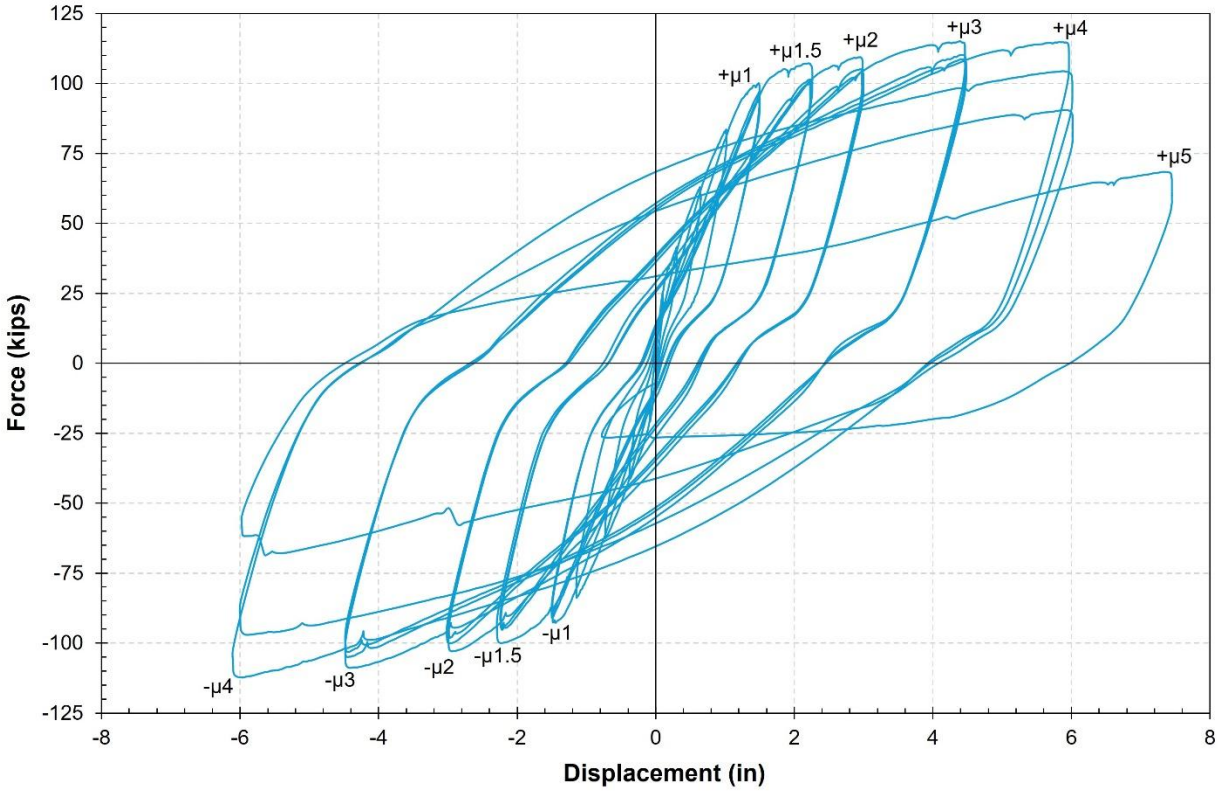


Figure 3-81. Force-displacement response of SJS 1

3.5.2. Instrumentation

Global displacement measurements of the specimens were obtained using two string potentiometers strategically positioned at the center and edge of the cap beam to monitor potential twisting of the specimen. Figure 3-82 provides a close-up of the string potentiometer locations.

The longitudinal bars in the external socket wall were equipped with 12 strain gauges to measure the strains in the reinforcement. Figure 3-83 illustrates the placement of these strain gauges on the socket longitudinal bars.

To measure the displacement response of the RC columns, the Optotrak Certus HD system was employed, utilizing 288 LED markers placed on exposed reinforcing steel at the anticipated plastic hinge locations of the specimens. Calibrated cameras recorded the LEDs, allowing for the capture of the three-dimensional displacement history of the longitudinal bars and spirals. This

data facilitated the determination of the axial and bending strain of the column reinforcing steel, as well as the shear deformation of the specimen. Figure 3-84 shows the distribution of LED markers on the extreme reinforcing steel of the column.



Figure 3-82. Actual location of string potentiometers

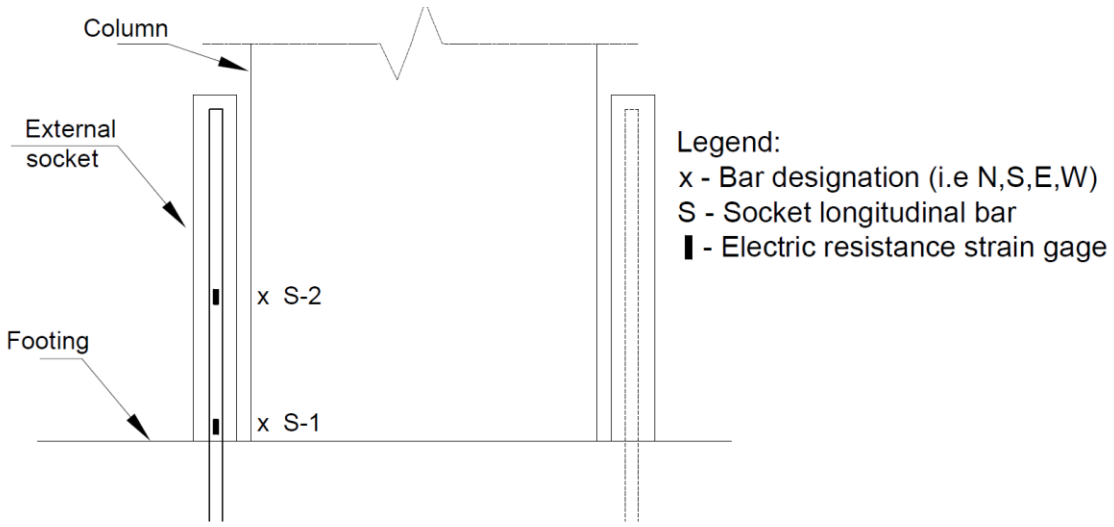


Figure 3-83. Typical layout of strain gages for external socket longitudinal bars



Figure 3-84. Distribution of LED markers on the south face of the column

Additionally, Digital Image Correlation (DIC) was used to monitor displacements and strains of the external socket sleeve and the steel tube of the RCFST during testing. Two sets of cameras captured approximately two-thirds of the circumference of both the external socket sleeves and the RCFST column at the expected plastic hinge region. Figure 3-85 shows the areas captured by the two sets of cameras for the external socket sleeve. Figure 3-86 depicts the overall test setup and instrumentation.

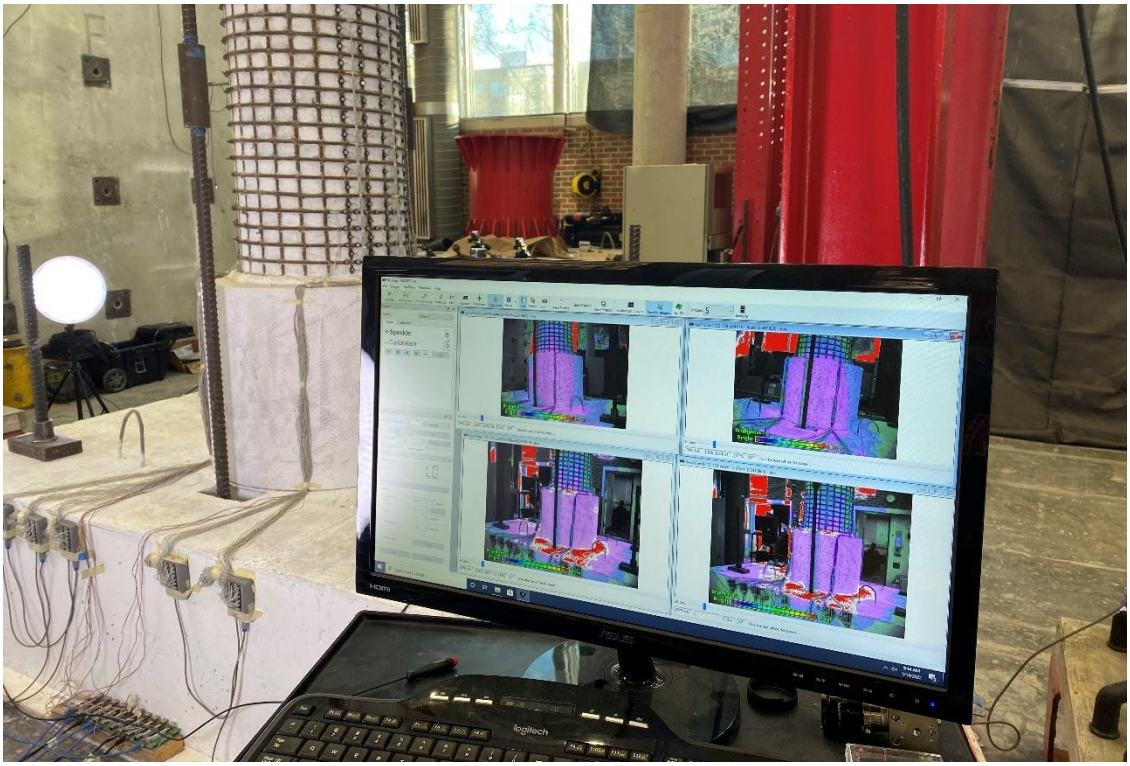


Figure 3-85. View of DIC cameras for an external socket sleeve

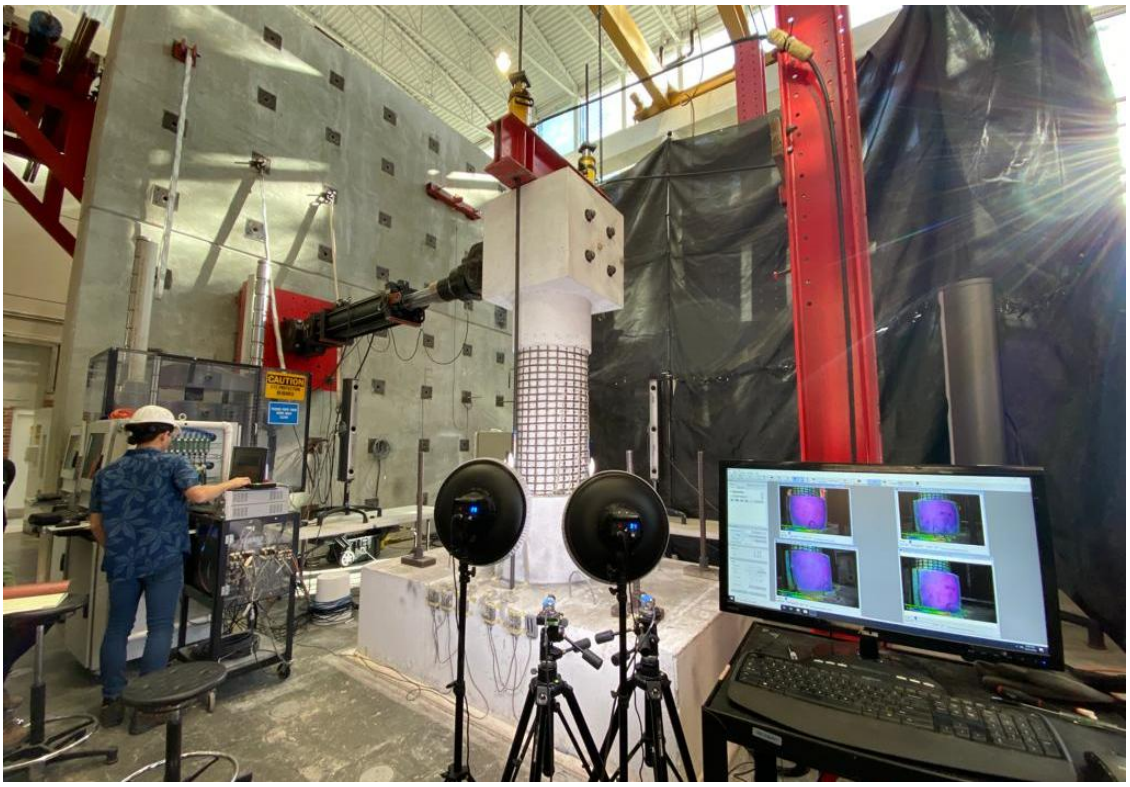


Figure 3-86. Test setup and instrumentation

Chapter 4: Global Response and Experimental Observations

This chapter discusses the global response of the eight large-scale tests by using moment-displacement curves. These curves offer a comprehensive understanding of the column behavior under cyclic lateral loads, providing insights into key characteristics such as stiffness, ductility, and strength degradation. The moment-displacement curve enhances our understanding of column behavior and informs the design process, ensuring that structures can withstand seismic forces and contribute to overall safety and resilience in earthquake-prone regions. Additionally, this chapter includes observations on damage progression throughout the tests. To accurately identify damage to the longitudinal reinforcement, each reinforcing bar was labeled as shown in Figure 4-1. Table 4-1 summarizes the global response and failure modes for specimens SJS 1 through SJS 8.

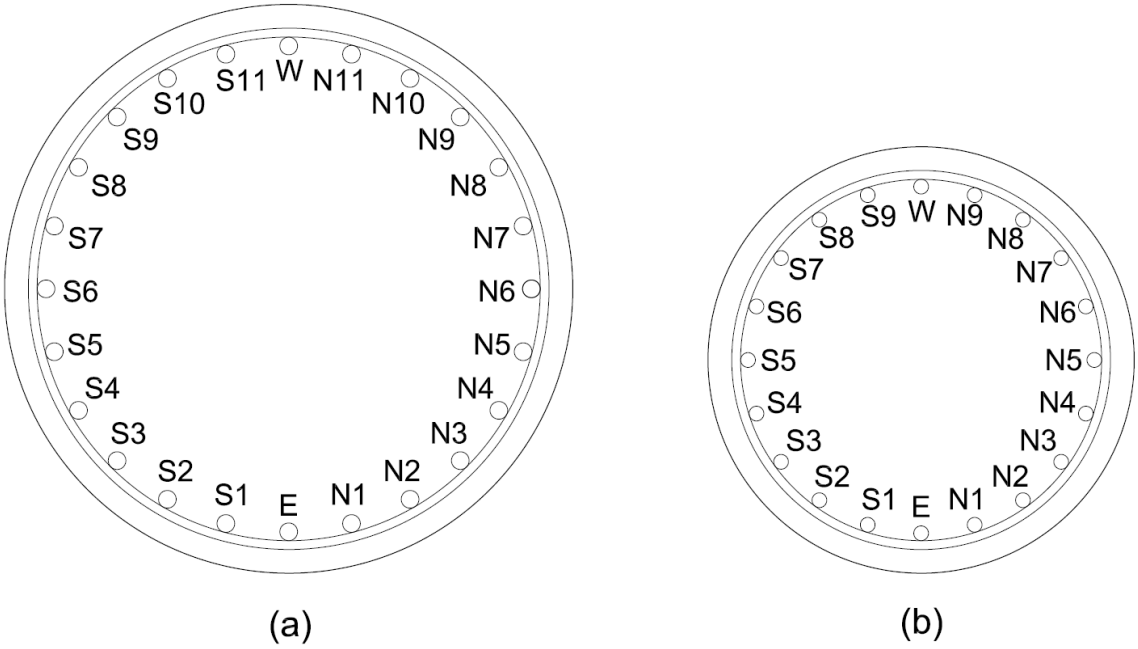


Figure 4-1. Label of longitudinal reinforcing bar. a) For SJS 1 to SJS 4. b) For SJS 5 y SJS6

Additionally, the external socket wall remained without significant damage, with only minor radial cracks appearing in the concrete and grout prior to the first yield displacement for all the specimens. The footing also sustained no visible damage and remained as a capacity-protected element for SJS1 to SJS8.

Table 4-1. Summary of global response of test SJS1 to SJS8

Test	Column nominal capacity (kip-ft)	Peak moment of the column (kip-ft)	Failure mode (Reached limit state)	Ductility at limit state	Drift at limit state
SJS 1 (1.0Dc)	598.8	632.9	Flexural failure of the column. Bar fracture	$-\mu 4^3$	6.6%
SJS 2 (0.75Dc)	598.8	476.4	Grout crushing	$+\mu 1.5^2$	5.9%
SJS 3 (0.85Dc)	598.8	562.6	Grout crushing	$+\mu 3^3$	4.9%
SJS 4 (0.85Dc)	598.8	631.7	Grout crushing	$+\mu 4^1$	6.9%
SJS 5 (0.85Dc)	254.3	256.7	Shear failure of the column inside the external socket	$+\mu 3^3$	5.3%
SJS 6 (0.85Dc)	254.3	271.7	Flexural failure of the column. Bar fracture	$-\mu 4.4^2$	7.8%
SJS 7 (0.85Dc)	301.7	315.7	Shear failure of the column inside the external socket	$+\mu 5^3$	6.2%
SJS 8 (1.22Dc)	308.5	318.6	Flexural failure of the column. Bar fracture	$+\mu 7^1$	7.5%

For tests that include the external socket connection, references to ‘column yield’ and ‘ductility increments’ should not be interpreted as indicative of traditional column yielding. This is because the global displacement includes the effects of rocking and rotation at the external socket, rather than solely the column flexural displacement. As a result, terms like ‘ductility four’ should not be taken to imply that the column reached four times its flexural yielding displacement. Instead, it is more appropriate to consider the loading increments in terms of lateral displacement or drift. However, the term ‘ductility increment’ is retained because of familiarity with engineering practices.

4.1. Specimen SJS1

Column test SJS1 was performed on Friday, January 14, 2022, at the Constructed Facilities Laboratory at NCSU. A summary of the key parameters for SJS1 is provided in Table 4-2.

Table 4-2. Summary of SJS1 parameters

Column parameters	
Longitudinal steel detailing	24#6 A706 (ρ_l=2.34%)
Transverse steel	#3 spirals @ 2 inches (ρ_s=1.04%)
Longitudinal steel yield strength	68.4 ksi
Concrete strength	6.0 ksi
Diameter of the column	24 in
Height of the column	90 in
Axial load ratio	5%
First yield displacement	1.08 in
Equivalent yield displacement	1.48 in
Maximum applied moment at socket interface	632.9 kip-ft
Failure mode	Rupture of longitudinal bars N5, N6, and N7
Socket parameters	
Longitudinal steel detailing	24#7 A706
Longitudinal steel yield strength	86.5 ksi
Steel sleeve yield strength	42.6 ksi
Thickness of steel sleeves	1/4 in
Concrete strength	12.9 ksi
Grout strength	7.9 ksi
Height of external socket	24 in (1.0 Diameter of the column)
Internal diameter	26 in
External diameter	32 in

The column had a clear height of 7'-6″ and a diameter of 24″, resulting in a height-to-diameter aspect ratio of 3.62, with a concrete cover of 1″. It was reinforced with 24 Grade 60-A706 #6 longitudinal bars (ρl = 2.34%), and the transverse reinforcement consisted of #3 spirals with a spacing of 2.0″ center to center (ρs = 1.04%).

The external socket had a height of 24″, resulting in a height-to-diameter ratio of 1.0 (1.0 Dc). The socket longitudinal reinforcement included 24 Grade 80-A706 #7 bars, and the concrete was confined with 1/4″ thick steel sleeves.

4.1.1. Loading Protocol of SJS1

The initial part of the loading history consisted of a single cycle at quarter, half, three-fourths, and full yield displacement. The experimentally measured first yield displacement was Δ'y = 1.08 in.

For cycles beyond the first yield, the loading protocol involved three cycles at increments of displacement ductility, as determined by Equation 3-1 and Equation 3-2. Table 4-3 presents the values of the ductility displacements applied to SJS1, and Figure 4-2 illustrates the load history for SJS1.

Table 4-3. Displacement ductility of SJS 1

Ductility	Δ (in)	Drift (%)
μ_1	1.48	1.6
$\mu_{1.5}$	2.23	2.5
μ_2	2.97	3.3
μ_3	4.45	4.9
μ_4	5.93	6.6
μ_5	7.42	8.2

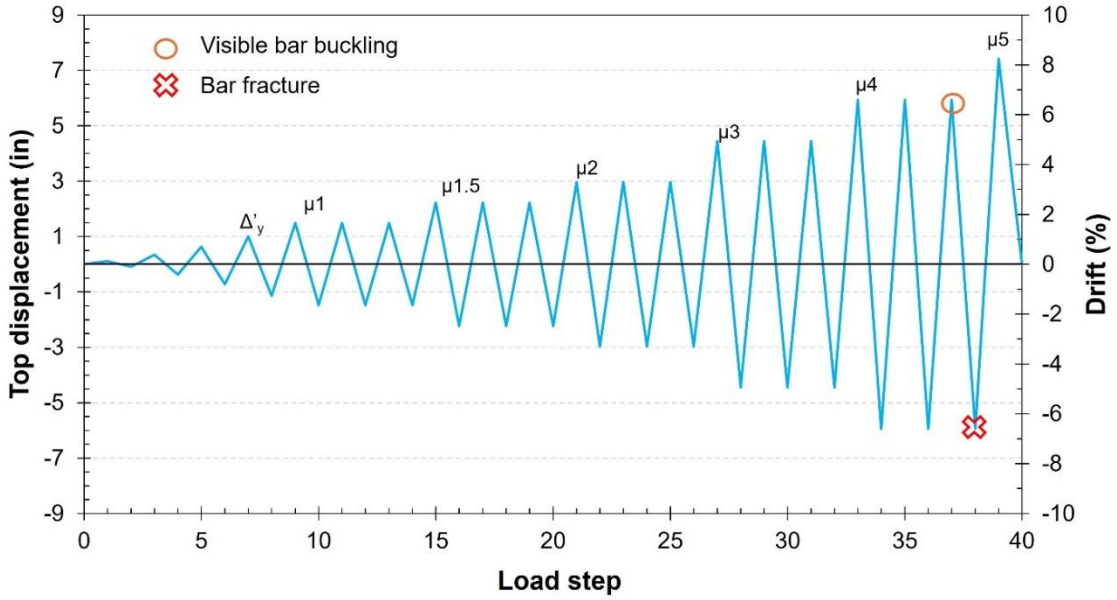


Figure 4-2. Displacement history of SJS1

4.1.2. Global Response of SJS1

Figure 4-3 presents the moment-displacement response of the column at the socket interface for SJS1. This specimen achieved a displacement ductility of five, with the maximum applied moment reaching 632.9 kip-ft at ductility three. At this stage, the column concrete core began to experience crushing. During ductility four, noticeable strength degradation occurred as bar buckling initiated, leading to the fracture of longitudinal bars N5, N6, and N7 during the third negative cycle of ductility four. A drop of approximately 40% from the maximum moment was observed during the first cycle of ductility 5, at which point the test was concluded. Notably, the plastic hinge successfully formed on the column above the interface of the external socket connection, with a socket height of 1.0 Dc.

Figure 4-4 compares the predicted response of a CIP column, derived from moment-curvature analysis using the same material properties as the experimental test, with the envelope of the moment response for SJS1 during the first and third cycles of each ductility displacement. The maximum moment reached by SJS1 was 5.7% higher than the nominal capacity of a CIP column. Strength degradation became evident at a drift of 6.6%, coinciding with the onset of bar buckling.

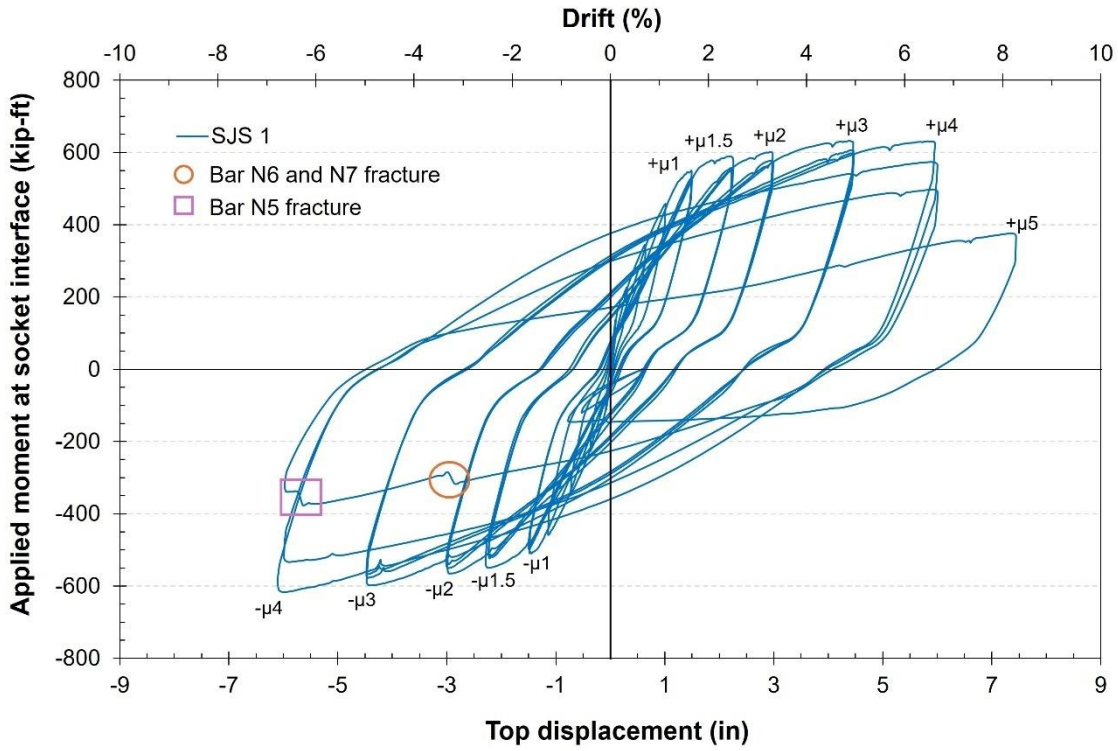


Figure 4-3. Moment-displacement response of SJS 1

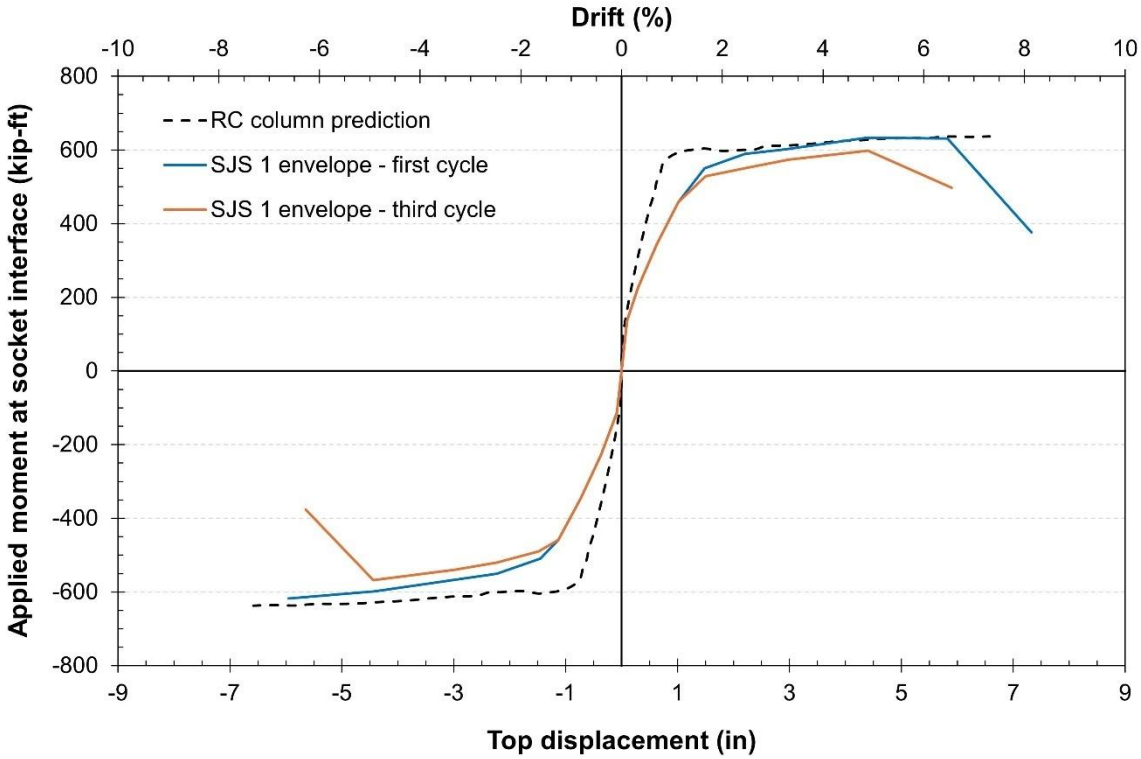


Figure 4-4. SJS 1 experimental envelopes compared to an RC column prediction

4.1.3. Damage progression of SJS1

The first cracks occurred at half of the first yield displacement, appearing only at the external socket wall in a radial direction, as shown in Figure 4-5. The cracks marked in red are related to the positive loading direction, while black cracks represented those that occurred during the pull direction of loading.

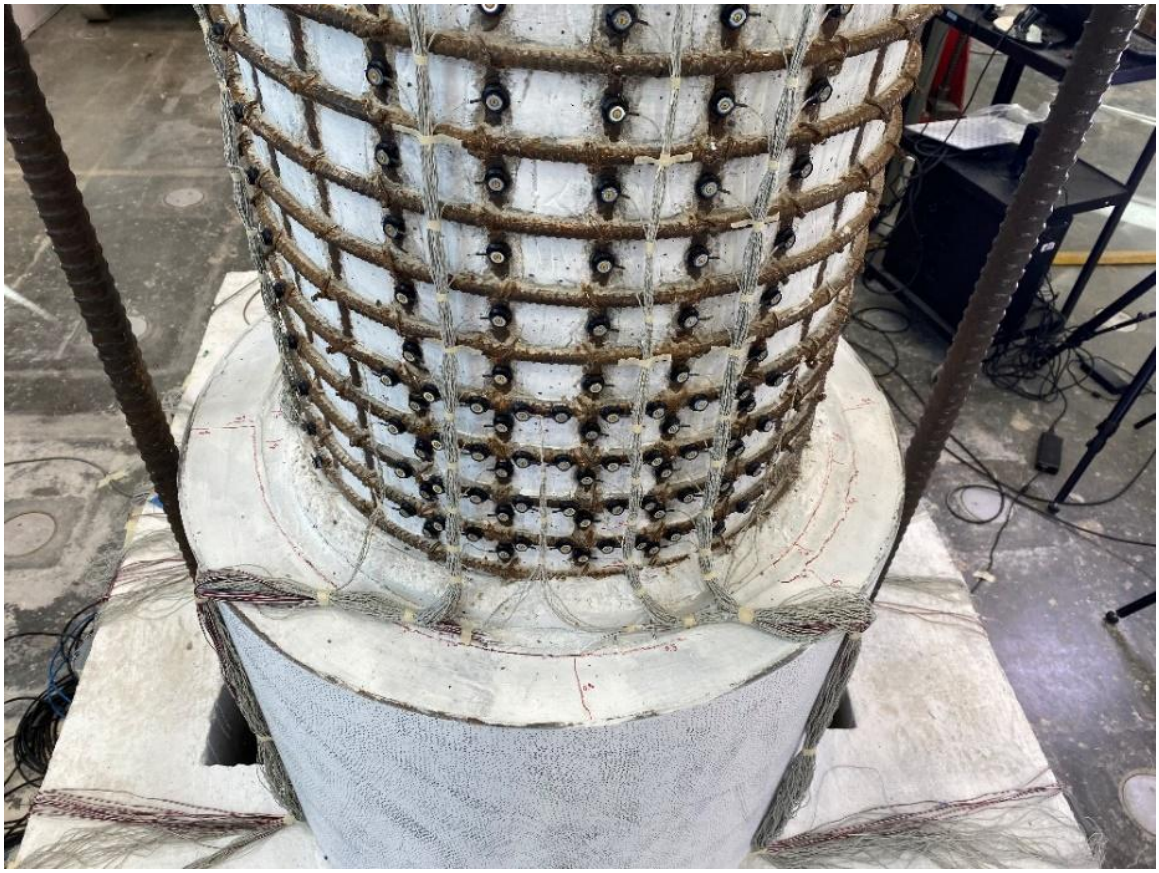


Figure 4-5. Cracks at external socket connection at half of the first yield displacement

A 0.079” (2.0 mm) gap between the steel sleeves and the concrete of the external socket appeared at the end of the three cycles of ductility one, as shown in Figure 4-6. The column itself had crack widths of at most 0.016” (0.4 mm) thickness. Additionally, a 0.039” (1 mm) uplift of the column relative to the top of the socket was noted. Figure 4-7 shows the crack pattern of the specimen at the last cycle of ductility one.

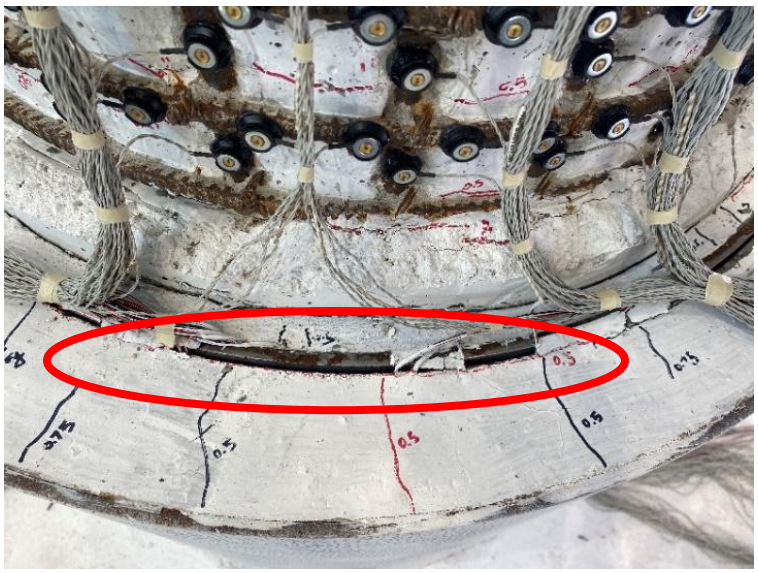


Figure 4-6. Gap between the steel sleeve and concrete on south face of the socket at ductility one



Figure 4-7. Crack pattern on south surface at last cycle of ductility one

The concrete cover that was in contact with the external socket started to crush at ductility 2 while the gap between the steel sleeve and the concrete of the socket increased to 0.138” (3.5 mm). Additionally, the flexural cracks on the columns near the external socket increased in width to 0.024” (0.6 mm). Figure 4-8 shows the crack pattern of the specimen at the last cycle of ductility two.

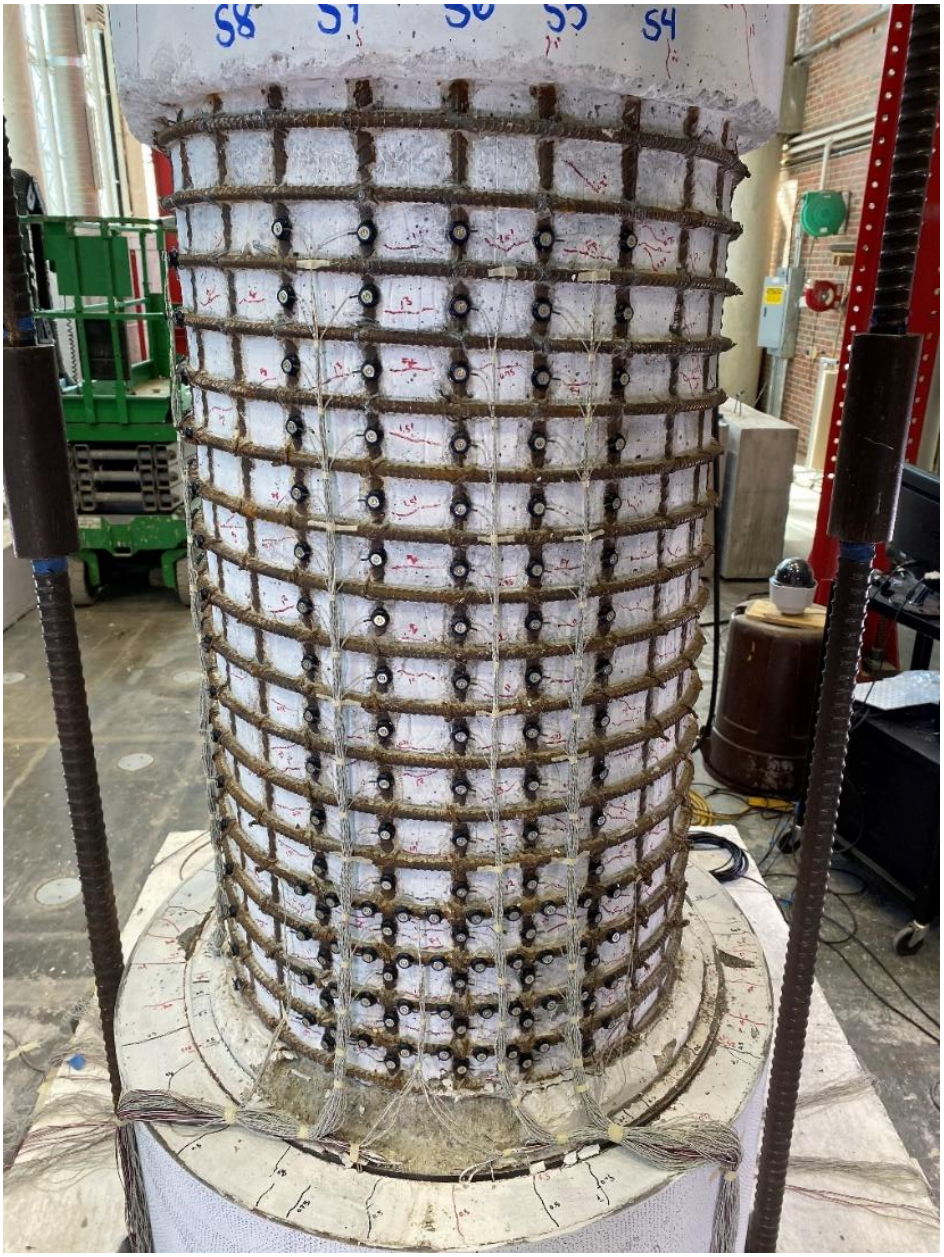


Figure 4-8. The crack pattern on the south surface at last cycle of ductility two

Crushing of the core was first observed at ductility 3, while the gap between the steel sleeve and the concrete of the socket increased to 0.177” (4.5 mm). Figure 4-9 presents the damage of the specimen at ductility three.

Reinforcing bar buckling occurred during the third positive cycle of ductility four when bars N4, N5, N6, N7, and N8 experienced buckling, as shown in Figure 4-10. Upon opposite direction loading (third negative cycle of ductility four), bars N5, N6 and N7 fractured, as shown in Figure 4-11.



Figure 4-9. Damage of the specimen on the south surface at ductility three



Figure 4-10. Buckling of longitudinal bars on north surface at ductility four



Figure 4-11. Fracture of longitudinal bars on the north surface at ductility four

The last loading cycle was at ductility five. The remaining bars on the north surface experienced large buckling deformation, as noted in Figure 4-12.



Figure 4-12. Buckled bars on the north surface of the column at ductility five

The footing did not present any significant cracks through the test. Additionally, the grout between the column and the socket did not present any damage. The concrete of the external socket presented only the radial cracks that appeared at the beginning of the test. Figure 4-13 shows the damage of the footing and external socket connection.

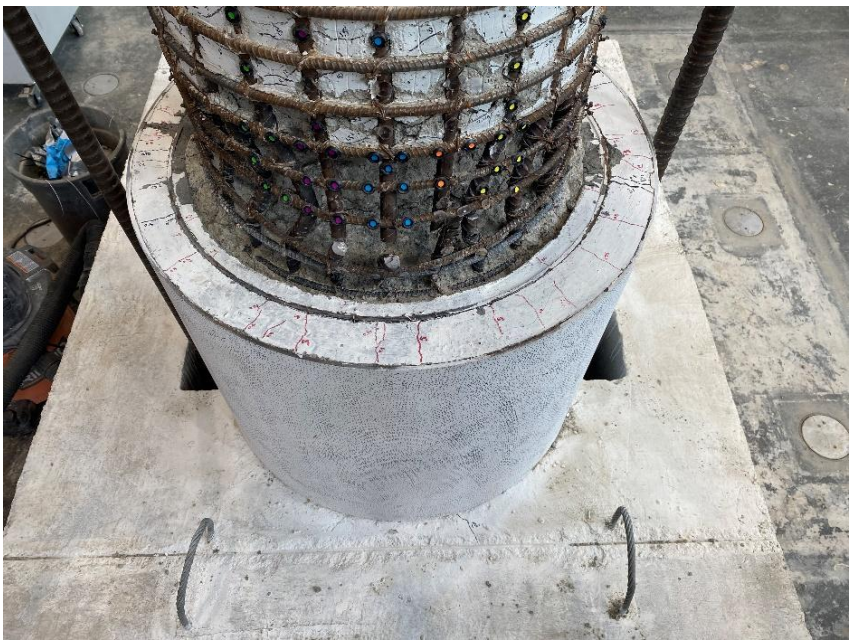


Figure 4-13. Damage on the footing and the external socket

Figure 4-14 shows the spread of damage on the north face of the column, with visible concrete crushing extending 10 in (255 mm) from the socket surface.

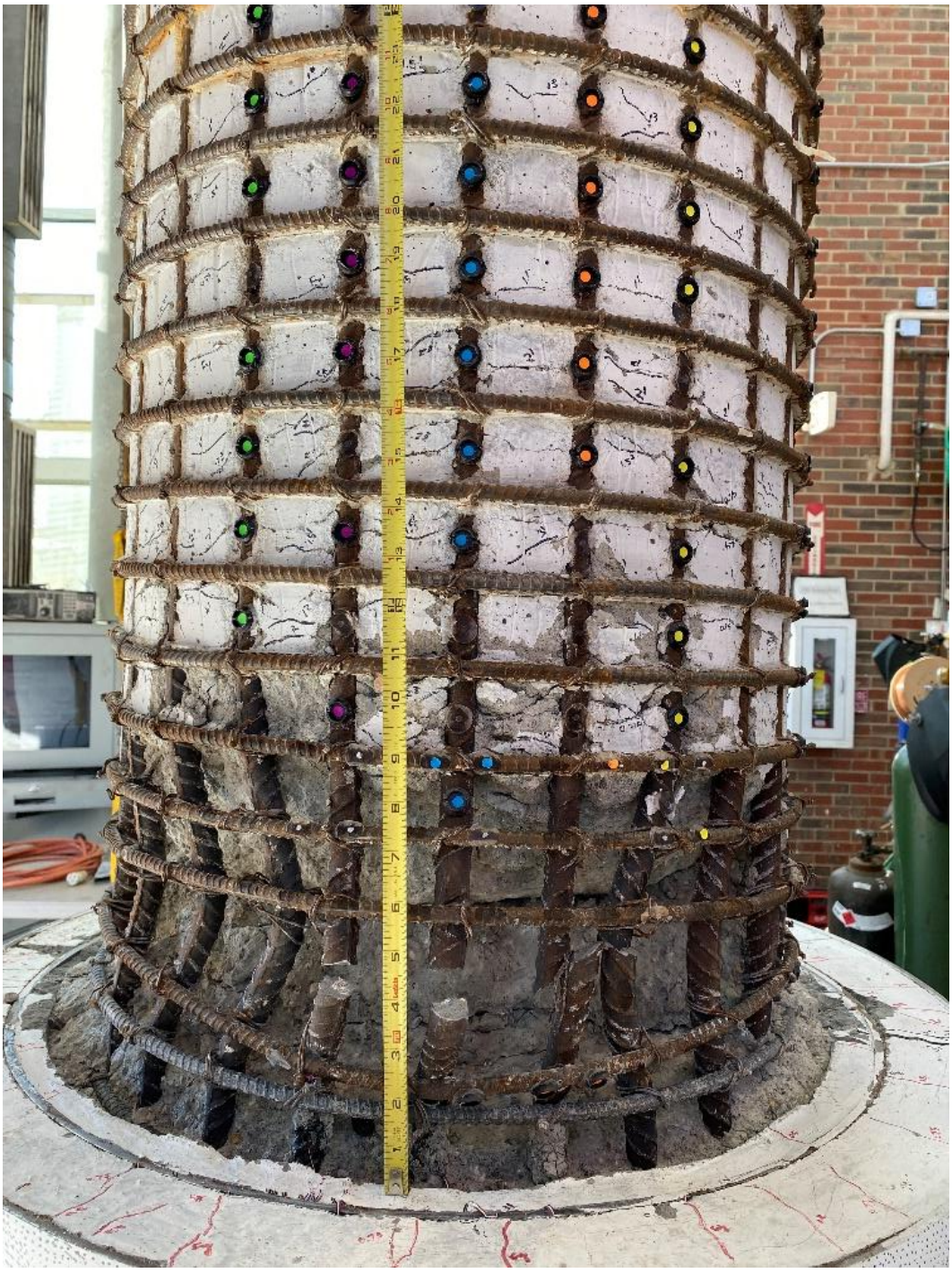


Figure 4-14. Spread of damage on the column at the north face

4.2. Specimen SJS-2

Column test SJS2 was performed on Tuesday, May 24, 2022, at the Constructed Facilities Laboratory at NCSU. A summary of the key parameters for SJS2 is provided in Table 4-4.

Table 4-4. Summary of SJS2 parameters

Column parameters	
Longitudinal steel detailing	24#6 A706 (ρ_l=2.34%)
Transverse steel	#3 spirals @ 2 inches (ρ_s=1.04%)
Longitudinal steel yield strength	68.4 ksi
Concrete strength	6.0 ksi
Diameter of the column	24 in
Height of the column	90 in
Axial load ratio	5%
First yield displacement	2.58 in
Equivalent yield displacement	3.57 in
Maximum applied moment at socket interface	476.4 kip-ft
Failure mode	Crushing of grout, rocking of column
Socket parameters	
Longitudinal steel detailing	24#7 A706
Longitudinal steel yield strength	86.5 ksi
Steel sleeve yield strength	42.6 ksi
Thickness of the steel sleeves	1/4 in
Concrete strength	9.5 ksi
Grout strength	6.5 ksi
Height of external socket	18 in (0.75 Diameter of the column)
Internal diameter	26 in
External diameter	32 in

The column had a clear height of 7'-6″ and a diameter of 24″, resulting in a height-to-diameter aspect ratio of 3.62, with a concrete cover of 1″. It was reinforced with 24 Grade 60-A706 #6 longitudinal bars (ρl = 2.34%), and the transverse reinforcement consisted of #3 spirals with a spacing of 2.0″ center to center (ρs = 1.04%).

The external socket had a height of 18″, resulting in a height-to-diameter ratio of 0.75 (0.75 Dc). The socket longitudinal reinforcement included 24 Grade 80-A706 #7 bars, and the concrete was confined with 1/4″ thick steel sleeves.

4.2.1. Loading Protocol of SJS2

The initial part of the loading history consisted of a single cycle at a quarter, half, three-fourths, and the yield displacement. The experimentally measured first yield displacement was Δ'y=2.58 in.

For cycles beyond the first yield, the loading protocol involved three cycles at increments of displacement ductility, as determined by Equation 3-1 and Equation 3-2. Table 4-5 presents the values of the ductility displacements applied to SJS2, and Figure 4-15 illustrates the load history for SJS2.

Table 4-5. Displacement ductility of SJS 2

Ductility	Δ (in)	Drift (%)
μ_1	3.57	4.0
$\mu_{1.5}$	5.35	5.9
μ_2	7.13	7.9

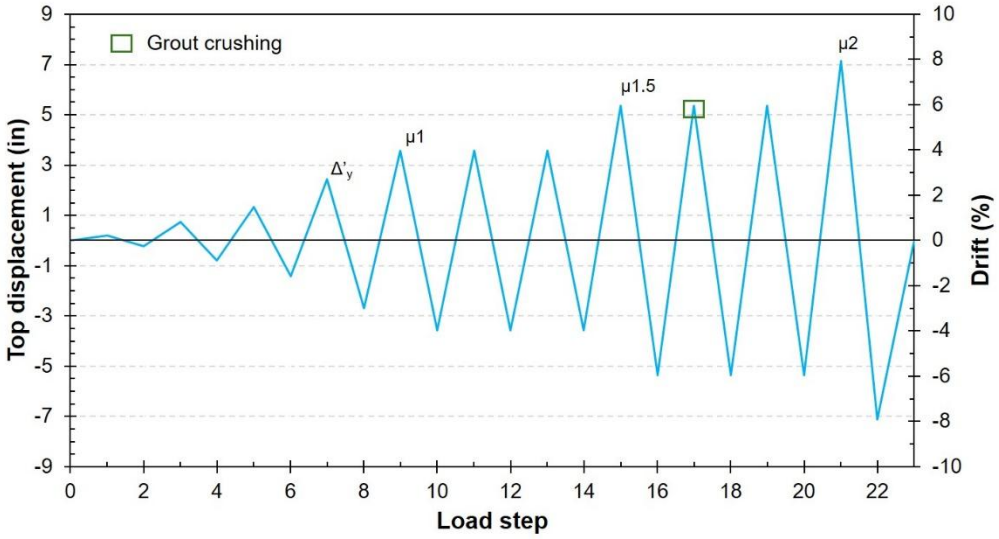


Figure 4-15. Displacement history of SJS 2

4.2.2. Global Response of SJS2

Figure 4-16 presents the moment-displacement response of the column at the socket interface for SJS2. This specimen experienced its highest applied moment of 476.4 kip-ft at ductility one, leading to grout crushing. Strength degradation was observed during ductility one, accompanied by rocking and grout crushing. A drop of approximately 60% from the maximum moment was observed during the third cycle of ductility one and a half. The test was concluded at the first cycle of ductility two. Notably, the column did not display significant cracks during the test. The external socket wall remained mostly undamaged, but some radial cracks appeared before reaching the first yield displacement. Additionally, the socket inner and outer steel sleeves exhibited inelastic deformations, while the footing had no visible damage and remained a capacity-protected element. However, the connection did not develop a plastic hinge in the column at the interface with the external socket.

Figure 4-17 compares the predicted response of a CIP column, derived from moment-curvature analysis using the same material properties as the experimental test, with the envelope of the moment response for SJS2 during the first and third cycles of each ductility displacement. The maximum moment reached by SJS2 was approximately 80% of the nominal capacity of a CIP

column. Strength degradation became evident at a drift of 4.0%, coinciding with the grout crushing.

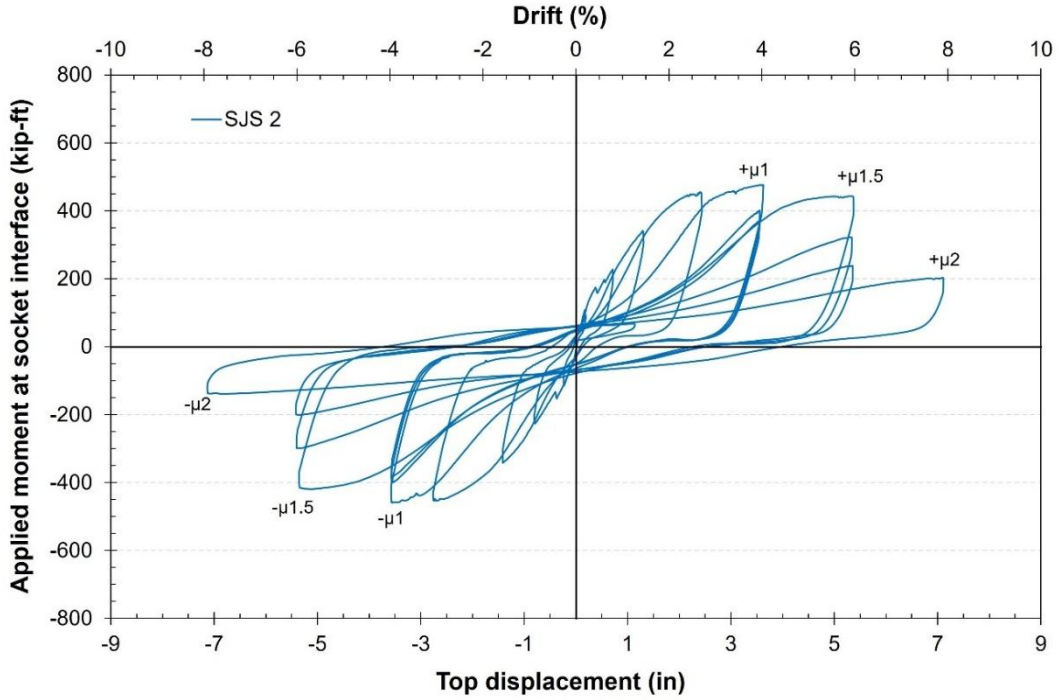


Figure 4-16. Moment-displacement response of SJS 2

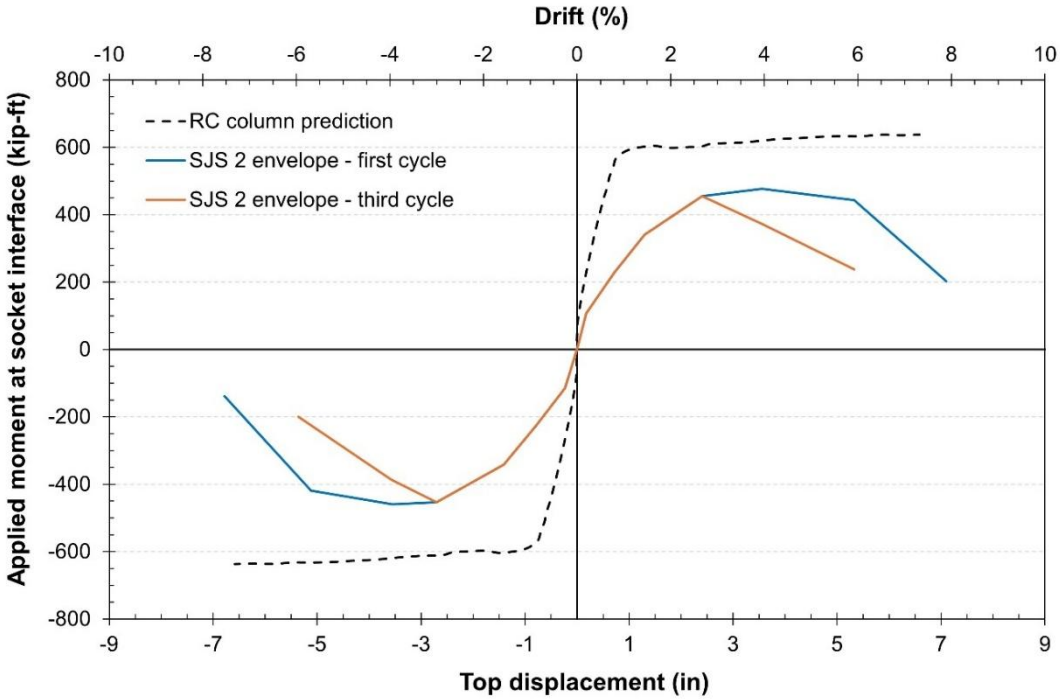


Figure 4-17. SJS 2 experimental envelopes compared to an RC column prediction

4.2.3. Damage progression of SJS2

As shown in Figure 4-18, the first cracks occurred at half the first yield displacement, appearing only at the external socket wall in a radial direction. The cracks marked in red are related to the positive loading direction, while black ones represent those that occurred during the negative loading direction.



Figure 4-18. Cracks at external socket connection at half of the first yield displacement

A 0.118″ (3.0 mm) gap between the grout and the concrete column appeared at three-quarters of the first yielding, as shown in Figure 4-19. The column had cracks thickness that were at most 0.008″ (0.2 mm). Additionally, Figure 4-20 exhibit a 0.295″ (7.5 mm) uplift of the column relative to the top of the grout. Figure 4-21 shows the crack pattern of the specimen at the first yielding.



Figure 4-19. Gap between the steel sleeve and concrete on the south surface of the socket at ductility one



Figure 4-20. Uplift of the column at three-quarters of the first yielding

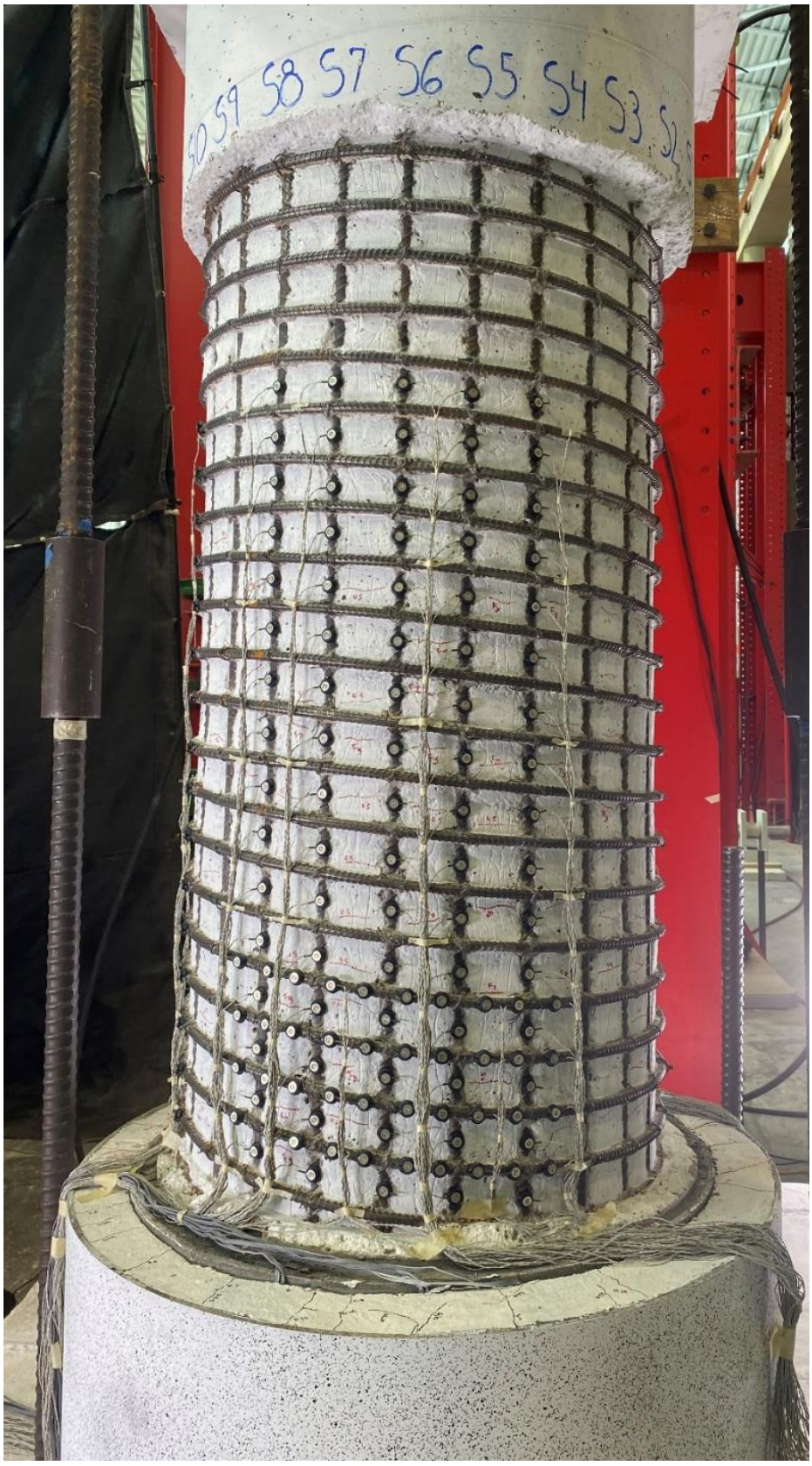


Figure 4-21. Crack pattern on the south surface at the first yielding

In the first cycle of ductility one, an uplift of the inner steel sleeve of 0.394″ (10 mm) with an additional 0.335″ (8.5 mm) uplift between the column and the grout was observed. Additionally, four gaps were observed between the different materials of the connection. Figure 4-22 shows the different gaps in the connection, while Figure 4-23 shows the sleeve and concrete column uplift.



Figure 4-22. Gaps at the external socket connection at the first cycle of ductility one



Figure 4-23. Uplift of steel sleeve and concrete column at the first cycle of ductility one

The grout between the column and the external socket started to crush at the third cycle of ductility one, while the gap between the inner steel sleeve and the concrete of the socket increased to 0.256″ (6.5 mm). Figure 4-24 depicts the damage to the external socket connection at the third cycle of ductility one. There were no additional flexural cracks on the column.



Figure 4-24. Damage of the socket connection at the third cycle of ductility one

At the end of ductility one and a half, the uplift of the column was approximately 2″ (50.8 mm). The grout crushing spread around the connection circumference, while the column did not

present additional damage. Figure 4-25 shows the deterioration of the column and the external socket connection at the last cycle of ductility one and a half.

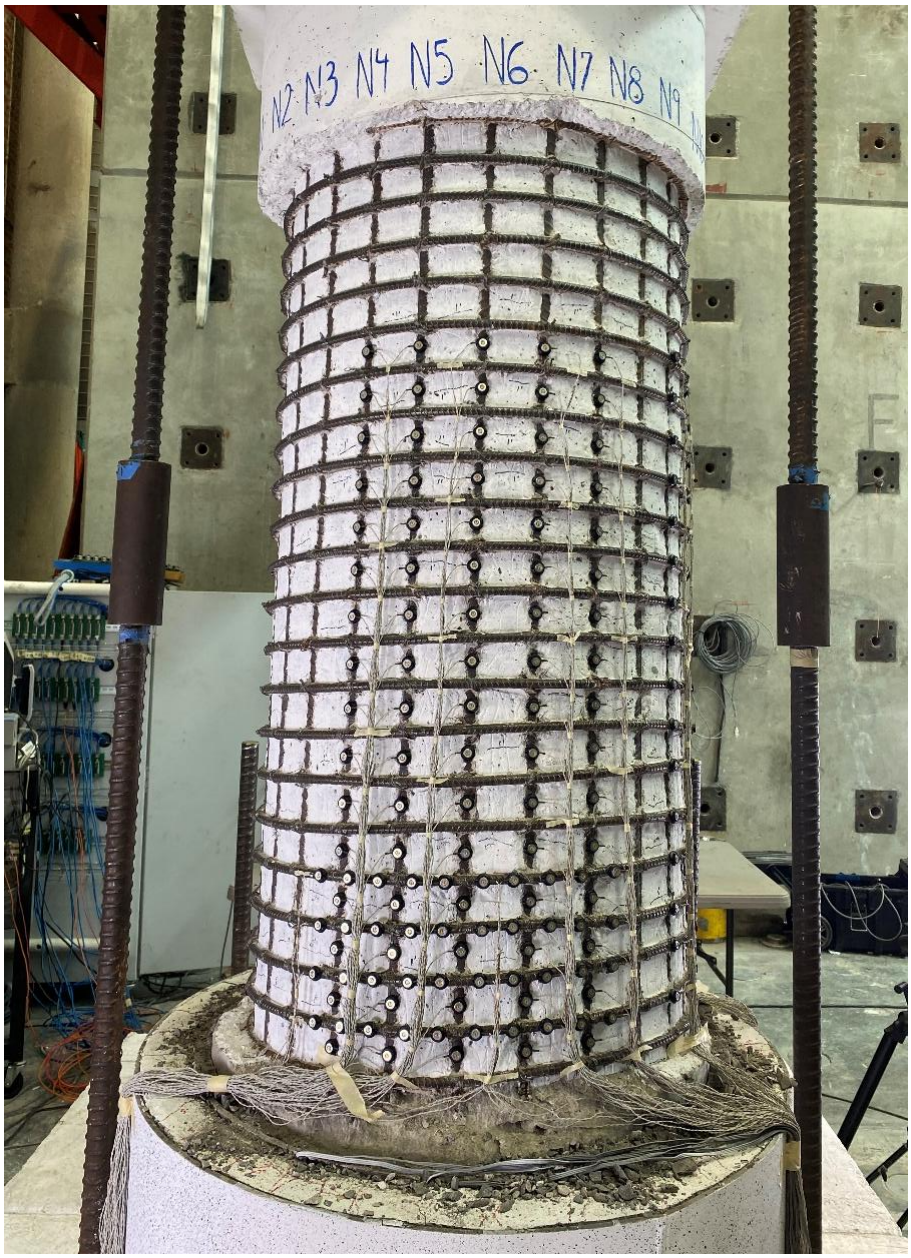


Figure 4-25. Damage of the specimen on the north surface at ductility one and a half

The last loading cycle was at ductility two, where no additional damage was observed, and the uplift of the column was approximately 2.5″ (63.5 mm). Figure 4-26 shows the displaced column and the uplift at the connection surface. The footing did not exhibit any significant cracks

throughout the test, and the external socket concrete presented only the radial cracks that appeared at the beginning of the test.

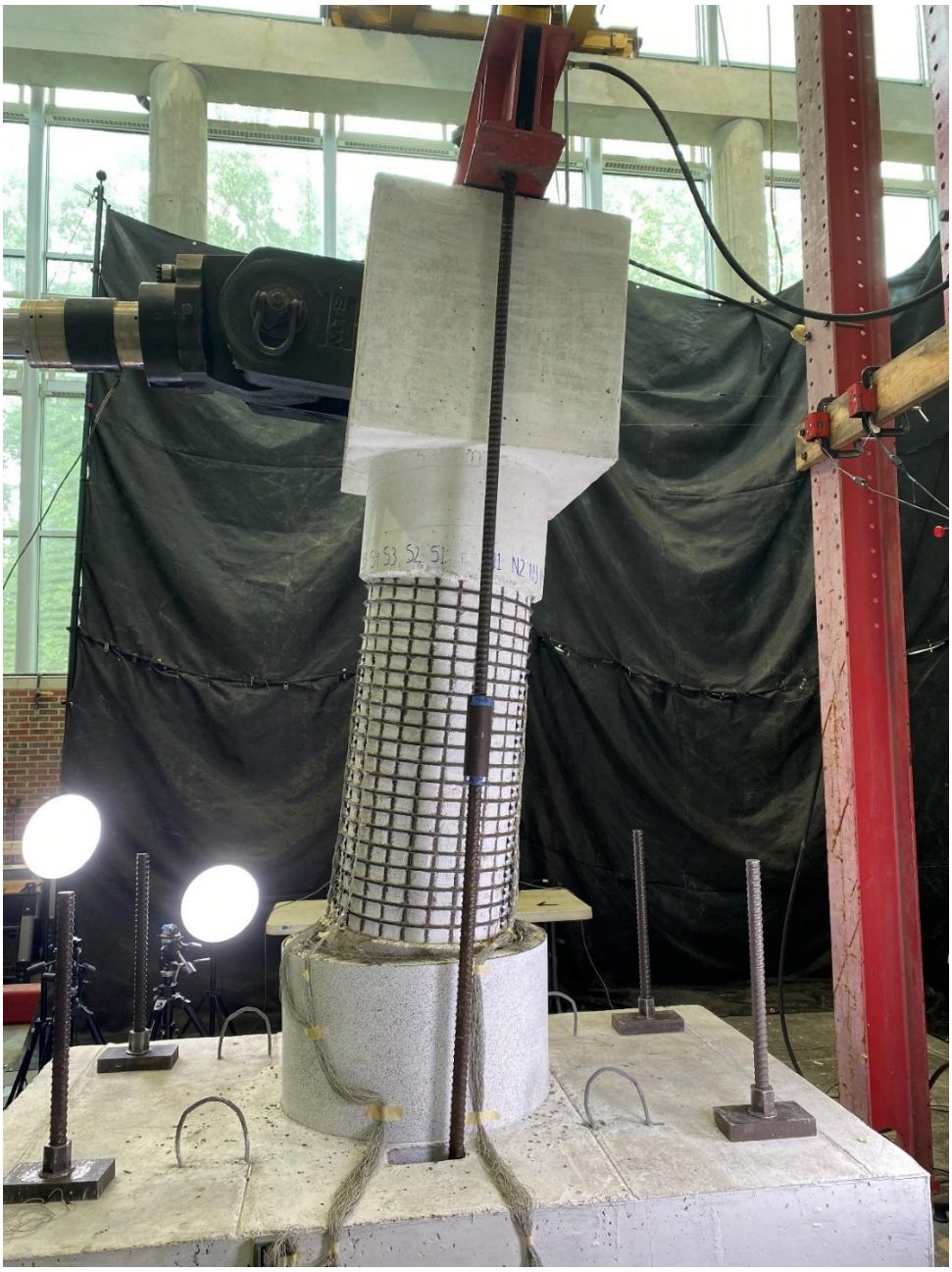


Figure 4-26. Uplift on the south surface of the column at ductility two

After the test, an inspection was conducted to investigate whether there was additional damage to the inside portion of the connection on the column. Figure 4-27 and Figure 4-28 depict the crushing of the portion of the column inside the socket.



Figure 4-27. Damage of the column inside the external socket connection



Figure 4-28. Damaged surface of the column inside the external socket connection

4.3. Specimen SJS-3

Column test SJS3 was performed on Friday, October 21, 2022, at the Constructed Facilities Laboratory at NCSU. A summary of the key parameters for SJS3 is provided in Table 4-6.

Table 4-6. Summary of SJS3 parameters

Column parameters	
Longitudinal steel detailing	24#6 A706 (ρ_l=2.34%)
Transverse steel	#3 spirals @ 2 inches (ρ_s=1.04%)
Longitudinal steel yield strength	68.4 ksi
Concrete strength (outside the socket)	6.0 ksi
Concrete strength (inside the socket)	10.0 ksi
Diameter of the column	24 in
Height of the column	90 in
Axial load ratio	5%
First yield displacement	1.59 in
Equivalent yield displacement	2.18 in
Maximum applied moment at socket interface	562.6 kip-ft
Failure mode	Crushing of grout, rocking of column
Socket parameters	
Longitudinal steel detailing	24#7 A706
Longitudinal steel yield strength	86.5 ksi
Socket sleeve steel yield strength	42.6 ksi
Thickness of steel sleeves	1/4 in
Concrete strength	12.1 ksi
Grout strength	9.1 ksi
Height of external socket	20.4 in (0.85 Dc)
Internal diameter	26 in
External diameter	32 in

The column had a clear height of 7'-6″ and a diameter of 24″, resulting in a height-to-diameter aspect ratio of 3.62, with a concrete cover of 1″. It was reinforced with 24 Grade 60-A706 #6 longitudinal bars (ρl = 2.34%), and the transverse reinforcement consisted of #3 spirals with a spacing of 2.0″ center to center (ρs = 1.04%).

The external socket had a height of 20 3/8″, resulting in a height-to-diameter ratio of 0.85 (0.85 Dc). The socket longitudinal reinforcement included 24 Grade 80-A706 #7 bars, and the concrete was confined with 1/4″ thick steel sleeves.

4.3.1. Loading Protocol of SJS 3

The initial part of the loading history consisted of a single cycle at a quarter, half, three-fourths, and the yield displacement. The experimentally measured first yield displacement was Δ'y=1.58 in.

For cycles beyond the first yield, the loading protocol involved three cycles at increments of displacement ductility, as determined by Equation 3-1 and Equation 3-2. Table 4-7 presents the values of the ductility displacements applied to SJS3, and Figure 4-29 illustrates the load history for SJS3.

Table 4-7. Displacement ductility of SJS 3

Ductility	Δ (in)	Drift (%)
μ_1	2.18	2.4
$\mu_{1.5}$	3.28	3.6
μ_2	4.37	4.9
μ_3	6.55	7.3

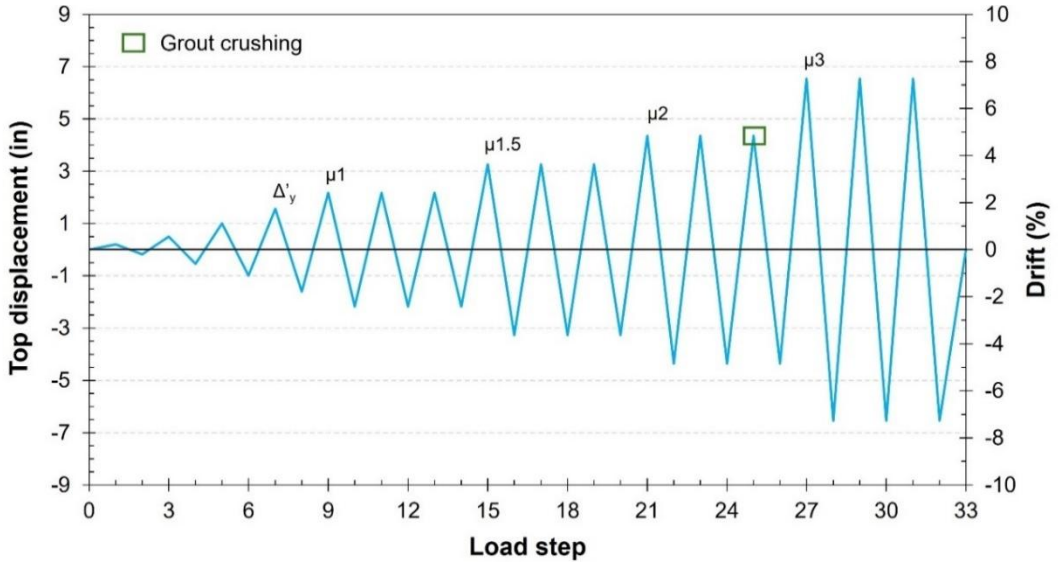


Figure 4-29. Displacement history of SJS 3

4.3.2. Global Response of SJS 3

Figure 4-30 presents the moment-displacement response of the column at the socket interface for SJS3. This specimen experienced its highest applied moment of 562.6 kip-ft at ductility two, initiating grout crushing. Strength degradation was observed during ductility two, accompanied by rocking and grout crushing. A drop of approximately 65% from the maximum moment was observed during the second cycle of ductility three. The test was concluded at the third cycle of ductility three. Notably, the column did not exhibit significant cracks throughout the test. The external socket wall concrete sustained minimal damage, with radial cracks appearing before reaching the column first yield displacement. Additionally, the socket inner and outer steel sleeves did not exhibit inelastic deformations, while the footing had no visible damage and remained a capacity-protected element. However, the connection did not develop a plastic hinge in the column at the interface with the external socket.

Figure 4-31 compares the predicted response of a CIP column, derived from moment-curvature analysis using the same material properties as the experimental test, with the envelope of the moment response for SJS3 during the first and third cycles of each ductility displacement. The maximum moment reached by SJS3 was approximately 94% of the nominal capacity of a CIP column. Strength degradation became evident at a drift of 4.9%, coinciding with grout crushing.

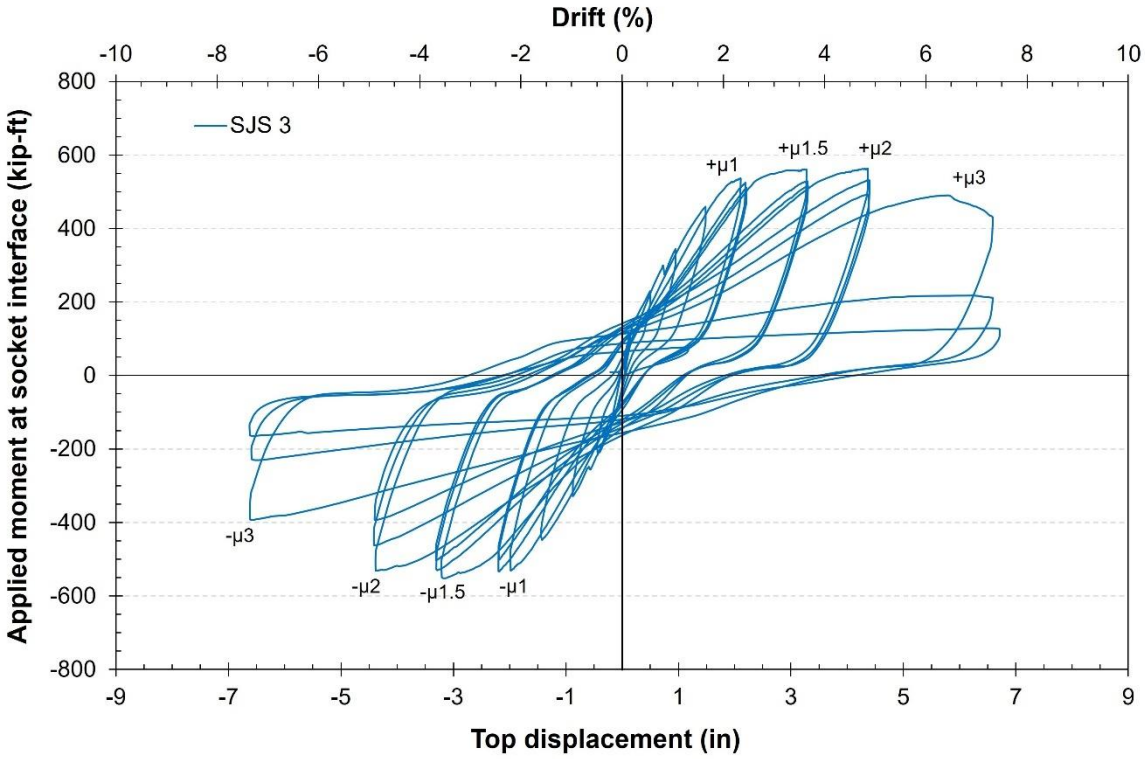


Figure 4-30. Moment-displacement response of SJS 3

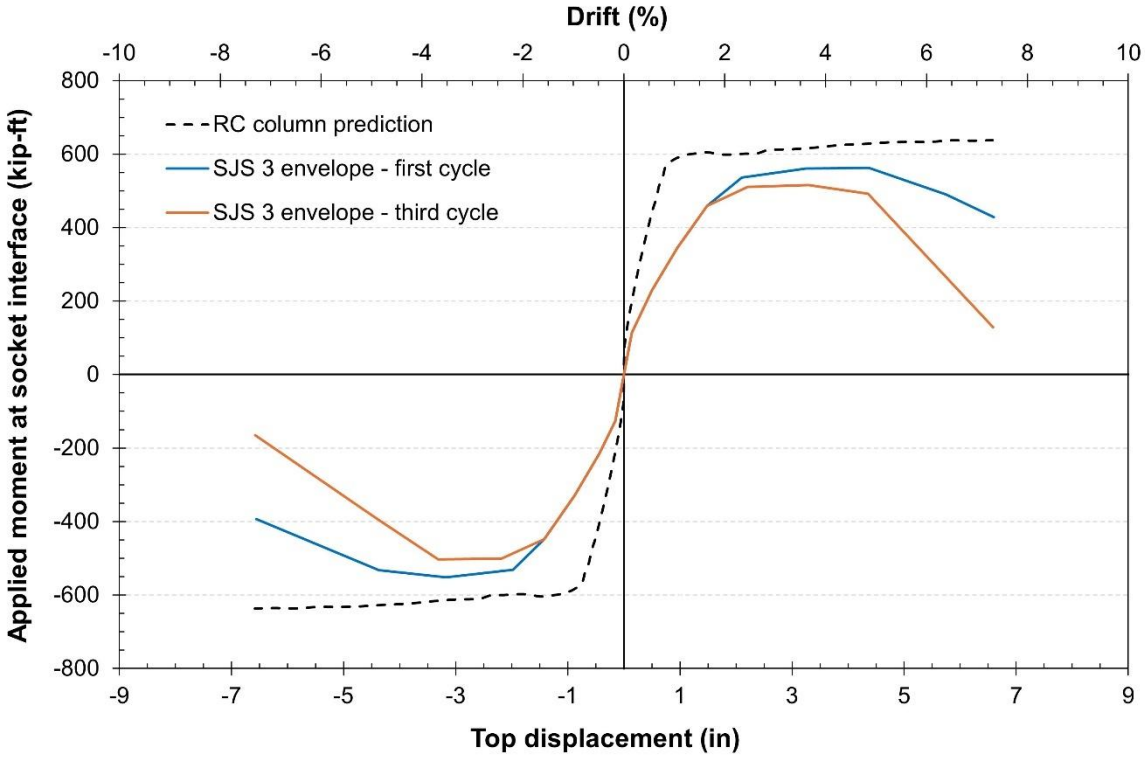


Figure 4-31. SJS 3 experimental envelopes compared to an RC column prediction

4.3.3. Damage progression of SJS 3

The first cracks occurred at half the first yield displacement, appearing at the external socket wall in a radial direction, and hairline cracks at the base of the column, as shown in Figure 4-32. The cracks marked in red are related to the positive loading direction, while black ones represent those that occurred during the negative loading direction.

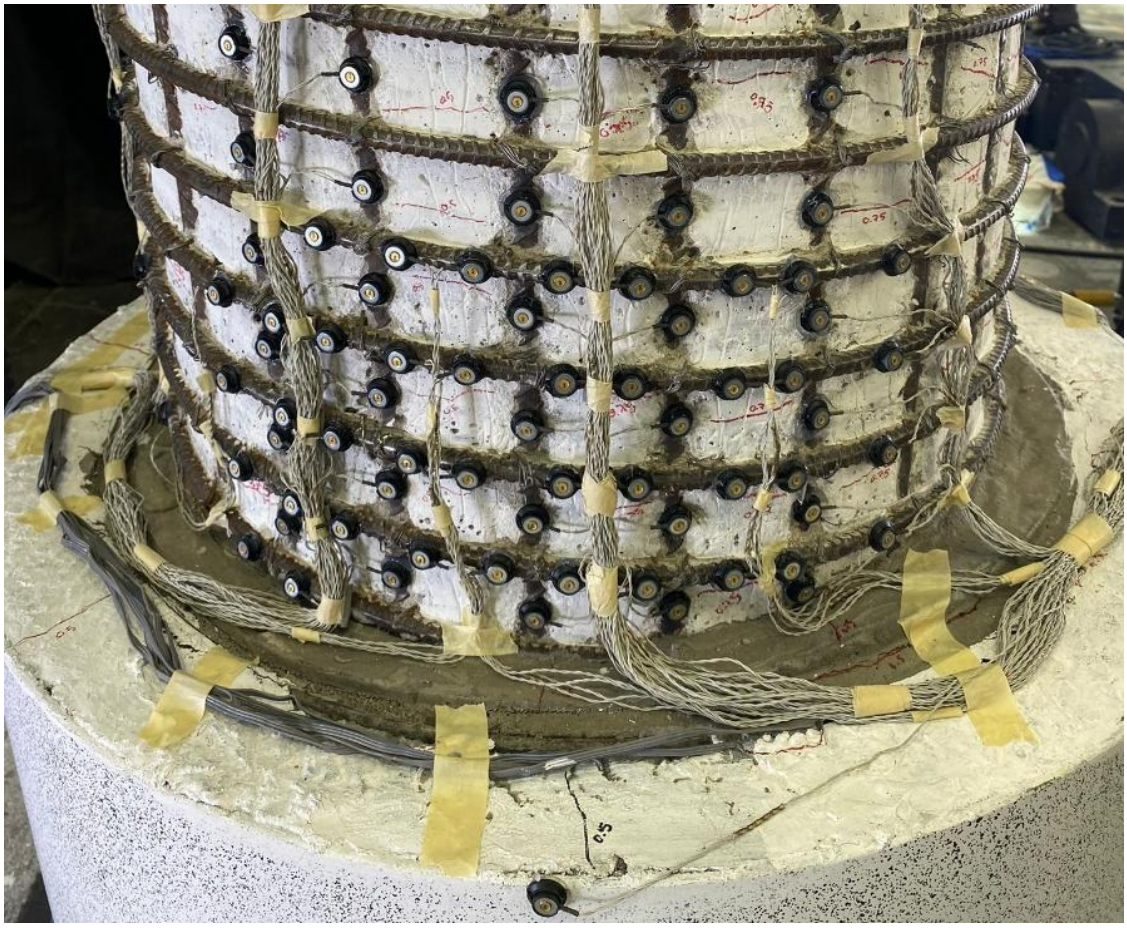


Figure 4-32. Cracks in external socket connection at half of the first yield displacement

A 0.032″ (0.8 mm) gap between the grout and the steel sleeve of the external socket appeared at the third cycle of ductility one, as shown in Figure 4-33. The column had crack widths that were at most 0.008″ (0.2 mm). Additionally, Figure 4-34 exhibits a 0.197″ (5.0 mm) column uplift relative to the top of the grout. Figure 4-35 shows the crack pattern of the specimen at the last cycle of ductility one.

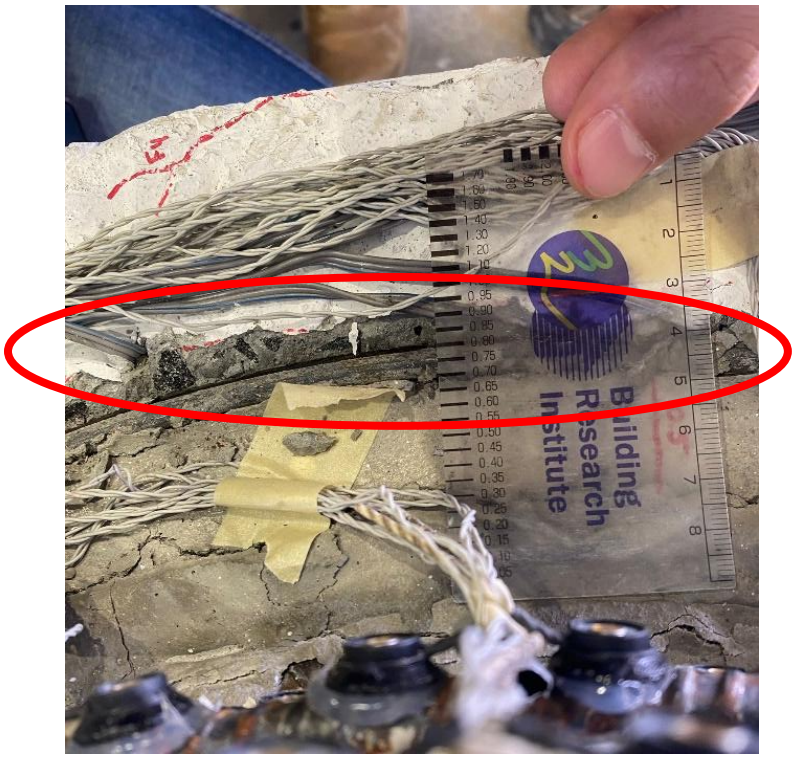


Figure 4-33. Gap between the steel sleeve and grout on the south surface at ductility one



Figure 4-34. Uplift of the column at the last cycle of ductility one

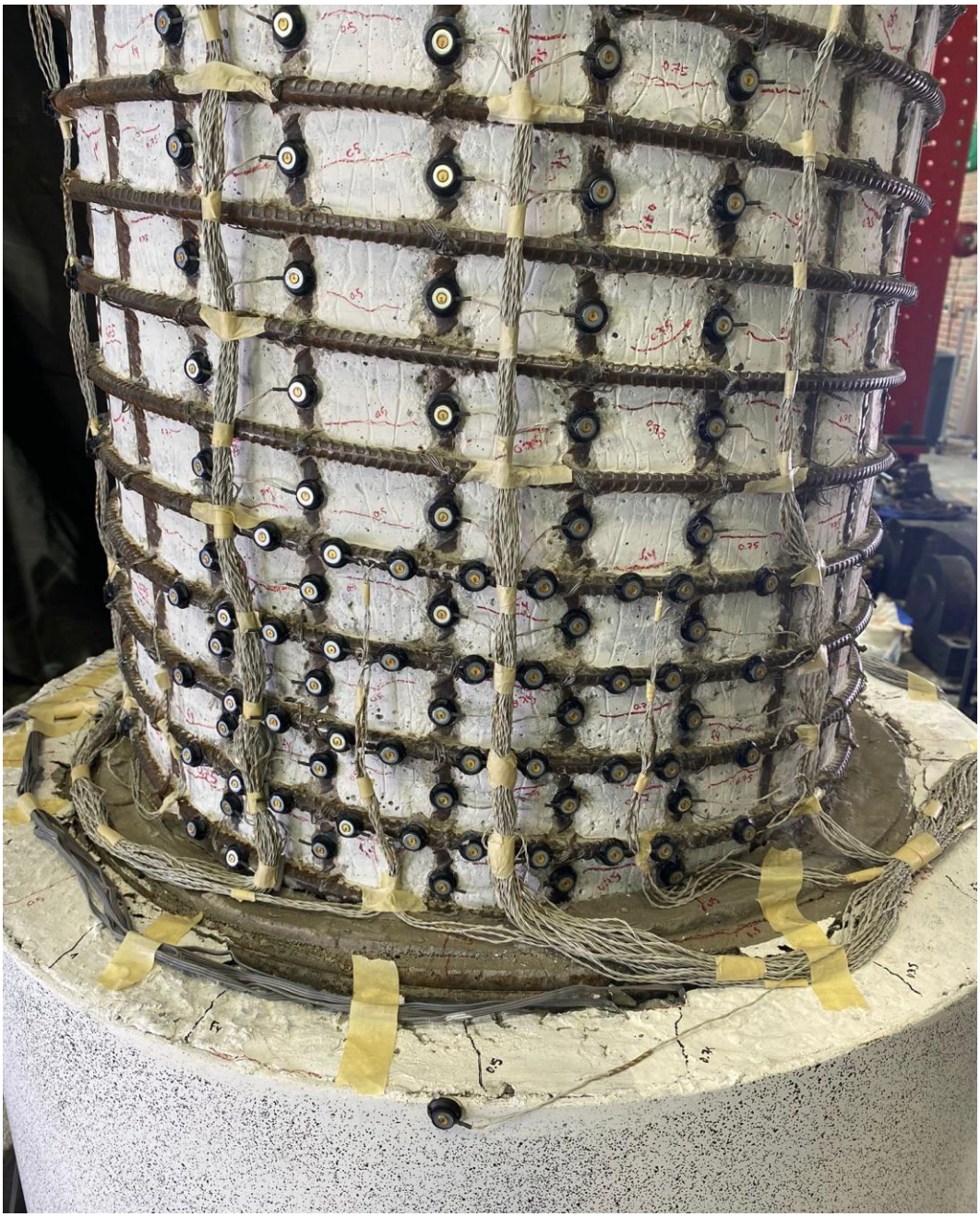


Figure 4-35. Crack pattern on the south surface at the last cycle of ductility one

In the last cycle of ductility 1.5, an uplift of 0.748″ (19 mm) between the column and the grout was observed. Additionally, three gaps were observed between the different materials of the connection. Figure 4-36 shows the different gaps in the connection while Figure 4-37 shows the grout uplift and the damage on the column, which started to present damage as flaking of the concrete at the interface with the external socket connection.

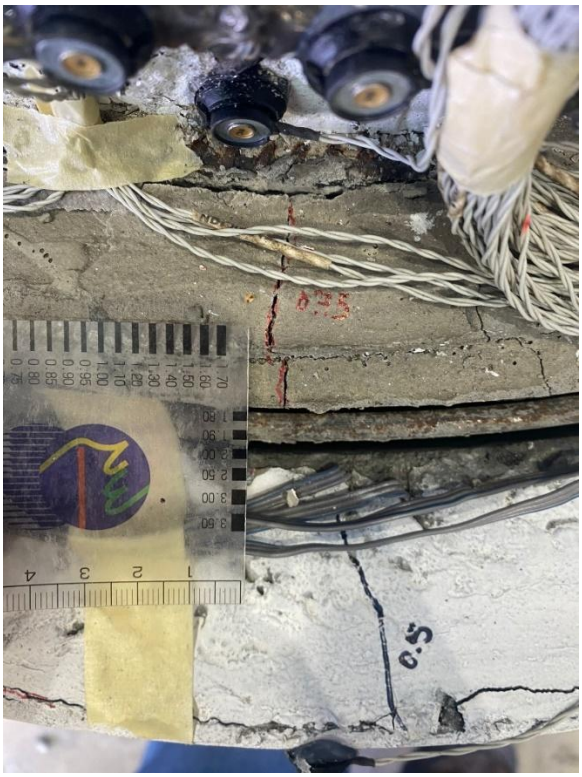


Figure 4-36. Gaps at the external socket connection at the last cycle of ductility one and a half

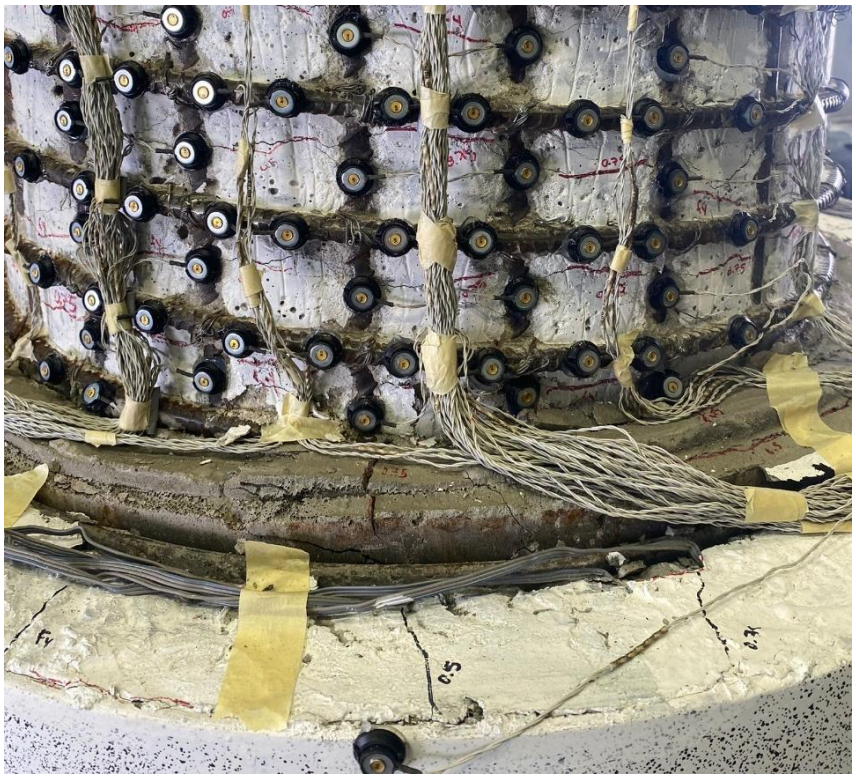


Figure 4-37. Damage of the column and uplift of grout at the last cycle of ductility one and a half

The grout between the column and the external socket started to crush at the third cycle of ductility two. Figure 4-38 depicts the damage to the external socket connection at the third cycle of ductility two. There was no additional damage on the column.

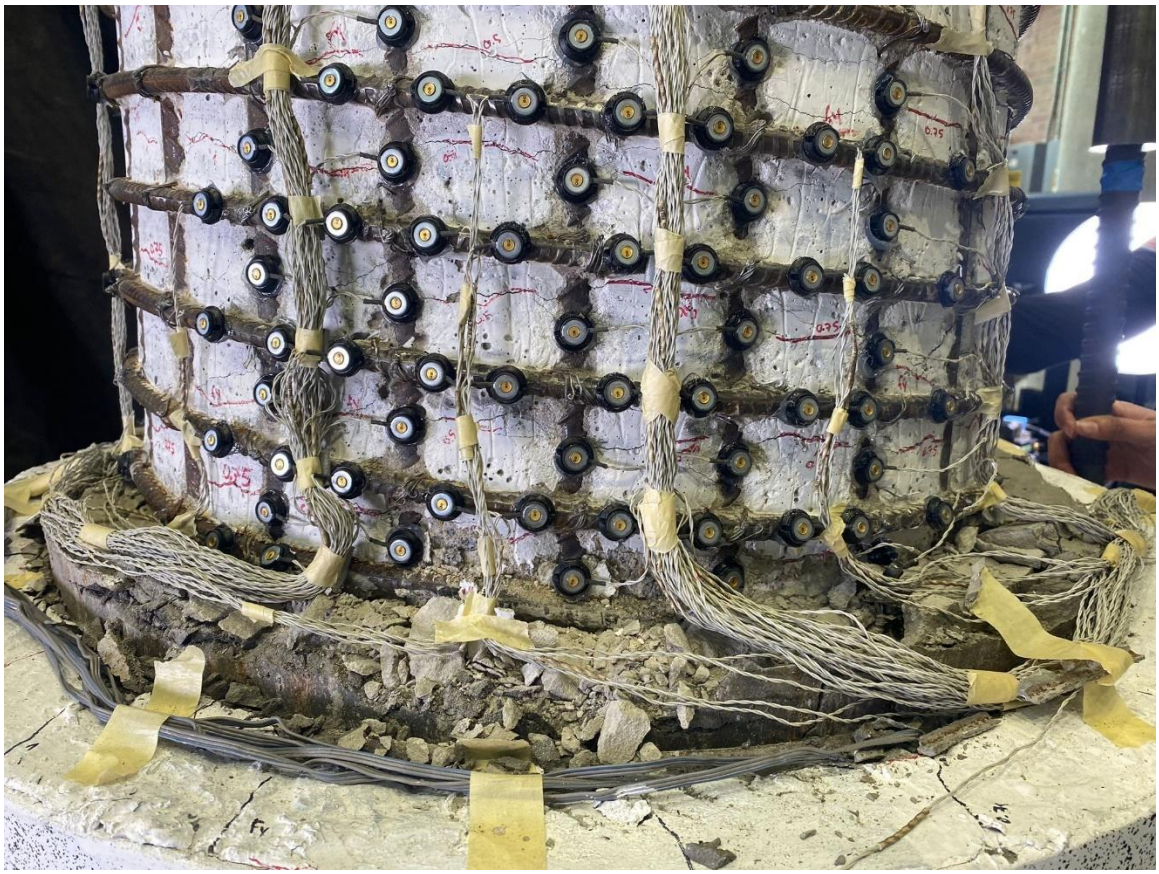


Figure 4-38. Damage of the socket connection at the third cycle of ductility two

No additional damage was observed after the last loading cycle of ductility three, and the column uplift was approximately 2.5″ (63.5 mm). The grout crushing spread around the connection circumference, while the column did not present additional damage. Figure 4-39 shows the column deterioration and the external socket connection at the last cycle of ductility three.

Figure 4-40 shows the displaced column and the uplift at the connection surface. The footing did not exhibit any significant cracks throughout the test, and the external socket concrete presented only the radial cracks that appeared at the beginning of the test.



Figure 4-39. Damage of the specimen on the south surface at ductility three

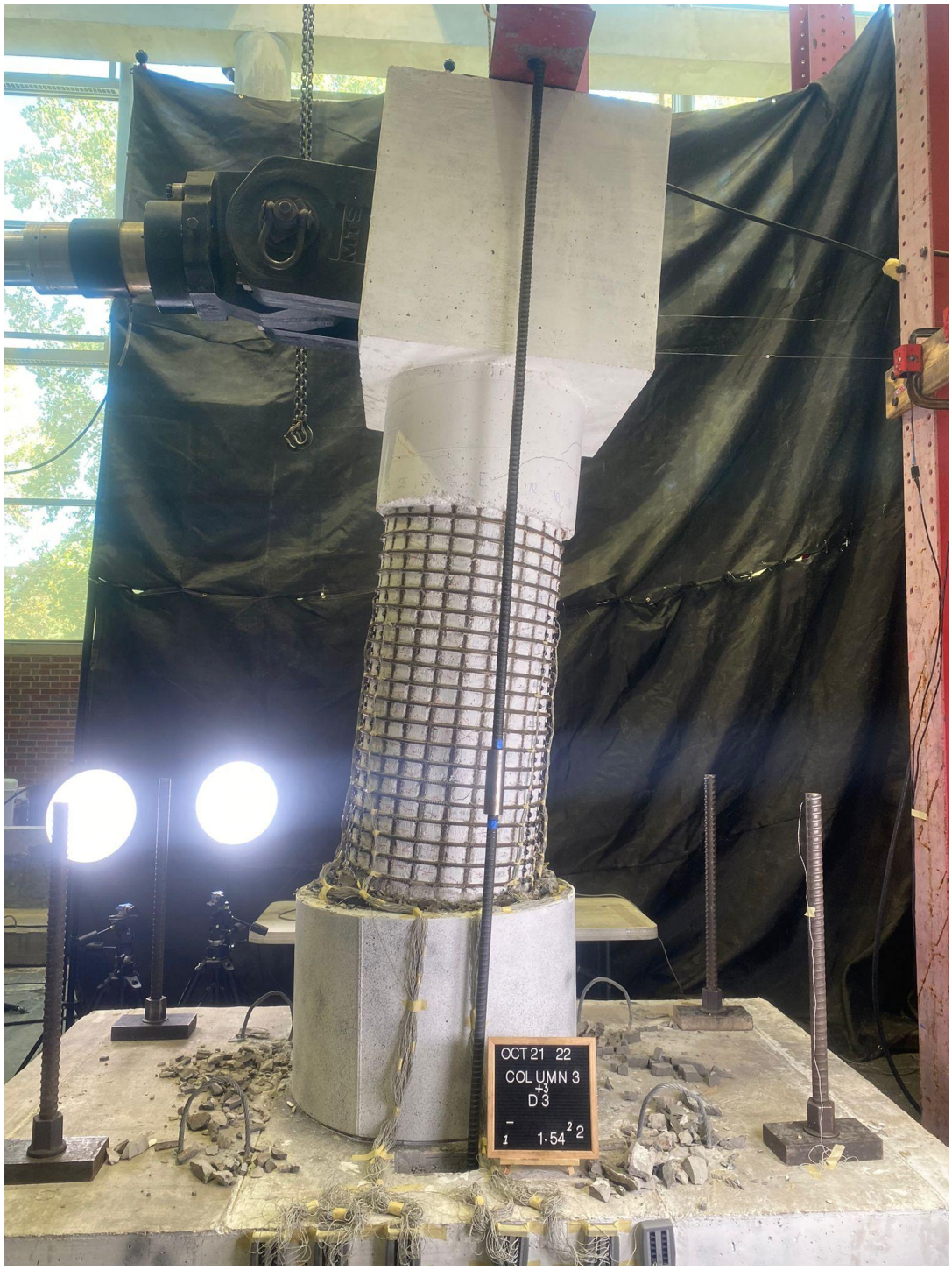


Figure 4-40. Displaced column at the third cycle of ductility three

After the test, an inspection was conducted to investigate whether there was additional damage to the inside portion of the connection on the column. Figure 4-41 and Figure 4-42 show the crushing of the portion of the column inside the socket.



Figure 4-41. Damage of the column inside the external socket connection



Figure 4-42. Damaged surface of the column inside the external socket connection

4.4. Specimen SJS-4

Column test SJS4 was performed on Friday, May 5, 2023, at the Constructed Facilities Laboratory at NCSU. A summary of the key parameters for SJS4 is provided in Table 4-8.

Table 4-8. Summary of SJS4 parameters

Column parameters	
Longitudinal steel detailing	24#6 A706 (ρ_l=2.34%)
Transverse steel	#3 spirals @ 2 inches (ρ_s=1.04%)
Longitudinal steel yield strength	68.4 ksi
Concrete strength (outside the socket)	6.0 ksi
Concrete strength (inside the socket)	8.3 ksi
Diameter of the column	24 in
Height of the column	90 in
Axial load ratio	5%
First yield displacement	1.51 in
Equivalent yield displacement	2.08 in
Maximum applied moment at socket interface	631.7 kip-ft
Failure mode	Crushing of grout, rocking of column
Socket parameters	
Longitudinal steel detailing	24#7 A706
Longitudinal steel yield strength	86.5 ksi
Socket sleeve steel yield strength	42.6 ksi
Thickness of steel sleeves	1/4 in
Concrete strength	12.1 ksi
Grout strength	9.7 ksi
Height of external socket	20.4 in (0.85 Dc)
Internal diameter	26 in
External diameter	32 in

The column had a clear height of 7’-6″ and a diameter of 24″, resulting in a height-to-diameter aspect ratio of 3.62, with a concrete cover of 1″. It was reinforced with 24 Grade 60-A706 #6 longitudinal bars (ρl = 2.34%), and the transverse reinforcement consisted of #3 spirals with a spacing of 2.0″ center to center (ρs = 1.04%).

The external socket had a height of 20 3/8″, resulting in a height-to-diameter ratio of 0.85 (0.85 Dc). The socket longitudinal reinforcement included 24 Grade 80-A706 #7 bars, and the concrete was confined with 1/4″ thick steel sleeves.

4.4.1. Loading Protocol of SJS 4

The initial part of the loading history consisted of a single cycle at a quarter, half, three-fourths, and the yield displacement. The experimentally measured first yield displacement was Δ’y=1.51 in.

For cycles beyond the first yield, the loading protocol involved three cycles at increments of displacement ductility, as determined by Equation 3-1 and Equation 3-2. Table 4-9 presents the values of the ductility displacements applied to SJS4, and Figure 4-43 illustrates the load history for SJS4.

Table 4-9. Displacement ductility of SJS 4

Ductility	Δ (in)	Drift (%)
μ_1	2.08	2.3
$\mu_{1.5}$	3.11	3.5
μ_2	4.15	4.6
μ_3	6.23	6.9
μ_4	8.30	9.2

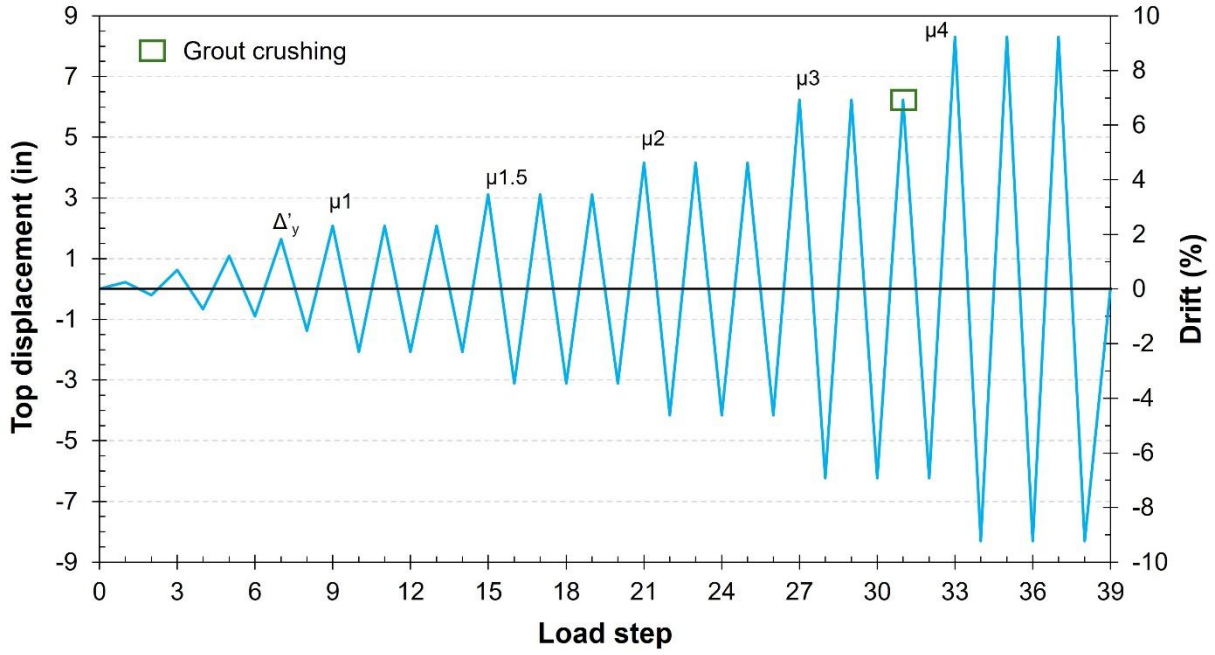


Figure 4-43. Displacement history of SJS 4

4.4.2. Global Response of SJS 4

Figure 4-44 presents the moment-displacement response of the column at the socket interface for SJS4. This specimen experienced its highest applied moment of 631.7 kip-ft at ductility three, initiating grout crushing. Strength degradation occurred during ductility three, accompanied by concrete core crushing, rocking, and grout crushing. A drop of approximately 55% from the maximum moment was observed during the second cycle of ductility four, leading to the conclusion of the test after the third cycle of ductility four. Notably, the column exhibited core crushing at the socket interface during the last cycle of ductility three.

The external socket wall sustained minimal damage, with radial cracks appearing when reaching the column first yield displacement. The inner and outer steel sleeves of the socket did not show any inelastic deformations, while the footing had no visible damage and remained a capacity-protected element.

However, it is important to note that while a plastic hinge began forming in the column at the socket interface, damage to the grout caused the column to rock, preventing the plastic hinge from fully developing.

Figure 4-45 compares the predicted response of a CIP column, derived from moment-curvature analysis using the same material properties as the experimental test, with the envelope of the moment response for SJS4 during the first and third cycles of each ductility displacement. The maximum moment reached by SJS4 was 5.5% higher than the nominal capacity of a CIP column. Strength degradation became evident at a drift of 6.9%, coinciding with grout crushing.

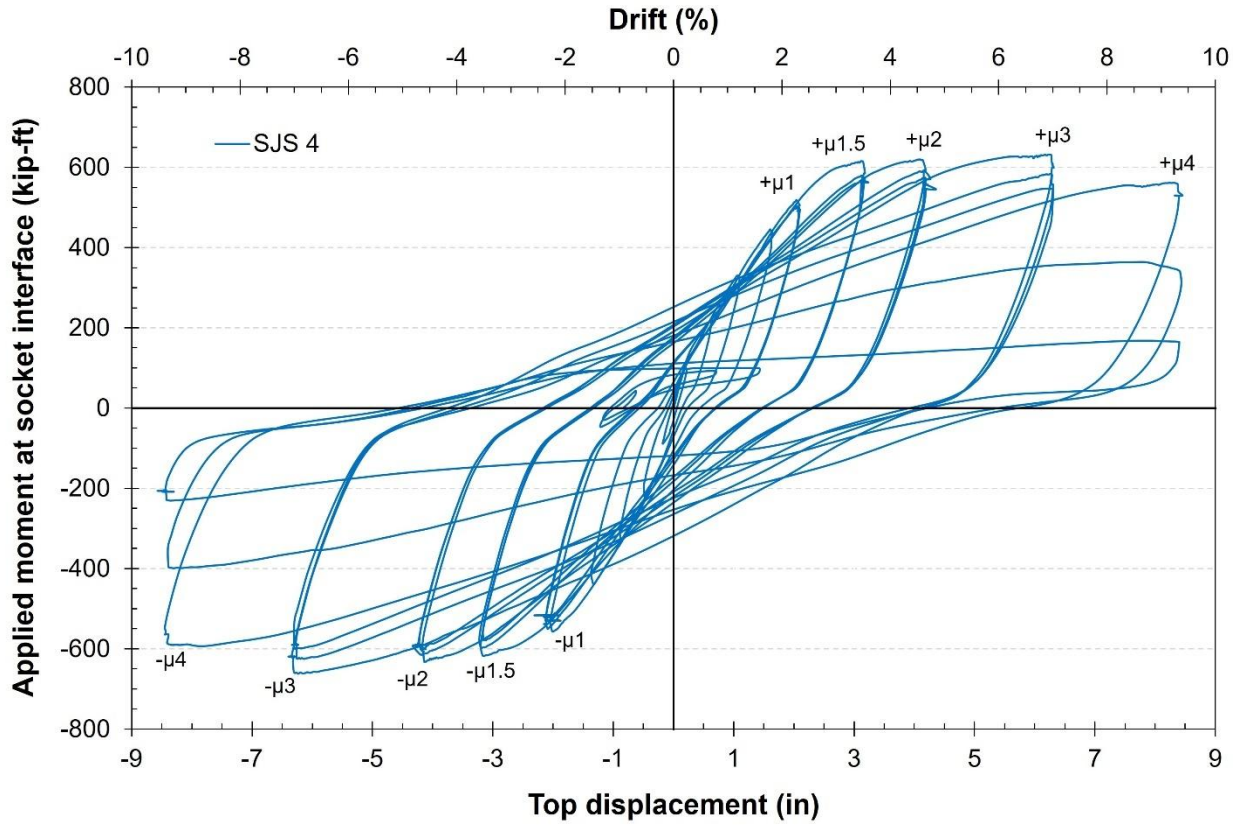


Figure 4-44. Moment-displacement response of SJS 4

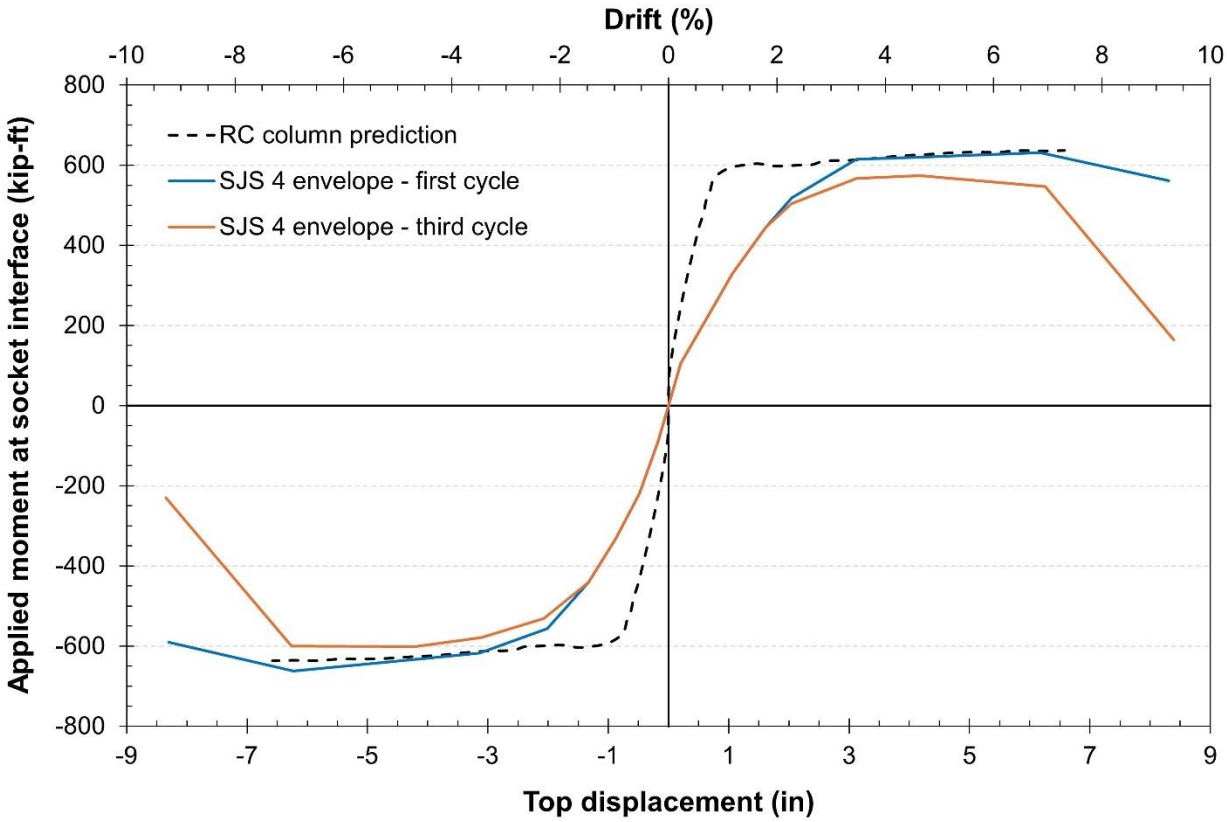


Figure 4-45. SJS 4 experimental envelopes compared to an RC column prediction

4.4.3. Damage progression of SJS 4

Figure 4-46 shows the existing damage to the column and socket wall from SJS3, with no new cracks observed before reaching the yield displacement. The cracks marked in red correspond to the positive loading direction, while those in black indicate cracks that occurred during the negative loading direction.

A 0.138″ (3.5 mm) gap between the grout and the steel sleeve of the external socket appeared at the first cycle of ductility one, as shown in Figure 4-47. The column had crack widths that were at most 0.008″ (0.2 mm). Additionally, Figure 4-48 exhibits a 0.158″ (4.0 mm) column uplift relative to the top of the grout. Figure 4-49 shows the crack pattern of the specimen at the last cycle of ductility one.



Figure 4-46. Damage on the column and socket wall at the start of SJS 4

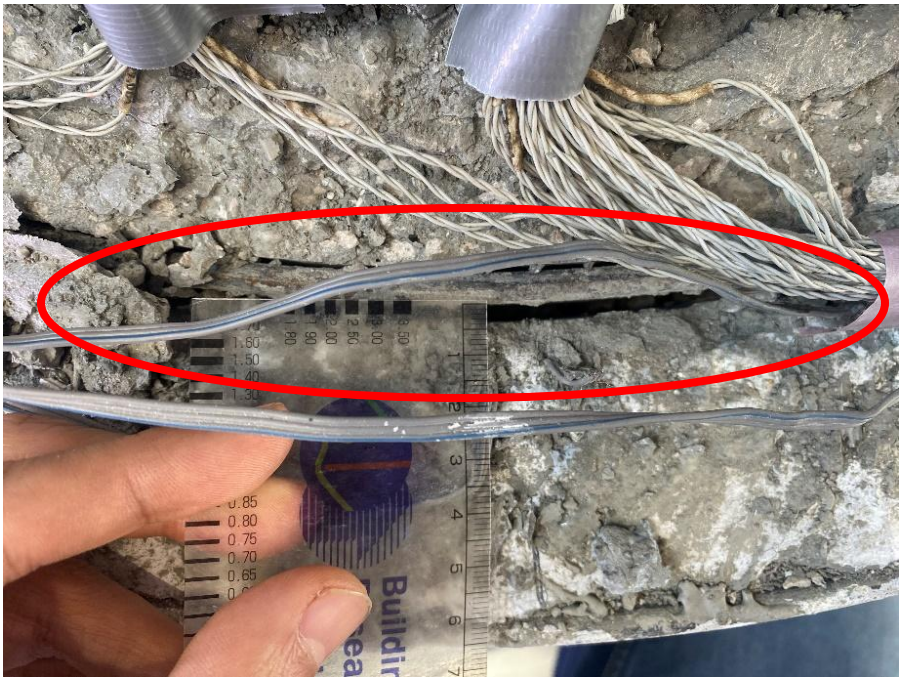


Figure 4-47. Gap between the steel sleeve and grout on the south surface at ductility one



Figure 4-48. Uplift of the column at the last cycle of ductility one

In the last cycle of ductility one and a half, an uplift of 0.394″ (10 mm) between the column and the grout was observed. Figure 4-50 shows a 0.197″ (5.0 mm) gap between the grout and the steel sleeve of the external socket, while Figure 4-51 shows the grout uplift and the damage on the grout, which started to present radial cracks due to compression.

The grout between the column and the external socket started to crush at the third cycle of ductility two. Figure 4-52 depicts the damage to the external socket connection at the third cycle of ductility two. The damage on the column started to present as flaking of the concrete at the interface with the external socket connection.

In the last cycle of ductility three, an uplift of 0.197″ (5 mm) between the footing and the socket sleeve was observed. Additionally, three gaps were observed between the different materials of the connection, with a maximum of 0.276″ (7 mm). Figure 4-53 shows the gaps in the connection that developed. Figure 4-54 shows grout crushing and the initiation of concrete core crushing at the column interface with the external socket connection.



Figure 4-49. Crack pattern on the south surface at the last cycle of ductility one



Figure 4-50. Gaps at the external socket connection at the last cycle of ductility one and a half



Figure 4-51. Damage of the column and uplift of grout at the last cycle of ductility one and a half



Figure 4-52. Damage of the socket connection at the third cycle of ductility two

At the end of ductility four, the grout crushing spread around the connection circumference, while the column did not present additional damage. Figure 4-55 shows the column and the external socket connection deterioration at the last cycle of ductility four.

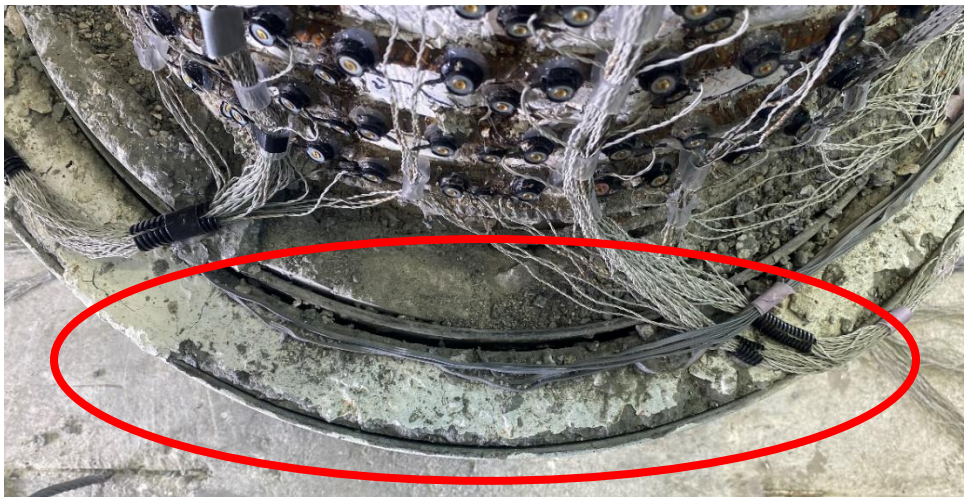


Figure 4-53. Gaps at the external socket connection at the last cycle of ductility three

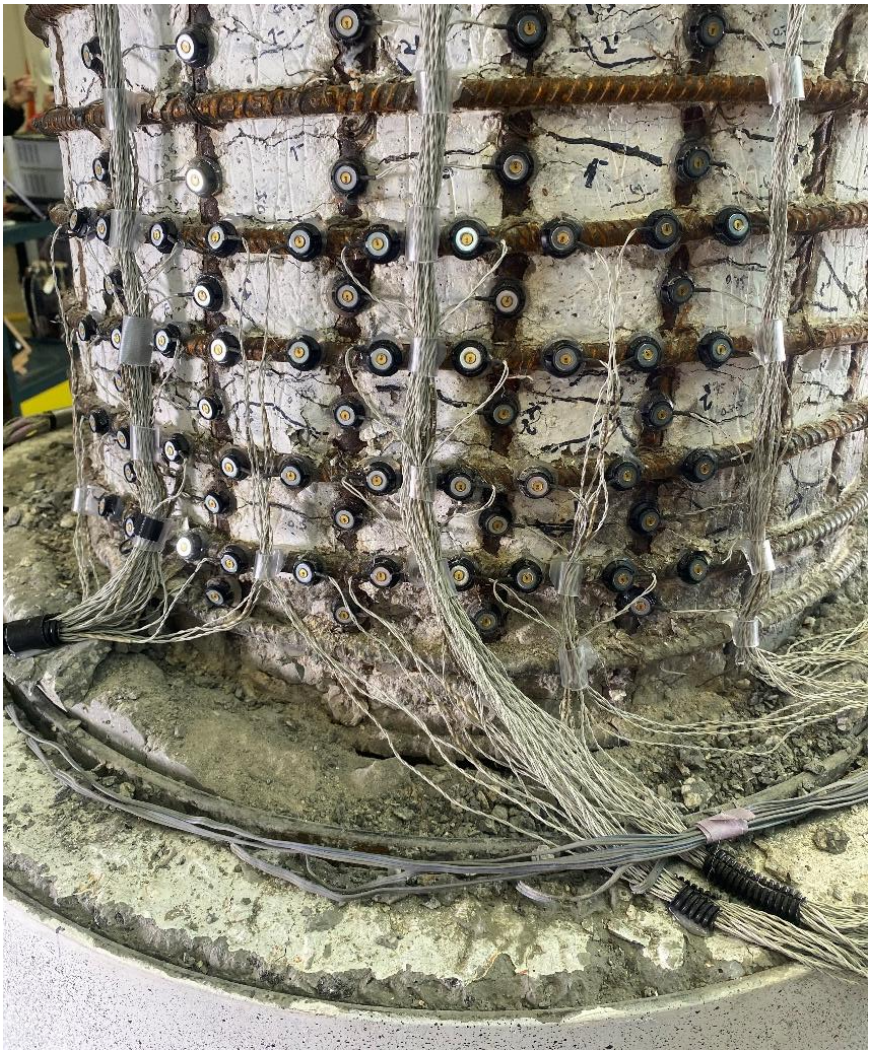


Figure 4-54. Damage of the socket connection at the third cycle of ductility three

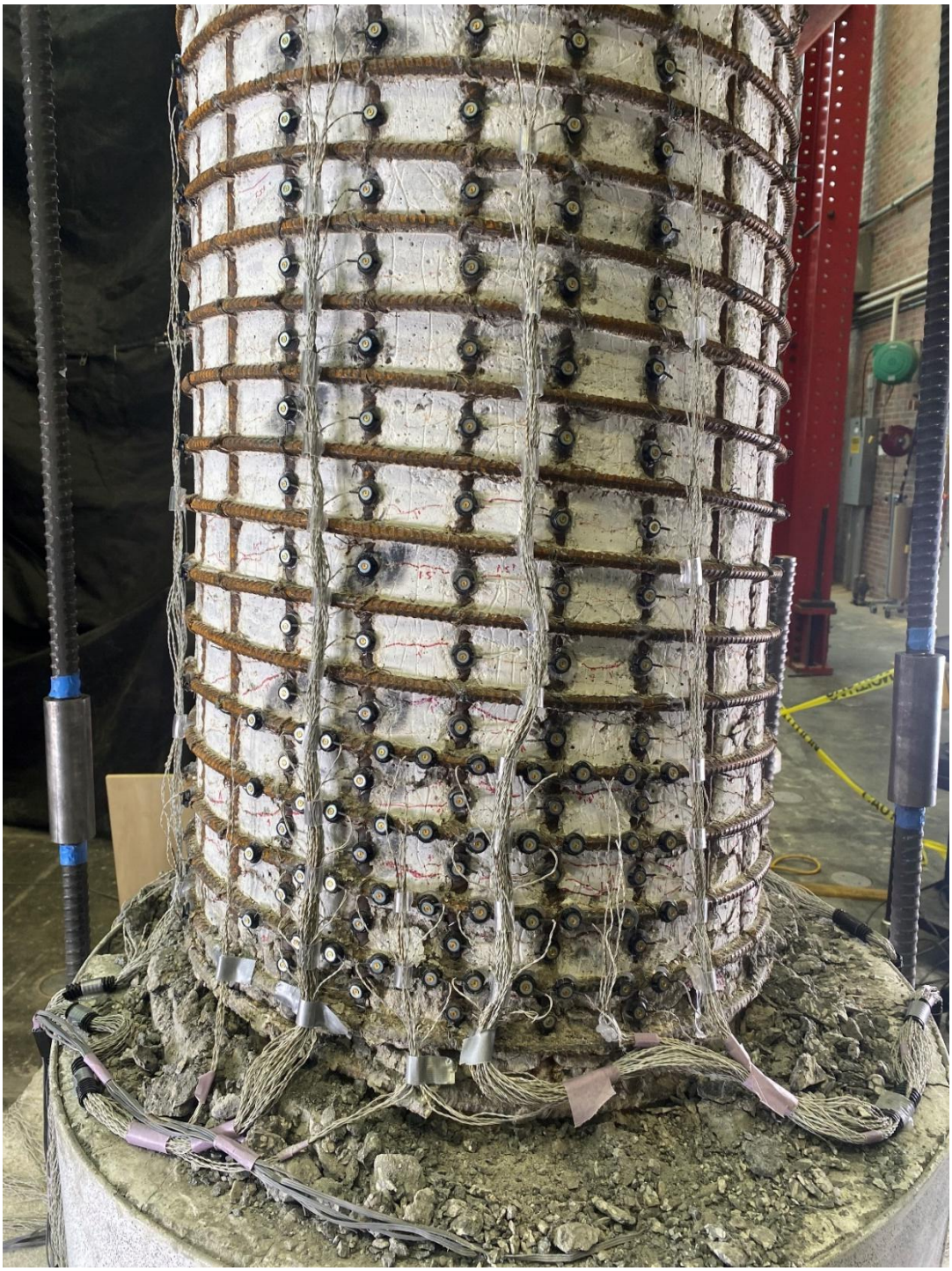


Figure 4-55. Damage of the specimen on the south surface at ductility four

Figure 4-56 shows the displaced column and the uplift at the connection surface. The footing did not exhibit any significant cracks throughout the test, and the external socket concrete presented only the radial cracks that appeared at the beginning of the test.



Figure 4-56. Displaced column at the third cycle of ductility four

After the test, an inspection was conducted to investigate whether there was additional damage to the inside portion of the connection on the column. Figure 4-57 and Figure 4-58 show the crushing of the portion of the column inside the socket and longitudinal bar deformed due to rocking of the column.



Figure 4-57. Damage of the column inside the external socket connection



Figure 4-58. Damaged surface of the column inside the external socket connection

4.5. Specimen SJS-5

Column test SJS5 was performed on Tuesday, November 21, 2023, at the Constructed Facilities Laboratory at NCSU. A summary of the key parameters for SJS5 is provided in Table 4-10.

Table 4-10. Summary of SJS5 parameters

Column parameters	
Longitudinal steel detailing	20#5 A706 (ρ_l=2.4%)
Transverse steel	#3 spirals @ 2 inches (ρs=1.3%)
Longitudinal steel yield strength	68.4 ksi
Concrete strength	6.8 ksi
Diameter of the column	18 in
Height of the column	90 in
Axial load ratio	5%
First yield displacement	1.15 in
Equivalent yield displacement	1.59 in
Maximum applied moment at socket interface	256.7 kip-ft
Failure mode	Crushing of concrete column inside the connection
Socket parameters	
Longitudinal steel detailing	20#6 A706
Longitudinal steel yield strength	86.5 ksi
Socket sleeve steel yield strength	55 ksi
Thickness of steel sleeves	1/4 in
Concrete strength	14.0 ksi
Grout strength	10.3 ksi
Height of external socket	15.3 in (0.85 Dc)
Internal diameter	20 in
External diameter	26.5 in

The column had a clear height of 7’-6″ and a diameter of 18″, resulting in a height-to-diameter aspect ratio of 5.0, with a concrete cover of 1″. It was reinforced with 20 Grade 60-A706 #5 longitudinal bars (ρl = 2.4%). The transverse reinforcement consisted of #3 spirals with a spacing of 2.0″ center to center (ρs = 1.3%).

The external socket had a height of 15.3″, resulting in a height-to-diameter ratio of 0.85 (0.85 Dc). The socket longitudinal reinforcement included 20 Grade 80-A706 #6 bars, and the concrete was confined with 1/4″ thick steel sleeves.

4.5.1. Loading Protocol of SJS 5

The initial part of the loading history consisted of a single cycle at a quarter, half, three-fourths, and the yield displacement. The experimentally measured first yield displacement was Δ’y=1.15 in.

For cycles beyond the first yield, the loading protocol involved three cycles at increments of displacement ductility, as determined by Equation 3-1 and Equation 3-2. Table 4-11 presents the values of the ductility displacements applied to SJS5, and Figure 4-59 illustrates the load history for SJS5.

Table 4-11. Displacement ductility of SJS 5

Ductility	Δ (in)	Drift (%)
μ_1	1.59	1.8
$\mu_{1.5}$	2.39	2.7
μ_2	3.18	3.5
μ_3	4.78	5.3
μ_4	6.34	7.0

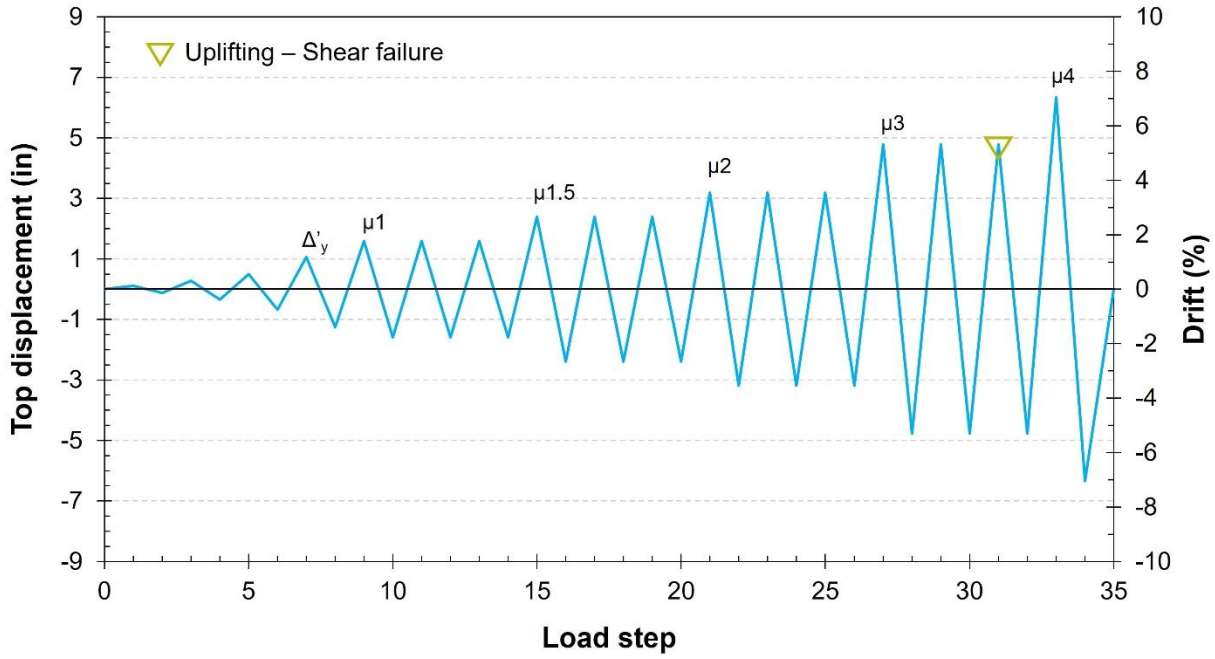


Figure 4-59. Displacement history of SJS 5

4.5.2. Global Response of SJS 5

Figure 4-60 presents the moment-displacement response of the column at the socket interface for SJS5. This specimen experienced its highest applied moment of 256.7 kip-ft at ductility three, which initiated grout splitting and shear failure inside the external socket connection. Strength degradation began during ductility three, accompanied by rocking, grout splitting, and lifting. A drop of approximately 55% from the maximum moment was observed during the first cycle of ductility four, leading to the conclusion of the test after the first negative cycle of ductility four. Notably, the column began to exhibit flaking of the concrete core at the socket interface during the first cycle of ductility three. By the second cycle of ductility three, the grout started to uplift, causing the column to rock.

The external socket wall sustained minimal damage, with radial cracks appearing before the column reached its first yield displacement. The inner and outer steel sleeves of the socket did not show any inelastic deformations, while the footing had no visible damage and remained a capacity-protected element.

However, it is important to note that while a plastic hinge was beginning to form at the socket interface, the splitting of the grout and the shear failure of the column portion inside the socket caused the column to rock, preventing the plastic hinge from fully developing.

Figure 4-61 compares the predicted response of a CIP column, derived from moment-curvature analysis using the same material properties as the experimental test, with the envelope of the moment response for SJS5 during the first and third cycles of each ductility displacement. The maximum moment reached by SJS5 was 1.0% higher than the nominal capacity of a CIP column. Strength degradation became evident at a drift of 5.3%, coinciding with the grout crushing.

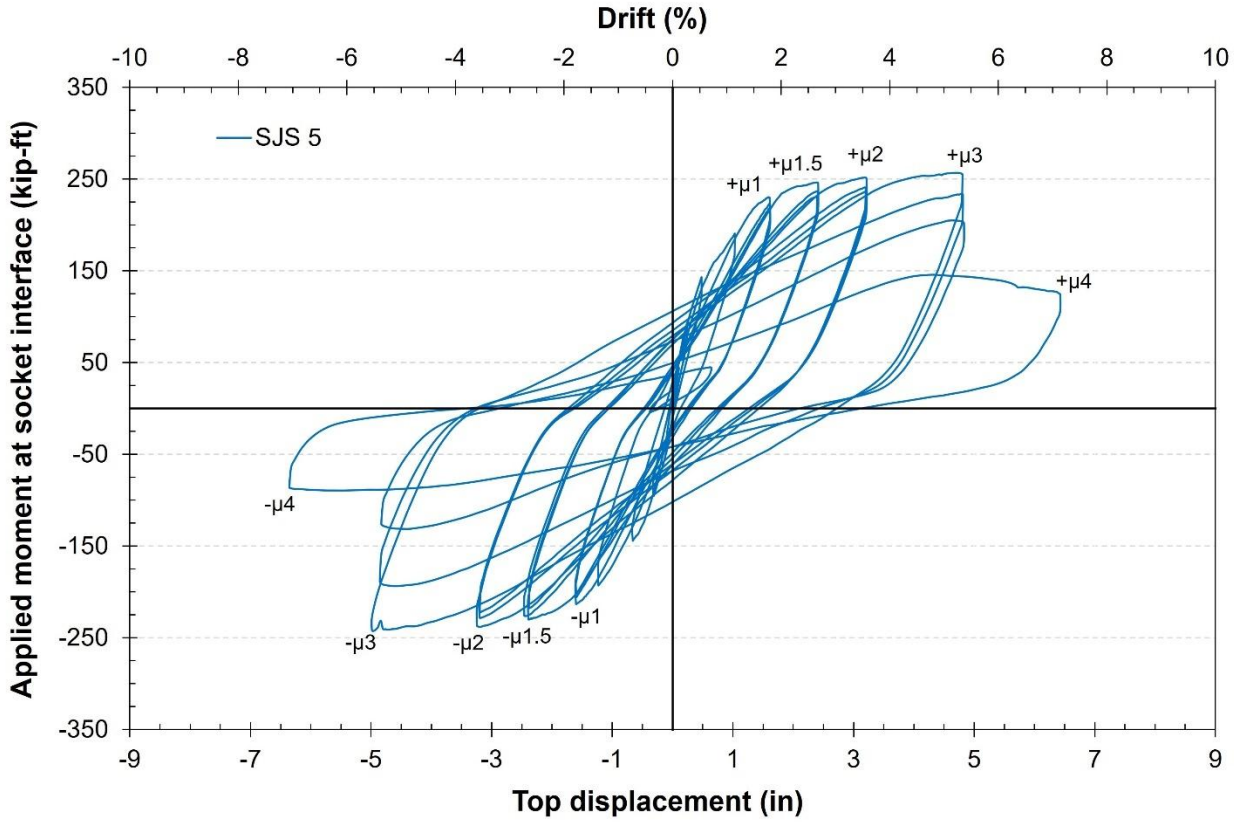


Figure 4-60. Moment-displacement response of SJS 5

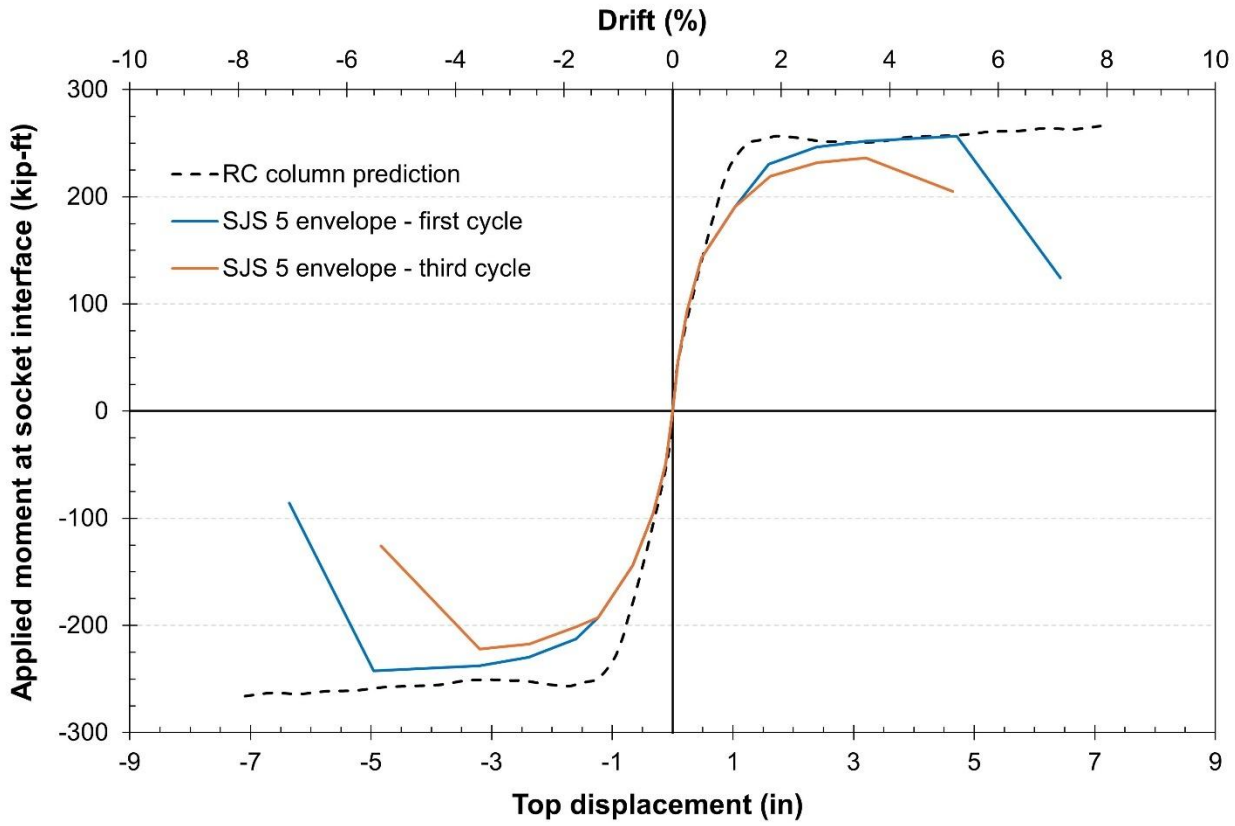


Figure 4-61. SJS 5 experimental envelopes compared to an RC column prediction

4.5.3. Damage progression of SJS 5

Figure 4-62 shows previous cracks on the column and socket wall, and no new cracks were found before the yielding displacement. However, a 0.032″ (0.8 mm) gap between the grout and the steel sleeve of the external socket appeared at the last cycle of ductility one, as shown in Figure 4-63.

The column had crack widths that were at most 0.008″ (0.2 mm) at the last cycle of ductility one. Additionally, there was no visible column uplift relative to the top of the grout. Figure 4-64 shows the crack pattern of the specimen at the last cycle of ductility one. The cracks marked in red are related to the positive loading direction, while black ones represent those that occurred during the negative loading direction.

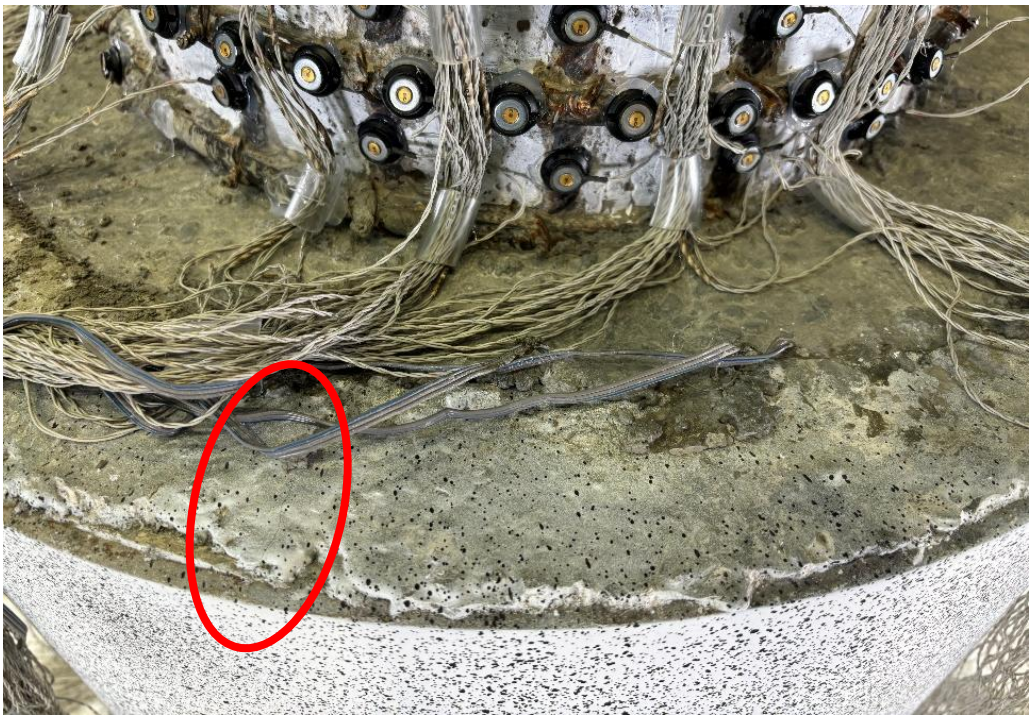


Figure 4-62. Initial cracks on the column and socket wall at the start of SJS 5

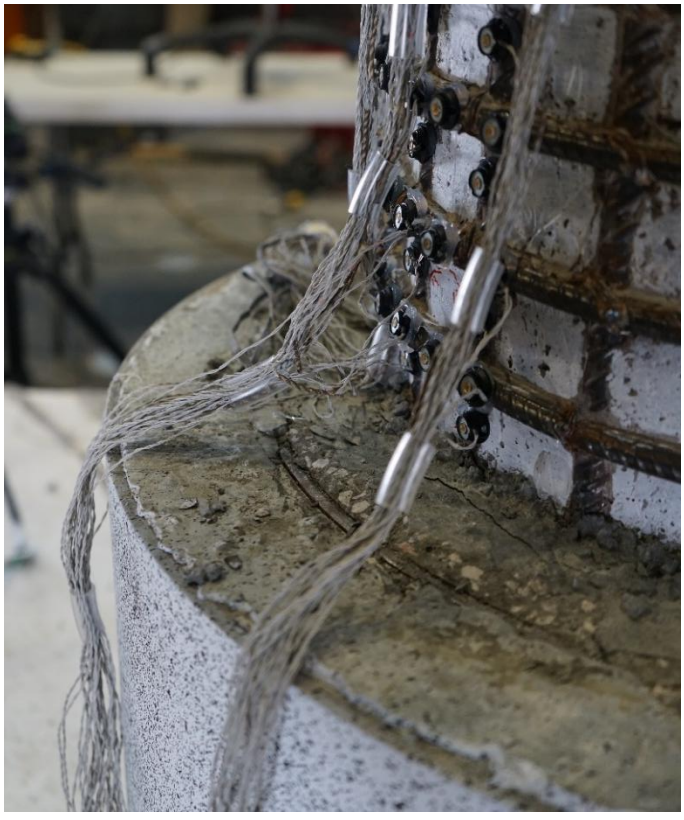


Figure 4-63. Gap between the steel sleeve and grout on the south surface at ductility one

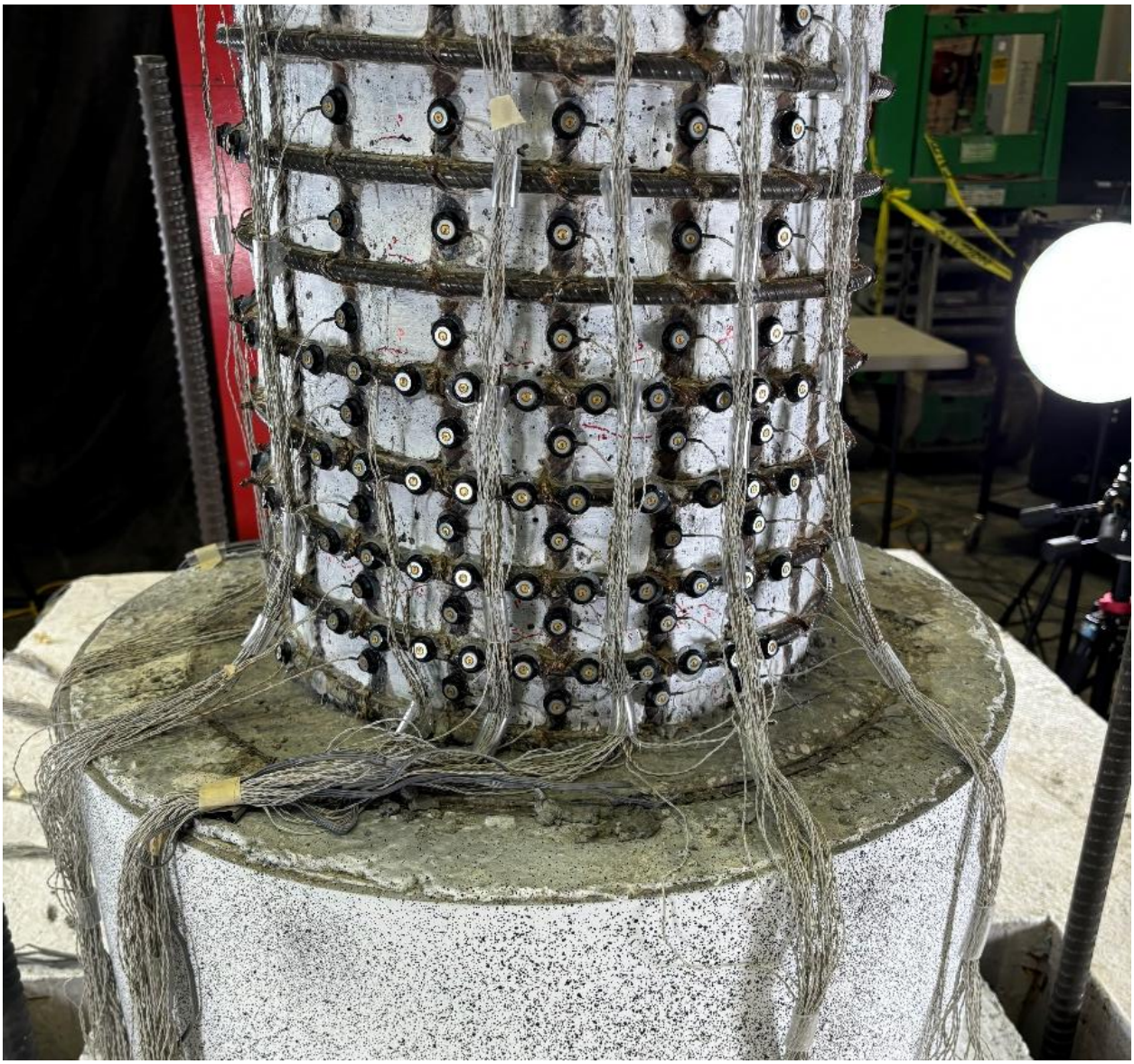


Figure 4-64. Crack pattern on the south surface at the last cycle of ductility one

In the last cycle of ductility 1.5, an uplift of 0.197″ (5 mm) between the column and the grout was observed. Additionally, the grout started to present radial cracks due to compression. Figure 4-65 shows the damage at the connection interface on the north side of the column and grout at the last cycle of ductility one and a half.

The grout between the column and the external socket had an uplift of 0.394″ (10 mm) at the third cycle of ductility two. Figure 4-66 depicts the damage to the external socket connection

at the third cycle of ductility two. The damage on the column started to present as flaking of the concrete at the interface with the external socket connection.

In the final cycle of ductility three, the grout started to split and uplift without presenting crushing of the material. Figure 4-67 and Figure 4-68 depict the damage to the column and the grout at the last cycle of ductility three.



Figure 4-65. Damage of the column at the last cycle of ductility one and a half

At the first cycle of ductility four, the splitting and uplifting of grout spread around the connection circumference, while the column did not present additional damage. Figure 4-69 shows the column and the external socket connection deterioration at the last cycle of ductility four.



Figure 4-66. Damage of the socket connection at the third cycle of ductility two

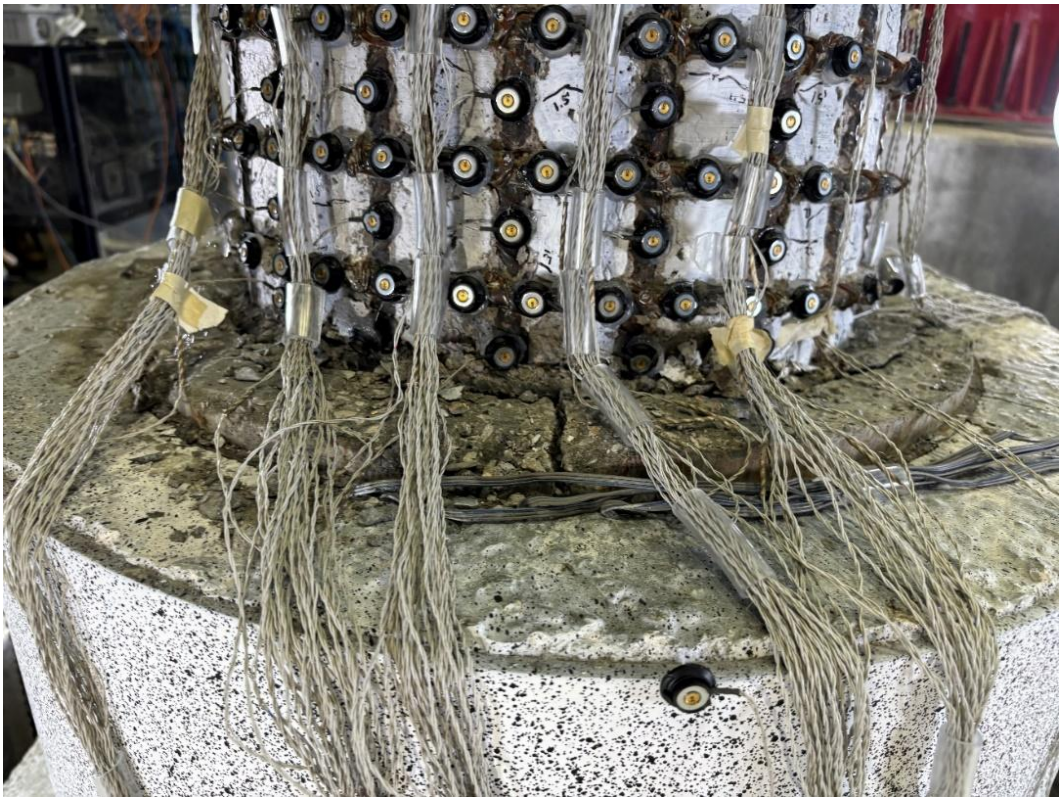


Figure 4-67. Splitting and uplifting of grout at the last cycle of ductility three



Figure 4-68. Damage of column and the socket connection at the third cycle of ductility three



Figure 4-69. Damage of the specimen on the south surface at ductility four

Figure 4-70 shows the displaced column and the uplift of the grout at the external socket interface. The footing did not exhibit any significant cracks throughout the test, and the external socket concrete presented only the radial cracks that appeared at the beginning of the test.

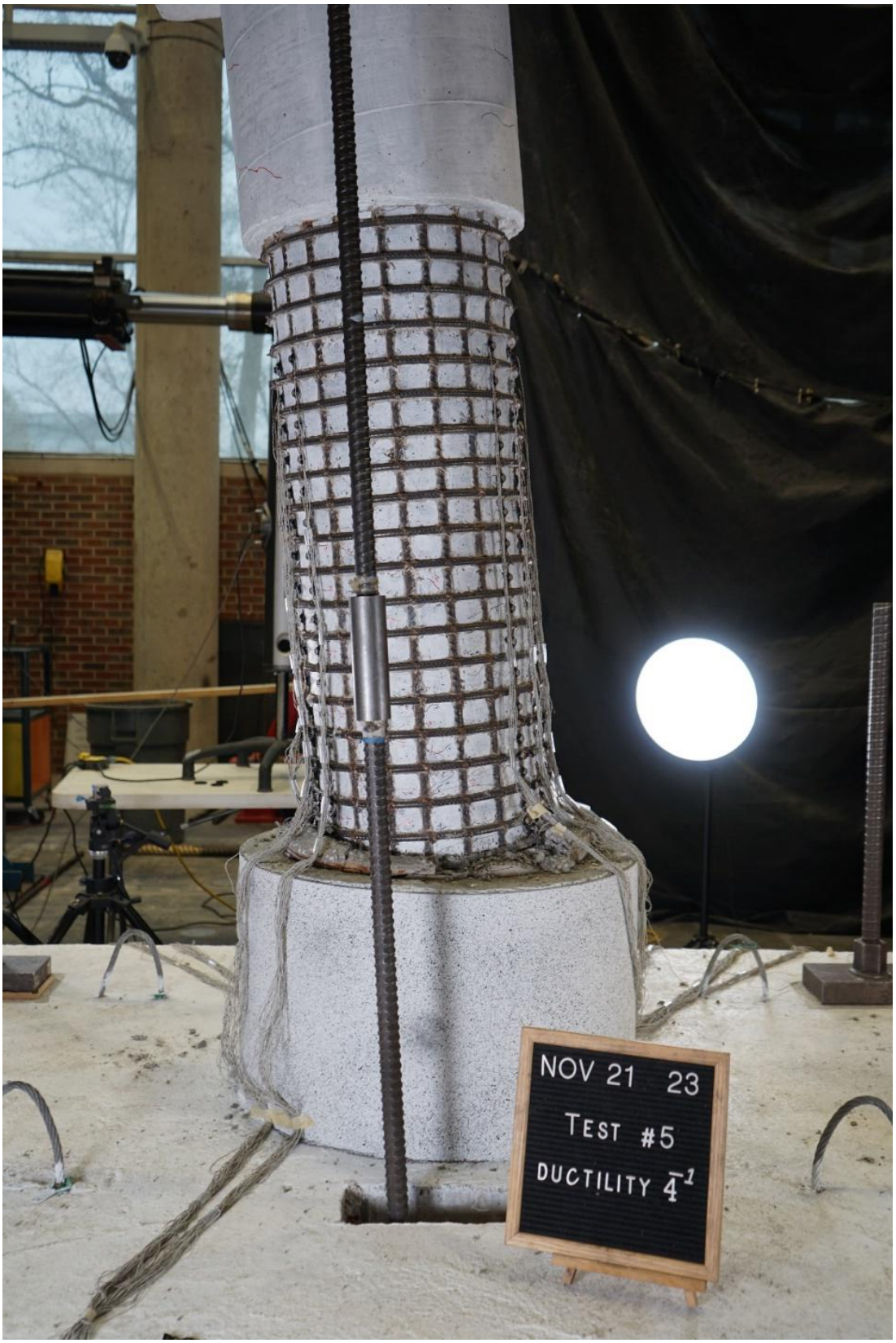


Figure 4-70. Displaced column at the first cycle of ductility four

After the test, an inspection was conducted to investigate if there was additional damage on the inside portion of the connection on the column. Figure 4-71 shows the crushing of the portion of the column inside the socket



Figure 4-71. Damage to the column inside the external socket connection

4.6. Specimen SJS-6

Column test SJS6 was performed on Tuesday, January 23, 2024, at the Constructed Facilities Laboratory at NCSU. A summary of the key parameters for SJS6 is provided in Table 4-12.

Table 4-12. Summary of SJS6 parameters

Column parameters	
Longitudinal steel detailing	20#5 A706 (ρ_l=2.4%)
Transverse steel	#3 spirals @ 2 inches (ρs=1.3%)
Longitudinal steel yield strength	68.4 ksi
Concrete strength (outside the socket)	6.8 ksi
Concrete strength (inside the socket)	9.2 ksi
Diameter of the column	18 in
Height of the column	90 in
Axial load ratio	5%
First yield displacement	1.15 in
Equivalent yield displacement	1.59 in
Maximum applied moment at socket interface	271.7 kip-ft
Failure mode	Rupture of N4, N5, N6 and N7 bars
Socket parameters	
Longitudinal steel detailing	20#6 A706
Longitudinal steel yield strength	86.5 ksi
Socket sleeve steel yield strength	55 ksi
Thickness of steel sleeves	1/4 in
Concrete strength	14.0 ksi
Grout strength	10.0 ksi
Height of external socket	15.3 in (0.85 Dc)
Internal diameter	20 in
External diameter	26.5 in

The column had a clear height of 7'-6″ and a diameter of 18″, resulting in a height-to-diameter aspect ratio of 5.0, with a concrete cover of 1″. It was reinforced with 20 Grade 60-A706 #5 longitudinal bars (ρl = 2.4%). The transverse reinforcement consisted of #3 spirals with a spacing of 2.0″ center to center (ρs = 1.3%).

The external socket had a height of 15.3″, resulting in a height-to-diameter ratio of 0.85 (0.85 Dc). The socket longitudinal reinforcement included 20 Grade 80-A706 #6 bars, and the concrete was confined with 1/4″ thick steel sleeves.

4.6.1. Loading Protocol of SJS 6

Since SJS6 is a repair of the column portion that was inserted into the socket connection from SJS5, and SJS5 exhibited significant non-linear behavior, the yield displacement for this test is based on the experimentally measured first yield displacement of SJS5, which was Δ'y=1.15 in.

The initial part of the loading history consisted of four single cycles that matched the applied moment at the socket at a quarter, half, three-quarters, and yield displacement of SJS5, for which the corresponding ductility values for SJS6 are shown in Table 4-13.

Table 4-13. Loading history for the single cycles of SJS 6

Applied moment at socket interface (kip-ft)	Δ (in)	Drift (%)	Ductility
48.2	0.24	0.3	0.5 Δ'y
96.5	0.62	0.7	0.75 Δ'y
145.0	1.15	1.3	Δ'y
193.0	1.59	1.8	μ_1

For cycles beyond the ductility one, the loading consisted of 3 cycles at increments of displacement ductility, as shown in Table 4-14. The load history for SJS6 is shown in Figure 4-72.

Table 4-14. Displacement ductility of SJS 6

Ductility	Δ (in)	Drift (%)
$\mu_{1.5}$	2.34	2.6
$\mu_{2.2}$	3.51	3.9
μ_{3}	4.72	5.2
$\mu_{4.4}$	7.01	7.8

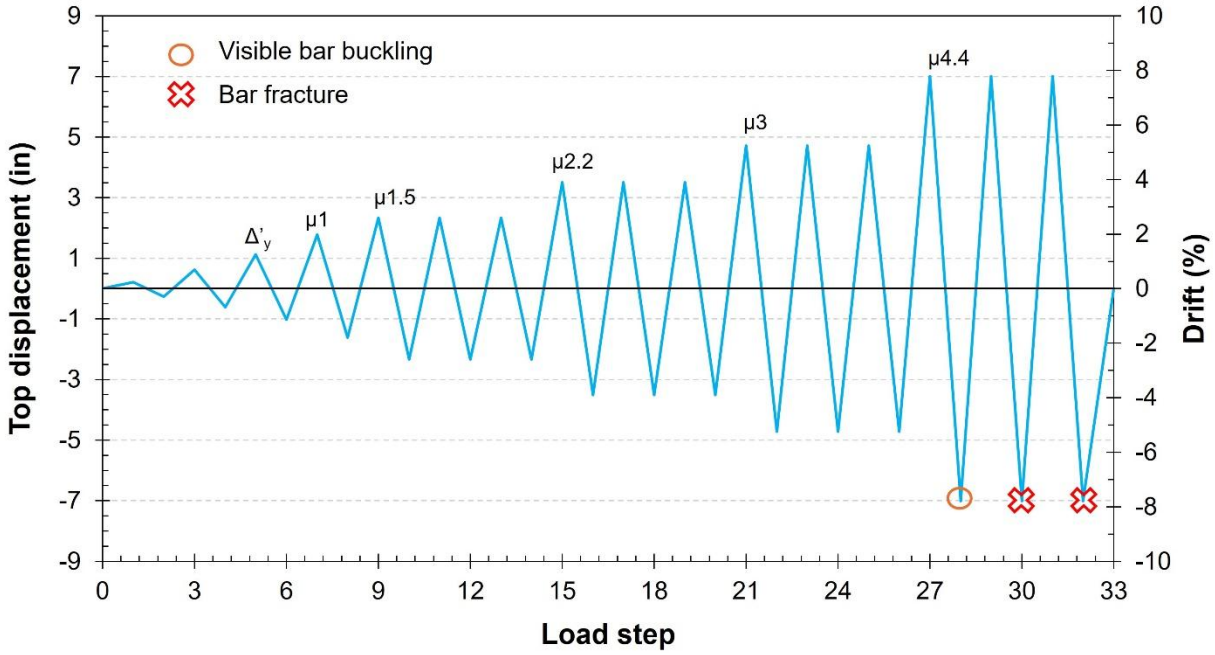


Figure 4-72. Displacement history of SJS 6

4.6.2. Global Response of SJS 6

Figure 4-73 presents the moment-displacement response of the column at the socket interface for SJS6. This specimen achieved a drift ratio of 7.8%, with the maximum applied moment reaching 271.7 kip-ft at ductility four point four. At this stage, the column concrete core began to experience crushing. During the second cycle of ductility four point four, noticeable strength degradation occurred as bar buckling initiated, leading to the fracture of longitudinal bars N5. During the third negative cycle of ductility four point four, three longitudinal bars N4, N6, and N7 fractured, leading to a drop of approximately 50% from the maximum moment, at which

point the test was concluded. Notably, the plastic hinge successfully formed on the column above the interface of the external socket connection, with a socket height of 0.85 Dc.

The external socket wall sustained minimal damage, with no new radial cracks beyond those observed in test SJS5. The inner and outer steel sleeves of the socket did not exhibit any inelastic deformations, and the footing showed no visible damage, remaining a capacity-protected element.

Figure 4-74 compares the predicted response of a CIP column, derived from moment-curvature analysis using the same material properties as the experimental test, with the envelope of the moment response for SJS6 during the first and third cycles of each ductility displacement. The maximum moment reached by SJS6 was 6.8% higher than the nominal capacity of a CIP column. Strength degradation became evident at a drift of 7.8%, coinciding with the onset of bar buckling.

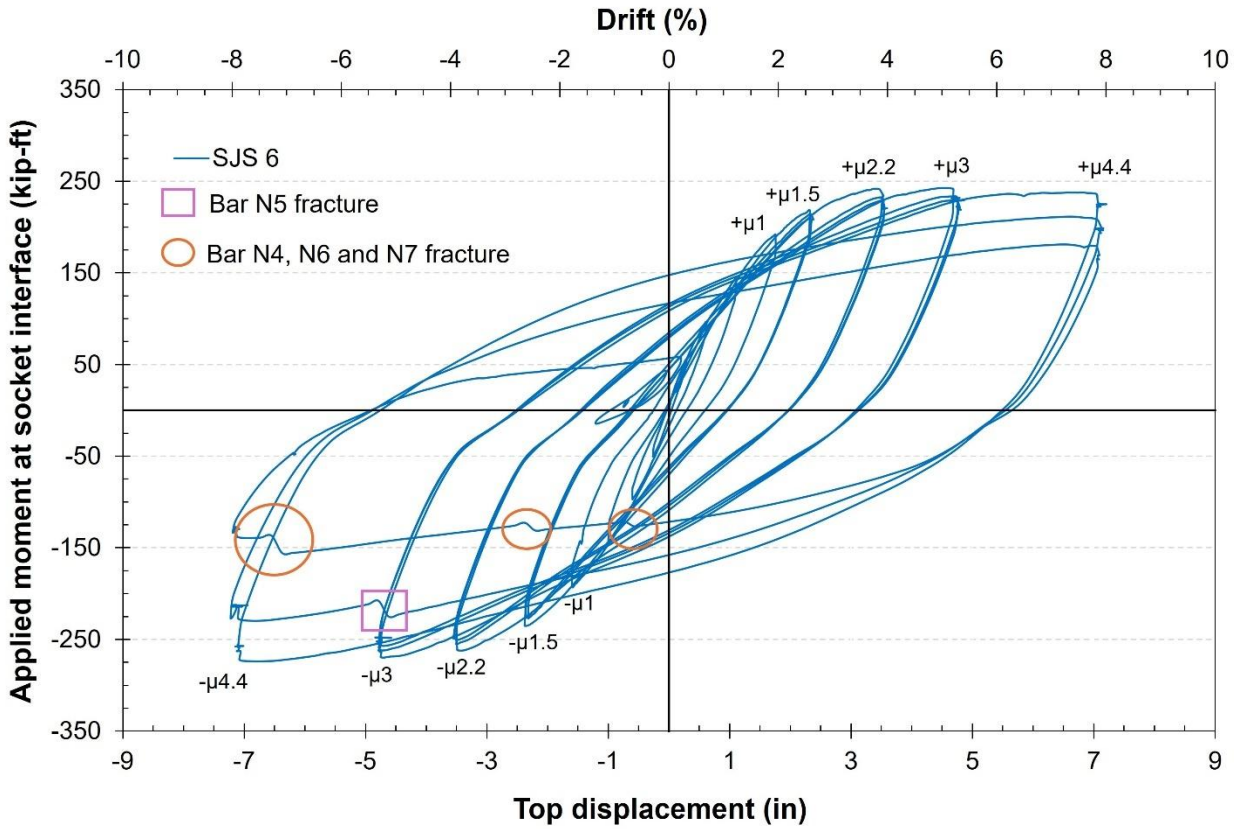


Figure 4-73. Moment-displacement response of SJS 6

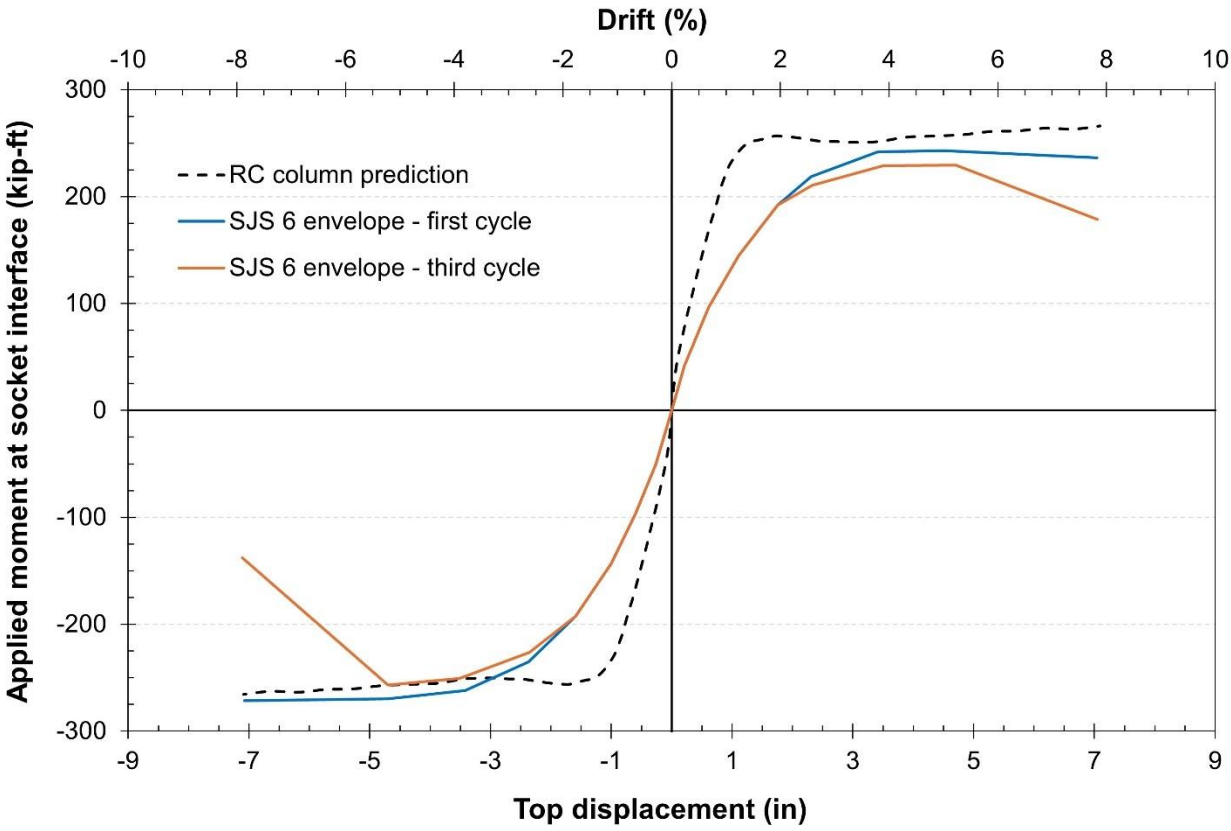


Figure 4-74. SJS 6 experimental envelopes compared to an RC column prediction

4.6.3. Damage progression of SJS 6

Figure 4-75 shows previous cracks on the column and socket wall, and no new cracks were found before the yielding displacement. The column had previous damage from the experimental test of SJS-5, where the initiation of crushing was observed; thus, in SJS-6, we focused on cracks developed on the connection.

At the end of ductility two, a 0.197″ (5 mm) uplift between the grout and the external socket wall was observed. Additionally, the grout started to present radial cracks due to compression. Figure 4-76 shows the uplift of the grout at the last cycle of ductility two.

The grout between the column and the external socket had an uplift of 0.394″ (10 mm) at the third cycle of ductility three. Figure 4-77 depicts the damage to the external socket connection at the third cycle of ductility three. Spalling of the concrete at the interface with the external socket

connection was observed. The external socket wall did not present any damage by the end of ductility three.



Figure 4-75. Initial damage on the column and socket wall at the start of the SJS6



Figure 4-76. Uplift of grout on the south surface at the last cycle of ductility two



Figure 4-77. Damage of the socket connection at the third cycle of ductility three

As shown in Figure 4-78, visible reinforcing bar buckling occurred during the first negative cycle of ductility four when bars S4 experienced buckling. Upon opposite direction of loading (second positive cycle of ductility four), bars N4, N5 and N6 buckled, as shown in Figure 4-79.

A bar fracture occurred at the second negative cycle of ductility four on the extreme bar (N5). Additionally, five bars on the south face of the column experienced buckling (S4, S5, S6, S7 and S8). Figure 4-80 shows the column and the external socket connection damage at the second cycle of ductility four.

At the last positive cycle of ductility 4, the bars N3, N4, N6, and N7 experienced large buckling deformation. Additionally, the grout at the surface of the external connection experienced splitting and uplifting. Figure 4-81 shows the column and the external socket connection damage at the last positive cycle of ductility four.

As shown in Figure 4-82, three longitudinal bars fractured on the third negative cycle of ductility four (N4, N6, N7). The longitudinal bars on the south side also experienced large buckling deformations, as shown in Figure 4-83.



Figure 4-78. Damage of column and the grout on the south side at the first cycle of ductility four



Figure 4-79. Damage of the column and the socket connection on the north side at the second cycle of ductility four



Figure 4-80. Damage of the column and the socket connection on the south side at the second cycle of ductility four



Figure 4-81. Damage of the column and the socket connection on the north side at the last positive cycle of ductility four



Figure 4-82. Damage of the column and the socket connection on the north side at the last negative cycle of ductility four



Figure 4-83. Damage of the column and the socket connection on the south side at the last negative cycle of ductility four

The footing did not present any significant cracks throughout the test. Additionally, the grout between the column and the socket experienced splitting just at the surface of the connection, while the grout remained without damage at one inch below the interface of the socket connection and the column. The concrete of the external socket wall did not present any damage. Figure 4-84 shows the damage of the footing and external socket connection of SJS 6.



Figure 4-84. Damage on the footing and the external socket connection at the end of the experimental test for SJS-6

Figure 4-85 presents the spread of damage to the south face of the column. The visible concrete crushing height was 8 inches (203 mm) measured from the socket surface.



Figure 4-85. Spread of damage on the column at the south face at the end of the experimental test for SJS-6

4.7. Specimen SJS-7

Column test SJS7 was performed on Monday, December 4, 2023, at the Constructed Facilities Laboratory at NCSU. A summary of the key parameters for SJS7 is provided in Table 4-15.

Table 4-15. Summary of SJS7 parameters

Column parameters	
Longitudinal steel detailing	20#5 A706 (ρ_l=2.4%)
Longitudinal steel yield strength	68.4 ksi
A606-4 steel yield strength	60.6 ksi
A709 steel yield strength	56.8 ksi
Thickness of steel tube inside socket	1/8 in
Thickness of steel tube outside socket	3/8 in
Concrete strength	5.6 ksi
Diameter of the column	18 in
Height of the column	90 in
Axial load ratio	5%
First yield displacement	1.15 in
Equivalent yield displacement	1.59 in
Maximum applied moment at socket interface	315.7 kip-ft
Failure mode	Crushing of concrete column inside the connection
Socket parameters	
Longitudinal steel detailing	20#6 A706
Longitudinal steel yield strength	86.5 ksi
Socket sleeve steel yield strength	55 ksi
Thickness of steel sleeves	1/4 in
Concrete strength	11.3 ksi

Table 4-15. Summary of SJS7 parameters (continued)

Socket parameters	
Grout strength	9.0 ksi
Height of external socket	15.3 in (0.85 Dc)
Internal diameter	20 in
External diameter	26.5 in

The column had a clear height of 7'-6″ and a diameter of 18″, resulting in a height-to-diameter aspect ratio of 5.0. The column was reinforced with 20 Grade 60-A706 #5 longitudinal bars (ρl=2.4%) and an external steel tube to confine the concrete. The clear distance between the longitudinal reinforcing steel and the inner surface of the tube was 1″. The resulting system is commonly referred to as RCFST. The RCSFT has two cross-sections with varying steel thicknesses. The portion of the column inside the external connection has a reduced steel thickness to minimize the forces transmitted to the external socket.

The external socket had a height of 15.3″, resulting in a height-to-diameter ratio of 0.85 (0.85 Dc). The socket longitudinal reinforcement included 20 Grade 80-A706 #6 bars, and the concrete was confined with 1/4″ thick steel sleeves.

4.7.1. Loading Protocol of SJS 7

The initial part of the loading history consisted of a single cycle at a quarter, half, three-fourths, and the yield displacement. The experimentally measured first yield displacement was Δ'y=0.805 in.

For cycles beyond the first yield, the loading protocol involved three cycles at increments of displacement ductility, as determined by Equation 3-1 and Equation 3-2. Table 4-16 presents the values of the ductility displacements applied to SJS7, and Figure 4-86 illustrates the load history for SJS7.

Table 4-16. Displacement ductility of SJS 7

Ductility	Δ (in)	Drift (%)
μ_1	1.11	1.2
$\mu_{1.5}$	1.66	1.8
μ_2	2.22	2.5
μ_3	3.33	3.7
μ_4	4.44	4.9
μ_5	5.55	6.2
μ_6	6.66	7.4

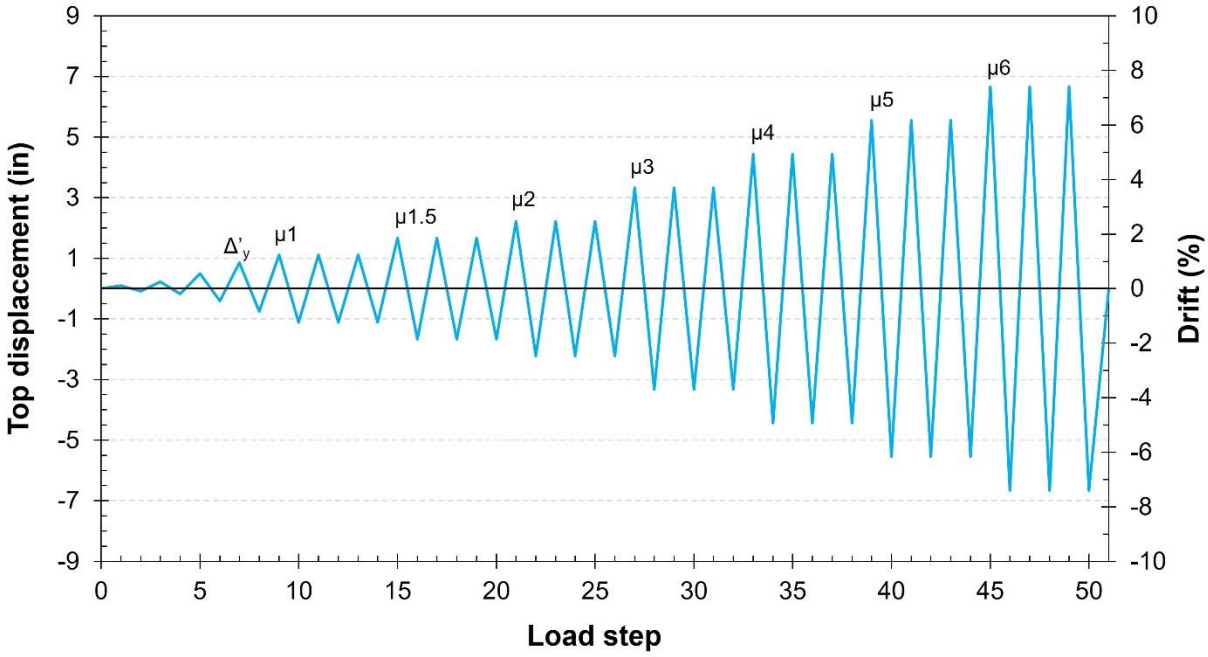


Figure 4-86. Displacement history of SJS 7

4.7.2. Global Response of SJS 7

Figure 4-87 presents the moment-displacement response of the column at the socket interface for SJS7. This specimen experienced its highest applied moment of 315.7 kip-ft at ductility five, initiating rocking and shear failure inside the external socket connection. Strength degradation began during ductility three when the column exhibited core crushing at the socket

interface. During the final cycle of ductility three, the steel tube inside the socket began to buckle at the gap between both steel tubes. A drop of approximately 55% from the maximum moment was observed during the second cycle of ductility six, coinciding with rocking and extensive concrete core crushing, leading to the conclusion of the test after the third cycle of ductility six.

The external socket wall sustained minimal damage, with radial cracks appearing before the column reached its first yield displacement. The inner and outer steel sleeves of the socket did not show any inelastic deformations at any location, and the footing remained free from visible damage, maintaining its capacity-protected status throughout the test.

However, it is important to note that while a plastic hinge developed at the socket interface, bar fracture was not achieved due to the shear failure of the column portion inside the socket. This failure caused the column to rock, preventing it from sustaining the additional force necessary to fracture the longitudinal bars.

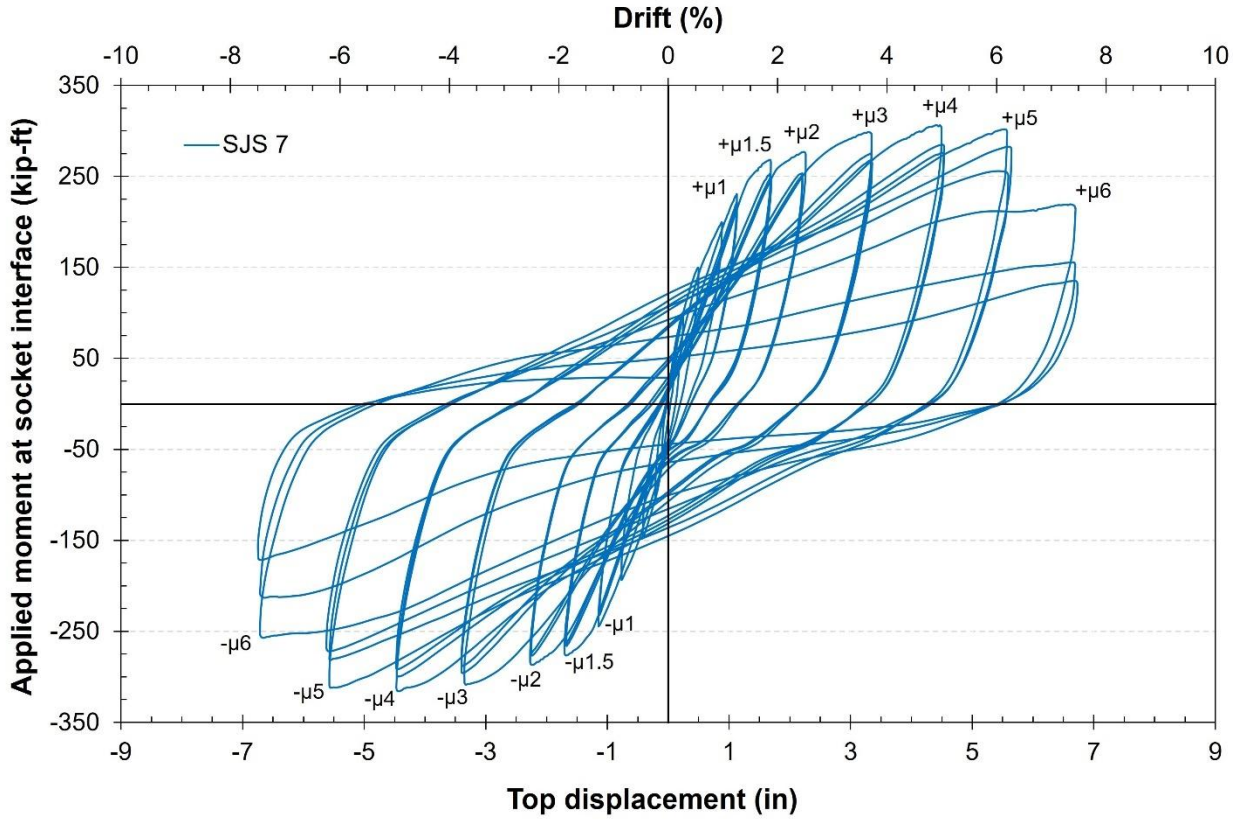


Figure 4-87. Moment-displacement response of SJS 7

Figure 4-88 compares the predicted response of a CIP column, derived from moment-curvature analysis using the same material properties as the experimental test, with the envelope of the moment response for SJS7 during the first and third cycles of each ductility displacement. The maximum moment reached by SJS7 was 5% higher than the nominal capacity of a CIP column. Force degradation became evident at a drift of 6.2%, coinciding with the extensive concrete crushing of the column.

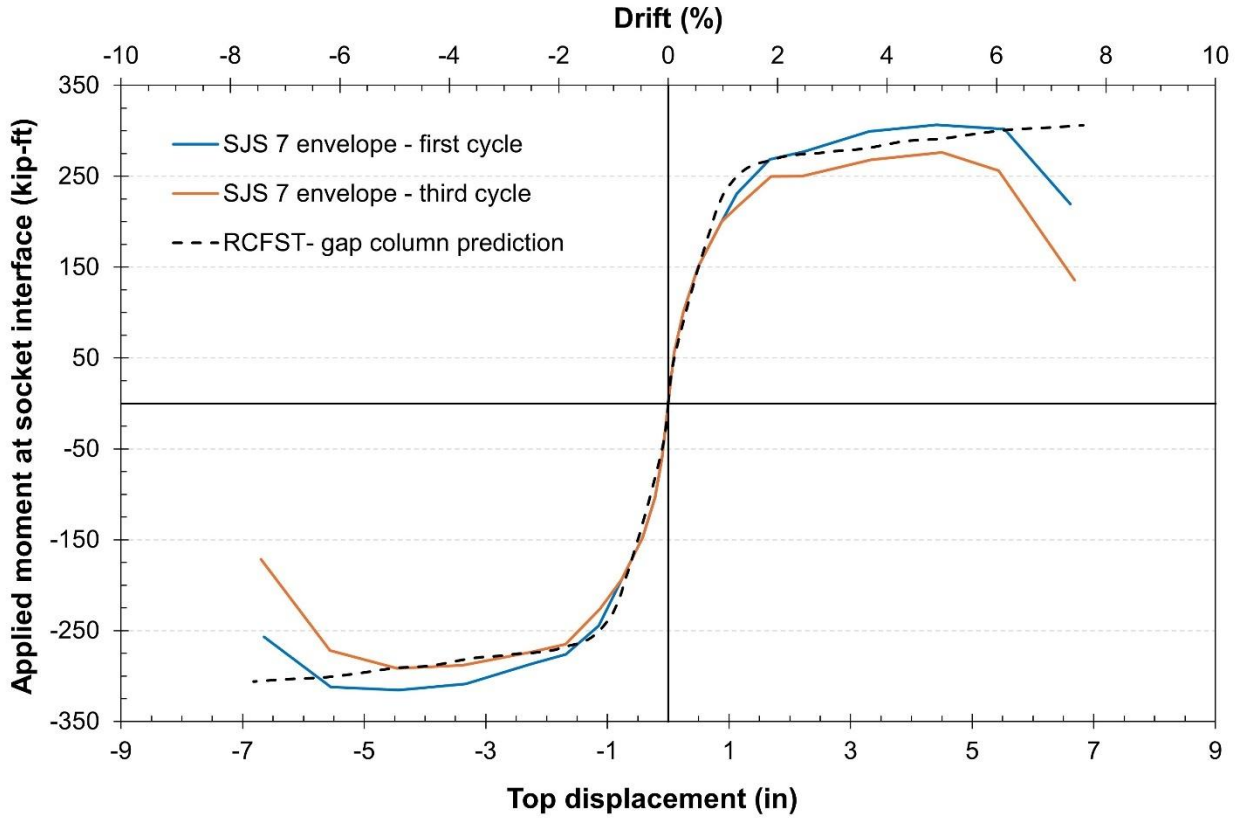


Figure 4-88. SJS 7 experimental envelopes compared to an RC column prediction

4.7.3. Damage progression of SJS 7

Before the test, the external socket wall and grout were inspected, revealing initial cracks as shown in Figure 4-89. No additional cracks were observed before reaching the yielding displacement. However, additional radial cracks appeared on the external socket wall in the last cycle of ductility one, as shown in Figure 4-90.



Figure 4-89. Initial cracks on the socket wall at the start of SJS 7

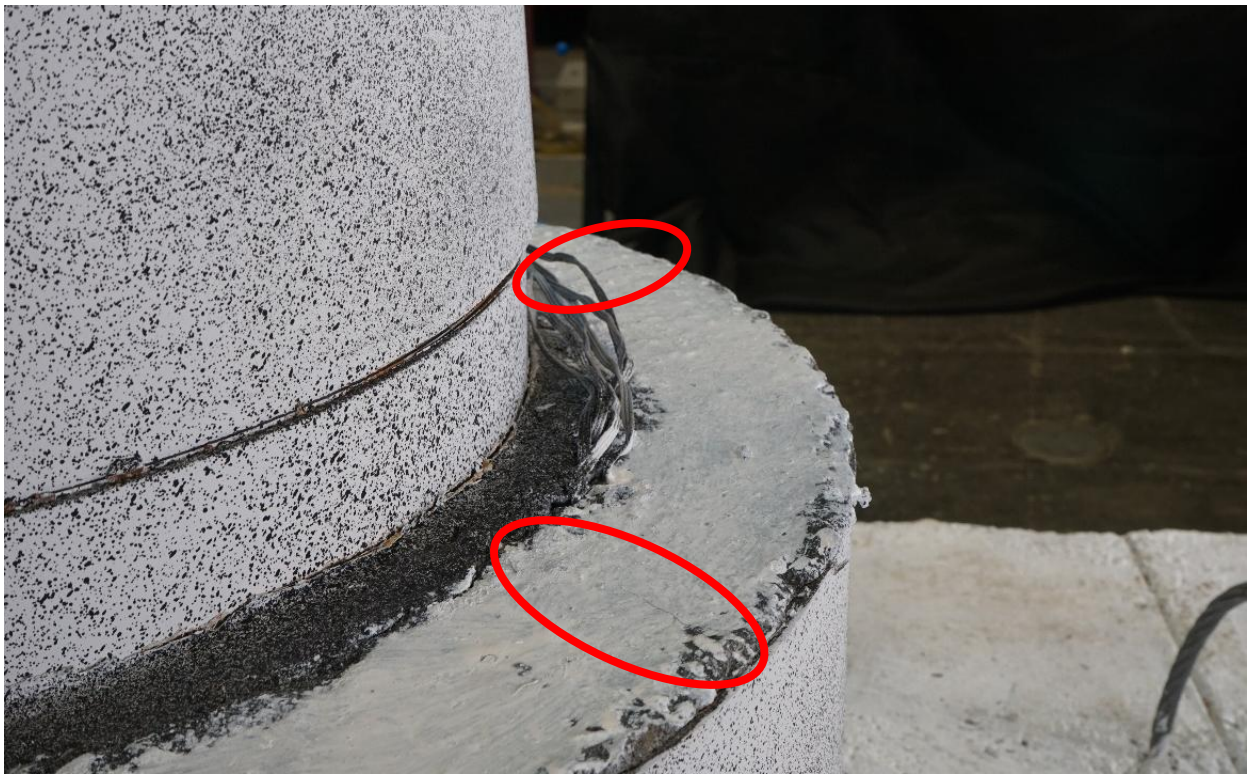


Figure 4-90. Radial cracks on the socket wall at the last cycle of ductility one

The external socket wall did not present additional damage at the end of ductility one and a half. Additionally, the column presented a 0.157″ (4 mm) gap between the steel tubes. Figure 4-91 shows the gap between steel tubes at the last cycle of ductility one and a half.



Figure 4-91. Crack pattern on the south surface at the last cycle of ductility one

In the last cycle of ductility two, a 0.354″ (9 mm) gap between the steel tubes was observed on the tension side of the column. At the same time, the steel tube inside the external socket connection also started to buckle when it was subjected to compression. Figure 4-92 shows the damage at the connection interface on the north side of the column at the last cycle of ductility two.

The gap between the steel tubes increased to 0.591″ (15 mm) at ductility three and 0.866″ (22 mm) at ductility four. Additionally, at the first cycle of ductility three, a 0.079″ (2 mm) crack was observed on the column at the interface between the steel tubes. Figure 4-93 and Figure 4-94 depict the damage to the column and external socket connection at the last cycle of ductility three and four, respectively.



Figure 4-92. Damage of the column and socket connection at the last cycle of ductility two



Figure 4-93. Damage of the column and socket connection at the last cycle of ductility three



Figure 4-94. Damage of the column and socket connection at the last cycle of ductility four

In the final cycle of ductility five, the gap between the steel tubes increased to 1.181″ (30 mm), and the concrete core had visible crushing at the interface between the two steel tubes. Figure 4-95 depicts the damage to the column and the external socket connection at the last cycle of ductility five.

At the last cycle of ductility six, the gap between the steel tubes increased to 1.654″ (42 mm), and the concrete core experienced additional crushing at the interface between the two steel tubes. Figure 4-96 shows the column and the external socket connection deterioration at the last cycle of ductility six.

Figure 4-97 shows the displaced column and the core crushing of the column at the interface between the two steel tubes. The footing and the grout of the gap between the column and socket did not exhibit any significant cracks throughout the test, and the external socket concrete presented only the radial cracks that appeared at the beginning of the test.



Figure 4-95. Damage of the column and the socket connection at the last cycle of ductility five



Figure 4-96. Damage of the column and the socket connection at the last cycle of ductility six



Figure 4-97. Displaced column at the last cycle of ductility six

After the test, an inspection was conducted to determine whether there was additional damage to the inside portion of the connection on the column. Figure 4-98 shows limited damage on the grout along the height of the socket, while Figure 4-99 shows the crushing of the portion of the column inside the socket with a total damage height of eight inches. Figure 4-100 shows the shear cracks on the column along the height of the socket.



Figure 4-98. Damage to the grout inside the external socket connection



Figure 4-99. Damage to the north face of the column inside the external socket connection



Figure 4-100. Damage to the west face of the column inside the external socket connection

4.8. Specimen SJS-8

Column test SJS8 was performed on Monday, May 20, 2024, at the Constructed Facilities Laboratory at NCSU. A summary of the key parameters for SJS8 is provided in Table 4-17.

Table 4-17. Summary of SJS8 parameters

Column parameters	
Longitudinal steel detailing	20#5 A706 (ρ_l=2.4%)
Longitudinal steel yield strength	68.4 ksi
A606-4 steel yield strength	60.6 ksi
A709 steel yield strength	56.8 ksi
Thickness of steel tube inside socket	1/8 in
Thickness of steel tube outside socket	3/8 in
Concrete strength	7.0 ksi
Diameter of the column	18 in
Height of the column	90 in
Axial load ratio	5%
First yield displacement	0.69 in
Equivalent yield displacement	0.96 in
Maximum applied moment at socket interface	318.6 kip-ft
Failure mode	Rupture of longitudinal bar S4, S5, S6, N4 and N5
Socket parameters	
Longitudinal steel detailing	20#6 A706
Longitudinal steel yield strength	86.5 ksi
Socket sleeve steel yield strength	46.6 ksi
Thickness of steel sleeves	1/4 in
Concrete strength	14.0 ksi
Grout strength	5.8 ksi

Table 4-17. Summary of SJS8 parameters (continued)

Socket parameters	
Height of external socket	22.0 in (1.22 Dc)
Internal diameter	20 in
External diameter	26.5 in

The column had a clear height of 7'-6″ and a diameter of 18″, resulting in a height-to-diameter aspect ratio of 5.0. The column was reinforced with 20 Grade 60-A706 #5 longitudinal bars (ρl= 2.4%) and an external steel tube to confine the concrete. The clear distance between the longitudinal reinforcing steel and the inner surface of the tube was 1″. The resulting system is commonly referred to as RCFST. The RCSFT has two cross-sections with varying steel thicknesses. The portion of the column inside the external connection has a reduced steel thickness to minimize the forces transmitted to the external socket.

The external socket had a height of 22″, resulting in a height-to-diameter ratio of 1.22 (1.22 Dc). The socket longitudinal reinforcement included 20 Grade 80-A706 #6 bars, and the concrete was confined with 1/4″ thick steel sleeves.

4.8.1. Loading Protocol of SJS 8

The initial part of the loading history consisted of a single cycle at a quarter, half, three-fourths, and the yield displacement. The experimentally measured first yield displacement was Δ'y= 0.697 in.

For cycles beyond the first yield, the loading protocol involved three cycles at increments of displacement ductility, as determined by Equation 3-1 and Equation 3-2. Table 4-18 presents the values of the ductility displacements applied to SJS8, and Figure 4-101 illustrates the load history for SJS8.

Table 4-18. Displacement ductility of SJS 7

Ductility	Δ (in)	Drift (%)
μ_1	0.96	1.1
$\mu_{1.5}$	1.44	1.6
μ_2	1.92	2.1
μ_3	2.88	3.2
μ_4	3.84	4.3
μ_5	4.80	5.3
μ_6	5.76	6.4
μ_7	6.72	7.5

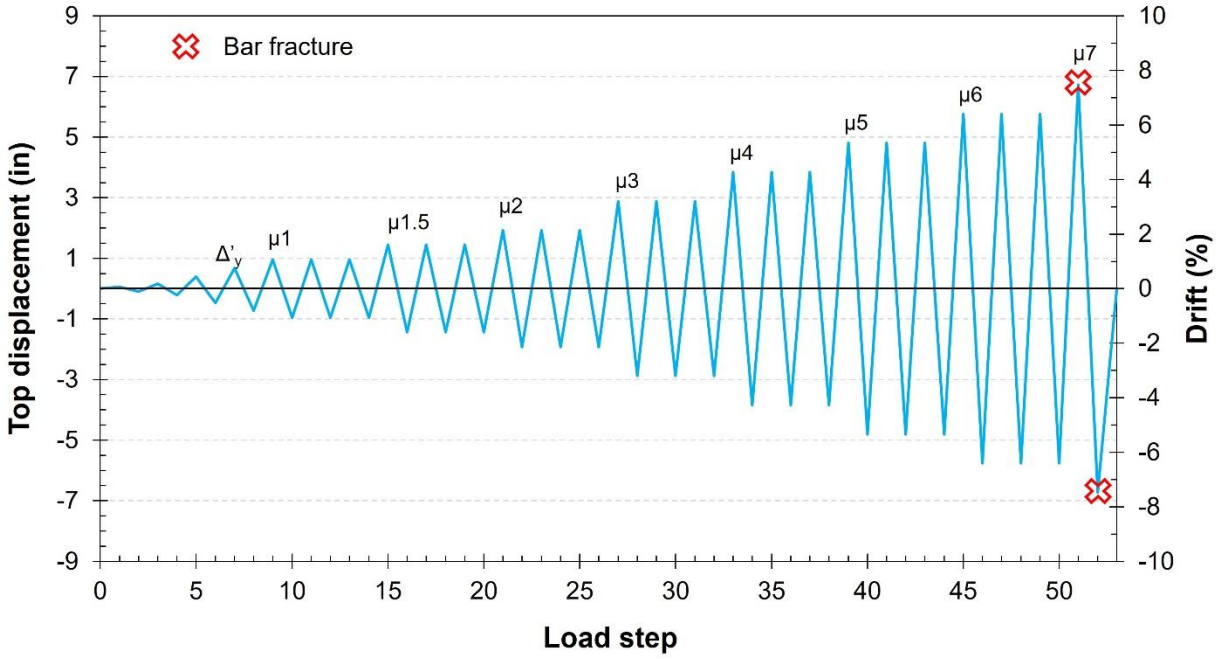


Figure 4-101. Displacement history of SJS 8

4.8.2. Global Response of SJS 8

Figure 4-102 presents the moment-displacement response of the column at the socket interface for SJS8. This specimen experienced its highest applied moment of 318.6 kip-ft at ductility five. During the final cycle of ductility three, the steel tube inside the socket began to

buckle at the interface between the two steel tubes. Force degradation began during the first cycle of ductility six when the column exhibited core crushing, and the gap between the steel tubes increased. A drop of approximately 45% from the maximum moment was observed during the first cycle of ductility seven. During this cycle, three bars were fractured on the south side during the first positive cycle of ductility seven, and two longitudinal bars were fractured during the first negative cycle of ductility seven, leading to the end of the experimental test. Notably, the plastic hinge successfully formed on the column and achieved bar fracture above the interface of the external socket connection, with a socket height of 1.2 DC.

The external socket wall and the grout used to fill the gap sustained minimal damage, with radial cracks appearing before the column reached its first yield displacement. The inner and outer steel sleeves of the socket did not show any inelastic deformations, and the footing remained free from visible damage, maintaining its capacity-protected status throughout the test.

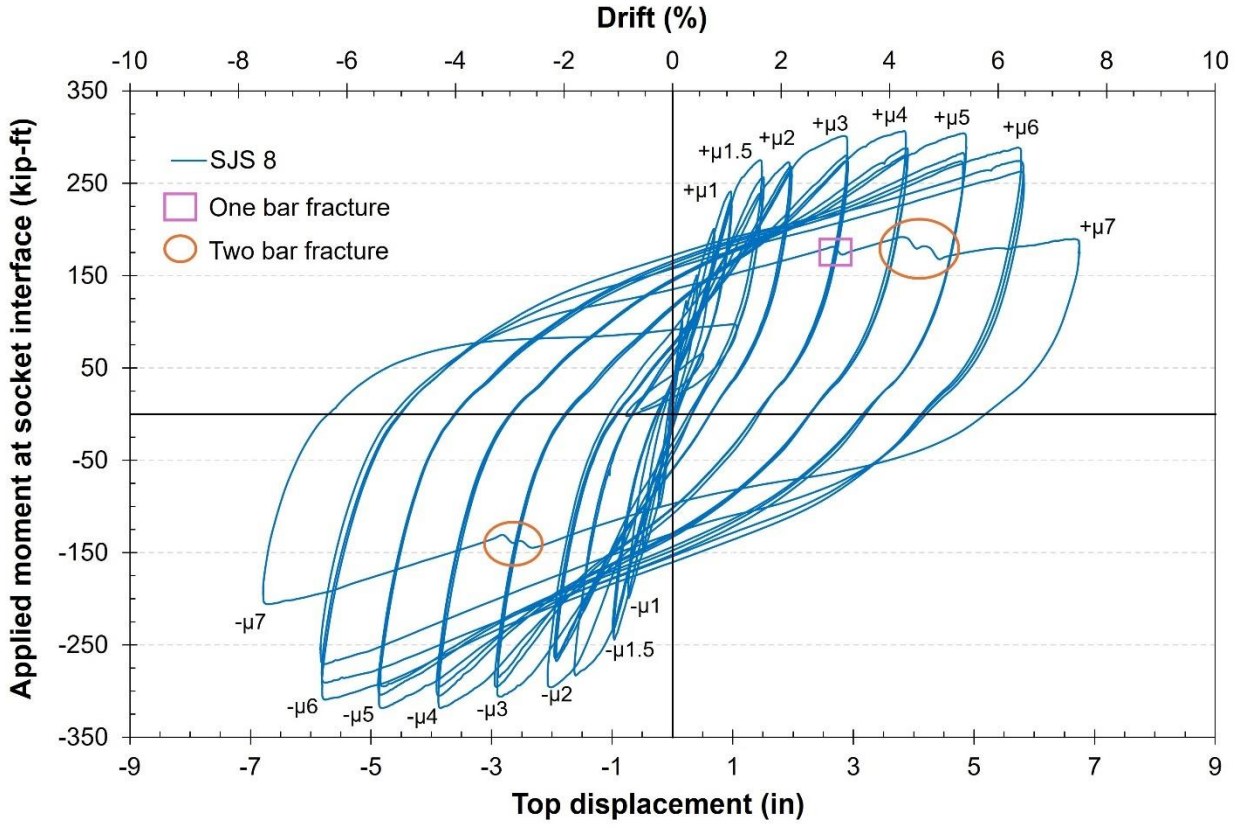


Figure 4-102. Moment-displacement response of SJS 8

Figure 4-103 compares the predicted response of a CIP column, derived from moment-curvature analysis using the same material properties as the experimental test, with the envelope of the moment response for SJS8 during the first and third cycles of each ductility displacement. The maximum moment reached by SJS8 was 3.3% higher than the nominal capacity of a CIP column. Strength degradation became evident at a drift of 6.4%, coinciding with the extensive concrete crushing of the column.

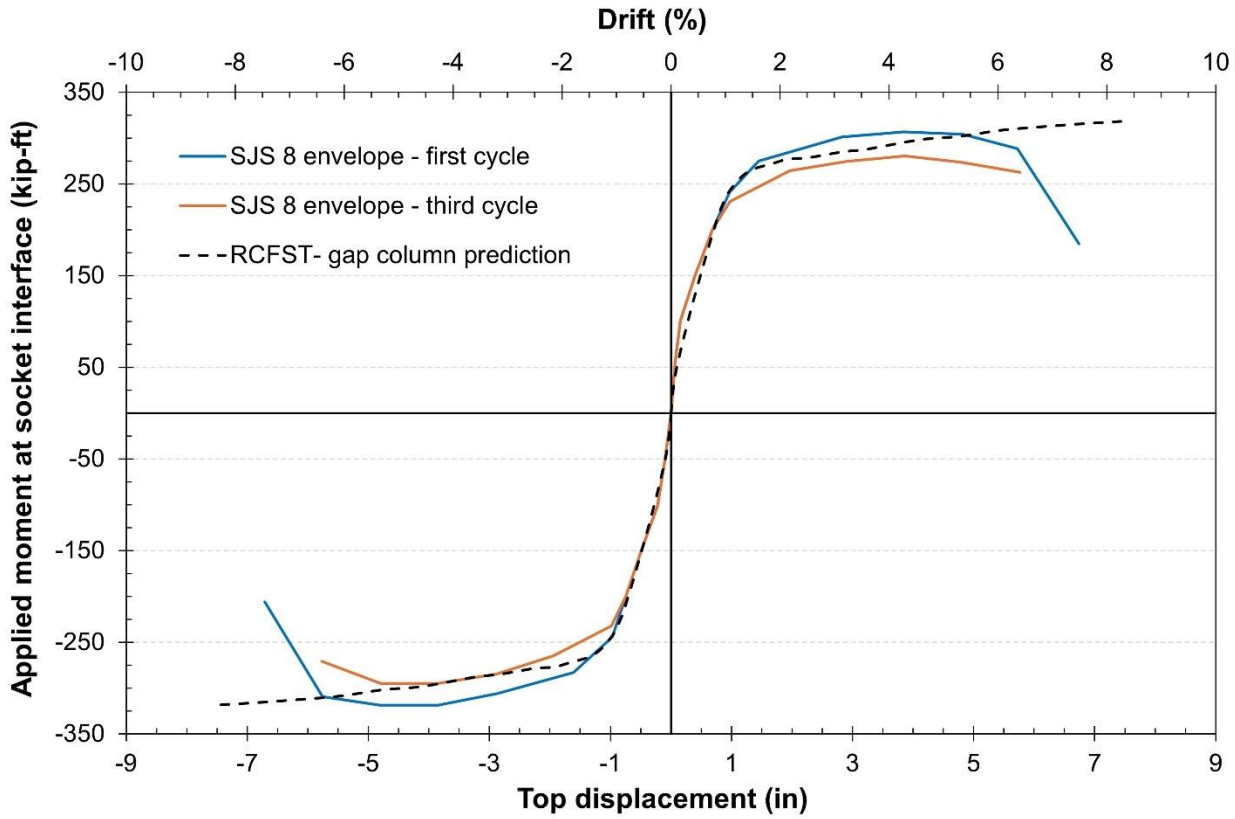


Figure 4-103. SJS 8 experimental envelopes compared to an RC column prediction

4.8.3. Damage progression of SJS 8

The external socket wall and grout were examined before the test, and no initial cracks were detected, as shown in Figure 4-104. No additional cracks were observed before reaching three-quarters of the yielding displacement. However, additional radial cracks appeared on the external socket wall at yield displacement, as depicted in Figure 4-105.



Figure 4-104. Socket wall at the start of SJS 8



Figure 4-105. Radial cracks on the socket wall at yield displacement

The external socket wall did not present additional damage after the yield displacement. Additionally, the column showed a 0.118″ (3 mm) gap between the steel tubes. Figure 4-106 illustrates the gap between steel tubes at the last cycle of ductility one.

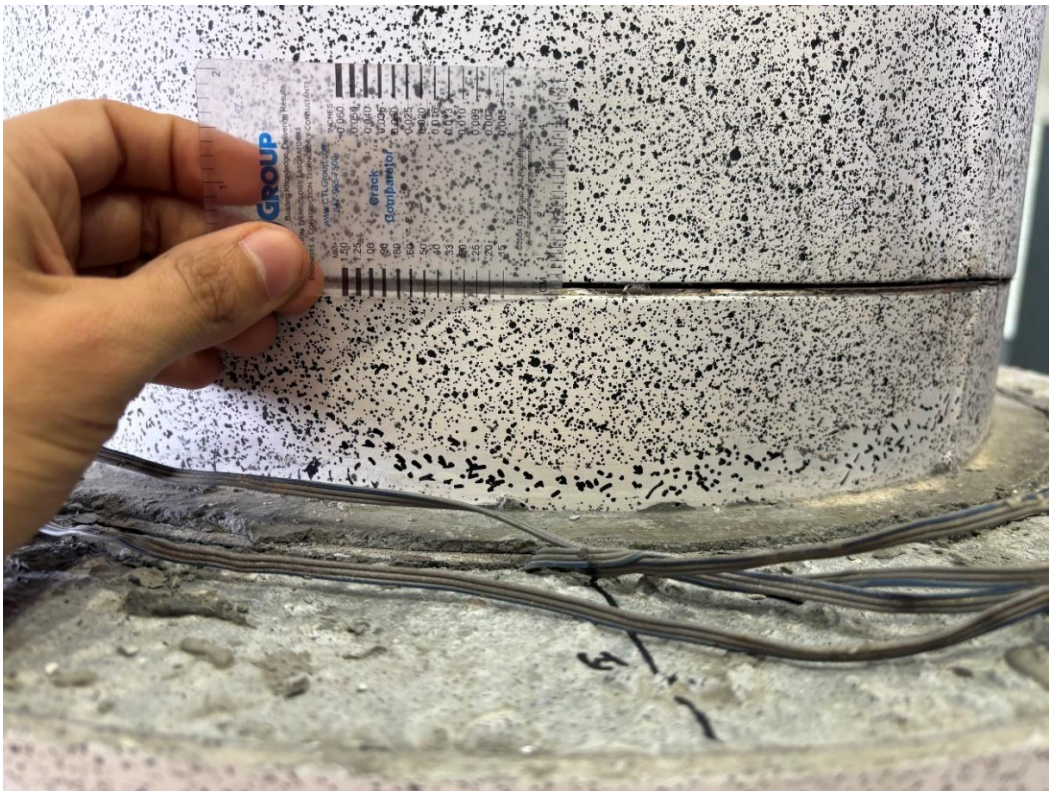


Figure 4-106. Gap between steel tubes at the last cycle of ductility one

In the last cycle of ductility two, a 0.433″ (11 mm) gap was observed between the steel tubes on the tension side of the column. Simultaneously, the steel tube inside the external socket connection began to buckle under compression. Figure 4-107 shows the damage at the connection interface on the south side of the column at the last positive cycle of ductility two.

The gap between the steel tubes increased to 0.591″ (15 mm) at ductility three and 0.866″ (22 mm) at ductility four. Additionally, at the first cycle of ductility three, a 0.079″ (2 mm) crack was observed on the column at the interface between the steel tubes. Figure 4-108 and Figure 4-109 depict the damage to the column and external socket connection at the last cycle of ductility three and four, respectively.



Figure 4-107. Damage of the column and the connection at the last cycle of ductility two



Figure 4-108. Damage of the column and the connection at the last cycle of ductility three



Figure 4-109. Damage of the column and the connection at the last cycle of ductility four

In the final cycle of ductility five, the gap between the steel tubes increased to 1.181″ (30 mm), and the concrete core had visible crushing at the interface between the two steel tubes. Figure 4-110 depicts the damage to the column and the external socket connection at the last cycle of ductility five.

At the last cycle of ductility six, the gap between the steel tubes increased to 1.654″ (42 mm), and the concrete core experienced additional crushing at the interface between the two steel tubes. Figure 4-111 shows the column and the external socket connection deterioration at the last cycle of ductility six.

At ductility seven, the column experienced three bar fractures on the south side and two on the north side. Due to the column external steel sleeves, it was impossible to observe which bars fractured during the test. Figure 4-112 shows the damage to the column at ductility seven when the bar fractures occurred.



Figure 4-110. Damage of the column and the connection at the last cycle of ductility five



Figure 4-111. Damage of the column and the connection at the last cycle of ductility six



Figure 4-112. Damage of column at the ductility seven

Figure 4-113 shows the displaced column at ductility seven. The footing and the grout of the gap between the column and socket did not exhibit any significant cracks throughout the test, and the external socket concrete presented only the radial cracks that appeared at the beginning of the test.



Figure 4-113. Displaced column at ductility seven

After the test, an inspection was conducted to determine whether there was additional damage to the inside portion of the connection on the column. Figure 4-114 and Figure 4-115 show limited damage to the grout and external wall along the height of the socket, respectively, while Figure 4-116 shows the crushing of the column and bar fracture.



Figure 4-114. Damage to the grout inside the external socket connection



Figure 4-115. Damage to the socket wall of the external socket connection



Figure 4-116. Damage to the column inside the external socket connection

4.9. Observed Failure modes for experimental tests

The experimental tests were categorized based on the observed failure modes, identified through experimental observations and post-test inspections, and corroborated by data analysis as detailed in Chapter 5 of this report. The failure modes considered include: (1) fracture of the longitudinal reinforcing bars above the interface of the external socket connection, (2) grout crushing, characterized by extensive compressive damage at the interface of the connection, and (3) shear failure of the portion of the column embedded within the external socket connection, which was identified after the test by lifting the column to inspect the damage. Figure 4-117 illustrates these failure modes and associates each with the corresponding experimental tests.

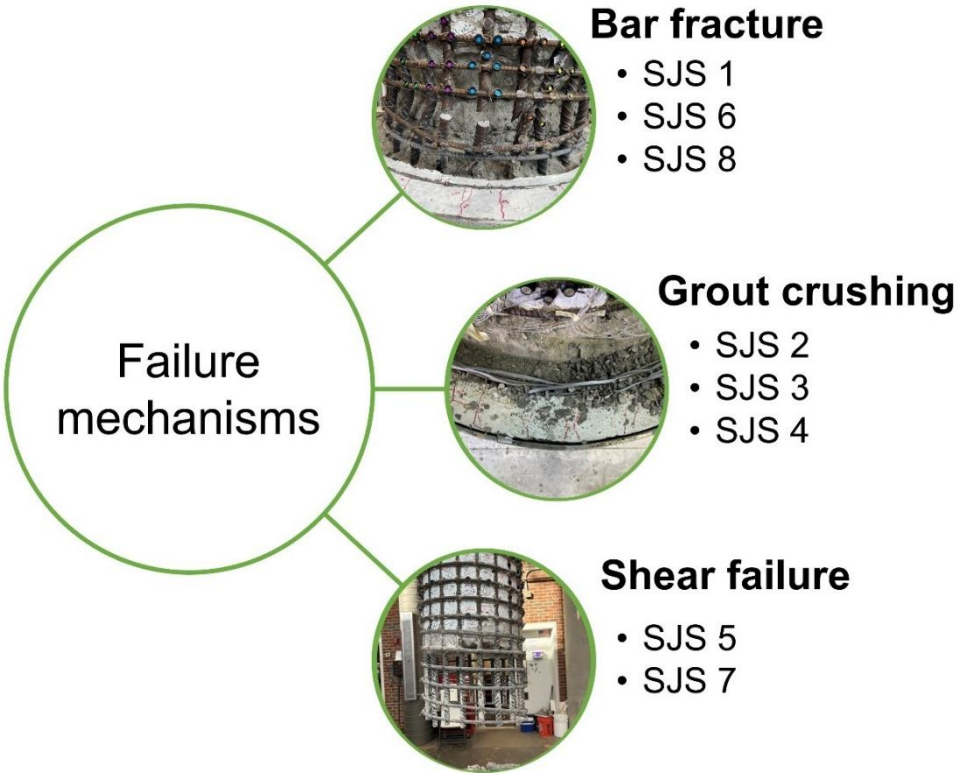


Figure 4-117. Failure mechanisms for the experimental program

The moment-displacement envelopes were used to compare the behavior across different failure modes. To account for the varying characteristics of the specimens, the applied moment was normalized relative to the nominal moment of each specimen. This normalization allows for a more accurate comparison between the different failure modes.

Figure 4-118 presents the normalized first cycle envelopes for SJS1, SJS6 and SJS8 that presented a bar fracture failure mechanism. The three experimental tests reached the nominal capacity of the columns at an approximate drift of 3%. The global behavior of SJS1 and SJS8 closely align, while SJS6 deviates slightly before reaching nominal capacity because SJS6 was a repair of SJS5, which had already experienced the initiation of concrete crushing. The three tests varied in socket heights and material strengths for the socket connection components (see Table 3-1, Table 3-4 to Table 3-7). The material strengths required to achieve a reinforcing bar fracture failure were derived from the analytical model presented in Chapter 6 of this report. The analytical model effectively predicted the required material strengths for this failure mode, considering the specific socket heights used in each test.

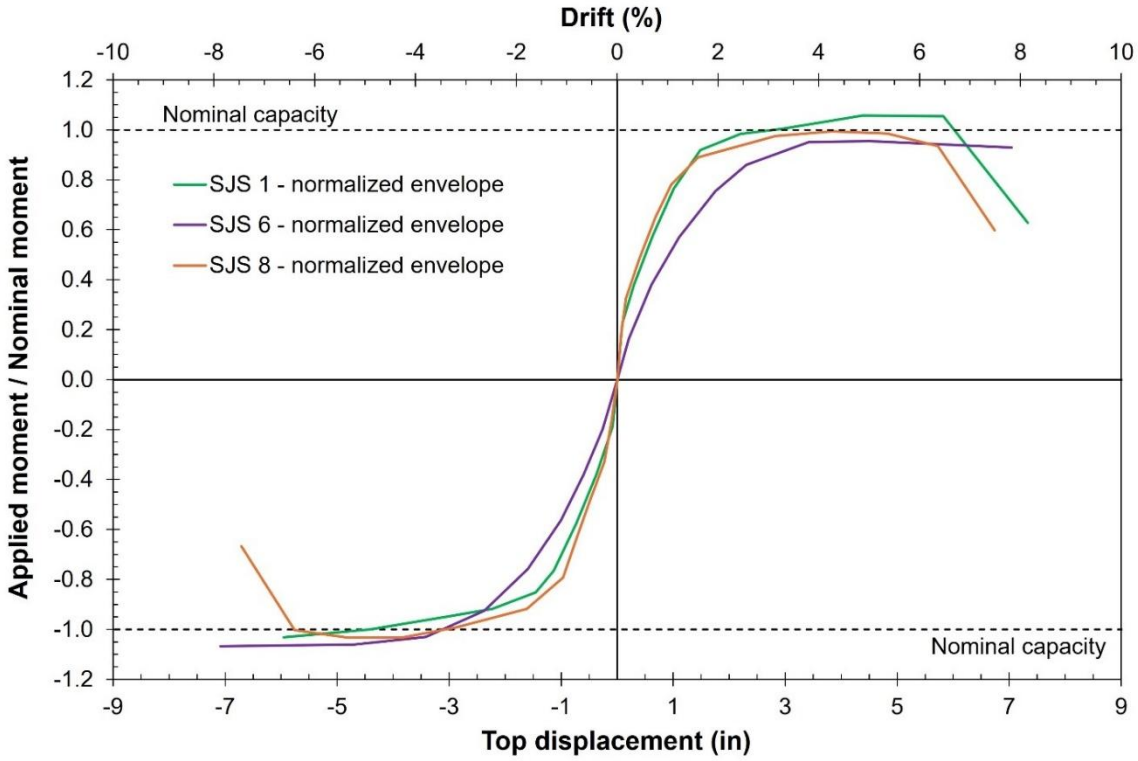


Figure 4-118. Envelopes of experimental tests exhibiting bar fracture

Figure 4-119 presents the normalized envelopes for the grout-crushing failure mechanism.

The experimental tests SJS2, SJS3 and SJS4 that presented grout crushing failure mechanism exhibit different behaviors due to variations in socket heights and material strengths

within the external connection components (see Table 3-1, Table 3-4 to Table 3-7). Among the specimens, SJS2 experienced the lowest applied moment at failure. With a socket height of 0.75 Dc and a grout strength of 6.5 ksi, the grout served as the weak link, leading to earlier failure. Specimens SJS3 and SJS4, both with a socket height of 0.85 Dc, had grout strengths of 9.1 ksi and 9.7 ksi, respectively. The behavior of SJS3 and SJS4 was similar until a drift of approximately 2%, at which point SJS3 experienced the initiation of grout crushing. Although SJS4 reached its nominal moment capacity, the grout could not sustain the applied forces without damage. According to the analytical model presented in Chapter 6, a grout strength exceeding 10.0 ksi would have been required to prevent grout failure at a socket height of 0.85 Dc, placing SJS4 on the borderline between different failure modes. Overall, the analytical model effectively predicts the material strengths necessary to avoid grout-crushing failure considering the specific socket heights used in each experimental test.

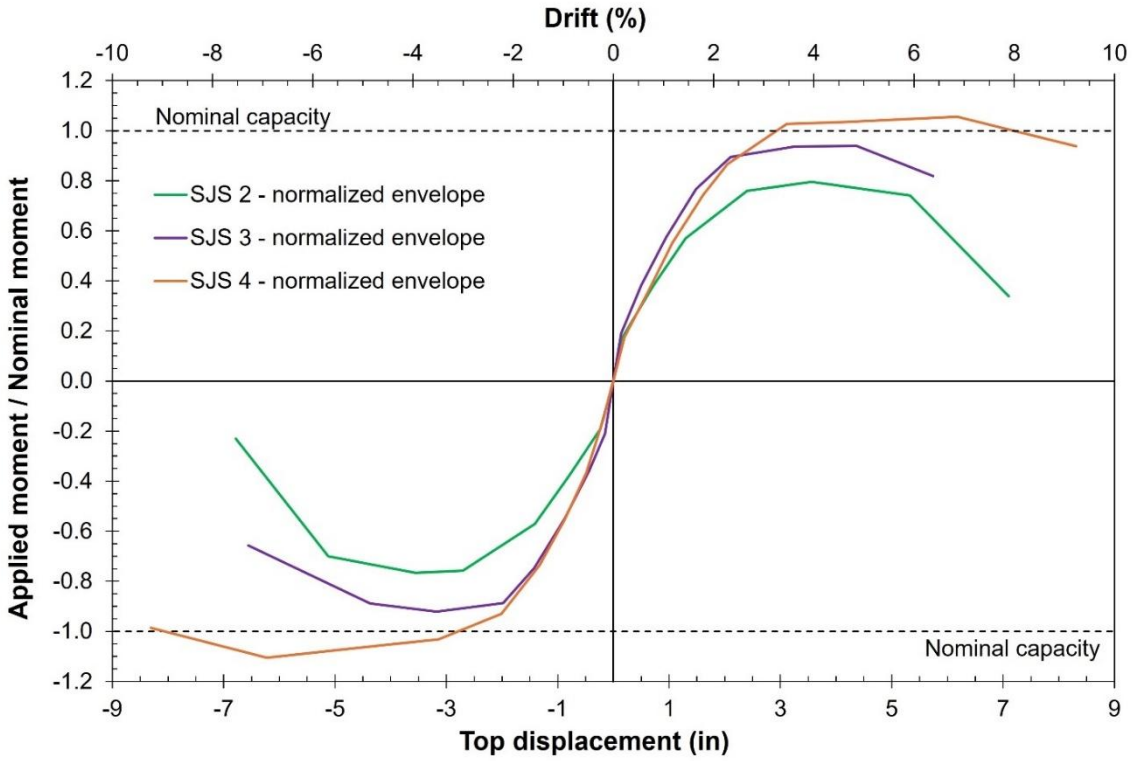


Figure 4-119. Envelopes of experimental tests exhibiting grout crushing

Figure 4-120 presents the normalized envelopes for SJS5 and SJS7 that presented shear failure mechanism, which occurred in the portion of the column embedded within the external

socket connection. When the grout has sufficient strength, the next vulnerable point becomes the shear capacity of the portion of the column within the socket connection. Although SJS5 is an RC column and SJS7 is an RCFST column, and despite variations in material strengths within the external connection components (see Table 3-4 to Table 3-7), the behavior of SJS5 and SJS7 remained similar. The socket height for both experimental tests was the same (0.85 Dc). The experimental tests for SJS5 and SJS7 reached the nominal moment of the column at approximately 4% drift. However, the longitudinal bars did not reach bar fracture because the shear capacity of the column was exceeded, leading to the shear failure mechanism. According to the analytical model presented in Chapter 6 of this report, a concrete strength exceeding 7.0 ksi would have been necessary to prevent shear failure at a socket height of 0.85 Dc, placing SJS5 and SJS7 on the borderline between different failure modes. The analytical model effectively predicted the required material strengths for this failure mode, considering the specific socket heights used in each test.

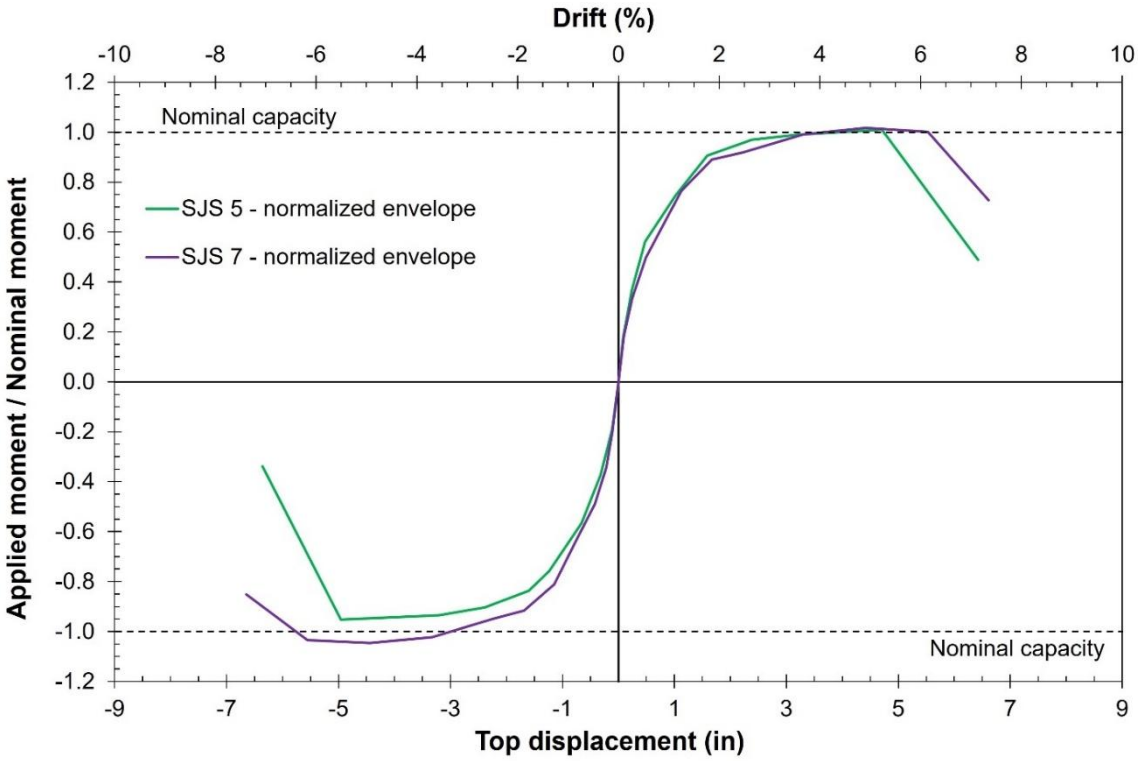


Figure 4-120. Envelopes of experimental tests exhibiting bar fracture

Figure 4-121 presents the moment-displacement curves for all eight experimental tests, providing a clear visualization of the varying responses and corresponding failure modes.

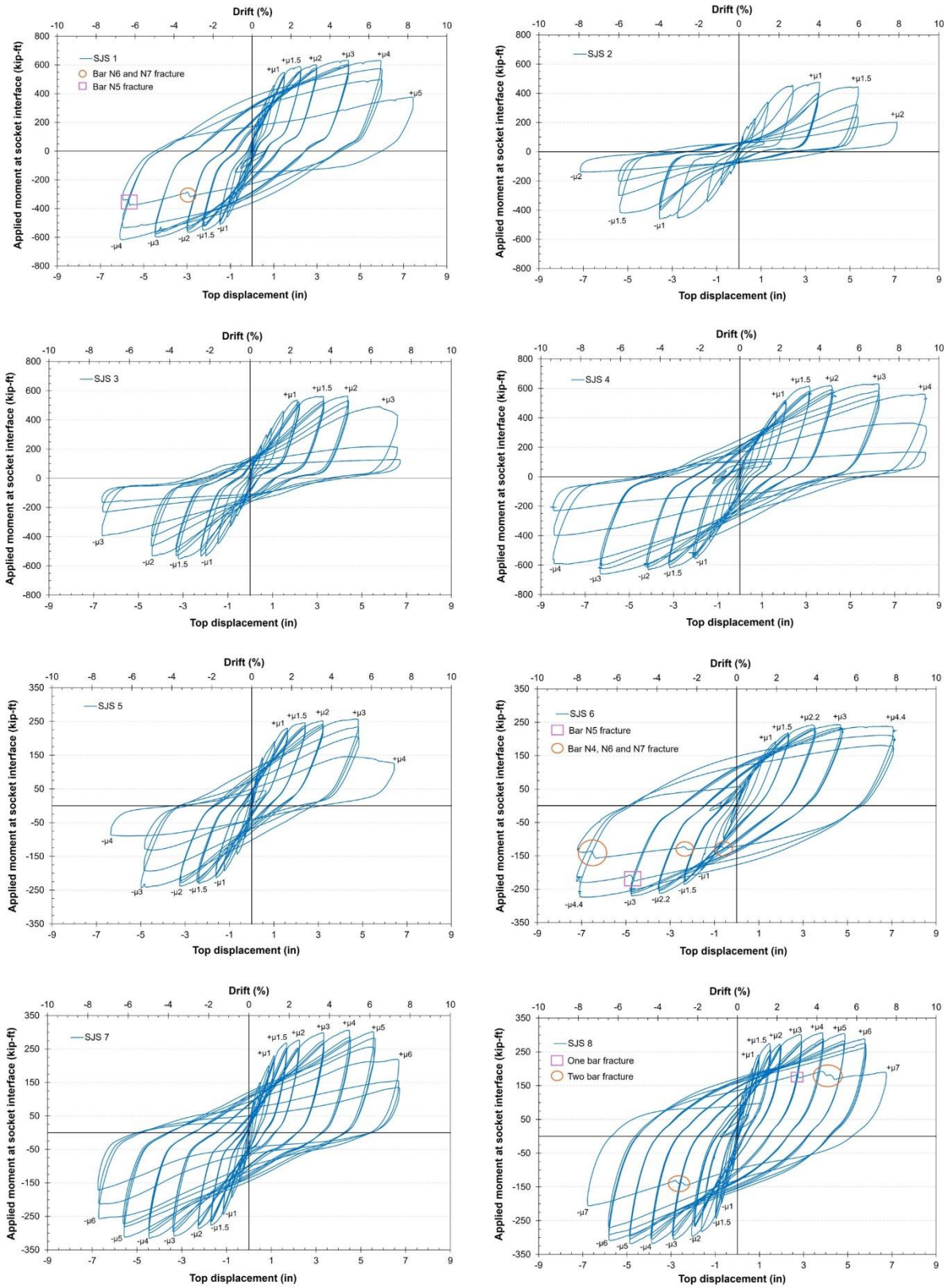


Figure 4-121. Moment-displacement curves for all eight experimental tests

Chapter 5: Analysis of Experimental Results

This chapter presents the analysis of experimental results from the data collected for each of the eight tests. The focus is on examining important aspects of the structural performance, including axial strain in both the column and the socket wall, energy dissipation of the column, hysteretic damping, displacement components, and the extent of plasticity. This chapter also outlines the methodology used to calculate these results, providing insight into the behavior of the external socket connection under the applied loading conditions.

5.1. Methodology for data analysis

This section details the approach used to process and interpret the data obtained from the instrumentation, including the calculation of axial strain, energy dissipation, hysteretic damping, displacement components, and the extent of plasticity.

5.1.1. Axial strain analysis

The axial strain analysis for the RC columns was conducted using the Optotrak Certus HD system, which captured the three-dimensional displacement history of the longitudinal bars throughout the experimental tests. To measure the strains on the longitudinal bars, the initial gauge length was determined by calculating the distance between two markers before the start of the test. During the experiment, the change in length between two markers (i and j) was calculated at each time step using the coordinates along the X, Y, and Z axes, as shown in Equation 5-1. Data recording was performed at a frequency of 1 hz.

Equation 5-1 $$L(t) = \sqrt{\left(x_j(t) - x_i(t)\right)^2 + \left(y_j(t) - y_i(t)\right)^2 + \left(z_j(t) - z_i(t)\right)^2}$$

Once the change in length for a specific time was determined, the axial strain was calculated by dividing the change in length by the initial gauge length (L_o), as expressed in

Equation 5-2. This approach allowed for precise monitoring of the strain behavior of the longitudinal bars throughout the loading cycles.

Equation 5-2 $$\varepsilon(t) = \frac{L(t) - L_o}{L_o}$$

Strains in the longitudinal reinforcement of the socket wall were directly measured using strain gauges, while strains on the steel tube in the RCFST were obtained through Digital Image Correlation (DIC) data processing.

Strain profiles were developed to visualize the distribution of strains along the instrumented height of the column. These profiles were generated by calculating the strains between each marker on the extreme longitudinal bars of the RC columns. To provide a clear comparison of strain behavior across different ductility displacements, strain profiles were obtained for cycles before and after yielding. This approach allows for a detailed examination of how strain evolves throughout the loading process. Figure 5-1 shows an example of a strain profile before yielding, with dashed lines representing the predicted values and solid lines representing the measured values. Figure 5-2 illustrates a strain profile after yielding. The strain profile examples represent the strains of SJS1.

The strain history for each gauge length was generated for all experimental tests; however, the presented strain histories focus on the extreme longitudinal bars at the locations where bar fracture occurred. If no bar buckling was observed in a specimen, the strain history was taken from a location centered 4 inches above the interface of the external socket connection. The strain history is crucial for identifying the onset of bar buckling or rocking behavior during the experimental test. For example, Figure 5-3 shows the strain history of the N6 bar for SJS1 at the location where bar buckling occurred. These strain histories provide valuable insights into the progression of deformation and the mechanisms leading to failure in the columns.

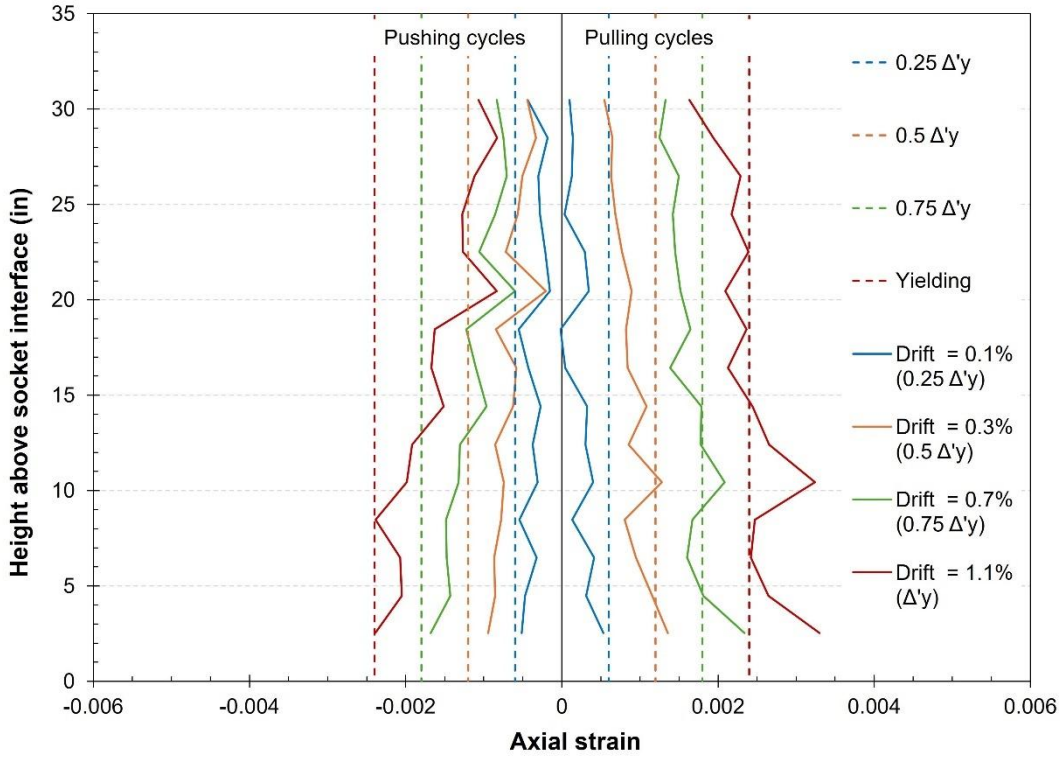


Figure 5-1. Example of strain profile up to first yield cycle

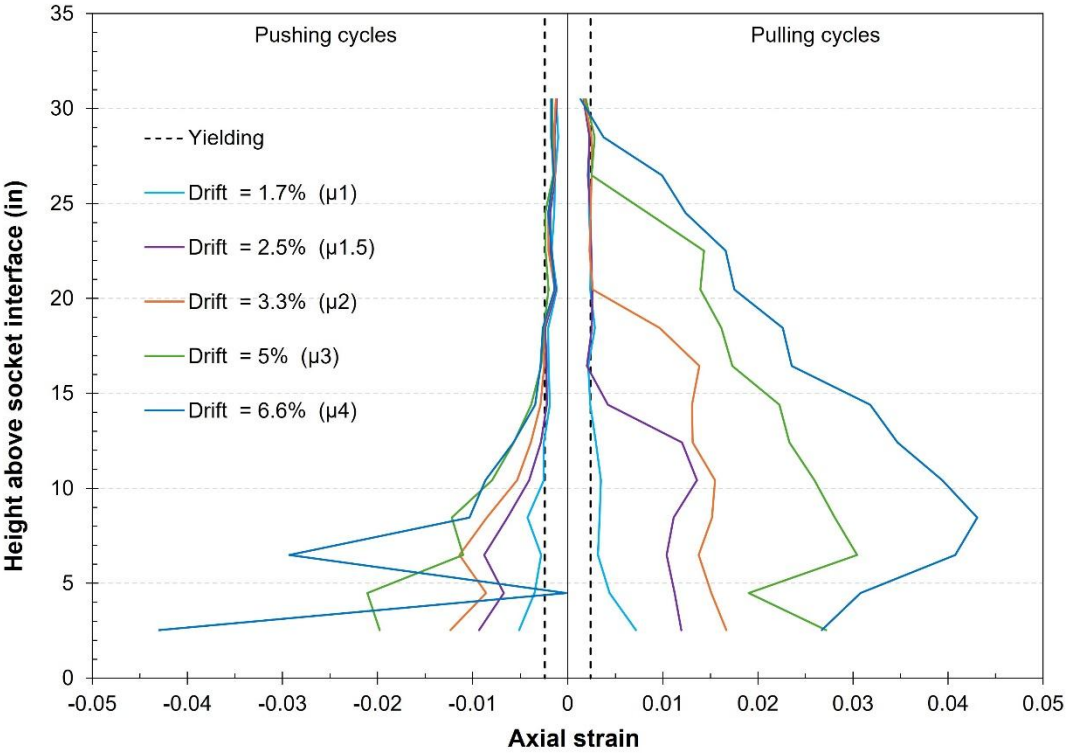


Figure 5-2. Example of strain profile for post-yield cycles

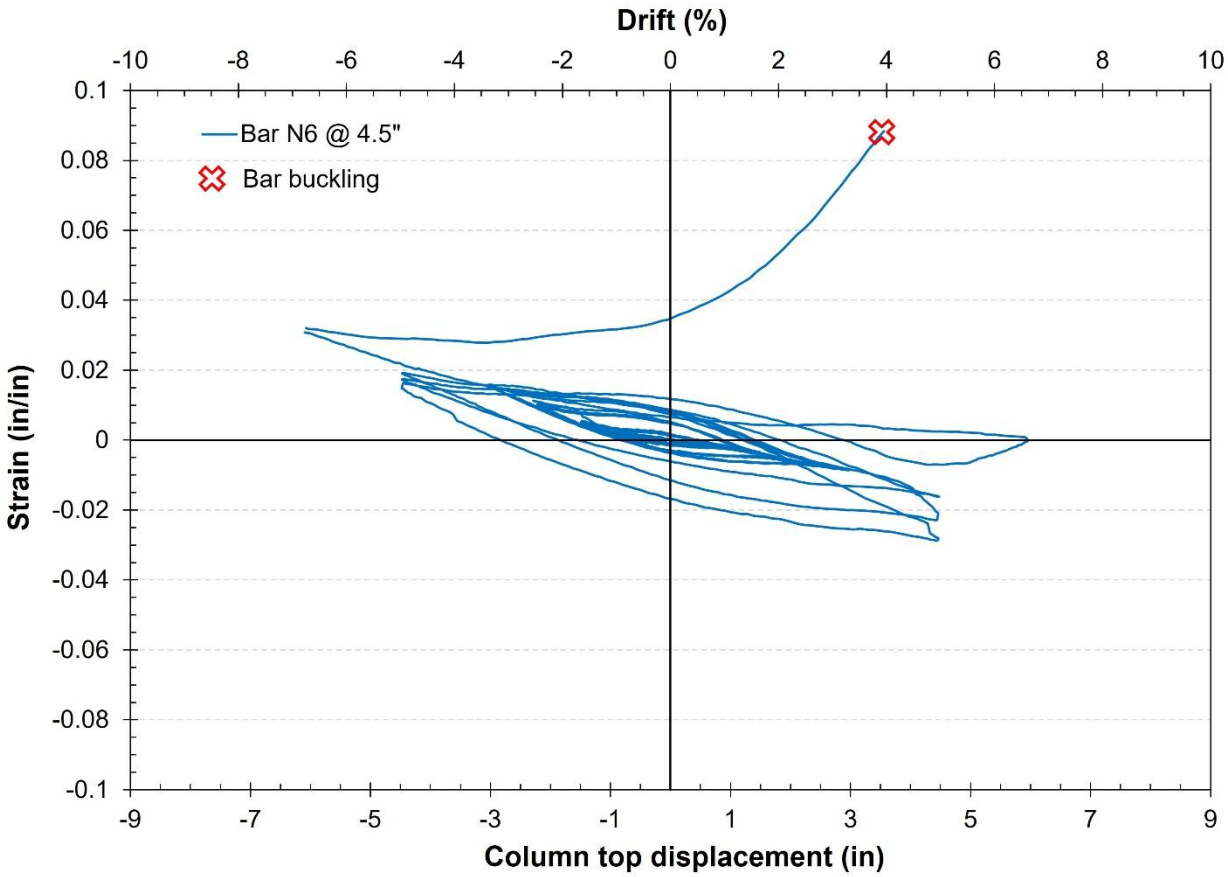


Figure 5-3. Example of strain vs displacement history

5.1.2. Energy dissipation and hysteretic damping

The energy dissipation of the system was calculated by evaluating the area within the force-displacement loop for each ductility cycle. The area of each loop, corresponding to the energy dissipated during that specific cycle, was determined using numerical integration. The total energy dissipation was then obtained by summing the results from all cycles. Figure 5-4 illustrates an example of a force-displacement loop from the first cycle of ductility three for specimen SJS1, highlighting the area used to calculate energy dissipation. Figure 5-5 presents the energy dissipation plot across all cycles, providing a comprehensive view of the system energy dissipation behavior.

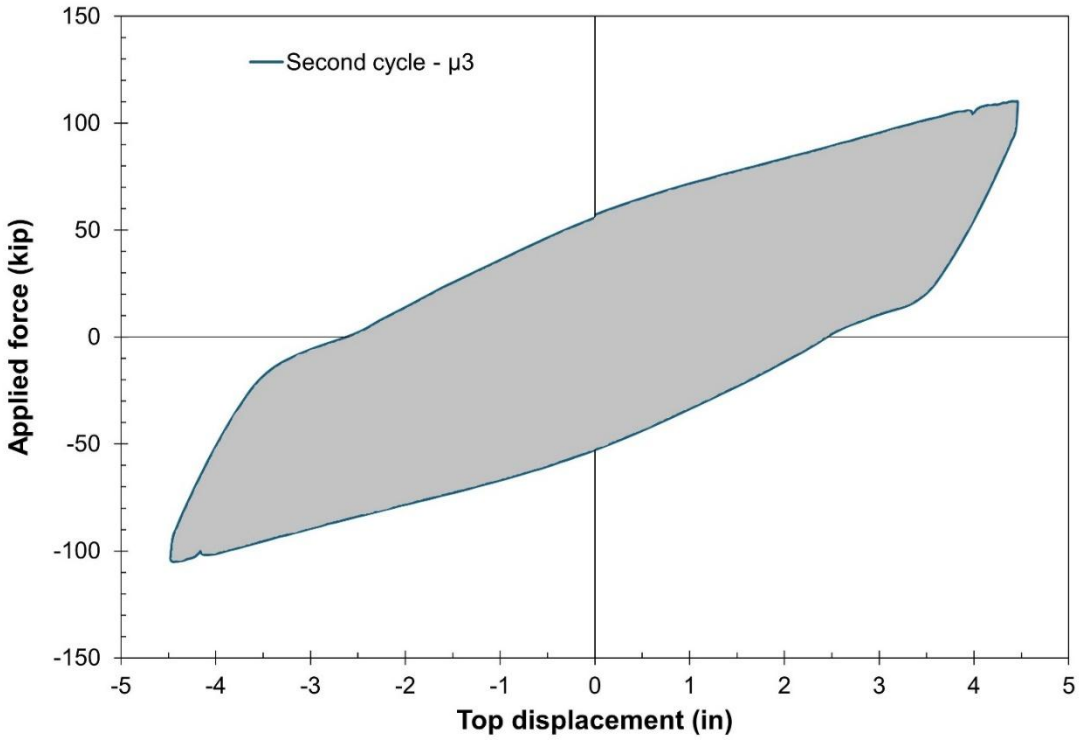


Figure 5-4. Example of force-displacement loop area for dissipated energy

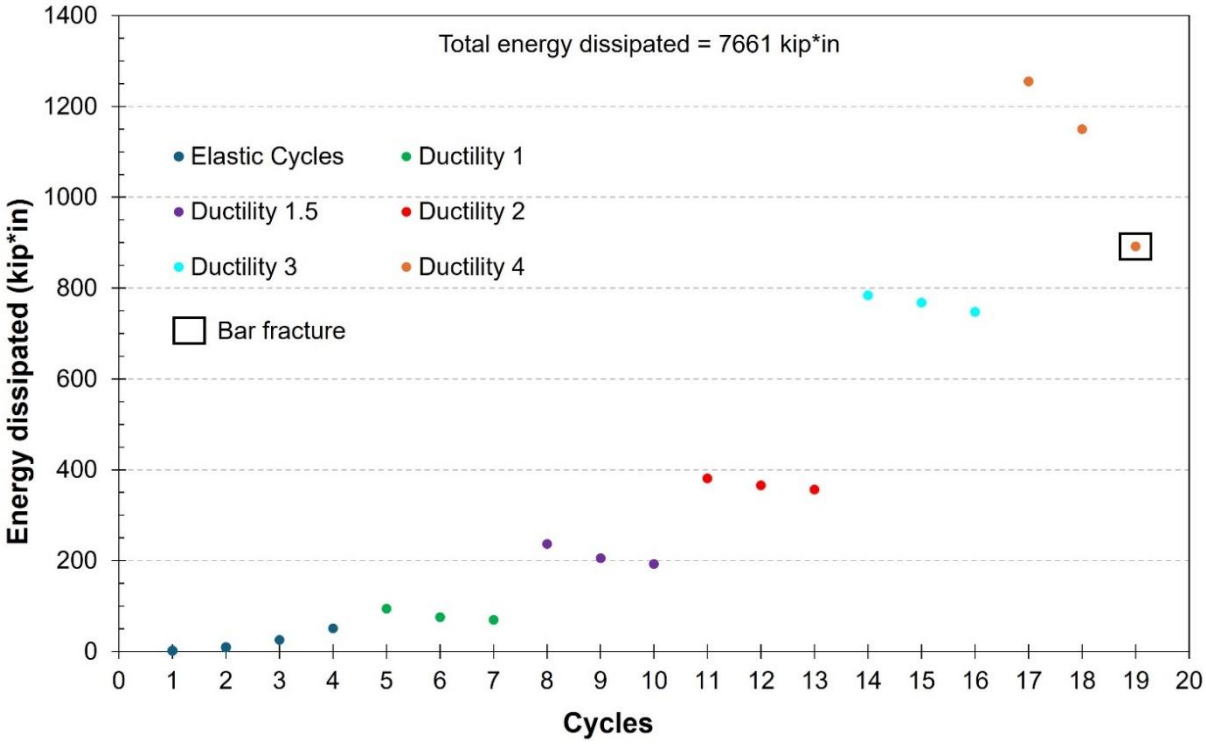


Figure 5-5. Example of energy dissipation plot

Hysteretic damping is an important parameter for characterizing energy dissipation in structures undergoing large inelastic deformations. It was calculated using the area-based hysteretic damping method defined by Jacobsen [23]. Equation 5-3 shows the calculation, which considers the area of the force-displacement loop (A1) and the area of the corresponding outlined rectangle (A2), as depicted in Figure 5-6. Additionally, Figure 5-7 presents the hysteretic damping calculated for all cycles of the experimental test, offering insights into the damping behavior throughout the experiment.

Equation 5-3 $$\xi_{hyst,jac} = \frac{2}{\pi} \times \frac{A_1}{A_2}$$

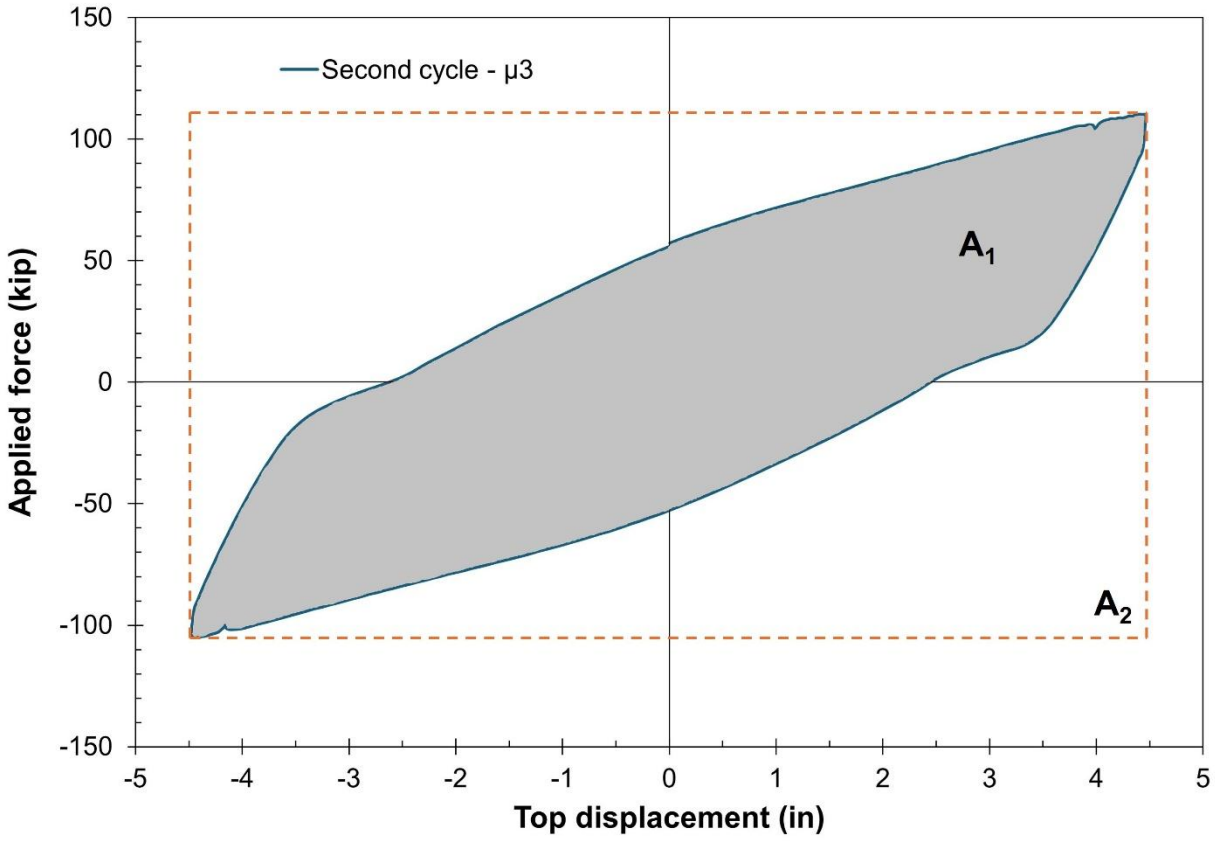


Figure 5-6. Example of Area 1 and Area 2 for Jacobsen hysteretic damping

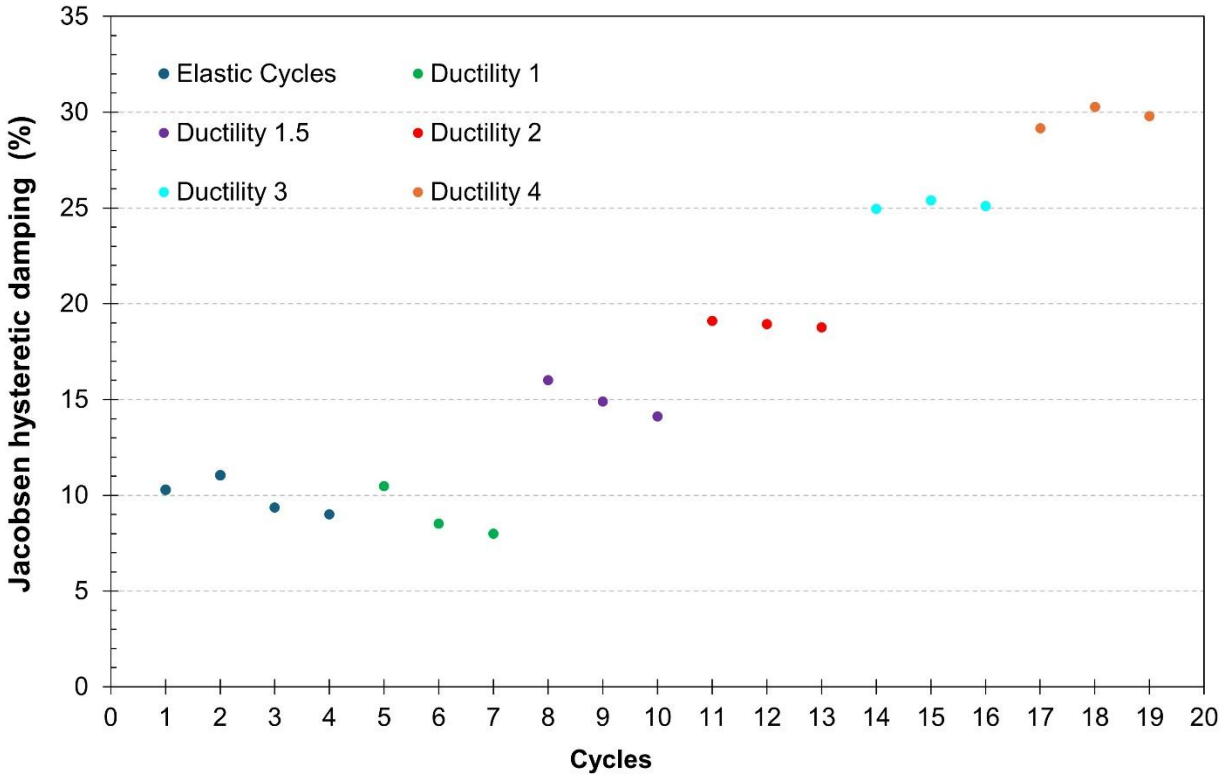


Figure 5-7. Example of hysteretic damping plot

5.1.3. Displacement components

The total lateral displacement is a result of multiple components, including the flexural deformation of the column, rotation due to strain penetration of the longitudinal bars, rocking of the column, shear deformation of the column, and rotation of the external socket connection. By isolating each component of the lateral displacement, we can gain a deeper understanding of the global behavior of the system. This section outlines the methodology used to calculate these individual displacement components.

The flexural component of the column displacement was calculated using the second theorem of the moment-area method, as expressed in Equation 5-4. The parameters involved in this calculation are illustrated in Figure 5-8 [24]. The integral required for this method was solved using numerical integration of the column curvature.

Equation 5-4 $$\Delta = \int_0^H \phi_{(h)} \cdot h \cdot dh$$

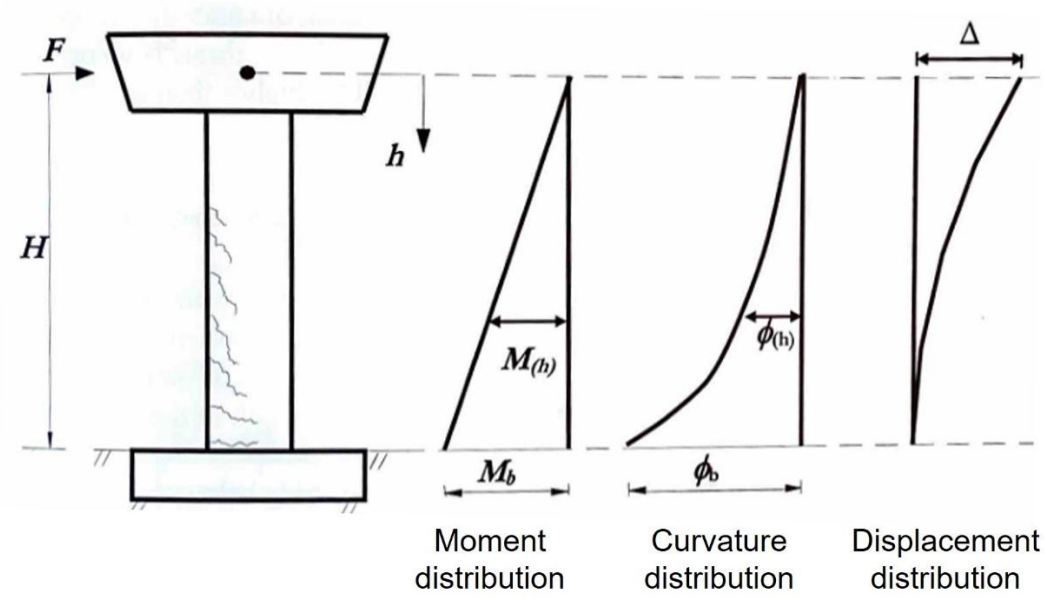


Figure 5-8. Displacements from curvature distribution [24]

The curvature was determined using the strains measured from the instrumented reinforcing bars of the column, focusing on the three most extreme bars on each side. Assuming that plane sections remain plane, the strain distribution across the column cross-section was treated as linear. Figure 5-9 illustrates the strain profile of the column cross-section and the corresponding curvature.

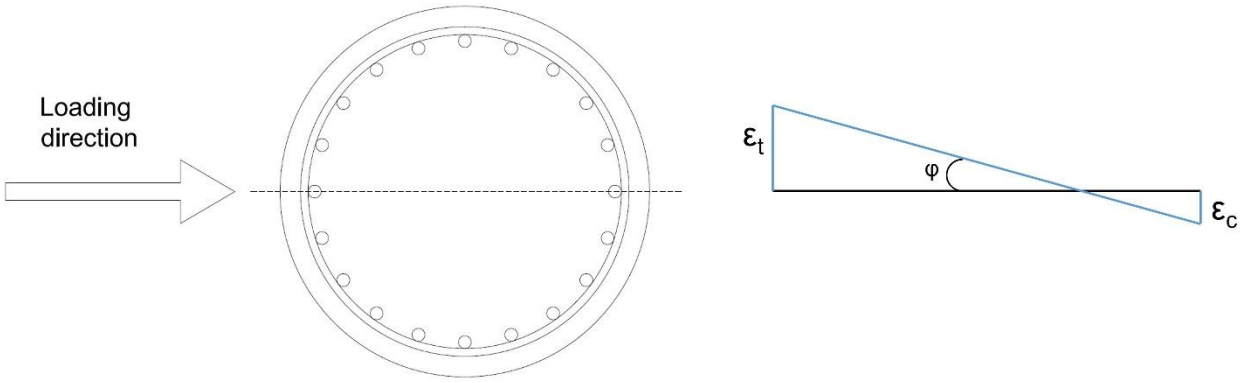


Figure 5-9. Strain profile for a cross-section in the loading direction

The strains of the three most extreme bars were plotted according to their positions in the loading direction to obtain the curvature at each cross-section. A line was then fit through the strain data, and the slope of this line was used to calculate the curvature, as shown in Figure 5-10 for specimen SJS1.

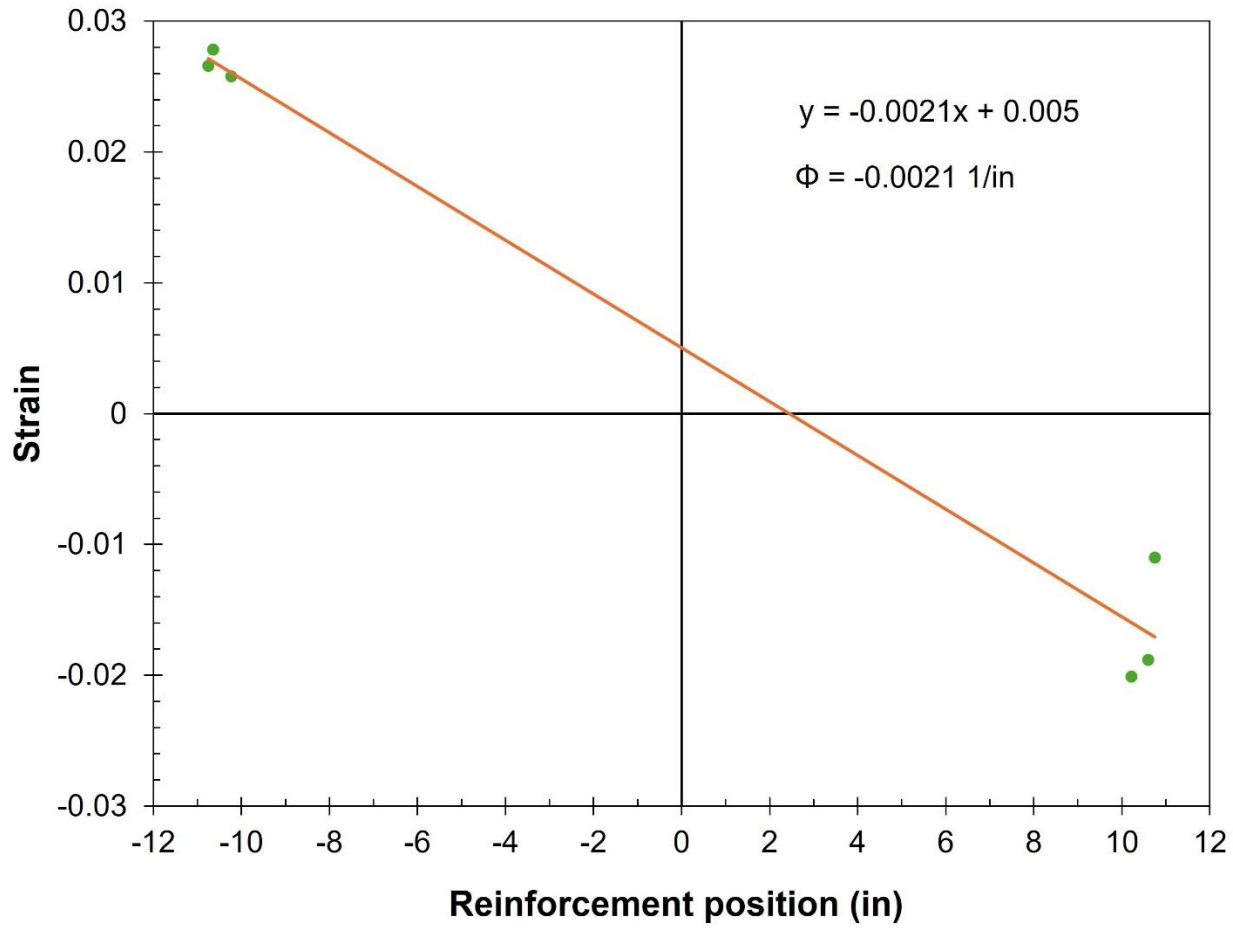


Figure 5-10. Example for curvature calculation

The curvature calculation was repeated for each gauge length along the height of the column during the first cycle of each ductility displacement and for both loading directions. The instrumented portion of the column began 2 inches above the socket interface. To determine the curvature at the socket interface, linear interpolation was performed using the curvature data along the height, as depicted in Figure 5-11.

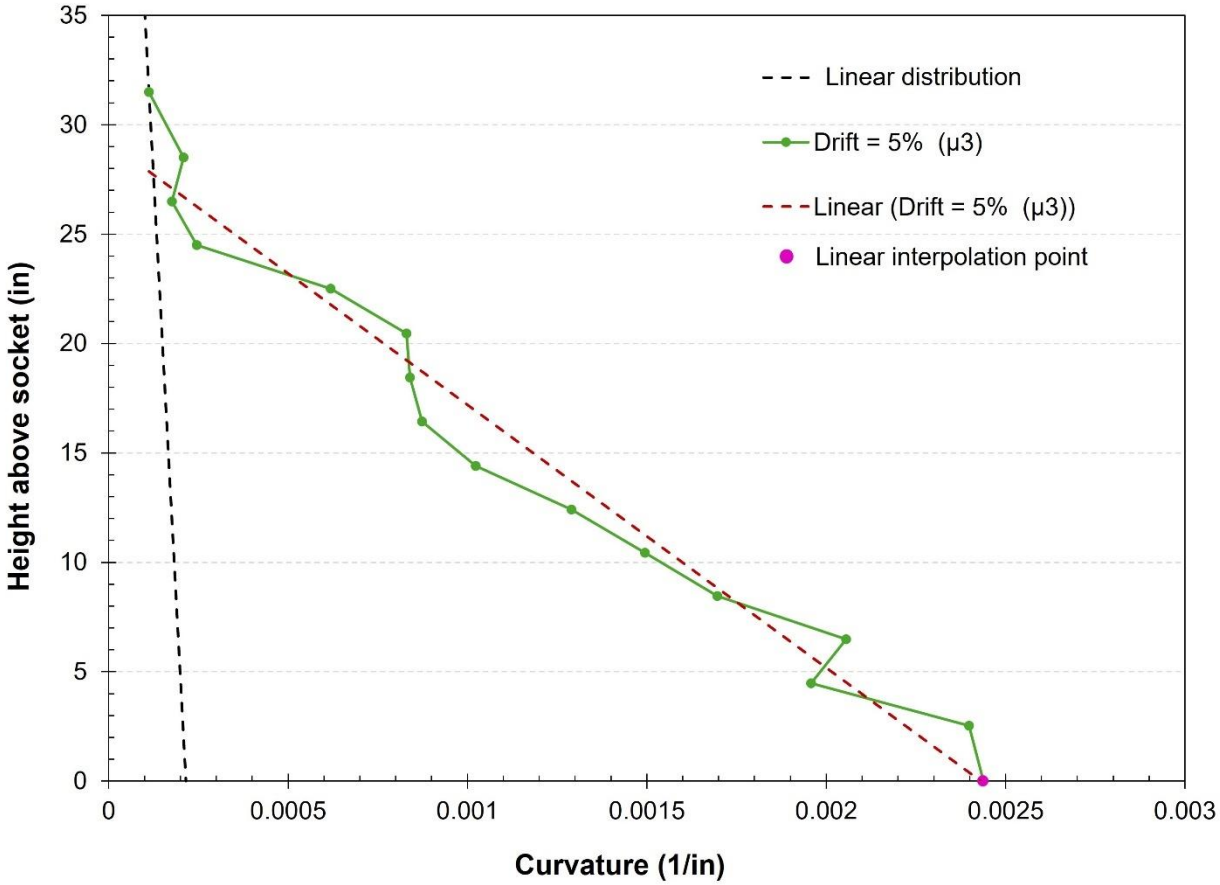


Figure 5-11. Example of linear interpolation in curvature profile

The resulting data provided a curvature profile along the column height, as shown in Figure 5-12 and Figure 5-13, illustrating the curvature before and after the first yield cycles. The curvature is defined as positive when the column is pushed toward its north face. The linear distribution line represents an elastic curvature distribution, starting from zero at the top of the column and increasing to the yield curvature at the socket interface.

The top portion of the column, expected to remain elastic, was not instrumented, and the curvature distribution in that region was assumed to be linear. Figure 5-14 provides an example of the curvature distribution along the height of the column. For the pre-yield cycles, the curvature was assumed to distribute linearly from the last measured curvature up to the column height. For post-yield cycles, the last measured curvature was extended until it reached the yield curvature, after which a linear distribution was assumed to follow the yield curvature line.

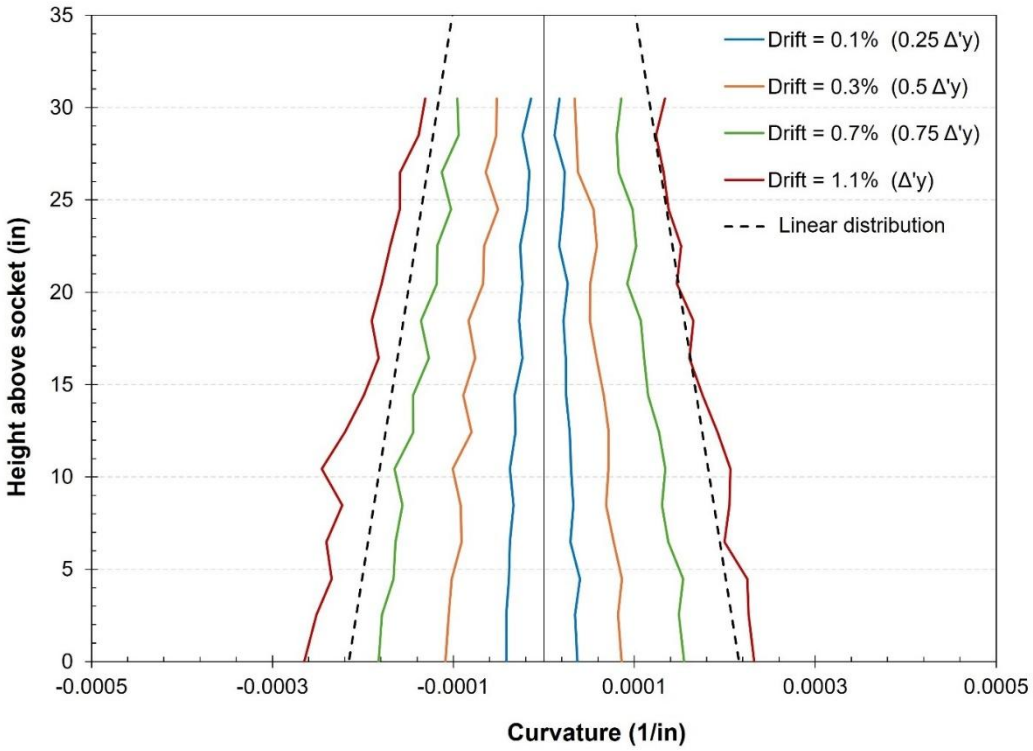


Figure 5-12. Example of curvature profile for cycles up to first yield

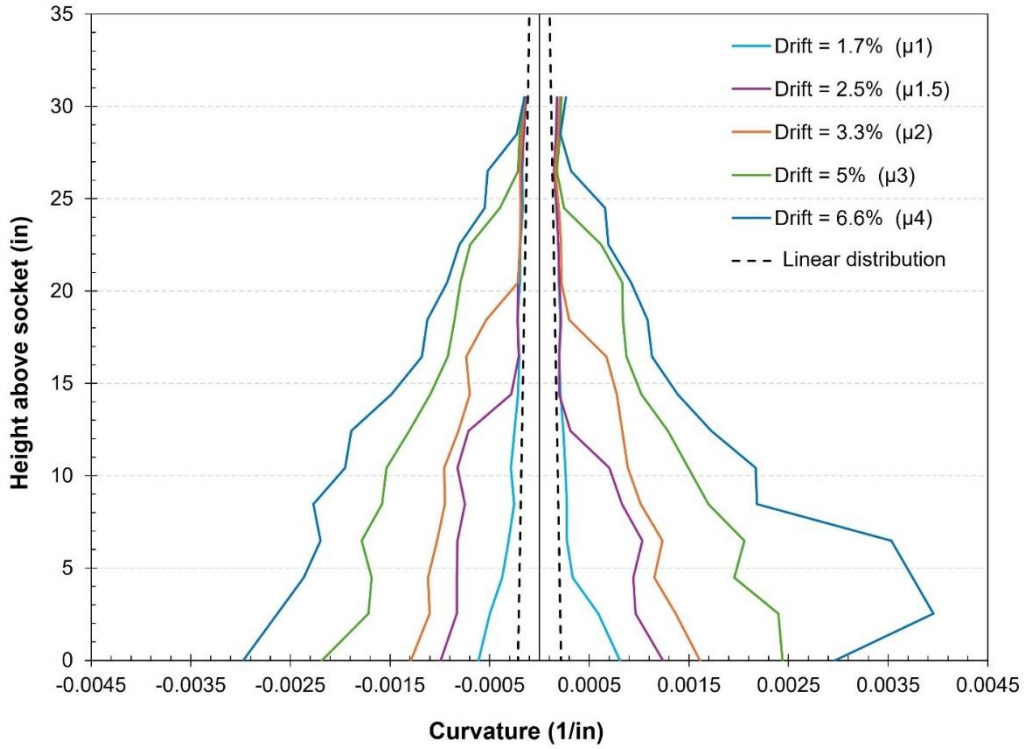


Figure 5-13. Example of curvature profile for post-yield cycles

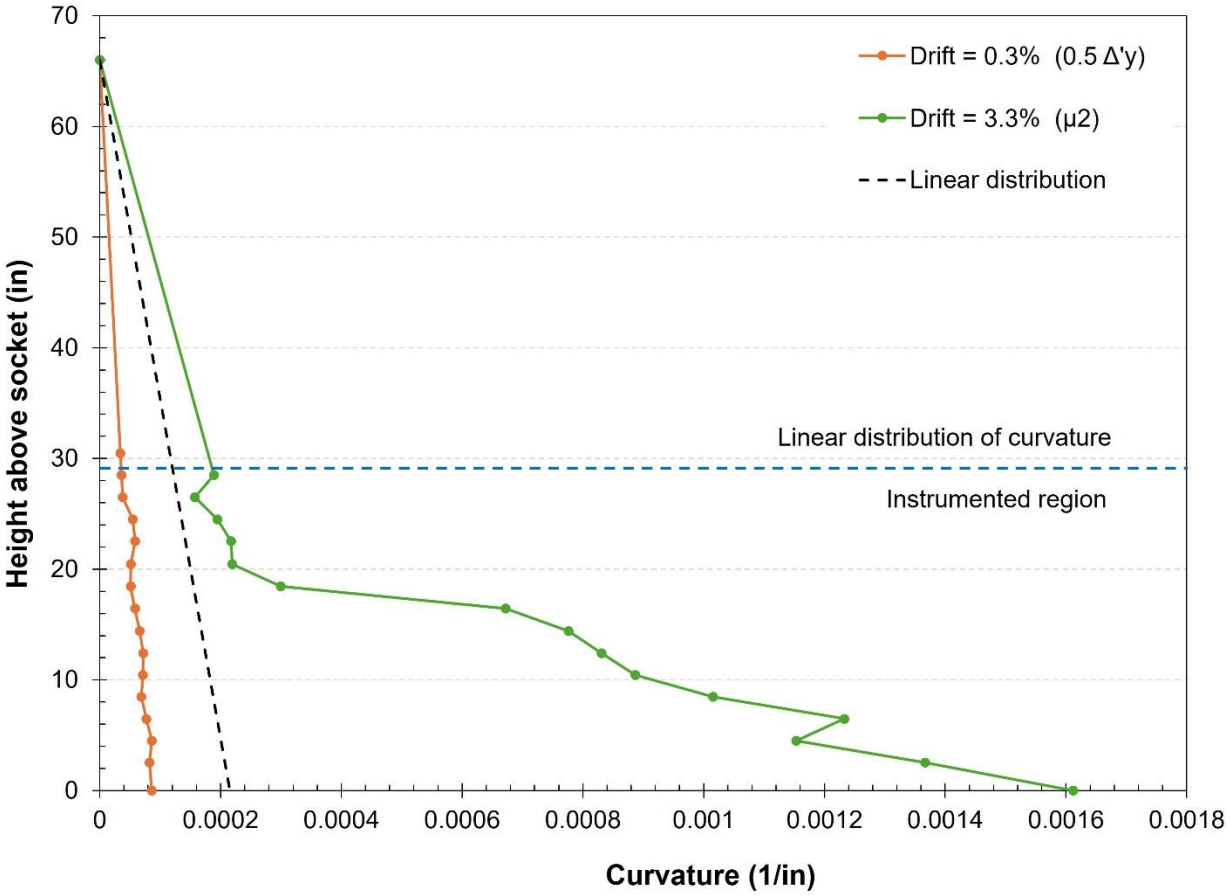


Figure 5-14. Example of curvature distribution along the height of the column

Once the curvature profile is obtained along the column height, the displacement calculation begins by integrating the area under the curvature curve. Numerical integration is employed, where the gauge length defines the height of each integration segment, and the curvature values between these gauge lengths determine the segment area.

After determining the integrated area for each section, the second theorem of the moment-area method is applied to calculate the displacement. According to this method, the displacement between two tangents to a deformed shape is calculated by considering the moment of the area under the curvature curve between the points (see Figure 5-8). Specifically, the method involves measuring the distance from the top of the column to the centroid of the previously calculated area. This procedure is repeated for the entire column height, providing the flexural component of the displacement.

The displacement component due to strain penetration and rocking of the column was determined by tracking the vertical change in position (slip) of an LED marker placed at the bottom of the column on the three extreme bars on each side. The initial height of each LED marker was recorded at the beginning of the test to establish a baseline. During the test, the baseline height was subtracted from the recorded height to calculate the change in position for each LED marker. This calculation was performed for the first cycle of each ductility displacement and for each loading direction.

A line was then fit through the slip data of the three extreme bars, and the slope provided the rotation angle resulting from strain penetration and rocking of the column. Figure 5-15 shows an example of the slip data and the fit line for SJS1 when the force was applied toward the north side of the column.

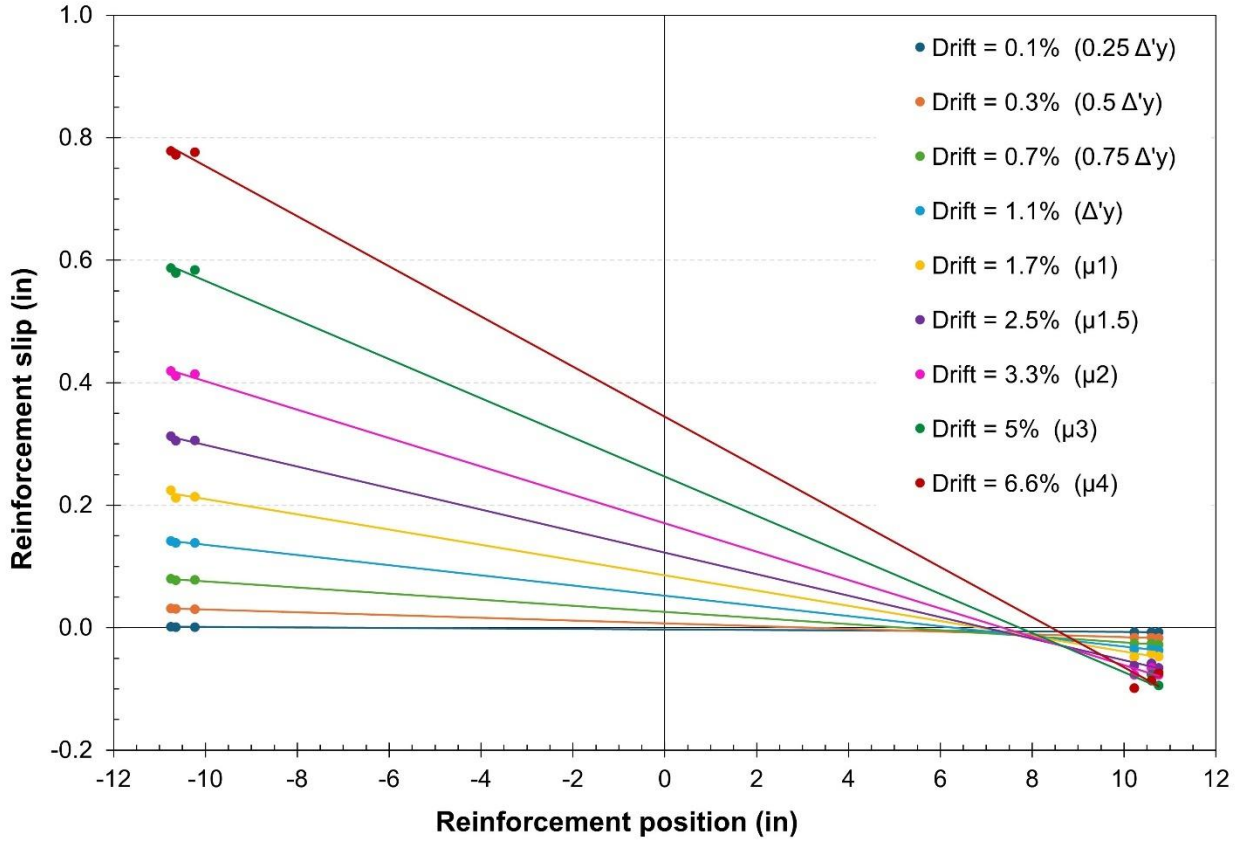


Figure 5-15. Example of rotation of the column at the socket interface

The displacement component due to strain penetration and rocking was calculated by multiplying the rotation angle by the column height measured from the interface of the external socket connection. The calculation of this displacement component is shown in Equation 5-5.

Equation 5-5 $$\Delta_{SP-R} = \theta_{SP-R} \cdot (H_{total} - H_s)$$

A grid of LED markers was utilized to calculate the shear deformation of the column, with the markers specifically placed on the west side of the column, as shown in Figure 5-16.



Figure 5-16. LED grid position for shear strain calculation

For each grid, the strains in the horizontal, vertical, and diagonal directions were calculated using Equation 5-1 and Equation 5-2. The horizontal and vertical strains were averaged, with the two horizontal strains averaged to represent ε1, and the two vertical strains to represent ε2. Figure 5-17 provides an example of the strain distribution for a grid.

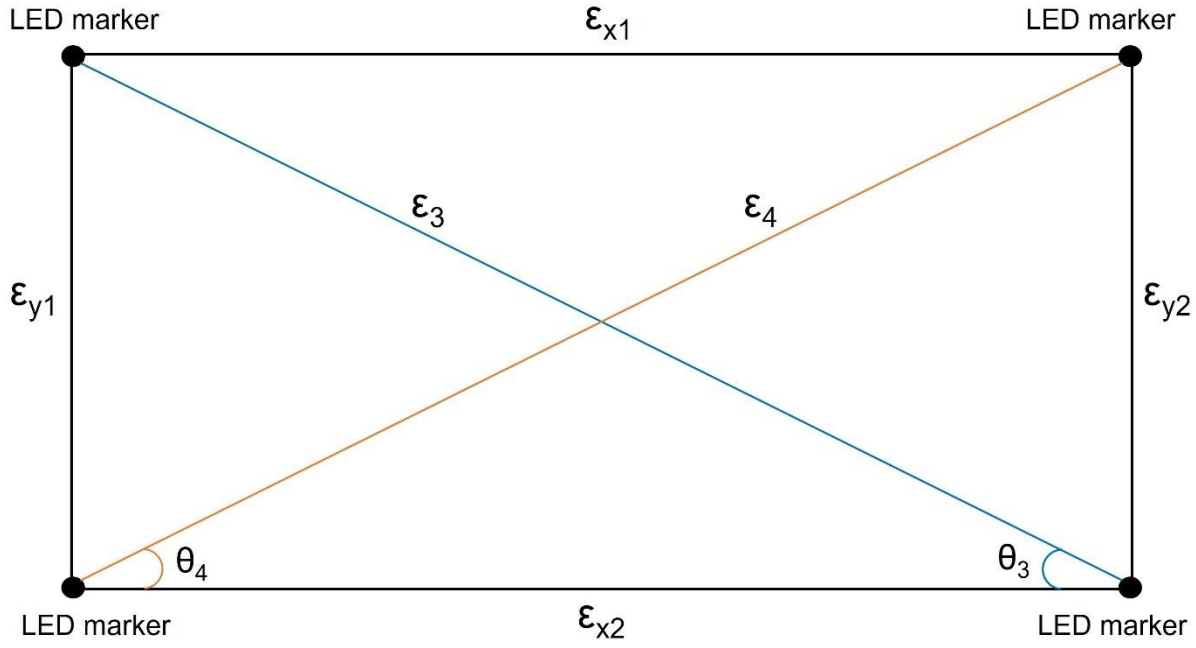


Figure 5-17. Example of strains measured on a grid

These calculated values represent axial strains, which are positioned on the horizontal axis of the Mohr circle. The shear strain is zero for strains ε1 and ε2, as these correspond to the principal stresses. However, for the strains measured in the inclined directions, denoted as ε3 and ε4, their respective shear strains were determined using the properties of the Mohr circle and geometry. To accurately obtain the Mohr circle properties, a best-fit approach was applied [25], where the radius and center of the Mohr circle were adjusted to minimize the error (see Equation 5-6) in the projected shear strain for ε3 and ε4. Figure 5-18 illustrates the Mohr circle and the projected errors.

Equation 5-6 $$find\ r, c\ \rightarrow \min(\sum_1^4 e_i)\ \rightarrow\ \gamma_{xy}$$

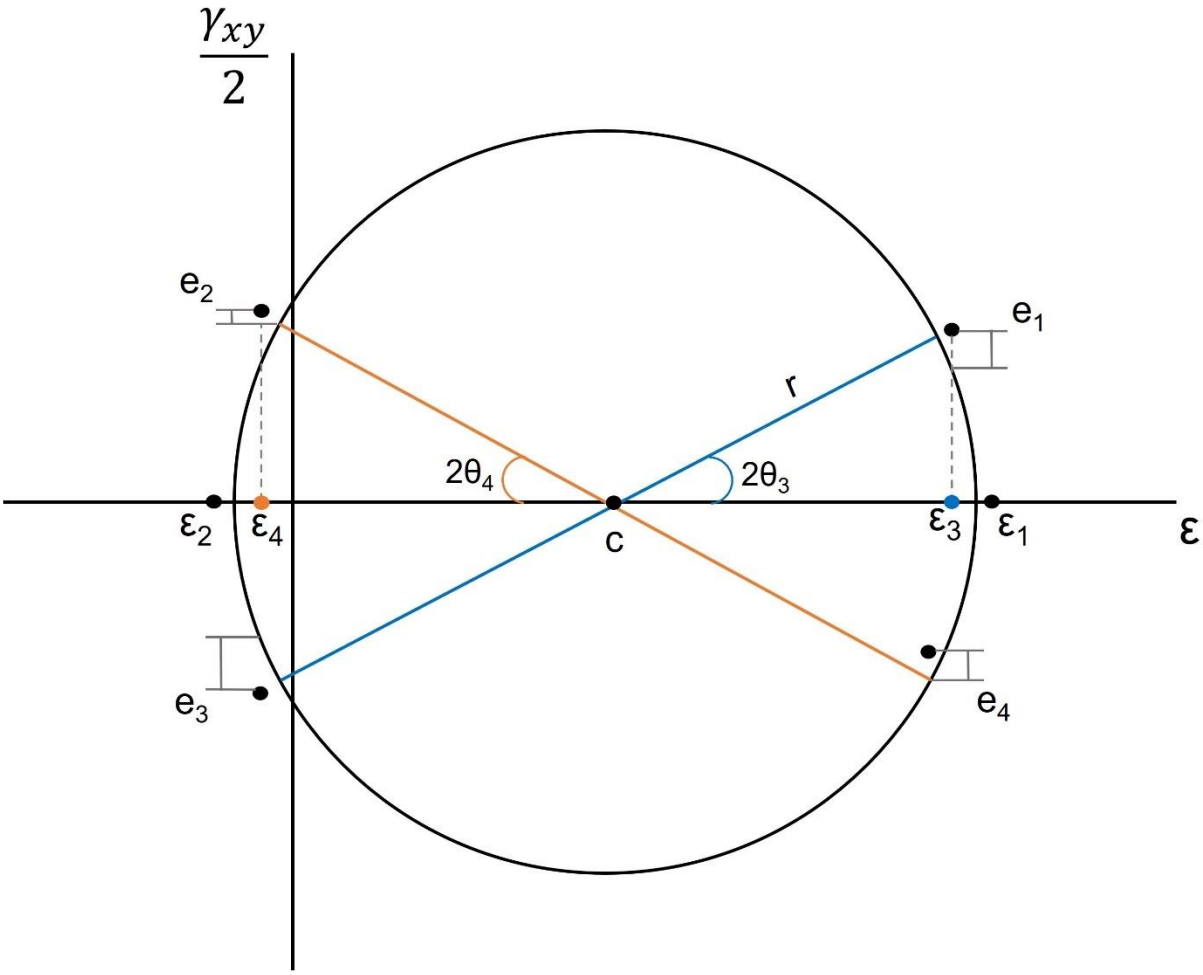


Figure 5-18.Example of a best fit of the Mohr circle

Once the center and radius of the Mohr circle were determined, the shear strain for each grid was calculated using Mohr circle principles, as outlined in Equation 5-7. This procedure was repeated for each grid on the column. Since three grids were positioned every two inches along the column height, the shear strain at each height was obtained by averaging the shear strains from these three grids. This process was repeated for the first cycle of each ductility displacement. Figure 5-19 illustrates an example of the shear strain distribution along the column of SJS1 for the last three ductility displacements.

Equation 5-7 $$\gamma_{xy} = 2 \cdot r$$

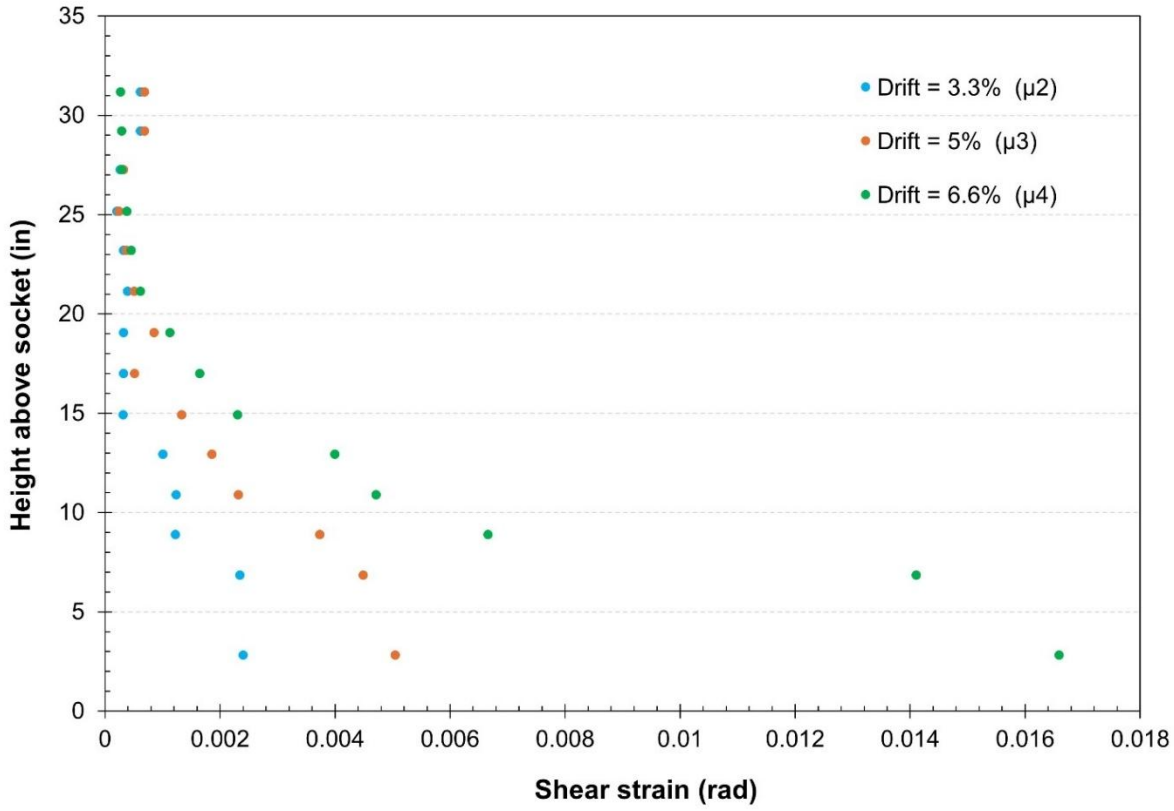


Figure 5-19. Example of shear strain distribution along the measured height of the column

Once the shear strains for each interval were determined, Equation 5-8 was used to calculate the shear displacement. In this equation, the shear strain for each interval was multiplied by the interval height, summing these contributions up to the top of the instrumented region. For the non-instrumented region, it was assumed that the last measured shear strain remained constant up to the top of the column. This procedure was performed for each loading direction.

Equation 5-8 $$\Delta_{shear} = \sum_{i=1}^{n} \left(\gamma_{xy(i)} \cdot h_i\right)$$

To calculate the displacement resulting from the rotation of the socket, VIC-3D software was used to analyze the rotation throughout the test. Figure 5-20 illustrates an area of interest with the selected points used to monitor the socket rotation. Figure 5-21 presents an example of the rotation measured on the north face of SJS1. It was observed that the rotation remained approximately constant along the height of the socket. Therefore, an average rotation from the five points was used for displacement calculation.

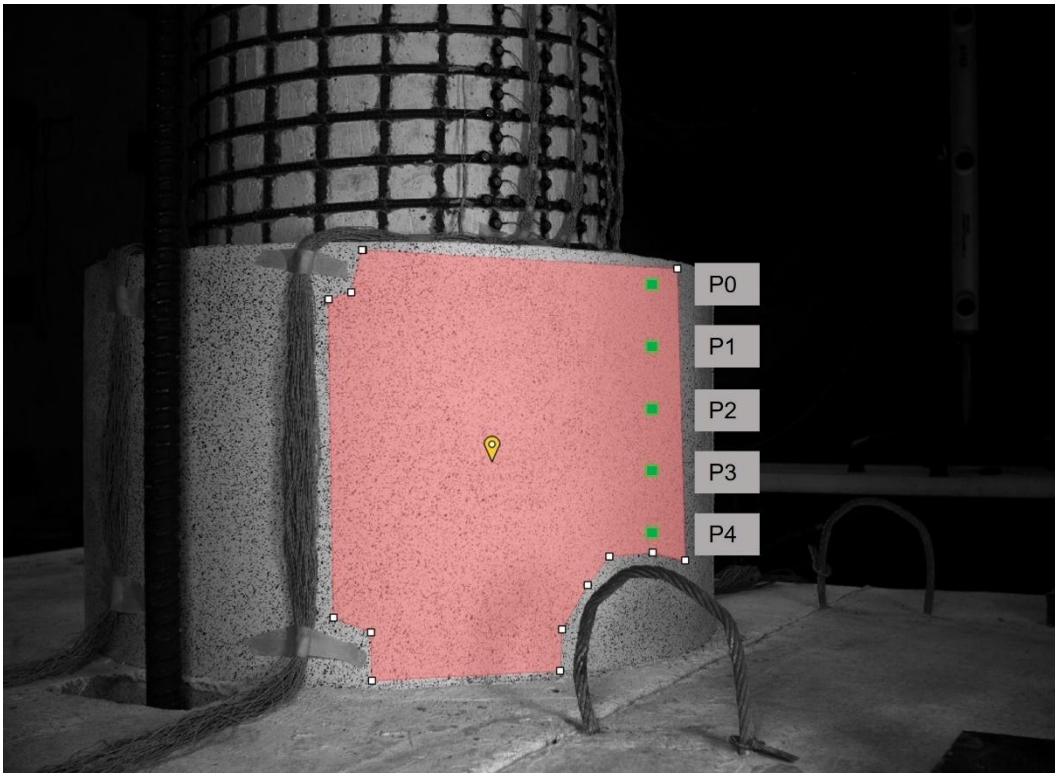


Figure 5-20. Example of area of interest for DIC analysis

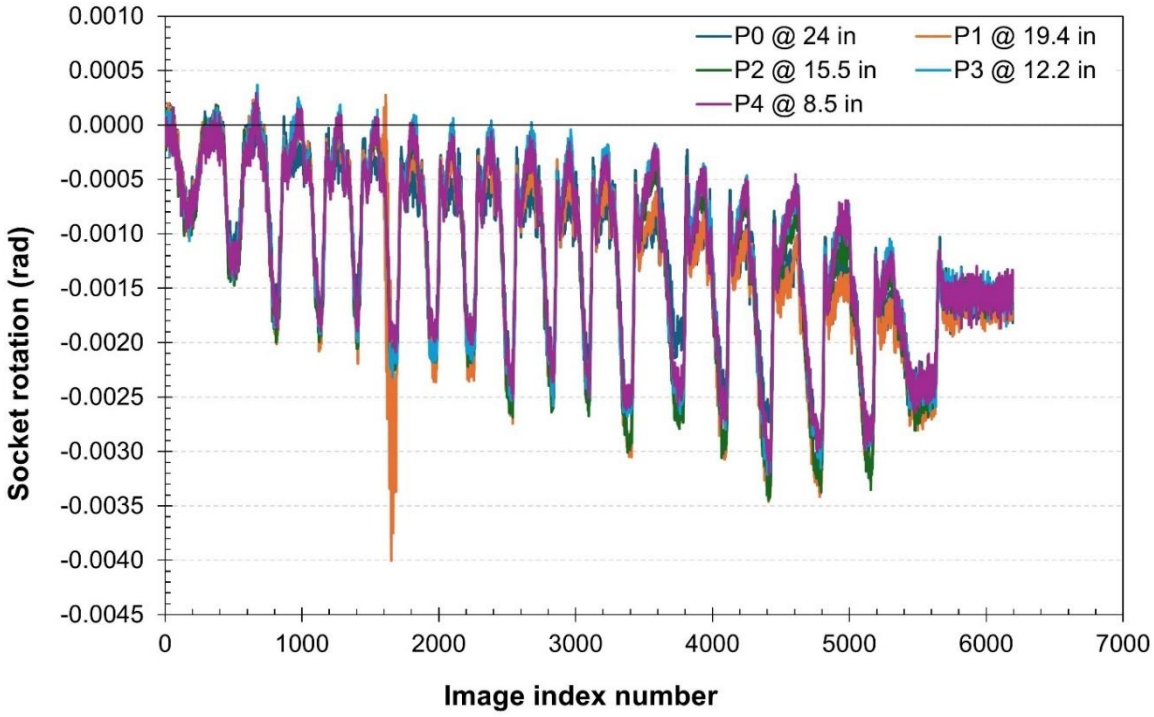


Figure 5-21. Example of socket rotation throughout the test

The influence of socket rotation on the column displacement was considered up to the socket height, and the rotation was multiplied by the socket height, as shown in Equation 5-9. This calculation was performed for both loading directions to capture the full extent of the socket rotation.

Equation 5-9 $$\Delta_{Socket} = \theta_{Socket} \cdot (H_s)$$

The contributions from flexural deformation, strain penetration, rocking, shear deformation, and socket rotation were compared with the measured displacement at each ductility level. Figure 5-22 presents an example of the measured displacement alongside each calculated displacement component. This analysis was performed for both loading directions. By comparing the measured displacement with the calculated displacement components, the accuracy of the calculation methods was validated, and the dominant displacement component for each experimental test was visually identified. While the measured displacement does not perfectly match the calculated components due to inherent calculation and instrumentation errors, the comparison provides valuable insights into the behavior of each test.

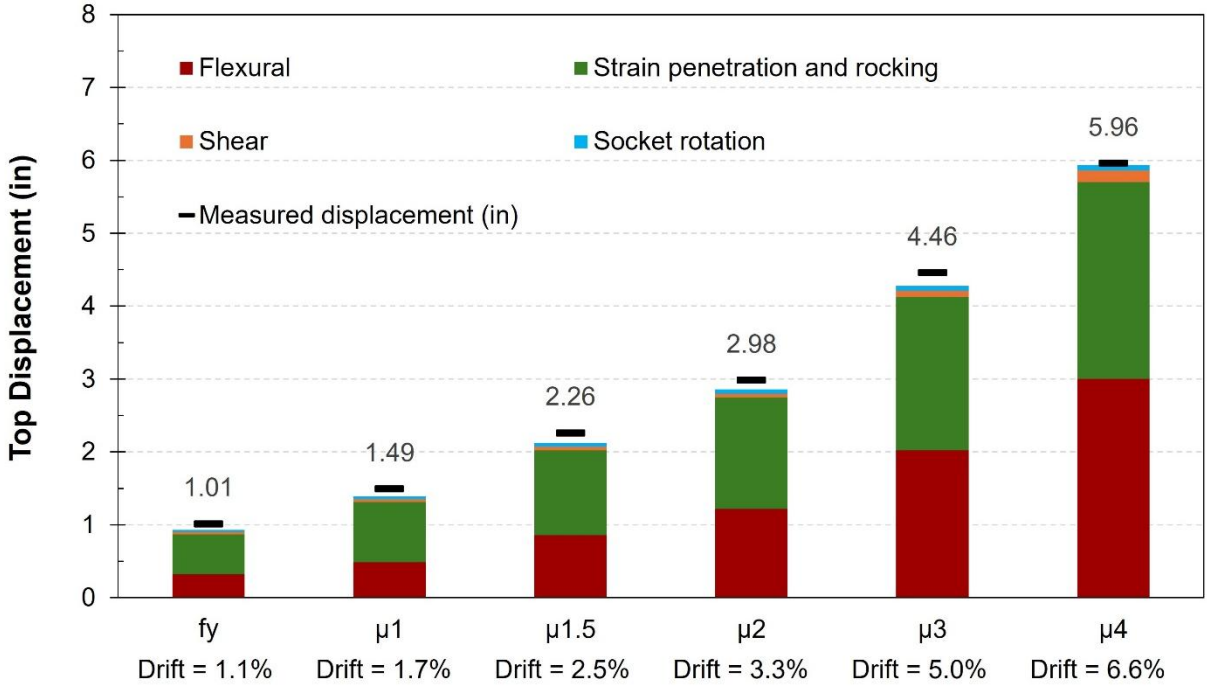


Figure 5-22. Example of displacement components for post-yield cycles

5.2. Experimental Results for Specimen SJS-1

In this section, the data analysis and experimental results previously discussed in this chapter will be specifically applied to the experimental test SJS1. The results for SJS1 will be presented in detail, focusing on axial strains on the column and external socket, hysteretic damping, and calculated displacement components. This analysis provides insights into the column performance and behavior under the applied loading conditions, contributing to a comprehensive understanding of the system response.

5.2.1. Axial strain analysis for SJS-1

The strain profiles were calculated to assess the strain distribution along the RC column during the first cycles of each ductility displacement for SJS1, considering both loading directions. In this context, ″Pushing Cycles″ refers to the strain profiles when force is applied toward the north face of the column, while ″Pulling Cycles″ refers to when force is applied toward the south face.

Figure 5-23 and Figure 5-24 present the strain profiles of the extreme bar located on the north face of the specimen for cycles up to yielding and post-yield cycles, respectively. Similarly, Figure 5-25 and Figure 5-26 depict the strain profiles for the extreme bar on the south side of the specimen for cycles up to yielding and post-yield cycles. The strain profiles are shown up to the cycle before bar fracture, beyond which data could not be recorded near the fracture area. These strain profiles indicate a spread of plasticity extending approximately 28 inches from the external socket interface.

The maximum axial strain in tension before bar fracture was approximately 4.5% on both sides of the specimen. On the north side, where bar fracture occurred, the maximum axial strain in compression was around 4.0%. In contrast, the maximum axial compression strain on the south side was significantly lower, reaching values of approximately 1.5%.

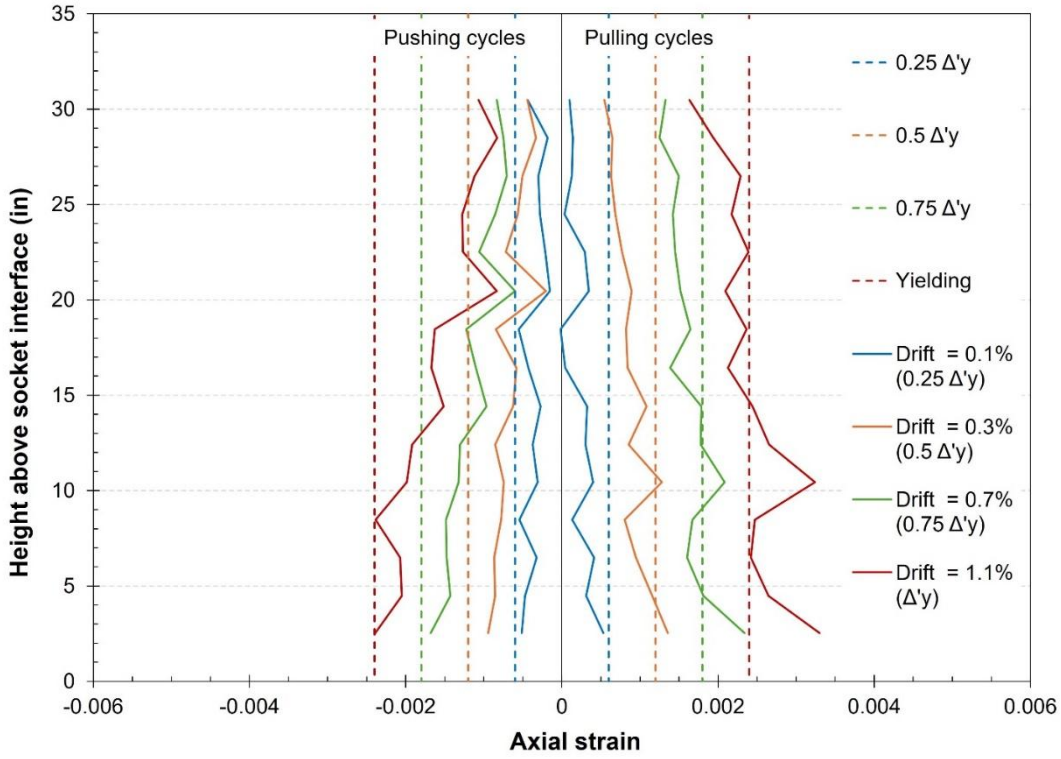


Figure 5-23. Strain profile up to first yield cycle for SJS1on the north side of the column

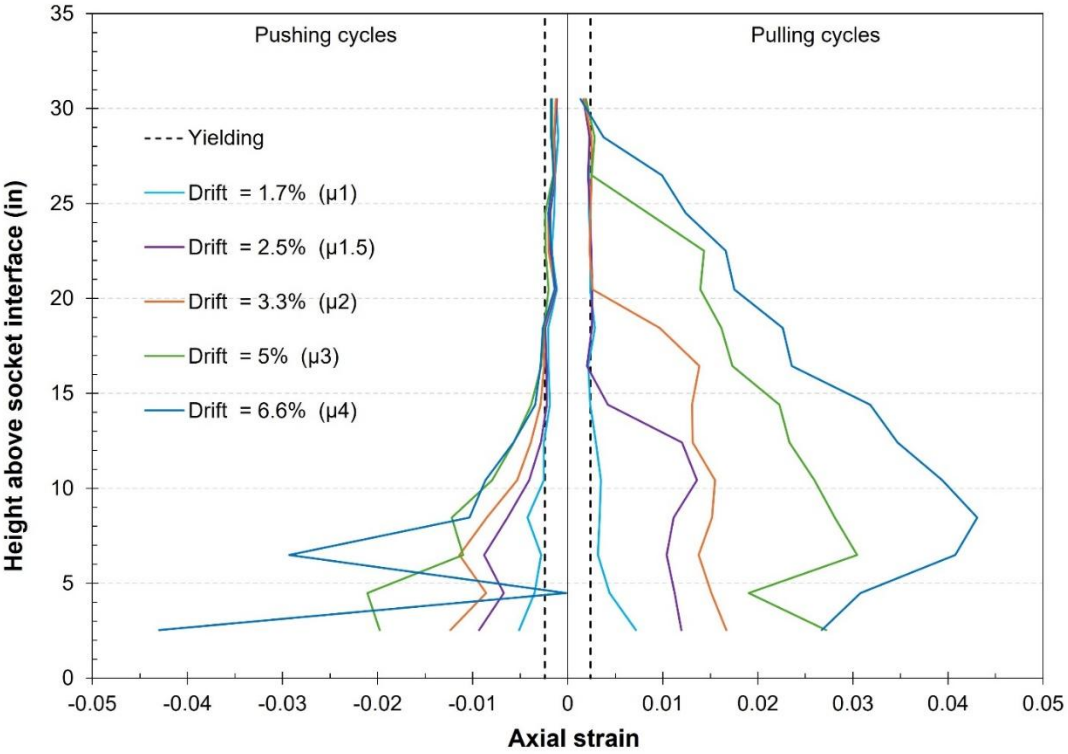


Figure 5-24. Strain profile for post-yield cycles for SJS1 on the north side of the column

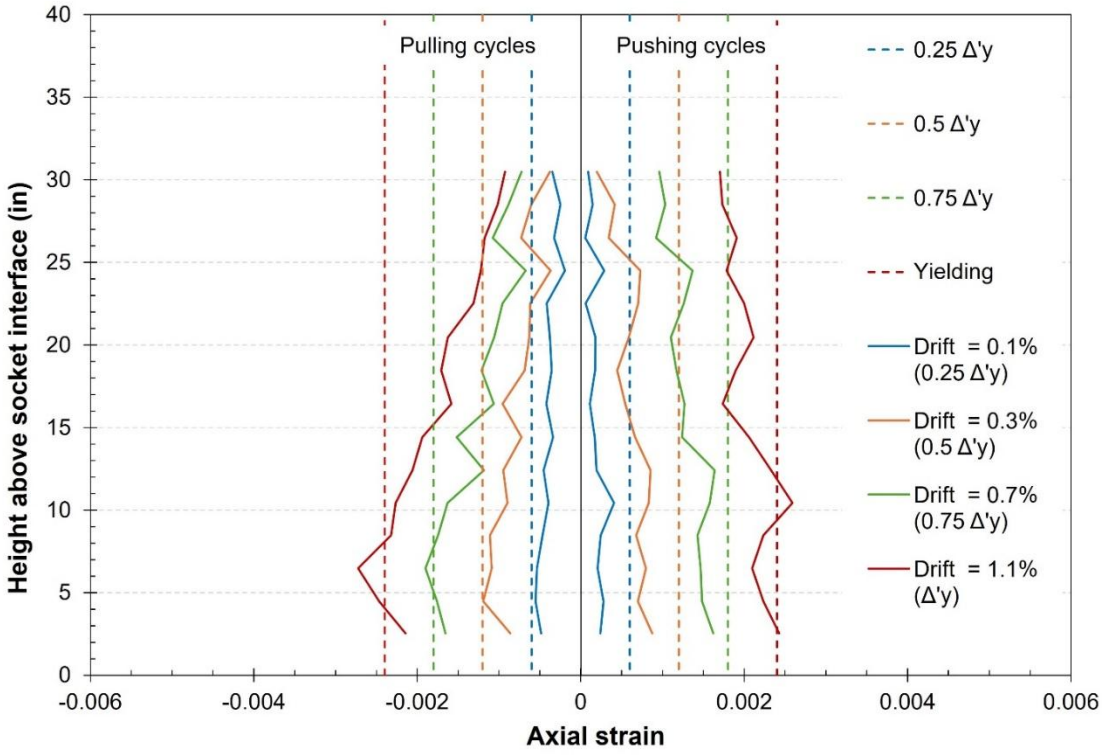


Figure 5-25. Strain profile up to first yield cycle for SJS1on the south side of the column

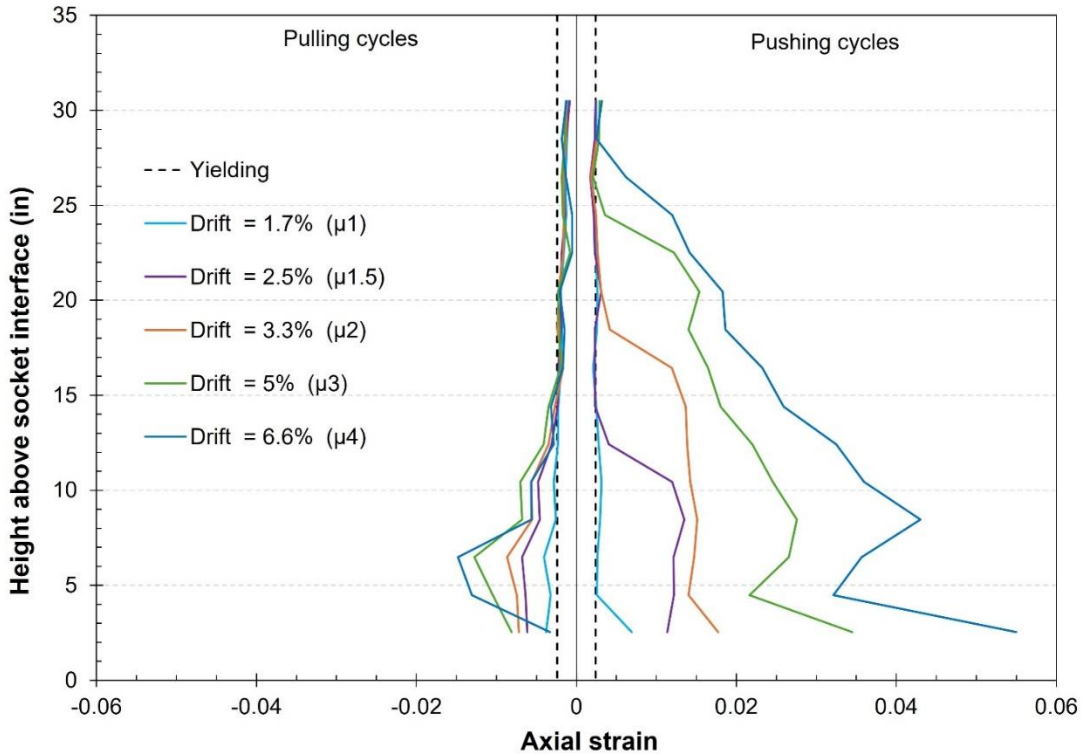


Figure 5-26. Strain profile for post-yield cycles for SJS1 on the south side of the column

A detailed examination of the strains on the reinforcing bars can be achieved by plotting the strain throughout the displacement history for each gauge length. Figure 5-27 and Figure 5-28 present the strain history of the extreme bars located on the north and south faces of the specimen, respectively, with the gauge length chosen at the points where the bars buckled and eventually fractured. For both extreme bars, it can be observed that once the strain in tension exceeded 3%, the reinforcement began to buckle. This buckling is evident when, instead of continuing to increase in compressive strains, the bars started to exhibit tension strains due to their deformed shape. After significant buckling occurred, the strain data was no longer plotted, as the resulting tension strains were no longer representative of the true behavior of the reinforcing bars.

Additionally, the strain history of the extreme bars in the external socket wall reinforcement was monitored using strain gauges placed 2 inches above the footing. Figure 5-29 and Figure 5-30 present the strain history for the extreme bars on the north and south faces, respectively. The data shows that the reinforcement in the external socket wall barely reached the yield point, indicating that the external socket wall remained elastic throughout the entire experimental test.

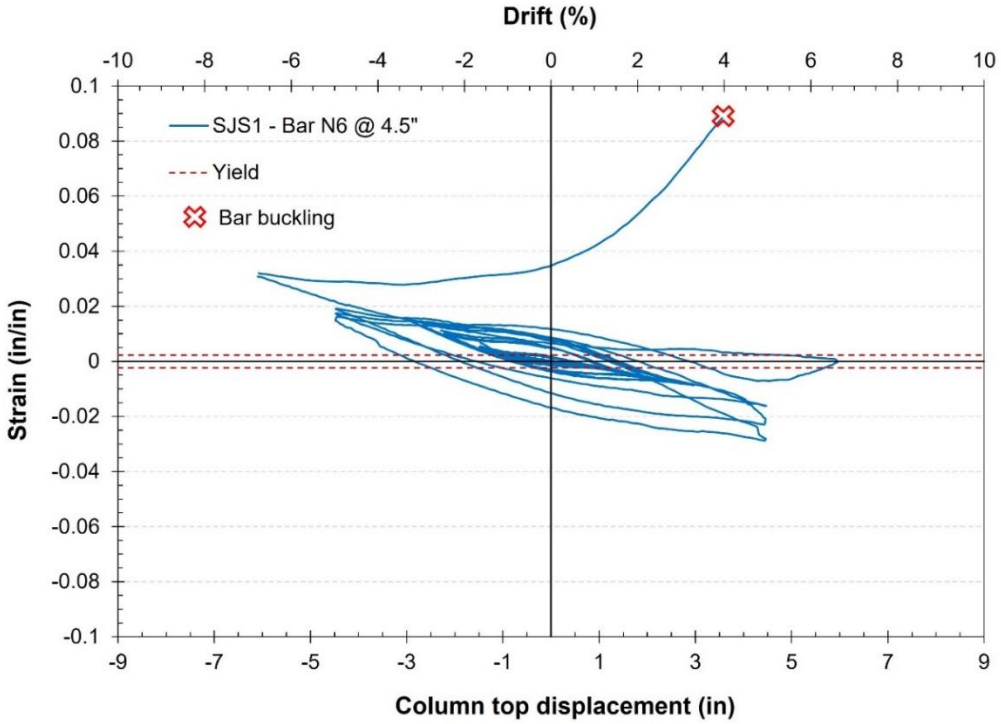


Figure 5-27. Strain vs displacement history for N6 of SJS1

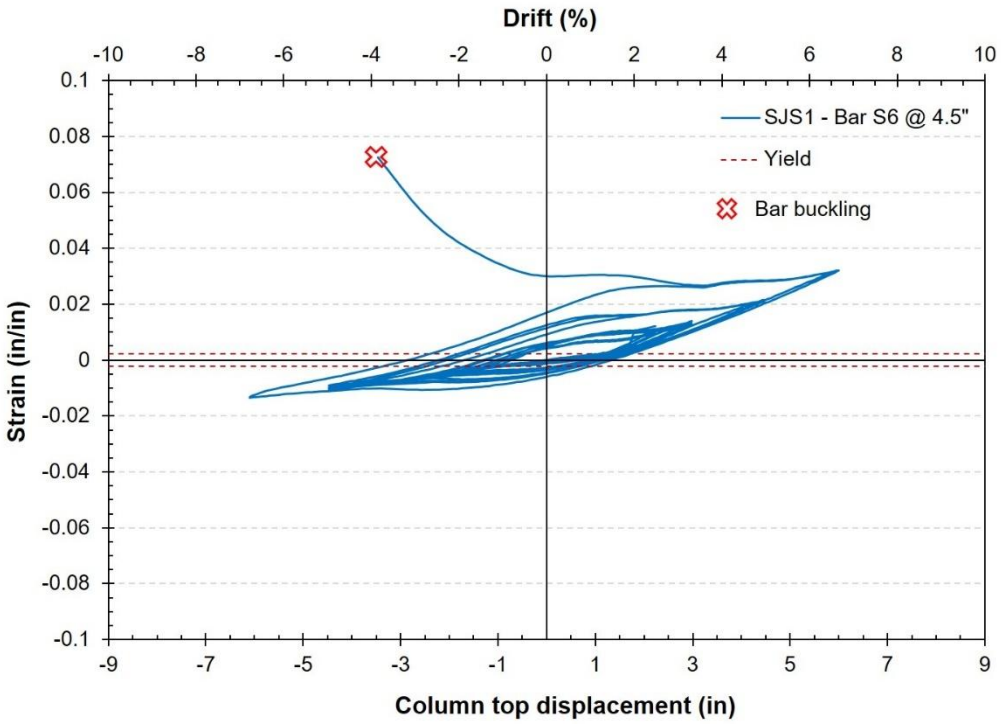


Figure 5-28. Strain vs displacement history for S6 of SJS1

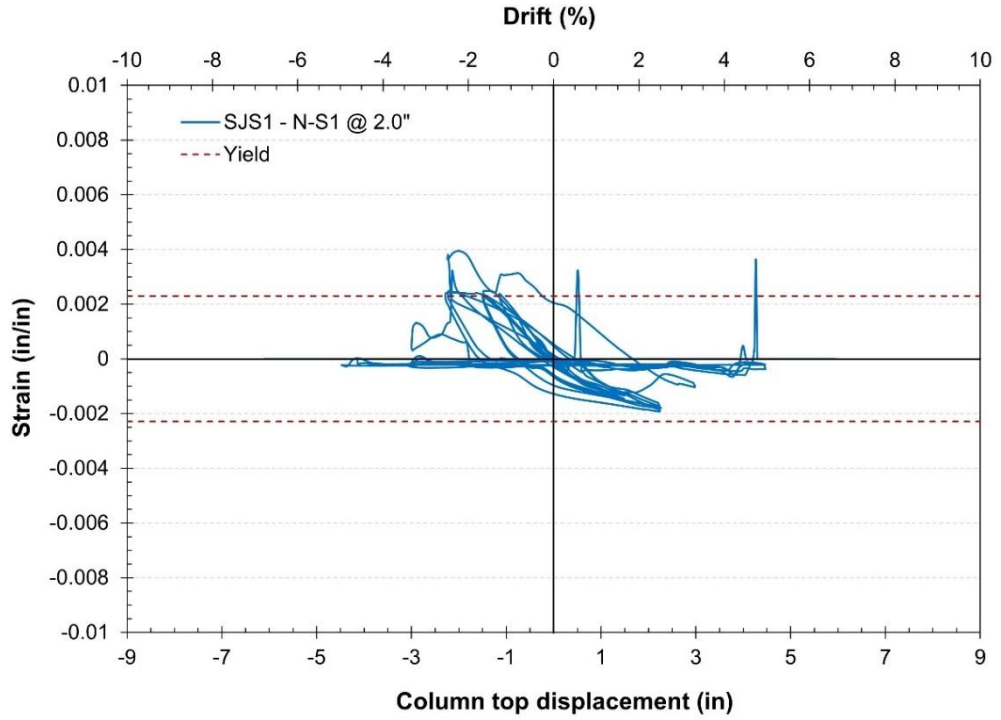


Figure 5-29. Strain vs displacement history for the extreme bar of socket wall reinforcement at the north side of SJS1

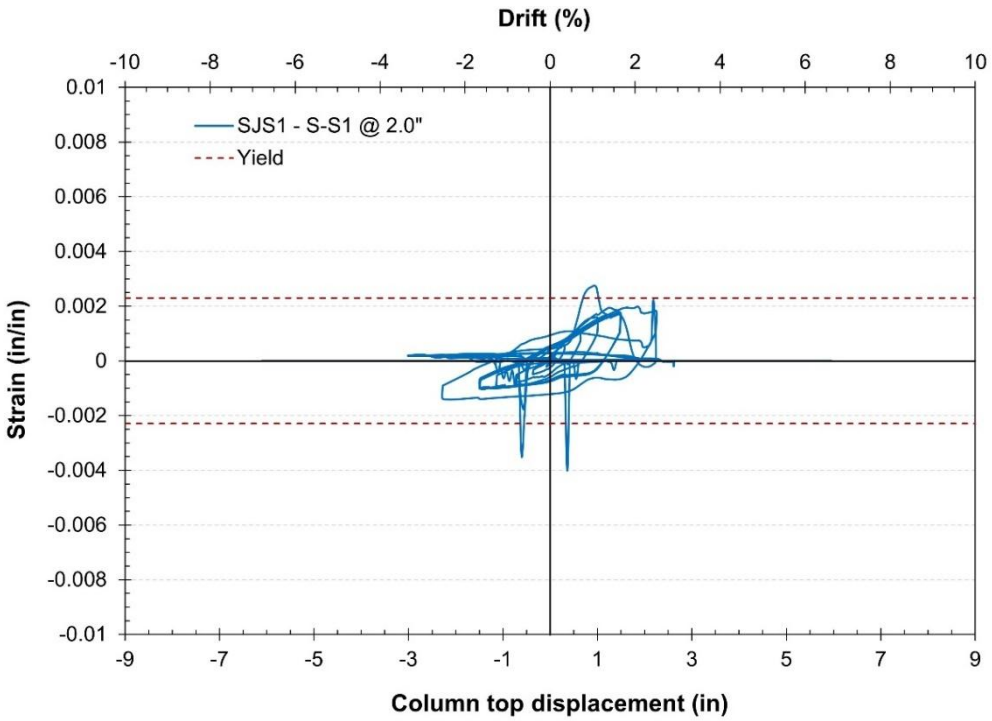


Figure 5-30. Strain vs displacement history for the extreme bar of socket wall reinforcement at the north side of SJS1

The axial strains on the external socket sleeve were measured using DIC. In this context, the horizontal strains correspond to the hoop forces acting around the circumference, while the vertical strains reflect any flexion sustained by the sleeves. Figure 5-31 and Figure 5-32 present the strains on the north face of the specimen while Figure 5-33 and Figure 5-34 show the strains on the south face.

The data shows that, for the horizontal strains, the top 4 inches of the socket experienced strain values twice that of yielding, while the remaining height of the socket remained elastic. The vertical strains remained elastic throughout the experimental test, indicating that the external socket sleeve did not contribute significantly to the flexural behavior of the external socket wall.

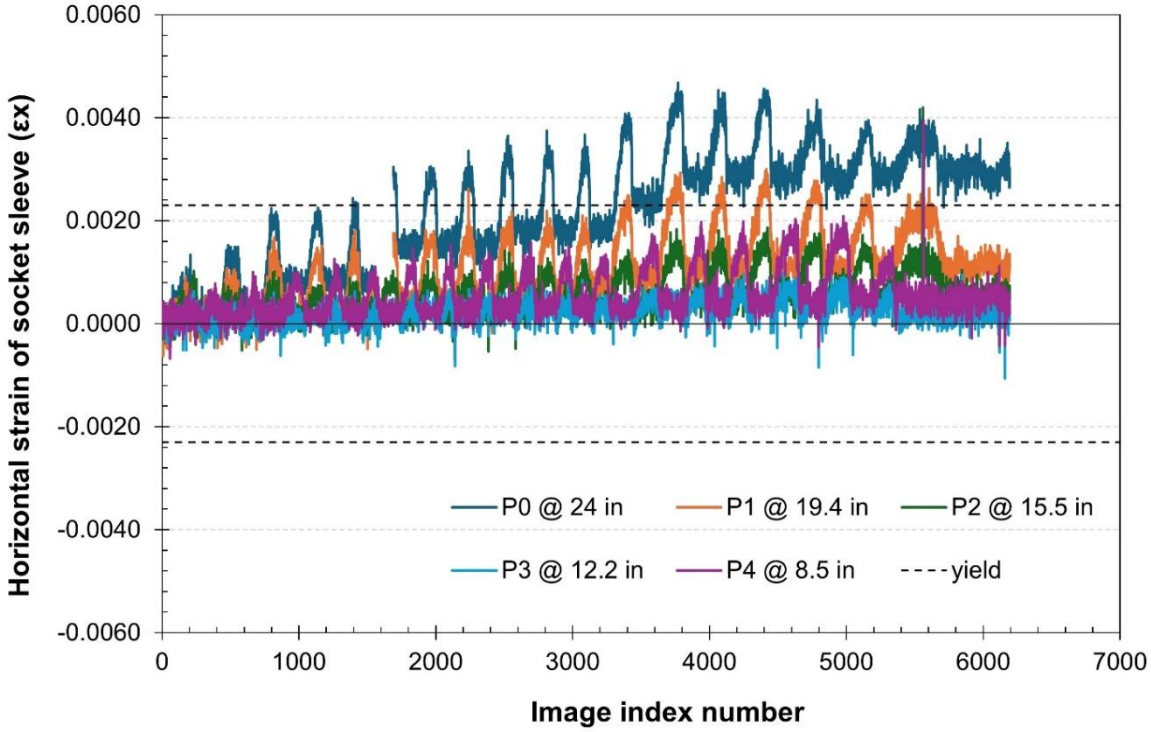


Figure 5-31. Horizontal strain history of external socket sleeve at the north side of SJS1

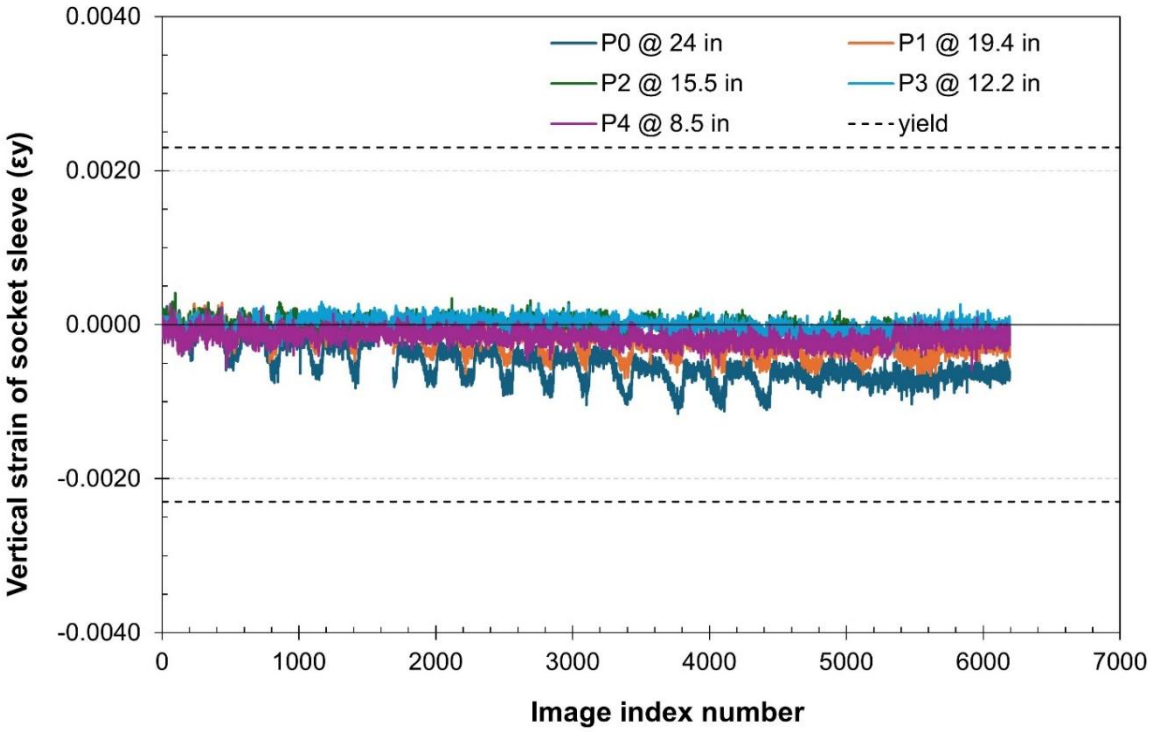


Figure 5-32. Vertical strain history of external socket sleeve at the north side of SJS1

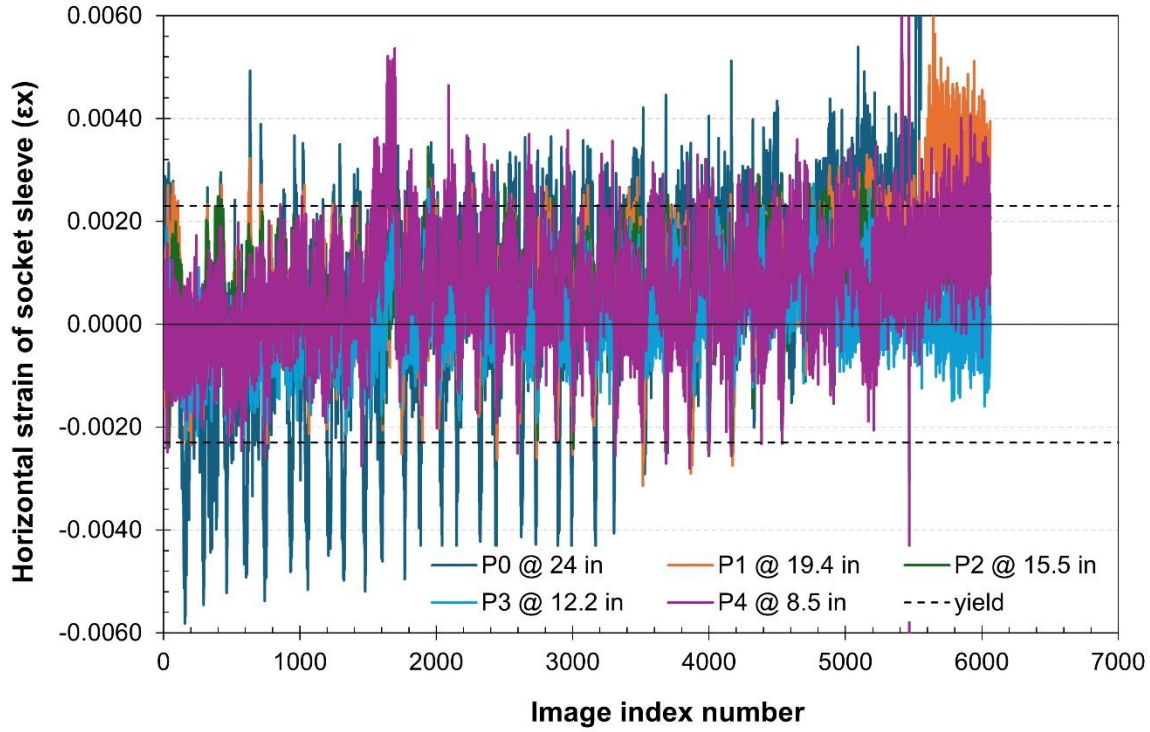


Figure 5-33. Horizontal strain history of external socket sleeve at the south side of SJS1

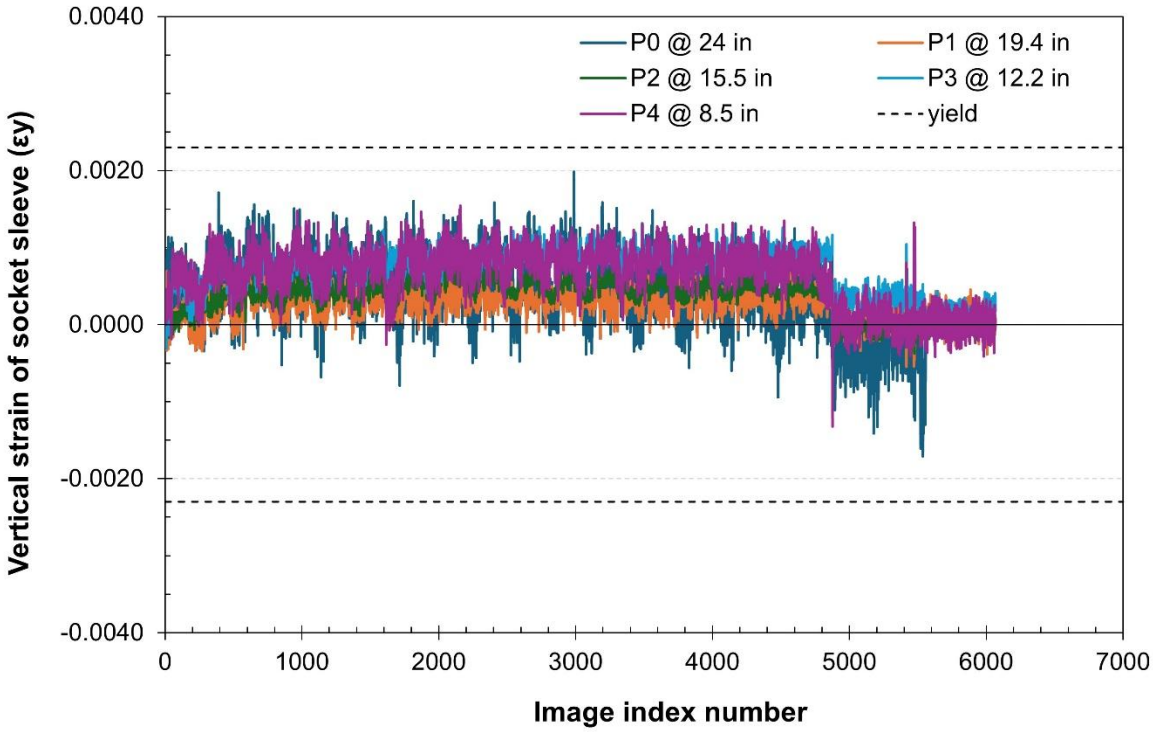


Figure 5-34. Vertical strain history of external socket sleeve at the south side of SJS1

5.2.2. Energy dissipation and hysteretic damping for SJS-1

Energy dissipation is important in understanding a structure seismic behavior because it relates to the structural element damage and energy dissipation capacity. Figure 5-35 illustrates the energy dissipation for all ductility displacement cycles for SJS1, with a total energy dissipation of 7661 kip-in. Notably, during the third cycle of ductility four, where bar fracture occurred, the energy dissipated was reduced by 30% compared to the first cycle at the same ductility level. This reduction highlights the impact of severe damage on the energy dissipation capacity of the column.

Additionally, Figure 5-36 presents the Jacobsen hysteretic damping values for SJS1, demonstrating that damping increases as the applied displacements grow and the column sustains more damage. Notably, the elastic damping for SJS1 was approximately 10%, which is 5% higher than what is typically observed in a CIP column, indicating enhanced energy dissipation during the structural element elastic behavior.

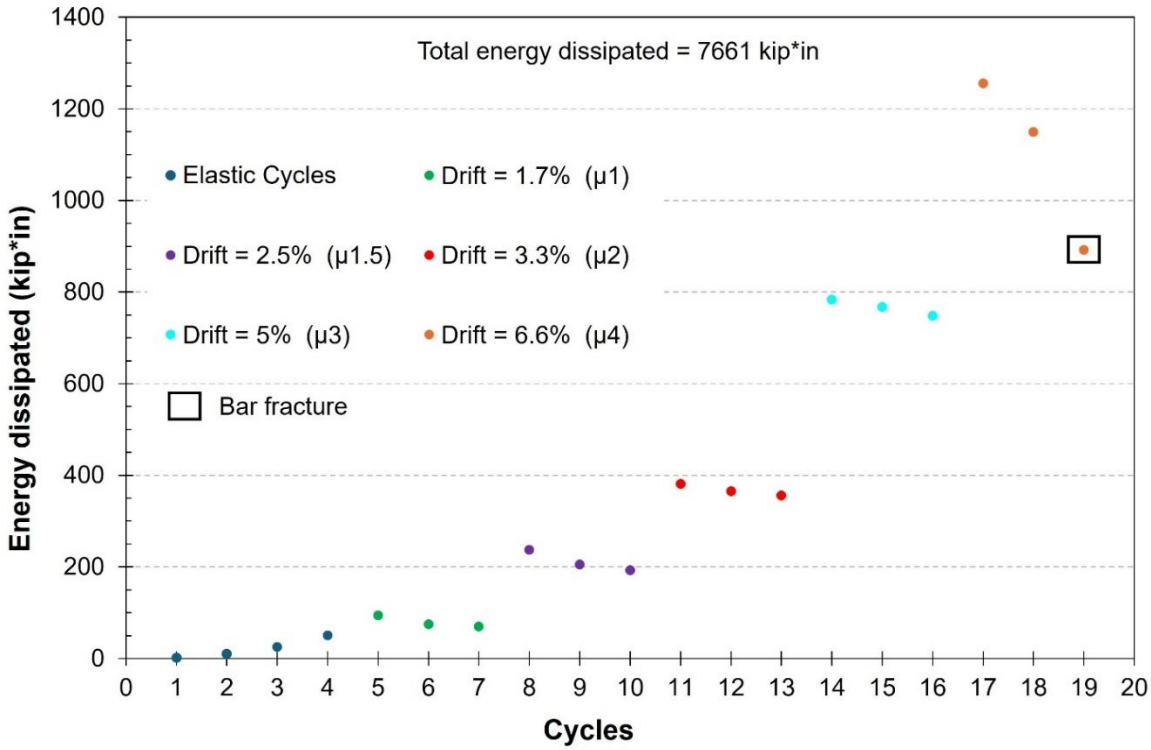


Figure 5-35. Energy dissipation plot for SJS1

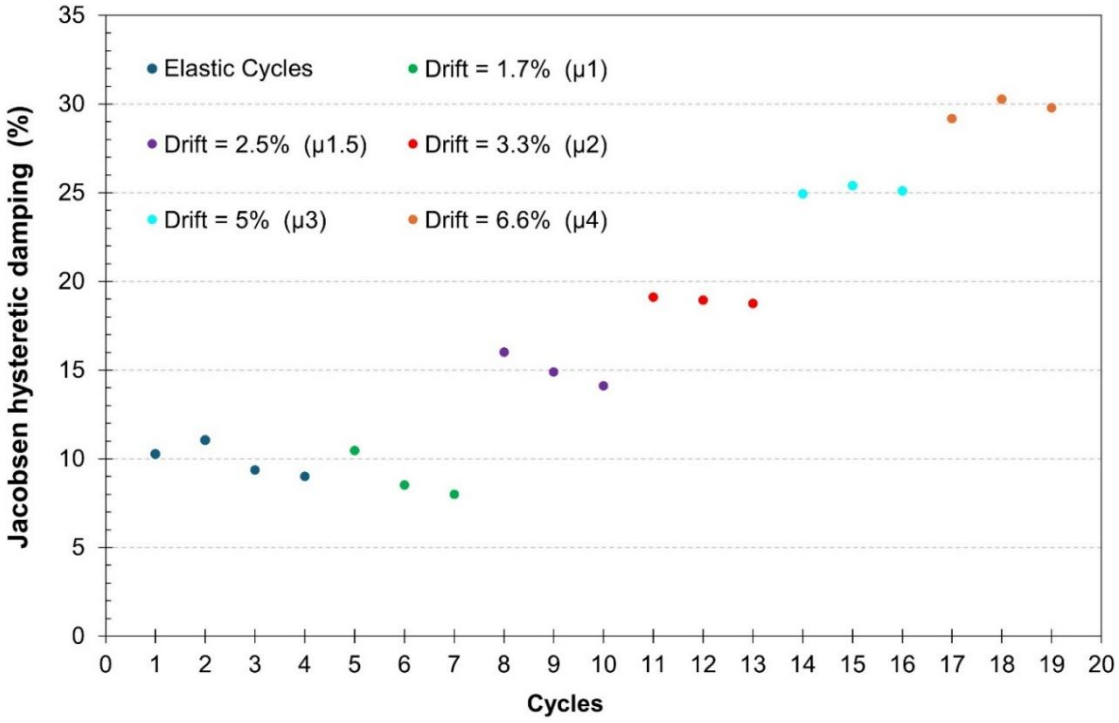


Figure 5-36. Hysteretic damping plot for SJS1

5.2.3. Displacement components for SJS-1

The displacement components considered in the calculations include flexural deformation, column rotation due to strain penetration and rocking, shear deformation of the column, and the deformation contribution resulting from socket rotation. The methodologies for these calculations have been detailed earlier in Section 5.1.3 of this report.

The flexural displacement component was derived from the column curvature, with the curvature profile shown in Figure 5-37 for the cycles up to yield and in Figure 5-38 for the post-yield cycles. The curvature is defined as positive when the column is pushed toward its north face. The dashed line in these figures represents the linear distribution of curvature, beginning at zero at the top of the column and reaching the yield curvature at the socket interface.

The displacement due to column rotation was calculated by determining the rotation angle at the base of the column and multiplying it by the column height above the socket. Figure 5-39 and Figure 5-40 present the column rotation for pushing and pulling cycles, respectively.

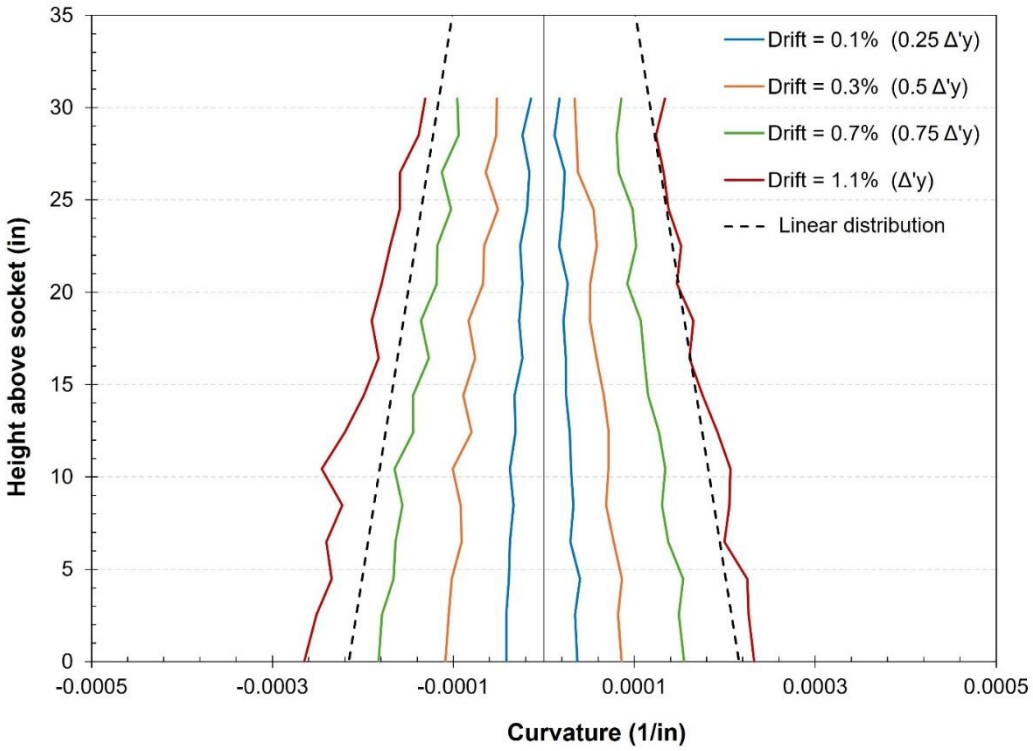


Figure 5-37. Curvature profile of the column up to the first yield cycle for SJS1

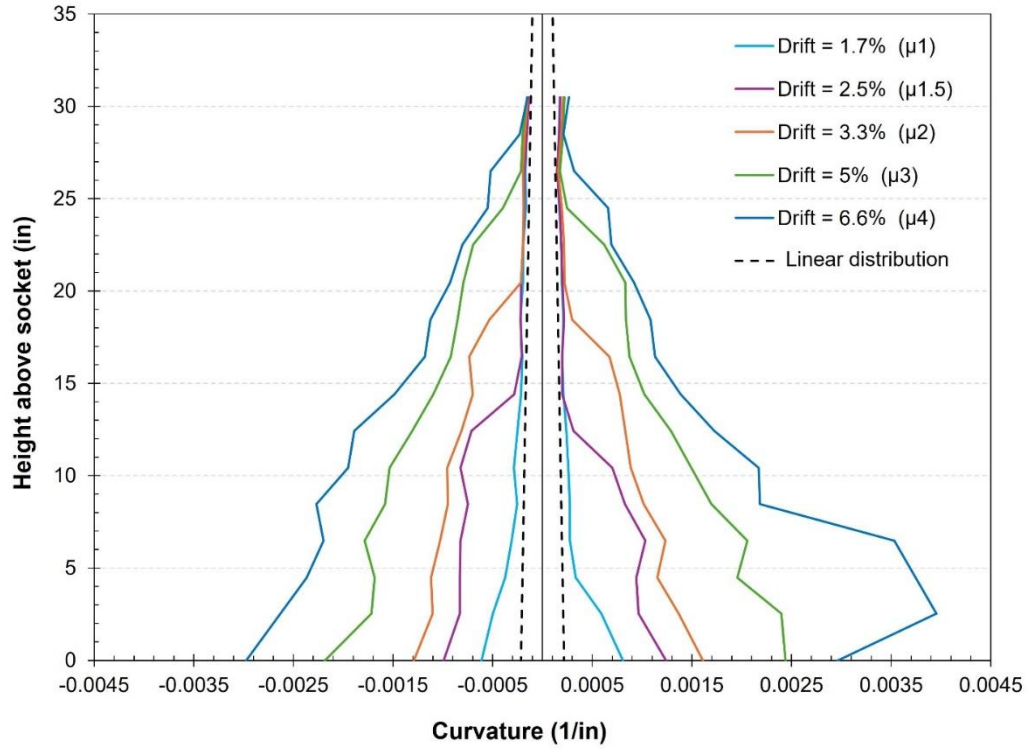


Figure 5-38. Curvature profile of the column for post-yield cycles for SJS1

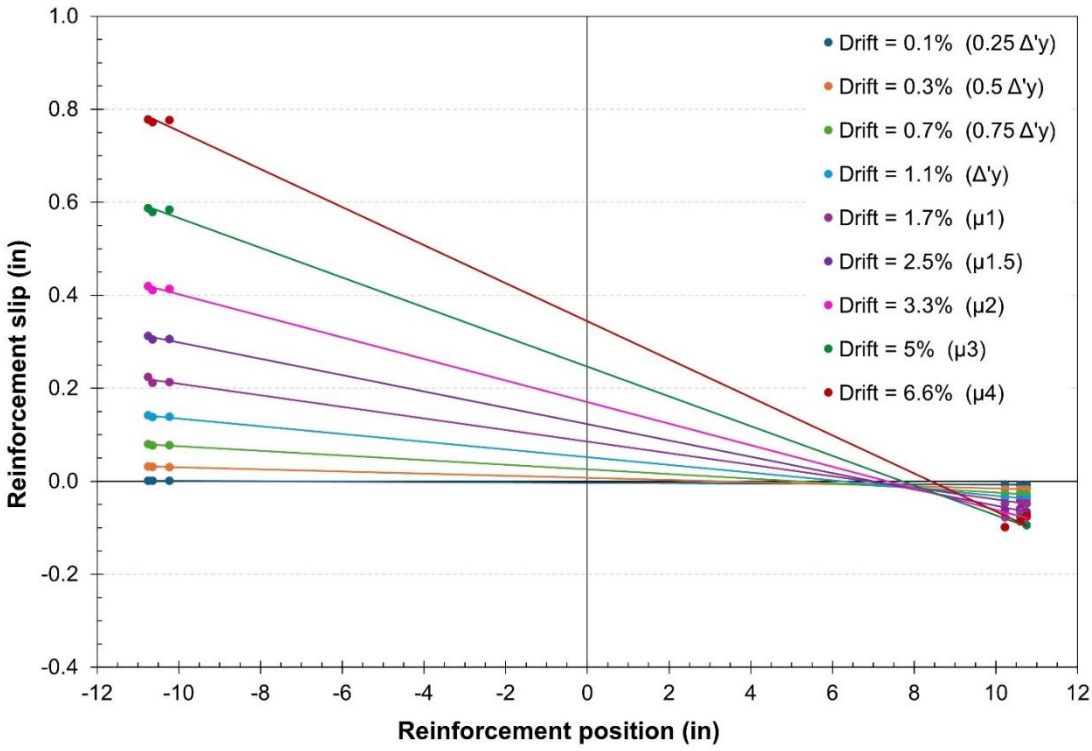


Figure 5-39. Rotation of the column for pushing cycles at the socket interface of SJS1

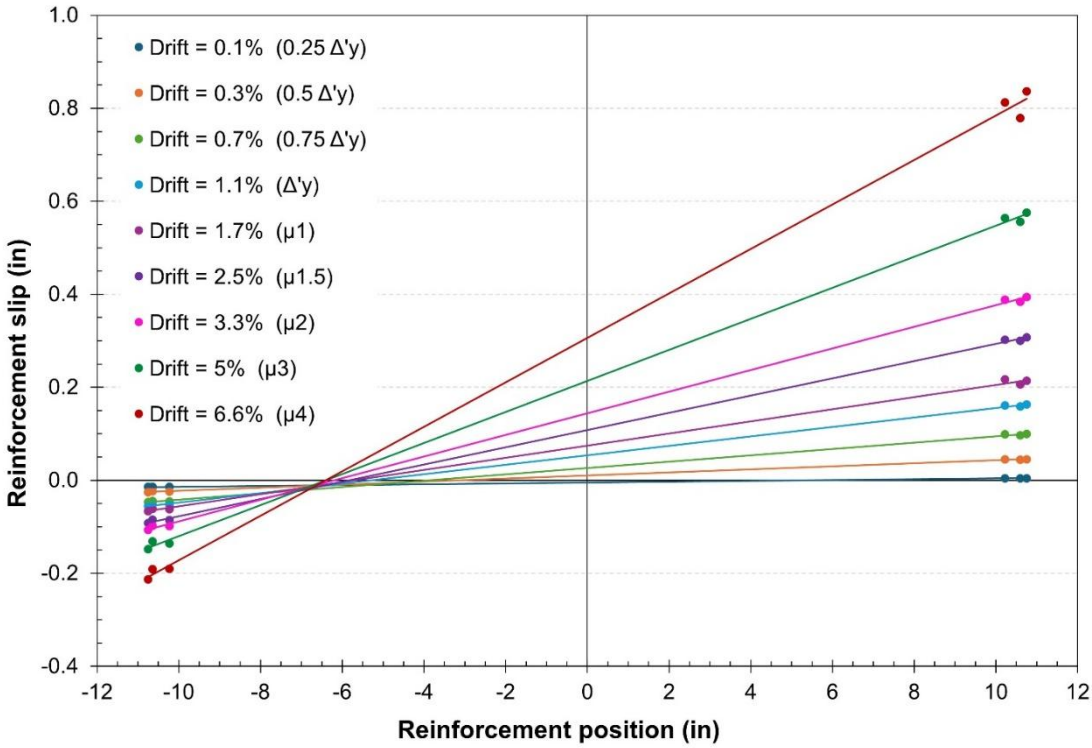


Figure 5-40. Rotation of the column for pulling cycles at the socket interface of SJS1

Figure 5-41 and Figure 5-42 present the shear strain distribution along the column height for the last three ductility displacements, as well as the yield displacement. These shear strains were then used to calculate the column shear displacement by multiplying the shear strain by the interval height. At 20 inches above the socket, the shear strains became constant, remaining approximately the same for all ductility displacements after yielding.

The displacement component resulting from socket rotation was obtained using DIC. Figure 5-43 and Figure 5-44 illustrate the socket rotation throughout the experimental test for the north and south faces, respectively. Socket rotation was measured at five different locations along the height, and an average value was used for displacement calculations due to the uniform distribution observed along the socket height. The averaged socket rotation, when multiplied by the socket height, provided the displacement component attributed to socket rotation.

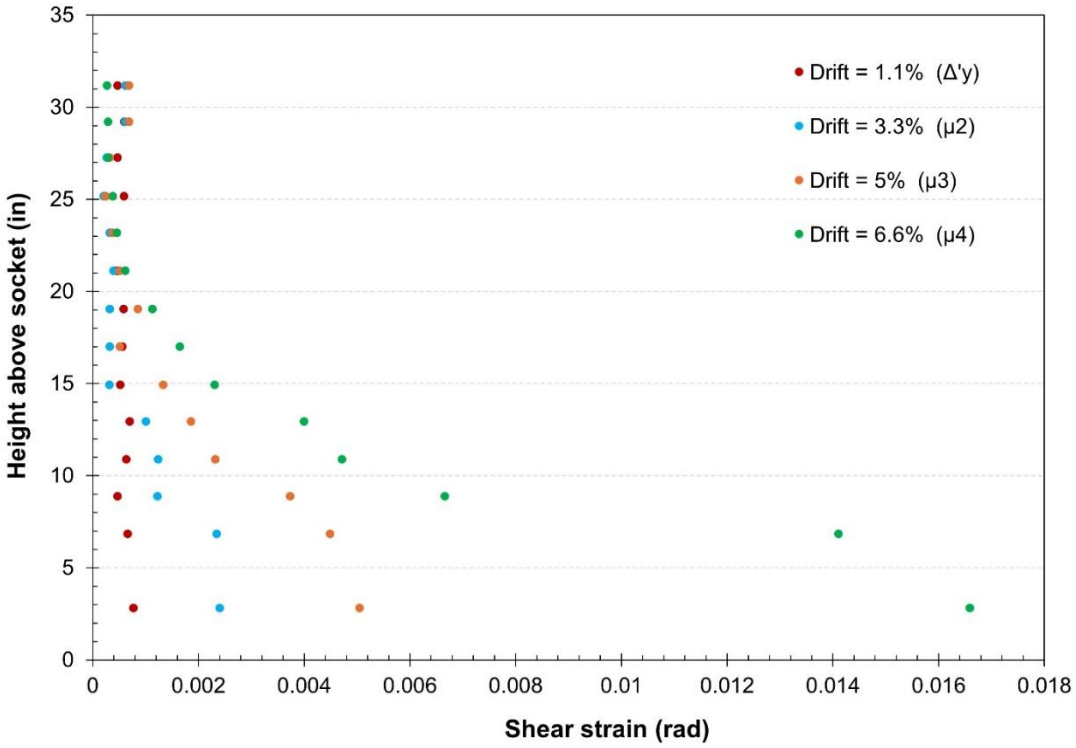


Figure 5-41. Shear strain distribution of the column for pushing cycles for SJS1

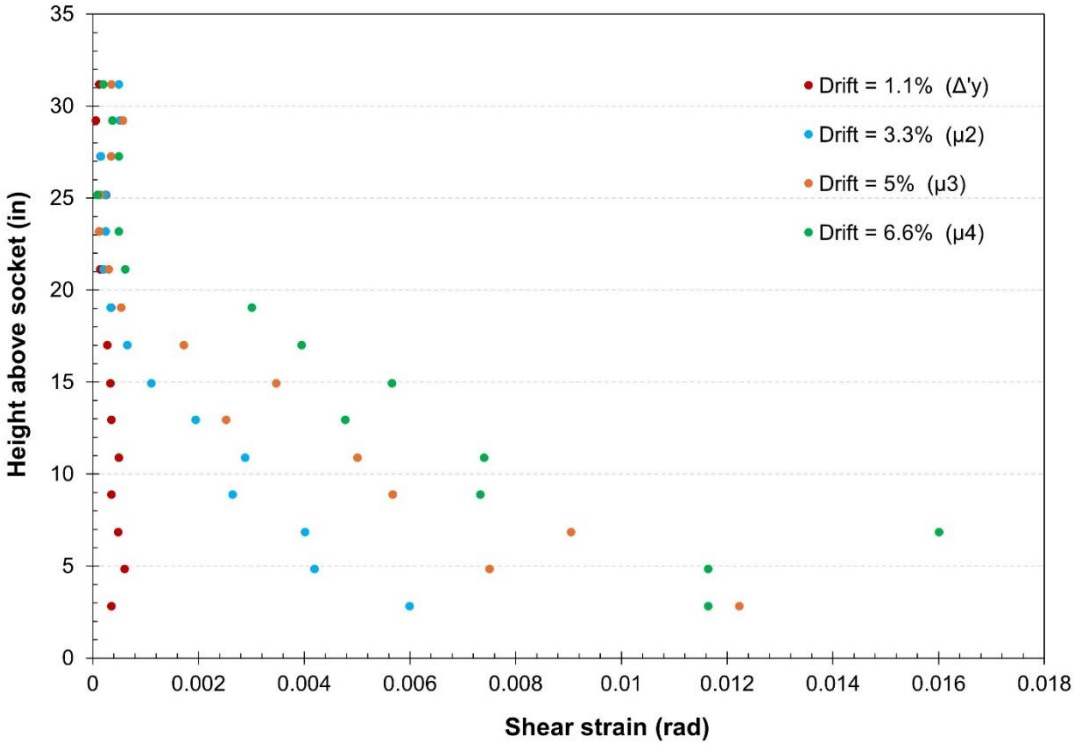


Figure 5-42. Shear strain distribution of the column for pulling cycles for SJS1

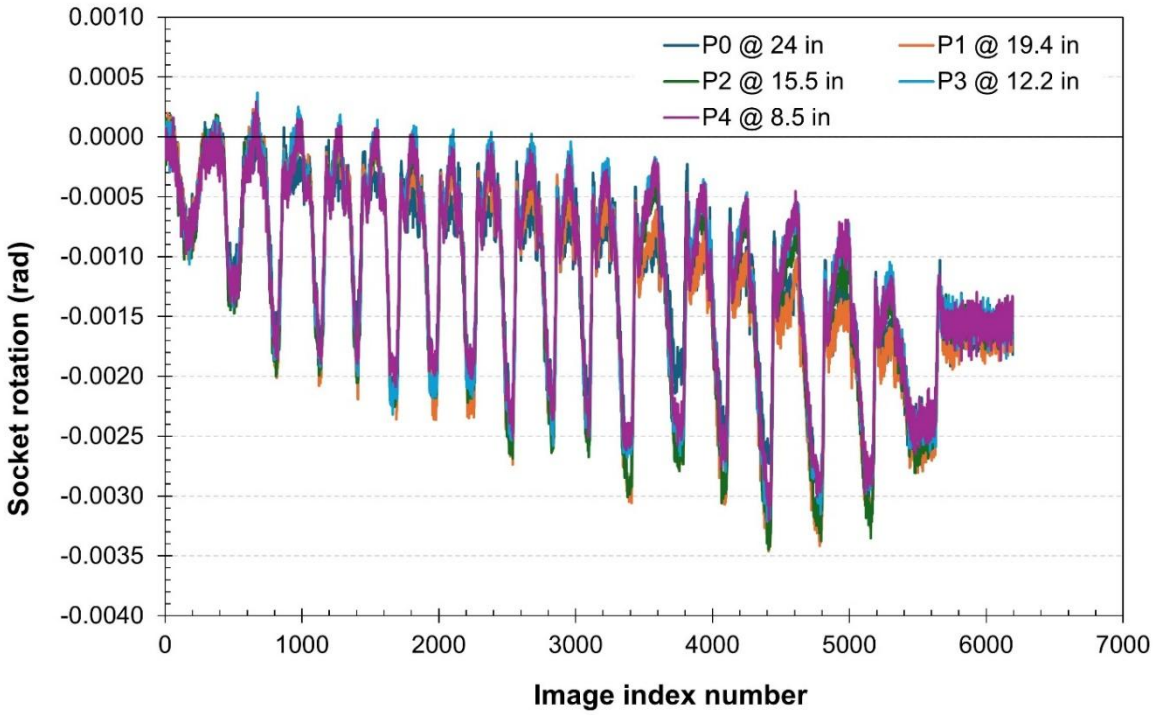


Figure 5-43. Socket rotation at the north side of SJS1

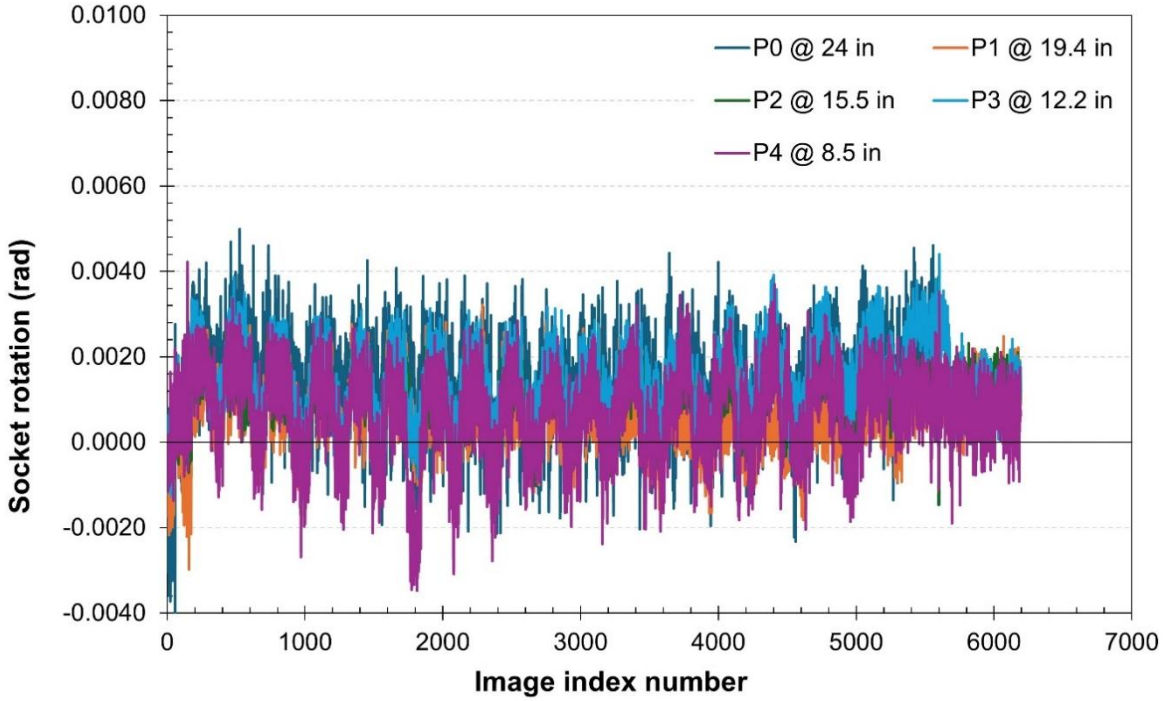


Figure 5-44. Socket rotation at the south side of SJS1

Table 5-1 and Table 5-2 present the contributions of the different components to the total displacement. Additionally, Figure 5-45 and Figure 5-46 illustrate the component displacements for pushing and pulling cycles following the first yield. The calculated displacement components closely match the measured values, validating the accuracy of the calculation methodology. The difference between the measured and calculated displacements is less than 5% for most ductility displacements.

Table 5-1. Displacement components for pushing cycles for SJS 1

Displacement component (in)	**Δ'y**	**μ1**	**μ1.5**	**μ2**	**μ3**	**μ4**
Measured displacement	1.01	1.49	2.26	2.98	4.46	5.96
Flexural	0.33	0.51	0.88	1.25	2.05	3.05
Strain penetration and rocking	0.55	0.82	1.16	1.53	2.11	2.70
Shear	0.03	0.04	0.05	0.05	0.08	0.16
Socket rotation	0.03	0.04	0.05	0.06	0.06	0.07
Calculated displacement error	0.07	0.08	0.11	0.09	0.15	-0.02
Calculated displacement error (%)	7.1%	5.3%	5.1%	3.2%	3.3%	-0.4%

Table 5-2. Displacement components for pulling cycles for SJS 1

Displacement component (in)	Δ'y	μ1	μ1.5	μ2	μ3	μ4
Measured displacement	1.14	1.49	2.29	2.98	4.48	6.10
Flexural	0.37	0.48	0.85	1.16	1.87	2.54
Strain penetration and rocking	0.67	0.86	1.22	1.53	2.20	3.16
Shear	0.01	0.03	0.08	0.07	0.12	0.16
Socket rotation	0.07	0.08	0.08	0.08	0.09	0.11
Calculated displacement error	0.02	0.03	0.06	0.14	0.18	0.13
Calculated displacement error (%)	1.9%	2.3%	2.6%	4.8%	4.1%	2.1%

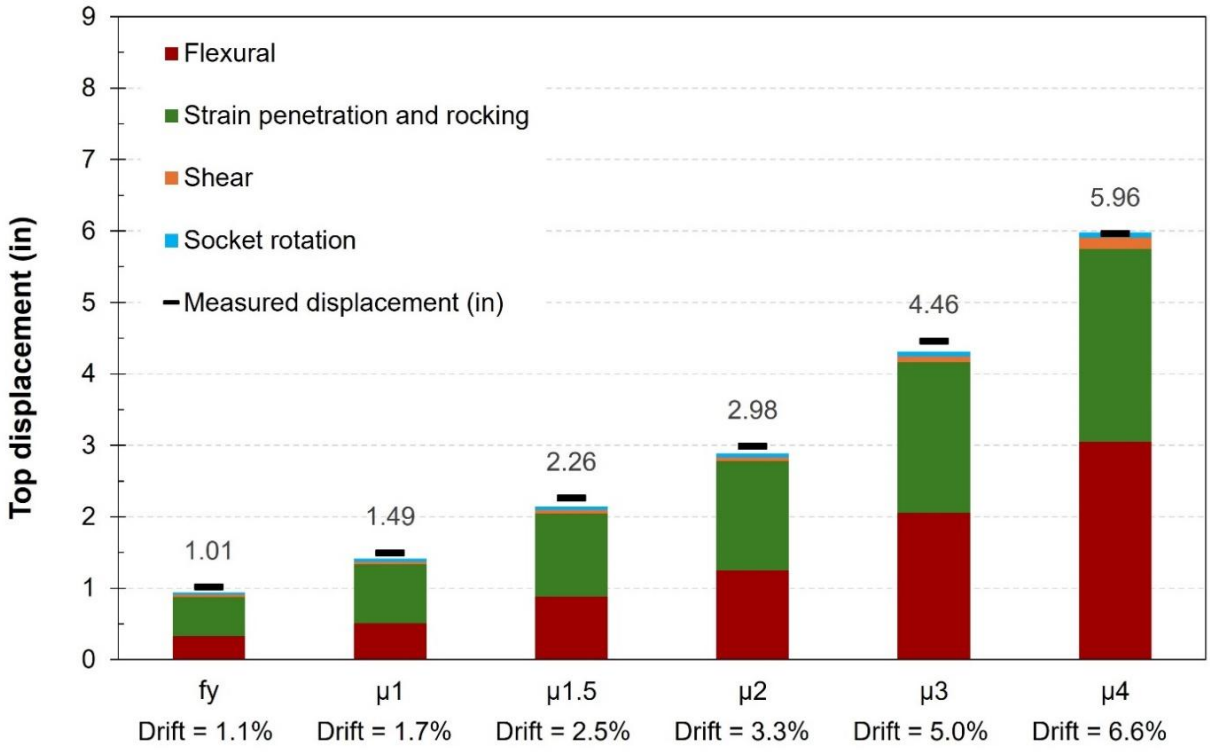


Figure 5-45. Displacement components for pushing cycles for SJS1

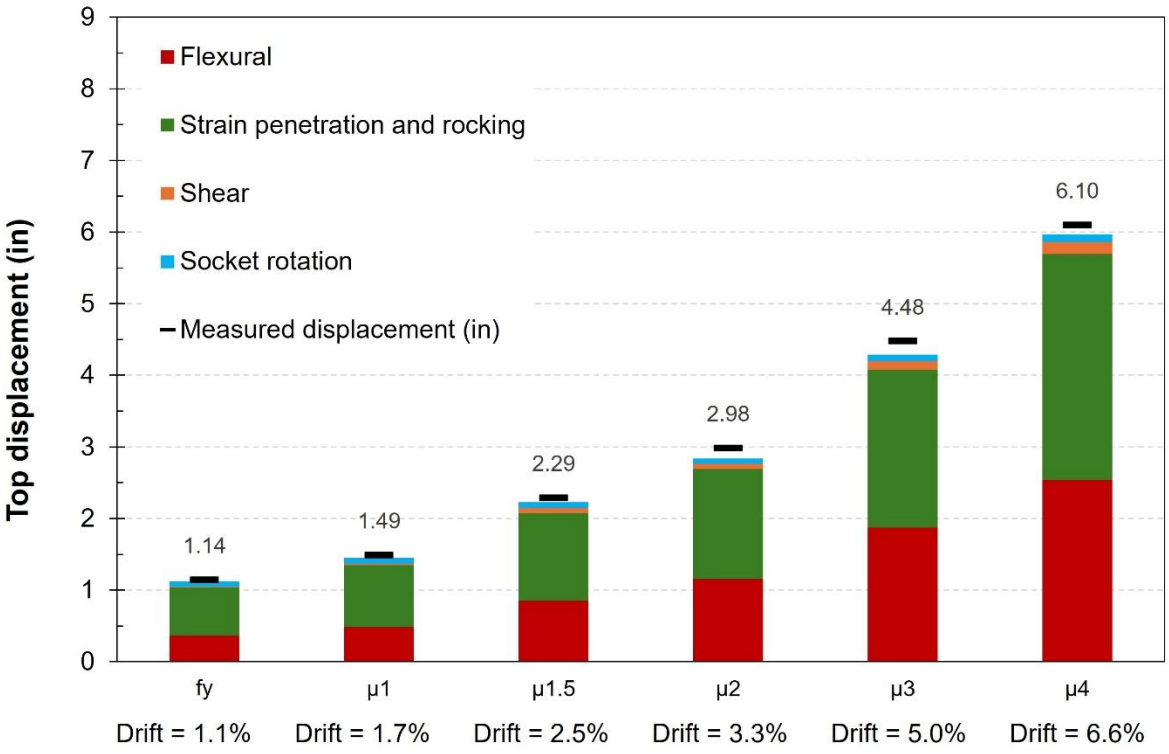


Figure 5-46. Displacement components for pulling cycles for SJS1

Comparing the displacement components, it was observed that the shear and socket rotation had a relatively small impact on the total displacement of the column. In contrast, the flexural deformation, strain penetration, and rocking of the column contributed significantly more, each having a comparable influence on the overall displacement. These findings highlight that while shear and socket rotation are present, the primary drivers of total column displacement are the flexural and rotational effects for a socket height of 1.0 Dc that developed the plastic hinge above the external socket connection.

5.2.4. Summary of Results for SJS-1

The tension strains in the longitudinal bars reached 4.5% before bar buckling occurred, followed by fracture in the subsequent cycle. This indicates that the plastic hinge was fully developed above the external socket interface. The strains in the external socket wall remained below the yield point throughout the test, confirming that the external socket connections effectively prevented plastic strains from reaching the foundation or cap beam. As a result, the

footing remained as a capacity-protected element. Horizontal strains in the external socket sleeve reached twice the yield strain at the top third of the socket height but remained elastic for the rest of the height. No visible damage was observed on the sleeves during the test, confirming that the sleeves did not experience significant inelastic deformation.

The elastic damping for SJS 1 was approximately 10%, which is higher than the 5% typically observed in CIP columns. This additional 5% damping may be attributed to the initial cracks in the socket wall and grout that occurred early in the test, as well as some unidentified noises observed during the cycles before the yield displacement.

The overall displacement behavior of SJS 1 was governed primarily by flexural deformation, strain penetration, and rocking. Flexural displacements accounted for approximately 40% of the total displacement, while strain penetration and rocking contributed around 50%. In comparison, CIP columns typically exhibit 65% flexural displacement and 30% strain penetration. This indicates that strain penetration and rocking have a more significant contribution to the total displacement of the column while having a socket connection than in CIP columns.

5.3. Experimental Results for Specimen SJS-2

In this section, the data analysis and experimental results previously discussed in this chapter will be specifically applied to the experimental test SJS2. The results for SJS2 will be presented in detail, focusing on axial strains on the column and external socket, hysteretic damping, and calculated displacement components. This analysis provides insights into the column performance and behavior under the applied loading conditions, contributing to a comprehensive understanding of the system response.

5.3.1. Axial strain analysis for SJS-2

The strain profiles were calculated to assess the strain distribution along the RC column during the first cycles of each ductility displacement for SJS2, considering both loading directions.

In this context, ″Pushing Cycles″ refers to the strain profiles when force is applied toward the north face of the column, while ″Pulling Cycles″ refers to when force is applied toward the south face.

Figure 5-47 and Figure 5-48 present the strain profiles of the extreme bar located on the north face of the specimen for cycles up to yielding and post-yield cycles, respectively. Similarly, Figure 5-49 and Figure 5-50 depict the strain profiles for the extreme bar on the south side of the specimen for cycles up to yielding and post-yield cycles. The maximum axial strain in both tension and compression before grout crushing occurred was approximately 0.23% on both sides of the specimen, which is the yield strain. These strain profiles indicate that the column remained elastic throughout the experimental test.

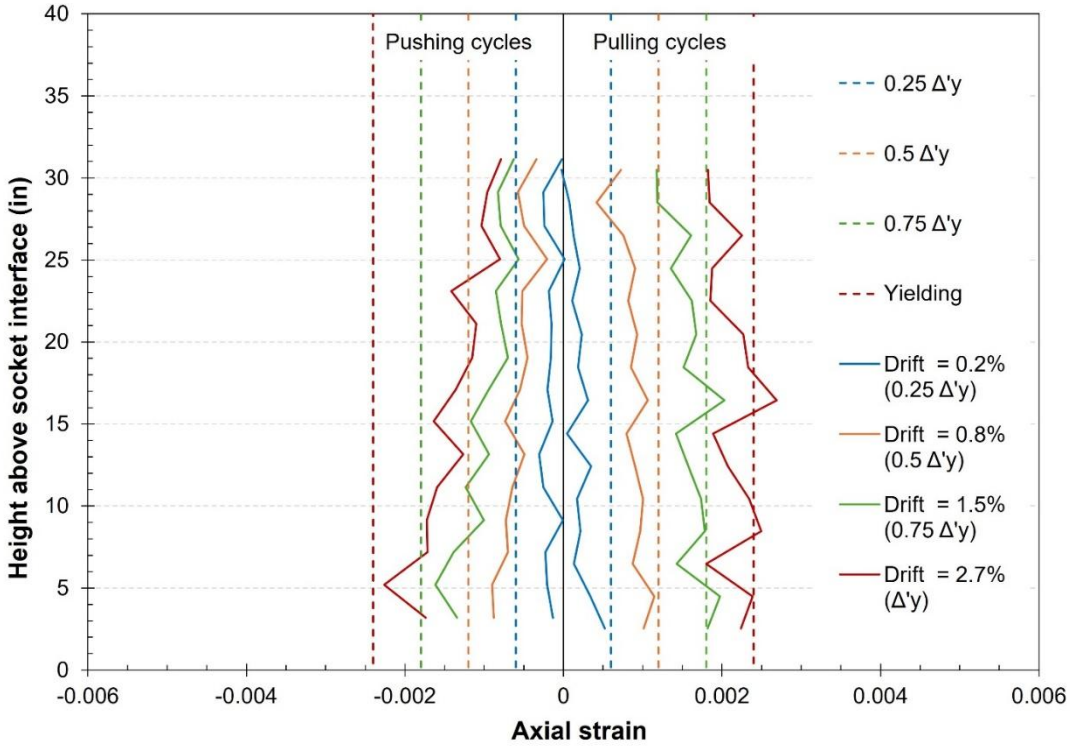


Figure 5-47. Strain profile up to first yield cycle for SJS2 on the north side of the column

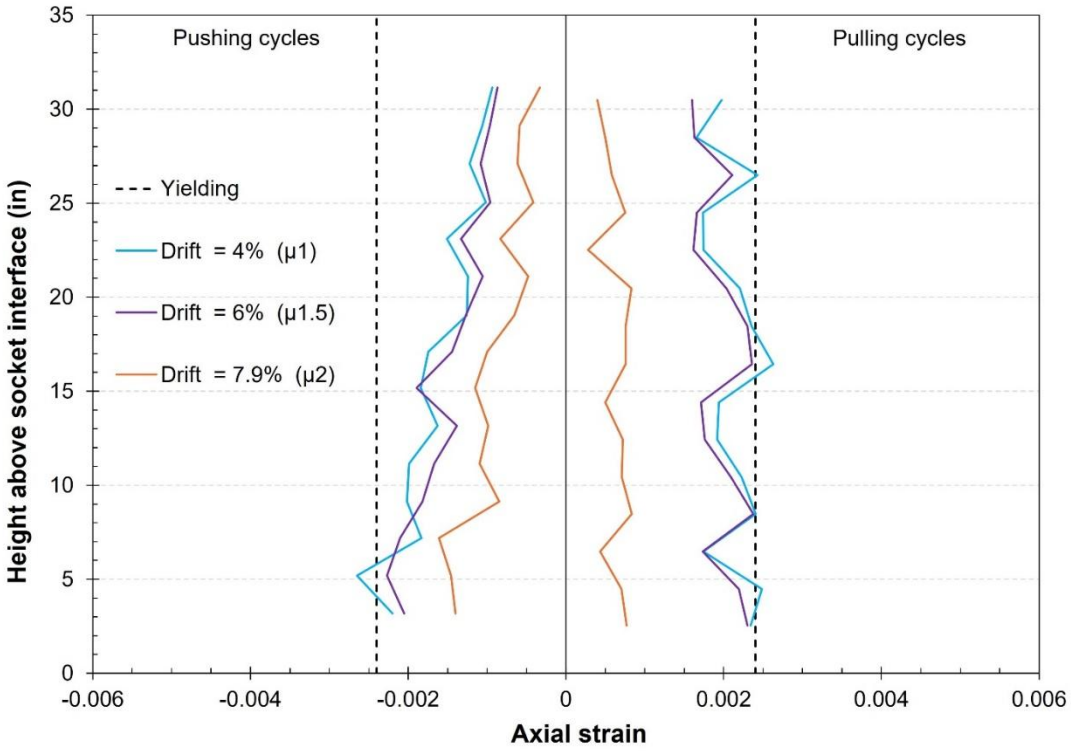


Figure 5-48. Strain profile for post-yield cycles for SJS2 on the north side of the column

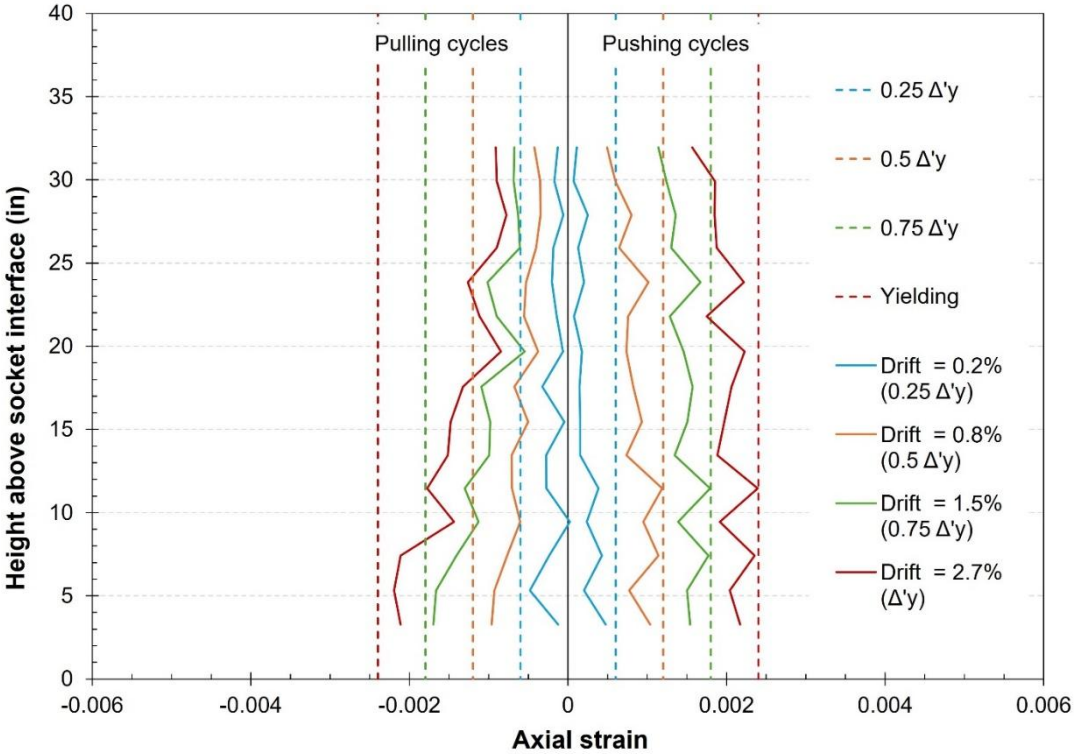


Figure 5-49. Strain profile up to first yield cycle for SJS2 on the south side of the column

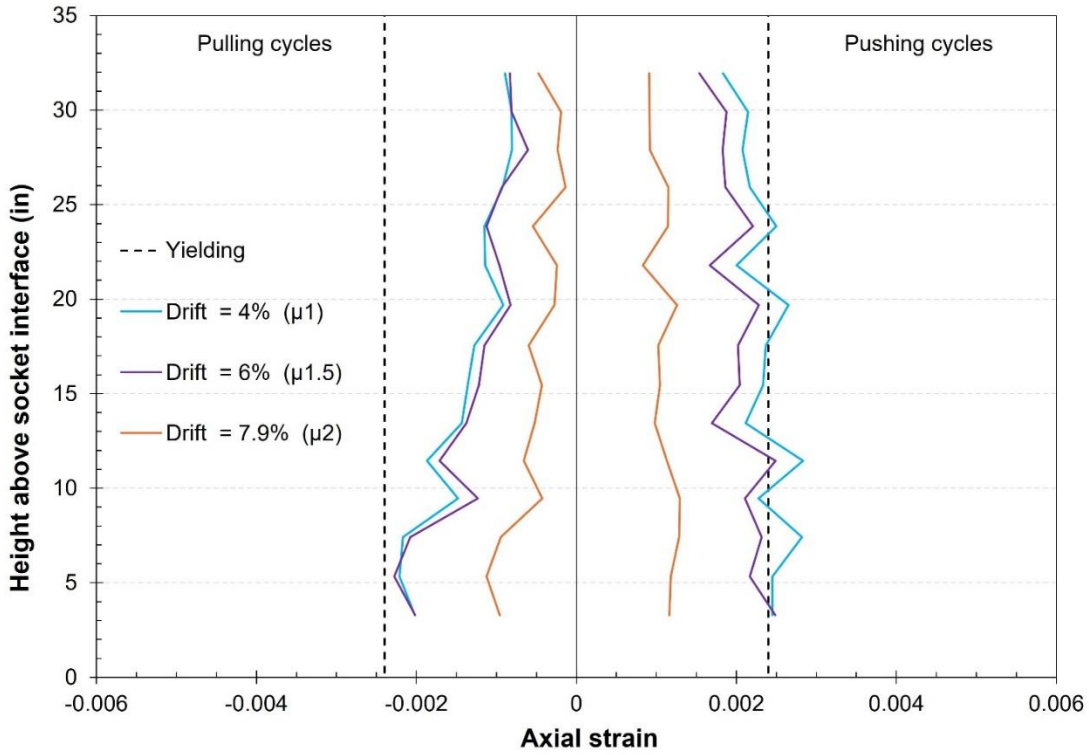


Figure 5-50. Strain profile for post-yield cycles for SJS2 on the south side of the column

A detailed examination of the strains on the reinforcing bars can be achieved by plotting the strain throughout the displacement history for each gauge length. Figure 5-51 and Figure 5-52 present the strain history of the extreme bars located on the north and south faces of the specimen at the first gauge length above the external socket. For both extreme bars, it was observed that the maximum strain reached during the experimental test was the yield strain. Following grout crushing, the column began to exhibit rocking behavior.

Additionally, the strain history of the extreme bars in the external socket wall reinforcement was monitored using strain gauges placed 2 inches above the footing. Figure 5-53 and Figure 5-54 present the strain history for the extreme bars on the north and south faces, respectively. The data shows that the reinforcement in the external socket wall barely reached the yield point, indicating that the external socket wall remained elastic throughout the entire experimental test.

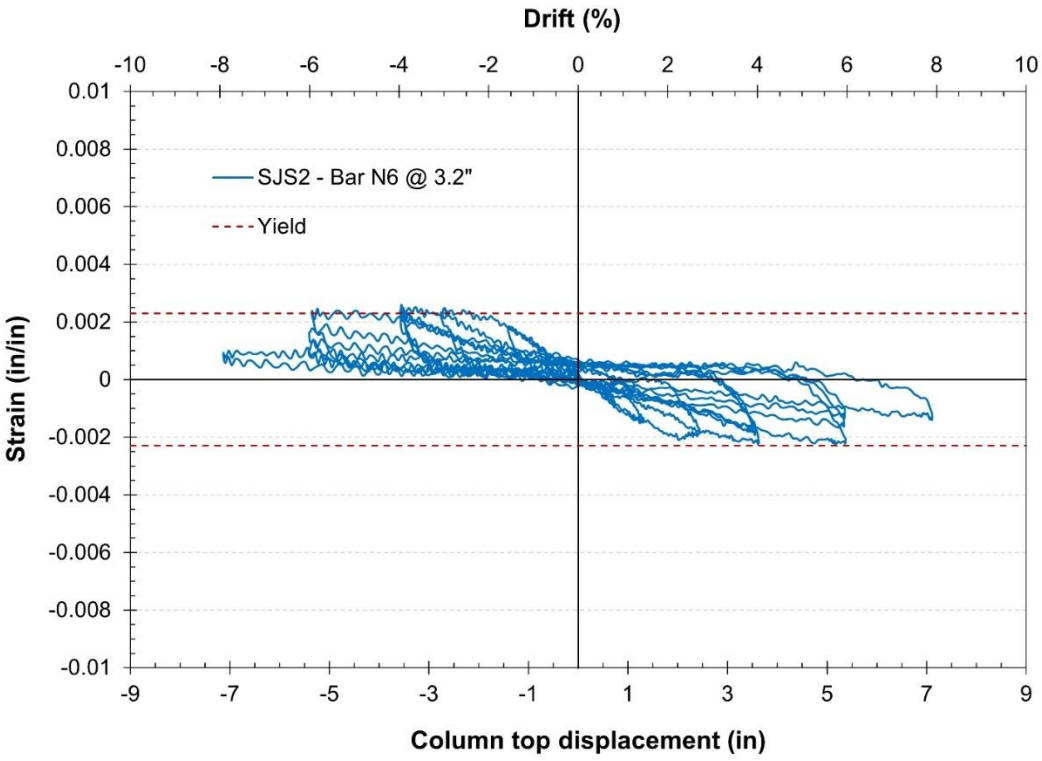


Figure 5-51. Strain vs displacement history for N6 of SJS2

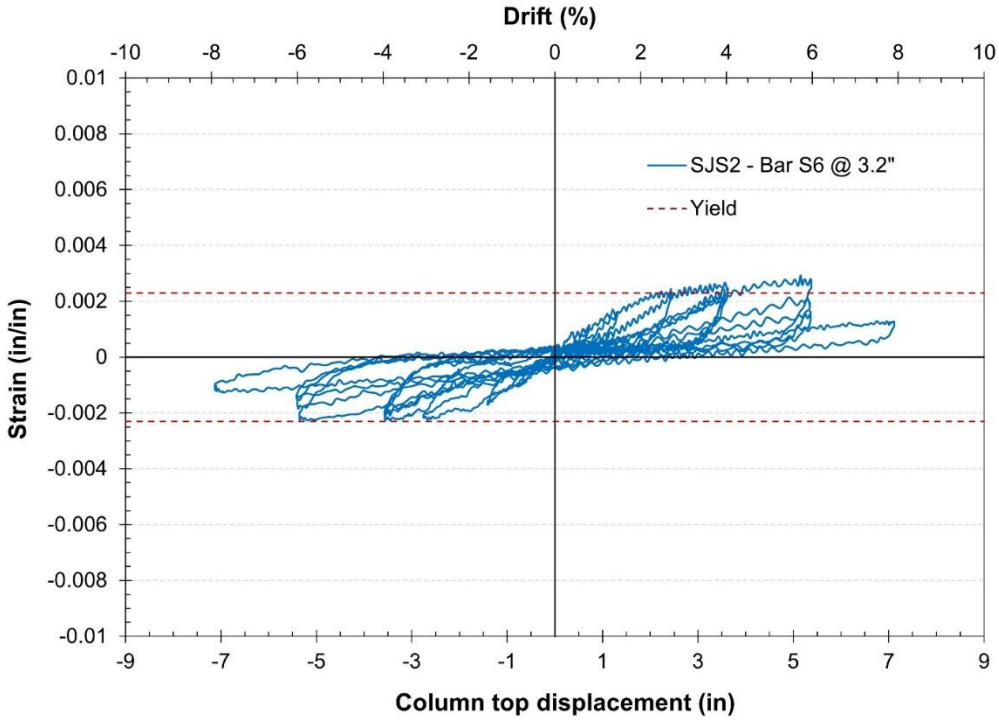


Figure 5-52. Strain vs displacement history for S6 of SJS2

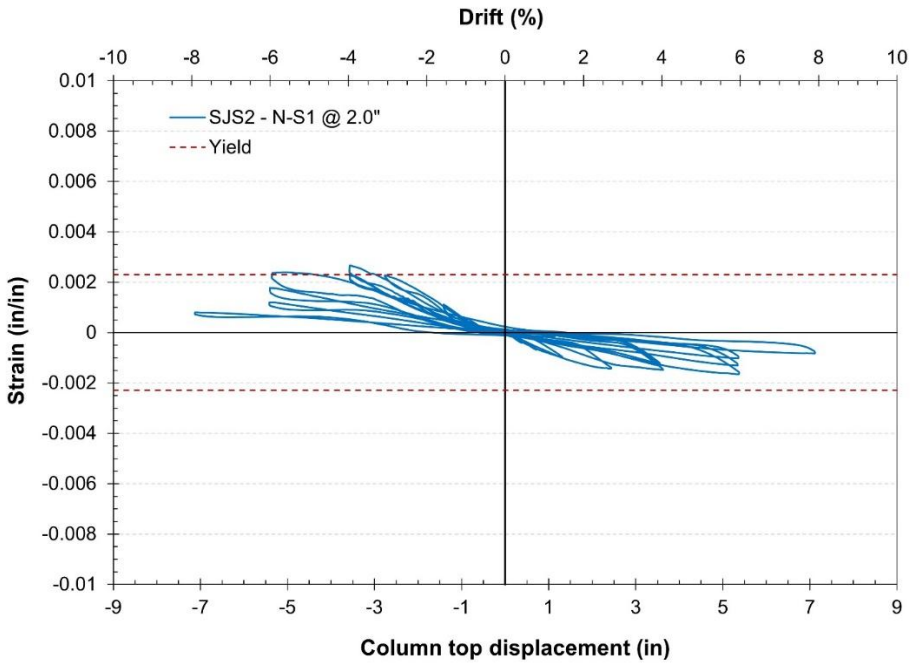


Figure 5-53. Strain vs displacement history for the extreme bar of socket wall reinforcement at the north side of SJS2

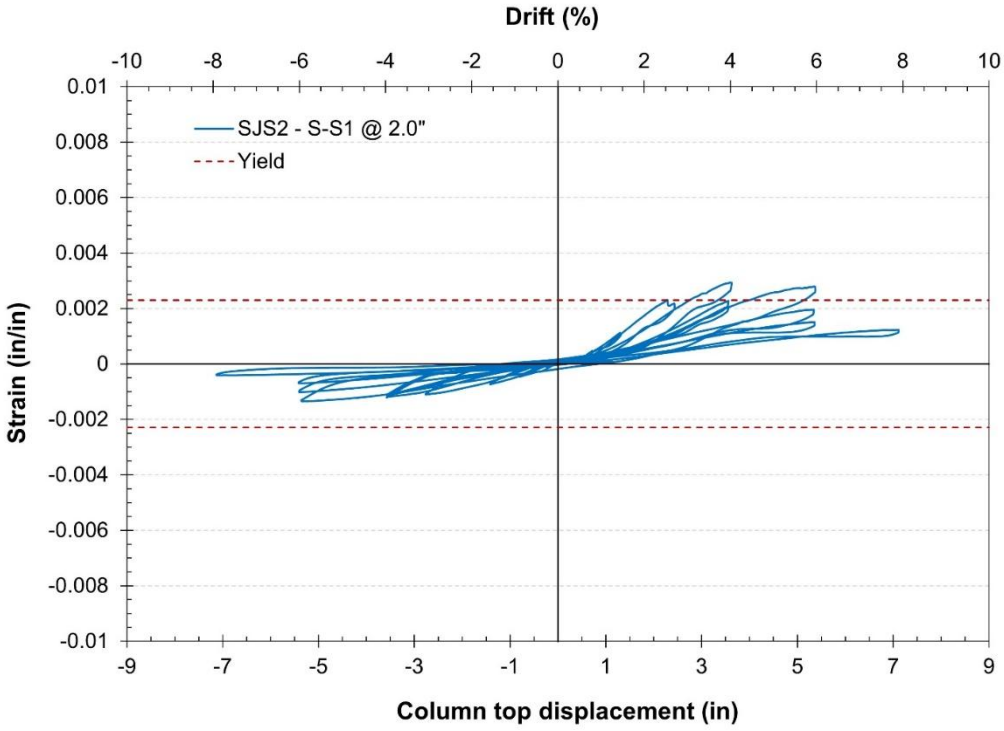


Figure 5-54. Strain vs displacement history for the extreme bar of socket wall reinforcement at the north side of SJS2

The axial strains on the external socket sleeve were measured using DIC. In this context, the horizontal strains correspond to the hoop forces acting around the circumference, while the vertical strains reflect any flexion sustained by the sleeves. Figure 5-55 and Figure 5-56 present the strains on the north face of the specimen while Figure 5-57 and Figure 5-58 show the strains on the south face. The data indicates that, for the horizontal strains, the top 4 inches of the socket experienced strain values of 1.2%, while the remainder of the socket height remained elastic. The vertical strains reached yielding at the top 2 inches of the socket, with the rest of the socket height staying elastic throughout the experimental test. These results suggest that the acting forces were concentrated in the top 4 inches of the steel sleeve.

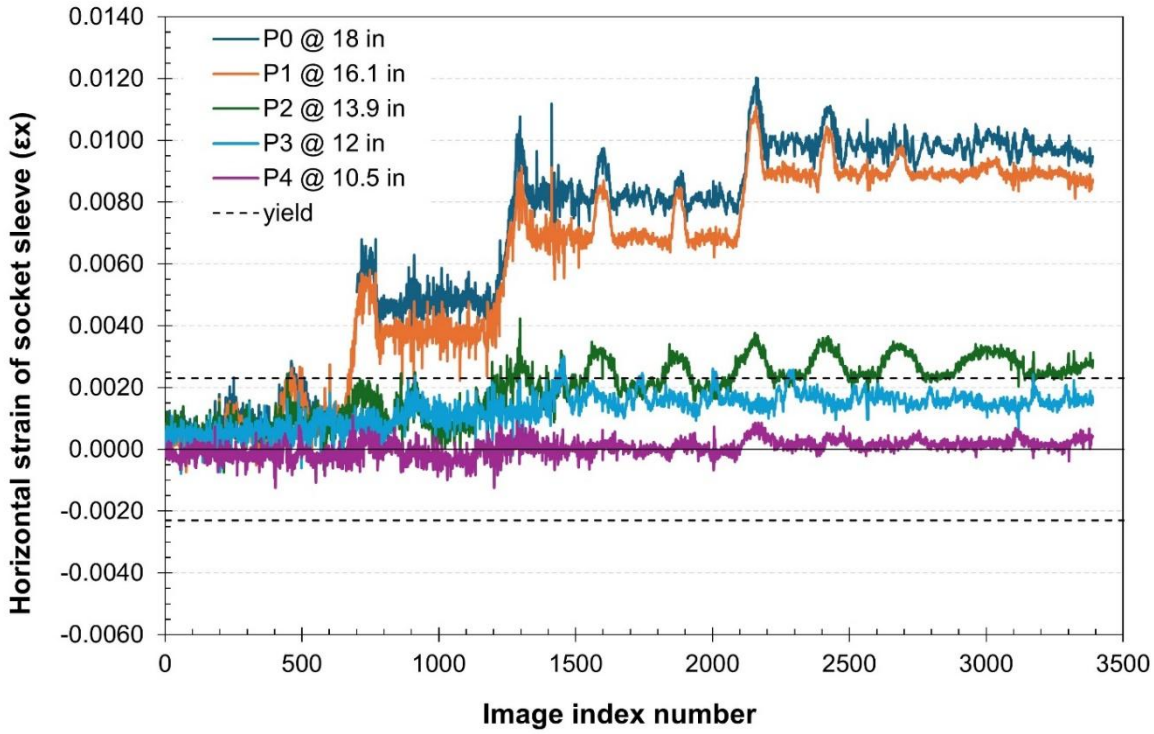


Figure 5-55. Horizontal strain history of external socket sleeve at the north side of SJS2

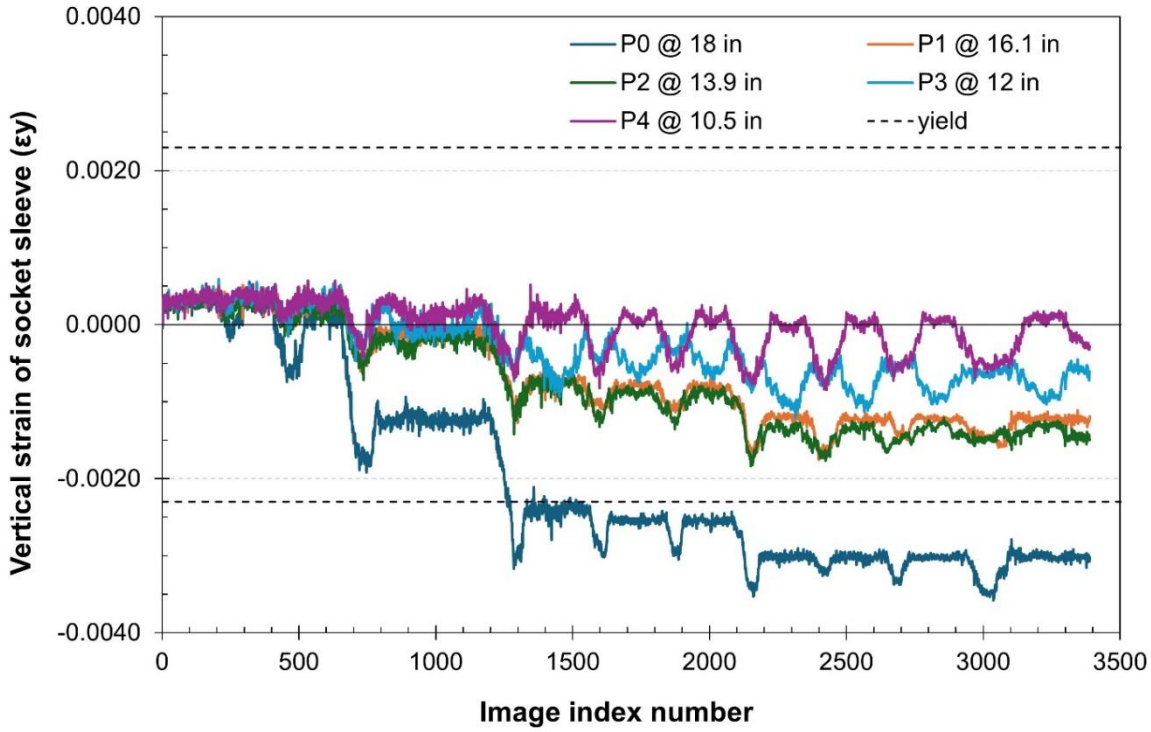


Figure 5-56. Vertical strain history of external socket sleeve at the north side of SJS2

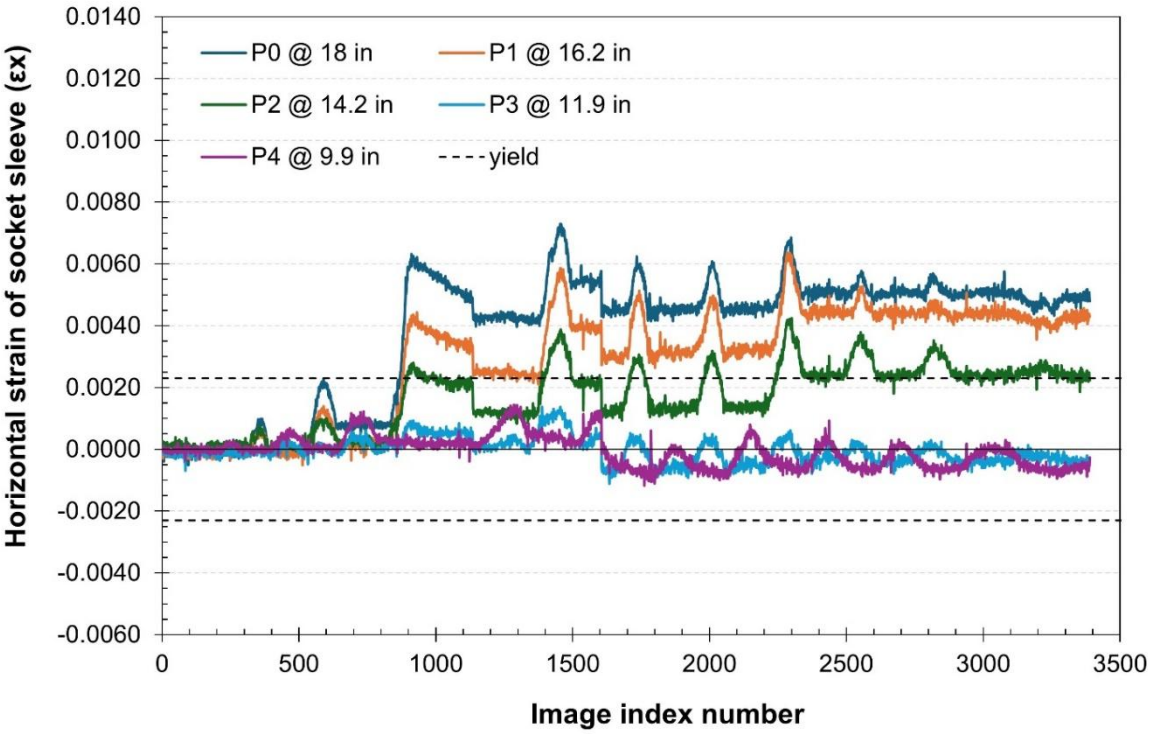


Figure 5-57. Horizontal strain history of external socket sleeve at the south side of SJS2

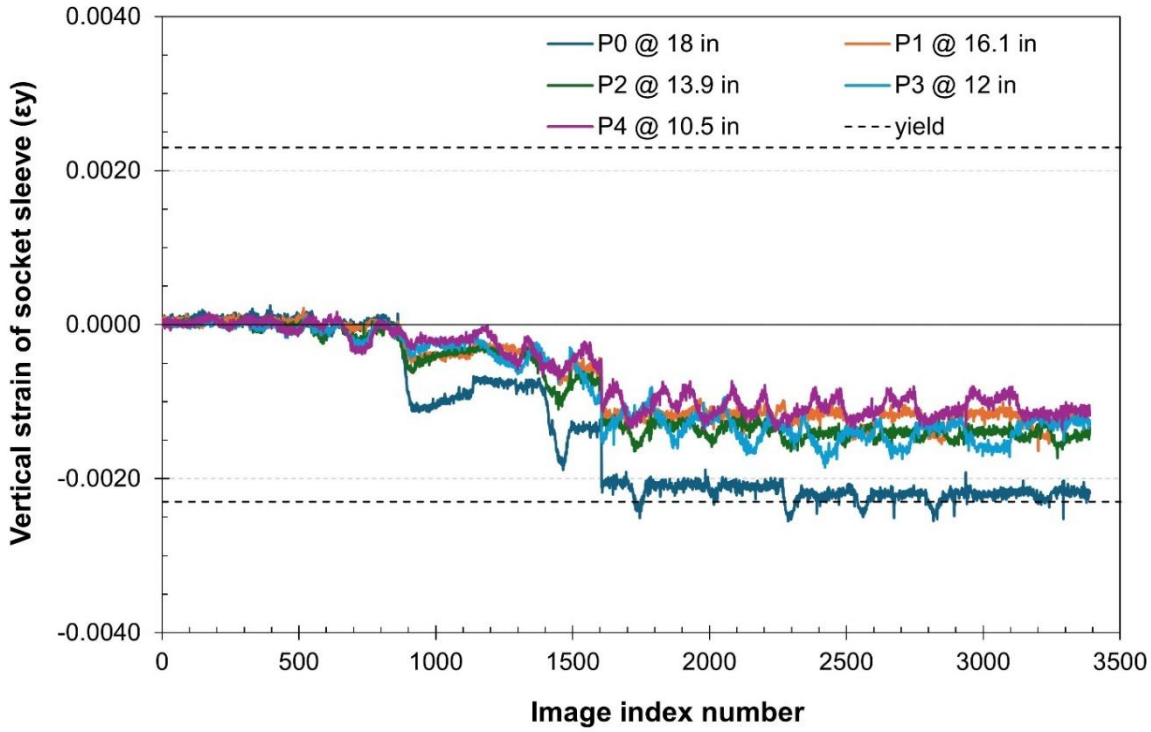


Figure 5-58. Vertical strain history of external socket sleeve at the south side of SJS2

5.3.2. Energy dissipation and hysteretic damping for SJS-2

Energy dissipation is important in understanding a structure seismic behavior because it relates to the structural element damage and energy dissipation capacity. Figure 5-59 illustrates the energy dissipation for all ductility displacement cycles for SJS2, with a total energy dissipation of 2118 kip-in. Notably, during the second cycle of ductility one and a half, where the grout was crushed, the energy dissipated was reduced by 35% compared to the first cycle at the same ductility level. This reduction highlights the impact of severe damage on the energy dissipation capacity of the column.

Additionally, Figure 5-60 presents the Jacobsen hysteretic damping values for SJS2, demonstrating that damping increases as the applied displacements grow and the column sustains more damage. Notably, the elastic damping for SJS2 was approximately 12%, which is 7% higher than what is typically observed in a CIP column, indicating enhanced energy dissipation during the structural element elastic behavior.

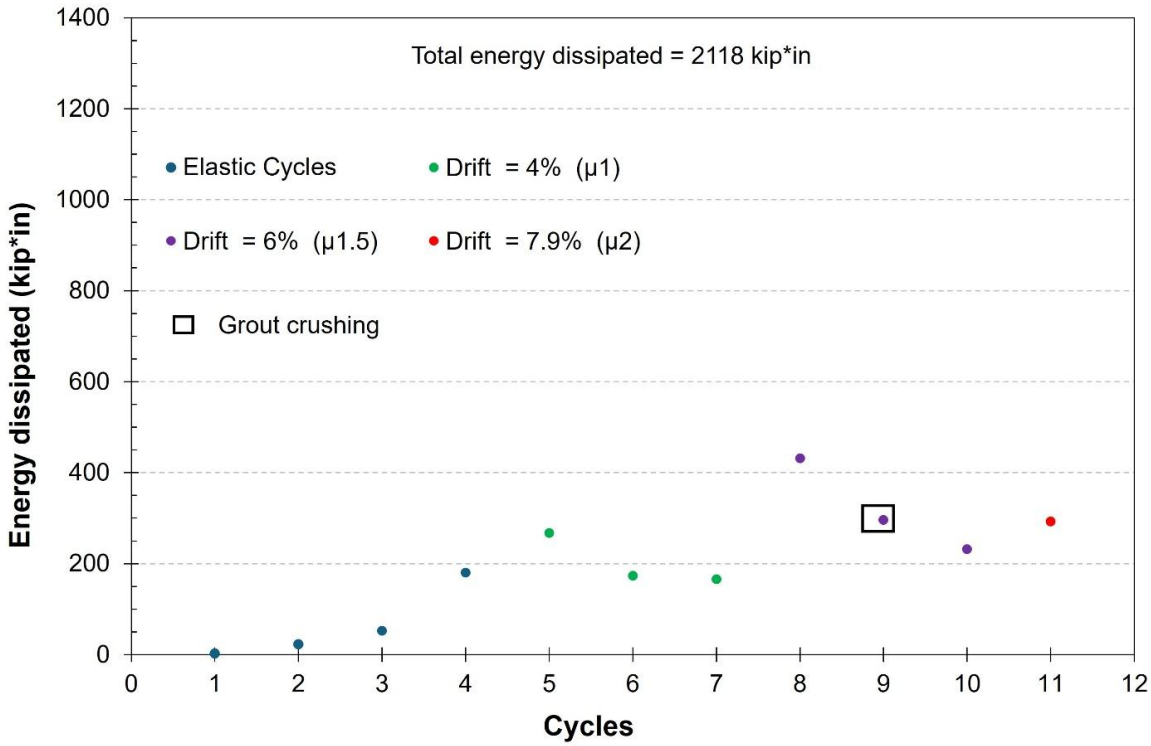


Figure 5-59. Energy dissipation plot for SJS2

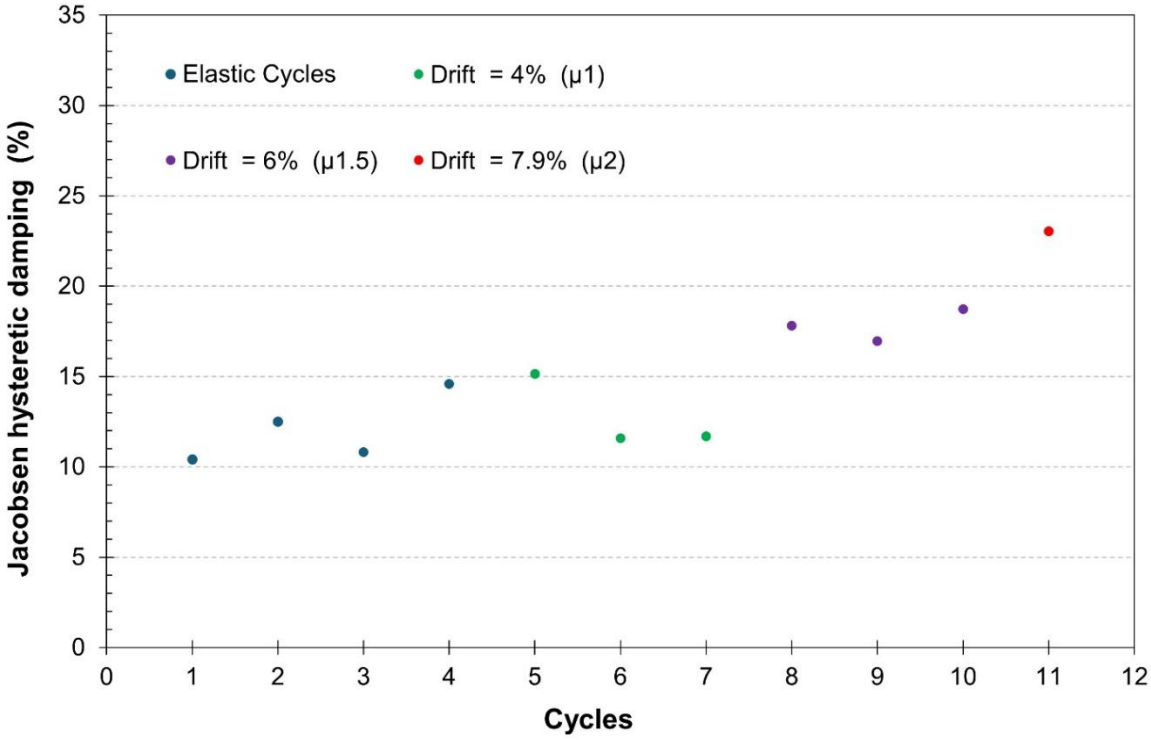


Figure 5-60. Hysteretic damping plot for SJS2

5.3.3. Displacement components for SJS-2

The displacement components considered in the calculations include flexural deformation, column rotation due to strain penetration and rocking, shear deformation of the column, and the deformation contribution resulting from socket rotation. The methodologies for these calculations have been detailed earlier in Section 5.1.3 of this report.

The flexural displacement component was derived from the column curvature, with the curvature profile shown in Figure 5-61 for the cycles up to yield and in Figure 5-62 for the post-yield cycles. The curvature is defined as positive when the column is pushed toward its north face. The dashed line in these figures represents the linear distribution of curvature, beginning at zero at the top of the column and reaching the yield curvature at the socket interface.

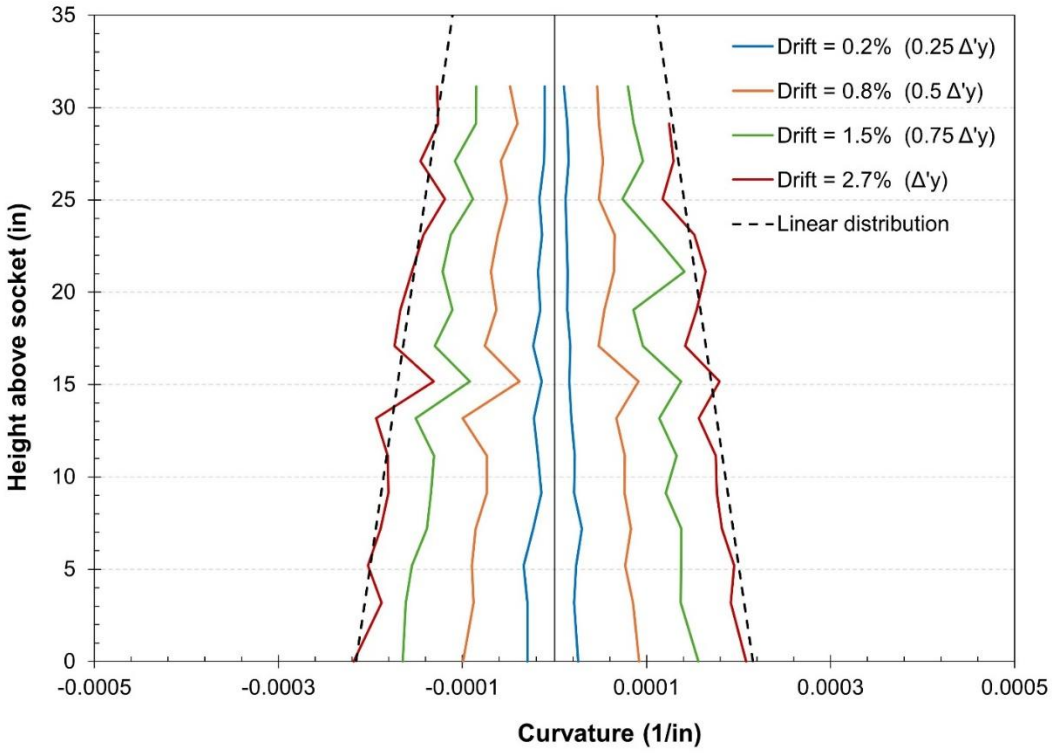


Figure 5-61. Curvature profile of the column up to the first yield cycle for SJS2

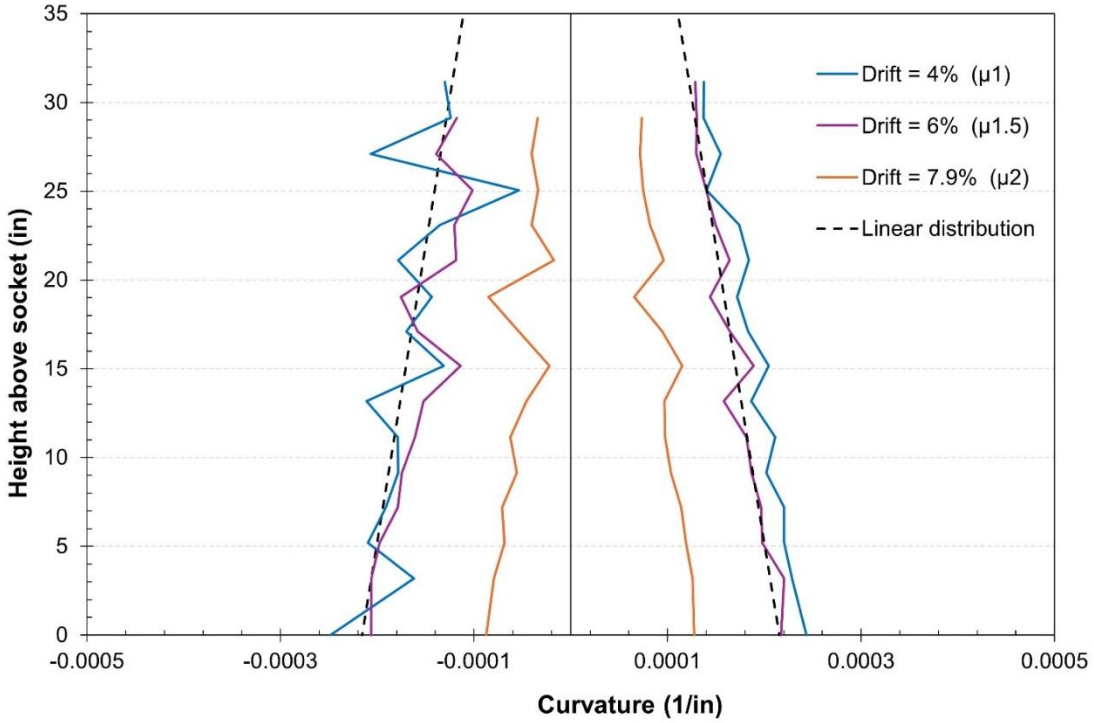


Figure 5-62. Curvature profile of the column for post-yield cycles for SJS2

The displacement due to column rotation was calculated by determining the rotation angle at the base of the column and multiplying it by the column height above the socket. Figure 5-63 and Figure 5-64 present the column rotation for pushing and pulling cycles, respectively.

Figure 5-65 and Figure 5-66 present the shear strain distribution along the column height for the last three ductility displacements, as well as the yield displacement. These shear strains were then used to calculate the column shear displacement by multiplying the shear strain by the interval height. The shear strains remained approximately constant for all ductility displacements after yielding.

The displacement component resulting from socket rotation was obtained using DIC. Figure 5-67 and Figure 5-68 illustrate the socket rotation throughout the experimental test for the north and south faces, respectively. Socket rotation was measured at five different locations along the height, and an average value was used for displacement calculations due to the uniform distribution observed along the socket height. The averaged socket rotation, when multiplied by the socket height, provided the displacement component attributed to socket rotation.

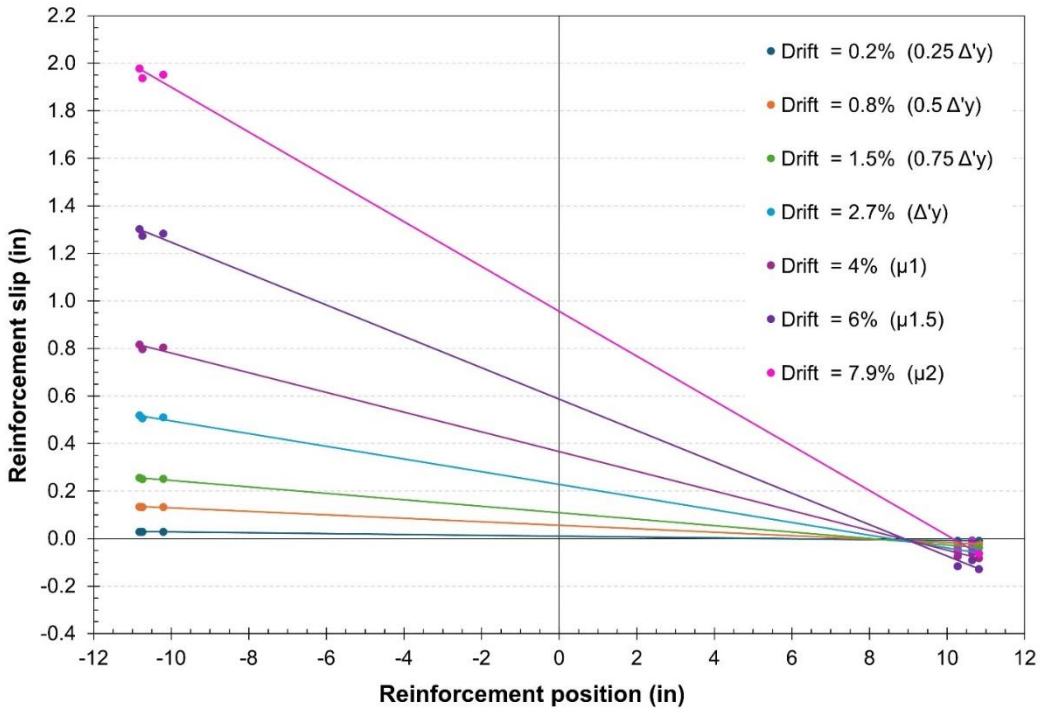


Figure 5-63. Rotation of the column for pushing cycles at the socket interface of SJS2

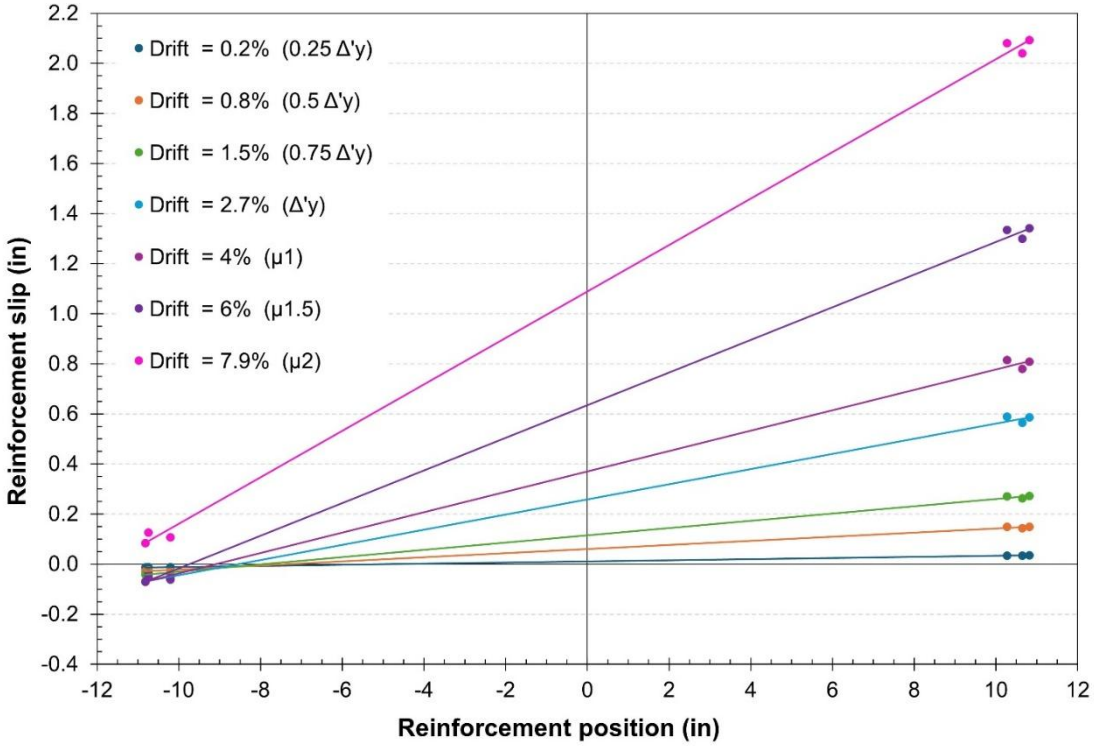


Figure 5-64. Rotation of the column for pulling cycles at the socket interface of SJS2

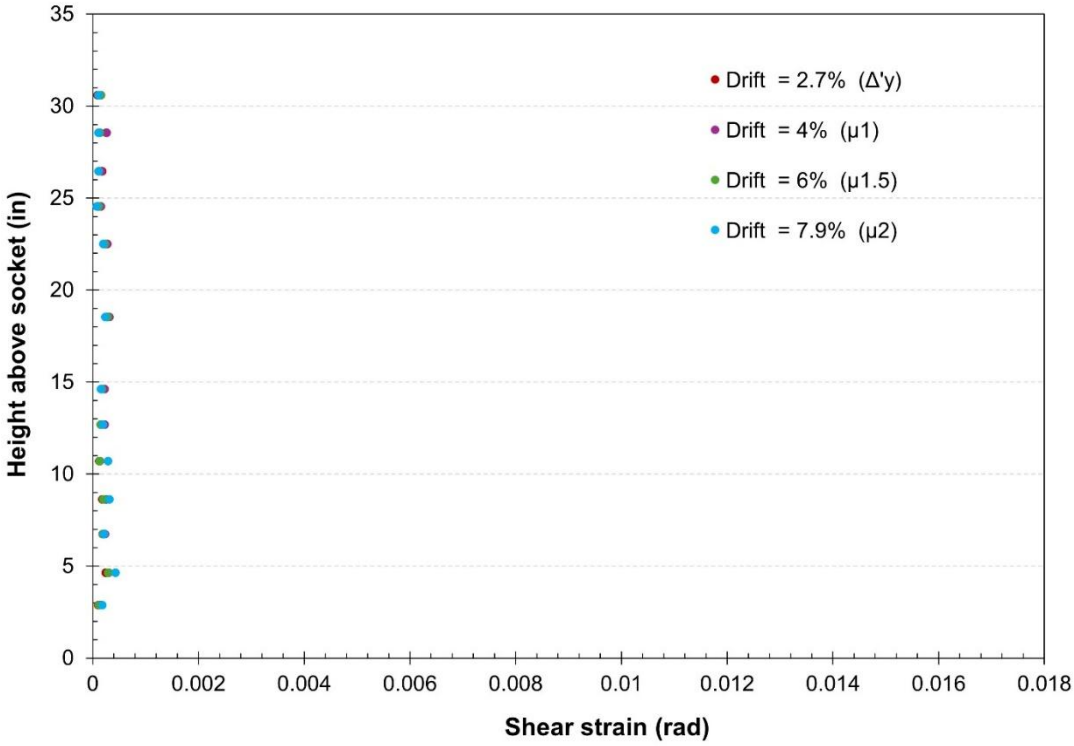


Figure 5-65. Shear strain distribution of the column for pushing cycles for SJS2

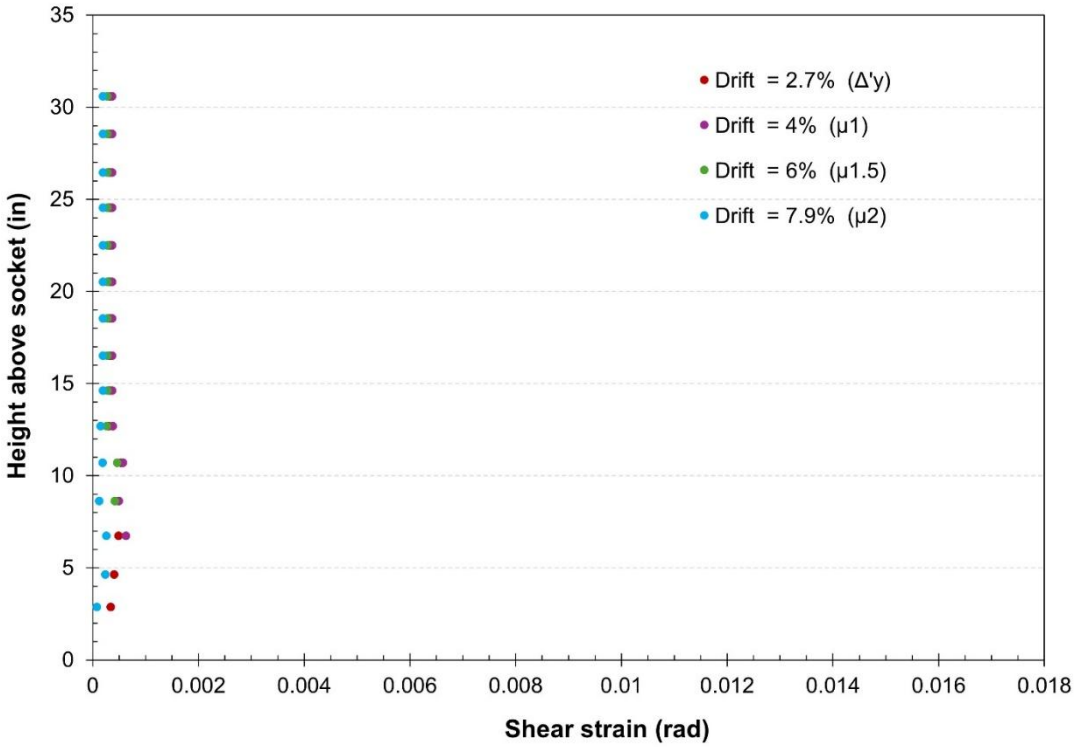


Figure 5-66. Shear strain distribution of the column for pulling cycles for SJS2

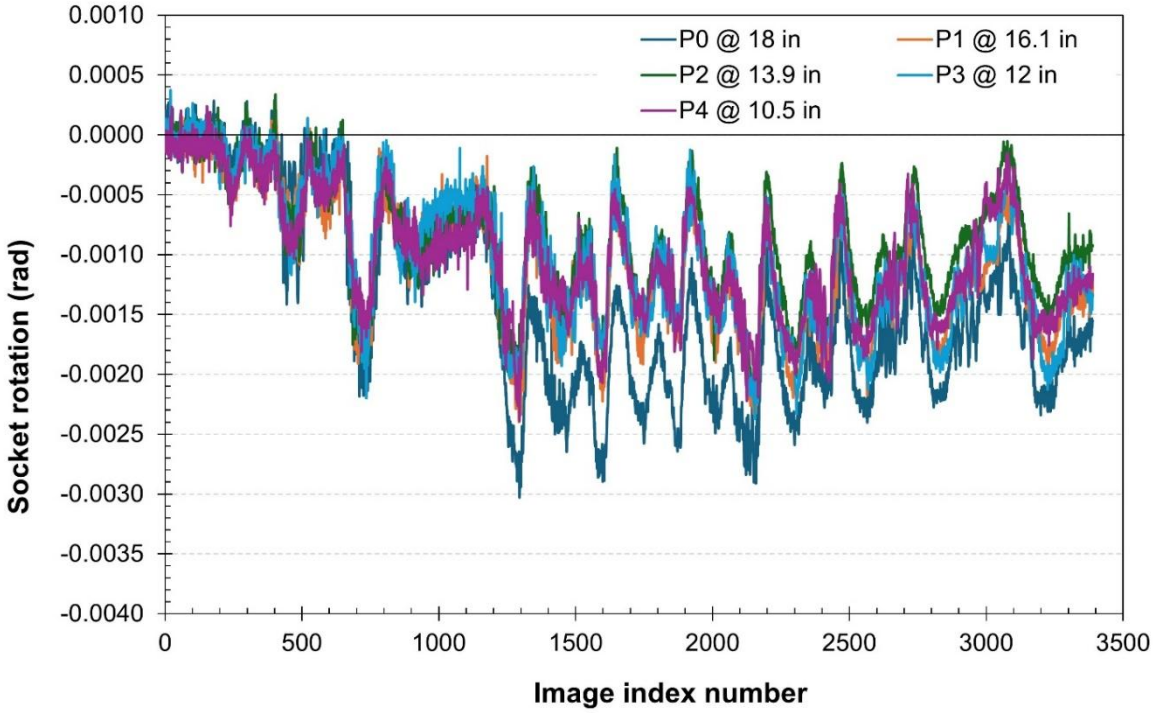


Figure 5-67. Socket rotation at the north side of SJS2

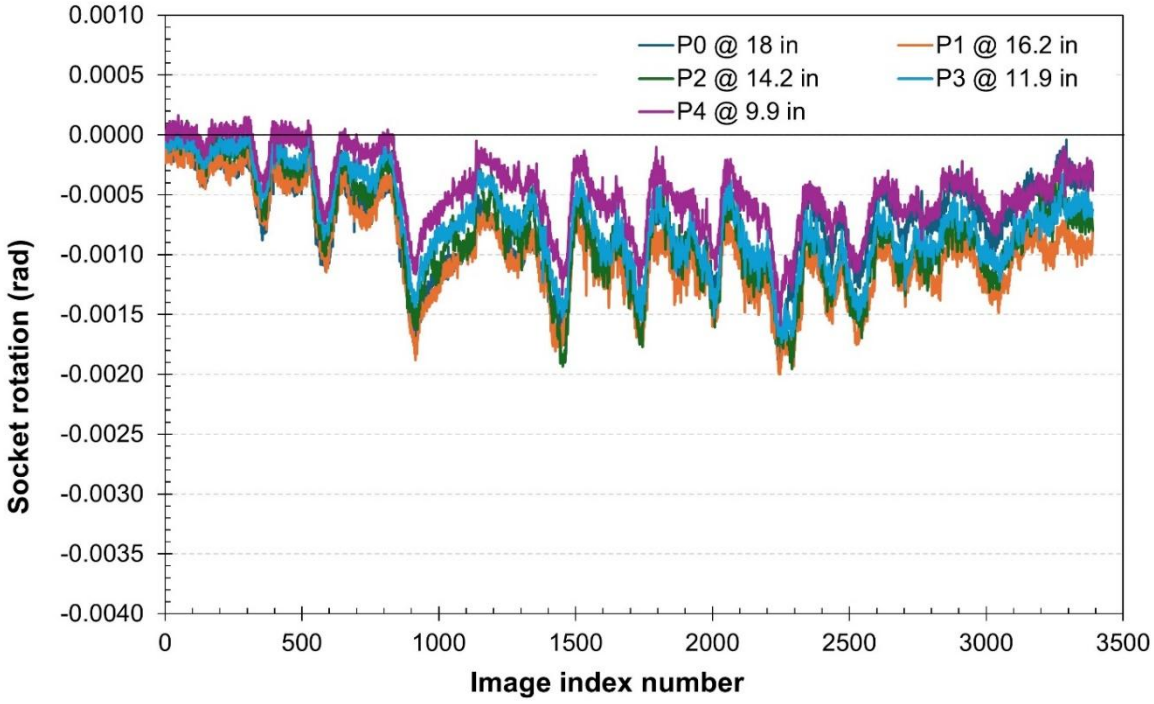


Figure 5-68. Socket rotation at the south side of SJS2

Table 5-3 and Table 5-4 present the contributions of the different components to the total displacement. Additionally, Figure 5-69 and Figure 5-70 illustrate the component displacements for pushing and pulling cycles following the first yield. The calculated displacement components closely match the measured values, validating the accuracy of the calculation methodology. The difference between the measured and calculated displacements is around 5.3% for most ductility displacements.

Table 5-3. Displacement components for pushing cycles for SJS 2

Displacement component (in)	**Δ'y**	**μ1**	**μ1.5**	**μ2**
Measured displacement	2.44	3.63	5.37	7.12
Flexural	0.34	0.40	0.37	0.21
Strain penetration and rocking	1.92	2.99	4.75	6.79
Shear	0.01	0.01	0.01	0.01
Socket rotation	0.03	0.04	0.04	0.03
Calculated displacement error	0.13	0.19	0.20	0.08
Calculated displacement error (%)	5.4%	5.1%	3.8%	1.1%

Table 5-4. Displacement components for pulling cycles for SJS 2

Displacement component (in)	**Δ'y**	**μ1**	**μ1.5**	**μ2**
Measured displacement	2.76	3.58	5.36	7.13
Flexural	0.36	0.36	0.33	0.12
Strain penetration and rocking	2.18	2.93	4.69	6.68
Shear	0.02	0.03	0.02	0.01
Socket rotation	0.03	0.03	0.03	0.02
Calculated displacement error	0.18	0.23	0.28	0.30
Calculated displacement error (%)	6.4%	6.5%	5.3%	4.2%

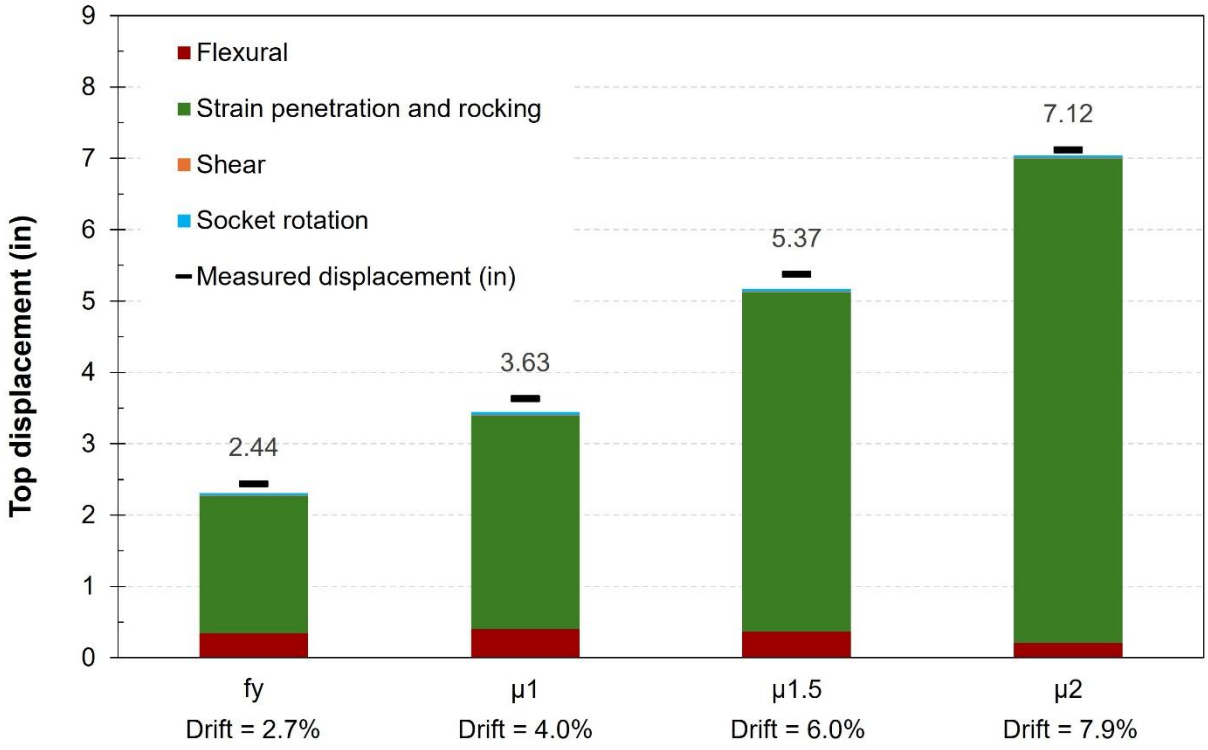


Figure 5-69. Displacement components for pushing cycles for SJS2

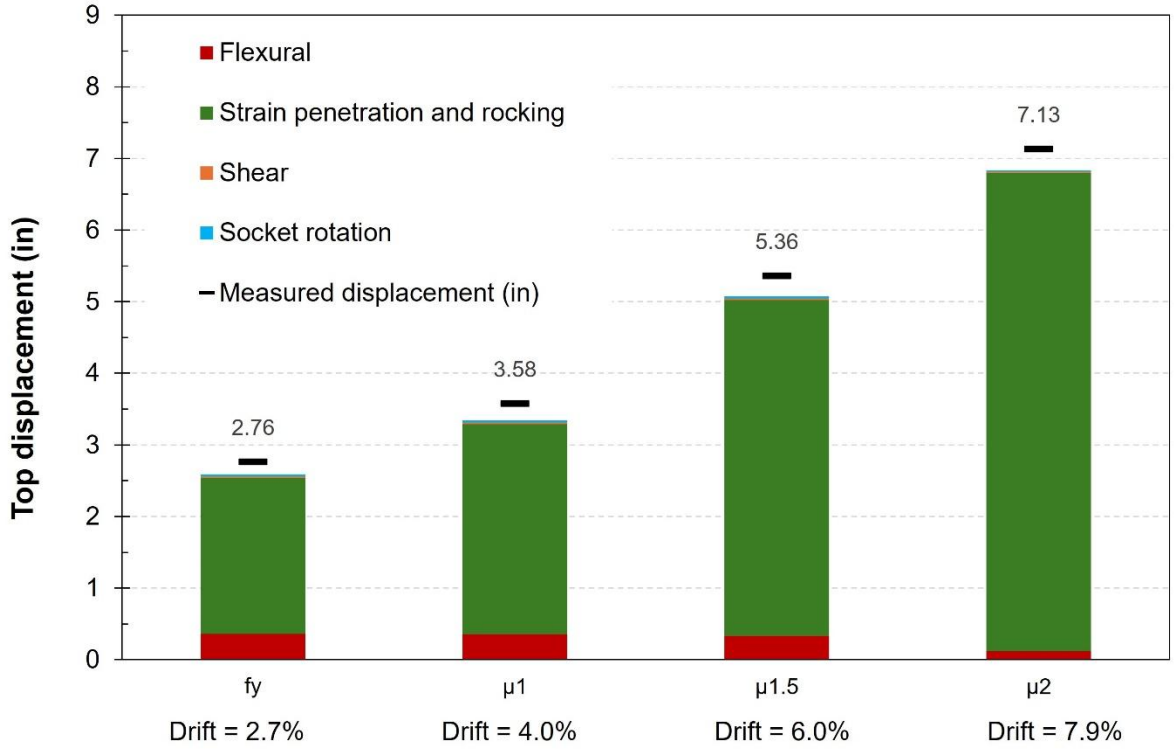


Figure 5-70. Displacement components for pulling cycles for SJS2

When comparing the displacement components, it was observed that shear and socket rotation had a relatively negligible impact on the column total displacement. Flexural displacement had a minimum effect, while strain penetration and rocking of the column contributed significantly to the overall displacement. Therefore, the primary displacement component was due to rotational effects, particularly for a socket height of 0.75 Dc, where the grout was crushed and the column remained elastic.

5.3.4. Summary of Results for SJS-2

The tension strains in the longitudinal bars reached yielding at the predicted yield displacement where grout crushing occurred and the column experienced rocking. This behavior prevented the development of the full plastic hinge above the external socket connection. The strains in the external socket wall remained below the yield point throughout the test, confirming that the external socket connections effectively prevented plastic strains from reaching the foundation or cap beam. As a result, the footing remained as a capacity-protected element.

Horizontal strains in the external socket sleeve reached 1% of strain at the top third of the socket height but remained elastic for the rest of the height. This aligns with the visible damage observed on the sleeves during the test, confirming that the sleeves experienced significant inelastic deformation.

The elastic damping for SJS 2 was approximately 12%, which is higher than the 5% typically observed in CIP columns. This additional 7% damping may be attributed to the initial cracks in the socket wall and grout that occurred early in the test, as well as some unidentified noises observed during the cycles before the yield displacement.

The overall displacement behavior of SJS 2 was governed primarily by strain penetration and rocking. Flexural displacements accounted for approximately 5% of the total displacement, while strain penetration and rocking contributed around 90%. This indicates that strain penetration and rocking play a more significant role in socket connections when the failure mechanism is attributed to grout crushing.

5.4. Experimental Results for Specimen SJS-3

In this section, the data analysis and experimental results previously discussed in this chapter will be specifically applied to the experimental test SJS3. The results for SJS3 will be presented in detail, focusing on axial strains on the column and external socket, hysteretic damping, and calculated displacement components. This analysis provides insights into the column performance and behavior under the applied loading conditions, contributing to a comprehensive understanding of the system response.

5.4.1. Axial strain analysis for SJS-3

The strain profiles were calculated to assess the strain distribution along the RC column during the first cycles of each ductility displacement for SJS2, considering both loading directions. In this context, ″Pushing Cycles″ refers to the strain profiles when force is applied toward the north face of the column, while ″Pulling Cycles″ refers to when force is applied toward the south face.

Figure 5-71 and Figure 5-72 present the strain profiles of the extreme bar located on the north face of the specimen for cycles up to yielding and post-yield cycles, respectively. Similarly, Figure 5-73 and Figure 5-74 depict the strain profiles for the extreme bar on the south side of the specimen for cycles up to yielding and post-yield cycles. The maximum axial strain in tension before grout crushing occurred was approximately 1.6%, while a maximum strain of 0.8% was reached in compression. These strain profiles indicate a spread of plasticity extending approximately 20 inches from the external socket interface.

A detailed examination of the strains on the reinforcing bars can be achieved by plotting the strain throughout the displacement history for each gauge length. Figure 5-75 and Figure 5-76 present the strain history of the extreme bars located on the north and south faces of the specimen at the first gauge length above the external socket. For both extreme bars, it was observed that the maximum strain reached during the experimental test was approximately 1.6% when the bar was in tension. Following grout crushing, the column began to exhibit rocking behavior.

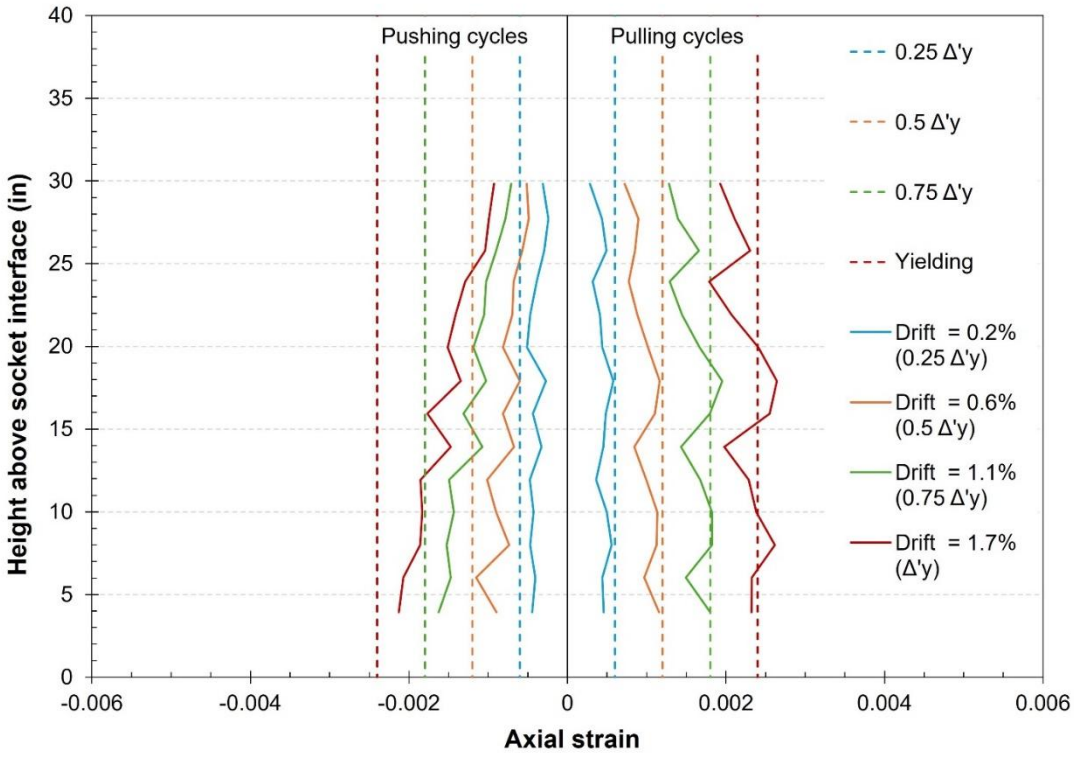


Figure 5-71. Strain profile up to first yield cycle for SJS3 on the north side of the column

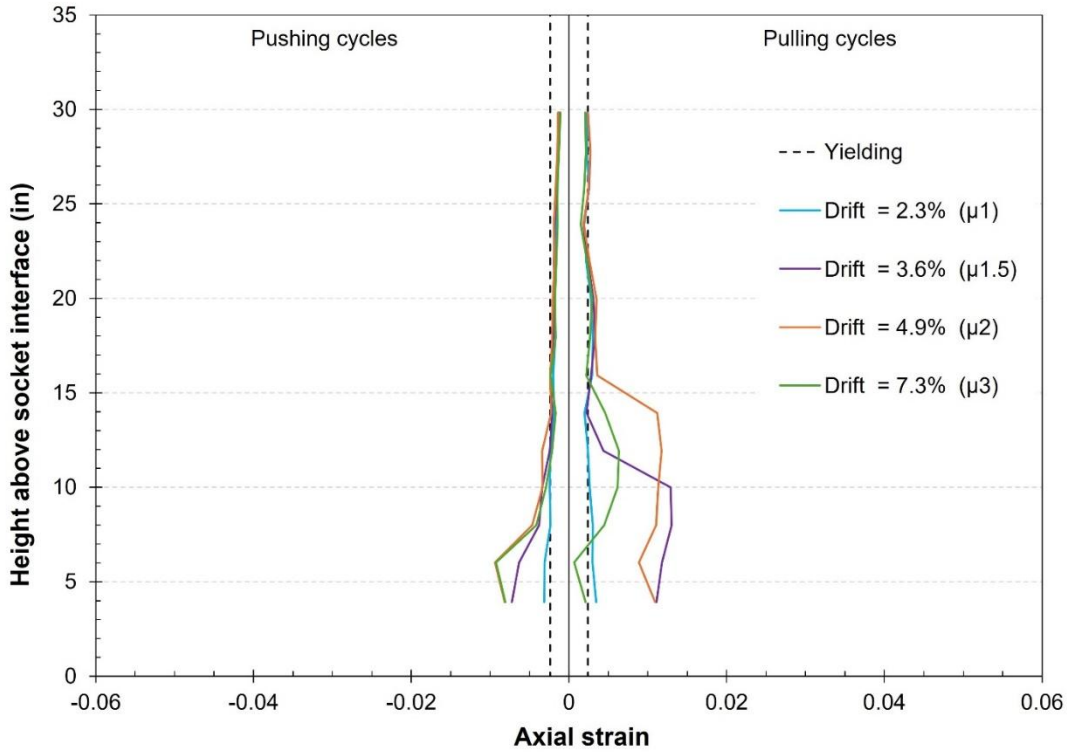


Figure 5-72. Strain profile for post-yield cycles for SJS3 on the north side of the column

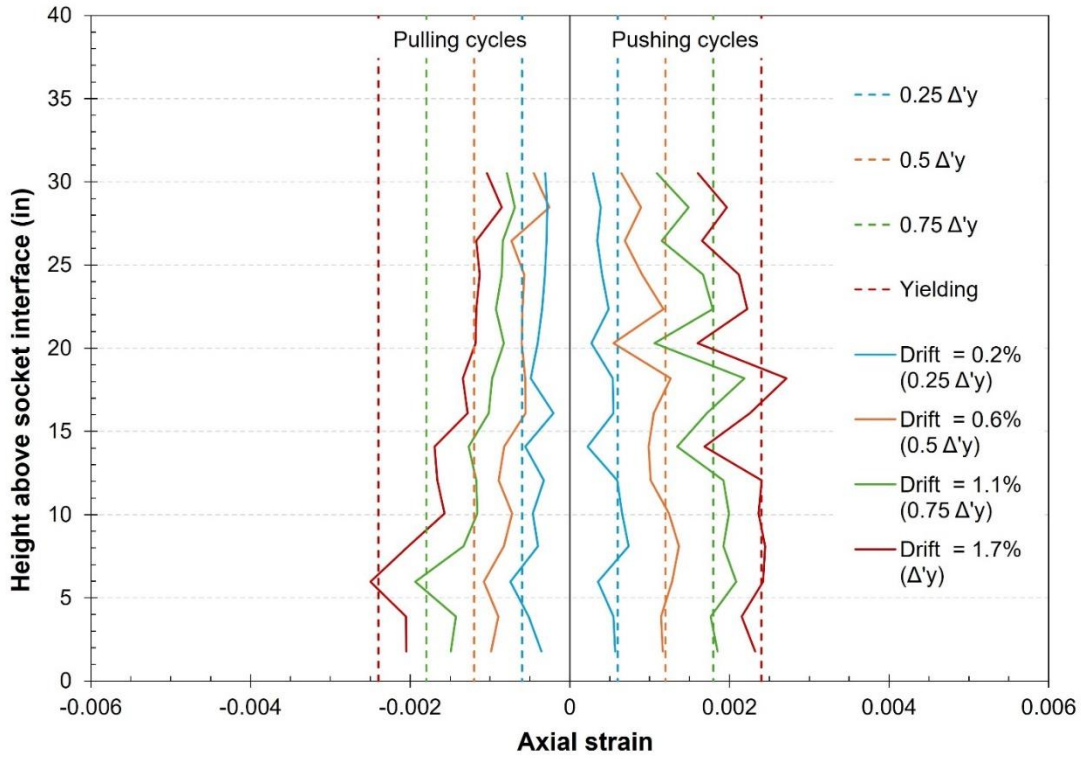


Figure 5-73. Strain profile up to first yield cycle for SJS3 on the south side of the column

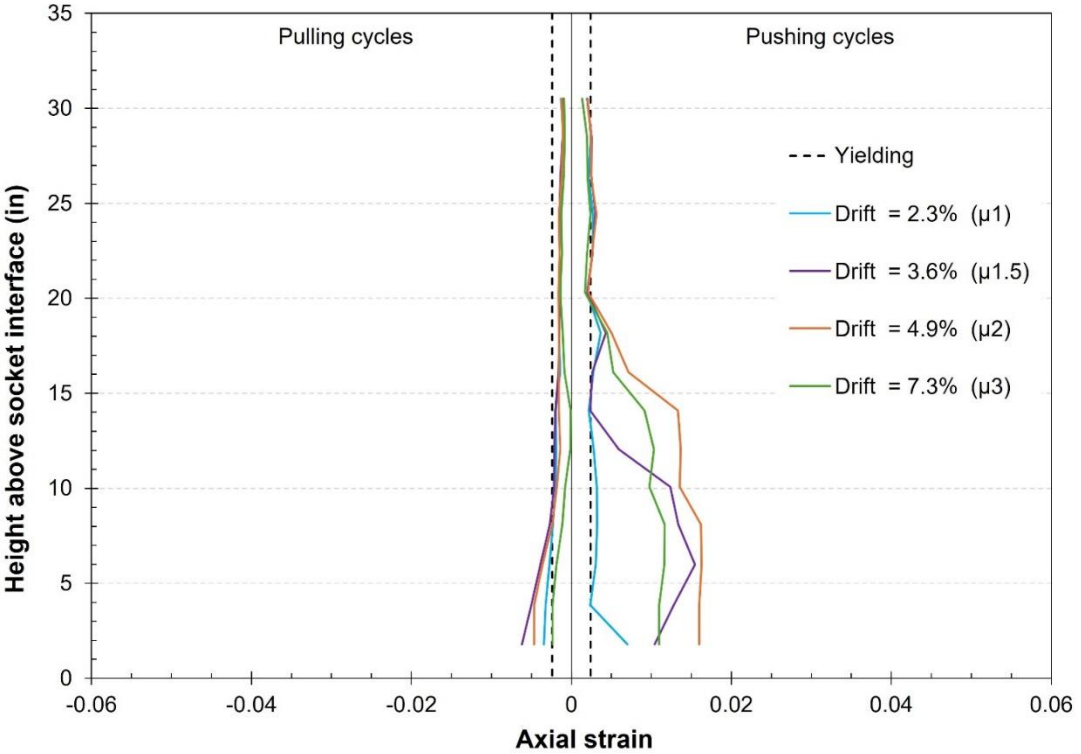


Figure 5-74. Strain profile for post-yield cycles for SJS3 on the south side of the column

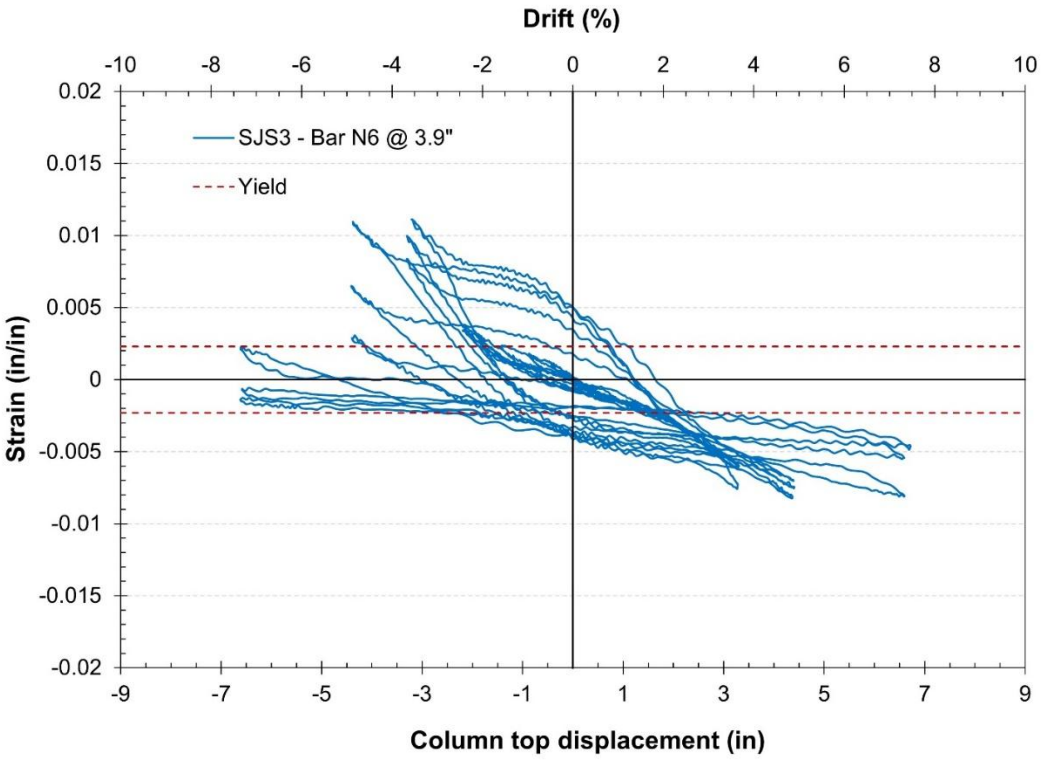


Figure 5-75. Strain vs displacement history for N6 of SJS3

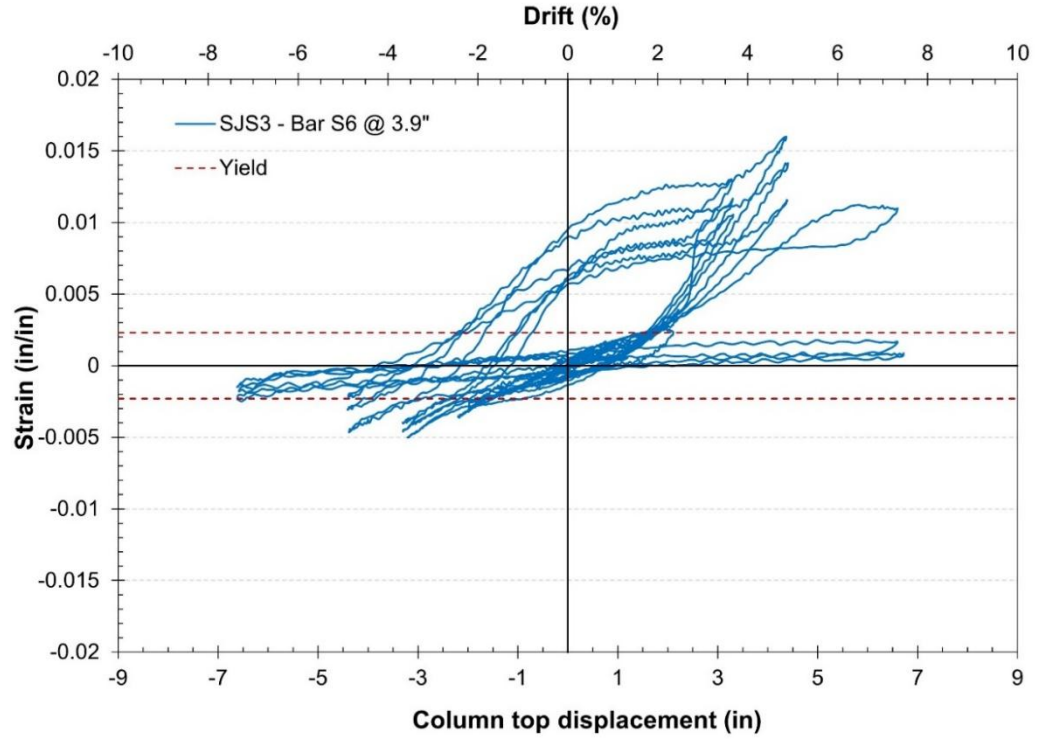


Figure 5-76. Strain vs displacement history for S6 of SJS3

Additionally, the strain history of the extreme bars in the external socket wall reinforcement was monitored using strain gauges placed 2 inches above the footing. Figure 5-77 and Figure 5-78 present the strain history for the extreme bars on the north and south faces, respectively. The data shows that the reinforcement in the external socket wall reached 1.5 the yield strain, indicating that the external socket wall remained mostly elastic throughout the entire experimental test.

The axial strains on the external socket sleeve were measured using DIC. In this context, the horizontal strains correspond to the hoop forces acting around the circumference, while the vertical strains reflect any flexion sustained by the sleeves. Figure 5-79 and Figure 5-80 present the strains on the north face of the specimen while Figure 5-81 and Figure 5-82 show the strains on the south face. The data indicates that, for the horizontal strains, the top 7 inches of the socket experienced strain values of 1.1%, while the remainder of the socket height remained elastic. The vertical strains reached yielding at the top 3 inches of the socket, with the rest of the socket height staying elastic throughout the experimental test. These results suggest that the acting forces were concentrated in the top 7 inches of the steel sleeve.

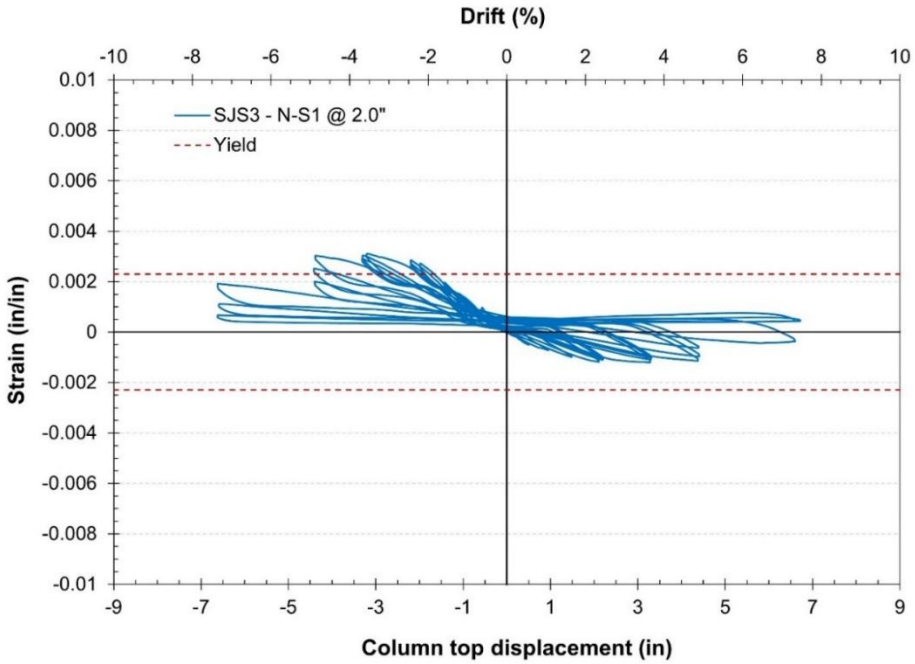


Figure 5-77. Strain vs displacement history for the extreme bar of socket wall reinforcement at the north side of SJS3

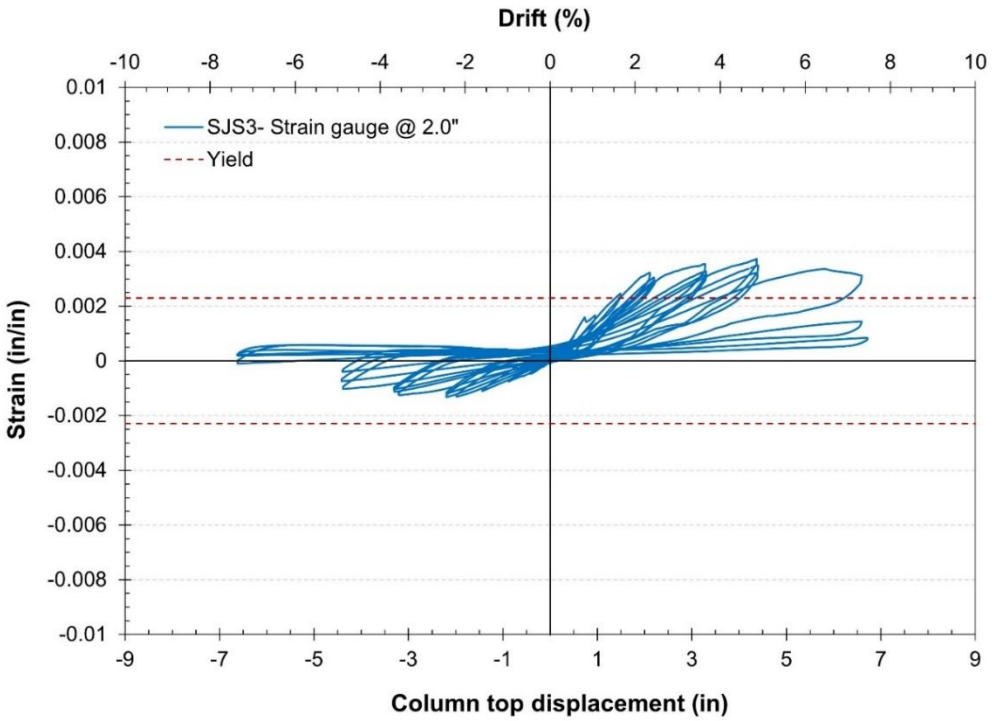


Figure 5-78. Strain vs displacement history for the extreme bar of socket wall reinforcement at the north side of SJS3

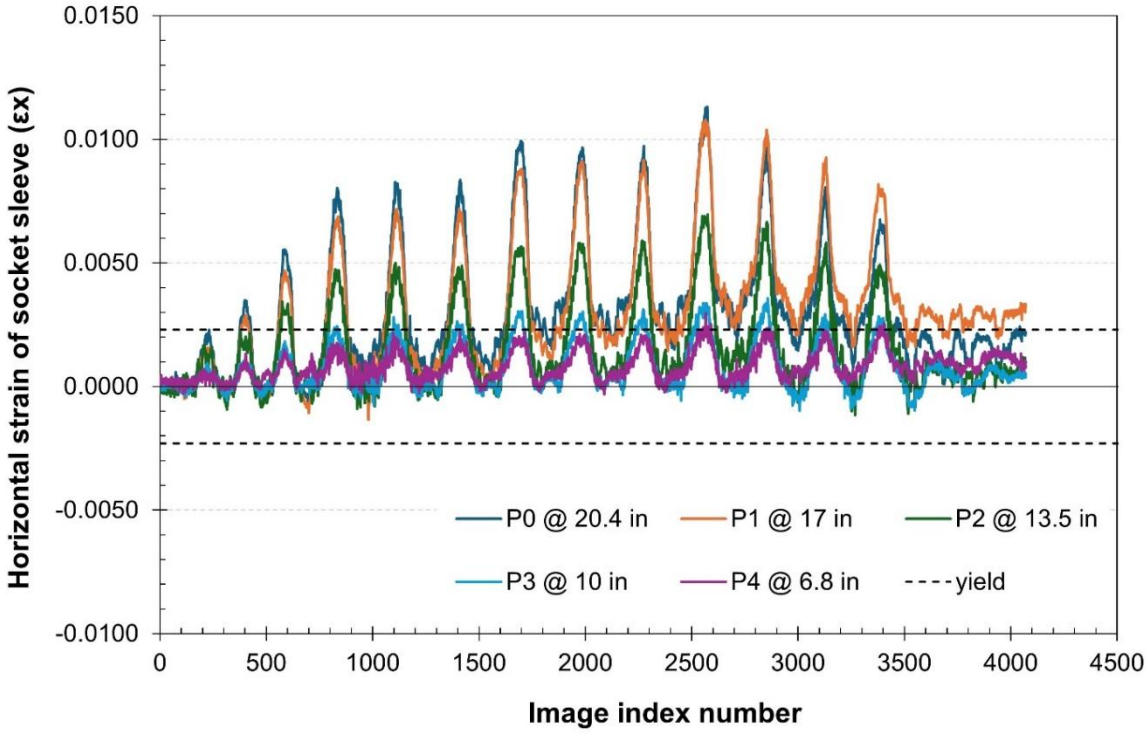


Figure 5-79. Horizontal strain history of external socket sleeve at the north side of SJS3

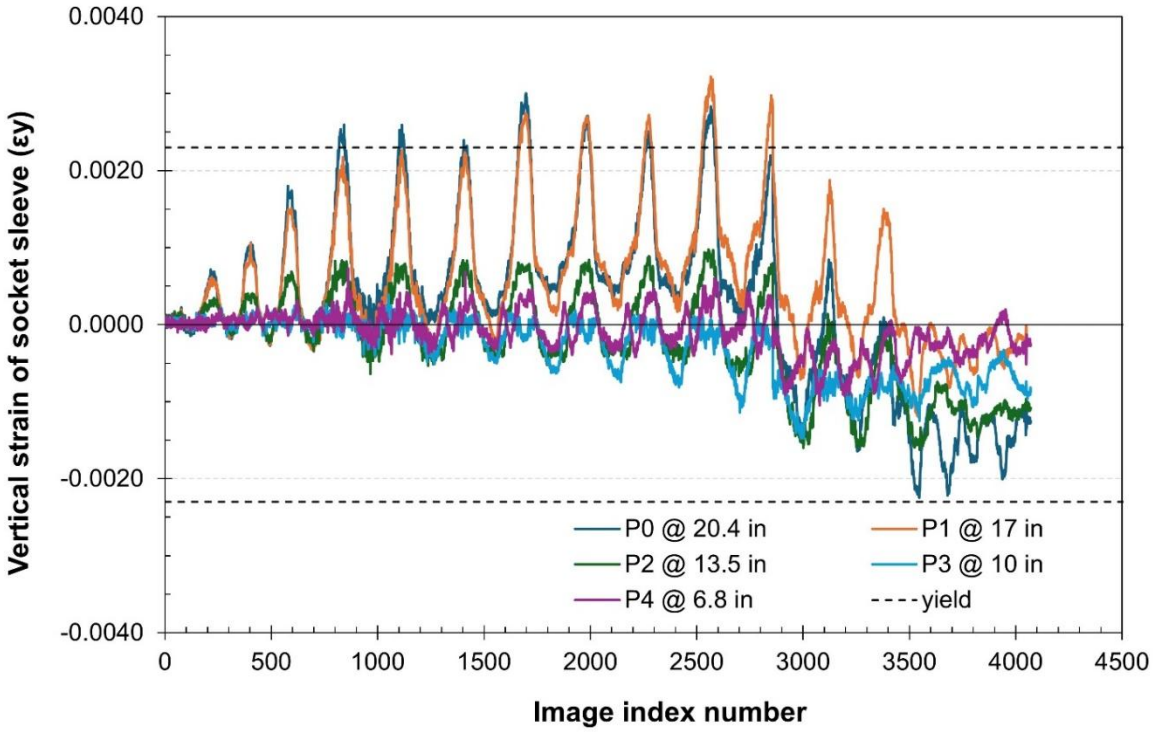


Figure 5-80. Vertical strain history of external socket sleeve at the north side of SJS3

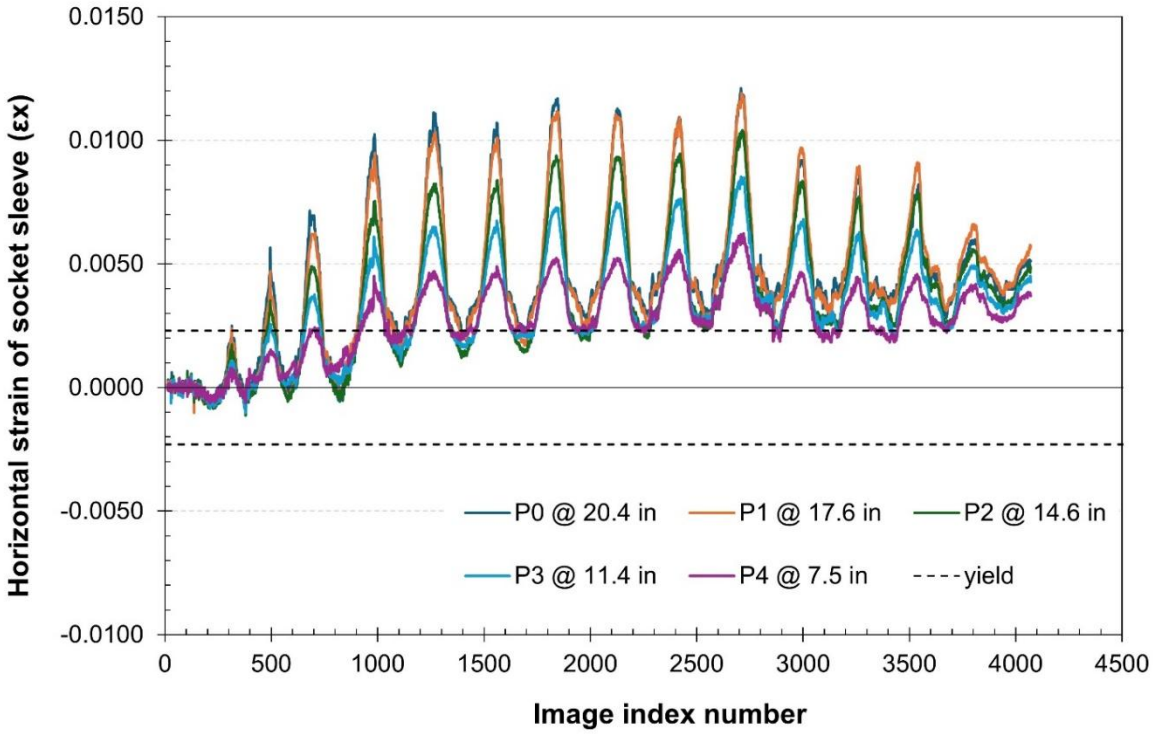


Figure 5-81. Horizontal strain history of external socket sleeve at the south side of SJS3

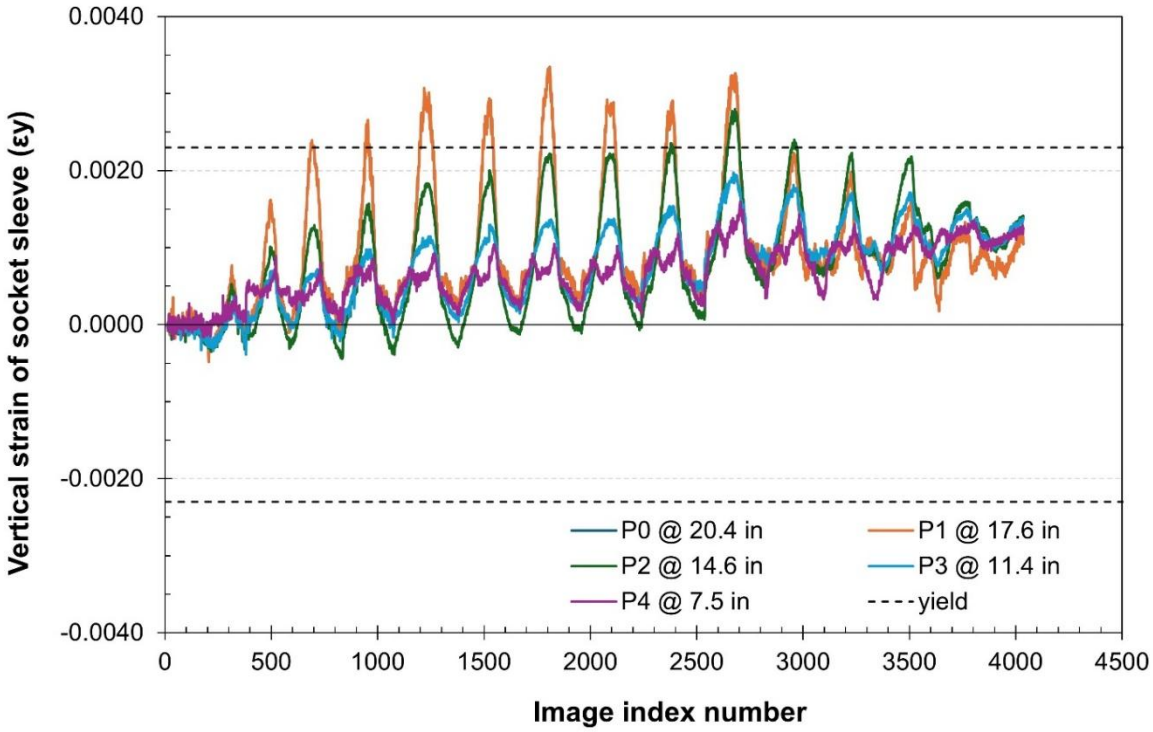


Figure 5-82. Vertical strain history of external socket sleeve at the south side of SJS3

5.4.2. Energy dissipation and hysteretic damping for SJS-3

Energy dissipation is important in understanding a structure seismic behavior because it relates to the structural element damage and energy dissipation capacity. Figure 5-83 illustrates the energy dissipation for all ductility displacement cycles for SJS3, with a total energy dissipation of 4113 kip-in. Notably, during the third cycle of ductility two, where the grout was crushed, the energy dissipated was reduced by 25% compared to the first cycle at the same ductility level. This reduction highlights the impact of severe damage on the energy dissipation capacity of the column.

Additionally, Figure 5-84 presents the Jacobsen hysteretic damping values for SJS3, demonstrating that damping increases as the applied displacements grow and the column sustains more damage. Notably, the elastic damping for SJS3 was approximately 10%, which is 5% higher than what is typically observed in a CIP column, indicating enhanced energy dissipation during the structural element elastic behavior.

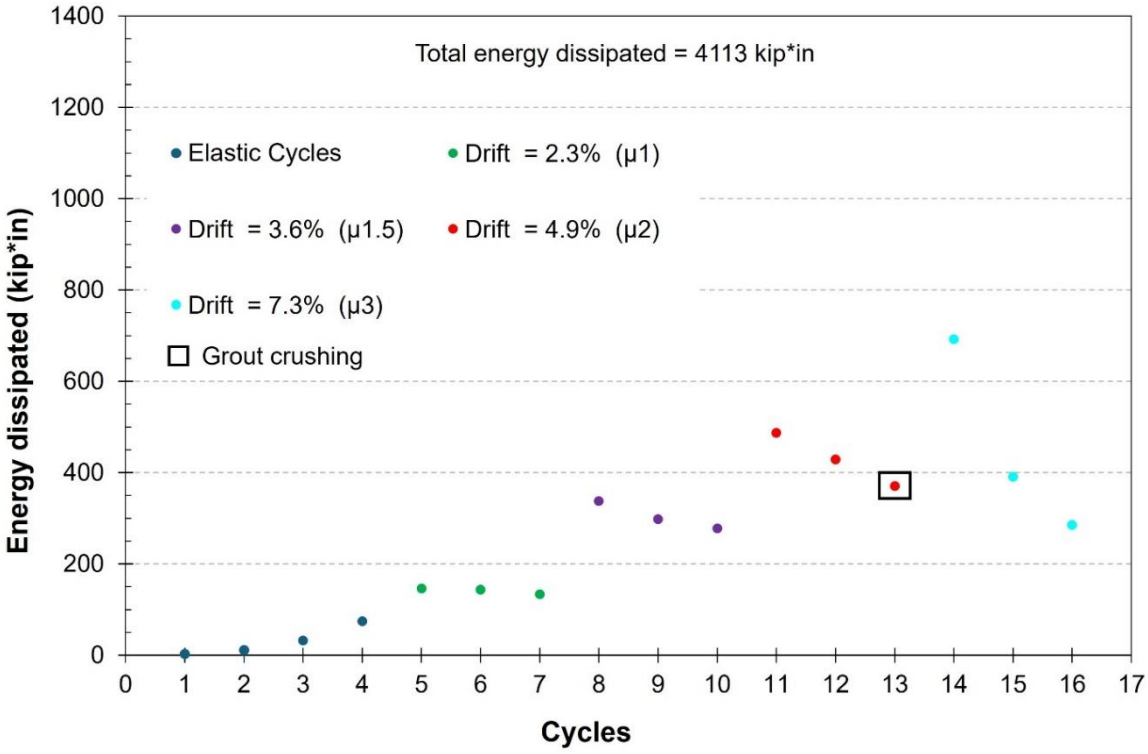


Figure 5-83. Energy dissipation plot for SJS3

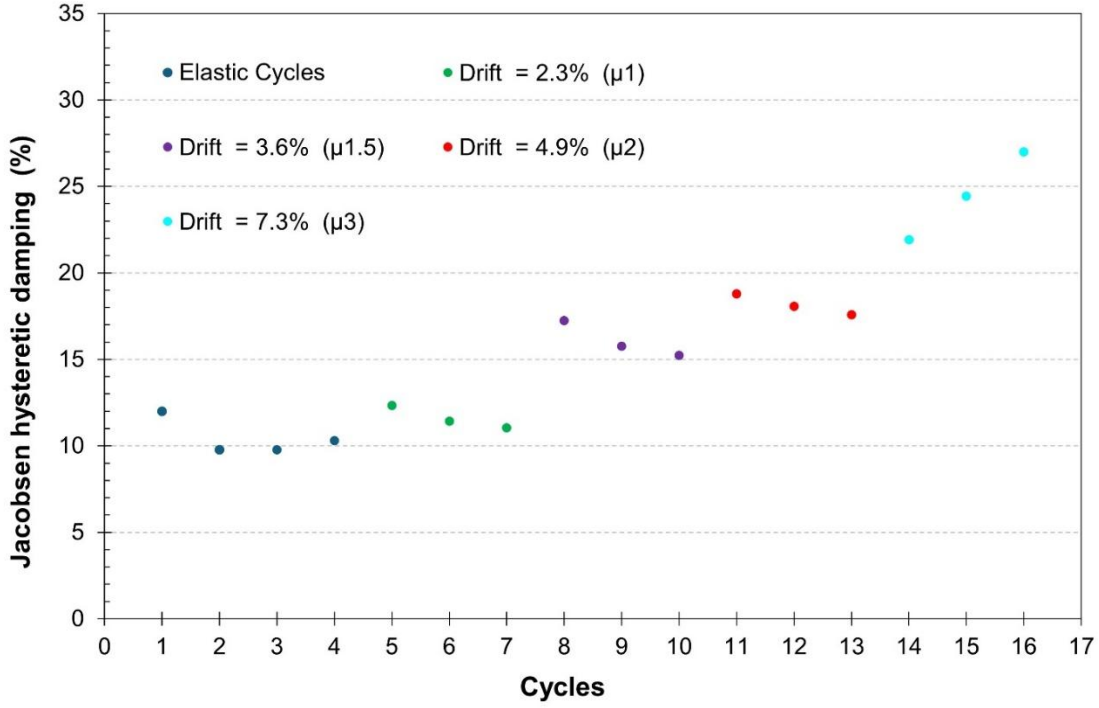


Figure 5-84. Hysteretic damping plot for SJS3

5.4.3. Displacement components for SJS-3

The displacement components considered in the calculations include flexural deformation, column rotation due to strain penetration and rocking, shear deformation of the column, and the deformation contribution resulting from socket rotation. The methodologies for these calculations have been detailed earlier in Section 5.1.3 of this report.

The flexural displacement component was derived from the column curvature, with the curvature profile shown in Figure 5-85 for the cycles up to yield and in Figure 5-86 for the post-yield cycles. The curvature is defined as positive when the column is pushed toward its north face. The dashed line in these figures represents the linear distribution of curvature, beginning at zero at the top of the column and reaching the yield curvature at the socket interface.

The displacement due to column rotation was calculated by determining the rotation angle at the base of the column and multiplying it by the column height above the socket. Figure 5-87 and Figure 5-88 present the column rotation for pushing and pulling cycles, respectively.

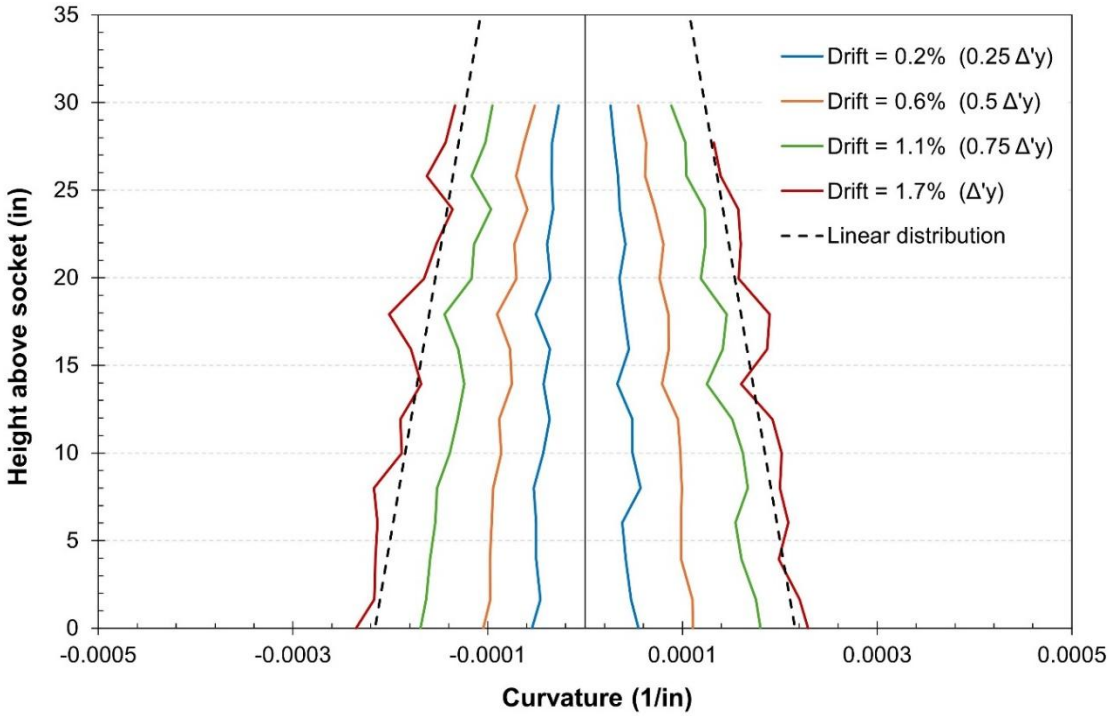


Figure 5-85. Curvature profile of the column up to the first yield cycle for SJS3

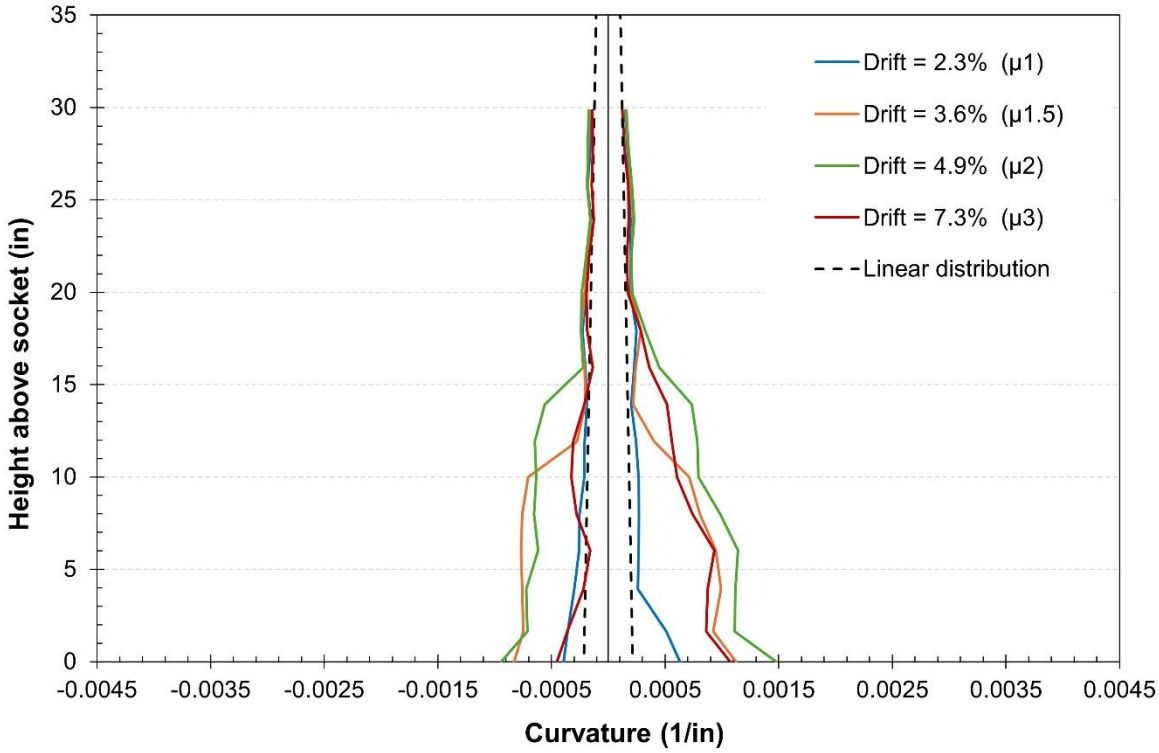


Figure 5-86. Curvature profile of the column for post-yield cycles for SJS3

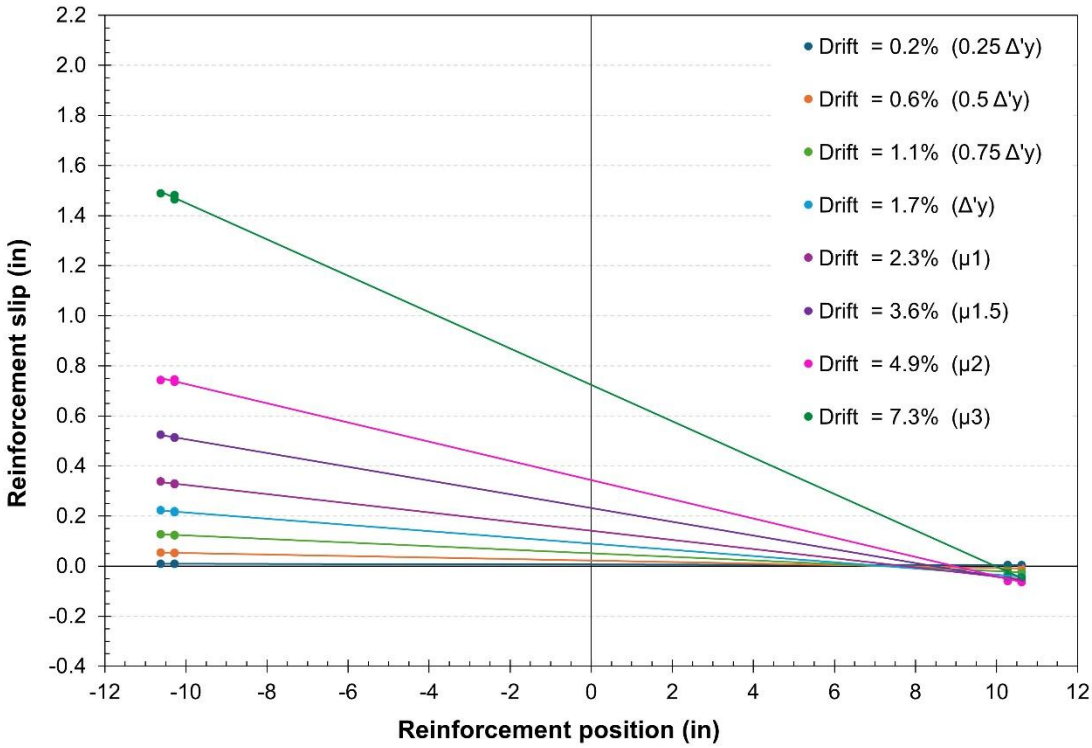


Figure 5-87. Rotation of the column for pushing cycles at the socket interface of SJS3

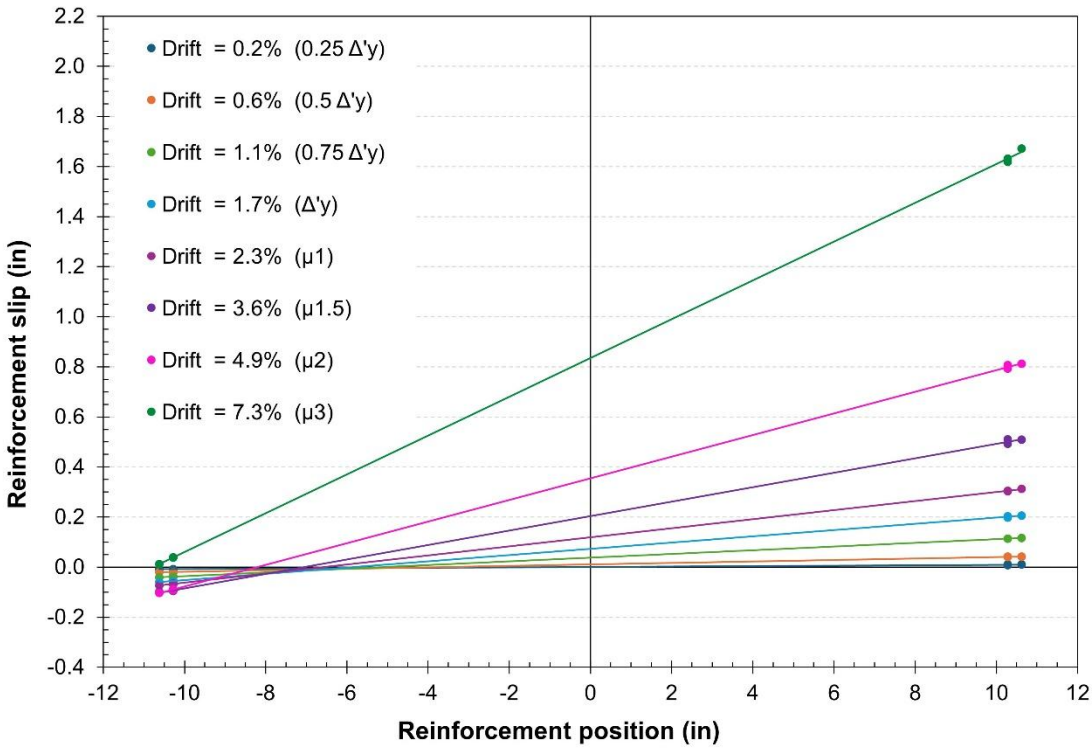


Figure 5-88. Rotation of the column for pulling cycles at the socket interface of SJS3

Figure 5-89 and Figure 5-90 present the shear strain distribution along the column height for the last three ductility displacements, as well as the yield displacement. These shear strains were then used to calculate the column shear displacement by multiplying the shear strain by the interval height. At 20 inches above the socket, the shear strains became constant, remaining approximately the same for all ductility displacements after yielding.

The displacement component resulting from socket rotation was obtained using DIC. Figure 5-91 and Figure 5-92 illustrate the socket rotation throughout the experimental test for the north and south faces, respectively. Socket rotation was measured at five different locations along the height, and an average value was used for displacement calculations due to the uniform distribution observed along the socket height. The averaged socket rotation, when multiplied by the socket height, provided the displacement component attributed to socket rotation.

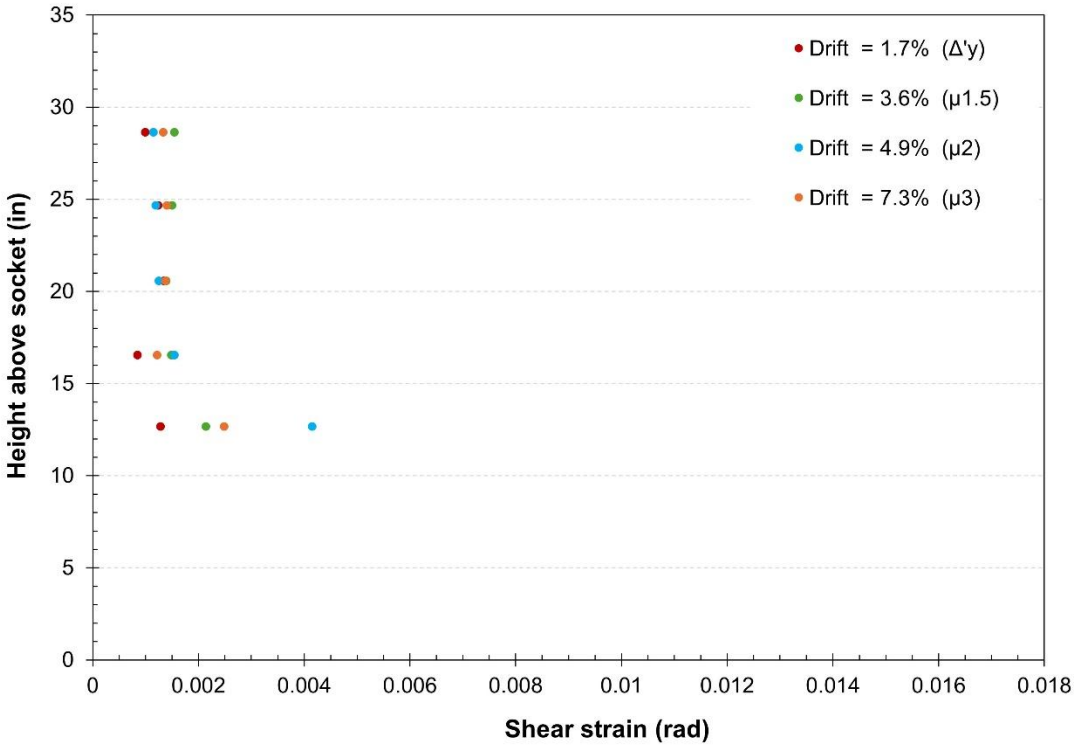


Figure 5-89. Shear strain distribution of the column for pushing cycles for SJS3

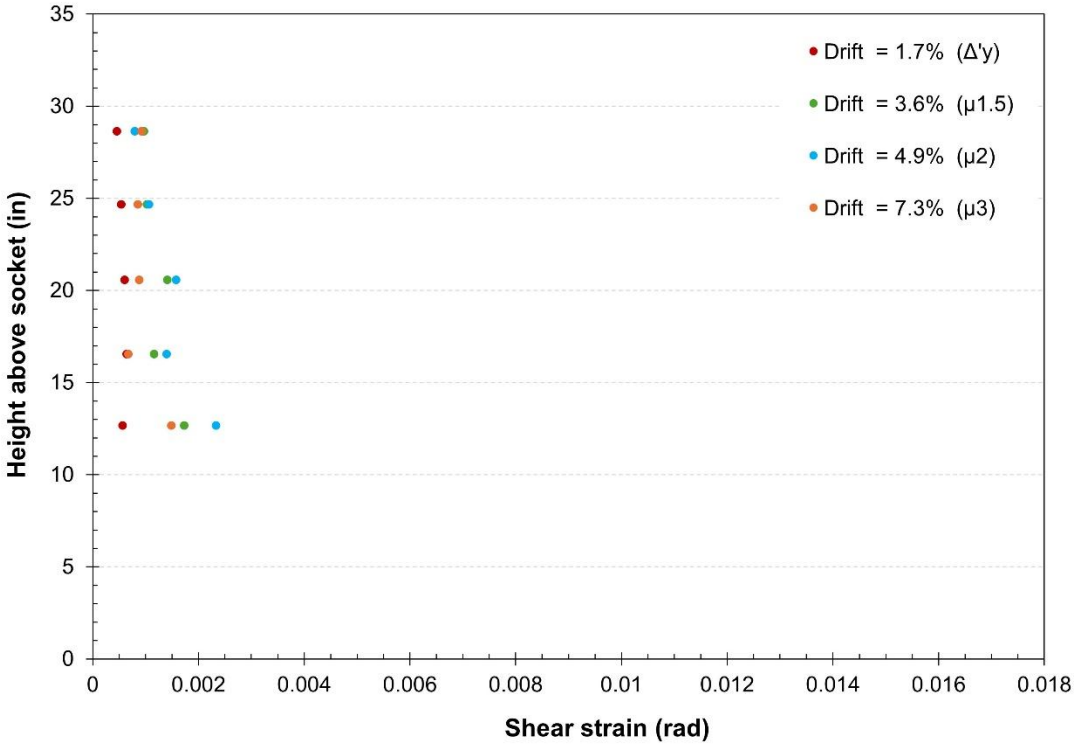


Figure 5-90. Shear strain distribution of the column for pulling cycles for SJS3

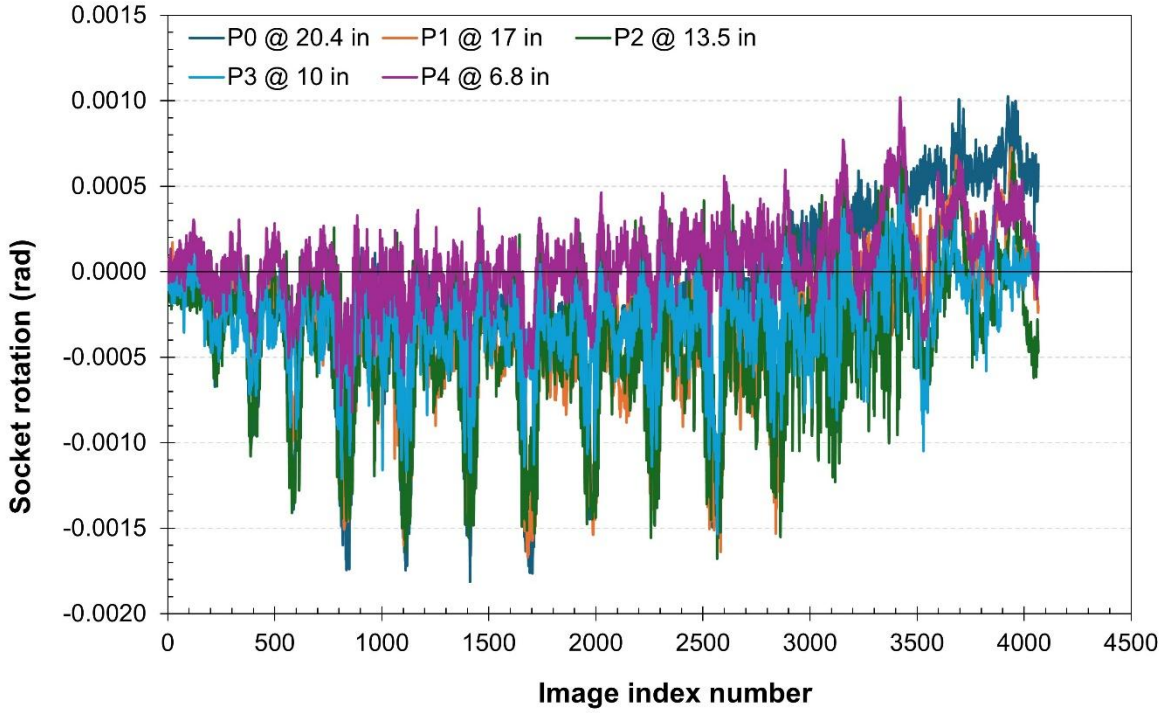


Figure 5-91. Socket rotation at the north side of SJS3

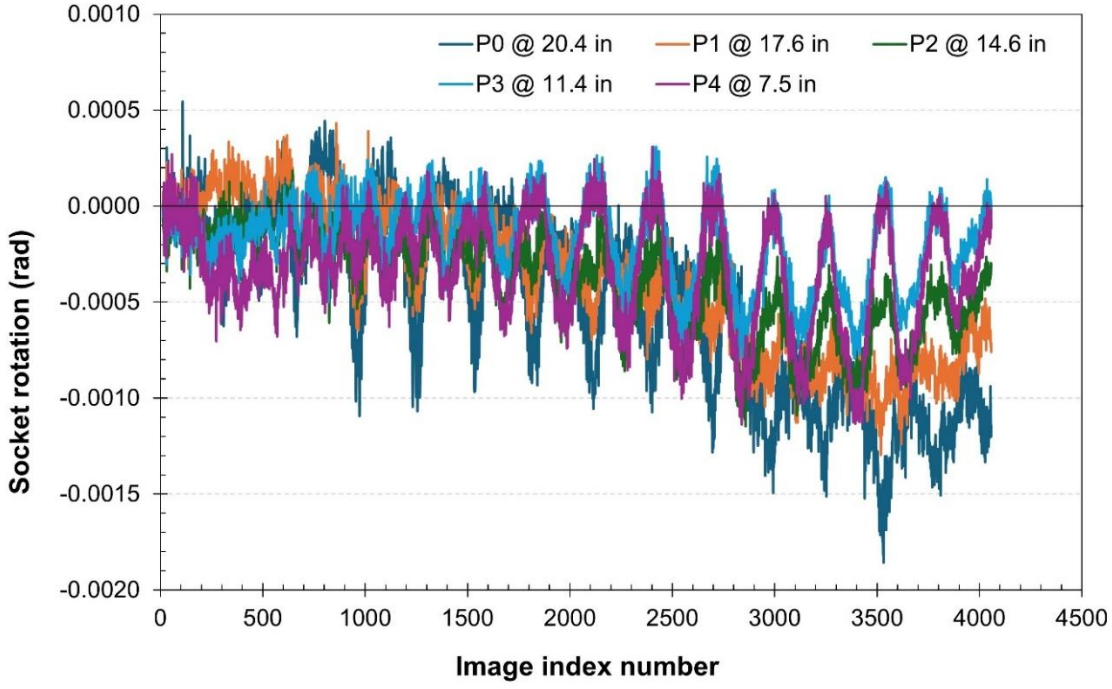


Figure 5-92. Socket rotation at the south side of SJS3

Table 5-5 and Table 5-6 present the contributions of the different components to the total displacement. Additionally, Figure 5-93 and Figure 5-94 illustrate the component displacements for pushing and pulling cycles following the first yield. The calculated displacement components closely match the measured values, validating the accuracy of the calculation methodology. The difference between the measured and calculated displacements is around 10% for most ductility displacements.

Table 5-5. Displacement components for pushing cycles for SJS 3

Displacement component (in)	**Δ'y**	**μ1**	**μ1.5**	**μ2**	**μ3**
Measured displacement	1.49	2.11	3.28	4.37	6.60
Flexural	0.35	0.50	0.92	1.18	0.91
Strain penetration and rocking	0.86	1.27	1.91	2.67	5.05
Shear	0.07	0.08	0.11	0.12	0.10
Socket rotation	0.03	0.04	0.04	0.03	0.02
Calculated displacement error	0.17	0.23	0.30	0.38	0.51
Calculated displacement error (%)	11.5%	10.7%	9.2%	8.6%	7.7%

Table 5-6. Displacement components for pulling cycles for SJS 3

Displacement component (in)	**Δ'y**	**μ1**	**μ1.5**	**μ2**	**μ3**
Measured displacement	1.42	1.99	3.21	4.38	6.62
Flexural	0.36	0.45	0.79	0.84	0.43
Strain penetration and rocking	0.87	1.26	2.01	3.01	5.39
Shear	0.03	0.05	0.08	0.08	0.07
Socket rotation	0.01	0.02	0.02	0.03	0.04
Calculated displacement error	0.15	0.21	0.31	0.43	0.69
Calculated displacement error (%)	10.3%	10.5%	9.8%	9.8%	10.4%

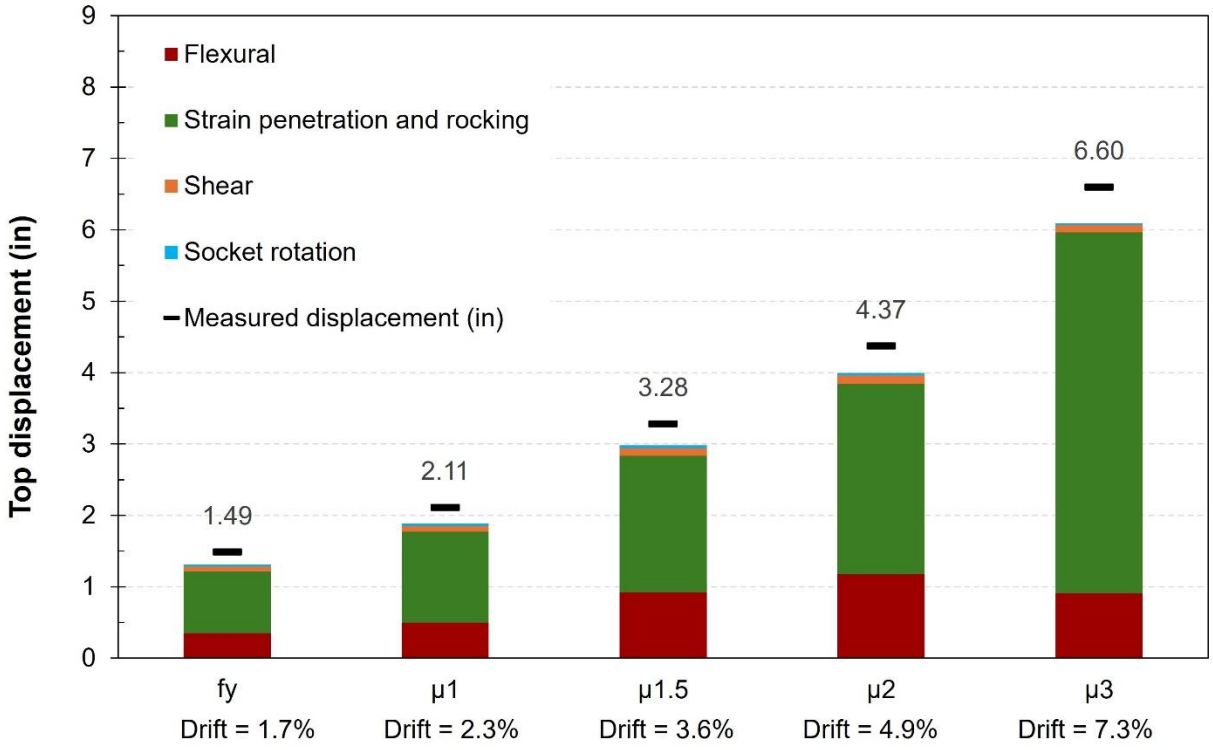


Figure 5-93. Displacement components for pushing cycles for SJS3

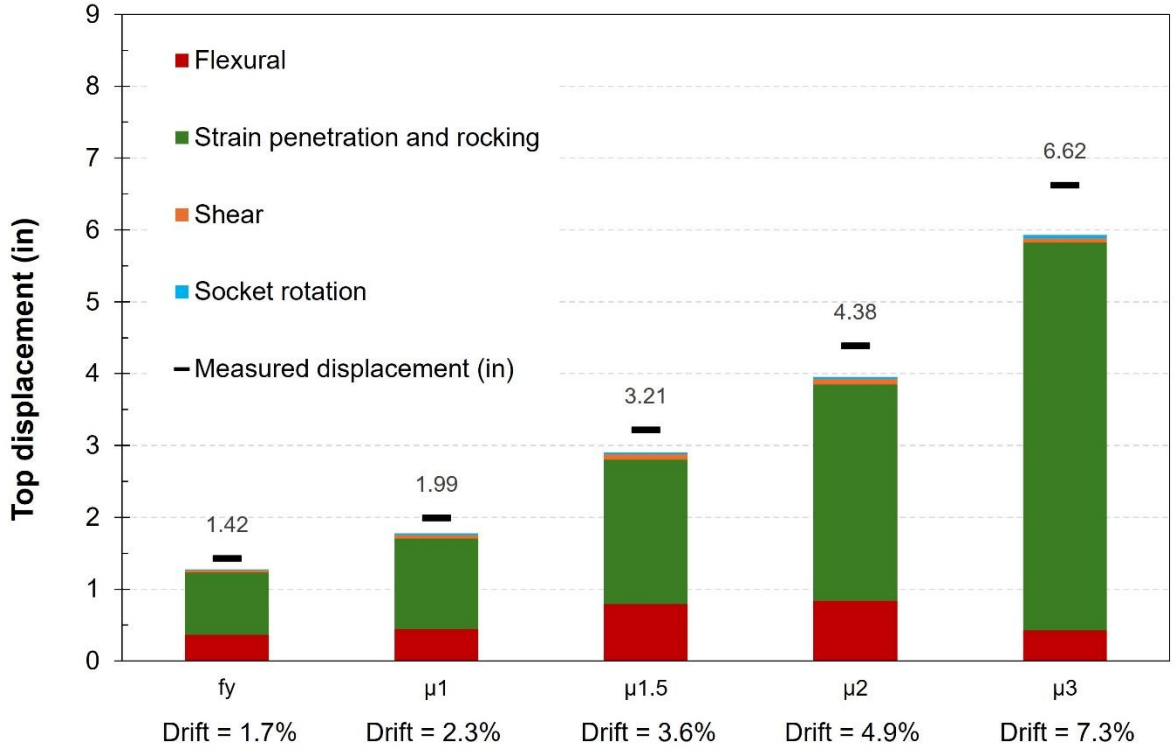


Figure 5-94. Displacement components for pulling cycles for SJS3

When comparing the displacement components, it was observed that shear and socket rotation had a relatively negligible impact on the column total displacement. Flexural displacement had a minimum effect, while strain penetration and rocking of the column contributed significantly to the overall displacement, with more than 65% of the total displacement. Therefore, the primary displacement component was due to rotational effects, particularly for a socket height of 0.85 Dc, where the failure mode was crushing of the grout.

5.4.4. Summary of Results for SJS-3

The tension strains in the longitudinal bars reached 1.6% before grout crushing occurred and the column experienced rocking. This behavior prevented the development of the full plastic hinge above the external socket connection. The strains in the external socket wall remained below the yield point throughout the test, confirming that the external socket connections effectively prevented plastic strains from reaching the foundation or cap beam. As a result, the footing remained as a capacity-protected element.

Horizontal strains in the external socket sleeve reached 1% of strain at the top third of the socket height but remained elastic for the rest of the height. This aligns with the visible damage observed on the sleeves during the test, confirming that the sleeves experienced significant inelastic deformation.

The elastic damping for SJS 3 was approximately 10%, which is higher than the 5% typically observed in CIP columns. This additional 5% damping may be attributed to the initial cracks in the socket wall and grout that occurred early in the test, as well as some unidentified noises observed during the cycles before the yield displacement.

The overall displacement behavior of SJS 3 was governed primarily by strain penetration and rocking. Flexural displacements accounted for approximately 25% of the total displacement, while strain penetration and rocking contributed around 65%. This indicates that strain penetration and rocking play a more significant role in socket connections when the failure mechanism is attributed to grout crushing.

5.5. Experimental Results for Specimen SJS-4

In this section, the data analysis and experimental results previously discussed in this chapter will be specifically applied to the experimental test SJS4. The results for SJS4 will be presented in detail, focusing on axial strains on the column and external socket, hysteretic damping, and calculated displacement components. This analysis provides insights into the column performance and behavior under the applied loading conditions, contributing to a comprehensive understanding of the system response.

5.5.1. Axial strain analysis for SJS-4

The strain profiles were calculated to assess the strain distribution along the RC column during the first cycles of each ductility displacement for SJS4, considering both loading directions. In this context, ″Pushing Cycles″ refers to the strain profiles when force is applied toward the north face of the column, while ″Pulling Cycles″ refers to when force is applied toward the south face.

Figure 5-95 and Figure 5-96 present the strain profiles of the extreme bar located on the north face of the specimen for cycles up to yielding and post-yield cycles, respectively. Similarly, Figure 5-97 and Figure 5-98 depict the strain profiles for the extreme bar on the south side of the specimen for cycles up to yielding and post-yield cycles. The maximum axial strain in tension before grout crushing occurred was approximately 4.0%, while a maximum strain of 2.0% was reached in compression. These strain profiles indicate a spread of plasticity extending approximately 28 inches from the external socket interface.

A detailed examination of the strains on the reinforcing bars can be achieved by plotting the strain throughout the displacement history for each gauge length. Figure 5-99 and Figure 5-100 present the strain history of the extreme bars located on the north and south faces of the specimen at the first gauge length above the external socket. For both extreme bars, it was observed that the maximum strain reached during the experimental test was approximately 3.5% when the bar was in tension. Following grout crushing, the column began to exhibit rocking behavior.

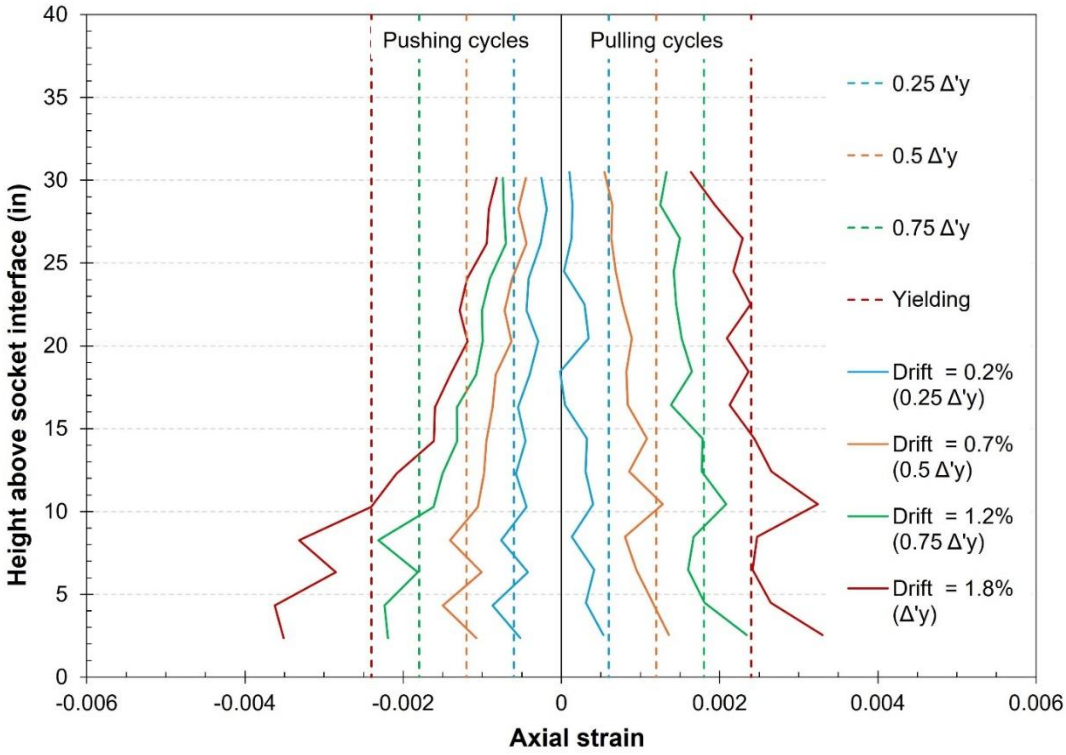


Figure 5-95. Strain profile up to first yield cycle for SJS4 on the north side of the column

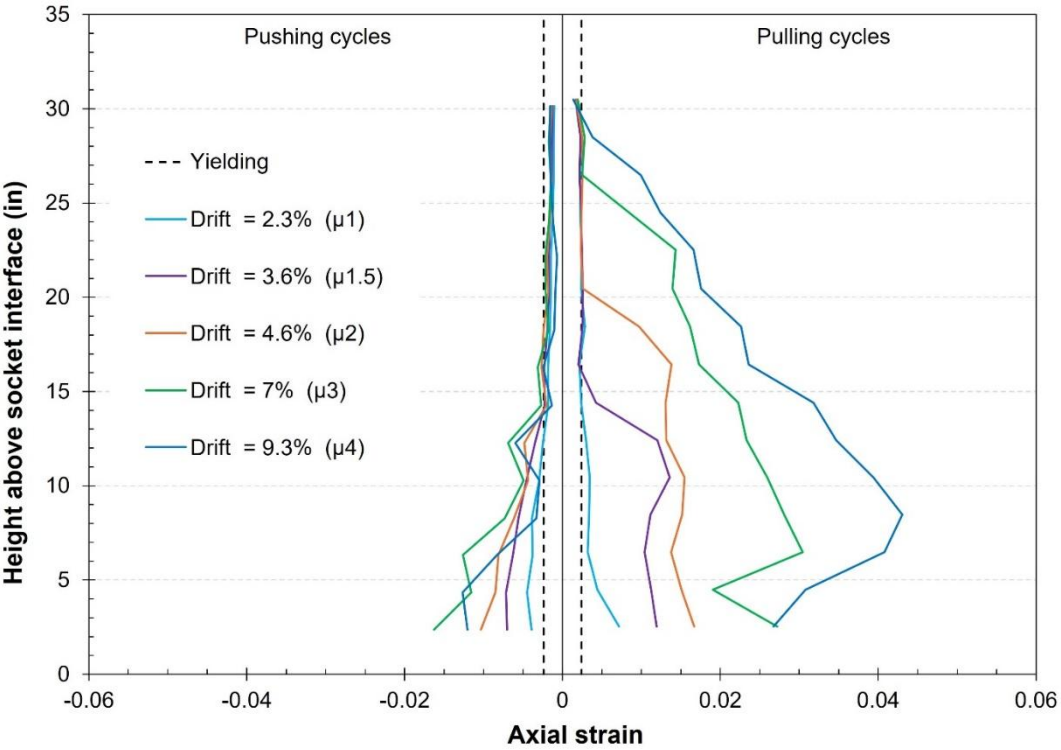


Figure 5-96. Strain profile for post-yield cycles for SJS4 on the north side of the column

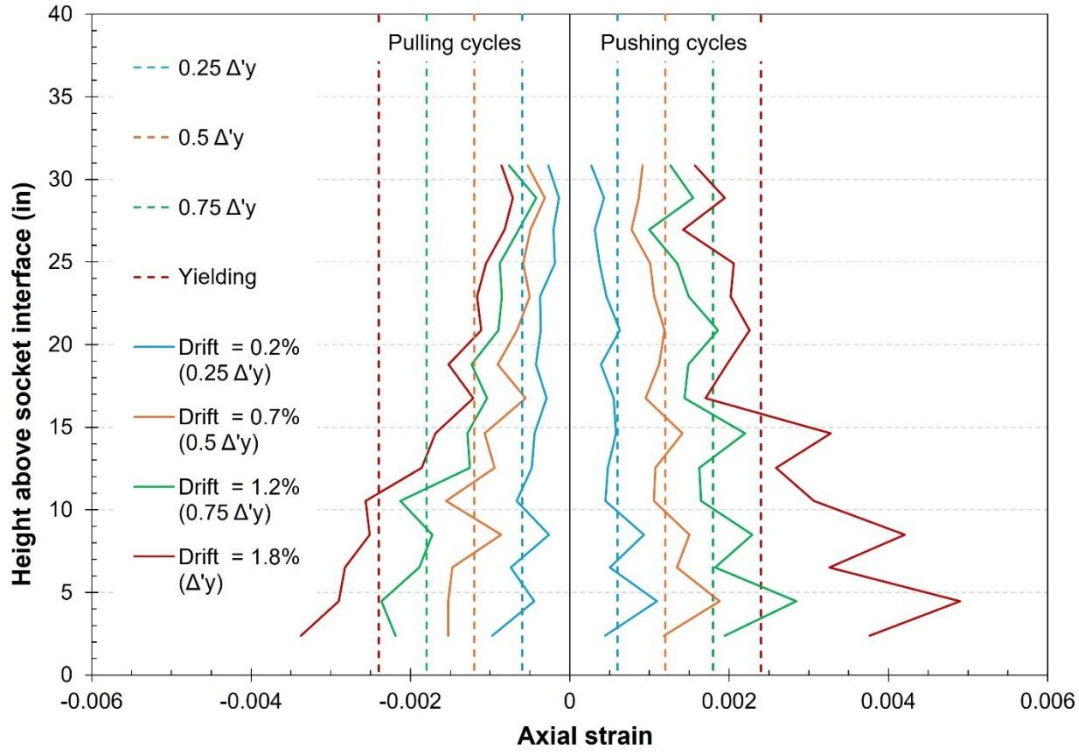


Figure 5-97. Strain profile up to first yield cycle for SJS4 on the south side of the column

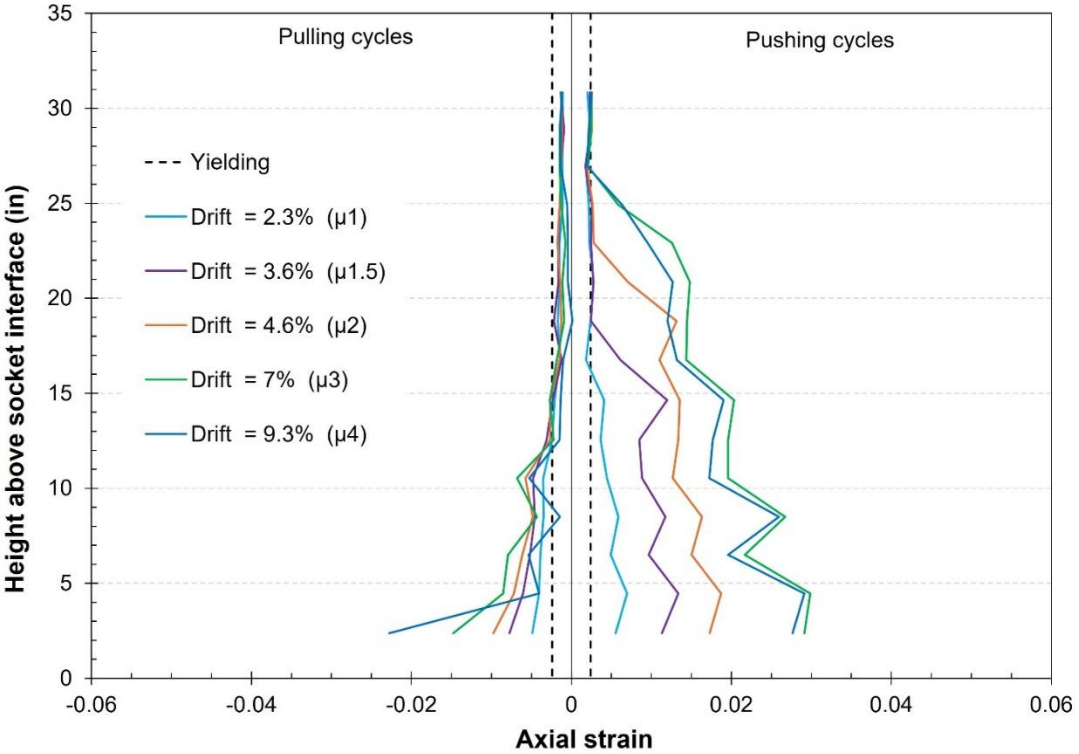


Figure 5-98. Strain profile for post-yield cycles for SJS4 on the south side of the column

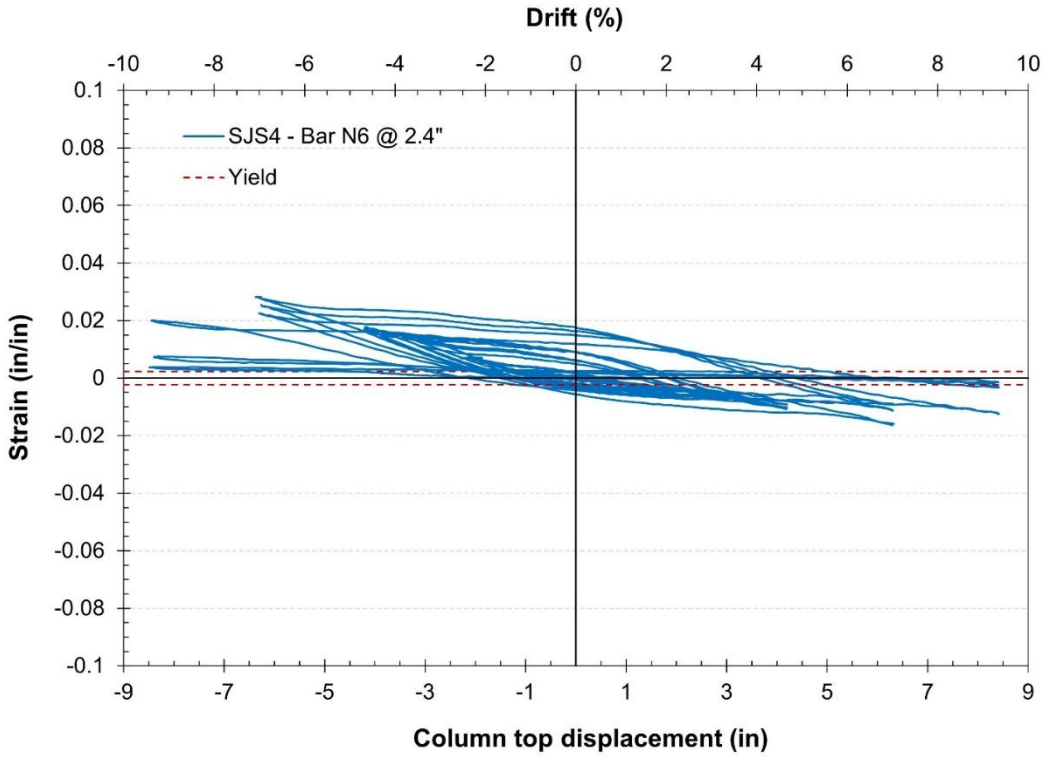


Figure 5-99. Strain vs displacement history for N6 of SJS4

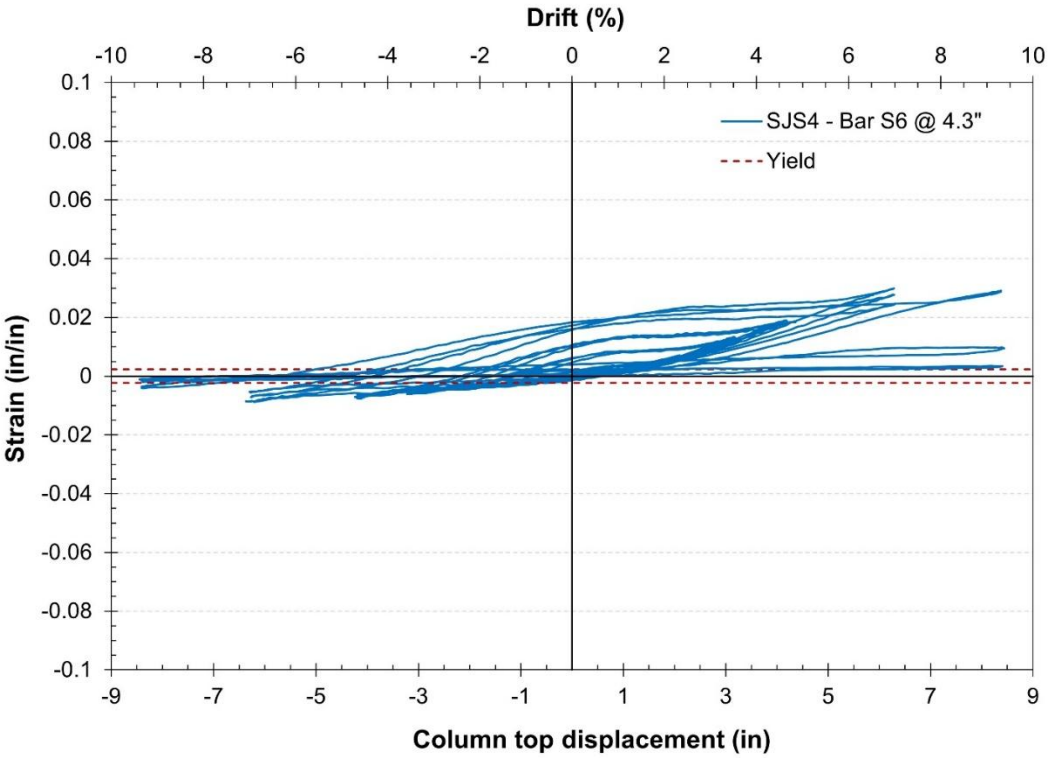


Figure 5-100. Strain vs displacement history for S6 of SJS4

Additionally, the strain history of the extreme bars in the external socket wall reinforcement was monitored using strain gauges placed 2 inches above the footing. Figure 5-101 and Figure 5-102 present the strain history for the extreme bars on the north and south faces, respectively. The data shows that the reinforcement in the external socket wall reached twice the yield strain on the north side. For the extreme bar on the south side, the strains were obtained at six inches above the footing, where the strains remained elastic.

The axial strains on the external socket sleeve were measured using DIC. In this context, the horizontal strains correspond to the hoop forces acting around the circumference, while the vertical strains reflect any flexion sustained by the sleeves. Figure 5-103 and Figure 5-104 present the strains on the north face of the specimen while Figure 5-105 and Figure 5-106 show the strains on the south face. The data indicates that, for the horizontal strains, the top 7 inches of the socket experienced strain values of 0.6%, while the remainder of the socket height remained elastic. The vertical strains reached yielding at the top 3 inches of the socket, with the rest of the socket height staying elastic throughout the experimental test.

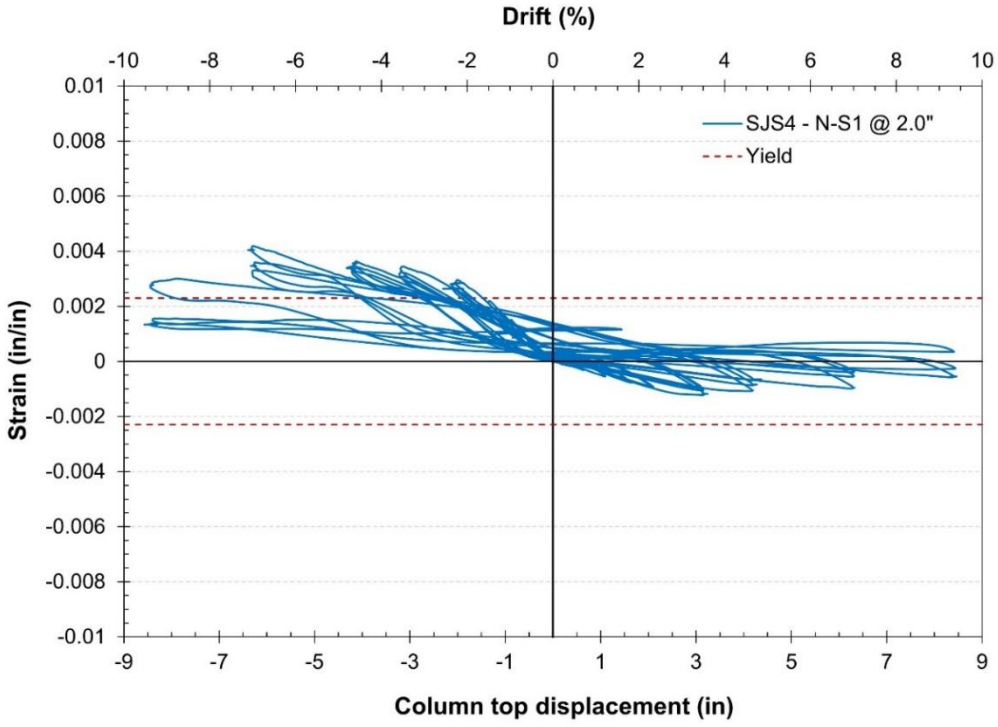


Figure 5-101. Strain vs displacement history for the extreme bar of socket wall reinforcement at the north side of SJS4

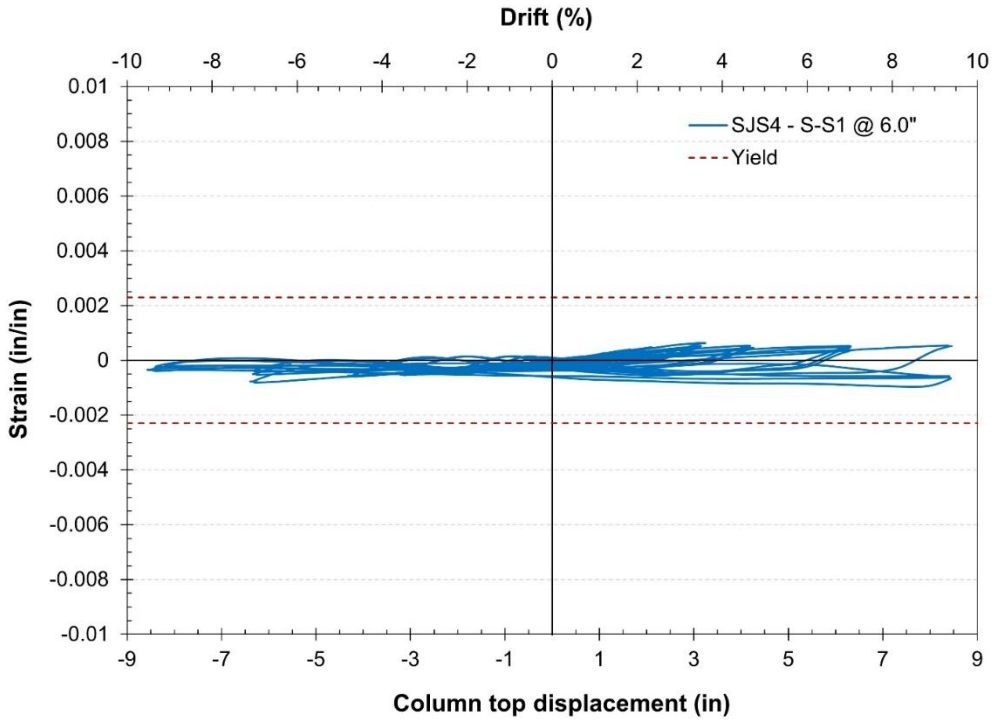


Figure 5-102. Strain vs displacement history for the extreme bar of socket wall reinforcement at the north side of SJS4

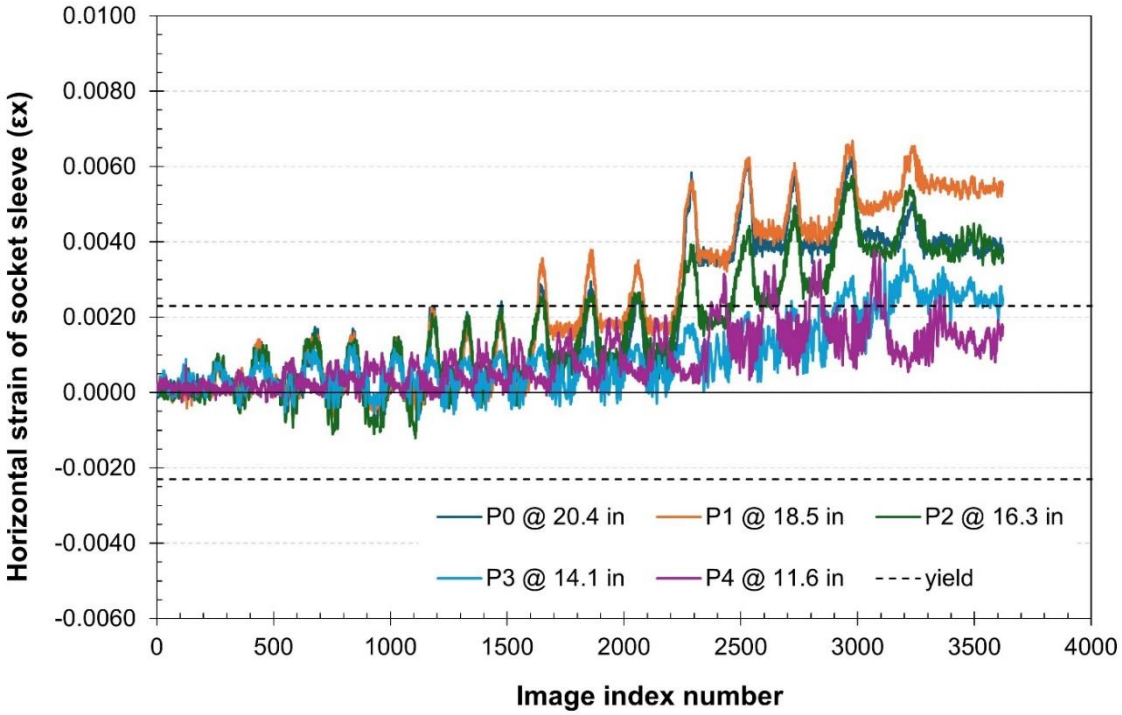


Figure 5-103. Horizontal strain history of external socket sleeve at the north side of SJS4

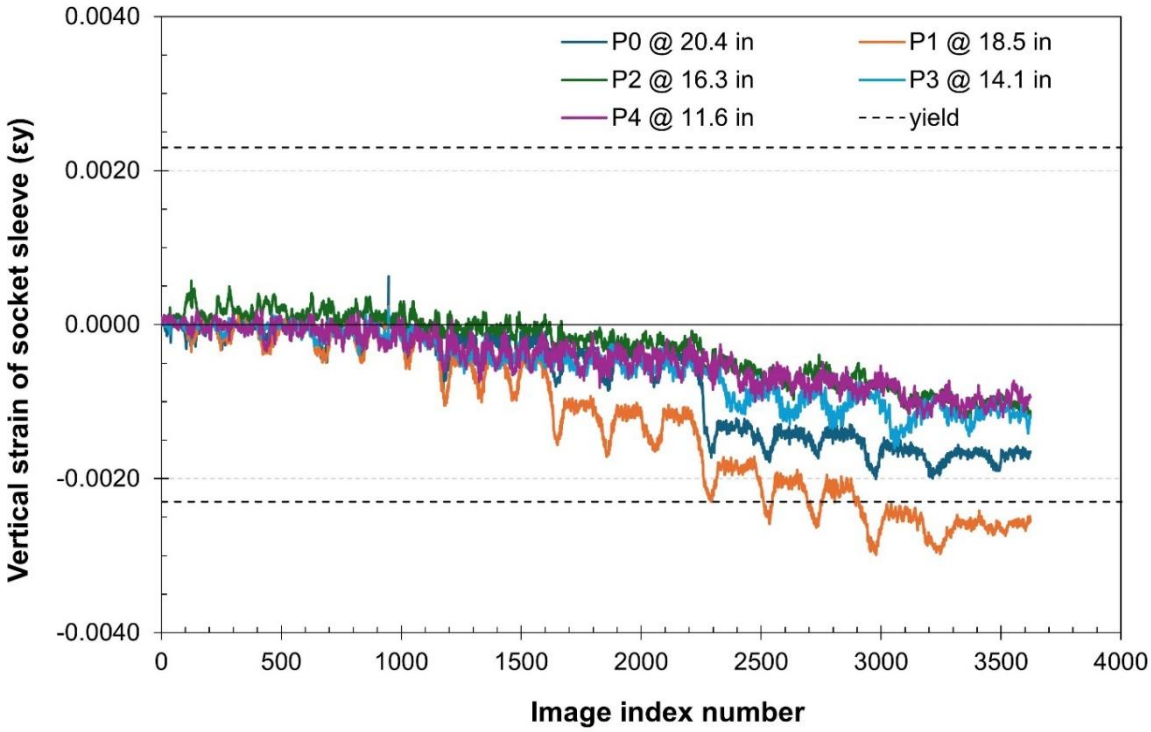


Figure 5-104. Vertical strain history of external socket sleeve at the north side of SJS4

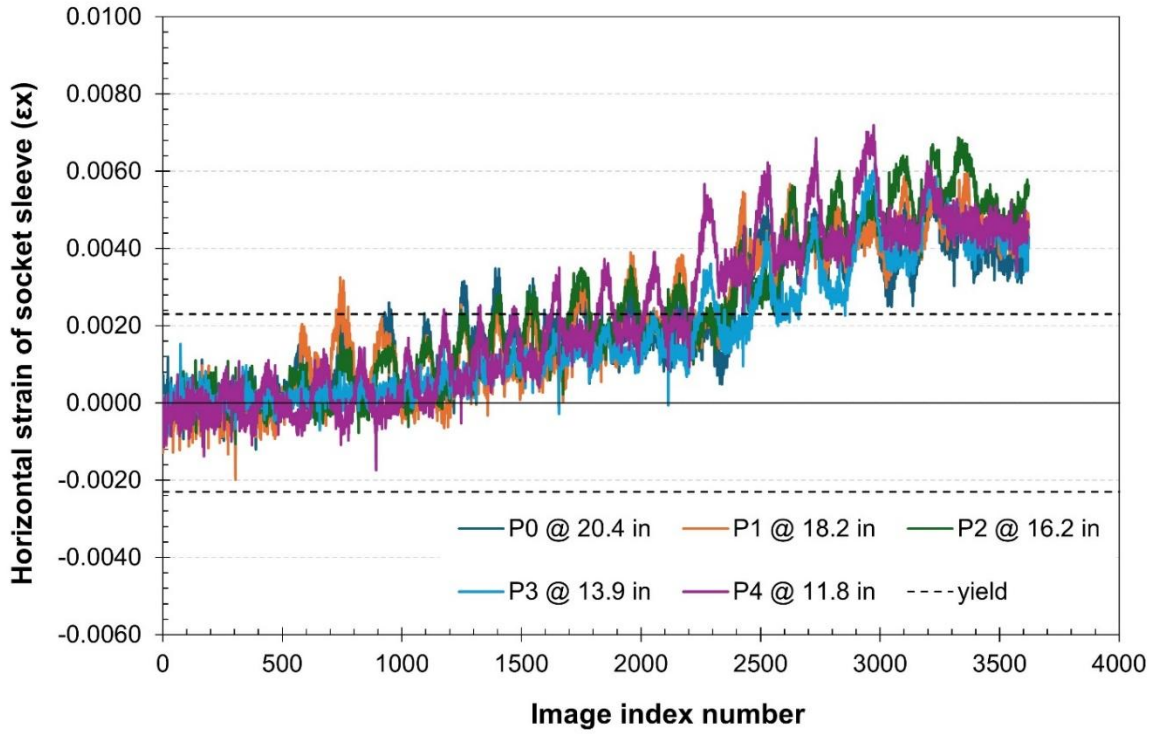


Figure 5-105. Horizontal strain history of external socket sleeve at the south side of SJS4

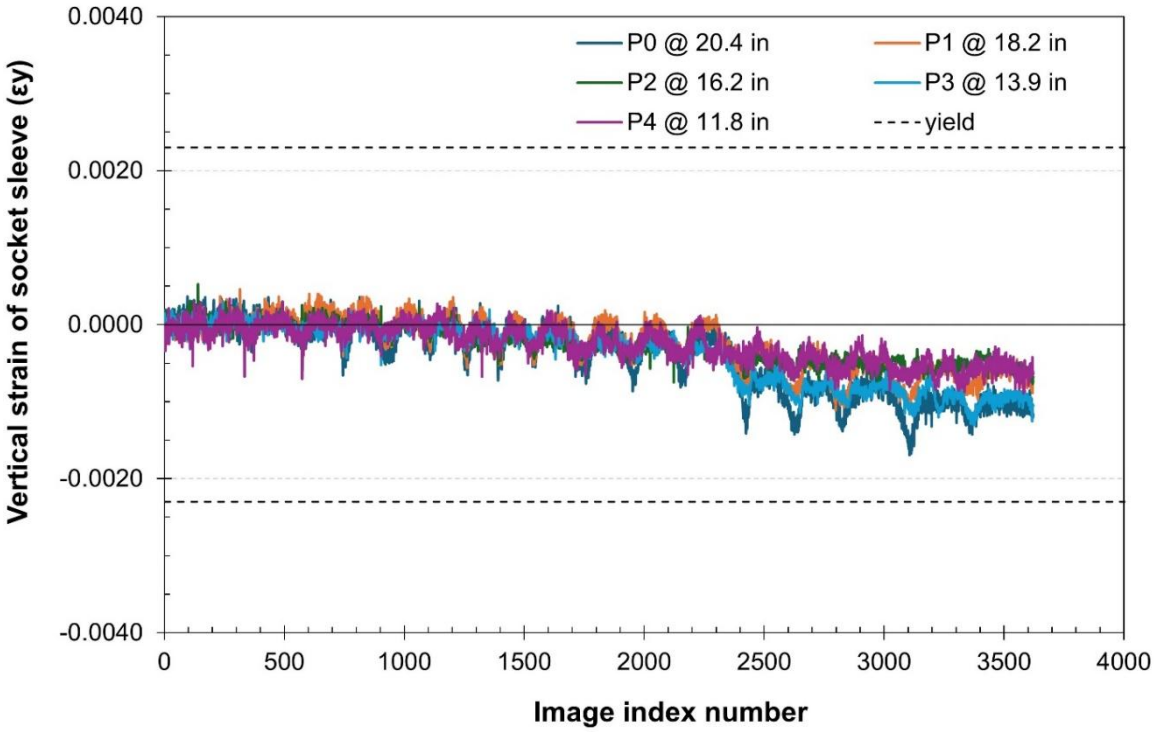


Figure 5-106. Vertical strain history of external socket sleeve at the south side of SJS4

5.5.2. Energy dissipation and hysteretic damping for SJS-4

Energy dissipation is important in understanding a structure seismic behavior because it relates to the structural element damage and energy dissipation capacity. Figure 5-107 illustrates the energy dissipation for all ductility displacement cycles for SJS4, with a total energy dissipation of 9053 kip-in. Notably, during the third cycle of ductility three, where the grout was crushed, the energy dissipated was reduced by 20% compared to the first cycle at the same ductility level. This reduction highlights the impact of severe damage on the energy dissipation capacity of the column.

Additionally, Figure 5-108 presents the Jacobsen hysteretic damping values for SJS4, demonstrating that damping increases as the applied displacements grow and the column sustains more damage. Notably, the elastic damping for SJS4 was approximately 11%, which is 6% higher than what is typically observed in a CIP column, indicating enhanced energy dissipation during the structural element elastic behavior.

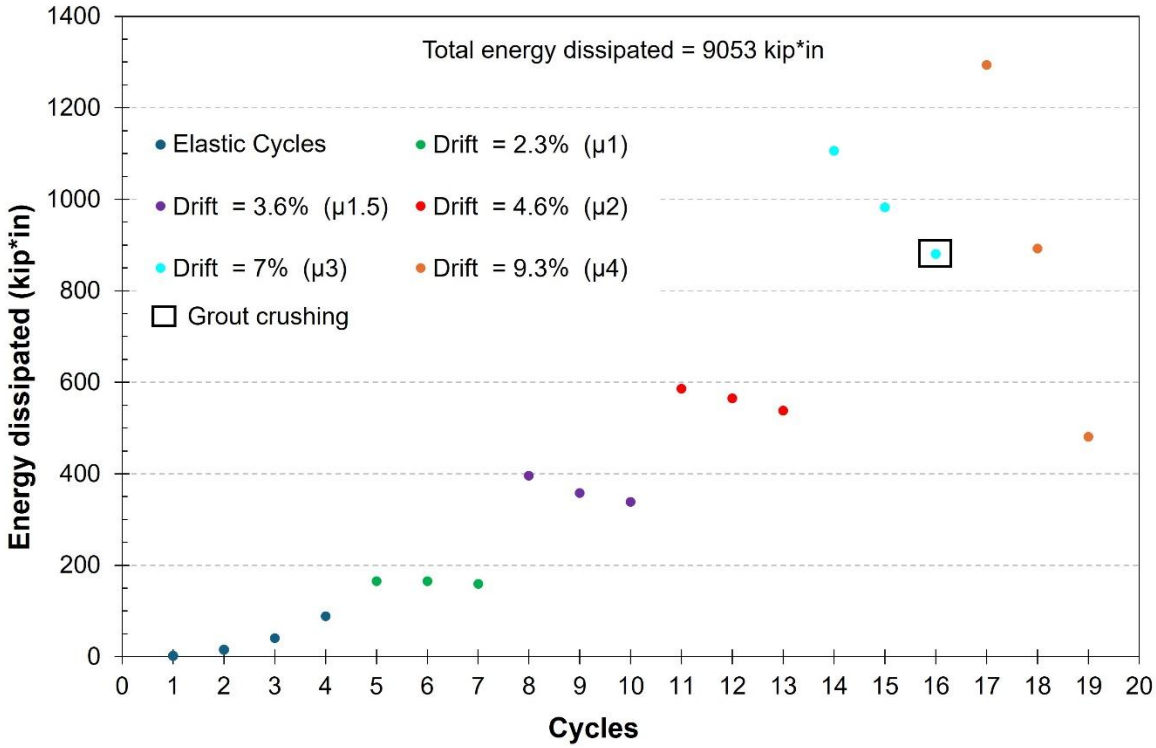


Figure 5-107. Energy dissipation plot for SJS4

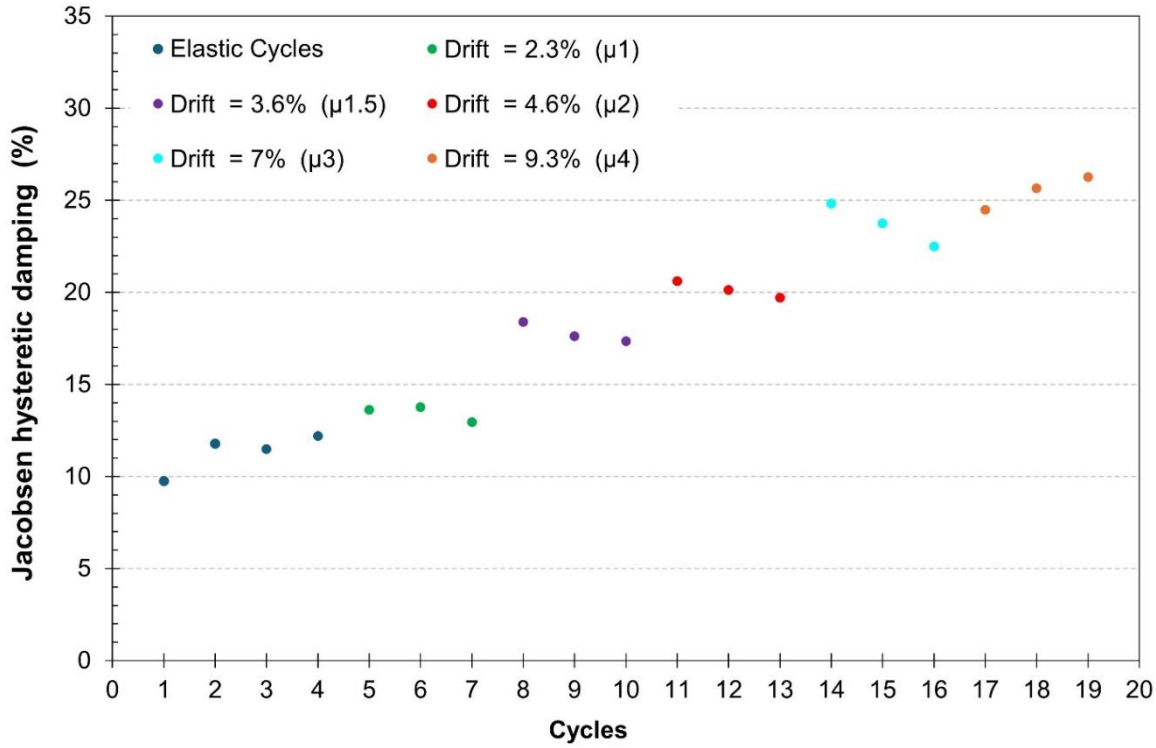


Figure 5-108. Hysteretic damping plot for SJS4

5.5.3. Displacement components for SJS-4

The displacement components considered in the calculations include flexural deformation, column rotation due to strain penetration and rocking, shear deformation of the column, and the deformation contribution resulting from socket rotation. The methodologies for these calculations have been detailed earlier in Section 5.1.3 of this report.

The flexural displacement component was derived from the column curvature, with the curvature profile shown in Figure 5-109 for the cycles up to yield and in Figure 5-110 for the post-yield cycles. The curvature is defined as positive when the column is pushed toward its north face. The dashed line in these figures represents the linear distribution of curvature, beginning at zero at the top of the column and reaching the yield curvature at the socket interface.

The displacement due to column rotation was calculated by determining the rotation angle at the base of the column and multiplying it by the column height above the socket. Figure 5-111 and Figure 5-112 present the column rotation for pushing and pulling cycles, respectively.

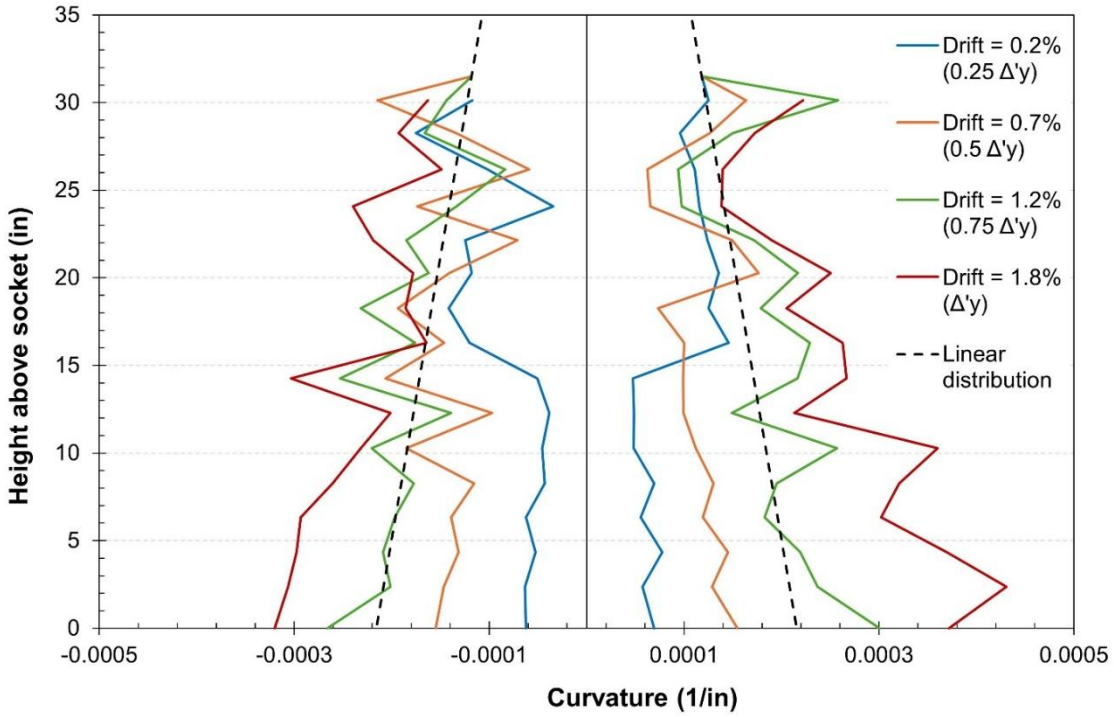


Figure 5-109. Curvature profile of the column up to the first yield cycle for SJS4

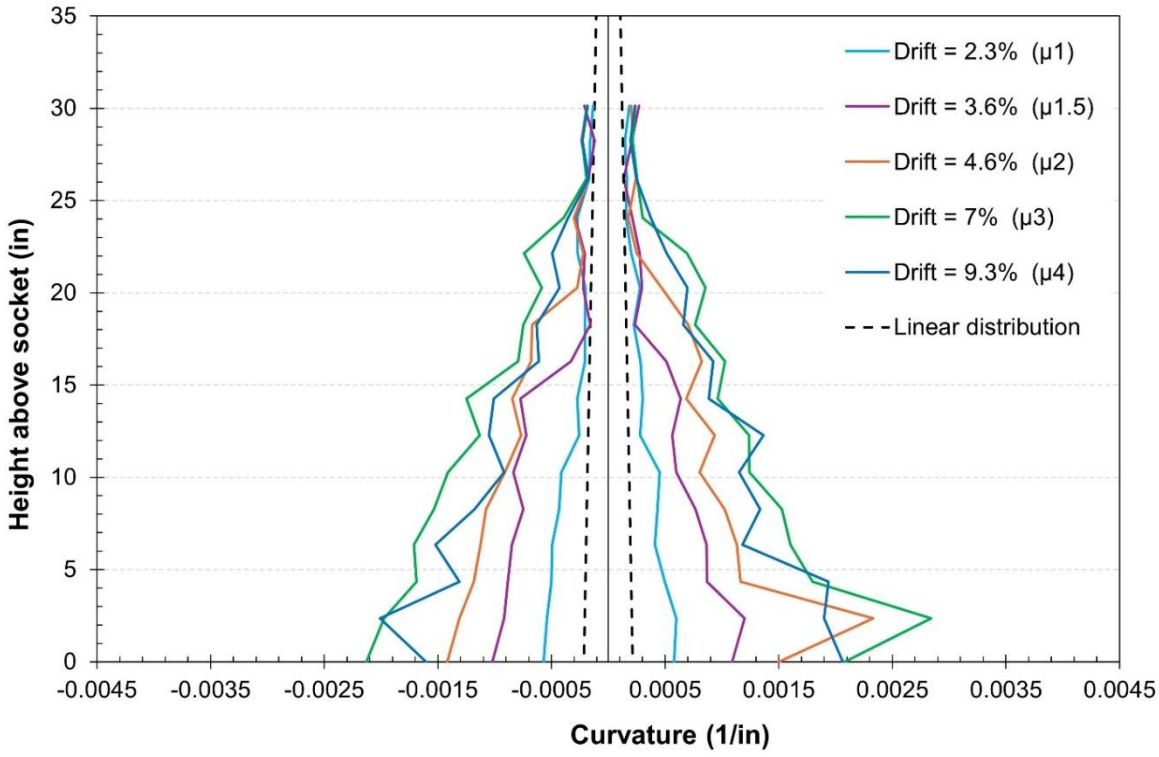


Figure 5-110. Curvature profile of the column for post-yield cycles for SJS4

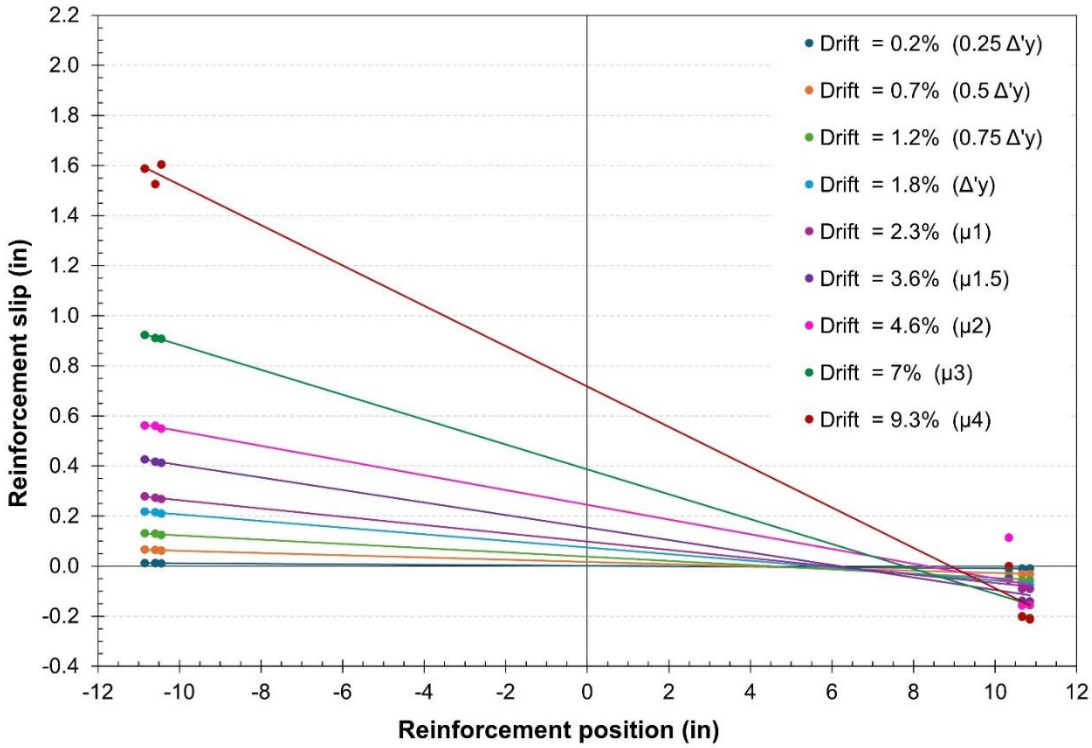


Figure 5-111. Rotation of the column for pushing cycles at the socket interface of SJS4

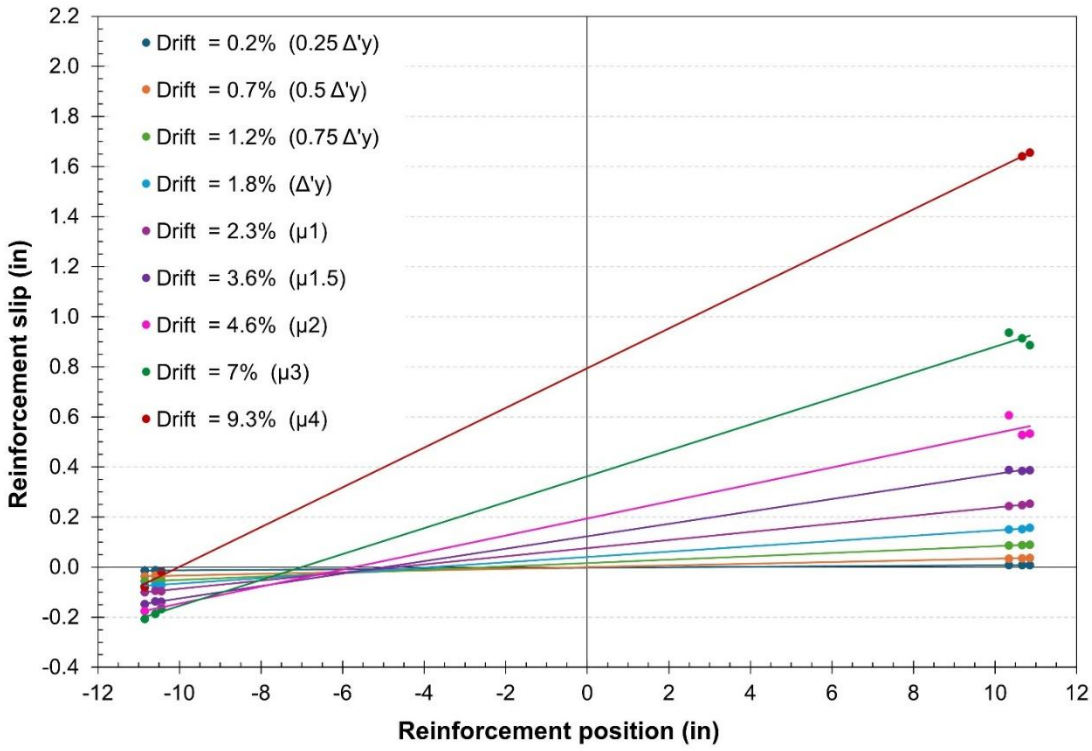


Figure 5-112. Rotation of the column for pulling cycles at the socket interface of SJS4

Figure 5-113 and Figure 5-114 present the shear strain distribution along the column height for the last three ductility displacements, as well as the yield displacement. These shear strains were then used to calculate the column shear displacement by multiplying the shear strain by the interval height. At 20 inches above the socket, the shear strains started to become constant, remaining approximately the same for all ductility displacements after yielding.

The displacement component resulting from socket rotation was obtained using DIC. Figure 5-115 and Figure 5-116 illustrate the socket rotation throughout the experimental test for the north and south faces, respectively. Socket rotation was measured at five different locations along the height, and an average value was used for displacement calculations due to the uniform distribution observed along the socket height. The averaged socket rotation, when multiplied by the socket height, provided the displacement component attributed to socket rotation.

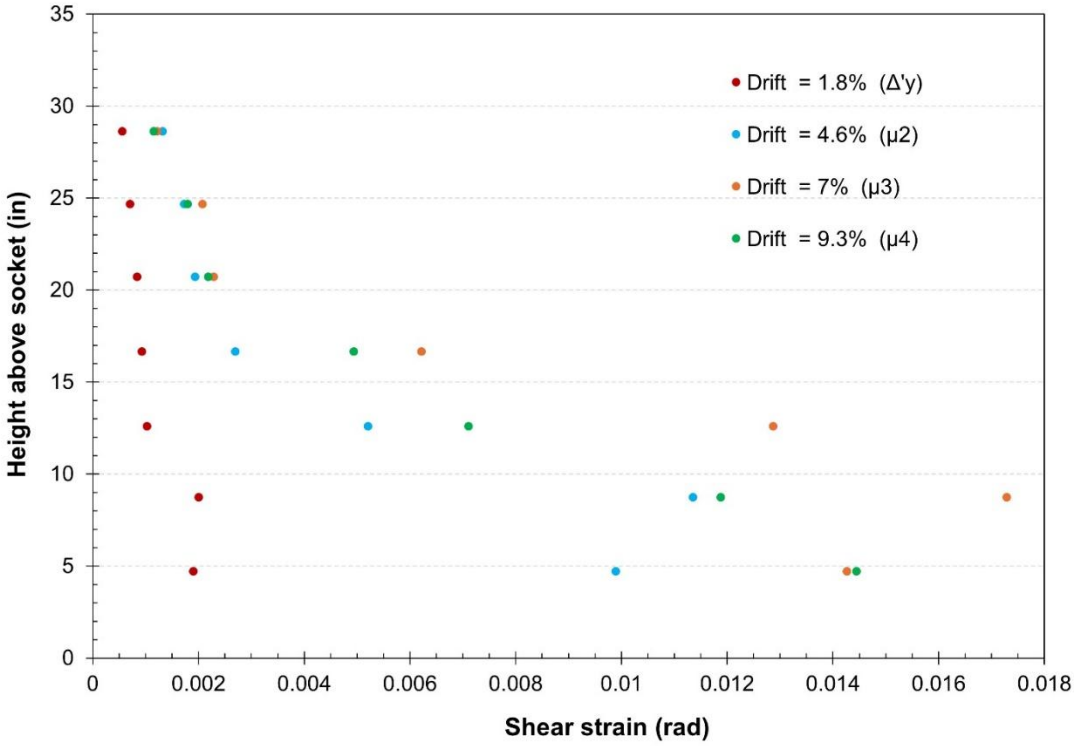


Figure 5-113. Shear strain distribution of the column for pushing cycles for SJS4

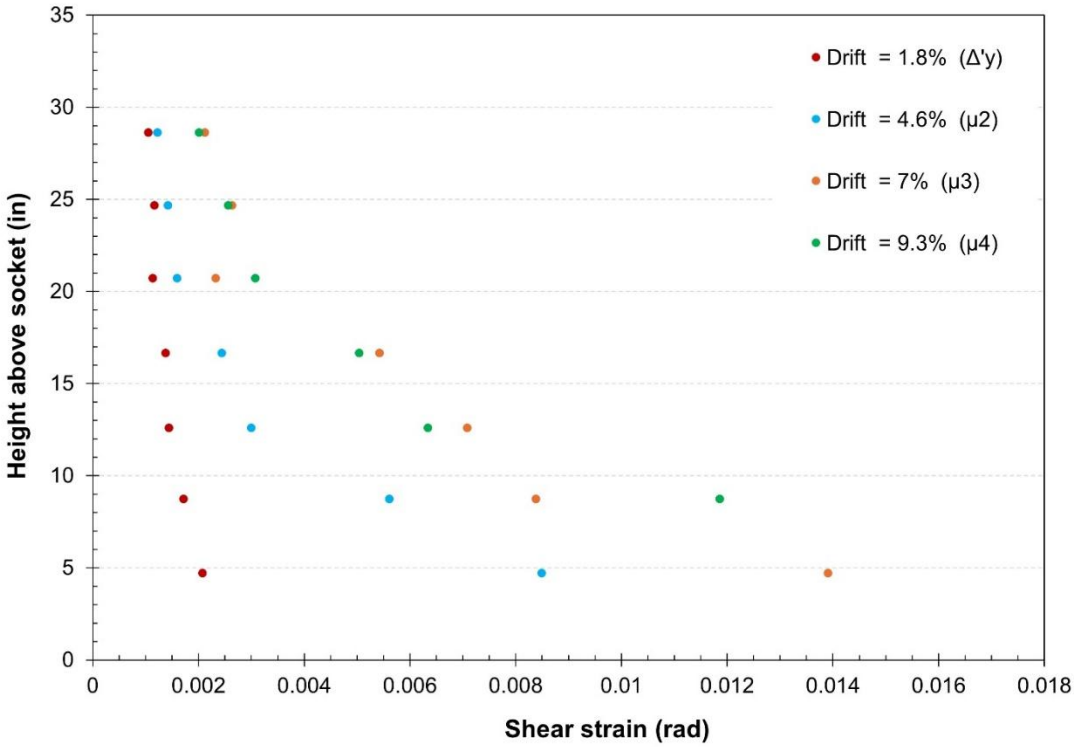


Figure 5-114. Shear strain distribution of the column for pulling cycles for SJS4

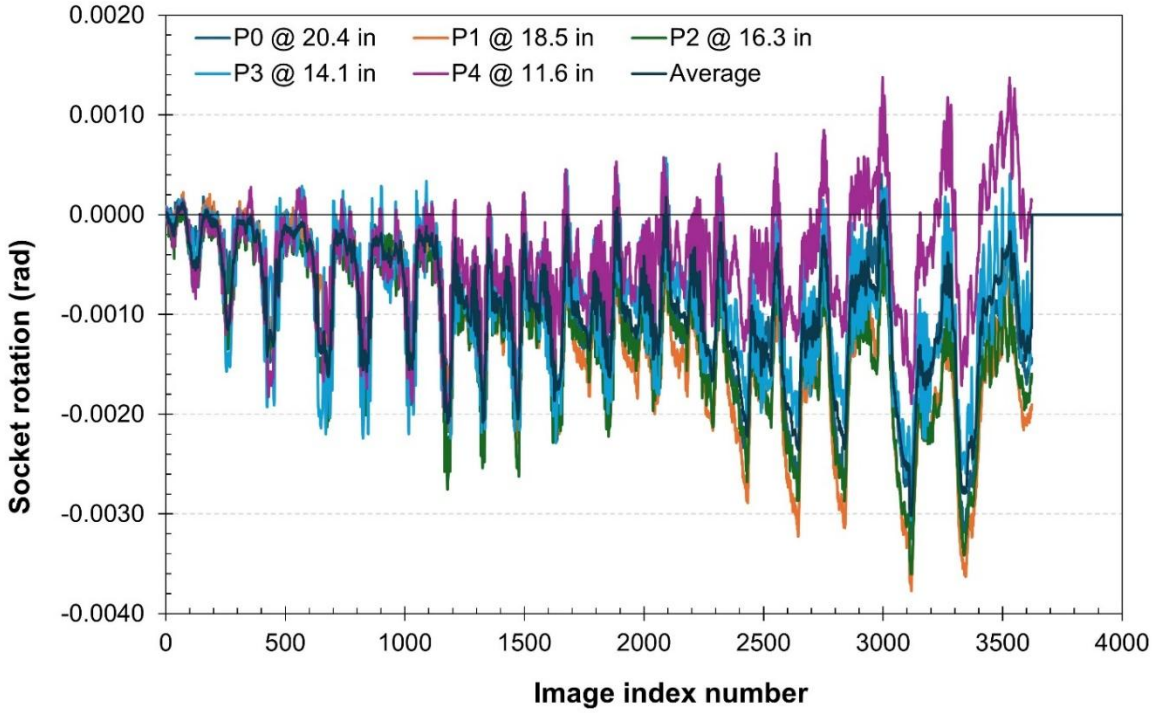


Figure 5-115. Socket rotation at the north side of SJS4

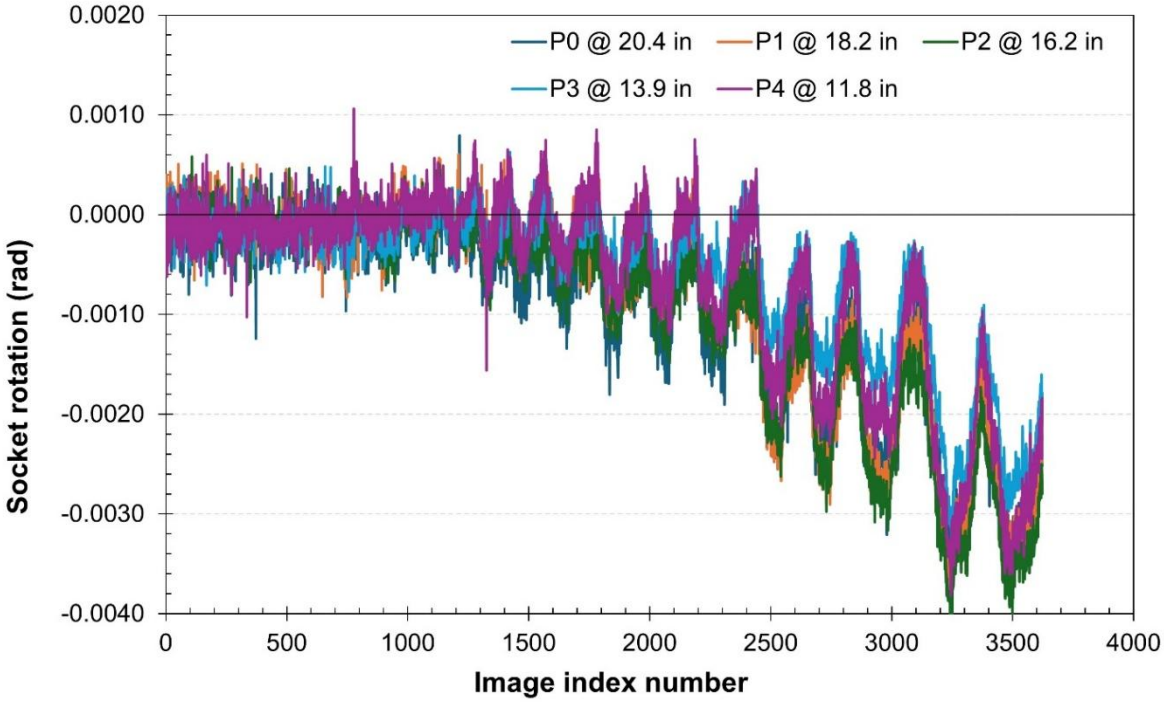


Figure 5-116. Socket rotation at the south side of SJS4

Table 5-7 and Table 5-8 present the contributions of the different components to the total displacement. Additionally, Figure 5-117 and Figure 5-118 illustrate the component displacements for pushing and pulling cycles following the first yield. The calculated displacement components closely match the measured values, validating the accuracy of the calculation methodology. The difference between the measured and calculated displacements is around 7% for most ductility displacements.

Table 5-7. Displacement components for pushing cycles for SJS 4

Displacement component (in)	**Δ'y**	**μ1**	**μ1.5**	**μ2**	**μ3**	**μ4**
Measured displacement	1.65	2.05	3.24	4.15	6.28	8.38
Flexural	0.54	0.64	1.08	1.53	2.10	1.85
Strain penetration and rocking	0.92	1.15	1.74	2.05	3.46	5.79
Shear	0.05	0.07	0.15	0.19	0.28	0.23
Socket rotation	0.04	0.04	0.05	0.05	0.06	0.07
Calculated displacement error	0.10	0.14	0.23	0.33	0.38	0.44
Calculated displacement error (%)	5.9%	7.0%	7.0%	8.0%	6.1%	5.3%

Table 5-8. Displacement components for pulling cycles for SJS 4

Displacement component (in)	**Δ'y**	**μ1**	**μ1.5**	**μ2**	**μ3**	**μ4**
Measured displacement	1.33	2.01	3.17	4.14	6.29	8.40
Flexural	0.46	0.61	1.03	1.35	1.95	1.63
Strain penetration and rocking	0.74	1.13	1.73	2.37	3.60	5.52
Shear	0.08	0.09	0.10	0.15	0.26	0.29
Socket rotation	0.01	0.01	0.02	0.03	0.05	0.08
Calculated displacement error	0.05	0.17	0.30	0.24	0.43	0.87
Calculated displacement error (%)	3.5%	8.5%	9.5%	5.7%	6.9%	10.4%

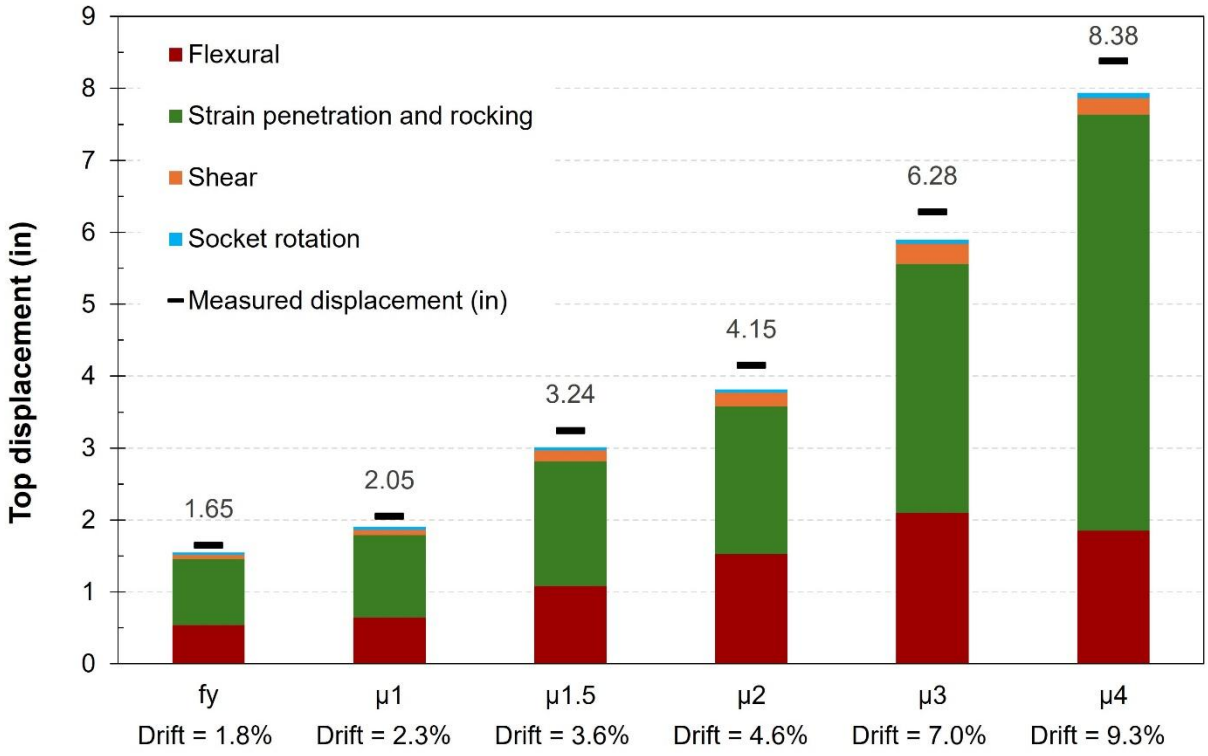


Figure 5-117. Displacement components for pushing cycles for SJS4

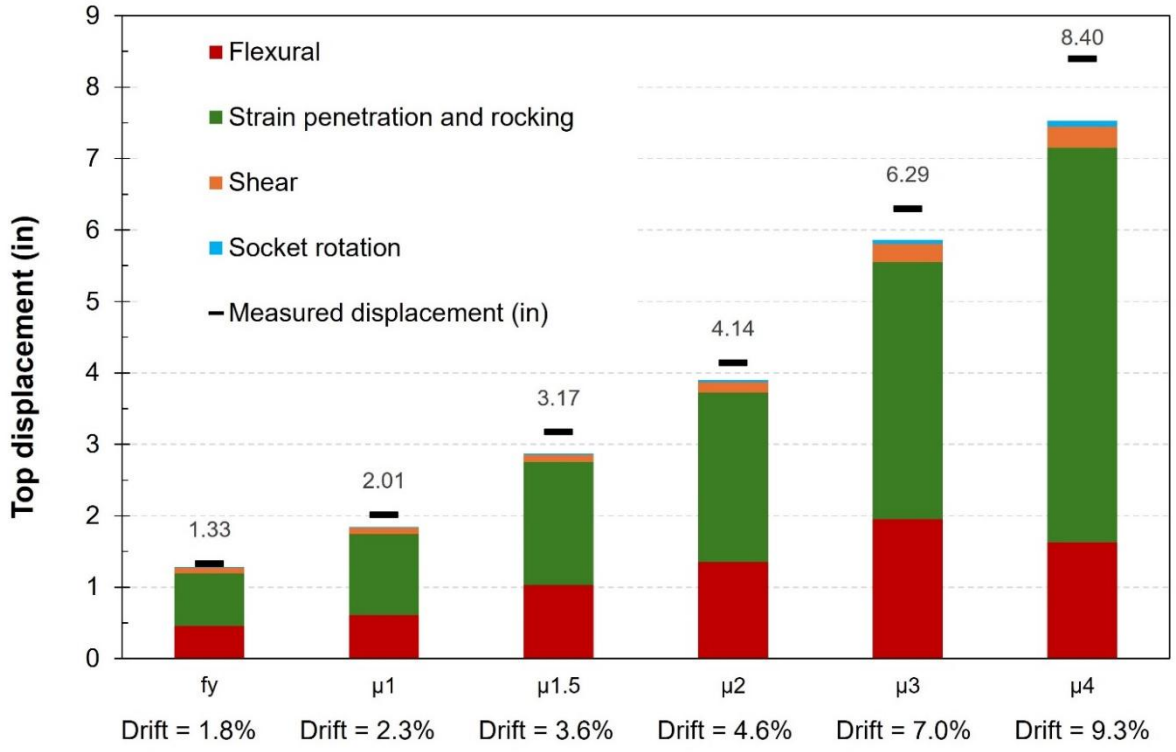


Figure 5-118. Displacement components for pulling cycles for SJS4

When comparing the displacement components, it was observed that shear and socket rotation had a relatively small impact on the column total displacement. Flexural displacement contributed around 30% of the total displacement, while strain penetration and rocking of the column contributed significantly to the overall displacement, with more than 55% of the total displacement. Therefore, the primary displacement component was due to rotational effects, particularly for a socket height of 0.85 Dc, where the failure mode was crushing of the grout.

5.5.4. Summary of Results for SJS-4

The tension strains in the longitudinal bars reached 4.0% before grout crushing occurred and the column experienced rocking. This behavior prevented the development of the full plastic hinge above the external socket connection. The strains in the external socket wall remained below the yield point throughout the test, confirming that the external socket connections effectively prevented plastic strains from reaching the foundation or cap beam. As a result, the footing remained as a capacity-protected element.

Horizontal strains in the external socket sleeve reached 0.6% of strain at the top third of the socket height but remained elastic for the rest of the height. This aligns with the visible damage observed on the sleeves during the test, confirming that the sleeves experienced significant inelastic deformation.

The elastic damping for SJS 4 was approximately 11%, which is higher than the 5% typically observed in CIP columns. This additional 6% damping may be attributed to the initial cracks in the socket wall and grout that occurred early in the test, as well as some unidentified noises observed during the cycles before the yield displacement.

The overall displacement behavior of SJS 4 was governed primarily by strain penetration and rocking. Flexural displacements accounted for approximately 30% of the total displacement, while strain penetration and rocking contributed around 55%. This indicates that strain penetration and rocking play a more significant role in socket connections when the failure mechanism is attributed to grout crushing.

5.6. Experimental Results for Specimen SJS-5

In this section, the data analysis and experimental results previously discussed in this chapter will be specifically applied to the experimental test SJS5. The results for SJS5 will be presented in detail, focusing on axial strains on the column and external socket, hysteretic damping, and calculated displacement components. This analysis provides insights into the column performance and behavior under the applied loading conditions, contributing to a comprehensive understanding of the system response.

5.6.1. Axial strain analysis for SJS-5

The strain profiles were calculated to assess the strain distribution along the RC column during the first cycles of each ductility displacement for SJS5, considering both loading directions. In this context, ″Pushing Cycles″ refers to the strain profiles when force is applied toward the north face of the column, while ″Pulling Cycles″ refers to when force is applied toward the south face.

Figure 5-119 and Figure 5-120 present the strain profiles of the extreme bar located on the north face of the specimen for cycles up to yielding and post-yield cycles, respectively. Similarly, Figure 5-121 and Figure 5-122 depict the strain profiles for the extreme bar on the south side of the specimen for cycles up to yielding and post-yield cycles. The maximum axial strain in tension before grout splitting occurred was approximately 2.5%, while a maximum strain of 2.0% was reached in compression. These strain profiles indicate a spread of plasticity extending approximately 25 inches from the external socket interface.

A detailed examination of the strains on the reinforcing bars can be achieved by plotting the strain throughout the displacement history for each gauge length. Figure 5-123 and Figure 5-124 present the strain history of the extreme bars located on the north and south faces of the specimen at the first gauge length above the external socket. For both extreme bars, it was observed that the maximum strain reached during the experimental test was approximately 2.5% when the bar was in tension. Following grout splitting, the column began to exhibit rocking behavior.

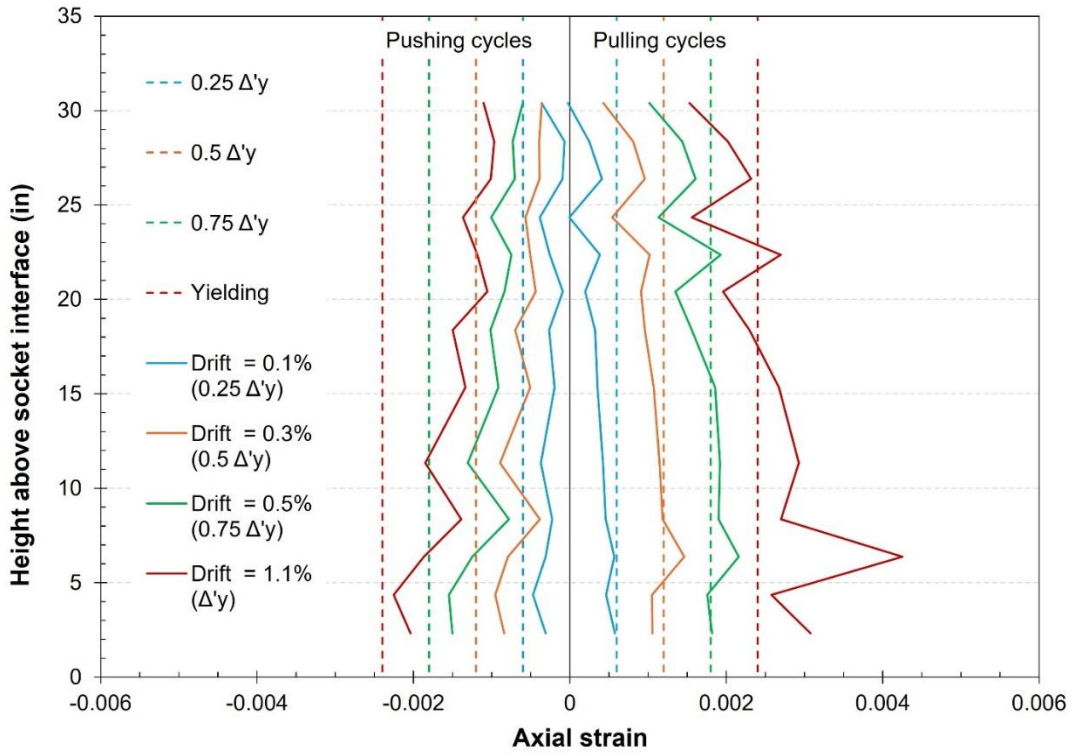


Figure 5-119. Strain profile up to first yield cycle for SJS5 on the north side of the column

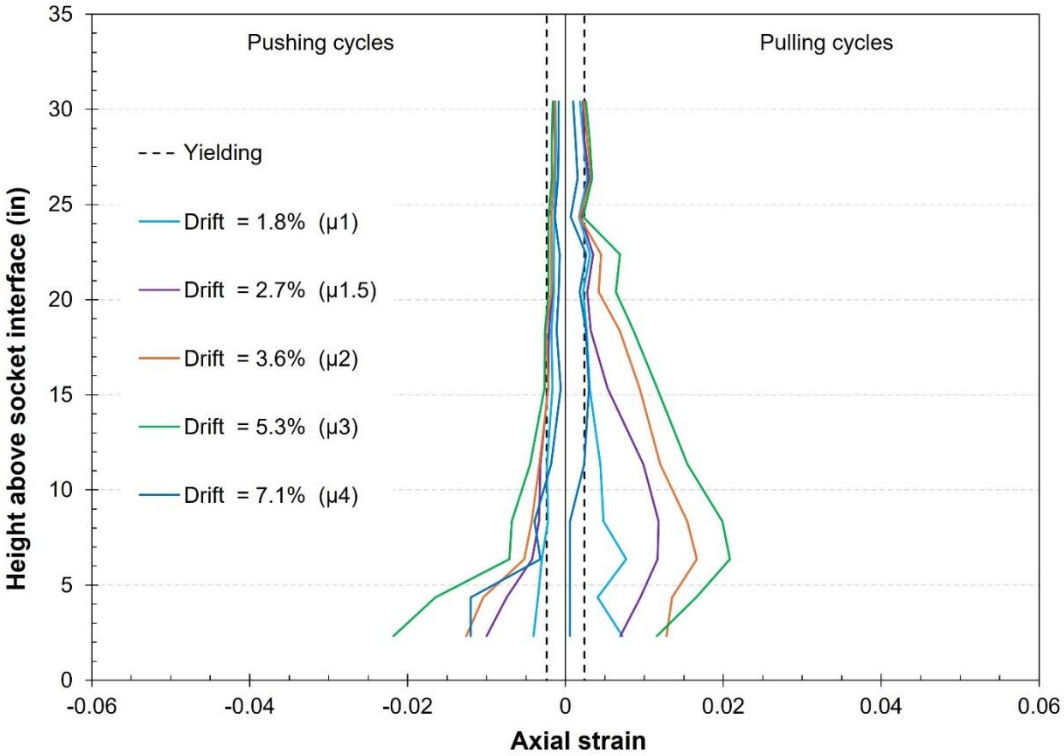


Figure 5-120. Strain profile for post-yield cycles for SJS5 on the north side of the column

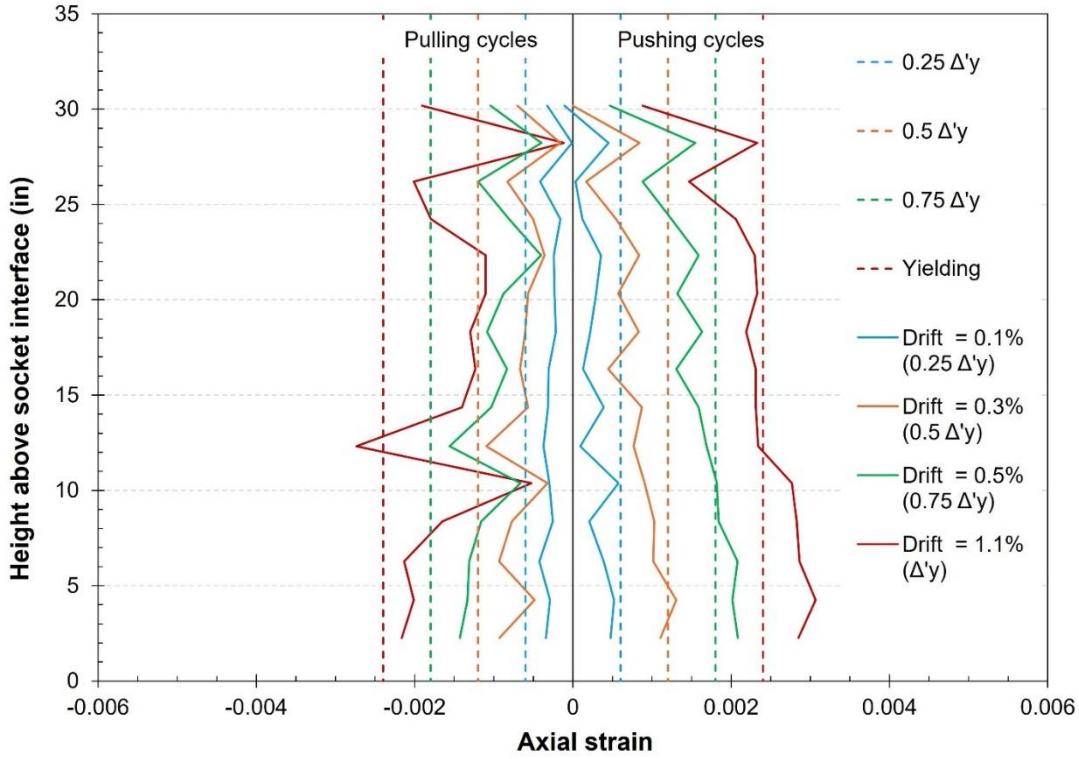


Figure 5-121. Strain profile up to first yield cycle for SJS5 on the south side of the column

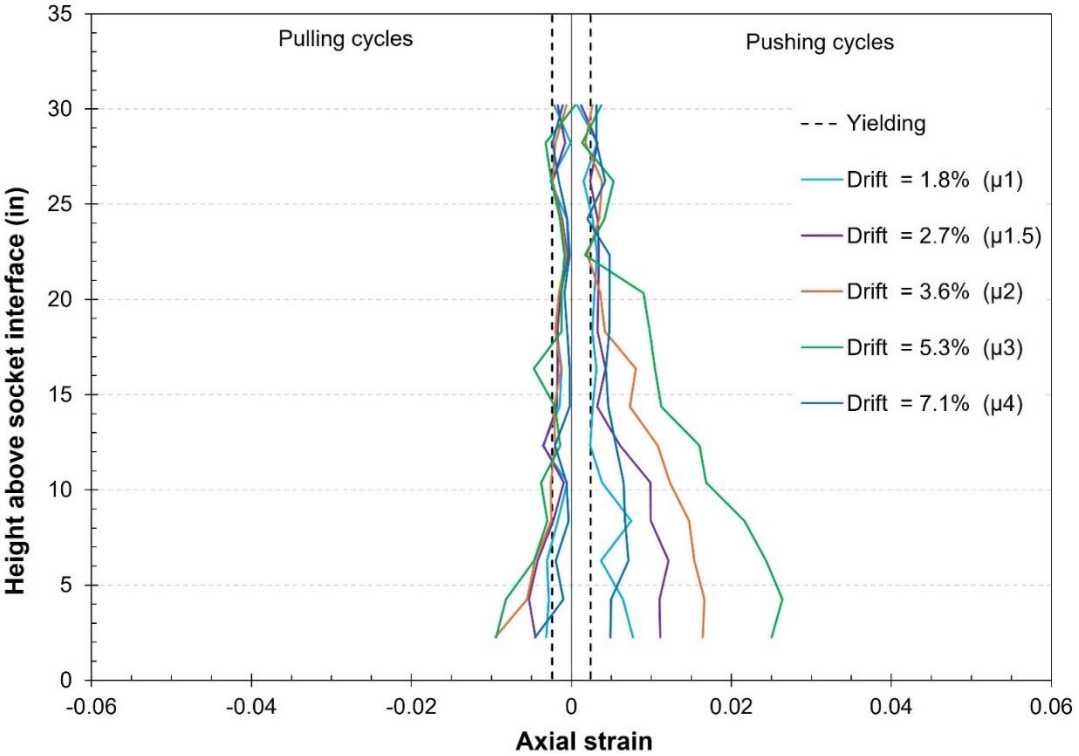


Figure 5-122. Strain profile for post-yield cycles for SJS5 on the south side of the column

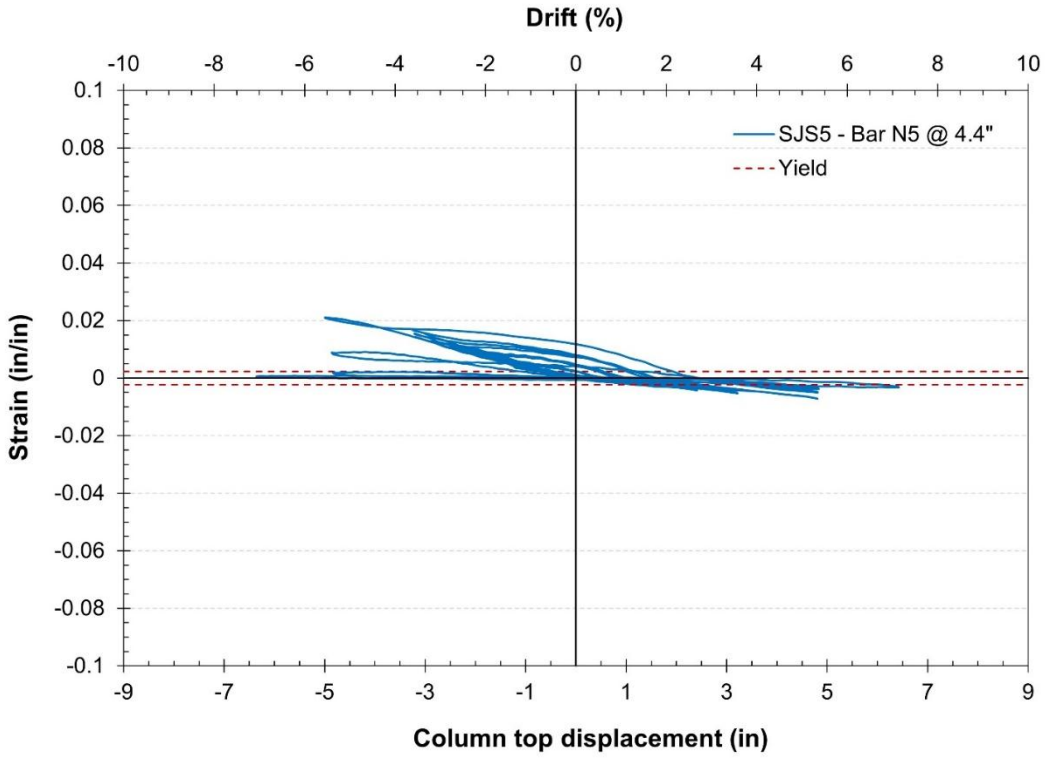


Figure 5-123. Strain vs displacement history for N5 of SJS5

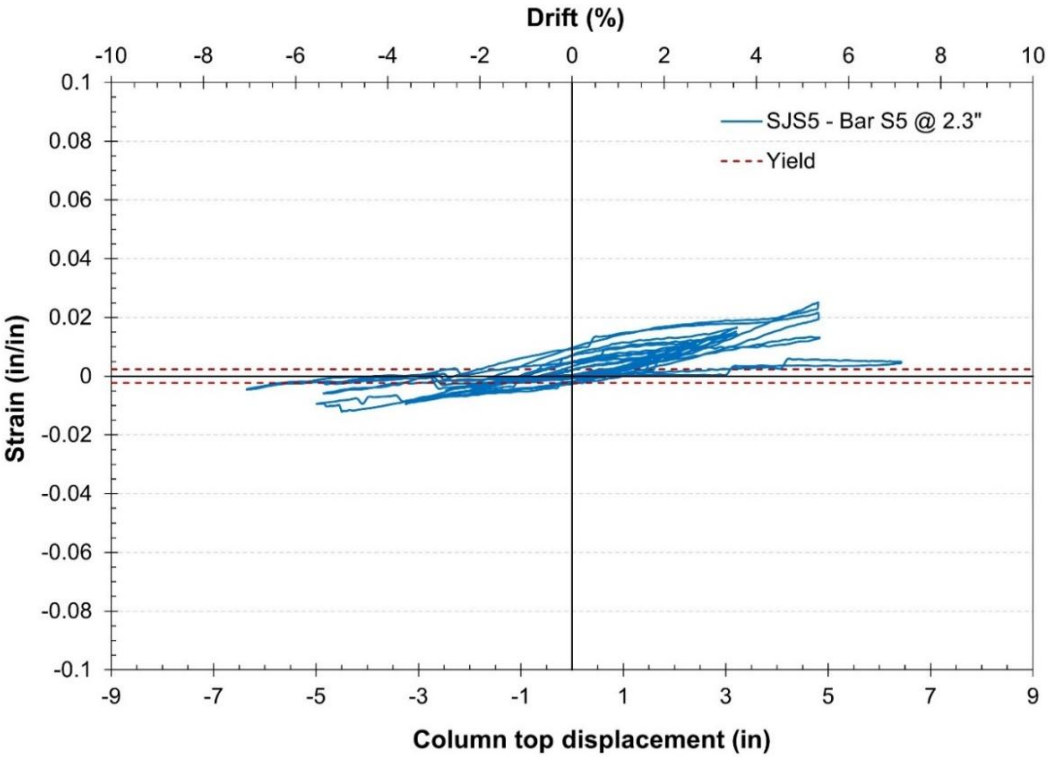


Figure 5-124. Strain vs displacement history for S5 of SJS5

Additionally, the strain history of the extreme bars in the external socket wall reinforcement was monitored using strain gauges placed 2 inches above the footing. Figure 5-125 and Figure 5-126 present the strain history for the extreme bars on the north and south faces, respectively. The data shows that the reinforcement in the external socket wall barely reached the yield point, indicating that the external socket wall remained elastic throughout the entire experimental test.

The axial strains on the external socket sleeve were measured using DIC. In this context, the horizontal strains correspond to the hoop forces acting around the circumference, while the vertical strains reflect any flexion sustained by the sleeves. Figure 5-127 and Figure 5-128 present the strains on the north face of the specimen while Figure 5-129 and Figure 5-130 show the strains on the south face. The data shows that, for the horizontal strains, the top 3 inches of the socket experienced the highest strain values, but the values were lower than the yield strain. Thus, the full height of the socket remained elastic on the horizontal strains. The vertical strains remained elastic throughout the experimental test, indicating that the external socket sleeve did not contribute significantly to the flexural behavior of the external socket wall.

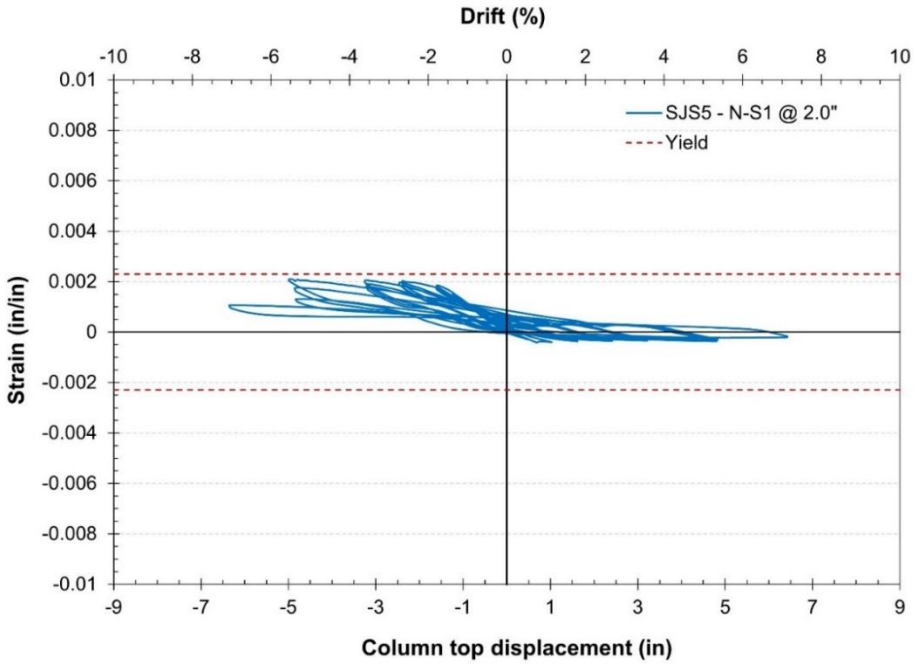


Figure 5-125. Strain vs displacement history for the extreme bar of socket wall reinforcement at the north side of SJS5

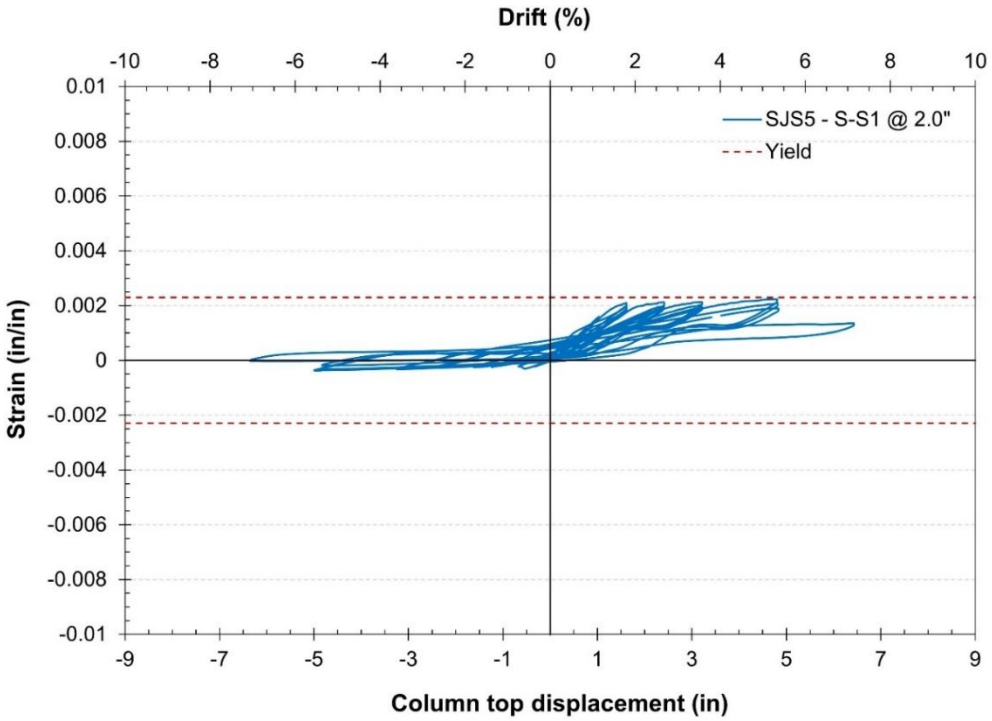


Figure 5-126. Strain vs displacement history for the extreme bar of socket wall reinforcement at the north side of SJS5

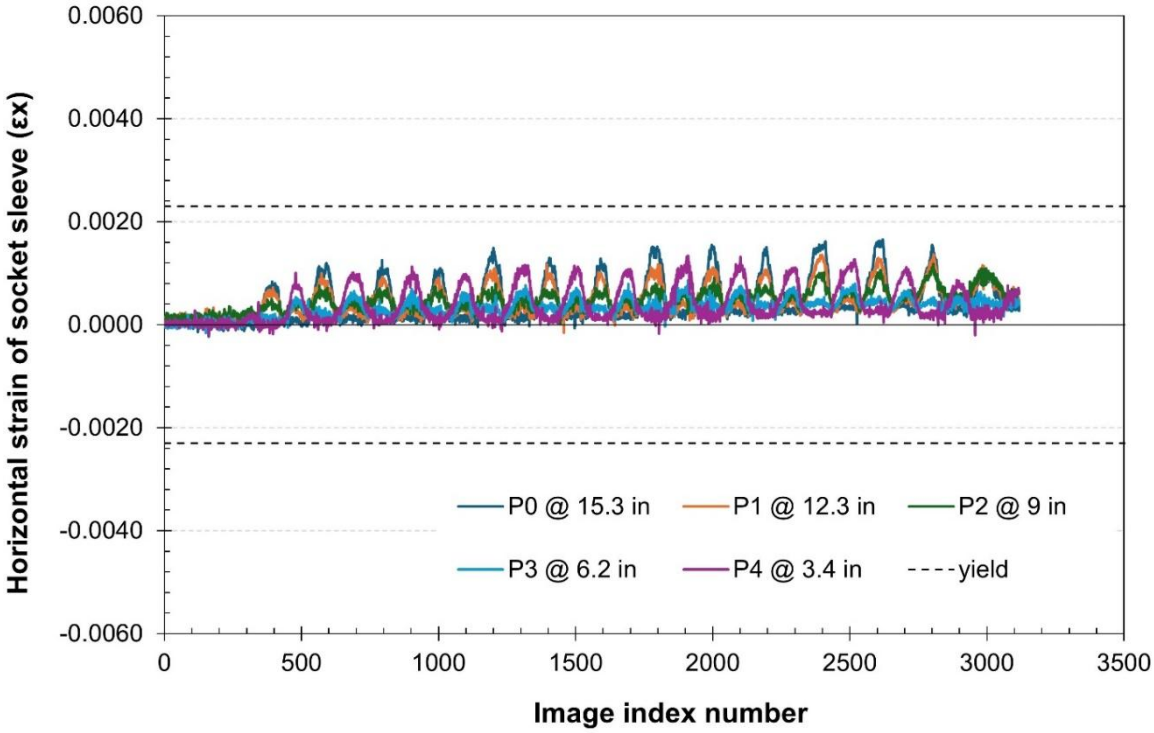


Figure 5-127. Horizontal strain history of external socket sleeve at the north side of SJS5

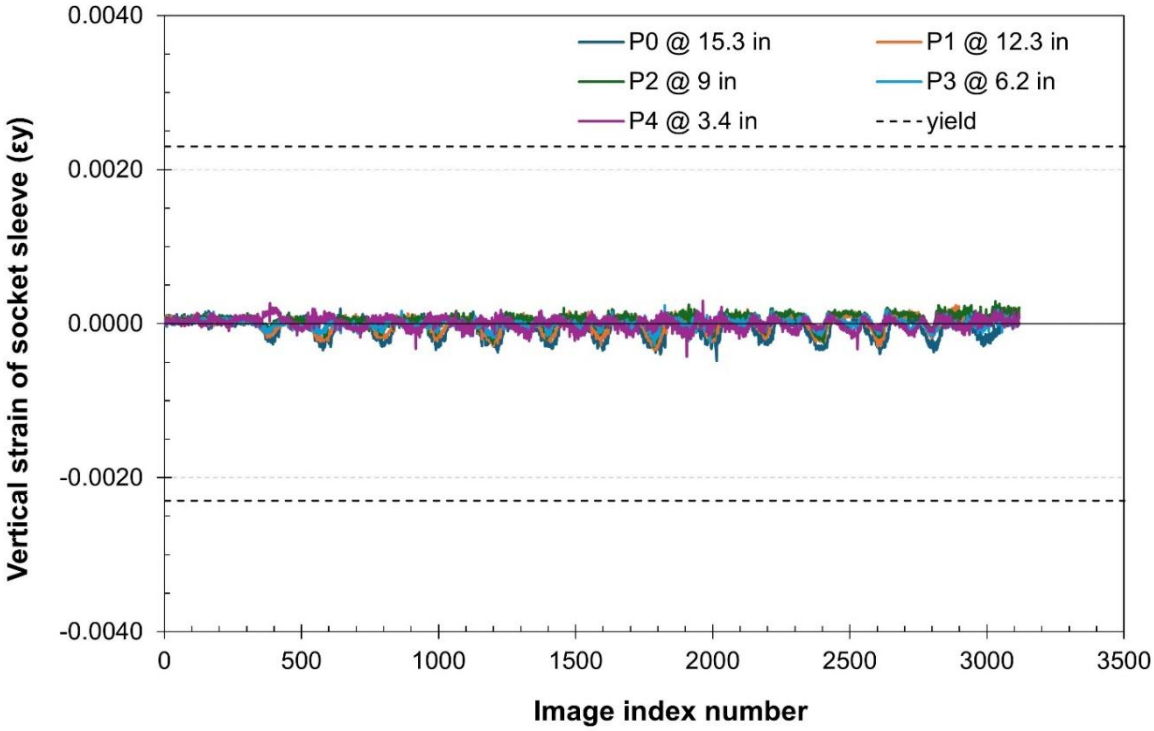


Figure 5-128. Vertical strain history of external socket sleeve at the north side of SJS5

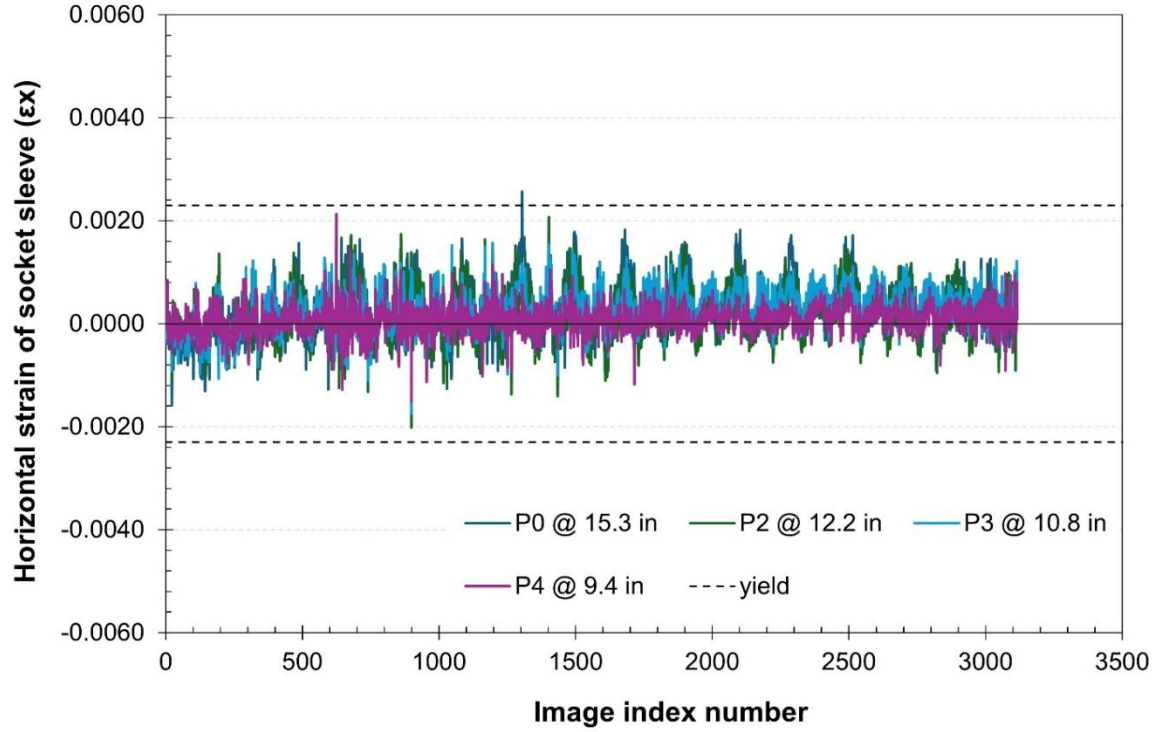


Figure 5-129. Horizontal strain history of external socket sleeve at the south side of SJS5

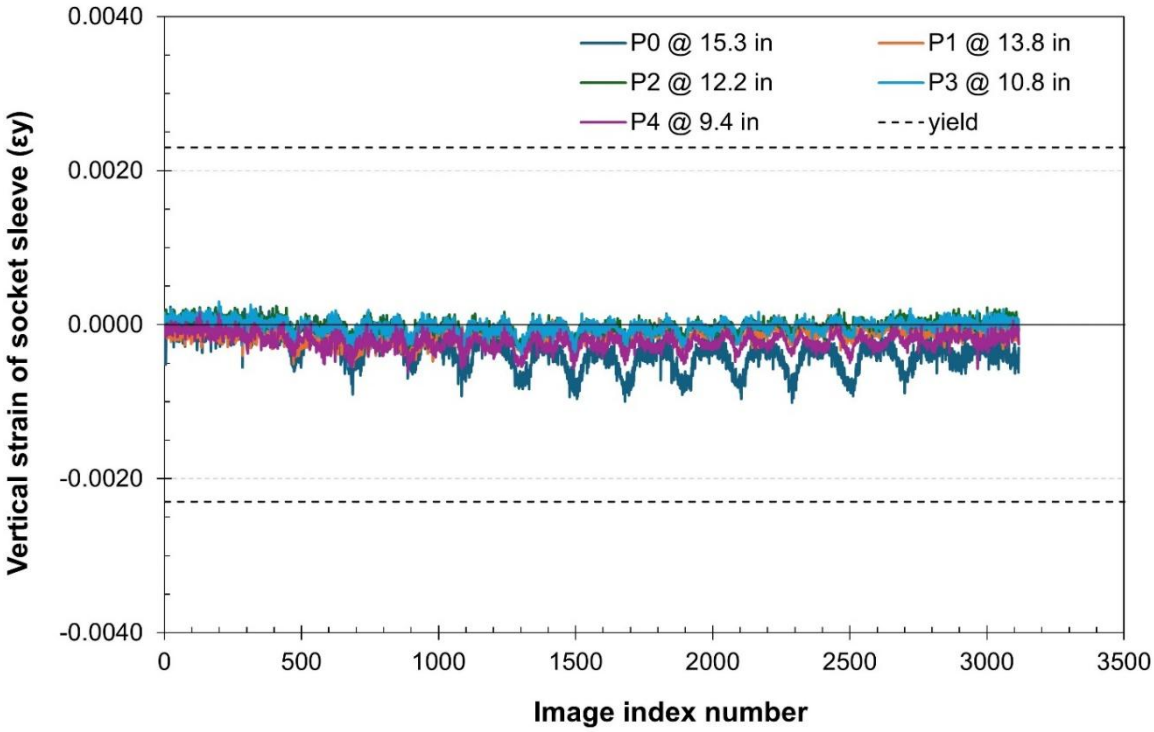


Figure 5-130. Vertical strain history of external socket sleeve at the south side of SJS5

5.6.2. Energy dissipation and hysteretic damping for SJS-5

Energy dissipation is important in understanding a structure seismic behavior because it relates to the structural element damage and energy dissipation capacity. Figure 5-131 illustrates the energy dissipation for all ductility displacement cycles for SJS5, with a total energy dissipation of 1726 kip-in. Notably, during the third cycle of ductility three, where the grout was split, the energy dissipated was reduced by 40% compared to the first cycle at the same ductility level. This reduction highlights the impact of severe damage on the energy dissipation capacity of the column.

Additionally, Figure 5-132 presents the Jacobsen hysteretic damping values for SJS5, demonstrating that damping increases as the applied displacements grow and the column sustains more damage. Notably, the elastic damping for SJS5 was approximately 9%, which is 4% higher than what is typically observed in a CIP column, indicating enhanced energy dissipation during the structural element elastic behavior.

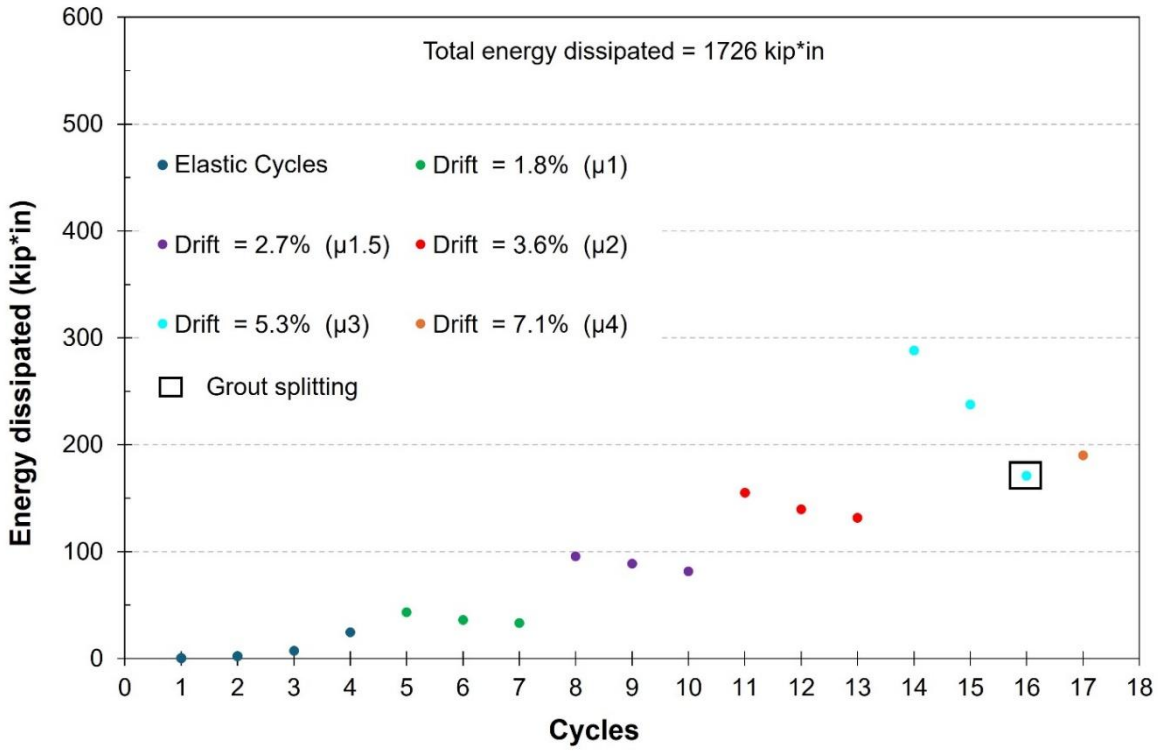


Figure 5-131. Energy dissipation plot for SJS5

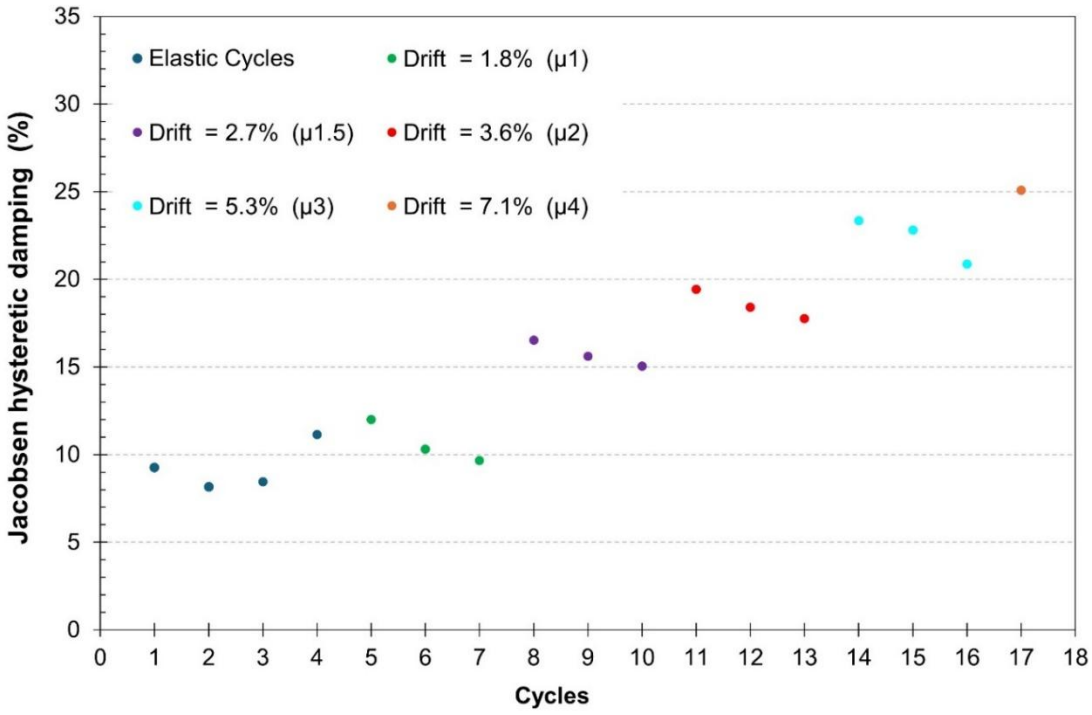


Figure 5-132. Hysteretic damping plot for SJS5

5.6.3. Displacement components

The displacement components considered in the calculations include flexural deformation, column rotation due to strain penetration and rocking, shear deformation of the column, and the deformation contribution resulting from socket rotation. The methodologies for these calculations have been detailed earlier in Section 5.1.3 of this report.

The flexural displacement component was derived from the column curvature, with the curvature profile shown in Figure 5-133 for the cycles up to yield and in Figure 5-134 for the post-yield cycles. The curvature is defined as positive when the column is pushed toward its north face. The dashed line in these figures represents the linear distribution of curvature, beginning at zero at the top of the column and reaching the yield curvature at the socket interface.

The displacement due to column rotation was calculated by determining the rotation angle at the base of the column and multiplying it by the column height above the socket. Figure 5-135 and Figure 5-136 present the column rotation for pushing and pulling cycles, respectively.

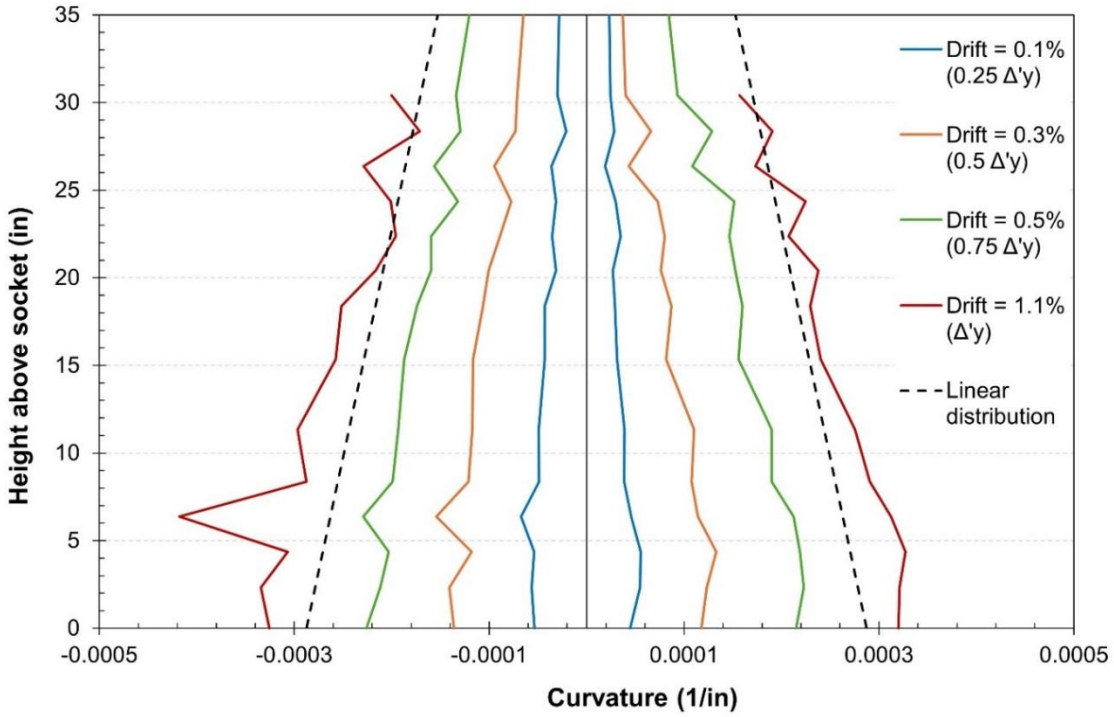


Figure 5-133. Curvature profile of the column up to the first yield cycle for SJS5

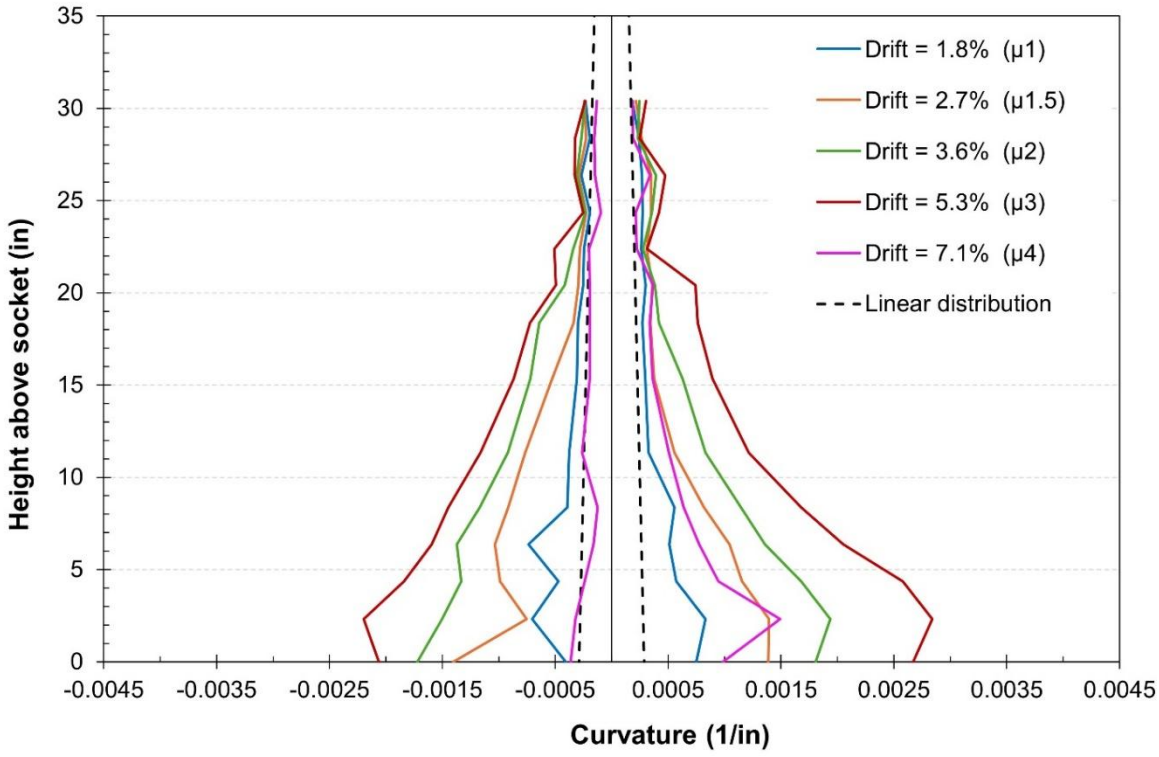


Figure 5-134. Curvature profile of the column for post-yield cycles for SJS5

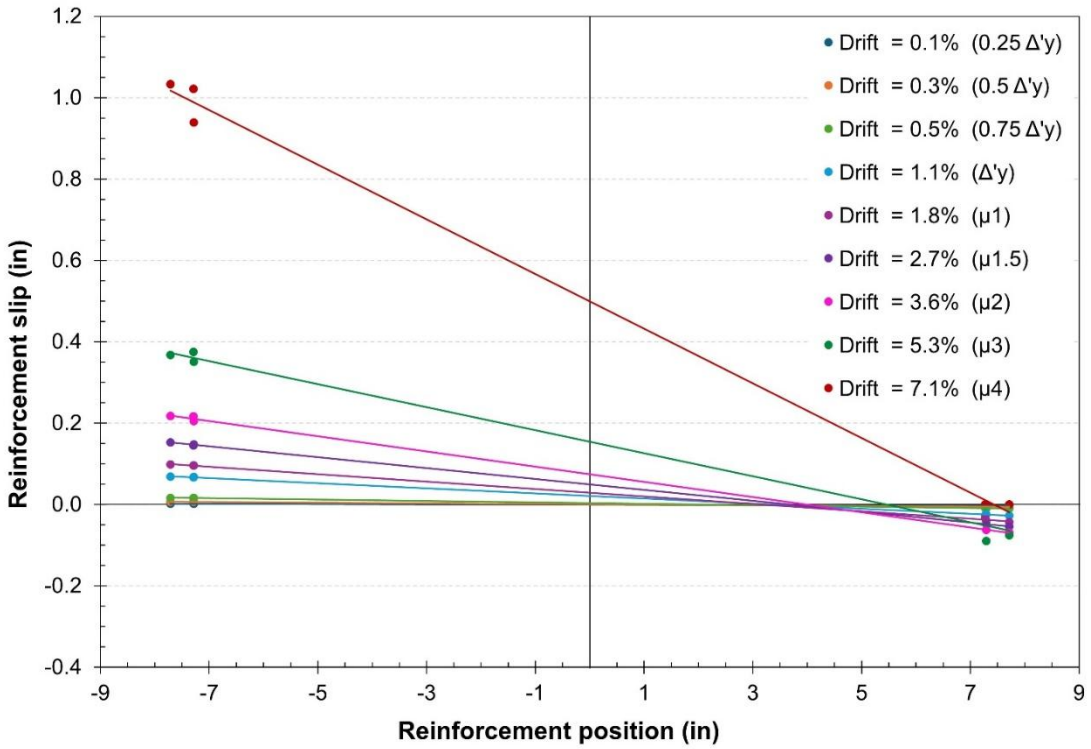


Figure 5-135. Rotation of the column for pushing cycles at the socket interface of SJS5

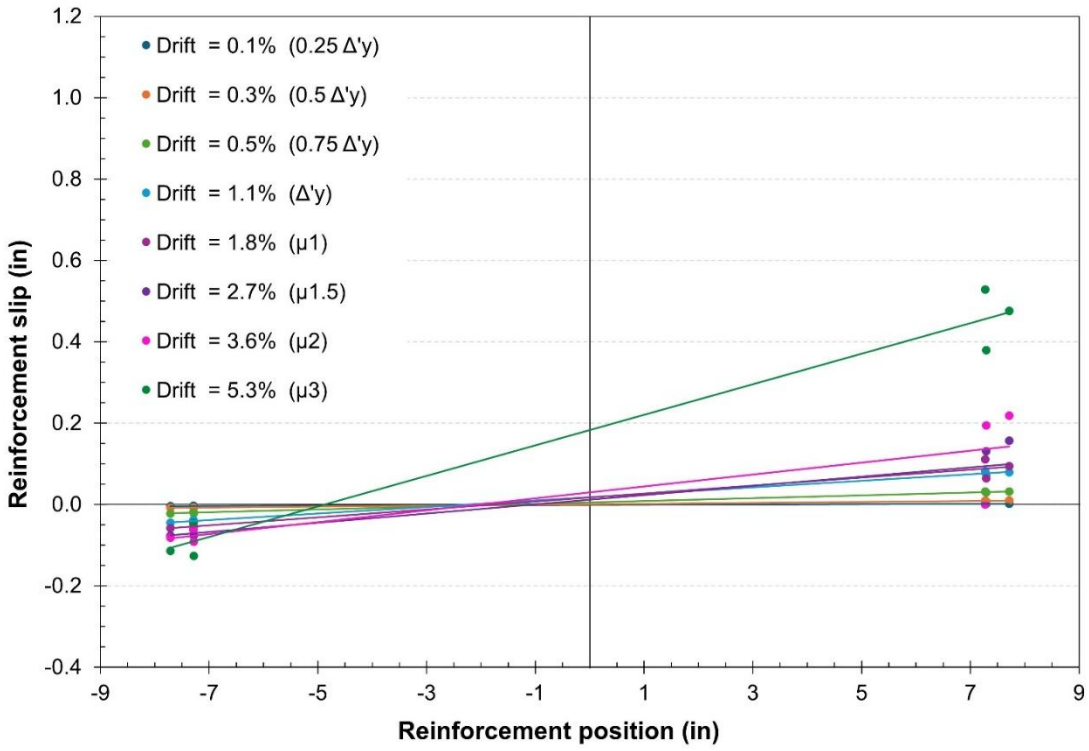


Figure 5-136. Rotation of the column for pulling cycles at the socket interface of SJS5

Figure 5-137 and Figure 5-138 present the shear strain distribution along the column height for the last three ductility displacements, as well as the yield displacement. These shear strains were then used to calculate the column shear displacement by multiplying the shear strain by the interval height. At 20 inches above the socket, the shear strains started to become constant, remaining approximately the same for all ductility displacements after yielding.

The displacement component resulting from socket rotation was obtained using DIC. Figure 5-139 and Figure 5-140 illustrate the socket rotation throughout the experimental test for the north and south faces, respectively. Socket rotation was measured at five different locations along the height, and an average value was used for displacement calculations due to the uniform distribution observed along the socket height. The averaged socket rotation, when multiplied by the socket height, provided the displacement component attributed to socket rotation.

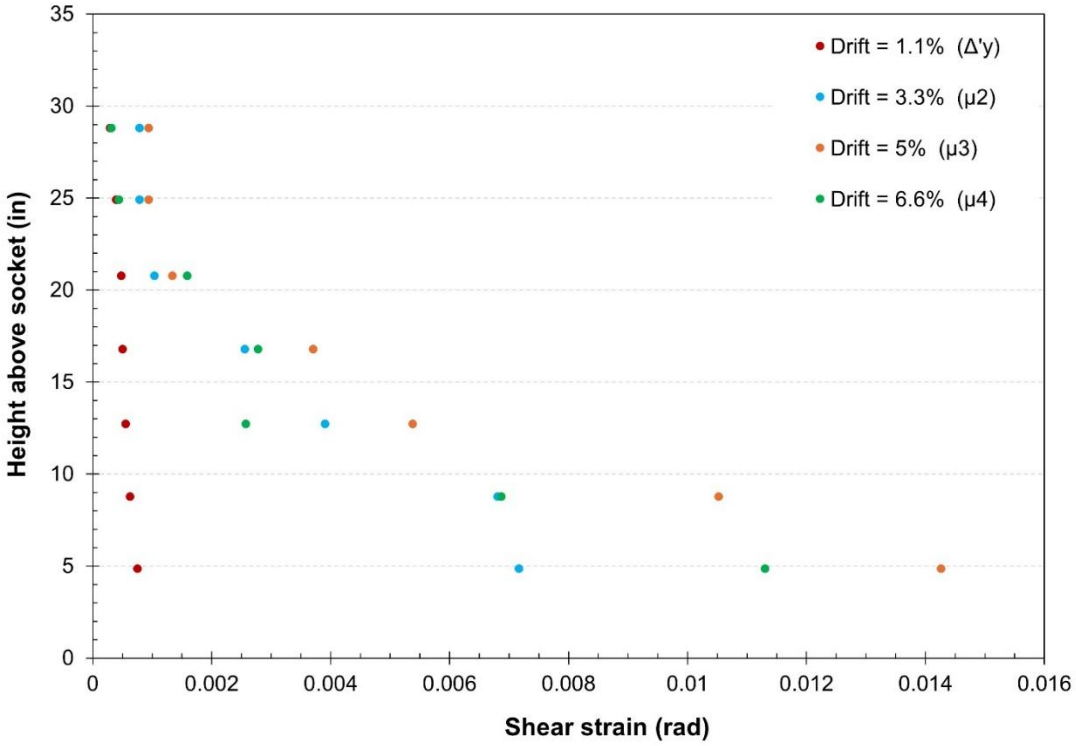


Figure 5-137. Shear strain distribution of the column for pushing cycles for SJS5

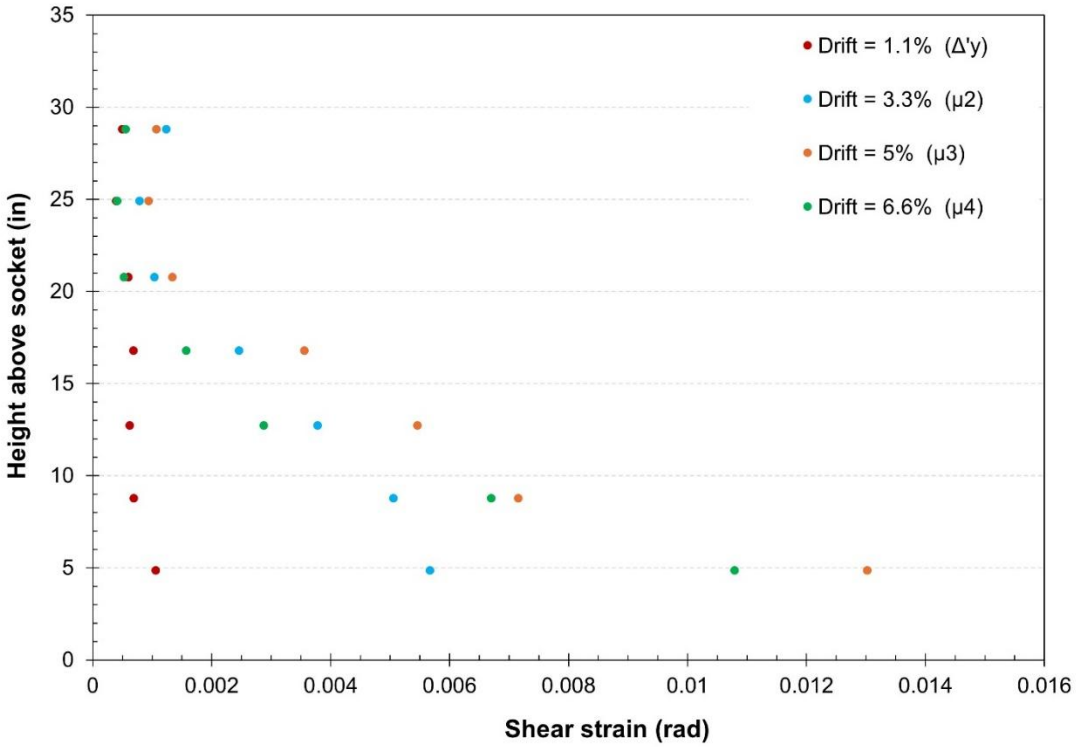


Figure 5-138. Shear strain distribution of the column for pulling cycles for SJS5

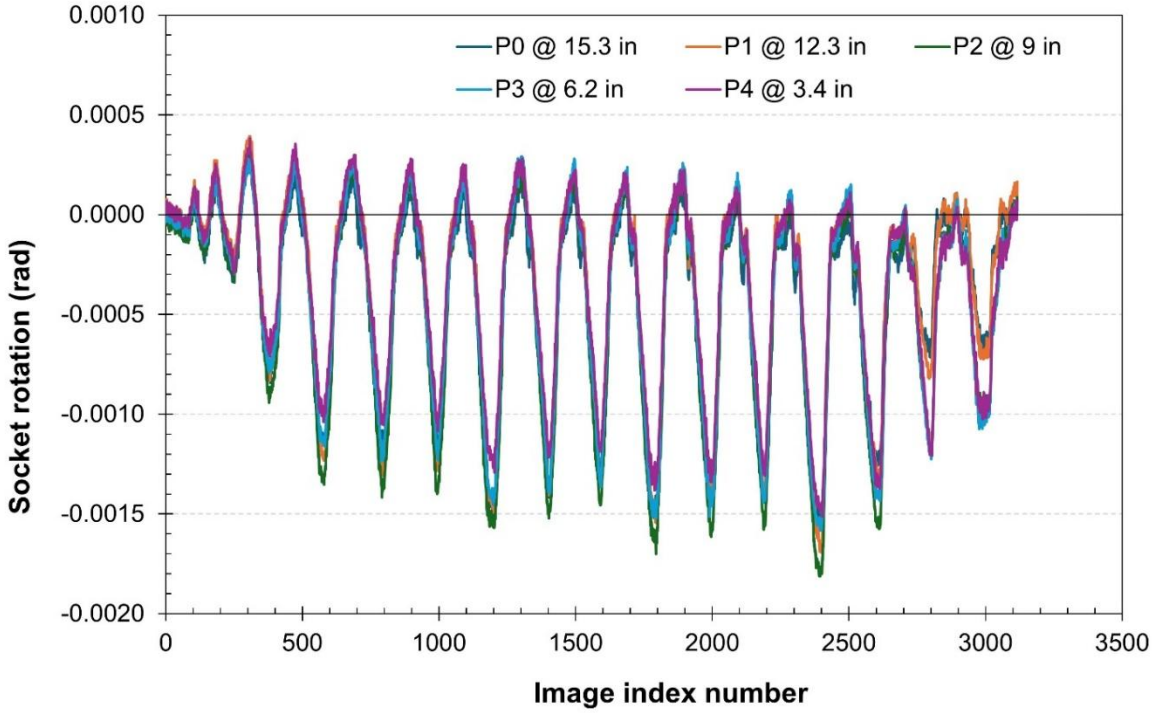


Figure 5-139. Socket rotation at the north side of SJS5

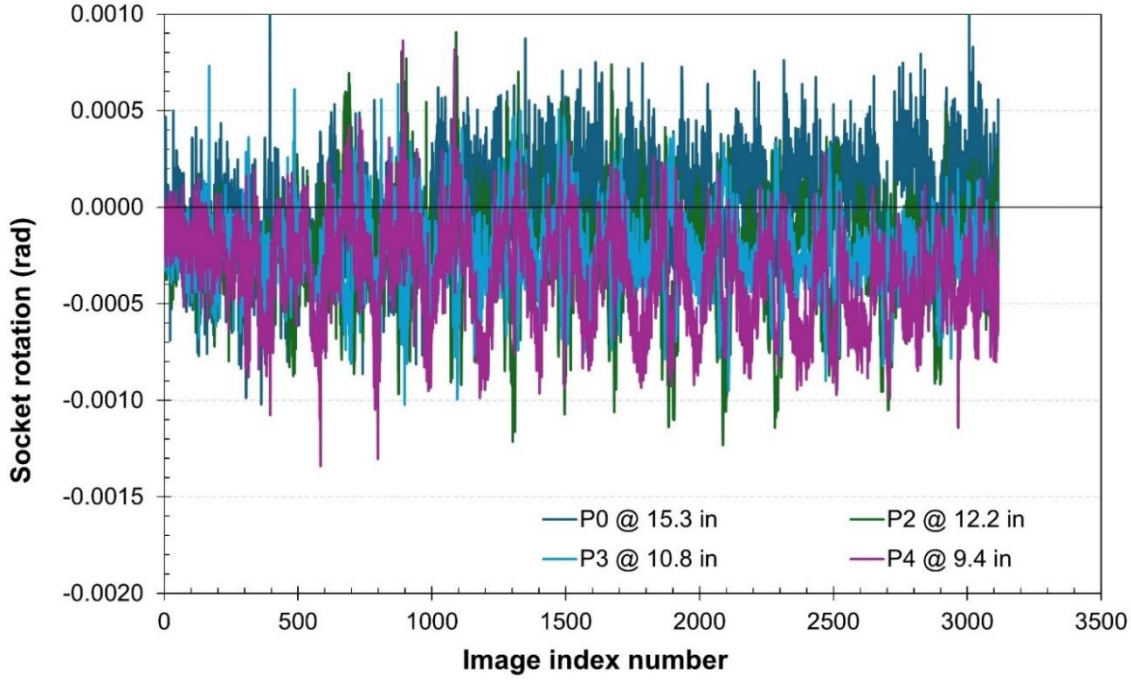


Figure 5-140. Socket rotation at the south side of SJS5

Table 5-9 and Table 5-10 present the contributions of the different components to the total displacement. Additionally, Figure 5-141 and Figure 5-142 illustrate the component displacements for pushing and pulling cycles following the first yield. The calculated displacement components closely match the measured values, validating the accuracy of the calculation methodology. The difference between the measured and calculated displacements is around 2% for most ductility displacements.

Table 5-9. Displacement components for pushing cycles for SJS 5

Displacement component (in)	**Δ'y**	**μ1**	**μ1.5**	**μ2**	**μ3**	**μ4**
Measured displacement	1.03	1.61	2.41	3.22	4.80	6.43
Flexural	0.55	0.84	1.31	1.74	2.55	1.06
Strain penetration and rocking	0.47	0.68	1.00	1.39	2.11	5.00
Shear	0.03	0.05	0.09	0.13	0.20	0.13
Socket rotation	0.01	0.02	0.02	0.03	0.03	0.02
Calculated displacement error	-0.03	0.02	0.00	-0.07	-0.08	0.23
Calculated displacement error (%)	-3.2%	1.0%	0.0%	-2.3%	-1.8%	3.6%

Table 5-10. Displacement components for pulling cycles for SJS 5

Displacement component (in)	**Δ'y**	**μ1**	**μ1.5**	**μ2**	**μ3**
Measured displacement	1.24	1.61	2.40	3.25	4.99
Flexural	0.60	0.82	1.27	1.69	2.11
Strain penetration and rocking	0.60	0.68	1.08	1.42	2.80
Shear	0.04	0.06	0.09	0.14	0.19
Socket rotation	0.01	0.01	0.01	0.01	0.01
Calculated displacement error	-0.02	0.06	-0.05	-0.01	-0.11
Calculated displacement error (%)	-1.2%	3.5%	-1.9%	-0.4%	-2.2%

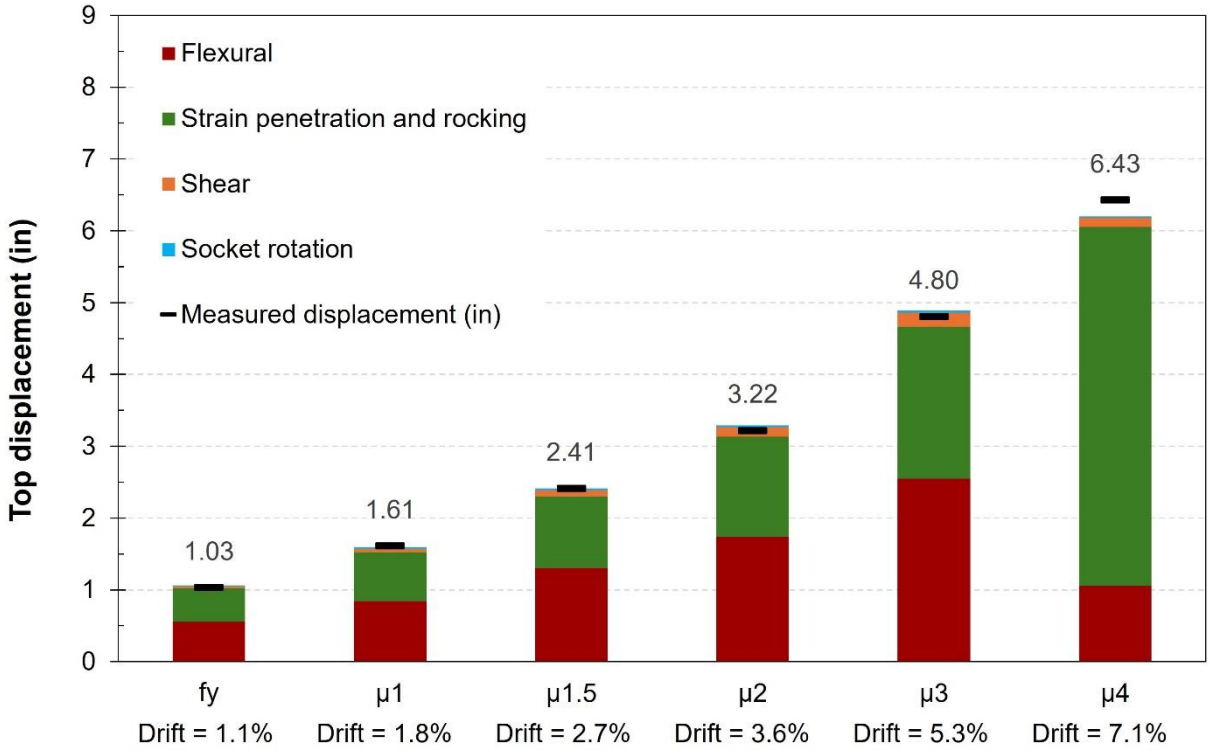


Figure 5-141. Displacement components for pushing cycles for SJS5

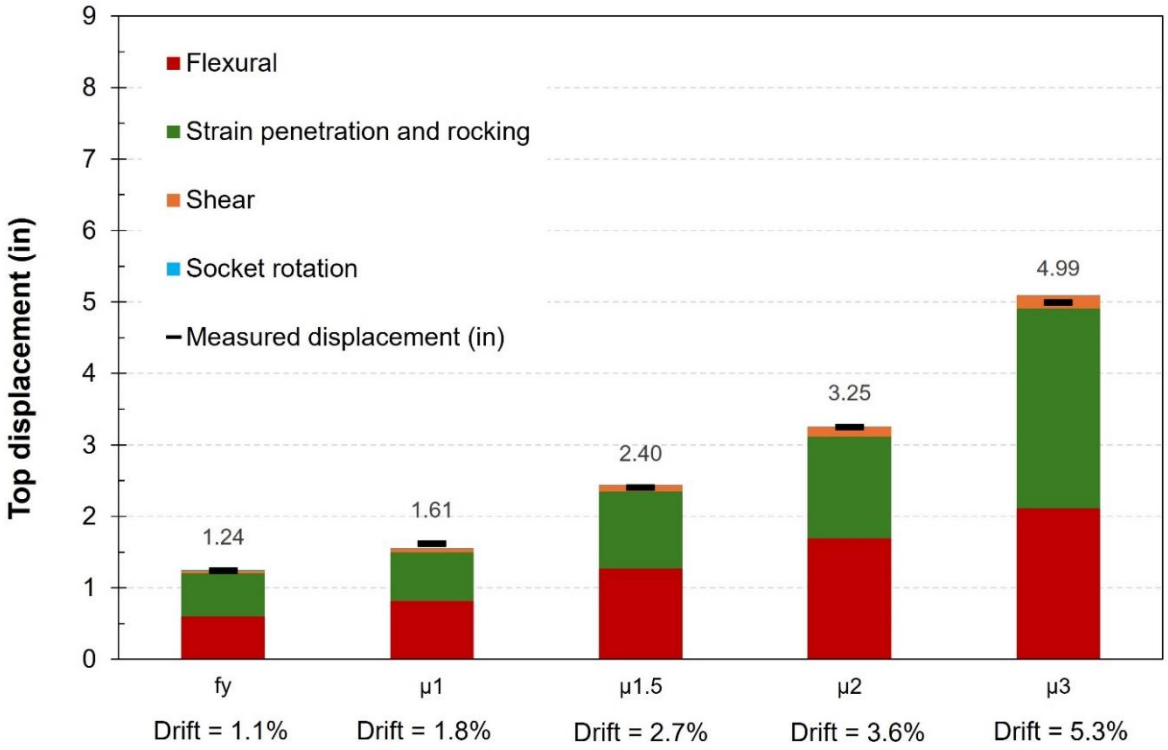


Figure 5-142. Displacement components for pulling cycles for SJS5

Comparing the displacement components, it was observed that the shear and socket rotation had a relatively small impact on the total displacement of the column. In contrast, the flexural deformation, strain penetration, and rocking of the column contributed significantly more, each having a comparable influence on the overall displacement until the grout started to split. At ductility four, the rocking became the main component of the total displacement, with 80% of the total displacement. In the case of the pulling cycles shown in Figure 5-142, the ductility four was not calculated because of the loss of markers due to the uplifting of the previous positive cycle.

5.6.4. Summary of Results for SJS-5

The tension strains in the longitudinal bars reached 2.5% before grout splitting occurred and the column experienced shear failure inside the external socket connection. This behavior prevented the development of the full plastic hinge above the external socket connection. The strains in the external socket wall remained below the yield point throughout the test, confirming that the external socket connections effectively prevented plastic strains from reaching the foundation or cap beam. As a result, the footing remained as a capacity-protected element. Horizontal strains in the external socket sleeve did not reach the yielding strain anywhere on the socket height. No visible damage was observed on the sleeves during the test, confirming that the sleeves did not experience significant inelastic deformation.

The elastic damping for SJS 5 was approximately 9%, which is higher than the 5% typically observed in CIP columns. This additional 4% damping may be attributed to the initial cracks in the socket wall and grout that occurred early in the test, as well as some unidentified noises observed during the cycles before the yield displacement. The overall displacement behavior of SJS 5 was governed primarily by flexural deformation, strain penetration, and rocking. Before the grout experienced splitting, the flexural displacements accounted for approximately 50% of the total displacement, while strain penetration and rocking contributed around 45%. After the grout splitting occurred, the flexural component was reduced to approximately 15% while the strain penetration and rocking increased approximately to 80% of the total displacement. This indicates that strain penetration and rocking play a more significant role in socket connections when the failure mechanism is attributed to shear failure of the column inside the socket connection.

5.7. Experimental Results for Specimen SJS-6

In this section, the data analysis and experimental results previously discussed in this chapter will be specifically applied to the experimental test SJS6. The results for SJS6 will be presented in detail, focusing on axial strains on the column and external socket, hysteretic damping, and calculated displacement components. This analysis provides insights into the column performance and behavior under the applied loading conditions, contributing to a comprehensive understanding of the system response.

5.7.1. Axial strain analysis for SJS-6

The strain profiles were calculated to assess the strain distribution along the RC column during the first cycles of each ductility displacement for SJS6, considering both loading directions. In this context, ″Pushing Cycles″ refers to the strain profiles when force is applied toward the north face of the column, while ″Pulling Cycles″ refers to when force is applied toward the south face.

Figure 5-143 and Figure 5-144 present the strain profiles of the extreme bar located on the north face of the specimen for cycles up to yielding and post-yield cycles, respectively. Similarly, Figure 5-145 and Figure 5-146 depict the strain profiles for the extreme bar on the south side of the specimen for cycles up to yielding and post-yield cycles. These strain profiles indicate a spread of plasticity extending approximately 20 inches from the external socket interface. The maximum axial strain in tension before bar fracture reached approximately 5.0% on both sides of the specimen, and the maximum compression strain was around 2.0%.

A detailed examination of the strains on the reinforcing bars can be achieved by plotting the strain throughout the displacement history for each gauge length. Figure 5-147 and Figure 5-148 present the strain history of the extreme bars located on the north and south faces of the specimen, respectively, with the gauge length chosen at the points where the bars buckled and eventually fractured. For both extreme bars, it can be observed that once the strain in tension exceeded 2%, the reinforcement began to buckle. This buckling is evident when, instead of continuing to increase in compressive strains, the bars started to exhibit tension strains due to their

deformed shape. After significant buckling occurred, the strain data was no longer plotted, as the resulting tension strains were no longer representative of the true behavior of the reinforcing bars.

The strains on the extreme bars of the external socket wall were not calculated, as the strain gauges were damaged during the repair process of SJS5. The axial strains on the external socket sleeve were measured using DIC. In this context, the horizontal strains correspond to the hoop forces acting around the circumference, while the vertical strains reflect any flexion sustained by the sleeves. Figure 5-149 and Figure 5-150 present the strains on the north face of the specimen while Figure 5-151 and Figure 5-152 show the strains on the south face.

The data shows that, for the horizontal strains, the top 4 inches of the socket experienced strain values close to yielding; thus, the full height of the socket remained elastic. The vertical strains remained elastic throughout the experimental test, indicating that the external socket sleeve did not contribute significantly to the flexural behavior of the external socket wall.

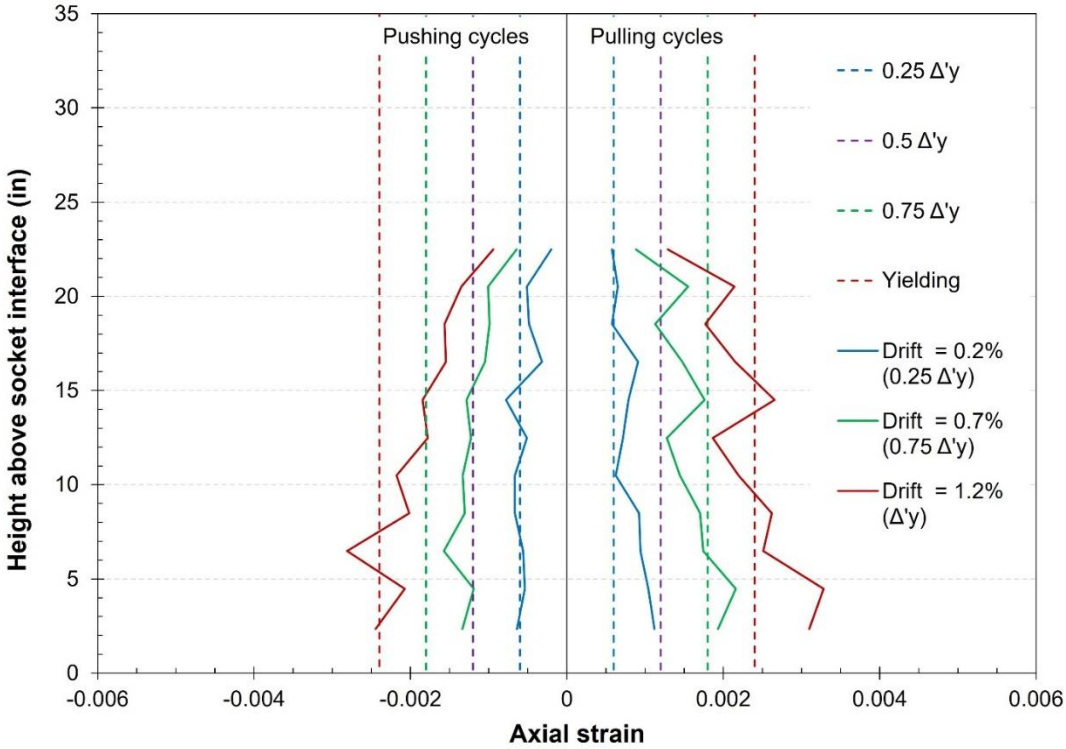


Figure 5-143. Strain profile up to first yield cycle for SJS6 on the north side of the column

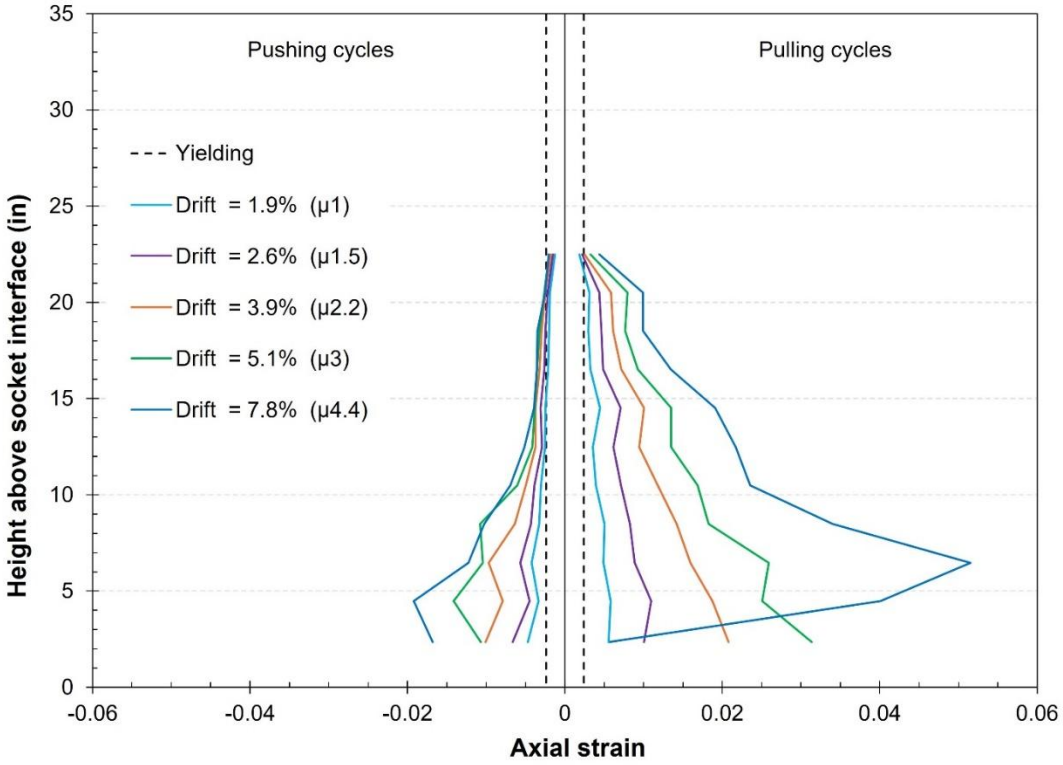


Figure 5-144. Strain profile for post-yield cycles for SJS6 on the north side of the column

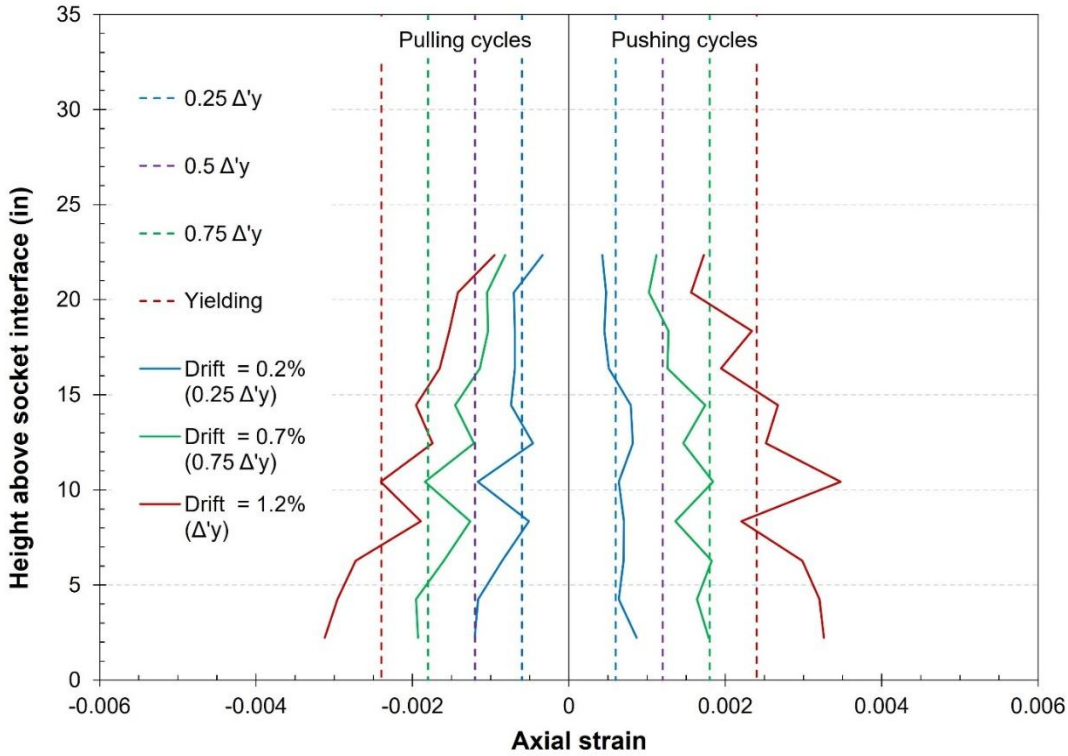


Figure 5-145. Strain profile up to first yield cycle for SJS6 on the south side of the column

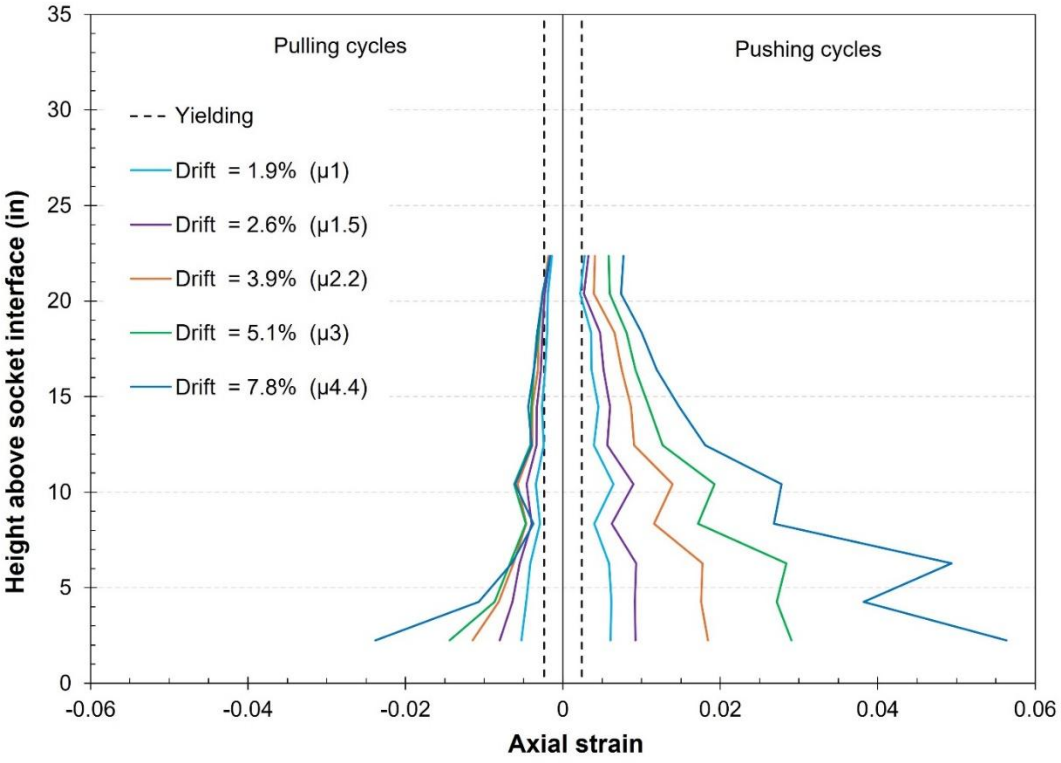


Figure 5-146. Strain profile for post-yield cycles for SJS6 on the south side of the column

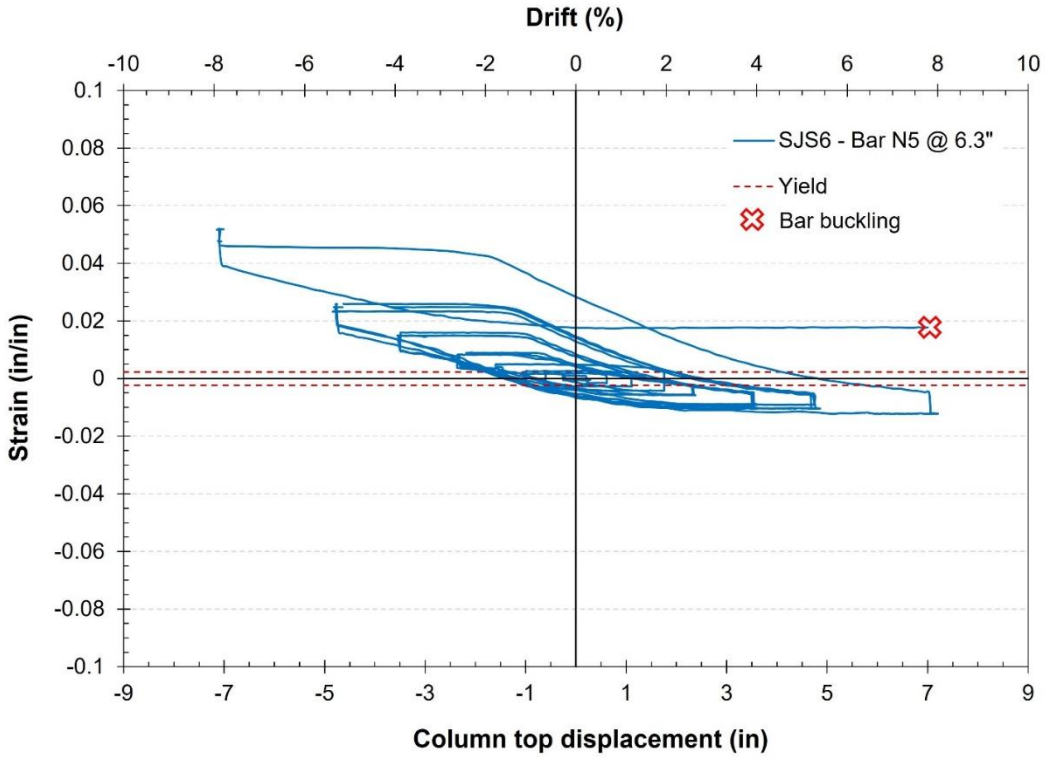


Figure 5-147. Strain vs displacement history for N5 of SJS6

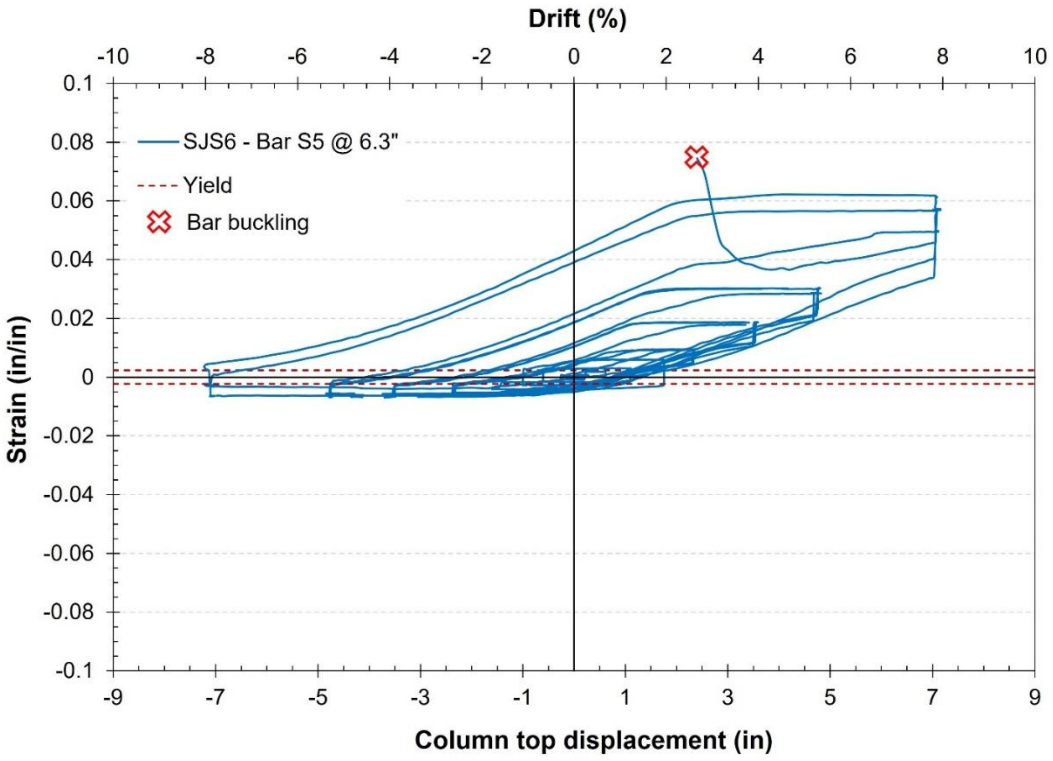


Figure 5-148. Strain vs displacement history for S5 of SJS6

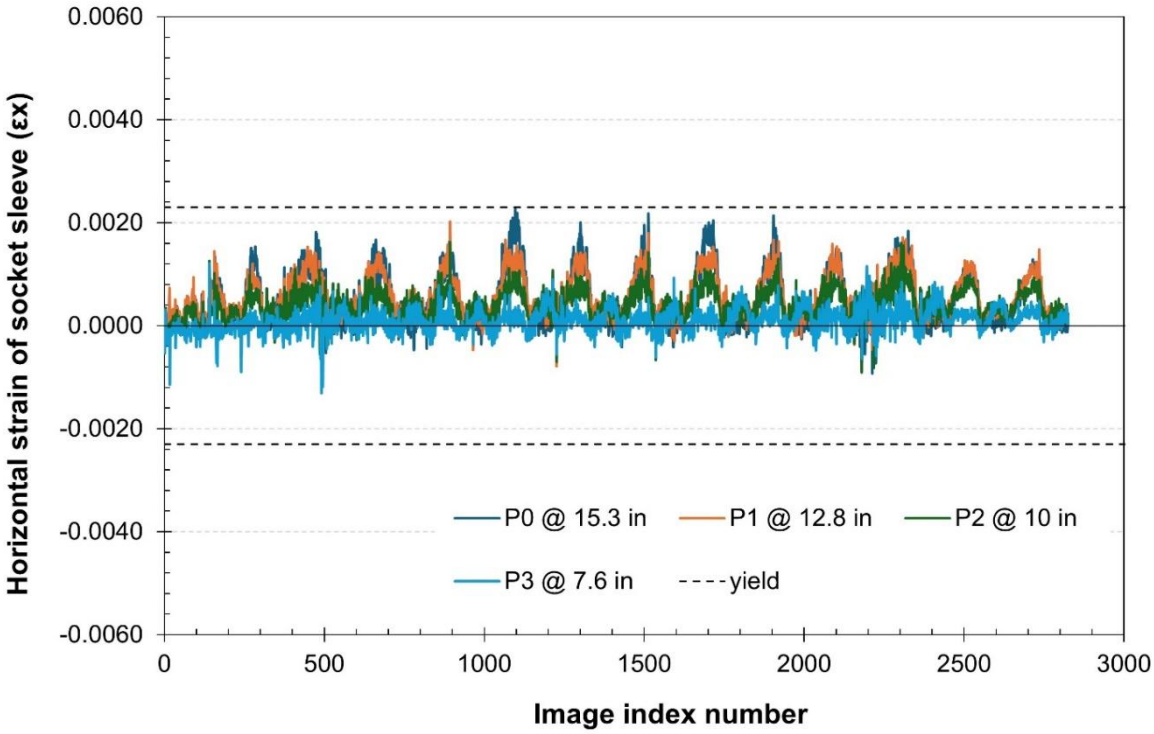


Figure 5-149. Horizontal strain history of external socket sleeve at the north side of SJS6

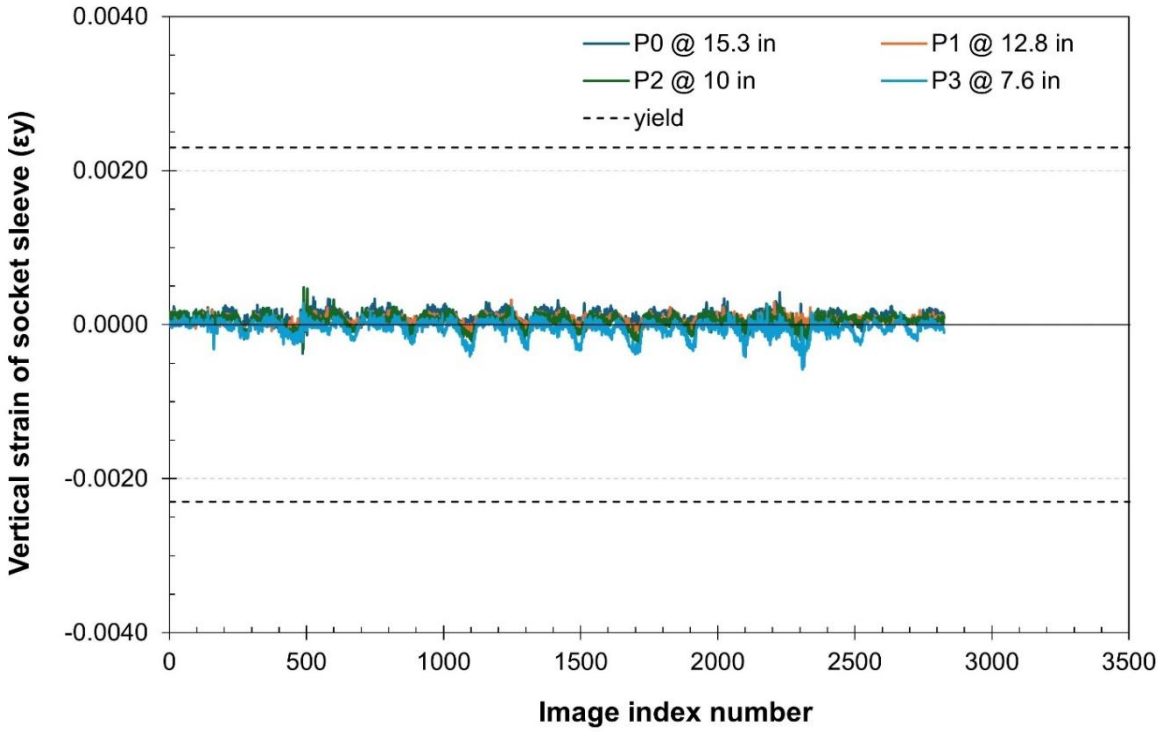


Figure 5-150. Vertical strain history of external socket sleeve at the north side of SJS6

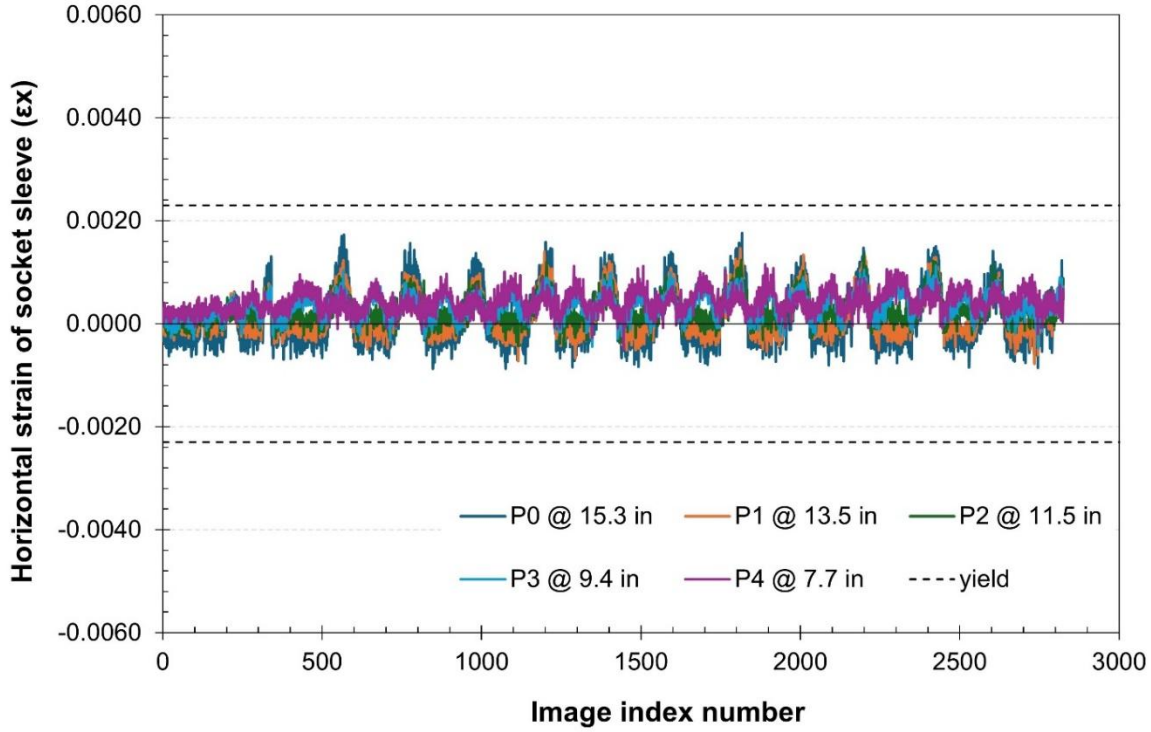


Figure 5-151. Horizontal strain history of external socket sleeve at the south side of SJS6

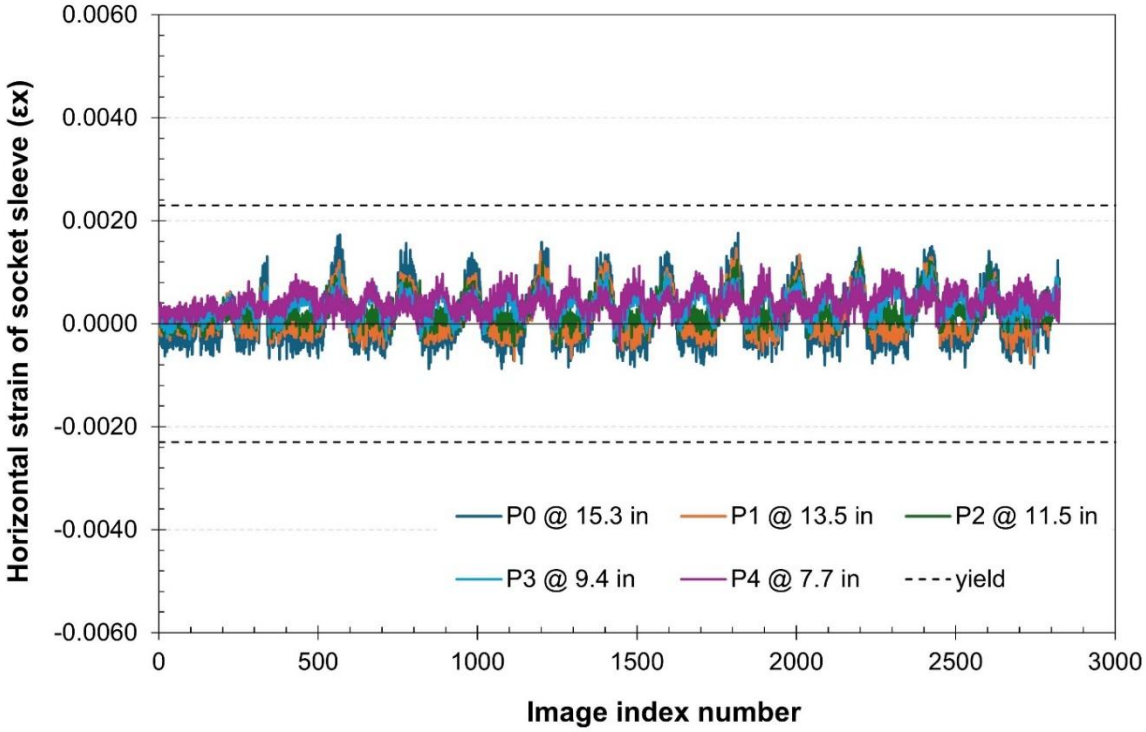


Figure 5-152. Vertical strain history of external socket sleeve at the south side of SJS6

5.7.2. Energy dissipation and hysteretic damping for SJS-6

Energy dissipation is important in understanding a structure seismic behavior because it relates to the structural element damage and energy dissipation capacity. Figure 5-153 illustrates the energy dissipation for all ductility displacement cycles for SJS6, with a total energy dissipation of 3209 kip-in. Notably, during the third cycle of ductility four, where bar fracture occurred, the energy dissipated was reduced by 40% compared to the first cycle at the same ductility level. This reduction highlights the impact of severe damage on the energy dissipation capacity of the column.

Additionally, Figure 5-154 presents the Jacobsen hysteretic damping values for SJS6, demonstrating that damping increases as the applied displacements grow and the column sustains more damage. Notably, the elastic damping for SJS6 was approximately 10%, which is 5% higher than what is typically observed in a CIP column, indicating enhanced energy dissipation during the structural element elastic behavior.

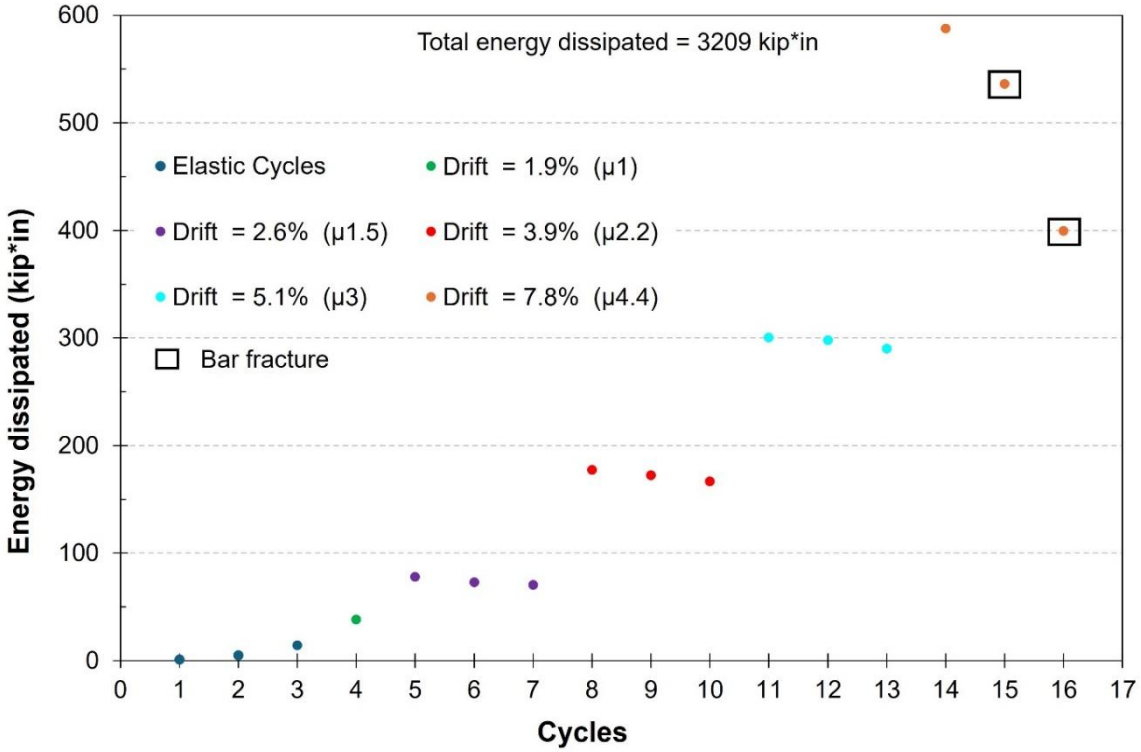


Figure 5-153. Energy dissipation plot for SJS6

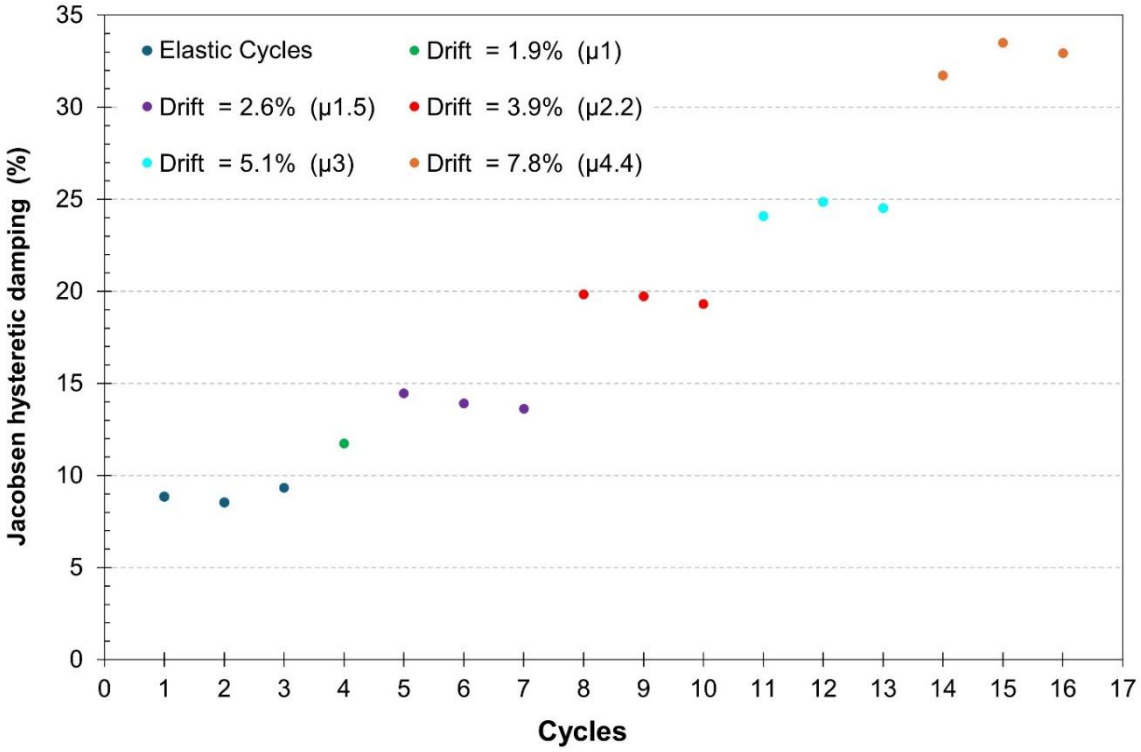


Figure 5-154. Hysteretic damping plot for SJS6

5.7.3. Displacement components for SJS-6

The displacement components considered in the calculations include flexural deformation, column rotation due to strain penetration and rocking, shear deformation of the column, and the deformation contribution resulting from socket rotation. The methodologies for these calculations have been detailed earlier in Section 5.1.3 of this report.

The flexural displacement component was derived from the column curvature, with the curvature profile shown in Figure 5-155 for the cycles up to yield and in Figure 5-156 for the post-yield cycles. The curvature is defined as positive when the column is pushed toward its north face. The dashed line in these figures represents the linear distribution of curvature, beginning at zero at the top of the column and reaching the yield curvature at the socket interface.

The displacement due to column rotation was calculated by determining the rotation angle at the base of the column and multiplying it by the column height above the socket. Figure 5-157 and Figure 5-158 present the column rotation for pushing and pulling cycles, respectively.

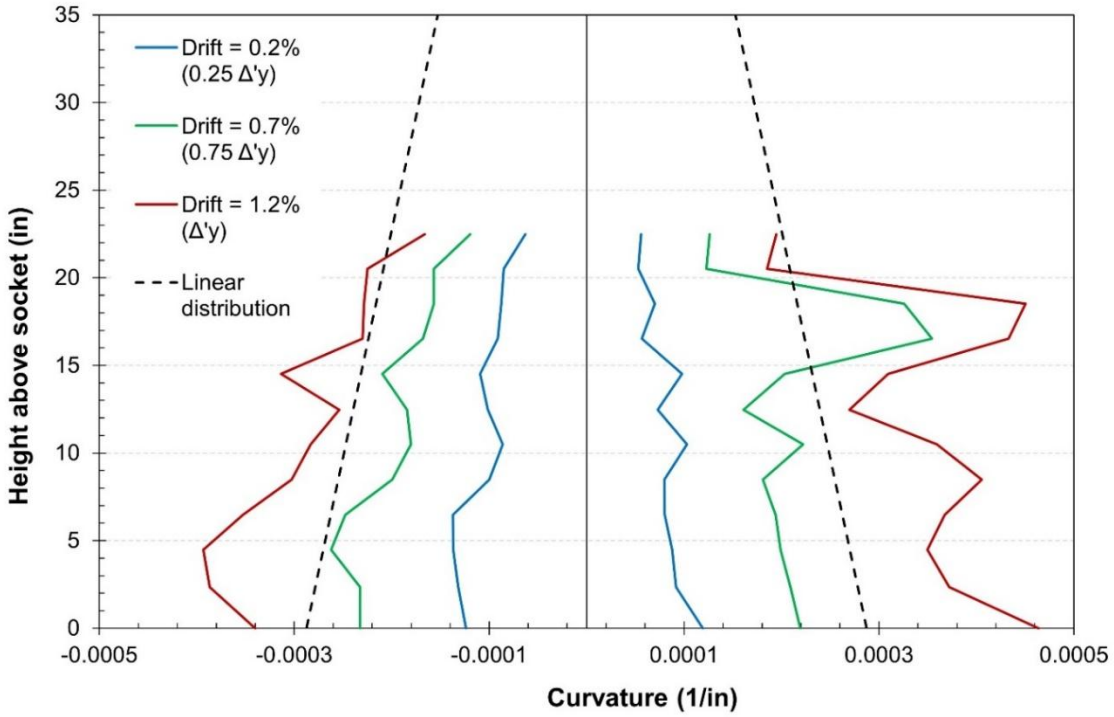


Figure 5-155. Curvature profile of the column up to the first yield cycle for SJS6

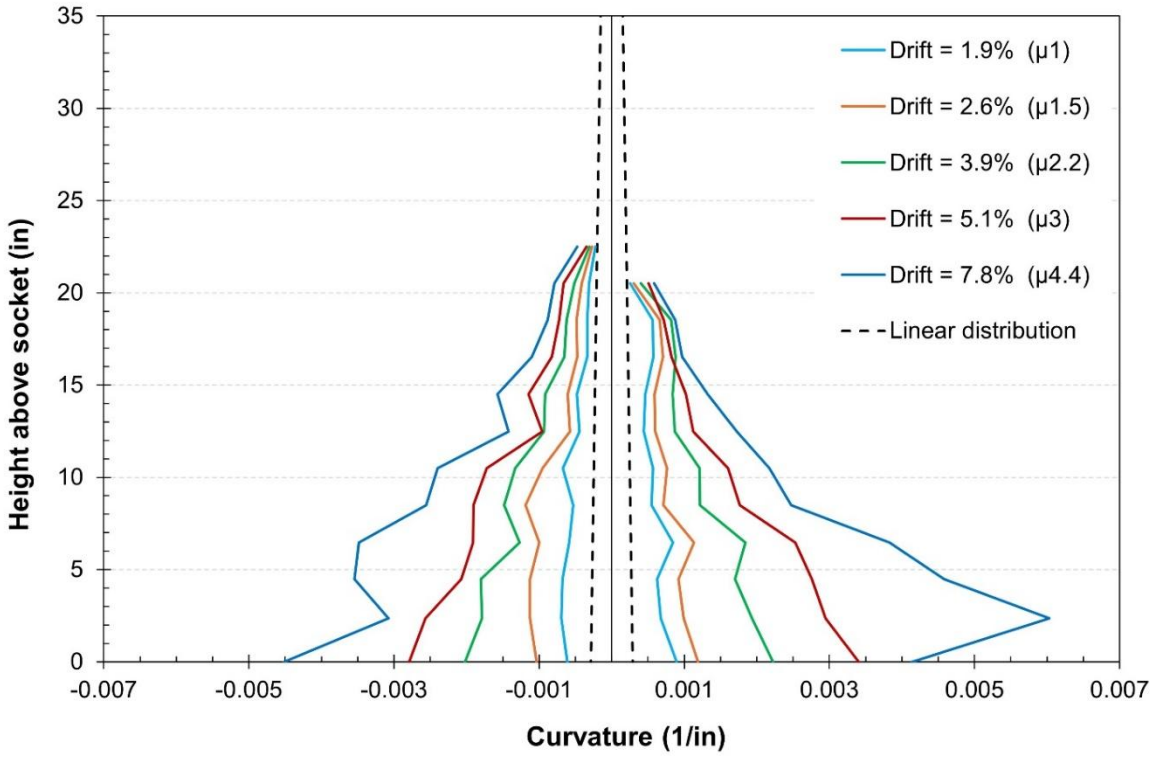


Figure 5-156. Curvature profile of the column for post-yield cycles for SJS6

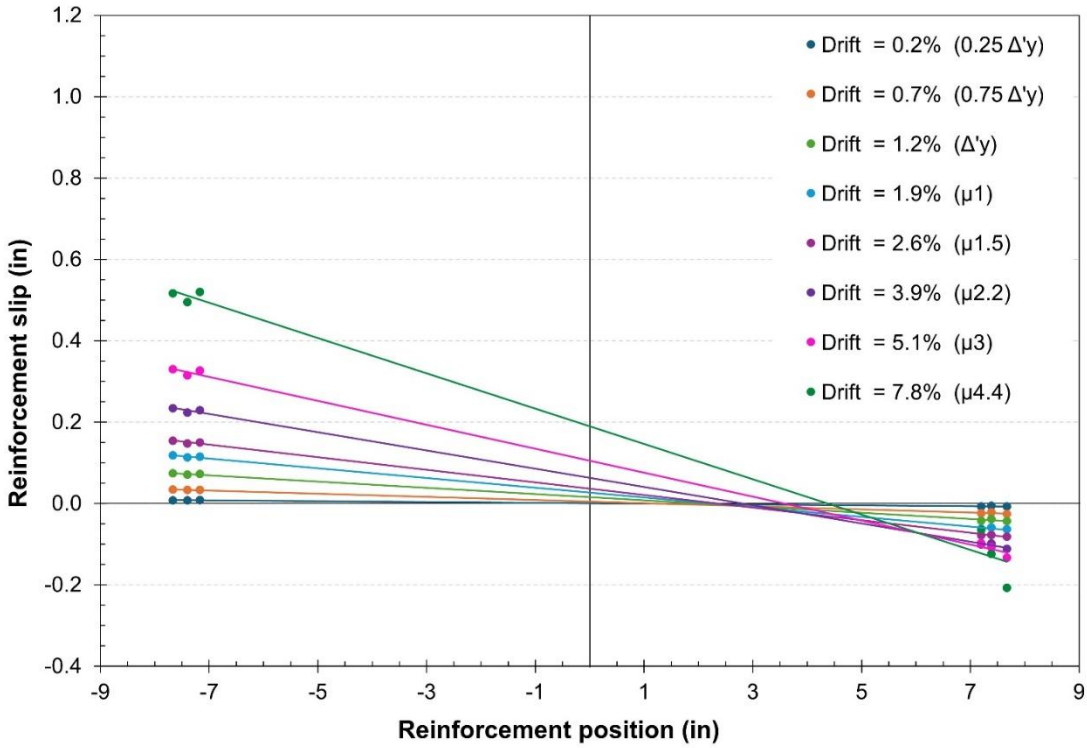


Figure 5-157. Rotation of the column for pushing cycles at the socket interface of SJS6

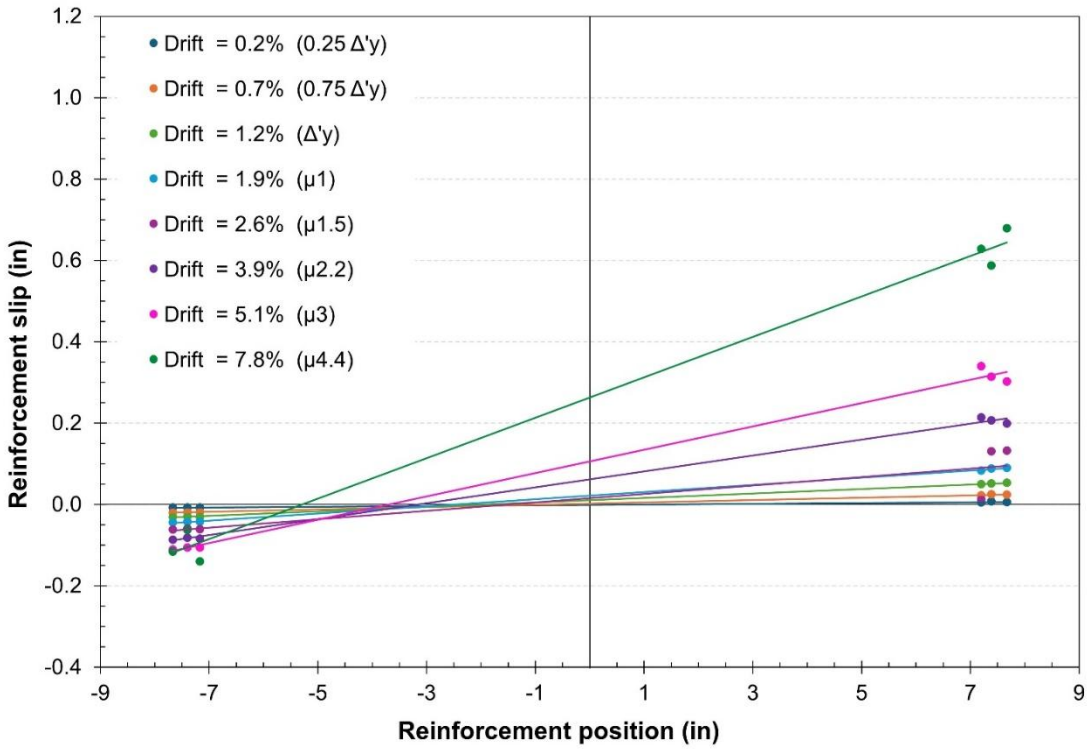


Figure 5-158. Rotation of the column for pulling cycles at the socket interface of SJS6

Figure 5-159 and Figure 5-160 present the shear strain distribution along the column height for the last three ductility displacements, as well as the yield displacement. These shear strains were then used to calculate the column shear displacement by multiplying the shear strain by the interval height. At 20 inches above the socket, the shear strains started to become constant, remaining approximately the same for all ductility displacements after yielding.

The displacement component resulting from socket rotation was obtained using DIC. Figure 5-161 and Figure 5-162 illustrate the socket rotation throughout the experimental test for the north and south faces, respectively. Socket rotation was measured at five different locations along the height, and an average value was used for displacement calculations due to the uniform distribution observed along the socket height. The averaged socket rotation, when multiplied by the socket height, provided the displacement component attributed to socket rotation.

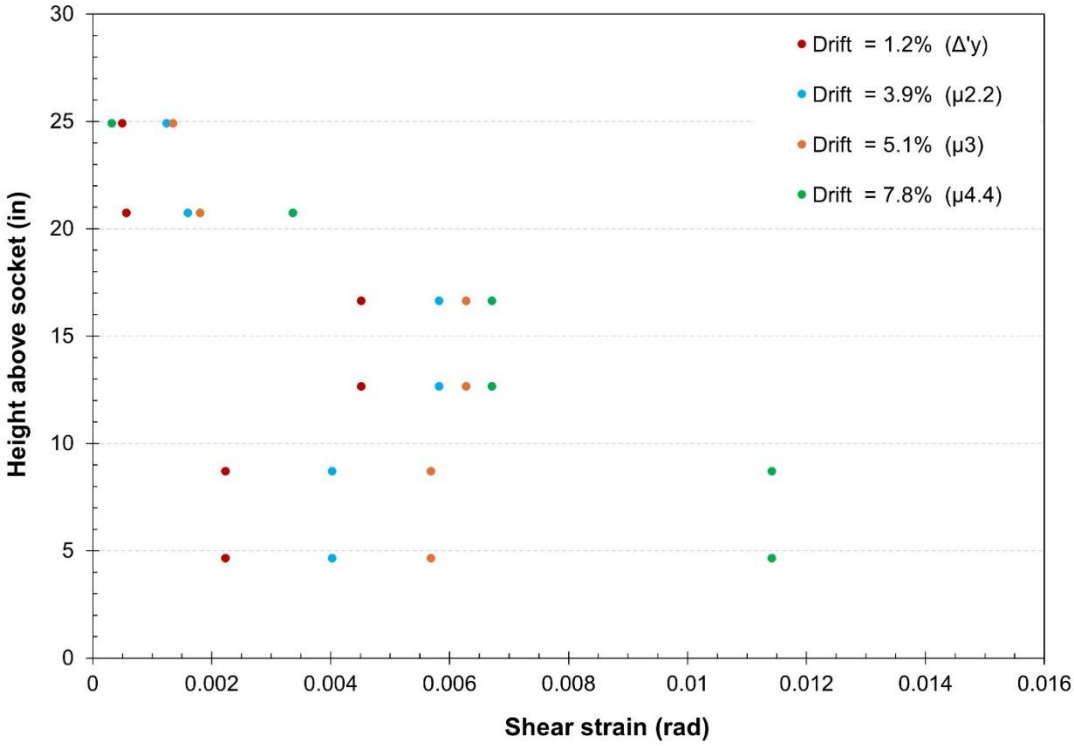


Figure 5-159. Shear strain distribution of the column for pushing cycles for SJS6

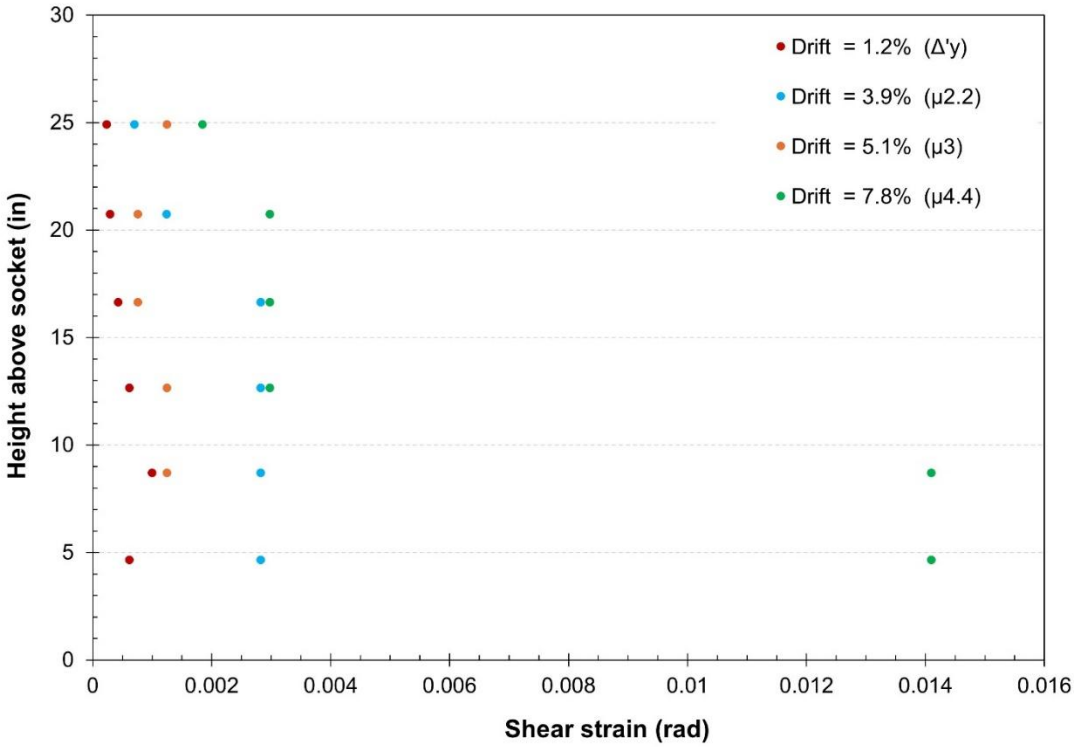


Figure 5-160. Shear strain distribution of the column for pulling cycles for SJS6

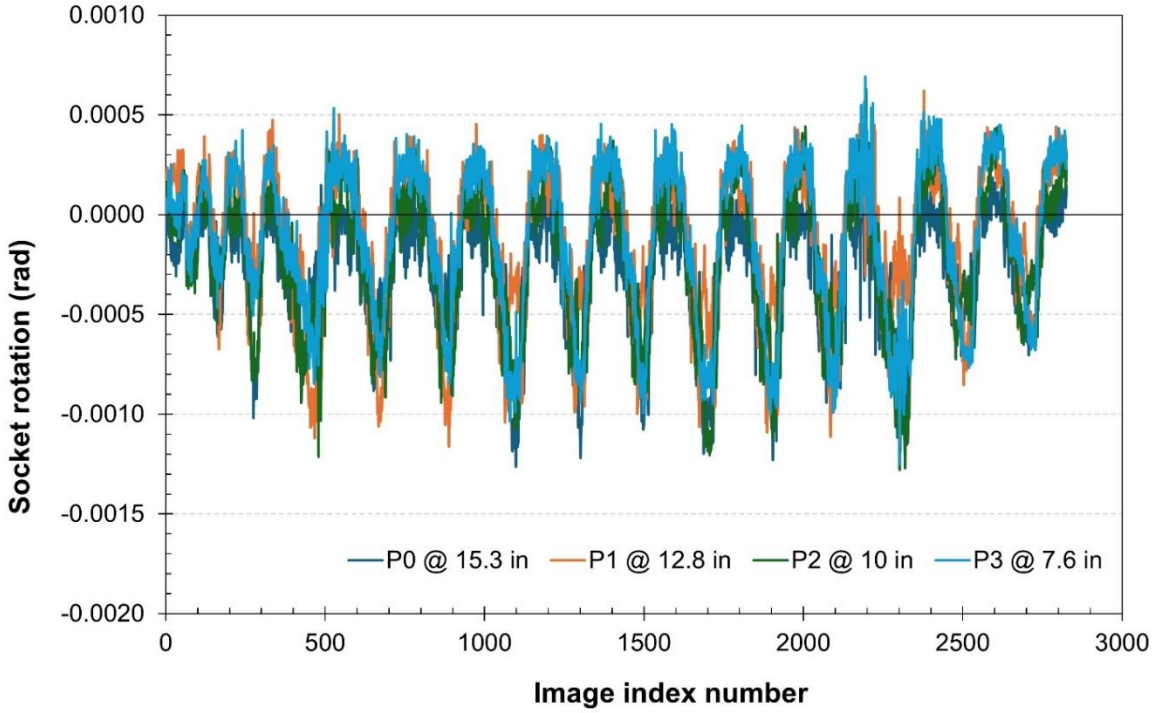


Figure 5-161. Socket rotation at the north side of SJS6

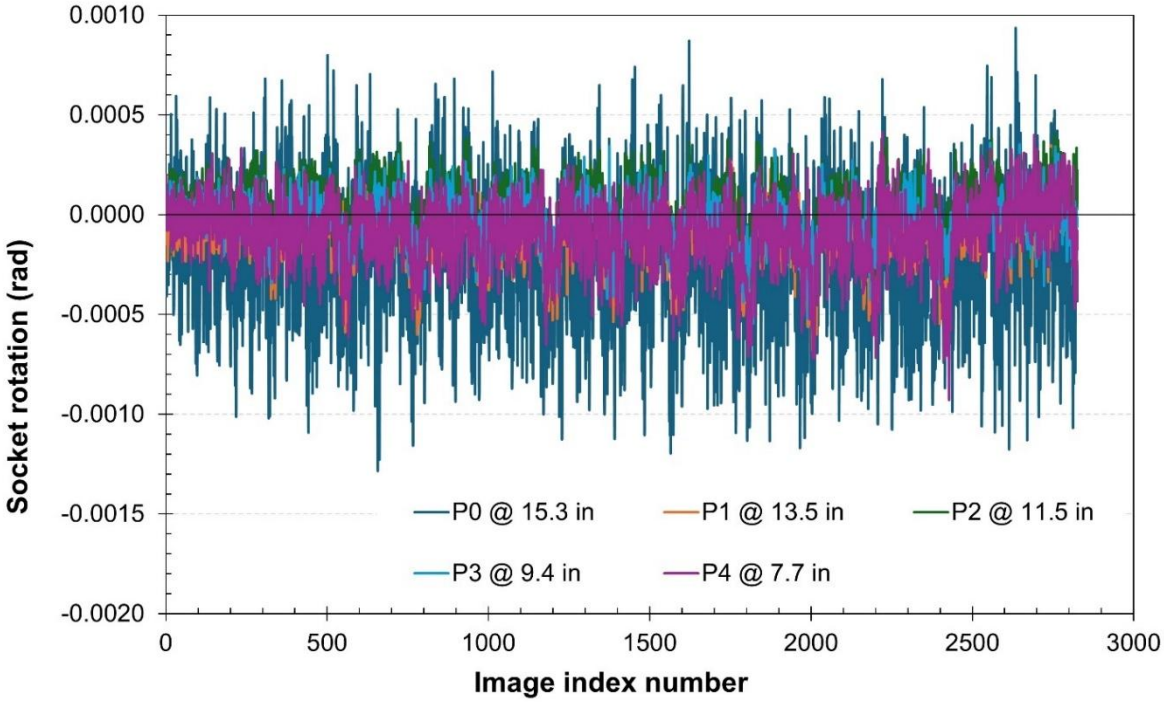


Figure 5-162. Socket rotation at the south side of SJS6

Table 5-11 and Table 5-12 present the contributions of the different components to the total displacement. Additionally, Figure 5-163 and Figure 5-164 illustrate the component displacements for pushing and pulling cycles following the first yield. The calculated displacement components closely match the measured values, validating the accuracy of the calculation methodology. The difference between the measured and calculated displacements was around 9% for most ductility displacements.

Table 5-11. Displacement components for pushing cycles for SJS 6

Displacement component (in)	**μ1**	**μ1.5**	**μ2.2**	**μ3**	**μ4.4**
Measured displacement	1.75	2.32	3.48	4.63	7.02
Flexural	0.96	1.23	1.92	2.61	3.94
Strain penetration and rocking	0.89	1.16	1.67	2.20	3.24
Shear	0.11	0.12	0.15	0.17	0.18
Socket rotation	0.01	0.02	0.02	0.02	0.02
Calculated displacement error	-0.21	-0.21	-0.29	-0.38	-0.37
Calculated displacement error (%)	-12.1%	-8.9%	-8.3%	-8.1%	-5.2%

Table 5-12. Displacement components for pulling cycles for SJS 6

Displacement component (in)	**μ1**	**μ1.5**	**μ2.2**	**μ3**	**μ4.4**
Measured displacement	1.60	2.38	3.42	4.72	7.10
Flexural	0.88	1.31	1.86	2.36	3.38
Strain penetration and rocking	0.66	0.77	1.46	2.14	3.71
Shear	0.04	0.06	0.09	0.14	0.25
Socket rotation	0.01	0.01	0.01	0.01	0.01
Calculated displacement error	0.01	0.22	0.00	0.06	-0.25
Calculated displacement error (%)	0.7%	9.4%	0.1%	1.2%	-3.6%

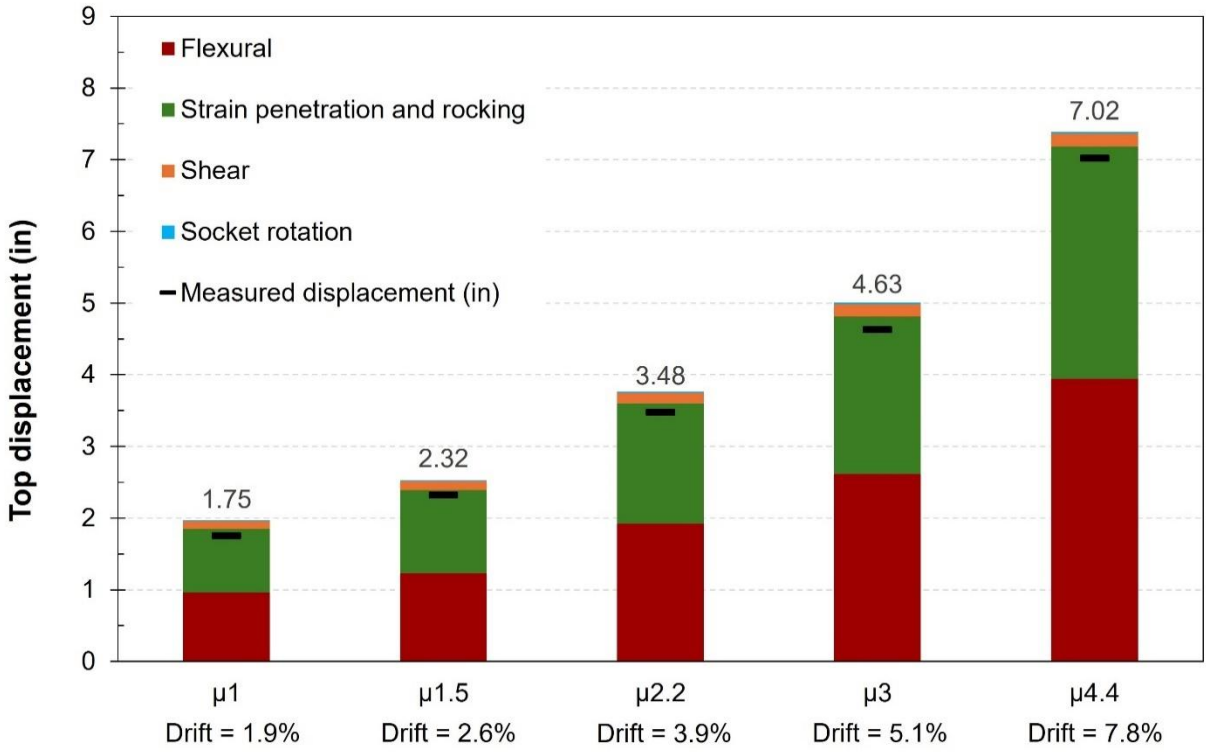


Figure 5-163. Displacement components for pushing cycles for SJS6

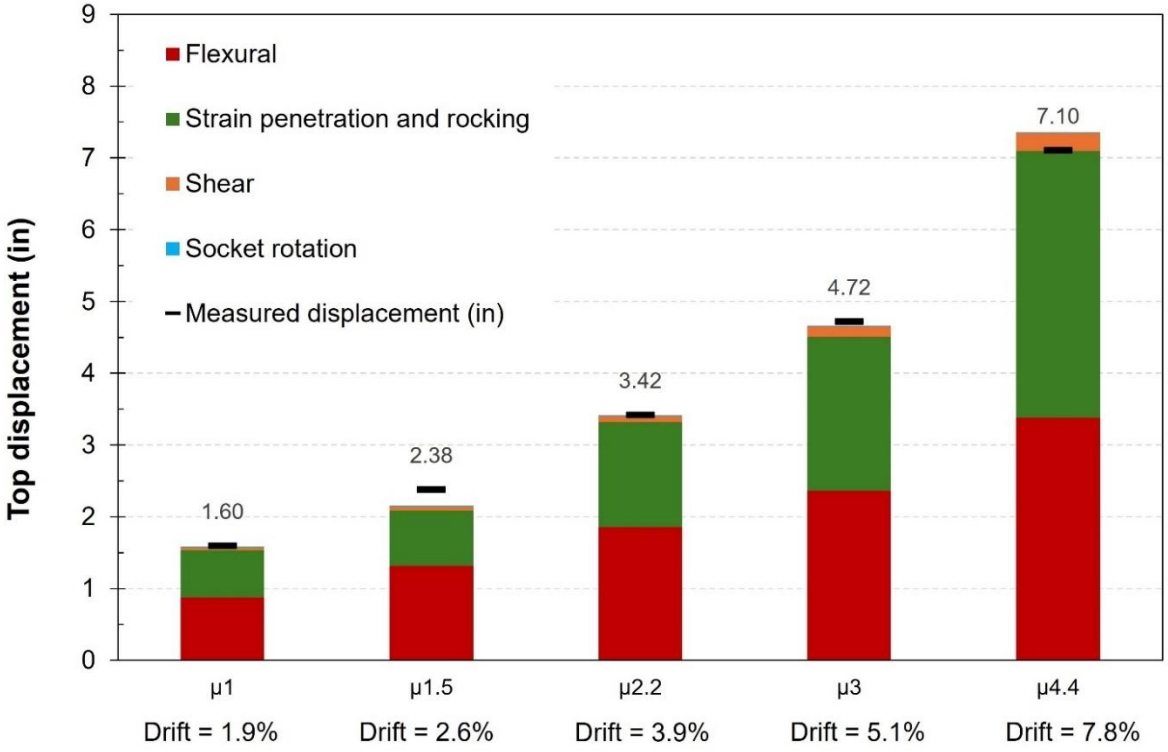


Figure 5-164. Displacement components for pulling cycles for SJS6

Comparing the displacement components, it was observed that the shear and socket rotation had a relatively small impact on the total displacement of the column. In contrast, the flexural deformation, strain penetration, and rocking of the column contributed significantly more, each having a comparable influence on the overall displacement. These findings highlight that while shear and socket rotation are present, the primary components of the total column displacement are the flexural and rotational effects for a socket height of 0.85 Dc that developed the plastic hinge above the external socket connection.

5.7.4. Discussion of Results for SJS-6

The tension strains in the longitudinal bars reached 5.0% before bar buckling occurred, followed by fracture in the subsequent cycle. This indicates that the plastic hinge was fully developed above the external socket interface. For this test, we did not have strain gages on the longitudinal reinforcing of the external socket wall, but during the test, there was no damage on the footing, remaining as a capacity-protected element. Horizontal strains in the external socket sleeve reached the yield strain at the top third of the socket height but remained elastic for the rest of the height. No visible damage was observed on the sleeves during the test, confirming that the sleeves did not experience significant inelastic deformation.

The elastic damping for SJS 6 was approximately 10%, which is higher than the 5% typically observed in CIP columns. This additional 5% damping may be attributed to the initial cracks in the socket wall and grout that occurred early in the test, as well as some unidentified noises observed during the cycles before the yield displacement.

The overall displacement behavior of SJS 6 was governed primarily by flexural deformation, strain penetration, and rocking. Flexural displacements accounted for approximately 50% of the total displacement, while strain penetration and rocking contributed around 45%. In comparison, CIP columns typically exhibit 65% flexural displacement and 30% strain penetration. This indicates that strain penetration and rocking have a more significant contribution to the total displacement of the column while having a socket connection than in CIP columns.

5.8. Experimental Results for Specimen SJS-7

In this section, the data analysis and experimental results previously discussed in this chapter will be specifically applied to the experimental test SJS7. The results for SJS7 will be presented in detail, focusing on axial strains on the RCFST column and external socket and hysteretic damping. This analysis provides insights into the column performance and behavior under the applied loading conditions, contributing to a comprehensive understanding of the system response.

5.8.1. Axial strain analysis for SJS-7

For the RCFST, the strains on the longitudinal bars were not obtained as in previous tests because the reinforcement could not be exposed due to the presence of the steel tube. However, the strain history of the extreme bars in the external socket wall reinforcement was monitored using strain gauges placed 2 inches above the footing. Figure 5-165 and Figure 5-166 present the strain history for the extreme bars on the north and south faces, respectively. The data indicates that the reinforcement in the external socket wall reached twice the yield strain, indicating that the external socket wall remained almost elastic throughout the entire experimental test.

The axial strains on the external socket sleeve were measured using DIC. In this context, the horizontal strains correspond to the hoop forces acting around the circumference, while the vertical strains reflect any flexion sustained by the sleeves. Figure 5-167 and Figure 5-168 present the strains on the north face of the specimen while Figure 5-169 and Figure 5-170 show the strains on the south face.

The data shows that, for the horizontal strains, the top 3 inches of the socket experienced strain values around 1.5 times the yielding strain; thus, the remaining height of the socket remained elastic. The vertical strains remained elastic throughout the experimental test, indicating that the external socket sleeve did not contribute significantly to the flexural behavior of the external socket wall.

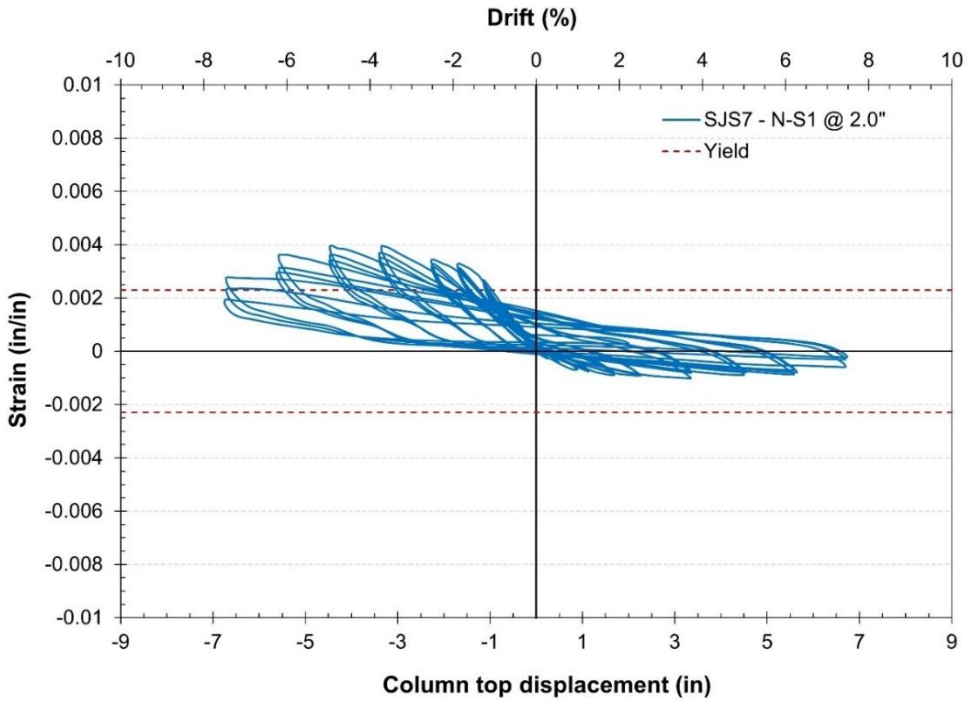


Figure 5-165. Strain vs displacement history for the extreme bar of socket wall reinforcement at the north side of SJS7

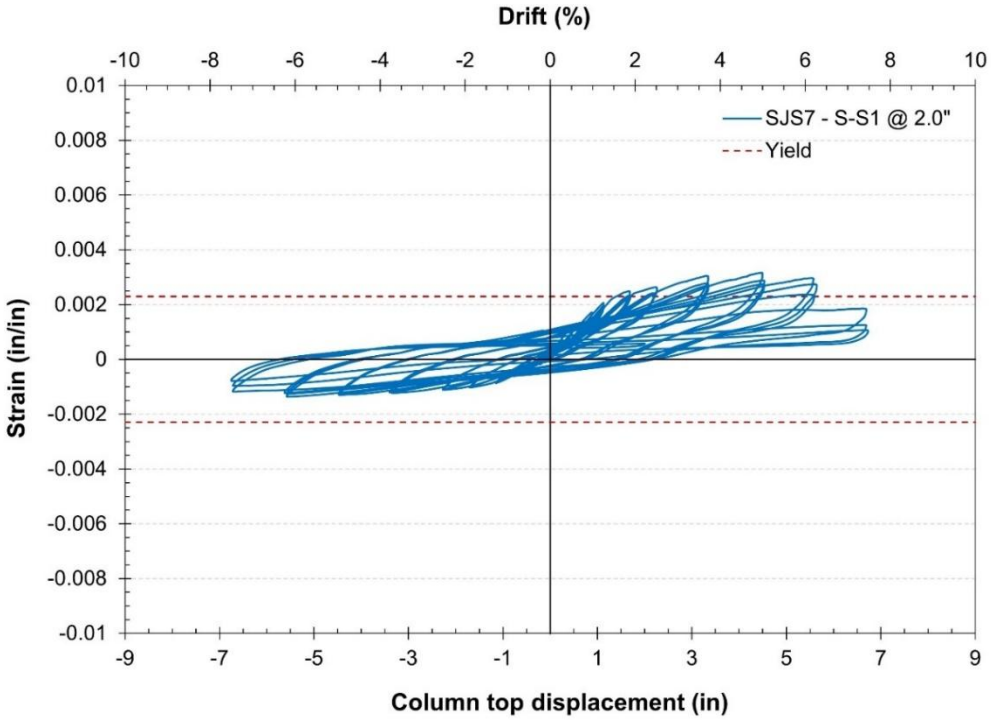


Figure 5-166. Strain vs displacement history for the extreme bar of socket wall reinforcement at the north side of SJS7

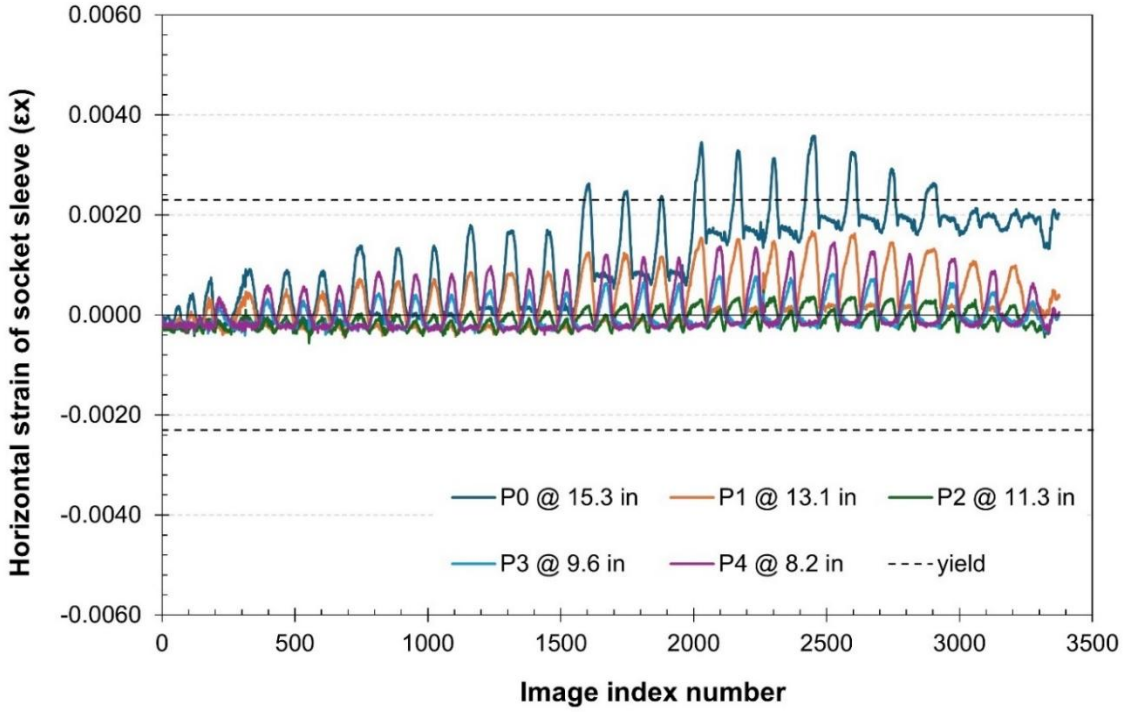


Figure 5-167. Horizontal strain history of external socket sleeve at the north side of SJS7

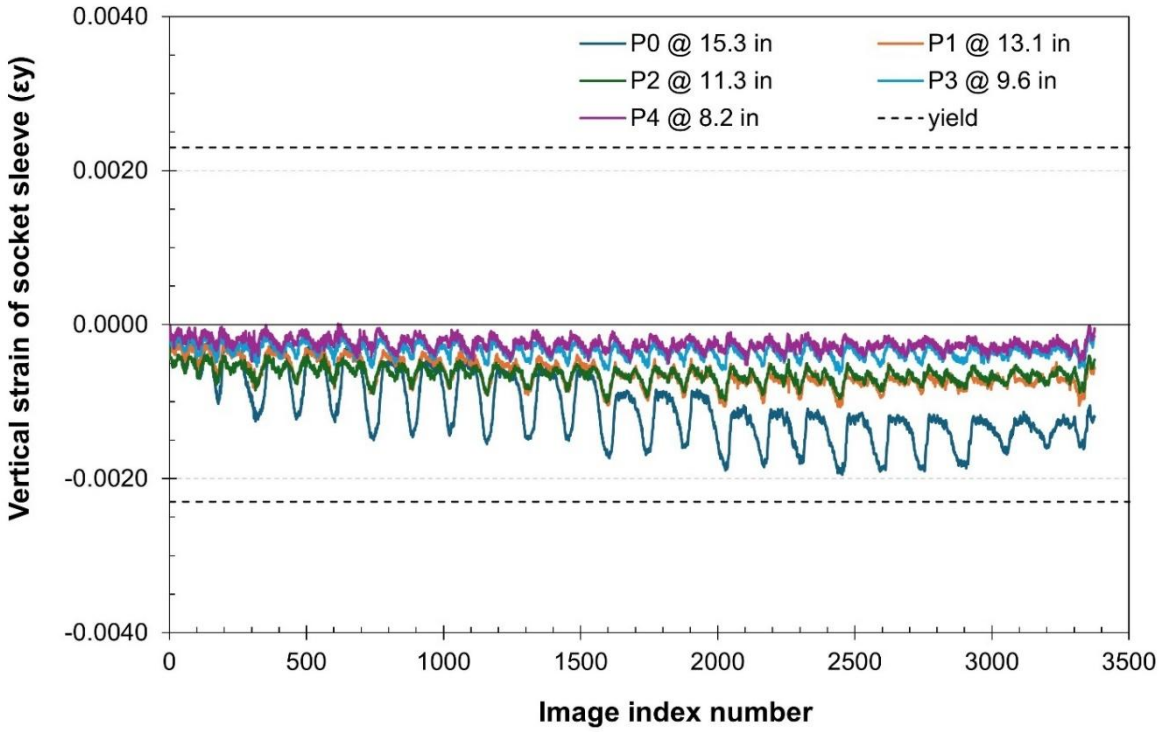


Figure 5-168. Vertical strain history of external socket sleeve at the north side of SJS7

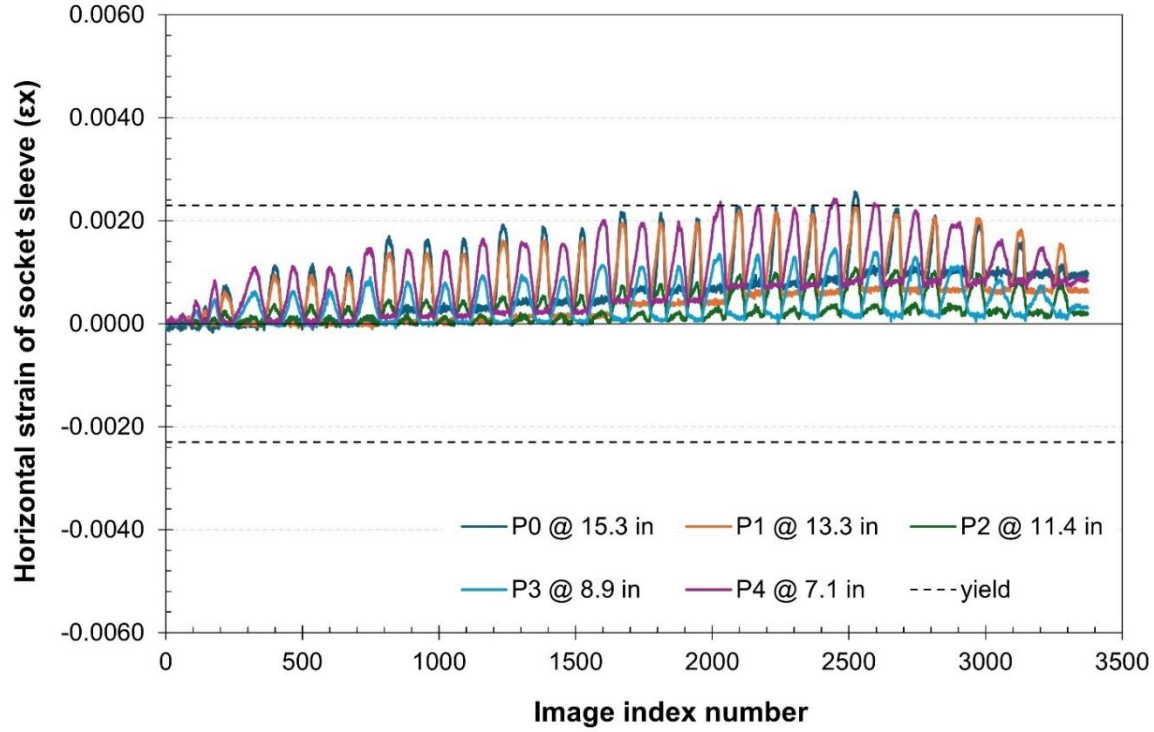


Figure 5-169. Horizontal strain history of external socket sleeve at the south side of SJS7

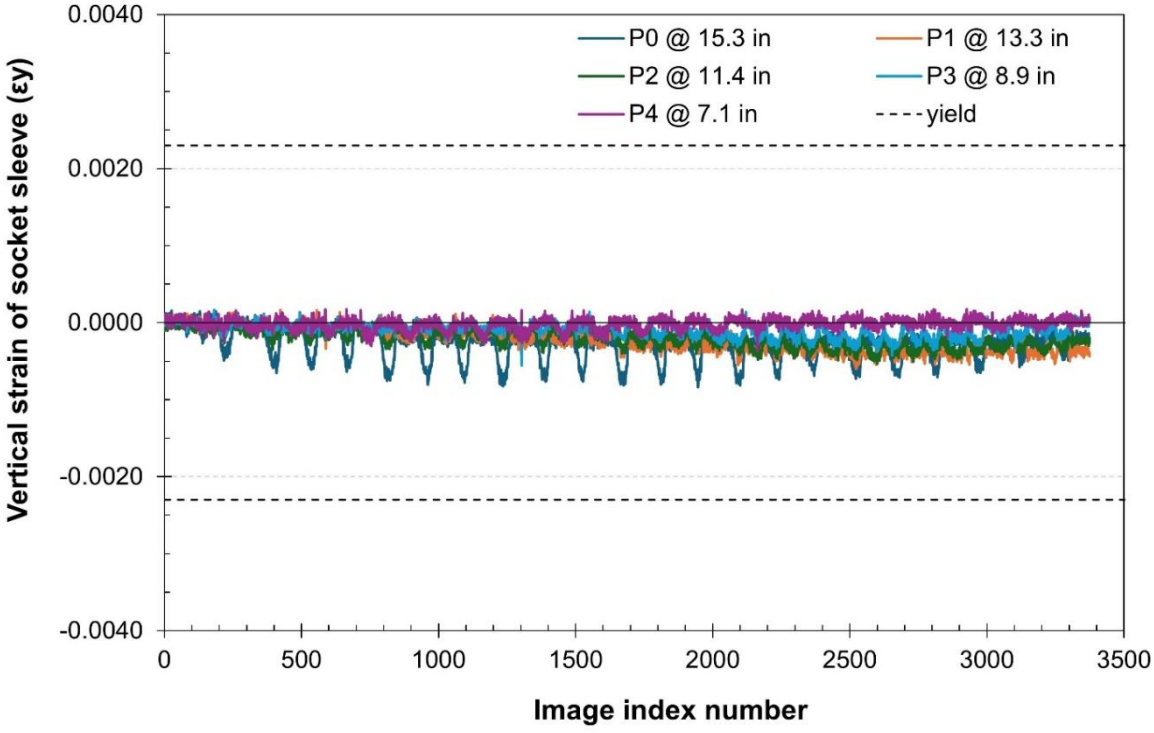


Figure 5-170. Vertical strain history of external socket sleeve at the south side of SJS7

The axial strains on the steel tube of the RCFST column were measured using DIC at the interface with the second steel tube, which has a smaller thickness designed to reduce the strains transmitted to the connection. Figure 5-171 and Figure 5-172 present the strains on the north face of the specimen while Figure 5-173 and Figure 5-174 show the strains on the south face. The data indicates that both the horizontal and vertical strains remained elastic throughout the experimental test, suggesting that the steel sleeve did not contribute significantly to the flexural behavior near the interface with the reduced thickness sleeve that extends into the external socket connection.

The axial strains on the steel tube with a reduced thickness sleeve, which extends into the external socket connection, were measured using DIC at the interface between the external socket connection and the steel tube of the RCFST column. Figure 5-175 and Figure 5-176 present the strains on the north face of the specimen while Figure 5-177 and Figure 5-178 show the strains on the south face. The data indicates that both the horizontal and vertical strains exceeded 1%, as expected, given that the steel sleeve served to confine the gap and was subjected to compressive contact forces from the RCFST column steel tube. However, once local buckling occurred, the strain data became unreliable, with values going off-scale.

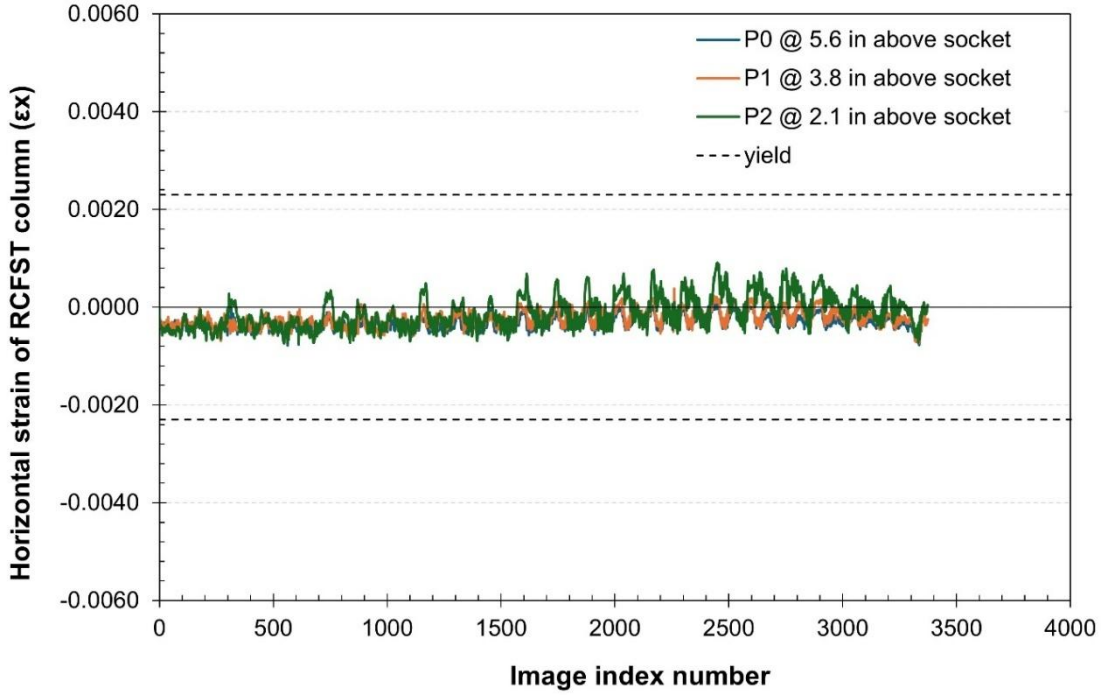


Figure 5-171. Horizontal strain history of RCFST column at the north side of SJS7

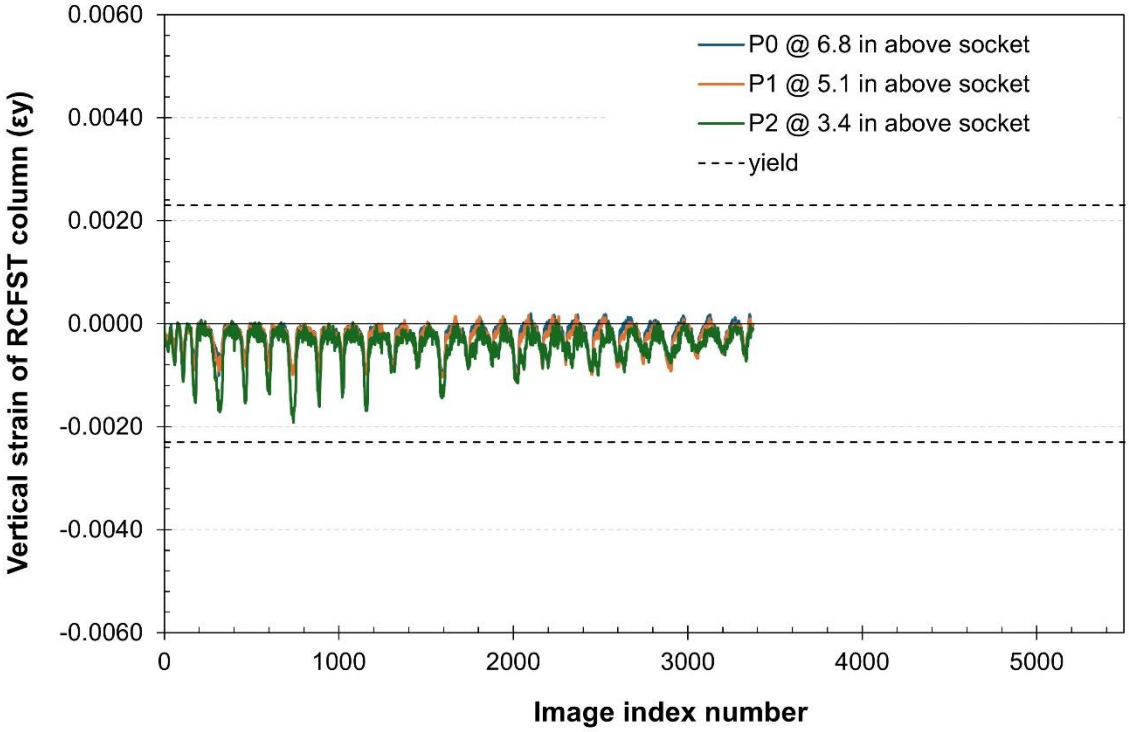


Figure 5-172. Vertical strain history of RCFST column at the north side of SJS7

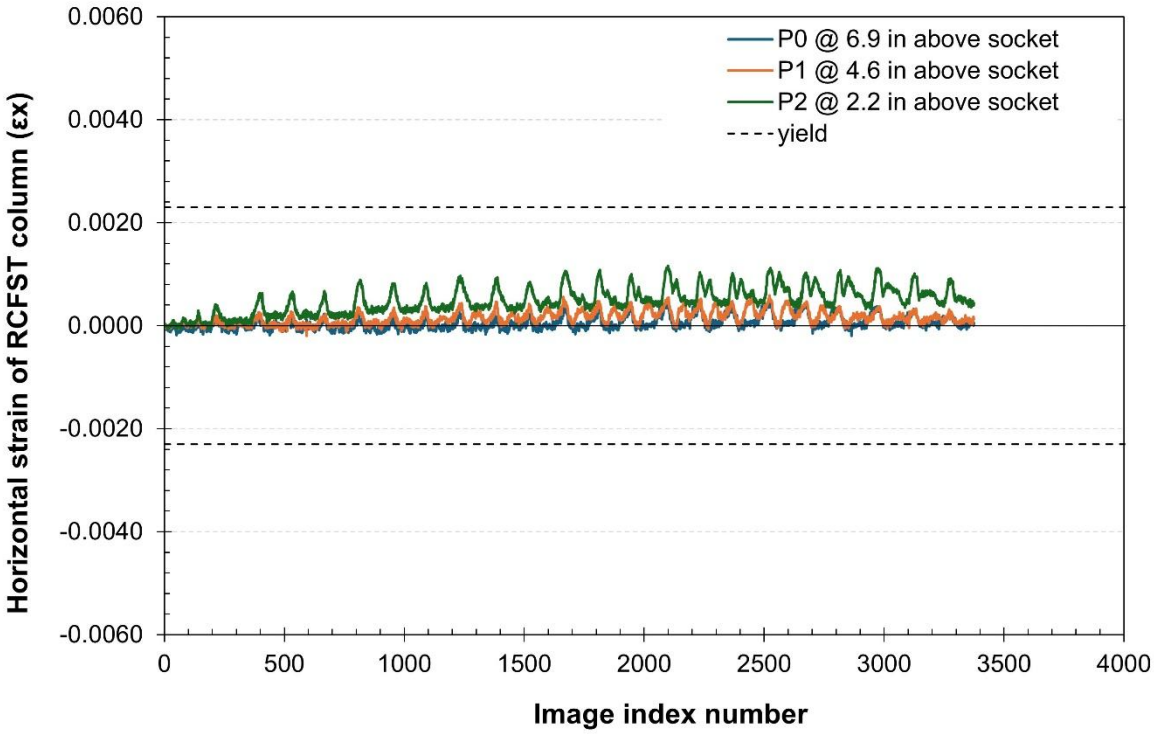


Figure 5-173. Horizontal strain history of RCFST column at the south side of SJS7

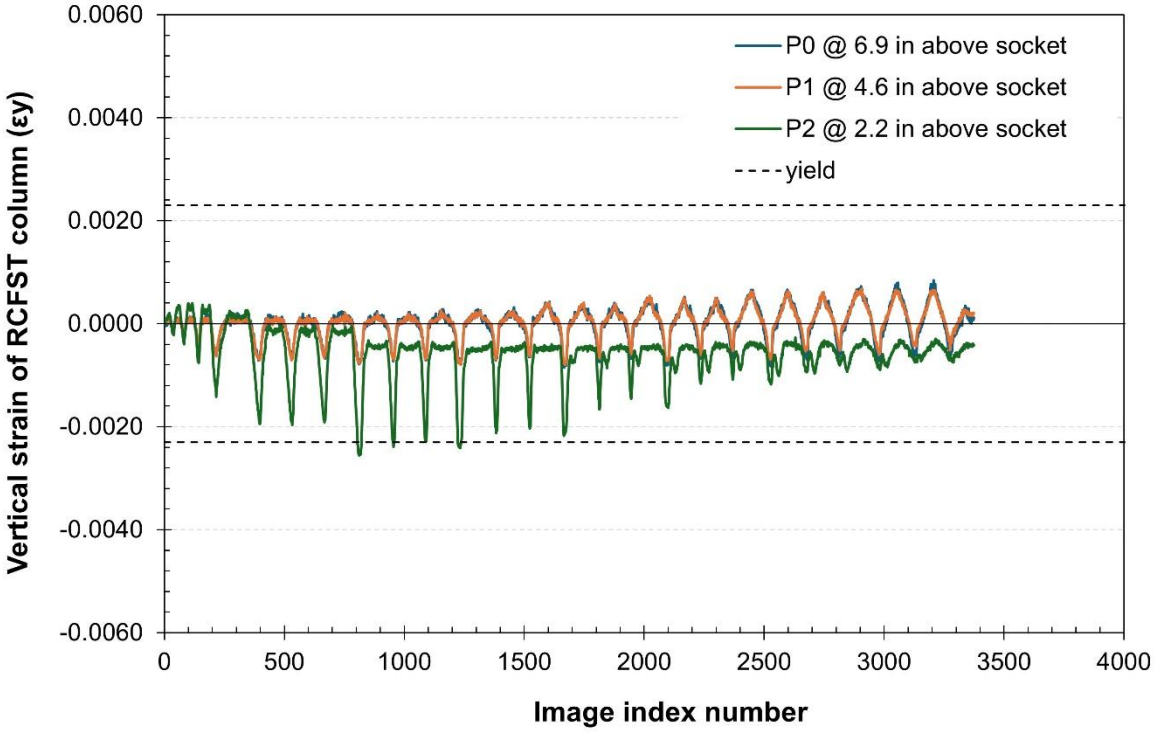


Figure 5-174. Vertical strain history of RCFST column at the south side of SJS7

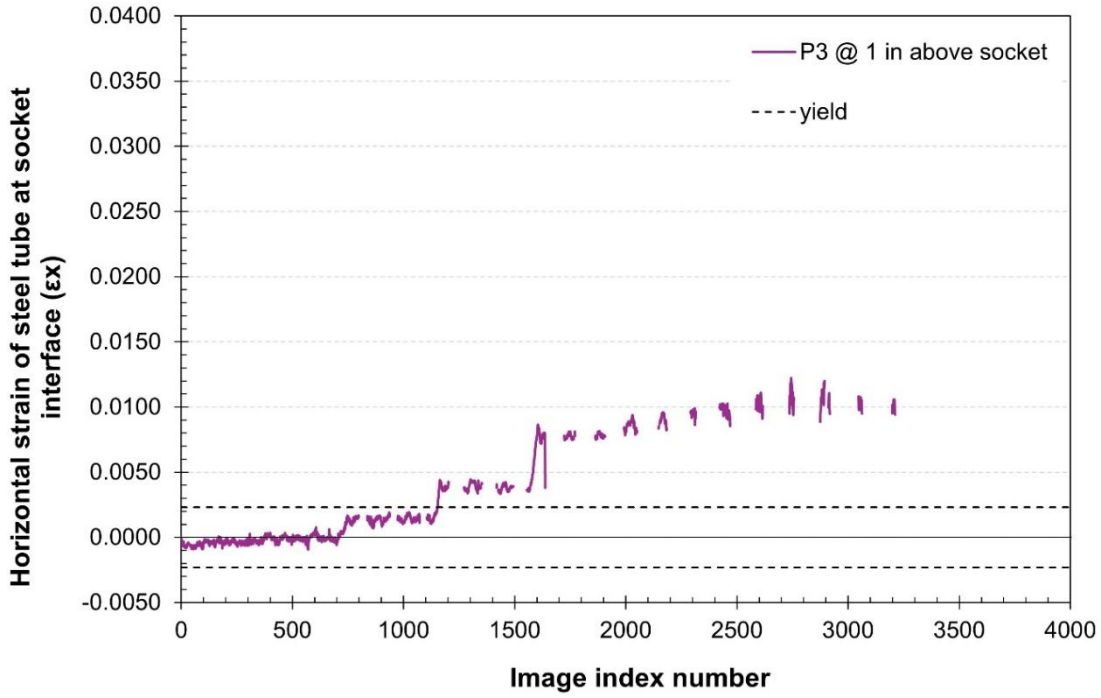


Figure 5-175. Horizontal strain history of steel tube at the socket interface at the north side of SJS7

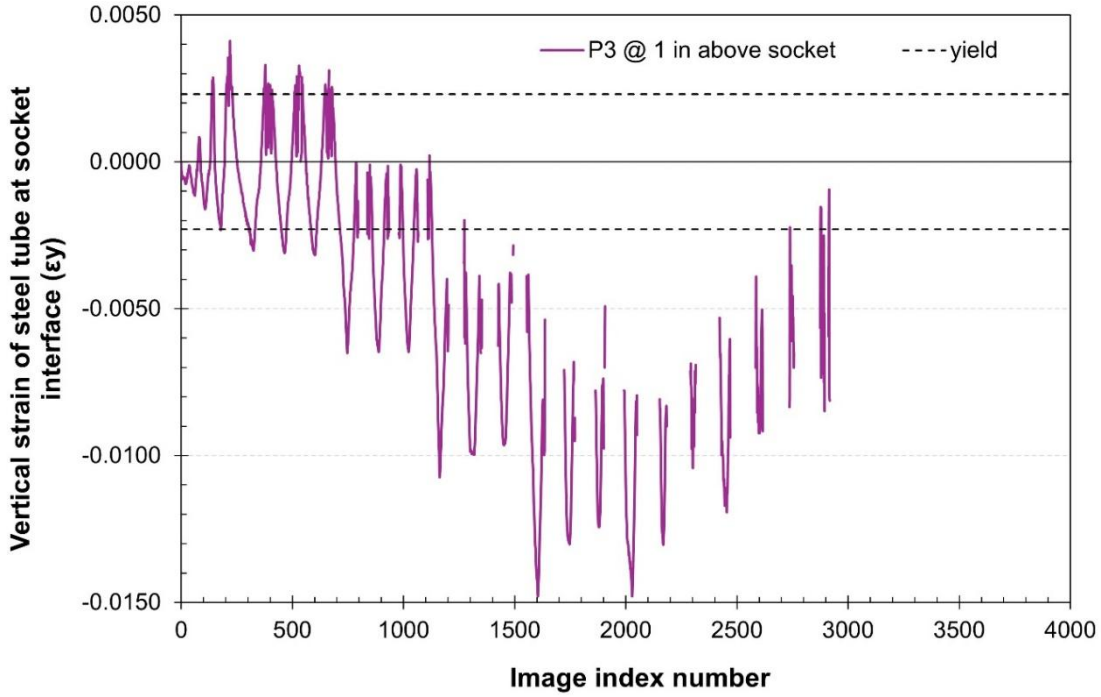


Figure 5-176. Vertical strain history of steel tube at the socket interface at the north side of SJS7

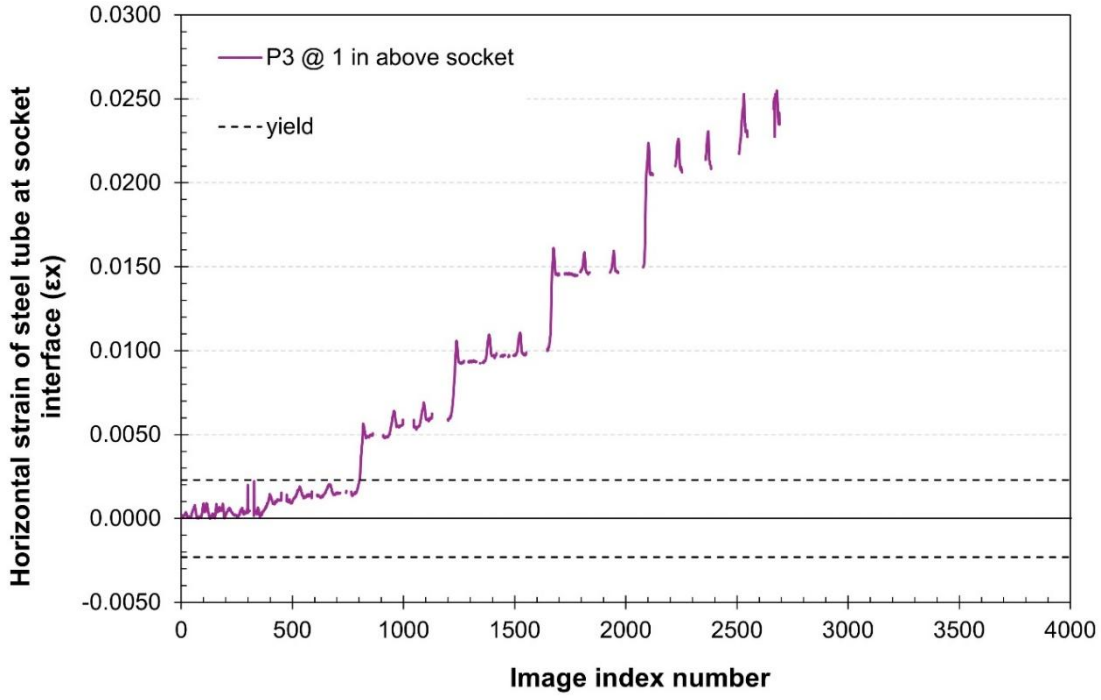


Figure 5-177. Horizontal strain history of steel tube at the socket interface at the south side of SJS7

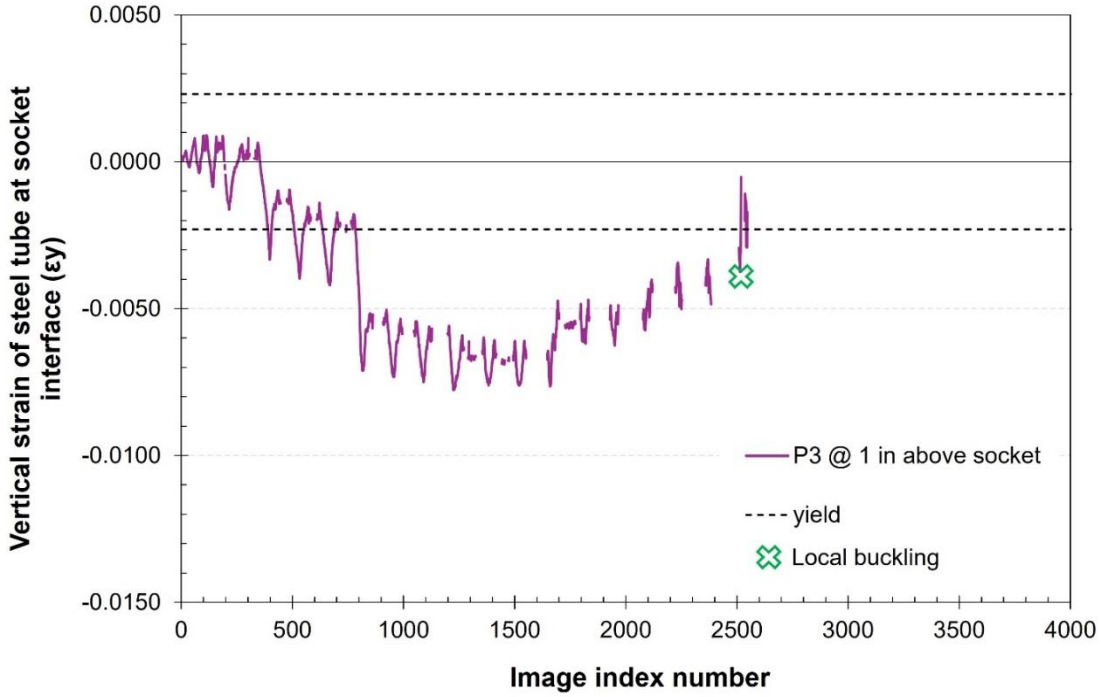


Figure 5-178. Vertical strain history of steel tube at the socket interface at the south side of SJS7

5.8.2. Energy dissipation and hysteretic damping for SJS-7

Energy dissipation is important in understanding a structure seismic behavior because it relates to the structural element damage and energy dissipation capacity. Figure 5-179 illustrates the energy dissipation for all ductility displacement cycles for SJS7, with a total energy dissipation of 4211 kip-in. Notably, during the third cycle of ductility six, when the shear failure of the column occurred, the energy dissipated was reduced by 50% compared to the first cycle at the same ductility level. This reduction highlights the impact of severe damage on the energy dissipation capacity of the column.

Additionally, Figure 5-180 presents the Jacobsen hysteretic damping values for SJS7, demonstrating that damping increases as the applied displacements grow and the column sustains more damage. Notably, the elastic damping for SJS7 was approximately 14%, which is 5% higher than what is typically observed in a CIP column, indicating enhanced energy dissipation during the structural element elastic behavior.

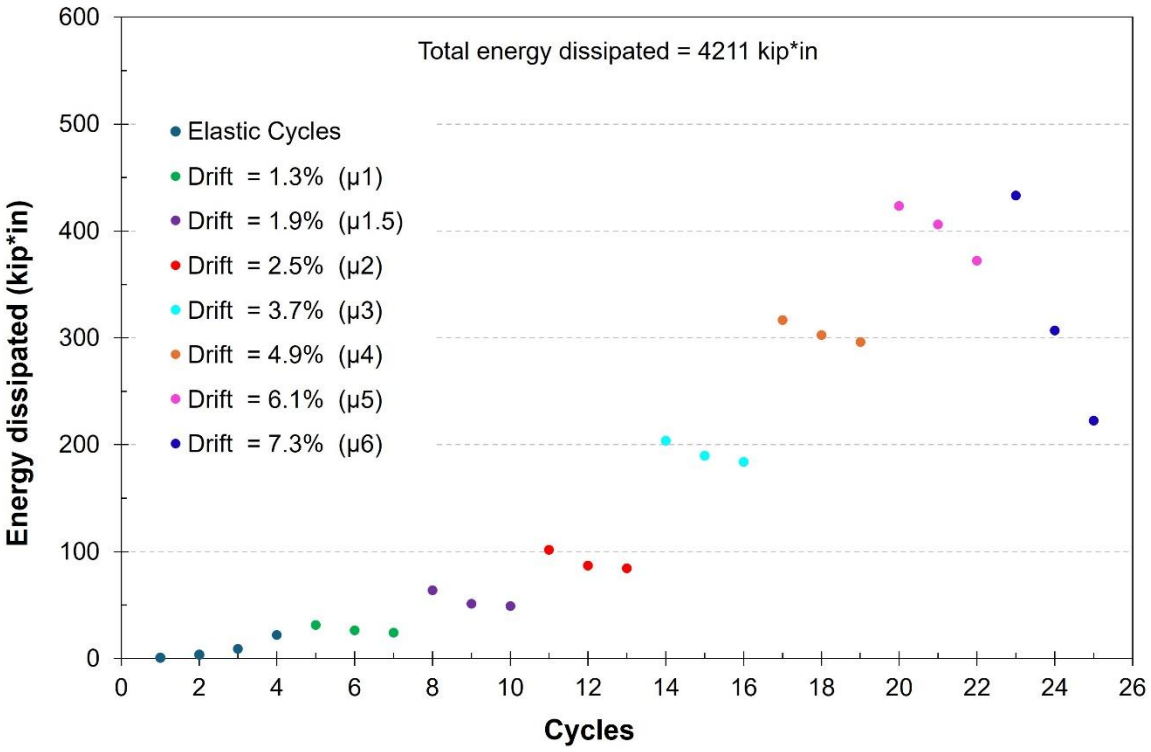


Figure 5-179. Energy dissipation plot for SJS7

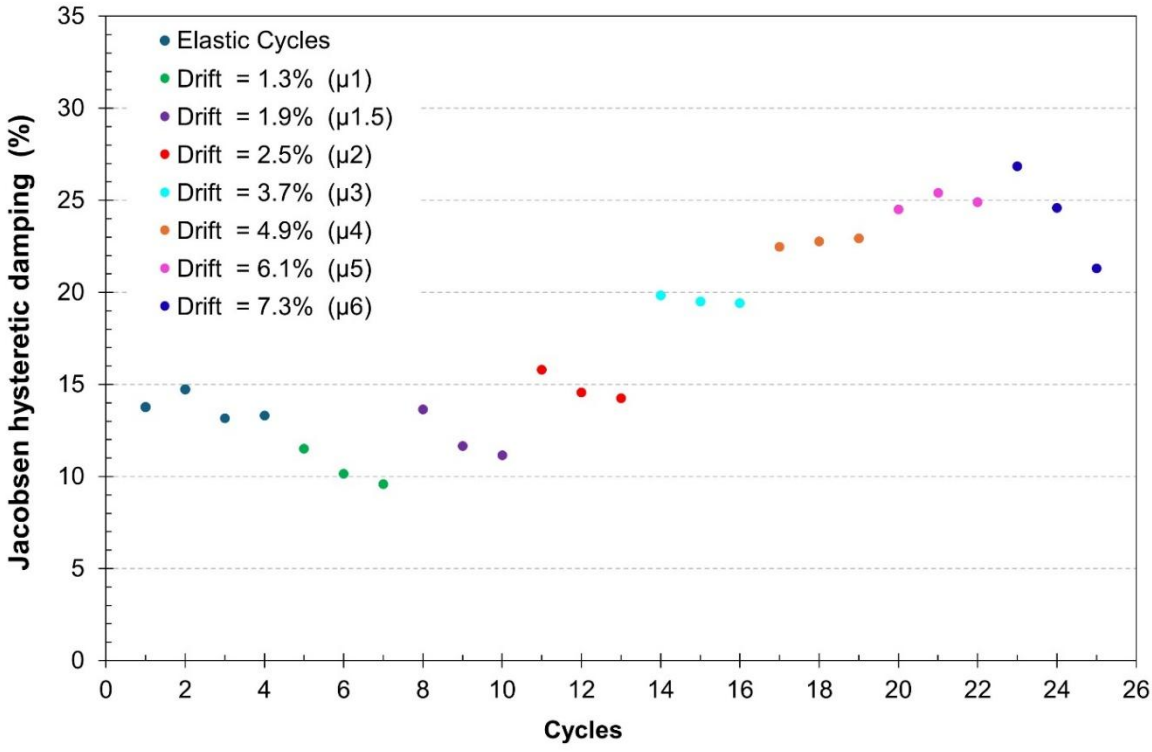


Figure 5-180. Hysteretic damping plot for SJS7

5.8.3. Socket rotation and RCFST gap opening for SJS-7

The socket rotation was measured using DIC, with Figure 5-181 and Figure 5-182 illustrating the rotation throughout the experimental test for the north and south faces, respectively. Measurements were taken at five different locations along the height of the socket. Although no specific calculations of displacement components were performed for the RCFST column, the socket rotation data was used to verify that the external socket connection exhibited behavior similar to that observed in previous tests. As shown in Figure 5-181 and Figure 5-182, the socket rotation is comparable to earlier results, indicating that socket rotation had a negligible impact on the total displacement.

Additionally, the gap between the two steel tubes was measured using DIC. Figure 5-183 shows the measured gap between the steel sleeves, which reached 1.1 inches upward during the final ductility displacement.

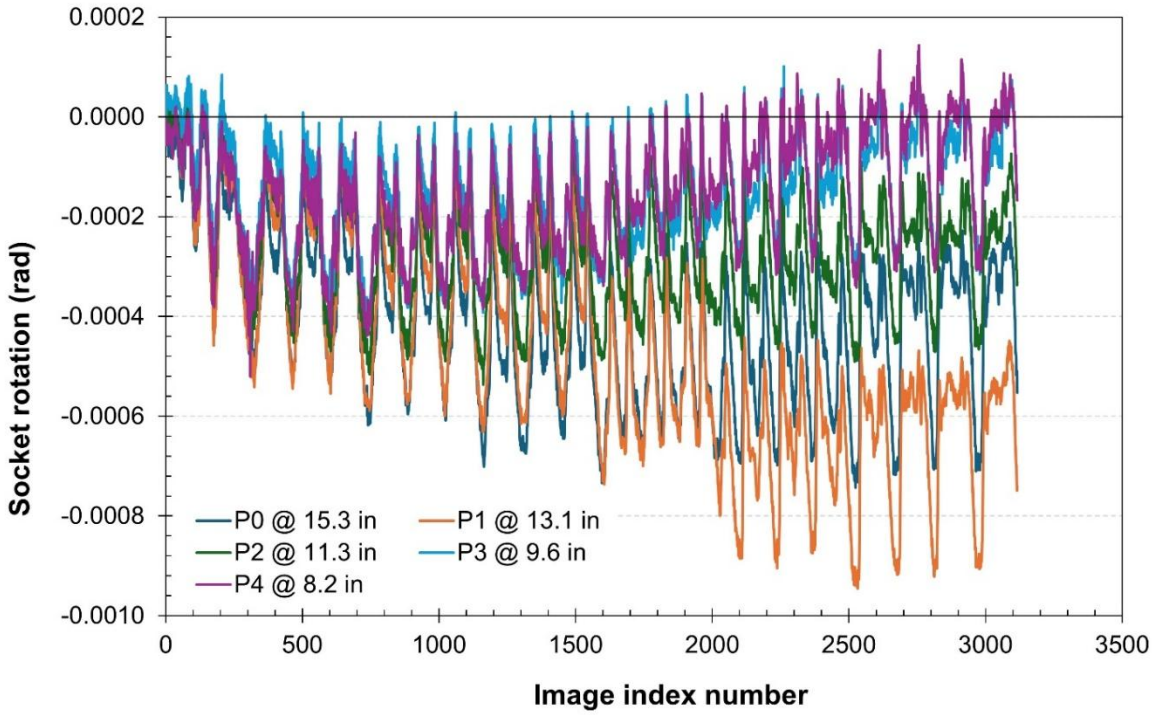


Figure 5-181. Socket rotation at the north side of SJS7

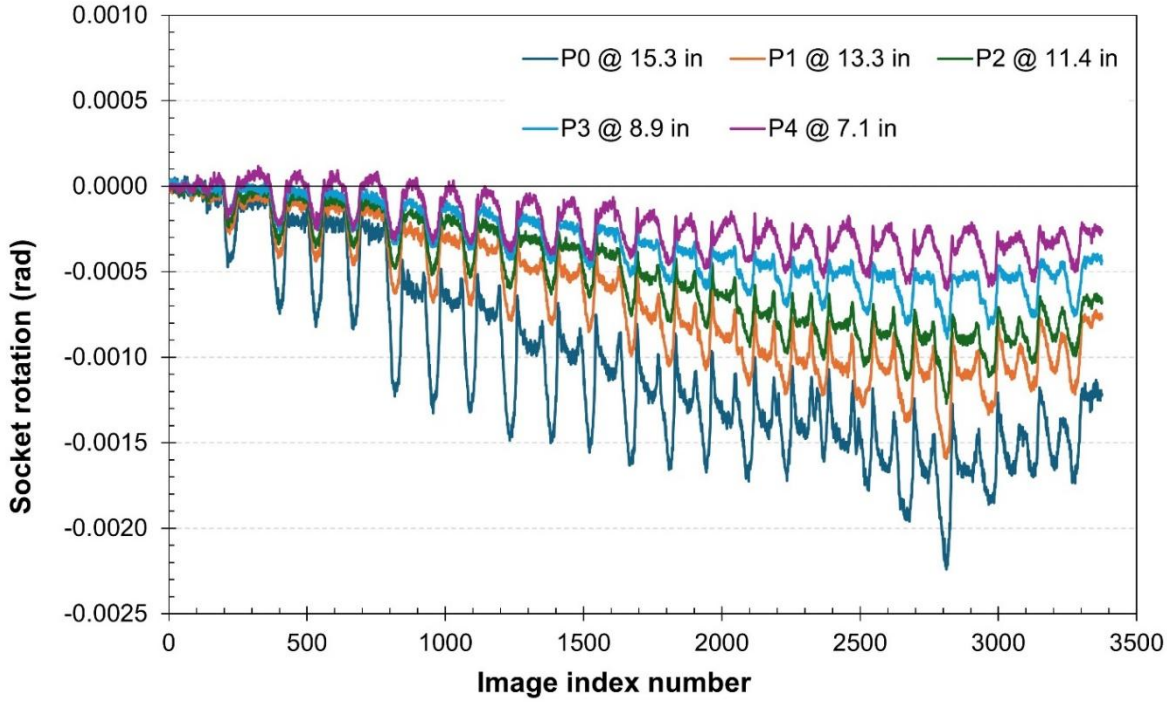


Figure 5-182. Socket rotation at the south side of SJS7

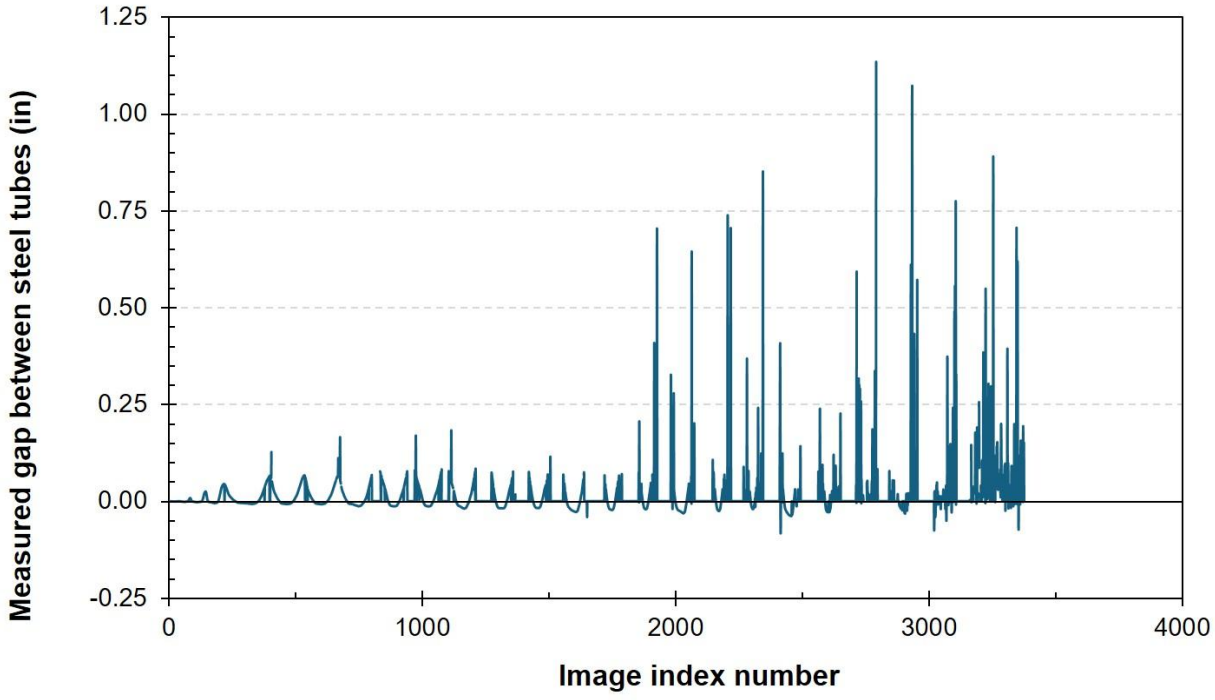


Figure 5-183. Opening of the gap between steel tubes at the north face of SJS7

5.8.4. Summary of Results for SJS-7

The tension strains on the longitudinal bars of the column were not obtained as in previous tests because the reinforcement could not be exposed due to the presence of the steel tube. The strains in the external socket wall reached twice the yield strain, indicating that the external socket connection effectively reduced plastic strains from reaching the foundation or cap beam. As a result, the footing remained as a capacity-protected element. Horizontal strains in the external socket sleeve reached 1.5 times the yield strain at the top third of the socket height but remained elastic for the rest of the height. No visible damage was observed on the sleeves during the test, confirming that the sleeves did not experience significant inelastic deformation.

The elastic damping for SJS 7 was approximately 14%, which is higher than the 5% typically observed in CIP columns. This additional 9% damping may be attributed to the initial cracks in the socket wall and grout that occurred early in the test, as well as some unidentified noises observed during the cycles before the yield displacement.

The gap between the two steel tubes was monitored throughout the test, reaching a maximum opening of 1.1 inches at the final ductility displacement. The gap became noticeable after the first cycle of ductility one and increased linearly until the onset of concrete crushing and the shear failure of the column.

5.9. Experimental Results of Specimen SJS-8

In this section, the data analysis and experimental results previously discussed in this chapter will be specifically applied to the experimental test SJS8. The results for SJS8 will be presented in detail, focusing on axial strains on the RCFST column and external socket and hysteretic damping. This analysis provides insights into the column performance and behavior under the applied loading conditions, contributing to a comprehensive understanding of the system response.

5.9.1. Axial strain analysis for SJS-8

For the RCFST, the strains on the longitudinal bars were not obtained as in previous tests because the reinforcement could not be exposed due to the presence of the steel tube. However, the strain history of the extreme bars in the external socket wall reinforcement was monitored using strain gauges placed 2 inches above the footing. Figure 5-184 and Figure 5-185 present the strain history for the extreme bars on the north and south faces, respectively. The data indicates that the reinforcement in the external socket wall reached 1.5 times the yield strain, indicating that the external socket wall remained almost elastic throughout the entire experimental test.

The axial strains on the external socket sleeve were measured using DIC. In this context, the horizontal strains correspond to the hoop forces acting around the circumference, while the vertical strains reflect any flexion sustained by the sleeves. Figure 5-186 and Figure 5-187 present the strains on the north face of the specimen while Figure 5-188 and Figure 5-189 show the strains on the south face. The data shows that, for the horizontal strains, the top 5 inches of the socket experienced strain similar to the yielding strain; thus, the remaining height of the socket remained elastic. The vertical strains remained elastic throughout the experimental test, indicating that the external socket sleeve did not contribute significantly to the flexural behavior of the external socket wall.

The axial strains on the steel tube of the RCFST column were measured using DIC at the interface with the second steel tube, which has a smaller thickness designed to reduce the strains transmitted to the connection. Figure 5-190 and Figure 5-191 present the strains on the north face of the specimen while Figure 5-192 and Figure 5-193 show the strains on the south face. The data indicates that both the horizontal and vertical strains remained elastic throughout the experimental test, suggesting that the steel sleeve did not contribute significantly to the flexural behavior near the interface with the reduced thickness sleeve that extends into the external socket connection.

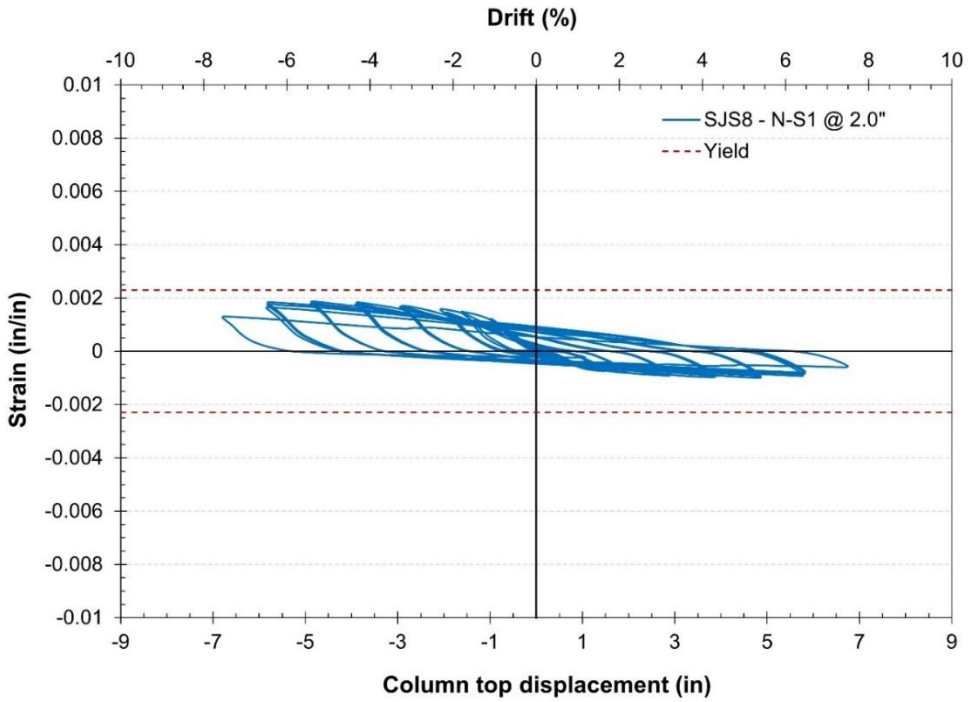


Figure 5-184. Strain vs displacement history for the extreme bar of socket wall reinforcement at the north side of SJS8

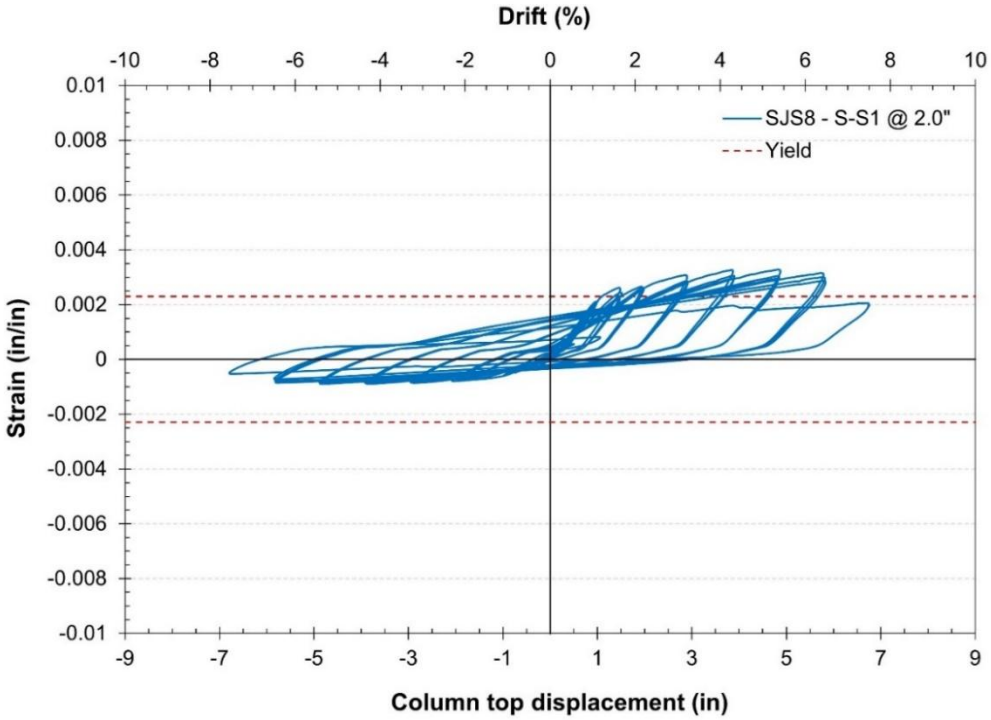


Figure 5-185. Strain vs displacement history for the extreme bar of socket wall reinforcement at the north side of SJS8

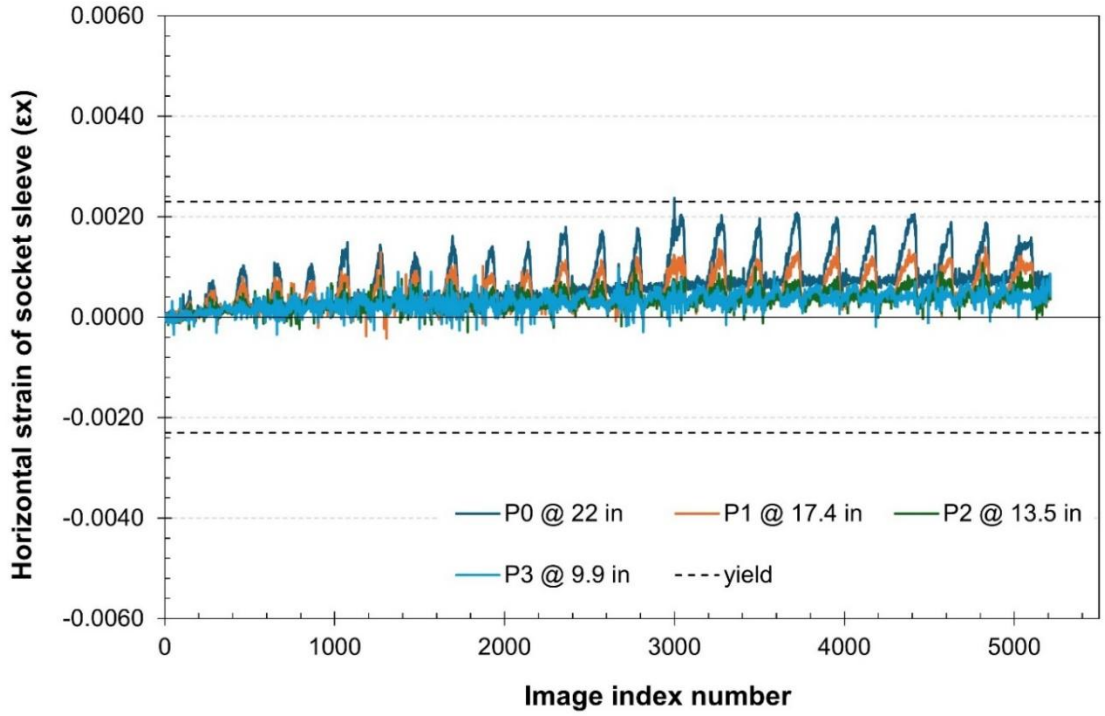


Figure 5-186. Horizontal strain history of external socket sleeve at the north side of SJS8

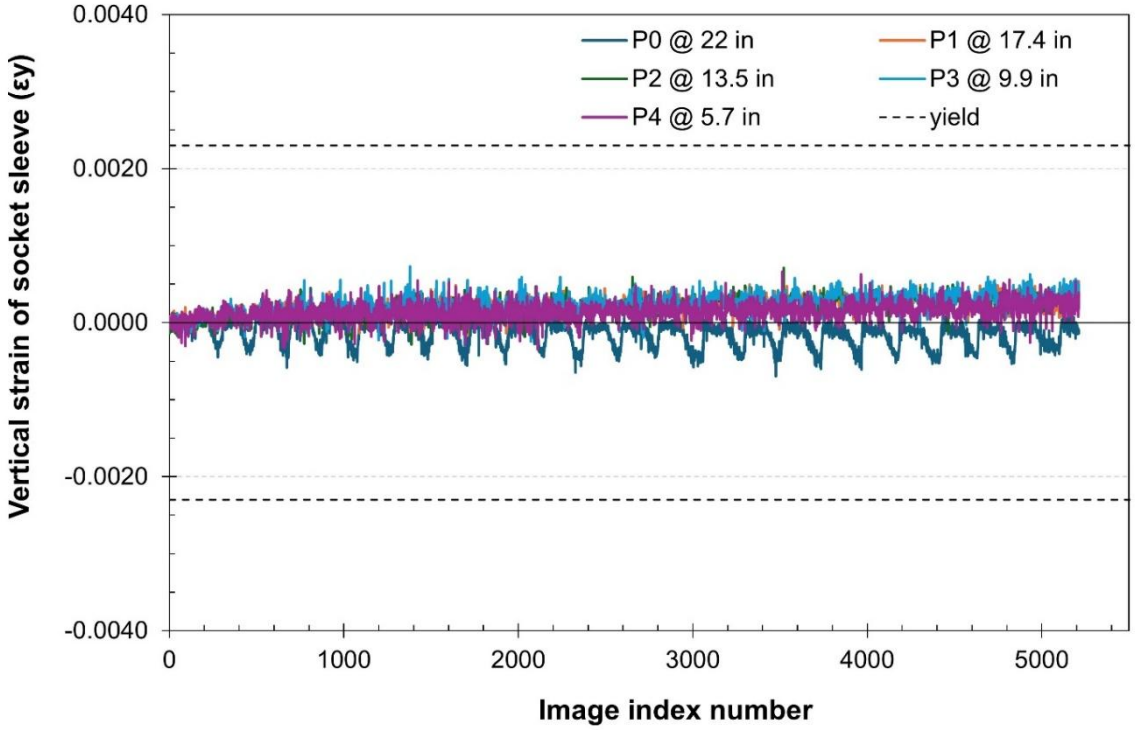


Figure 5-187. Vertical strain history of external socket sleeve at the north side of SJS8

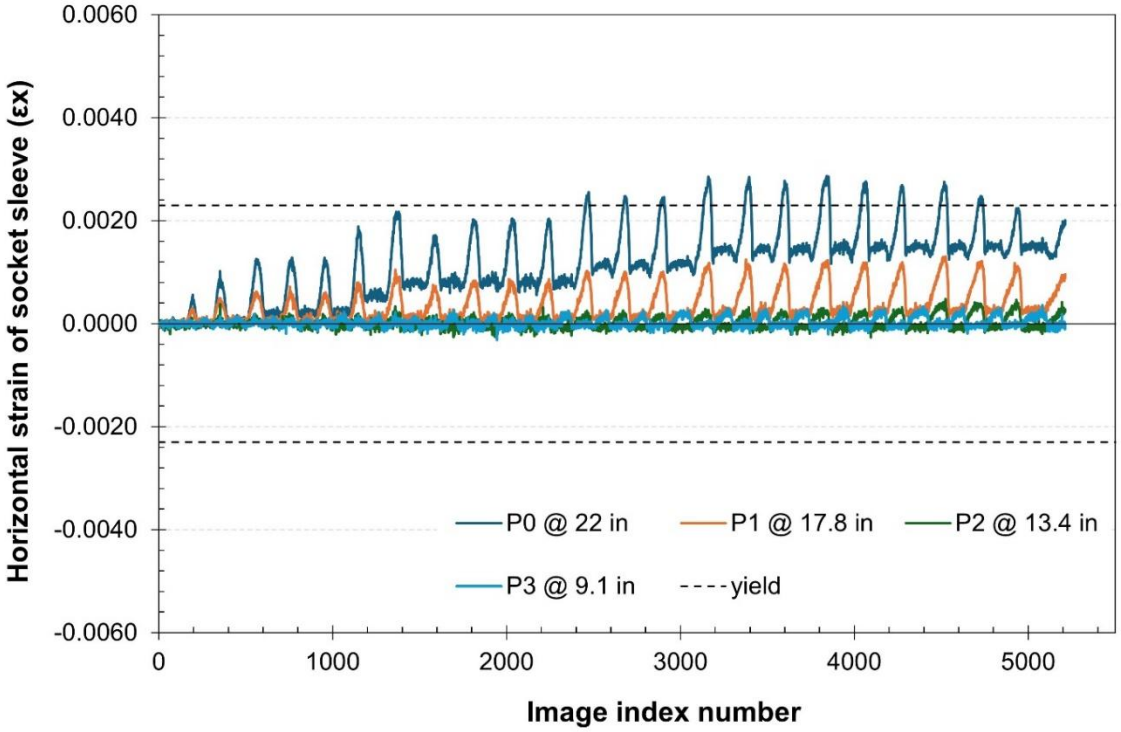


Figure 5-188. Horizontal strain history of external socket sleeve at the south side of SJS8

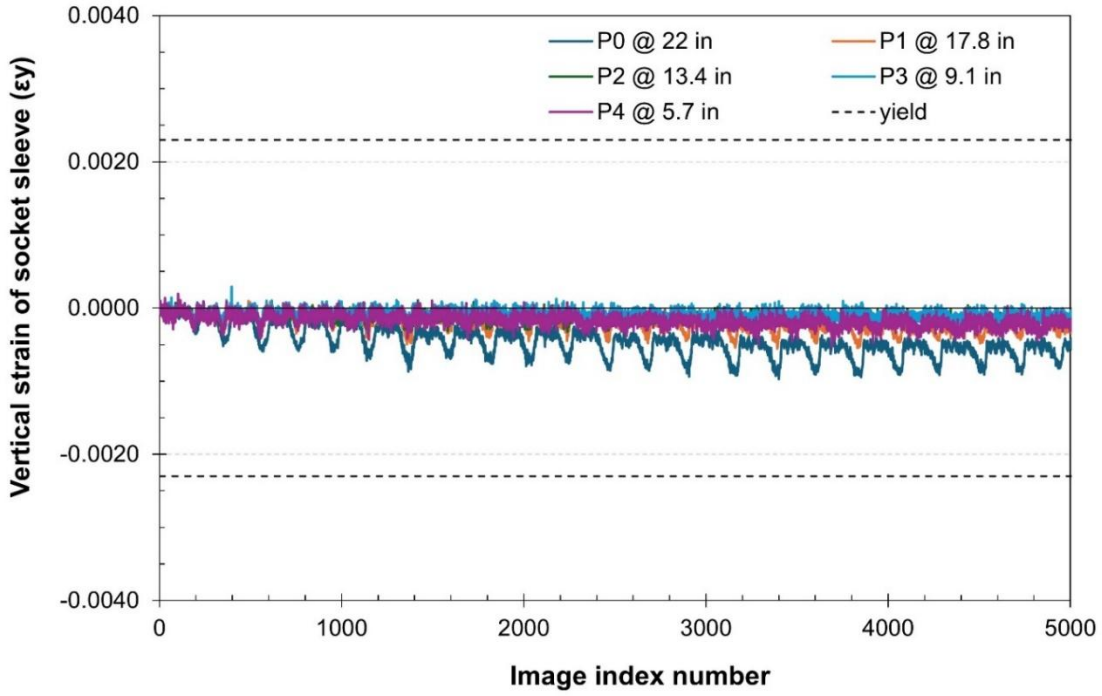


Figure 5-189. Vertical strain history of external socket sleeve at the south side of SJS8

The axial strains on the steel tube with a reduced thickness sleeve, which extends into the external socket connection, were measured using DIC at the interface between the external socket connection and the steel tube of the RCFST column. Figure 5-194 and Figure 5-195 present the strains on the north face of the specimen while Figure 5-196 and Figure 5-197 show the strains on the south face. The data indicates that both the horizontal and vertical strains exceeded 2%, as expected, given that the steel sleeve served to confine the gap and was subjected to compressive contact forces from the RCFST column steel tube. However, once local buckling occurred, the strain data became unreliable, with values going off-scale.

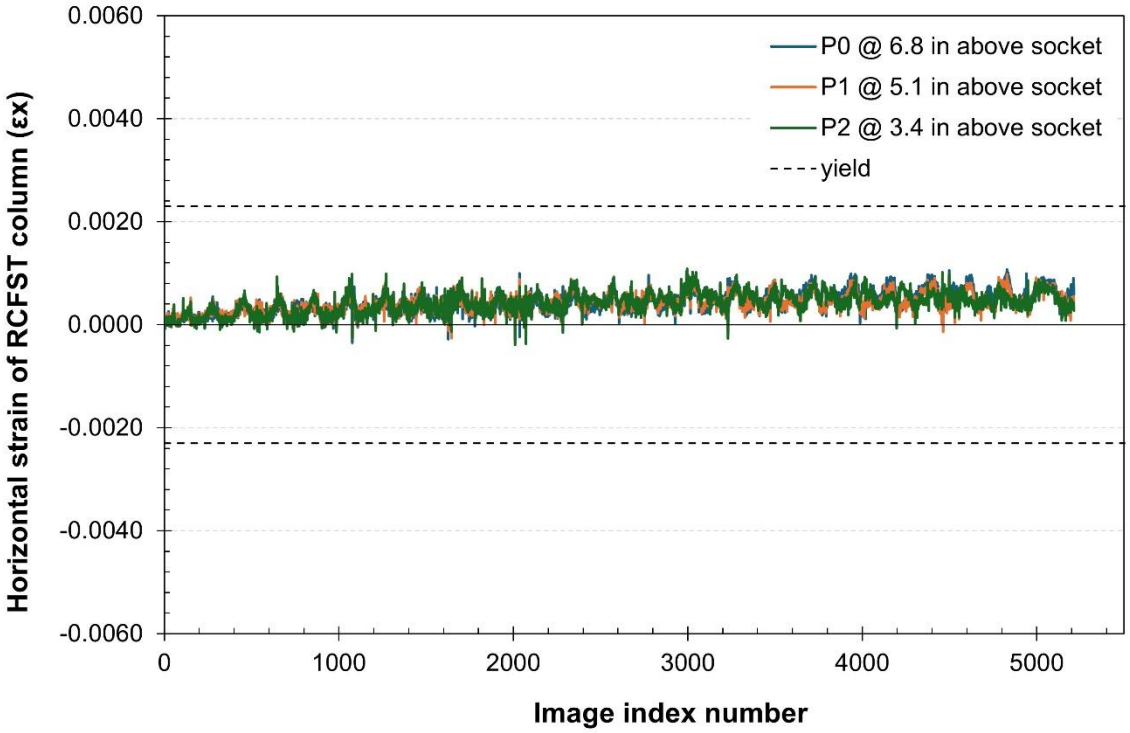


Figure 5-190. Horizontal strain history of RCFST column at the north side of SJS8

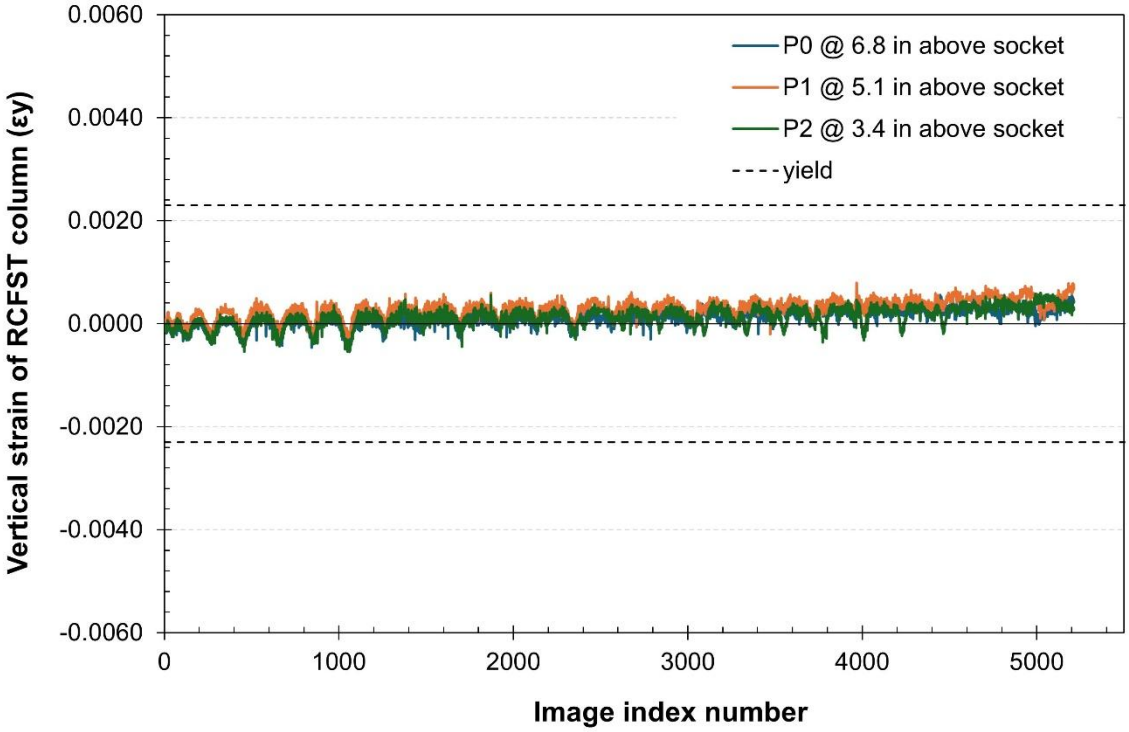


Figure 5-191 Vertical strain history of RCFST column at the north side of SJS8

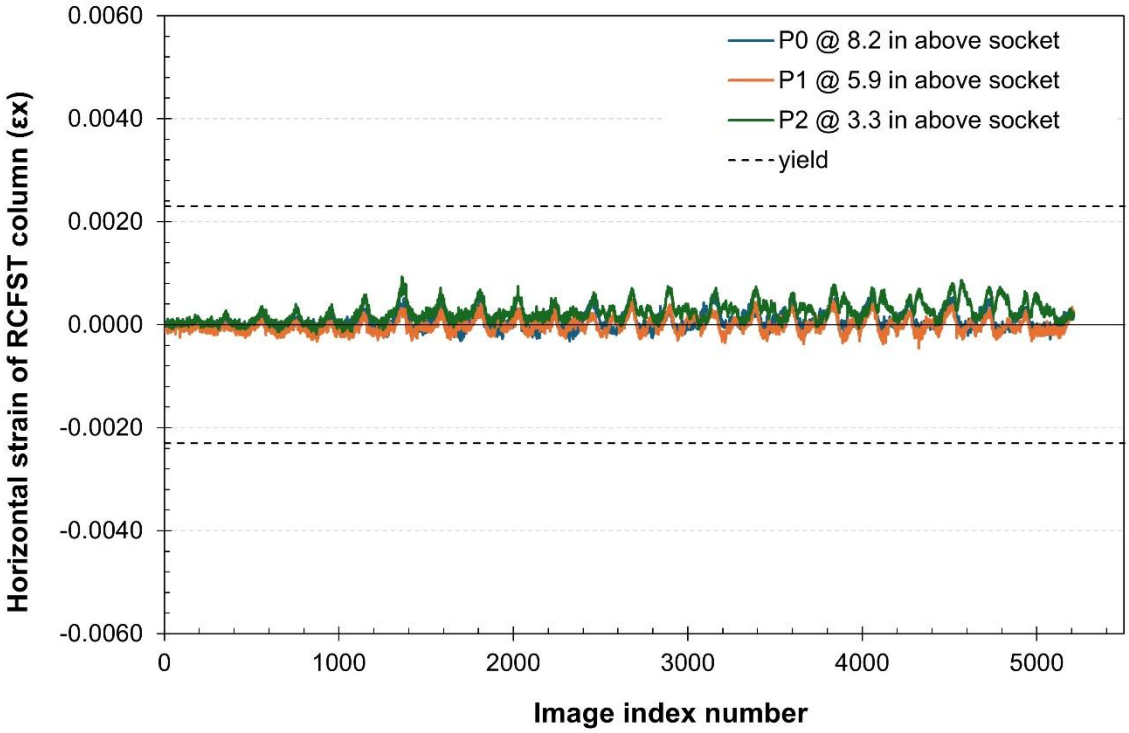


Figure 5-192. Horizontal strain history of RCFST column at the south side of SJS8

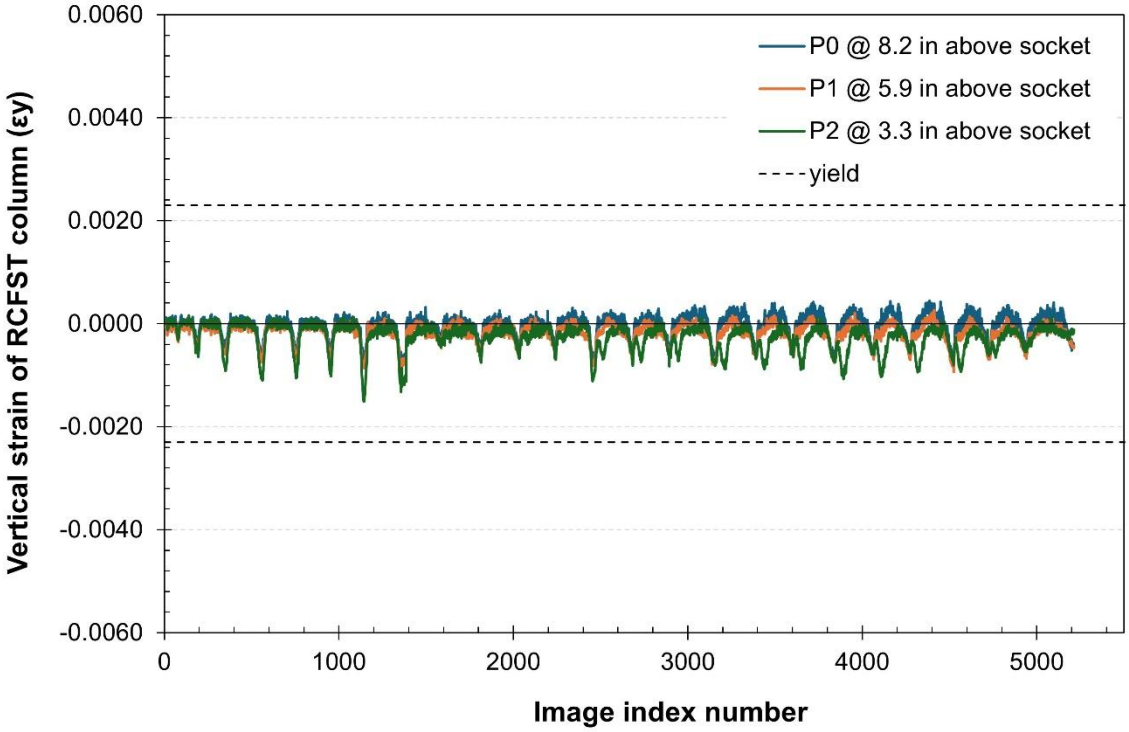


Figure 5-193. Vertical strain history of RCFST column at the south side of SJS8

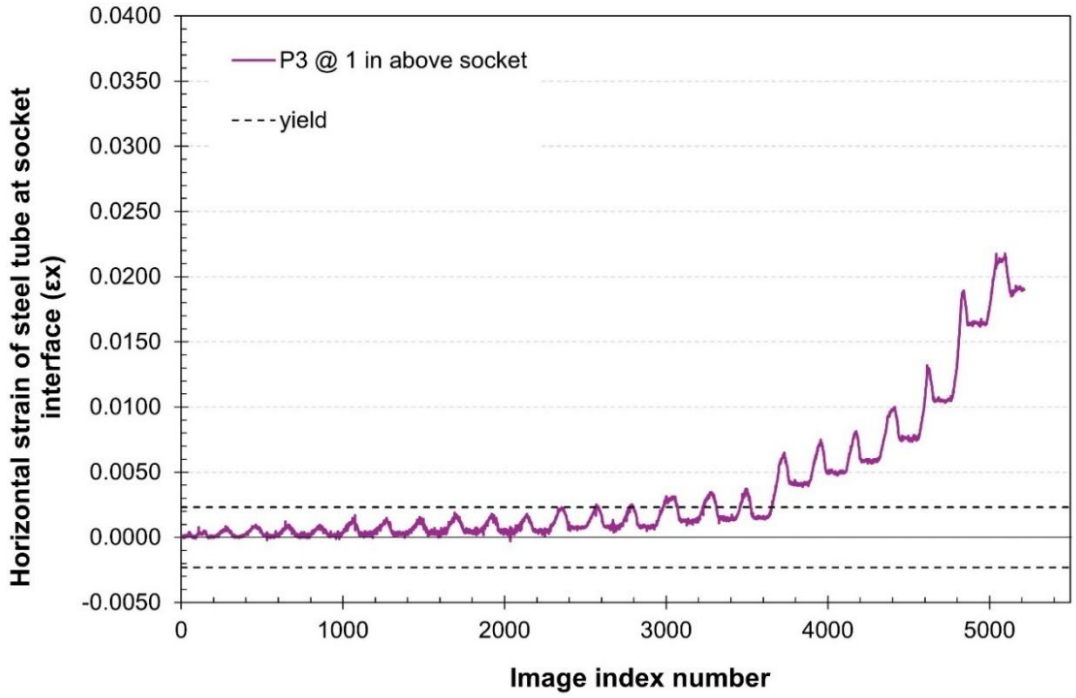


Figure 5-194 Horizontal strain history of steel tube at the socket interface at the north side of SJS8

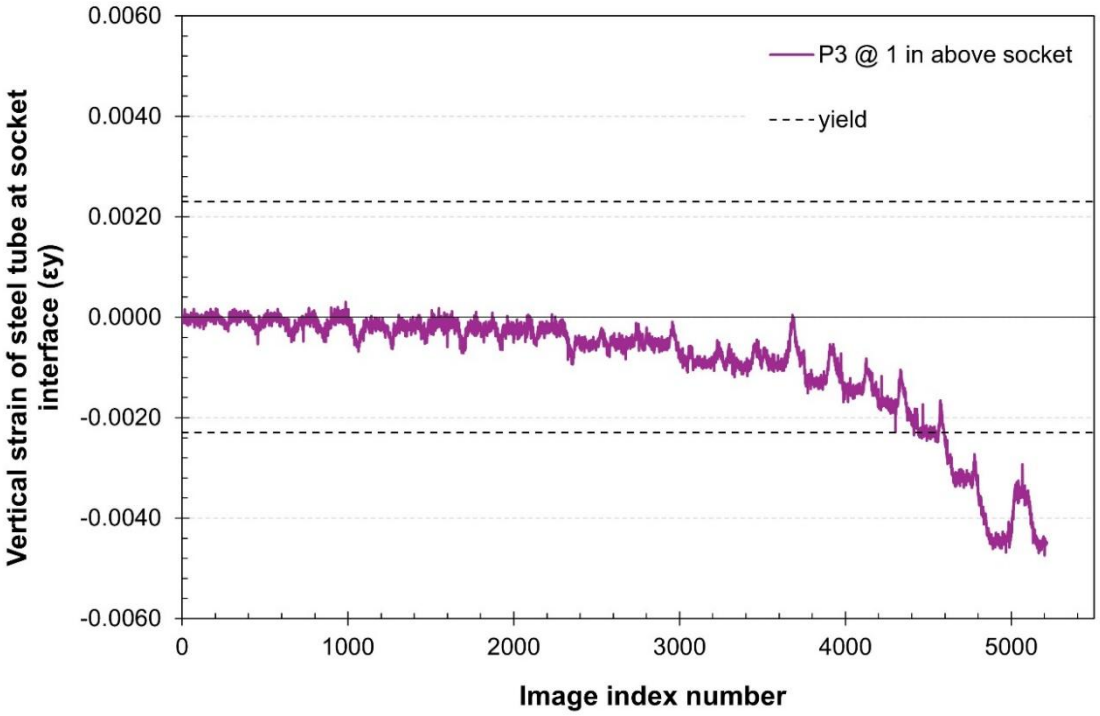


Figure 5-195. Vertical strain history of steel tube at the socket interface at the north side of SJS8

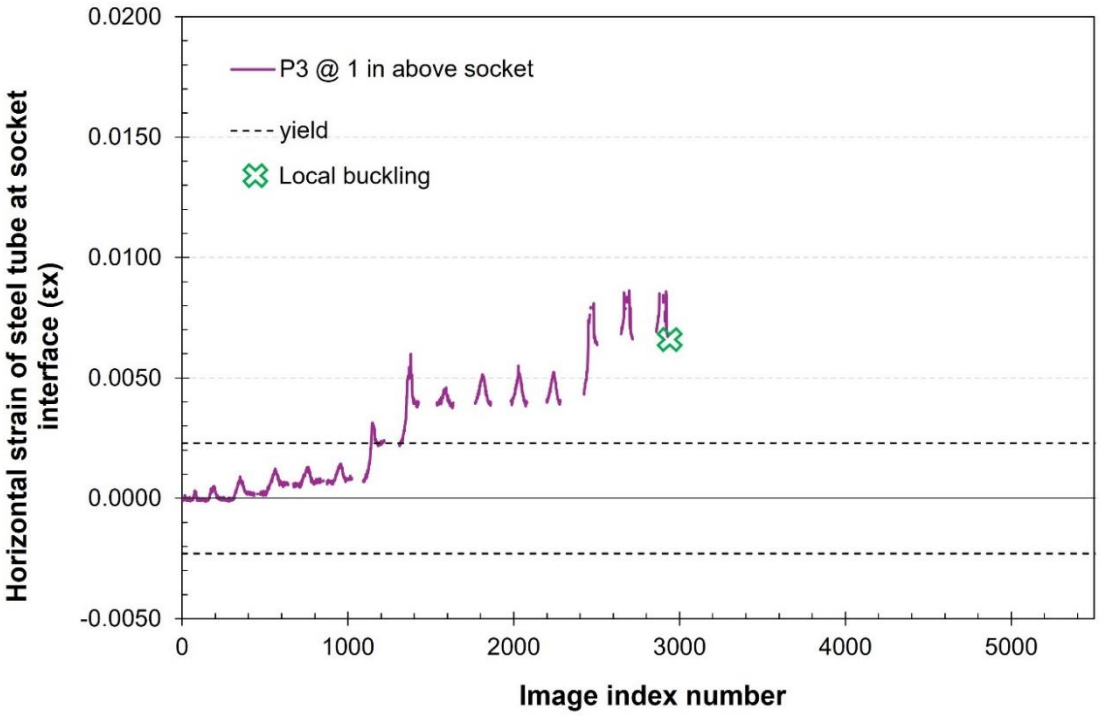


Figure 5-196. Horizontal strain history of steel tube at the socket interface at the south side of SJS8

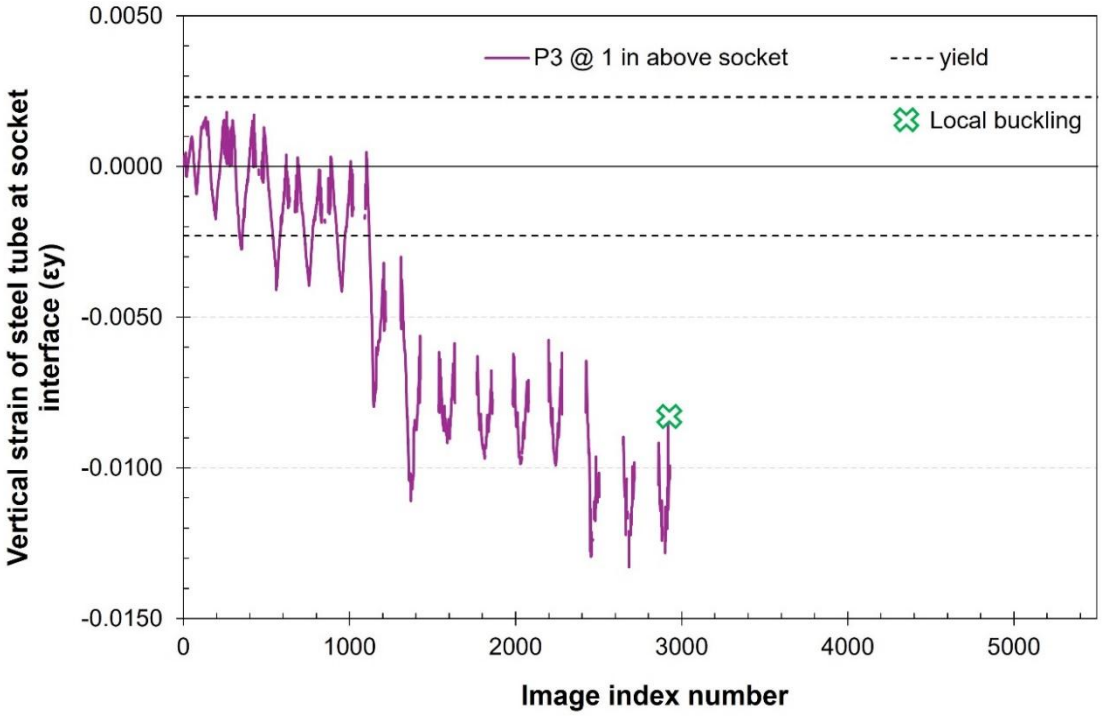


Figure 5-197. Vertical strain history of steel tube at the socket interface at the south side of SJS8

5.9.2. Energy dissipation and hysteretic damping for SJS-8

Energy dissipation is important in understanding a structure seismic behavior because it relates to the structural element damage and energy dissipation capacity. Figure 5-198 illustrates the energy dissipation for all ductility displacement cycles for SJS8, with a total energy dissipation of 5478 kip-in. Notably, during the first cycle of ductility seven, where bar fracture occurred, the energy dissipated was reduced by 20% compared to the first cycle of ductility six. This reduction highlights the impact of severe damage on the energy dissipation capacity of the column.

Additionally, Figure 5-199 presents the Jacobsen hysteretic damping values for SJS8, demonstrating that damping increases as the applied displacements grow and the column sustains more damage. Notably, the elastic damping for SJS8 was approximately 10%, which is 5% higher than what is typically observed in a CIP column, indicating enhanced energy dissipation during the structural element elastic behavior.

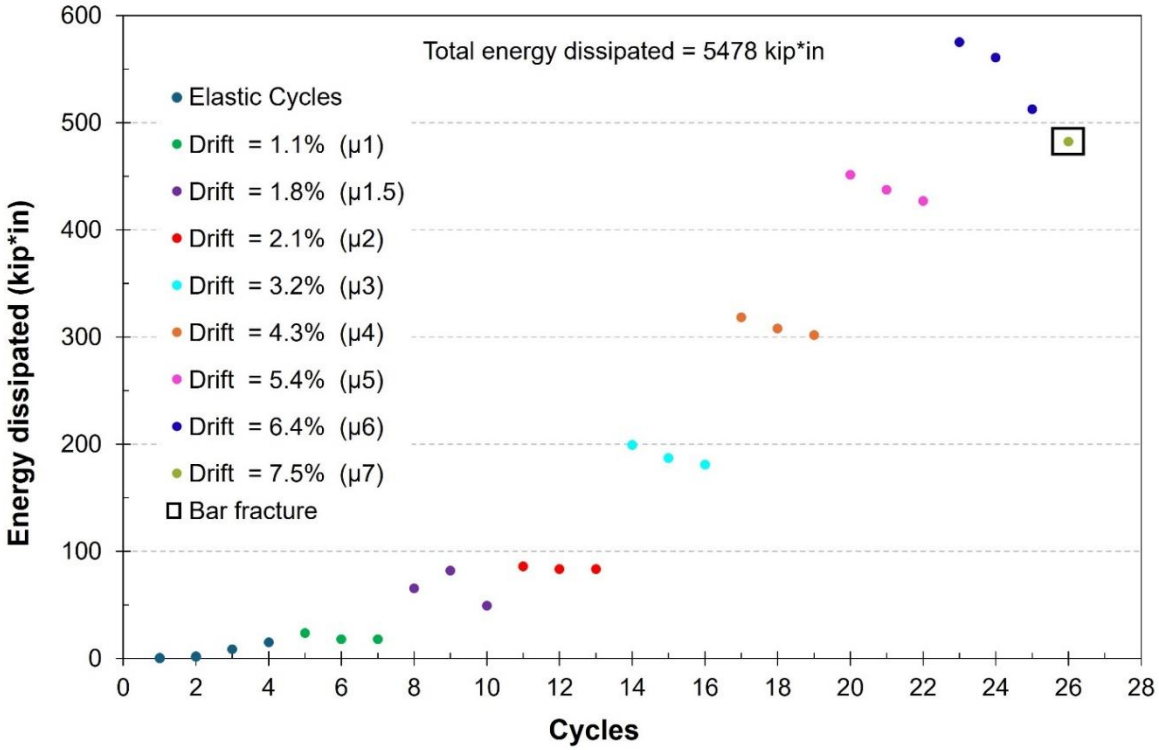


Figure 5-198. Energy dissipation plot for SJS8

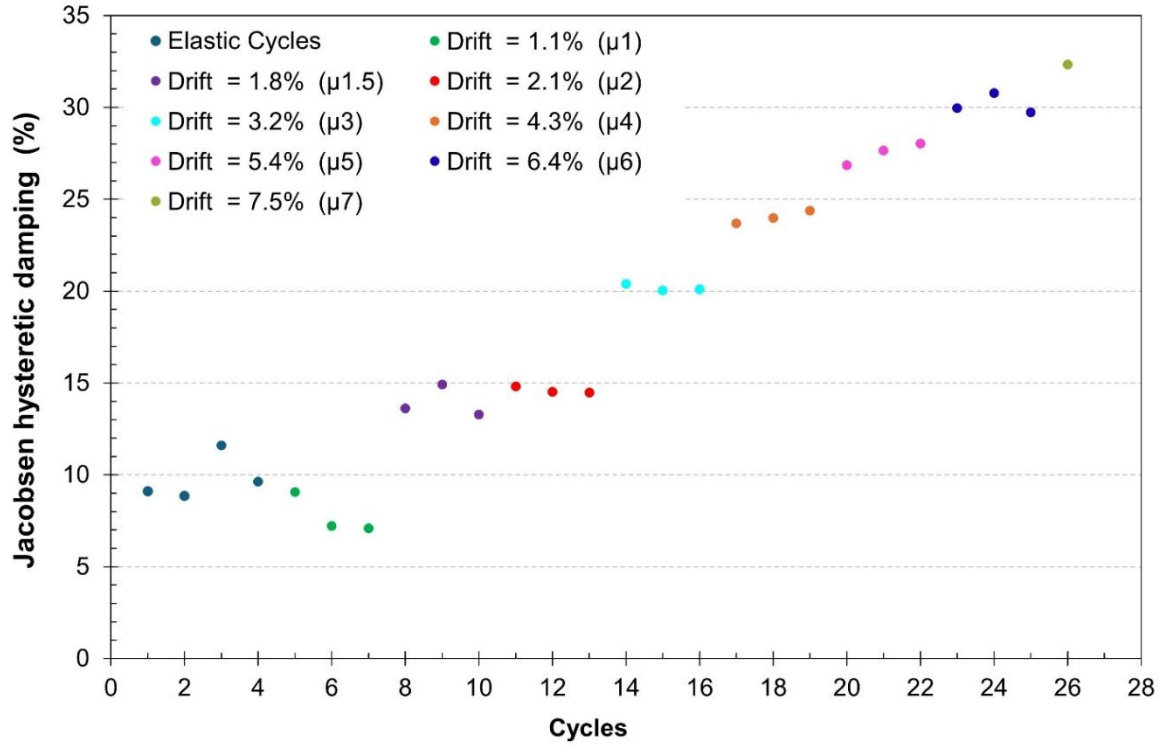


Figure 5-199. Hysteretic damping plot for SJS8

5.9.3. Socket rotation and RCFST gap opening for SJS-8

The socket rotation was measured using DIC, with Figure 5-200 and Figure 5-201 illustrating the rotation throughout the experimental test for the north and south faces, respectively. Measurements were taken at five different locations along the height of the socket. Although no specific calculations of displacement components were performed for the RCFST column, the socket rotation data was used to verify that the external socket connection exhibited behavior similar to that observed in previous tests. As shown in Figure 5-200 and Figure 5-201, the socket rotation is comparable to earlier results, indicating that socket rotation had a negligible impact on the total displacement.

Additionally, the gap between the two steel tubes was measured using DIC. Figure 5-202 shows the measured gap between the steel sleeves, which reached 1.2 inches upward during the final ductility displacement.

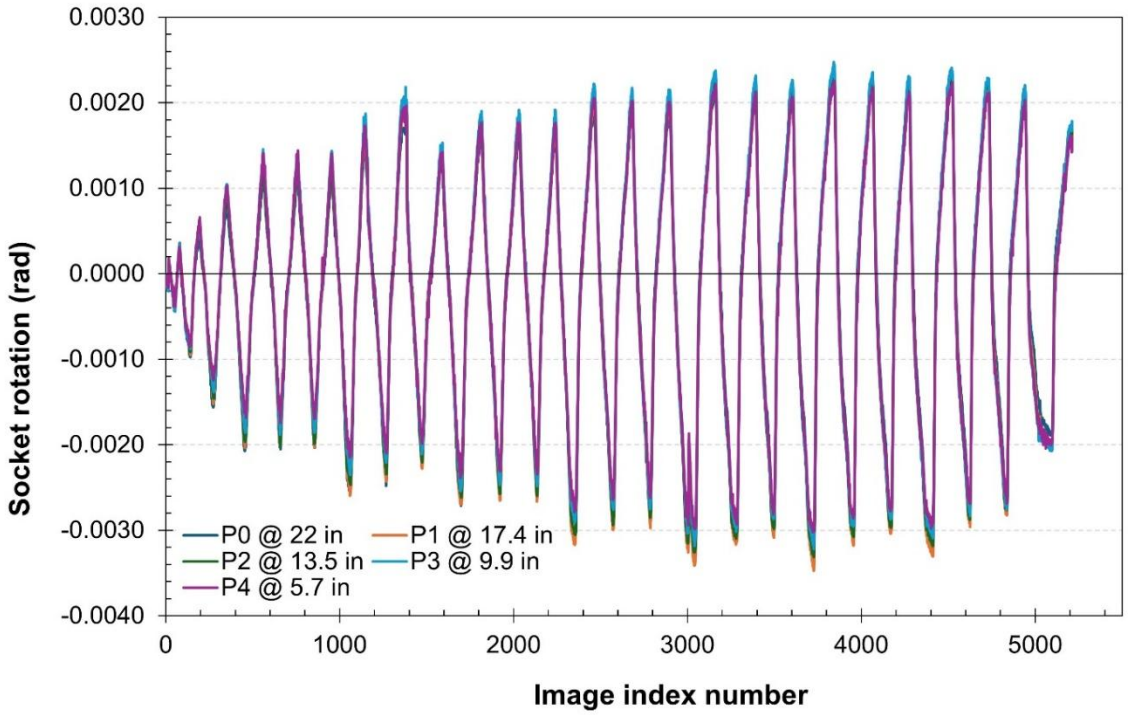


Figure 5-200. Socket rotation at the north side of SJS8

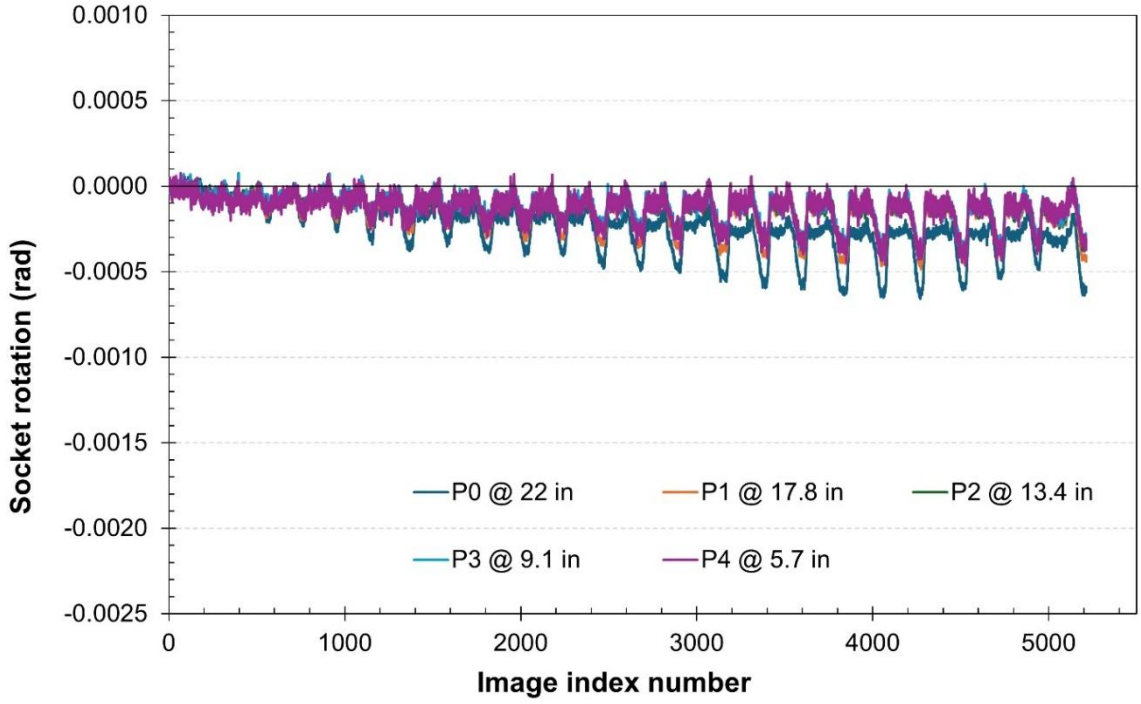


Figure 5-201. Socket rotation at the south side of SJS8

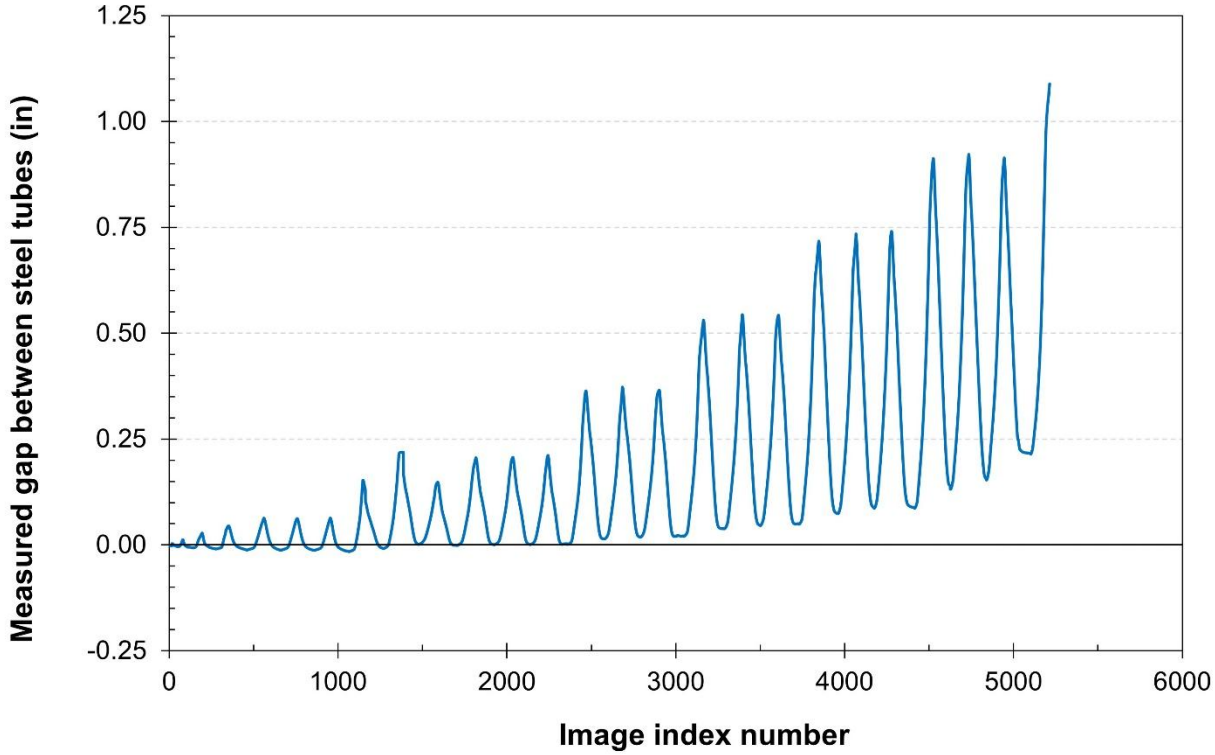


Figure 5-202. Opening of the gap between steel tubes at the north face of SJS8

5.9.4. Summary of Results for SJS-8

The tension strains on the longitudinal bars of the column were not obtained as in previous tests because the reinforcement could not be exposed due to the presence of the steel tube. The strains in the external socket wall reached 1.5 times the yield strain, indicating that the external socket connection effectively reduced plastic strains from reaching the foundation or cap beam. As a result, the footing remained as a capacity-protected element. Horizontal strains in the external socket sleeve remained elastic throughout the experimental test along the socket height. No visible damage was observed on the sleeves during the test, confirming that the sleeves did not experience significant inelastic deformation.

The elastic damping for SJS 8 was approximately 10%, which is higher than the 5% typically observed in CIP columns. This additional 5% damping may be attributed to the initial cracks in the socket wall and grout that occurred early in the test, as well as some unidentified noises observed during the cycles before the yield displacement.

The gap between the two steel tubes was monitored throughout the test, reaching a maximum opening of 1.2 inches at the final ductility displacement. The gap became noticeable after the first cycle of ductility one and increased linearly until the onset of concrete crushing and the shear failure of the column.

Chapter 6: Analytical model

While previous experimental studies have contributed to a better understanding of socket connections [4], [5], [6], [12], [14], significant gaps remain in comprehending their fundamental behavior, resulting in limited design guidance. To address these gaps and provide a more comprehensive analysis of external socket connections, this chapter introduces a Strut-and-Tie Model (STM). This model illustrates the influence of various design parameters, such as socket height, concrete strength, external socket wall thickness, and the strength of the filling material used to close the void between the socket and the precast element.

The STM offers a versatile design methodology based on a lower-bound approach, commonly applied in the analysis of disturbed regions (D-regions) within a structure [26]. These regions experience disturbed internal stress-strain distributions due to geometrical discontinuities or abrupt changes in load paths, as is the case with socket connections. Figure 6-1 depicts examples of these geometrical discontinuities. The following sections will explore the development and validation of the analytical model, providing insights into its practical applications and contributions to improving design methodologies for socket connections.

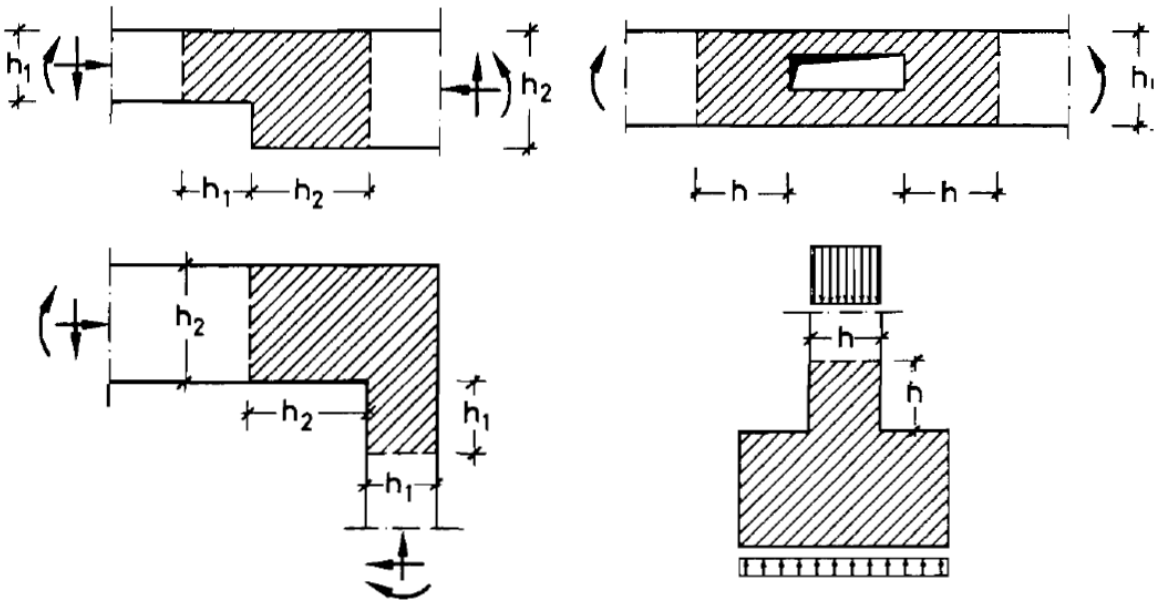


Figure 6-1. D-regions (shaded areas) due to geometrical discontinuities [27]

6.1. Strut and Tie Model

STMs are composed of three primary elements: struts, ties, and nodes. Struts represent compression elements, ties represent tension elements, and nodes are the points where struts and ties intersect. For structural stability, it is essential to ensure the external equilibrium of forces, adhering to the principles of statics while maintaining a statically determinate or indeterminate structure.

The proposed STM comprises three distinct statically determinate models that analyze forces within different regions: forces acting within the precast column (Figure 6-2), inclined tension force within the external socket (Figure 6-3), and inclined compressive force on the external socket wall (Figure 6-4). In Figure 6-2 through Figure 6-4, solid lines represent ties, dashed lines depict struts, and arrows illustrate simply supported reactions. As shown in Figure 6-2, the supports within the STM for the column are not designed to resist tension, given the lack of direct connection to the foundation. Therefore, only reaction forces r1 and r4 are transferred from the column to the STMs of the external socket, as illustrated in Figure 6-3 and Figure 6-4.

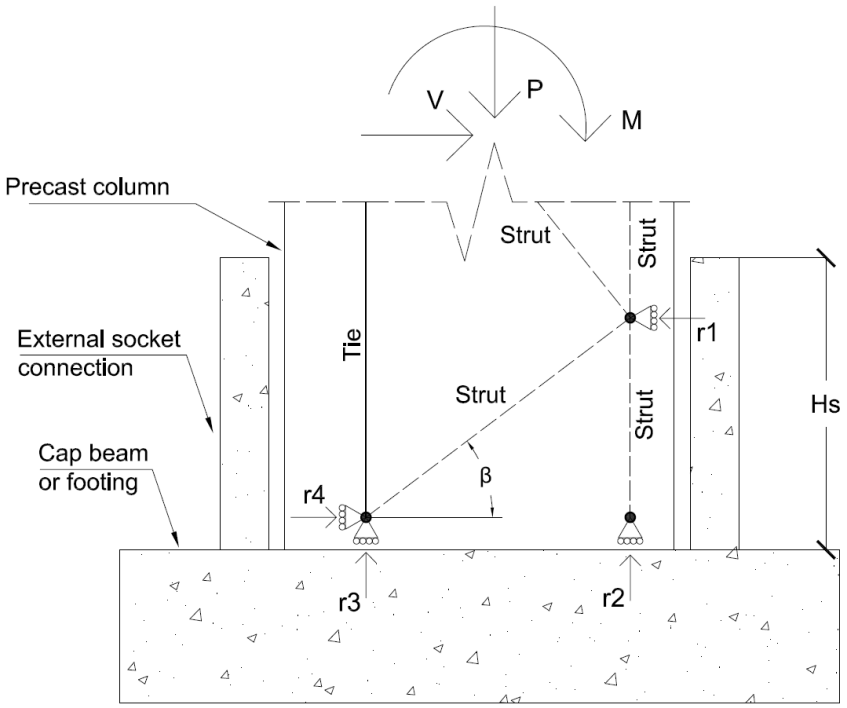


Figure 6-2. STM for the column

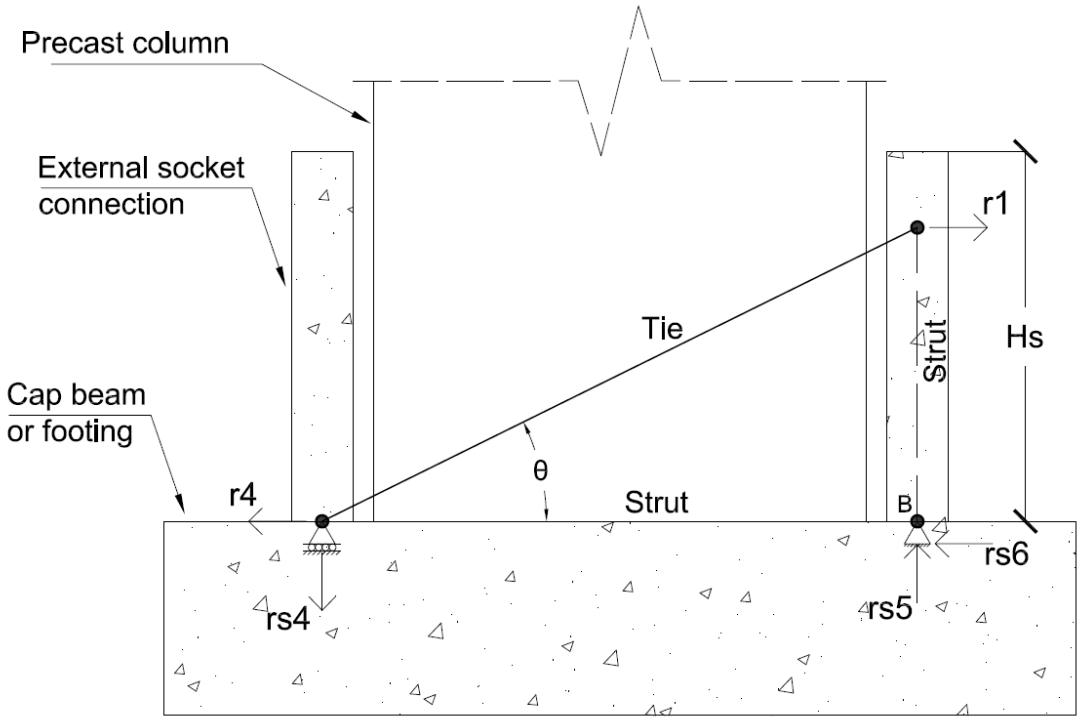


Figure 6-3. STM for external socket / Tension field

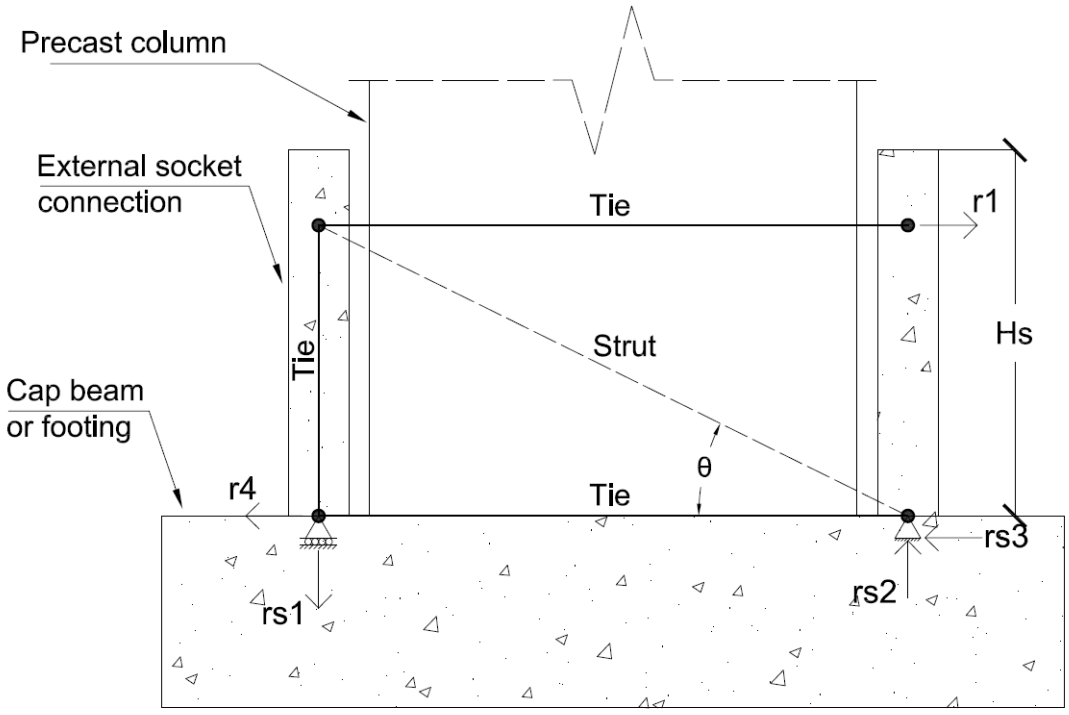


Figure 6-4. STM for external socket / Compression field

The reaction force r1 was considered at 1/6 of the socket height measured from the top of the external connection, representing the center of the compression zone where the column contacts the grout and transfers the forces to the external socket. Figure 6-5, from SJS8 with a socket height of 22 inches, shows that the compressive height was validated through post-test inspection of the experimental column. The observed damage is concentrated within the top 8 inches of the socket, with the center of the compressive force located approximately 4 inches below the socket interface, closely aligning with the considered 1/6 of the socket height.

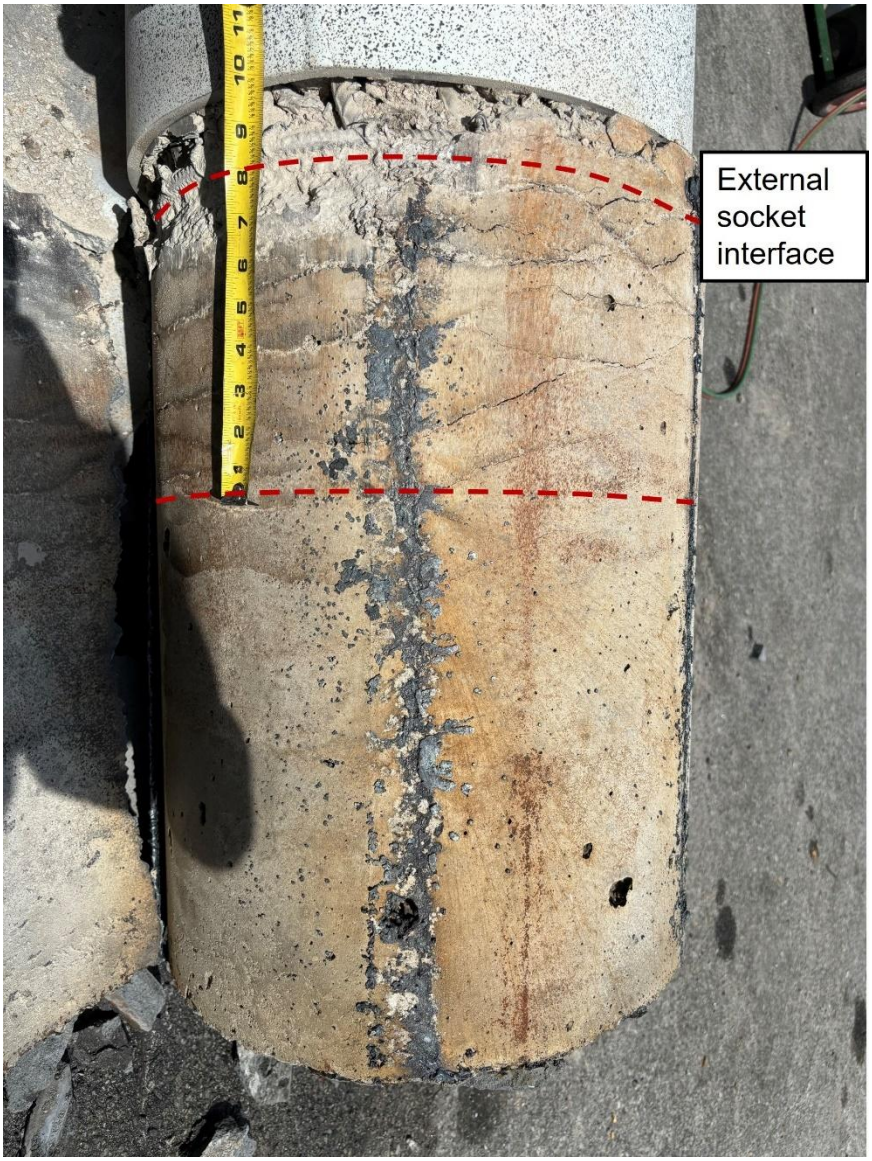


Figure 6-5. Compression zone at the top of the external socket of SJS8

The reaction force r4 was placed at 1/8 of the socket height measured from the bottom of the external connection, representing the center of the compression zone at the bottom of the external socket connection. Figure 6-6, from SJS7 with a socket height of 15.3 inches, shows the compressive height measured at 4.2 inches, with the center of the compressive force located at 2.1 inches. This aligns closely with the considered 1/8 of the socket height.



Figure 6-6. Compression zone at the bottom of the external socket of SJS7

The vertical strut of the column is located by first determining the neutral axis of the column at the nominal moment and then dividing this value by 2. A typical value for the location of the neutral axis is 0.2 Dc, placing the center of the compressive area at 0.1 Dc. Figure 6-7

illustrates the location of the strut within the column, along with the shaded compressive area used for calculating the stresses acting on the strut.

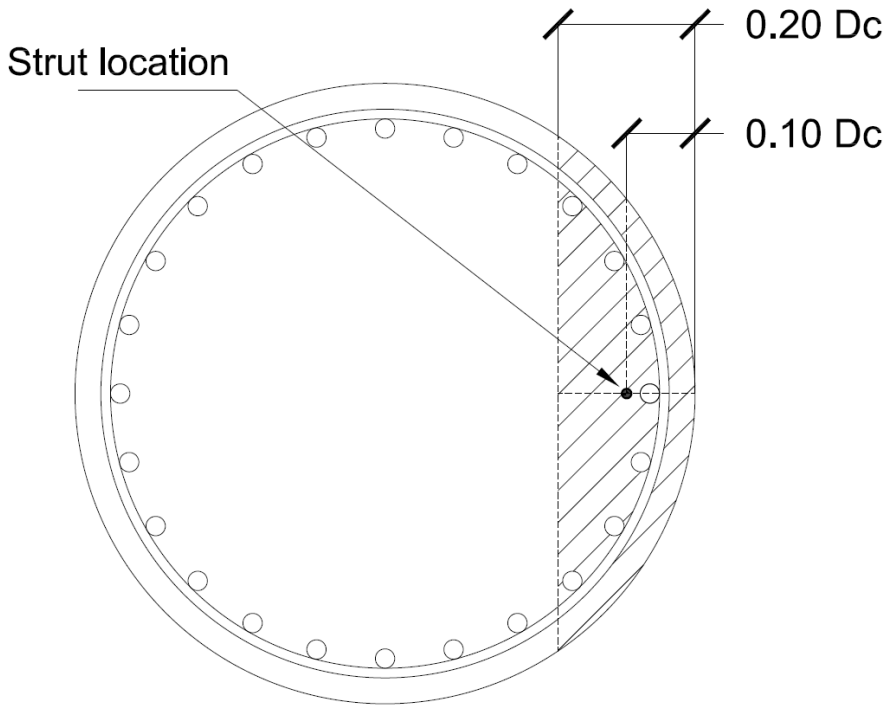


Figure 6-7. Location of the strut for the STM of the column

The location of the tie of the column is determined by taking 0.15 Dc, which represents the center of the tension region within the column. Figure 6-8 shows the position of the tie and highlights the shaded reinforcing bars that are considered part of the reinforcing area for calculating stresses acting on the tie. Figure 6-9 illustrates the location of the strut, tie, and reaction forces in STM of the column.

To calculate the stresses acting on the grout, a contact arc length of 0.4 Dc was used. This value was determined during the initial loading cycles of the experimental tests by measuring the distance between the first cracks that appeared in the grout. Figure 6-10 illustrates the contact arc length between the column and the grout. The height of the contact area was based on the height of the compression zone at r1, multiplied by a factor of 0.85. This factor was selected after inspecting the height of the damage in specimens that experienced grout crushing failure.

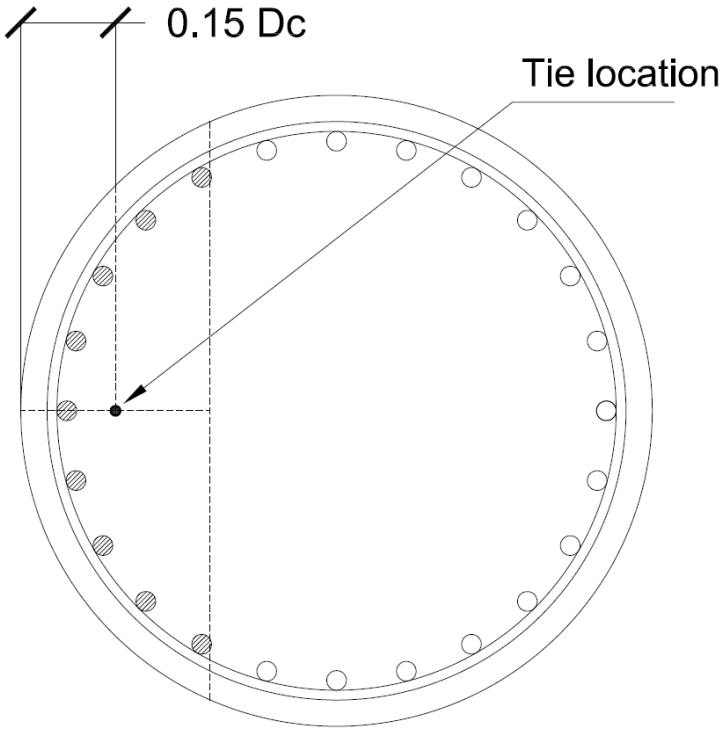


Figure 6-8. Location of the tie for the STM of the column

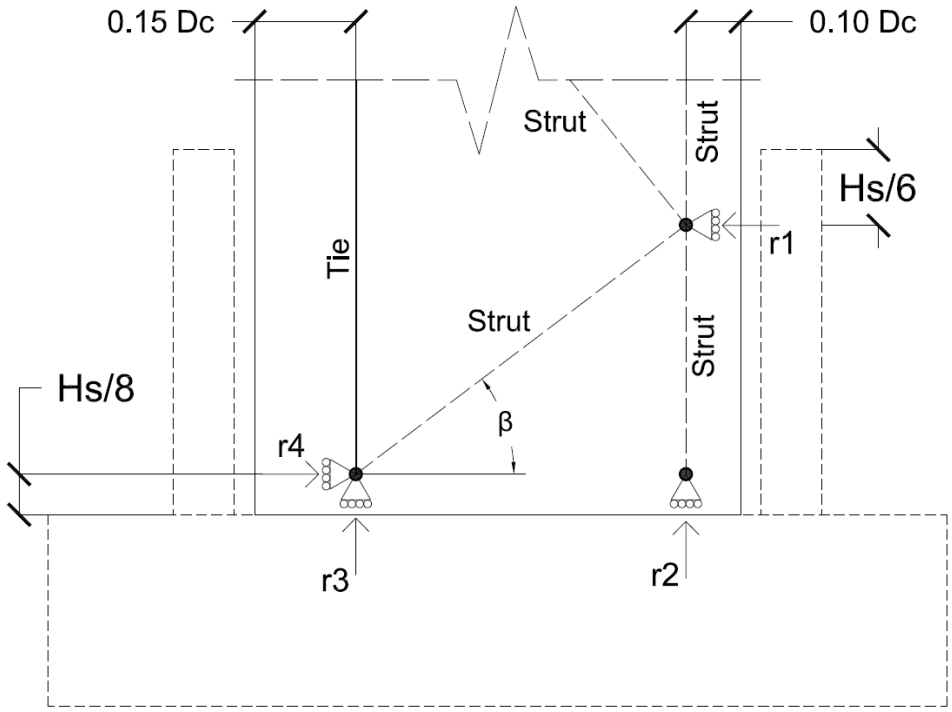


Figure 6-9. Location of strut, tie, and reaction forces of the analytical model for the column

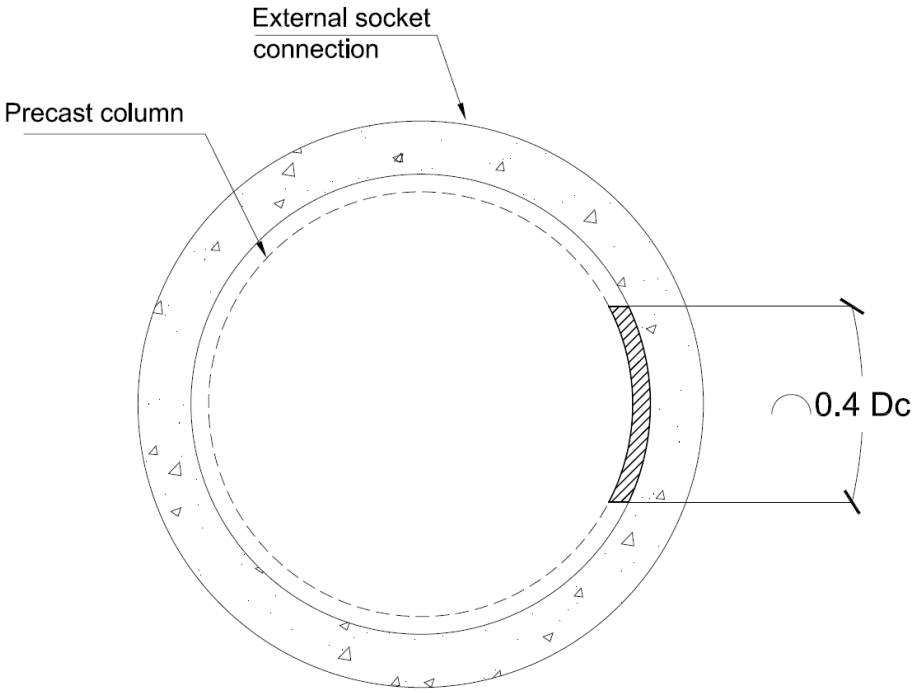


Figure 6-10. Considered compression contact arc length between grout and column

Figure 6-11, the shaded strut area represents the region used to calculate the compressive stresses acting on the portion of the column embedded within the external socket. The width of the strut is defined as 0.4 Dc * sin β, while the base of the inclined strut is taken as 0.7 Dc. The base of the inclined strut refers to the perpendicular distance to the width of the strut, creating the plane where the force acts perpendicularly.

For the inclined strut of the external socket wall, the width of the strut was considered half the socket height, with the base of the strut area taken as the thickness of the socket wall. Similarly, for the inclined tie of the external socket sleeve, the width was also considered as half the socket height, while the base of the tie area was four times the thickness of the sleeve, accounting for both the internal and external socket sleeves on both sides. Figure 6-12 and Figure 6-13 illustrate the width of the strut in the external socket wall and the width of the tie in the socket sleeves, respectively. For the horizontal tie of the socket sleeves, the width was set equal to the compressive height zone of the grout, aligning closely with the DIC results, which demonstrate the strain distribution in the horizontal direction. The data showed that the top portion of the socket experienced higher strains than the rest of the socket height. The base of the horizontal tie area

was considered the same as that of the inclined tie for the socket sleeves. Figure 6-14 illustrates the width of the horizontal tie for the external socket sleeve. In Figure 6-11 through Figure 6-14, the ties and struts follow the circumference of the external socket; however, a lateral view is provided for simplicity.

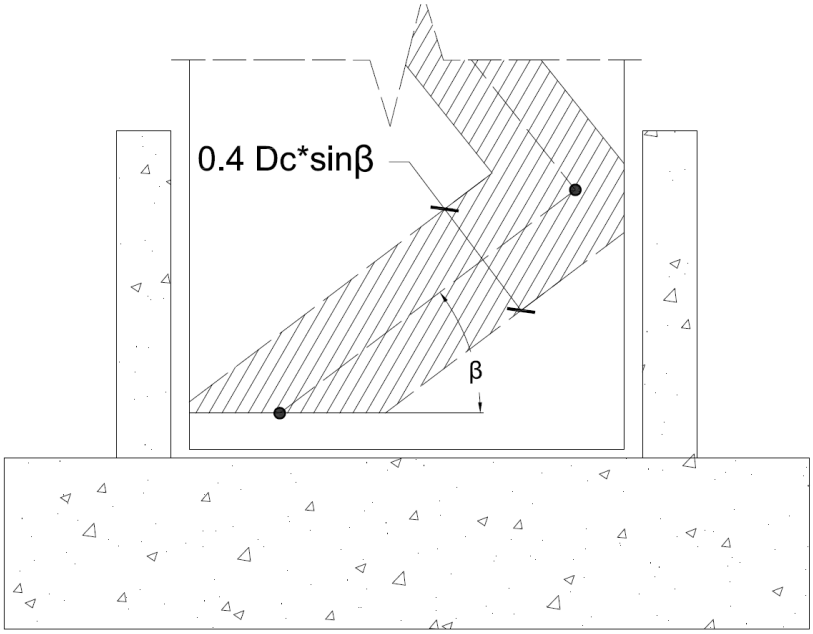


Figure 6-11. Width of the incline strut of the column inside the socket

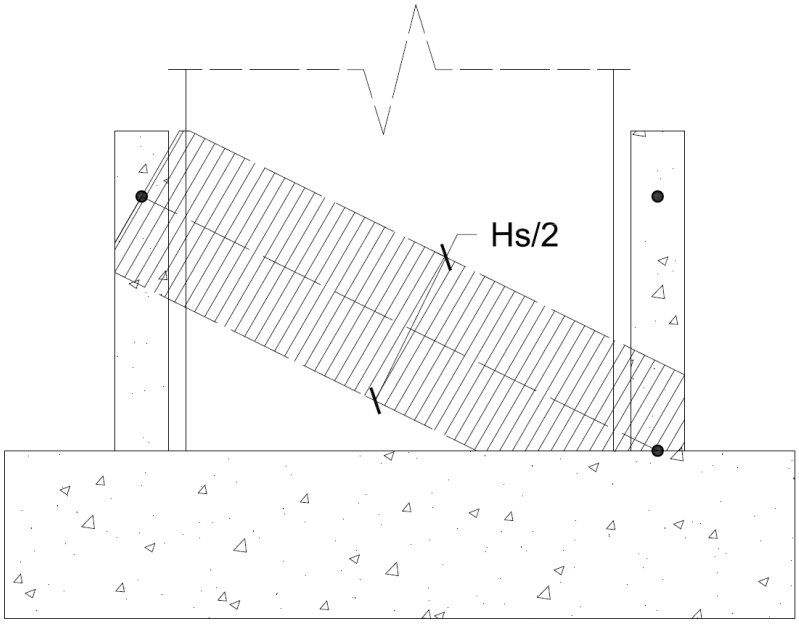


Figure 6-12. Width of the inclined strut of the external socket wall

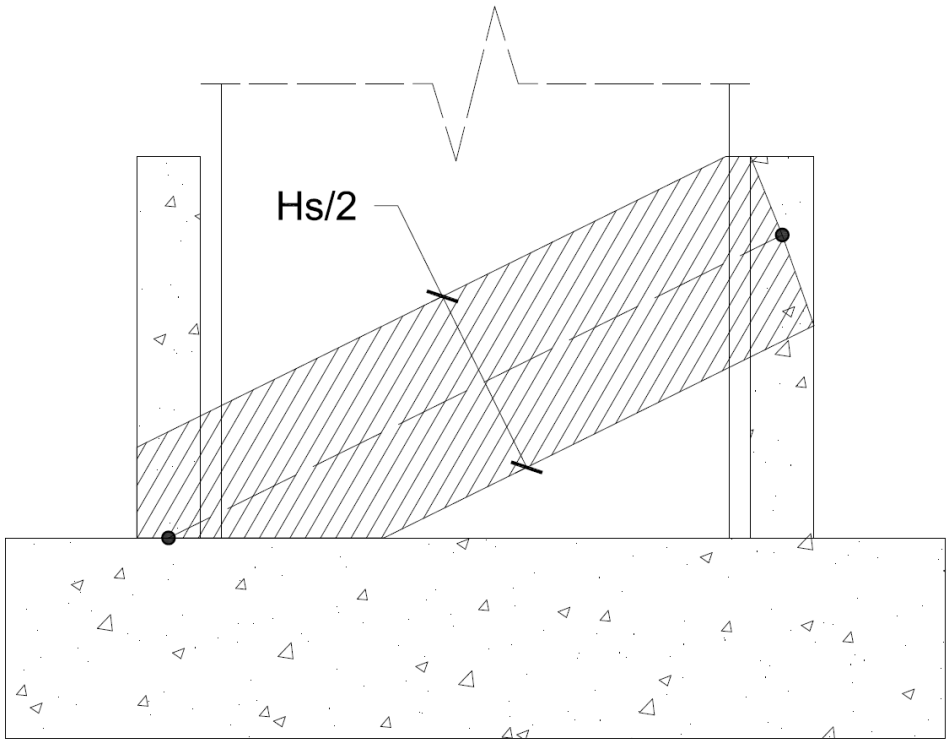


Figure 6-13. Width of the inclined tie of the external socket sleeves

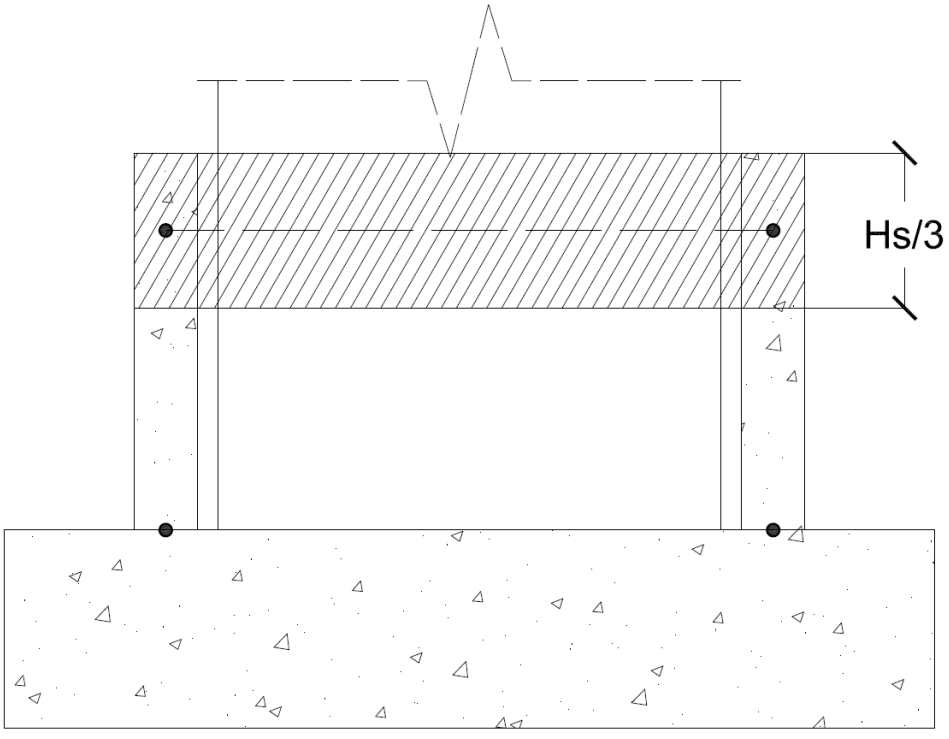


Figure 6-14. Width of the horizontal tie of the external socket sleeve

To calculate the stresses acting on the vertical strut of the socket concrete wall and the vertical tie for the socket reinforcement, a segment length of 1.0 Dc was used. This length was determined by inspecting the experimental test and measuring the distance between the first cracks that appeared on the socket wall. Figure 6-15 illustrates these initial cracks on SJS2, where the measured distance closely aligns with the 1.0 Dc assumption. The area of the vertical tie for the reinforcement was based on the amount of reinforcement located within the compression zone of the vertical strut in the socket concrete wall. Figure 6-16 shows the compressive area for the vertical strut and the corresponding reinforcing bars considered for the vertical tie of the socket reinforcement.

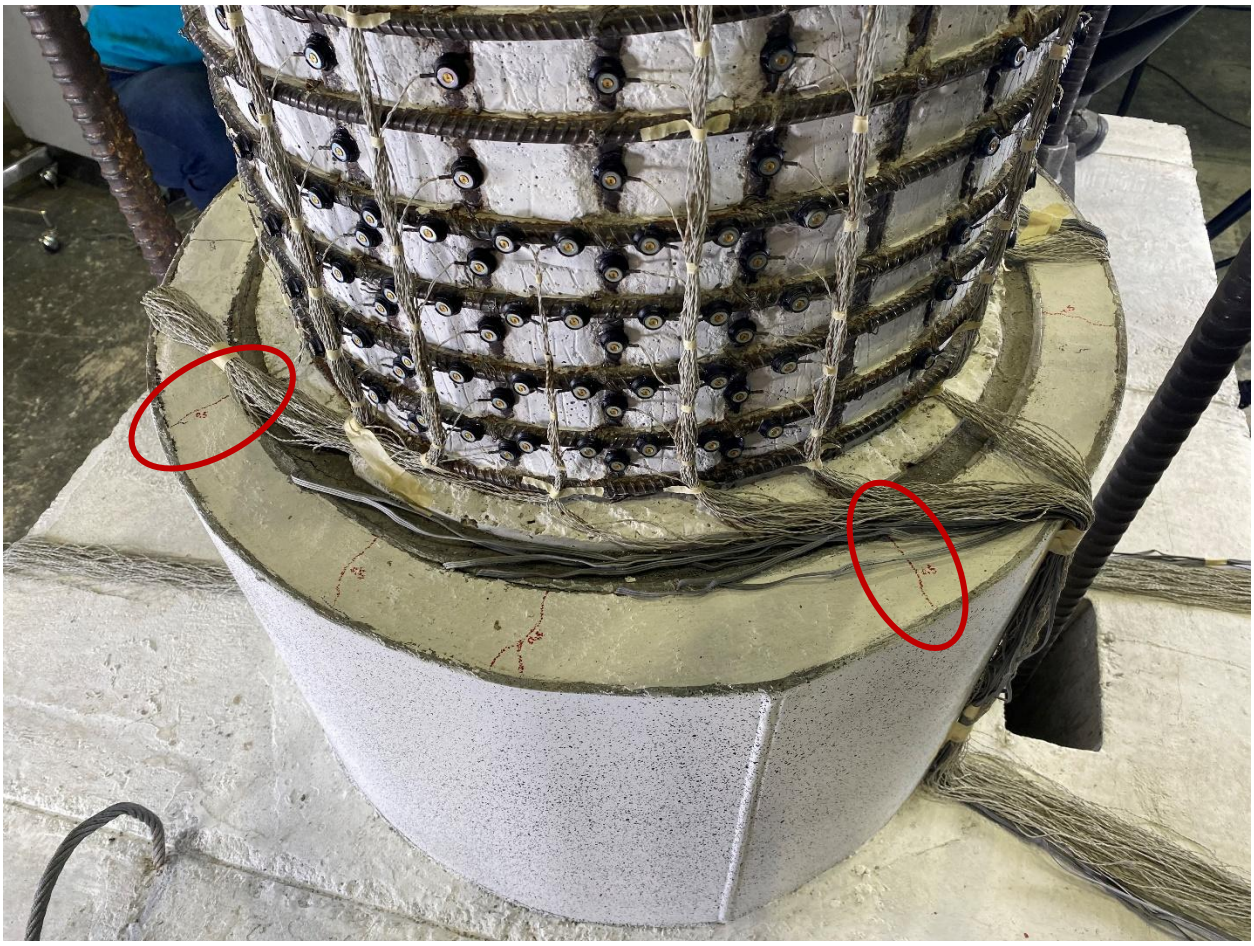


Figure 6-15. First cracks on external socket wall for SJS2

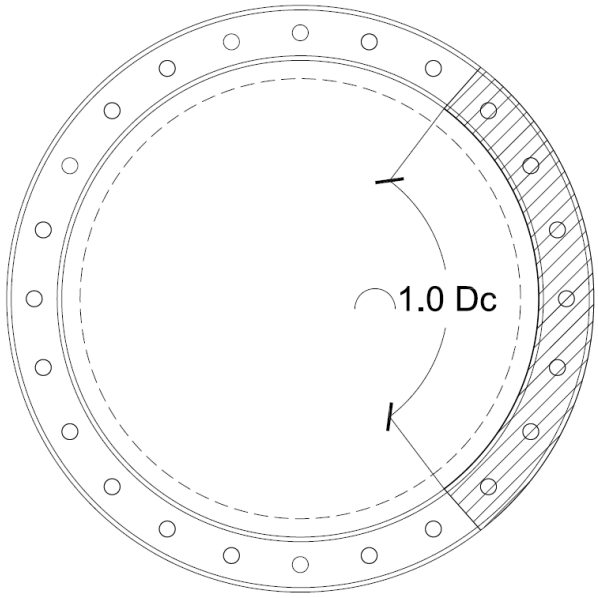


Figure 6-16. Compression area and reinforcing bar area for the external socket wall

The analytical model calculates the forces acting on each strut and ties for the three STMs. The areas calculated for each element, whether for struts or ties, were then used to compute the corresponding stresses. The STM calculations for the column and external socket connection are provided in Chapter 7.1, while the complete derivation of the equations is provided in the appendix.

6.2. Analytical Model Outputs

The outputs of the analytical model provide a valuable guide for designing external socket connections, especially in seismic conditions. These results enhance the understanding of the connection behavior and performance when subjected to seismic forces.

Applying STMs to analyze the column and external socket connection allowed us to establish a comprehensive correlation between socket height, applied moment, and critical stresses within the connection. We explored various socket heights to define practical limits for the stresses acting within the system, using the column and external socket details from tests SJS1 to SJS3 (section 3.2) as the basis for the STM calculations.

The results for all the struts and ties in the STMs for socket heights of 1.0 Dc (SJS1), 0.85 Dc (SJS3), and 0.85 Dc (SJS2) are presented in Figure 6-17 to Figure 6-26. Additionally, the nominal moment from the large-scale experiments, measured at 598.8 kip-ft for SJS1 to SJS3, is included as a reference point, allowing for direct comparison of the outcomes across different socket heights for a specific applied moment.

Figure 6-17 illustrates the influence of socket height on the tensile stresses in the longitudinal steel of the column. The results show that socket height has a minimal impact on the stresses acting on the longitudinal steel. In contrast, Figure 6-18 demonstrates the effect of socket height on the diagonal compressive stress within the precast column. The results indicate that as socket height decreases, the stresses increase, necessitating higher concrete strength in the column to develop the nominal moment. Figure 6-19 presents the shear forces acting on the portion of the column embedded within the socket connection, showing that a lower socket height results in higher shear forces within the system, which must be accounted for in design considerations.

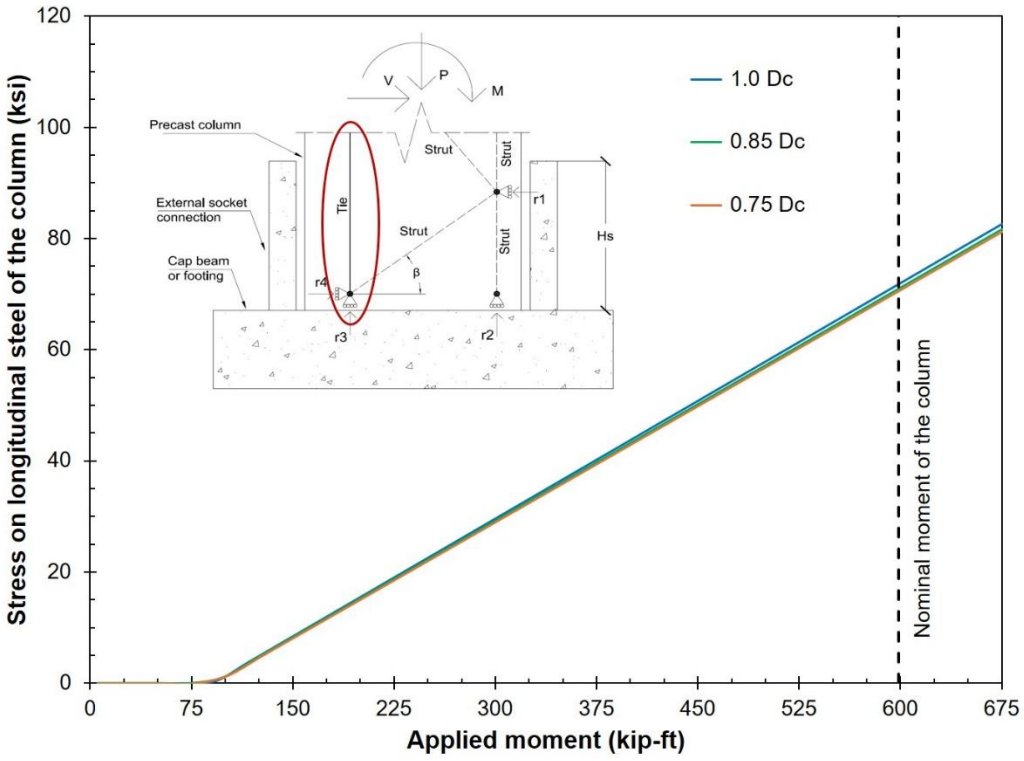


Figure 6-17. Example of STM results of tensile stress on longitudinal steel of the column

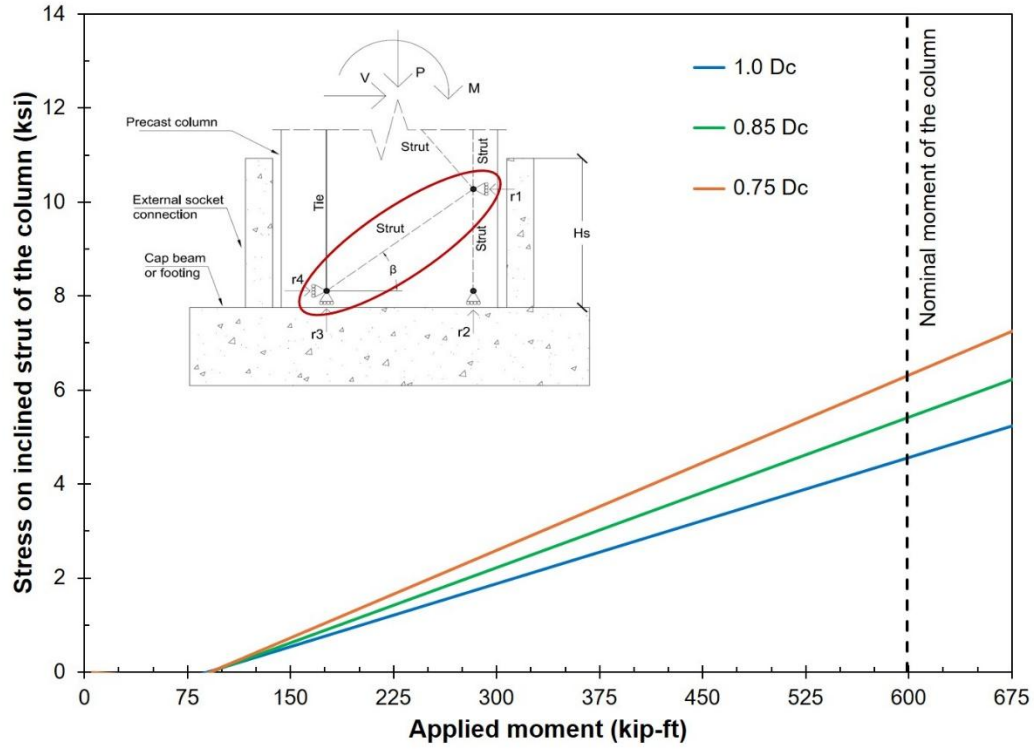


Figure 6-18. Example of STM results of diagonal compressive stress on the precast column

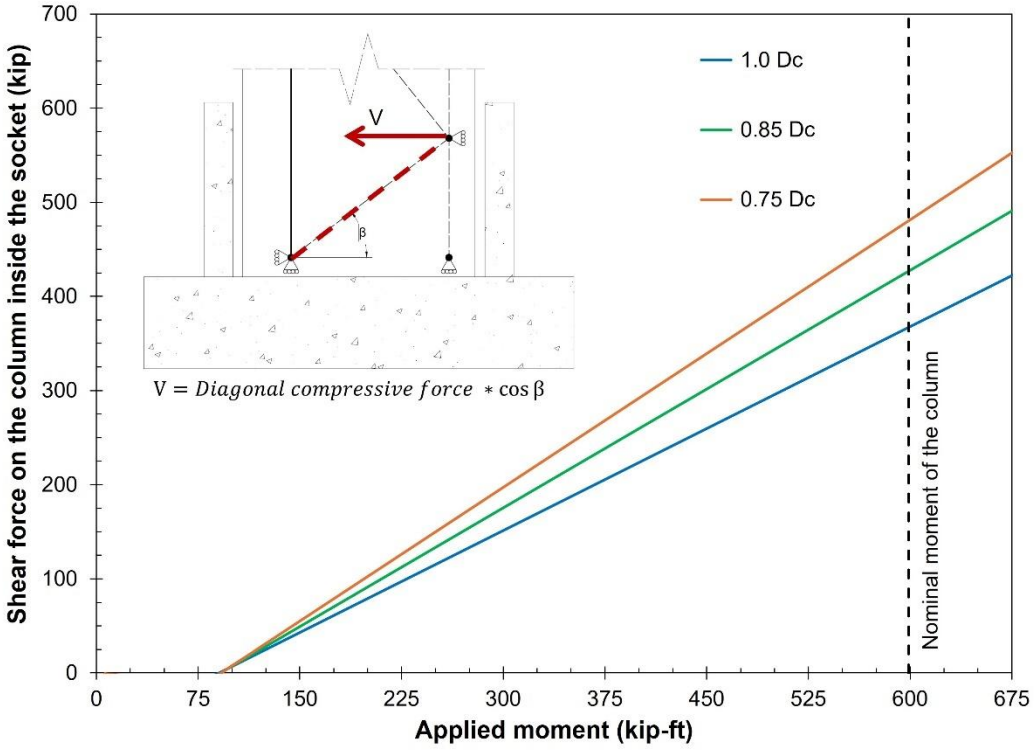


Figure 6-19. Example of STM results of shear forces on the precast column within the socket

Figure 6-20 presents the compressive stresses acting on the column at the socket interface. The results indicate that these stresses remain similar regardless of the socket height. Figure 6-21 illustrates the effect of socket height on the grout joining the column and the external socket wall. The results show that a lower socket height significantly increases the compressive stresses acting on the grout. To prevent grout failure, its compressive strength must be increased accordingly.

Figure 6-22 highlights the stresses acting on the longitudinal reinforcement of the external socket wall. As the socket height increases, the stress on the reinforcing steel also increases. To reduce these stresses, the number of reinforcing bars carrying the tension forces should be increased.

Figure 6-23 illustrates the influence of socket height on the horizontal stresses acting on the steel sleeve of the external socket. The results show that as socket height decreases, horizontal stress increases. To mitigate this stress, the thickness of the steel sleeves should be increased.

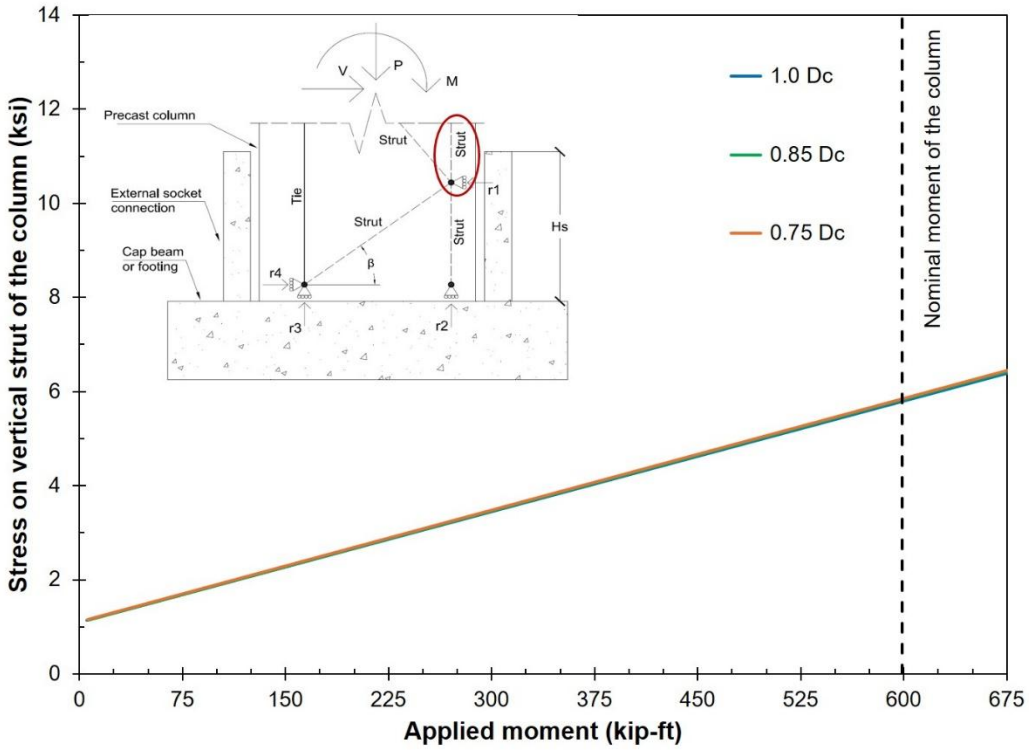


Figure 6-20. Example of STM results of vertical compressive stress on the precast column

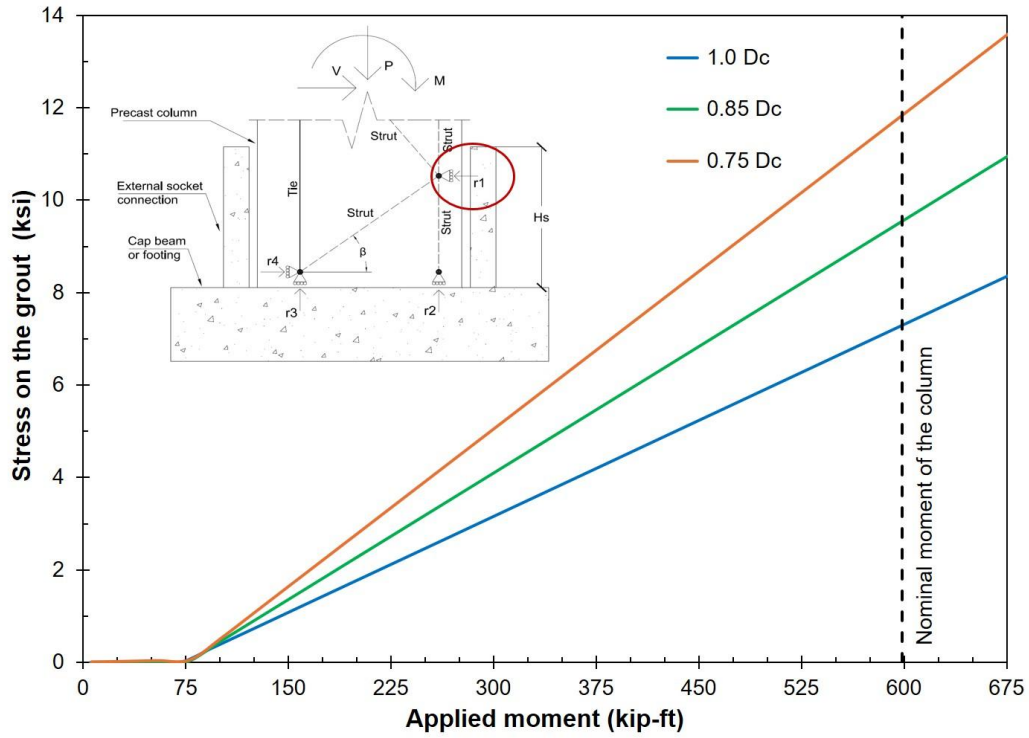


Figure 6-21. Example of STM results of compressive stress within the grout

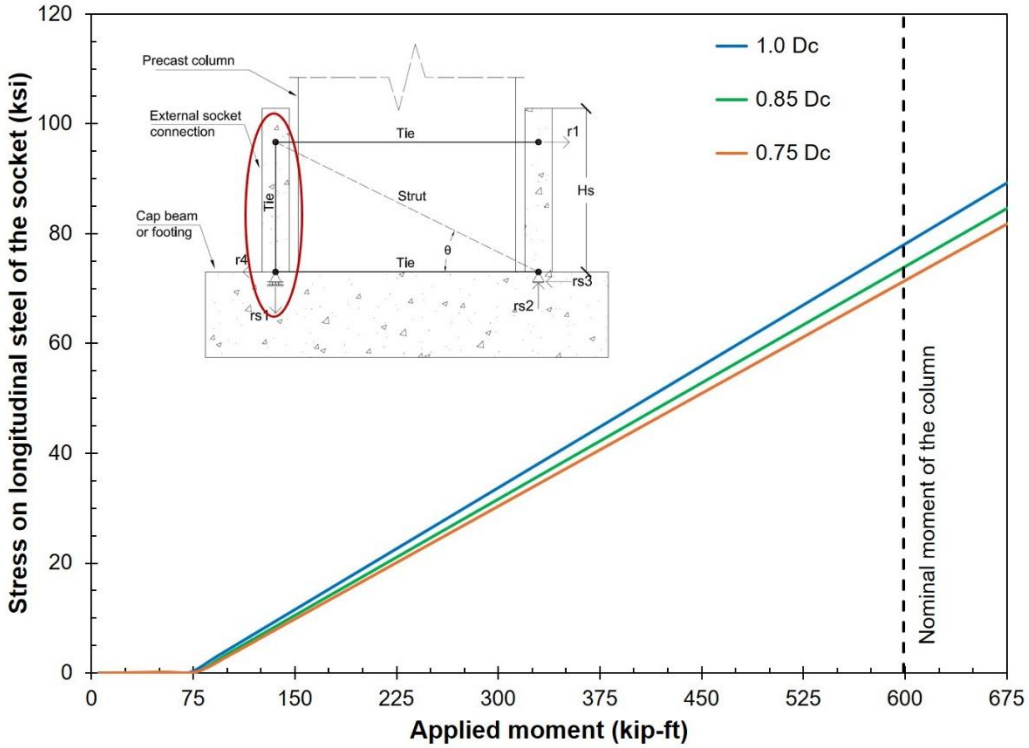


Figure 6-22. Example of STM results of tensile stress on longitudinal steel of the socket wall

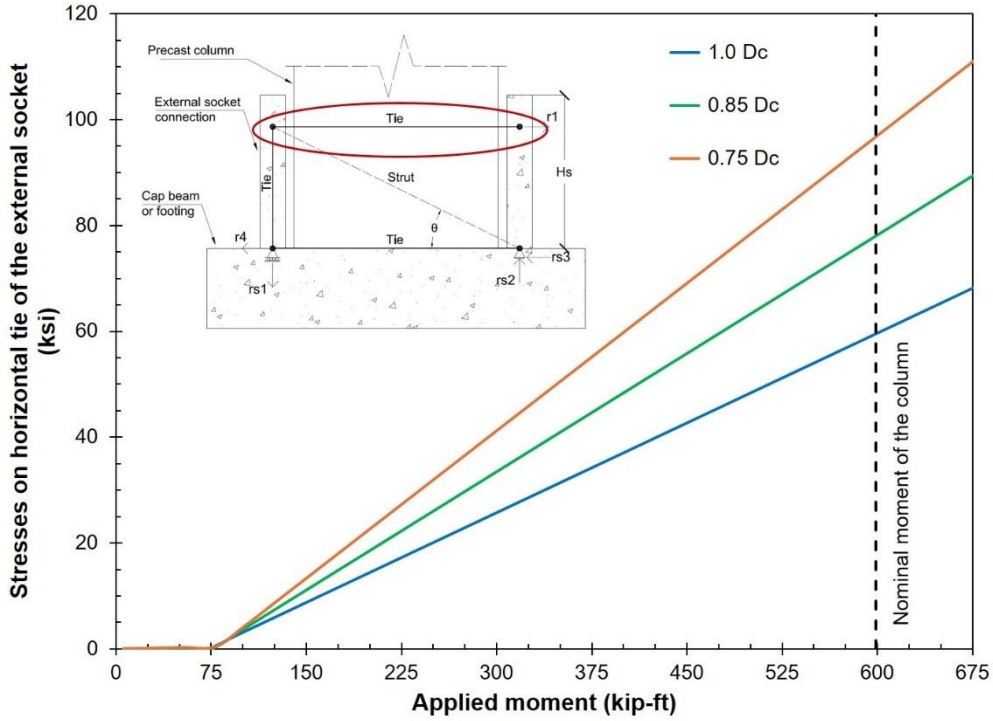


Figure 6-23. Example of STM results of horizontal tensile stress on the socket sleeves

Figure 6-24 illustrates the influence of socket height on the diagonal compressive stress acting on the external socket wall. The results show that the stress on the socket wall increases as socket height decreases. The concrete strength or the wall thickness must be increased to prevent failure in this component while decreasing the socket height. Figure 6-25 depicts how socket height affects the diagonal tensile stress on the external socket sleeves. As socket height decreases, the stress on the sleeves increases. To reduce the stress on this component, the thickness of the sleeves should be increased. Figure 6-26 presents the vertical compressive stress acting on the socket wall. The results show that socket height has a small impact on the compressive stresses within the socket wall.

Table 6-1 summarizes the results at the nominal moment of the large-scale experiments for the various connection components with varying socket heights. As socket height decreases, the stresses on the different components of the external socket connection and the precast column increase accordingly. However, the impact of socket height on the stresses in the longitudinal steel of both the column and the socket wall is relatively minor, with stresses remaining similar across different socket heights.

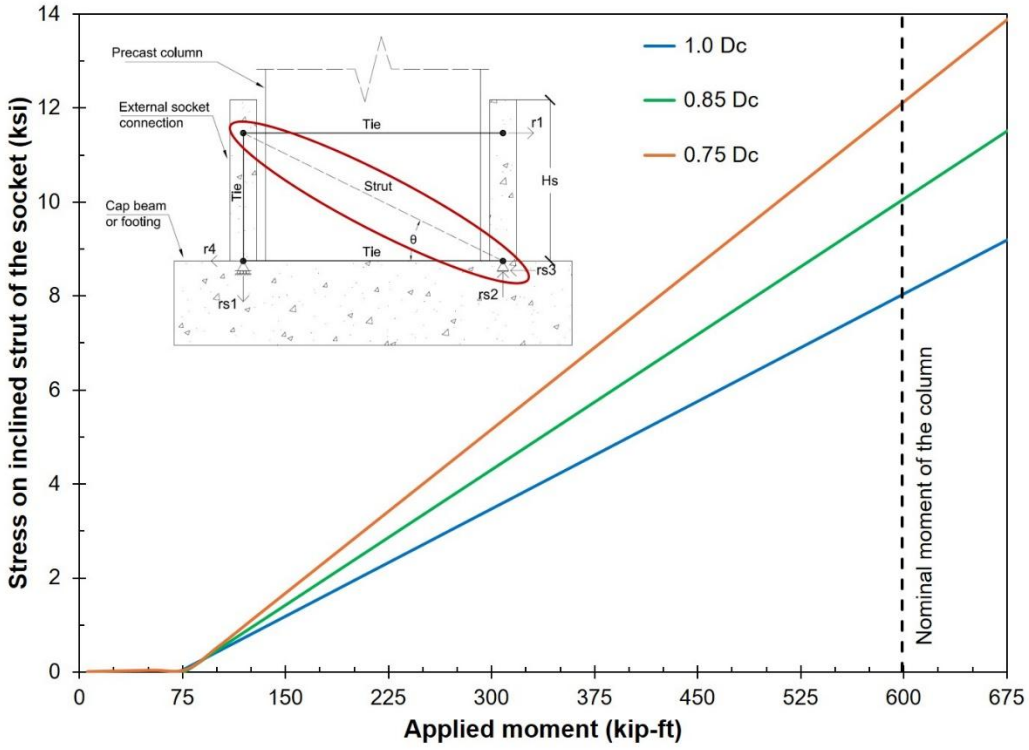


Figure 6-24. Example of STM results of diagonal compressive stress on the socket wall

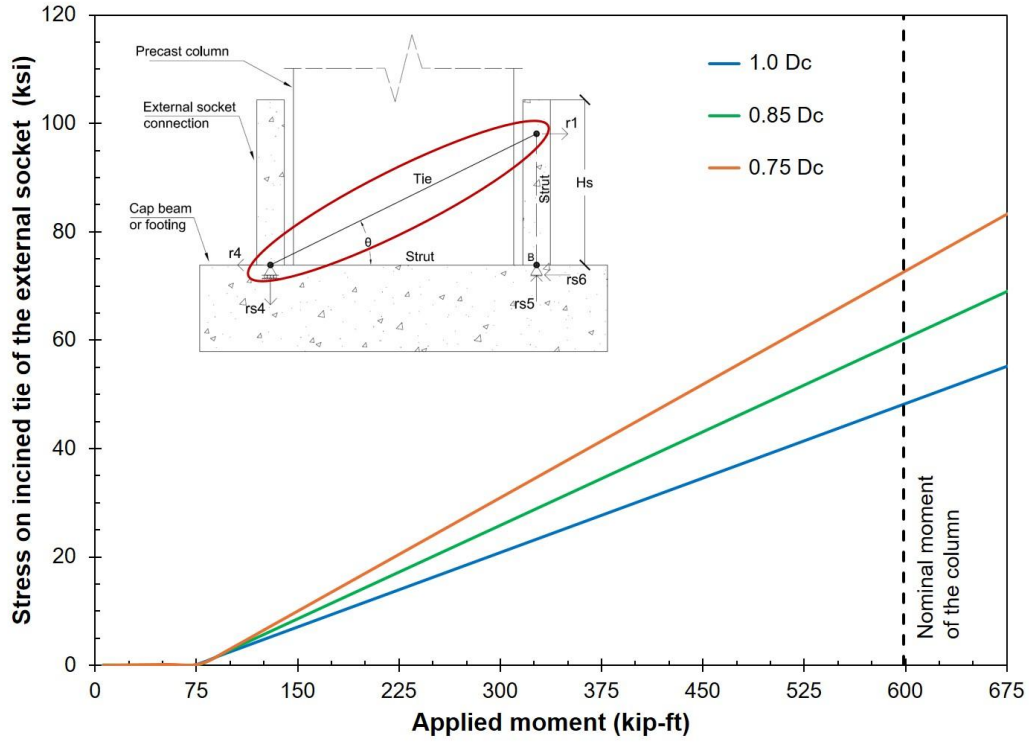


Figure 6-25. Example of STM results of diagonal tensile stress on the socket sleeves

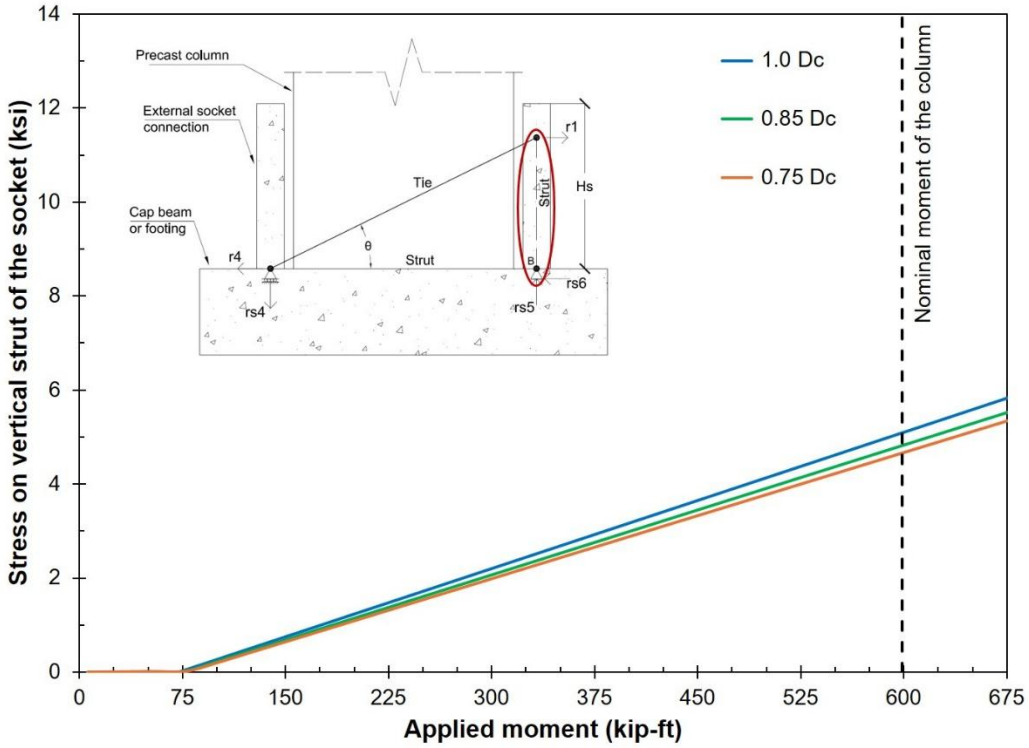


Figure 6-26. Example of STM results of vertical compressive stress on the socket wall

Table 6-1. STM results for the different components of the external socket connection with different socket heights

	1.0 Dc	0.85 Dc	0.75 Dc
Tensile stress on longitudinal steel of the column (ksi)	71.9	70.8	69.9
Diagonal compressive stress on the column (ksi)	4.6	5.4	6.3
Vertical compressive stress on the column (ksi)	5.8	5.8	5.8
Shear force on the column in the socket (kip)	367.7	425.8	475.8
Compressive stress in the grout (ksi)	7.3	9.5	11.7
Tensile stress on longitudinal steel of the socket (ksi)	78.1	73.7	70.6
Horizontal tensile stress on the socket sleeves (ksi)	59.6	77.8	95.8
Diagonal tensile stress on the socket sleeves (ksi)	48.3	60.1	71.9
Diagonal compressive stress on the socket wall (ksi)	8.0	10.0	12.0
Vertical compressive stress on the socket wall (ksi)	5.1	4.8	4.6

6.3. Comparison with Experimental Results

Using the detailing and material properties of the eight experimental tests described in Chapter 3 of this report, the analytical model was applied to evaluate the stresses developed in the different components of the connection. Each connection exhibited unique critical components influenced by the specific material properties required for the given socket height.

To compare the results from the STMs with the experimental tests, a plot was generated showing the ratio between demand and capacity for the most critical components, the nominal moment of the column, and the specimen failure during the experimental test. For the longitudinal reinforcing and the steel sleeves, the capacity was defined by the yield values listed in Table 3-8. For the concrete components of the column and socket connection, the capacity was determined using the material strengths reported in Table 3-3 through Table 3-7. The column' shear capacity was calculated using the revised UCSD shear model [28], and then multiplied by a factor of 1.3 to account for the additional confinement provided by the grout, which enhances the shear capacity. This factor of 1.3 was considered based on the observations of the experimental tests and the distribution of shear forces from the STMs.

Figure 6-27 presents the demand-capacity ratio versus the applied moment for SJS1 and shows that the tension in the longitudinal steel reaches its yield point, which is expected during the formation of a plastic hinge. The next component to reach the capacity is the compression in the column at the socket interface, indicating that the concrete will experience crushing. This suggests that the failure mode will follow a flexural behavior similar to a CIP column. The predicted failure moment was 98% of the actual failure moment observed in the experiment, and the predicted failure mode matched the observed failure mode of SJS1.

Figure 6-28 presents the demand-capacity ratio versus the applied moment for SJS2. The first component to reach the capacity is the grout in compression, indicating that the grout will experience crushing before the column reaches its nominal capacity. The STM results also predict that the longitudinal steel of the column will not reach yielding, and the concrete will not experience crushing or shear failure. The predicted failure moment was 76% of the actual failure

moment observed in the experiment, and the predicted failure mode matched the observed failure mode of SJS2. Notably, the longitudinal steel of the column barely reached the yield stress only at the extreme bar, as predicted by the analytical model.

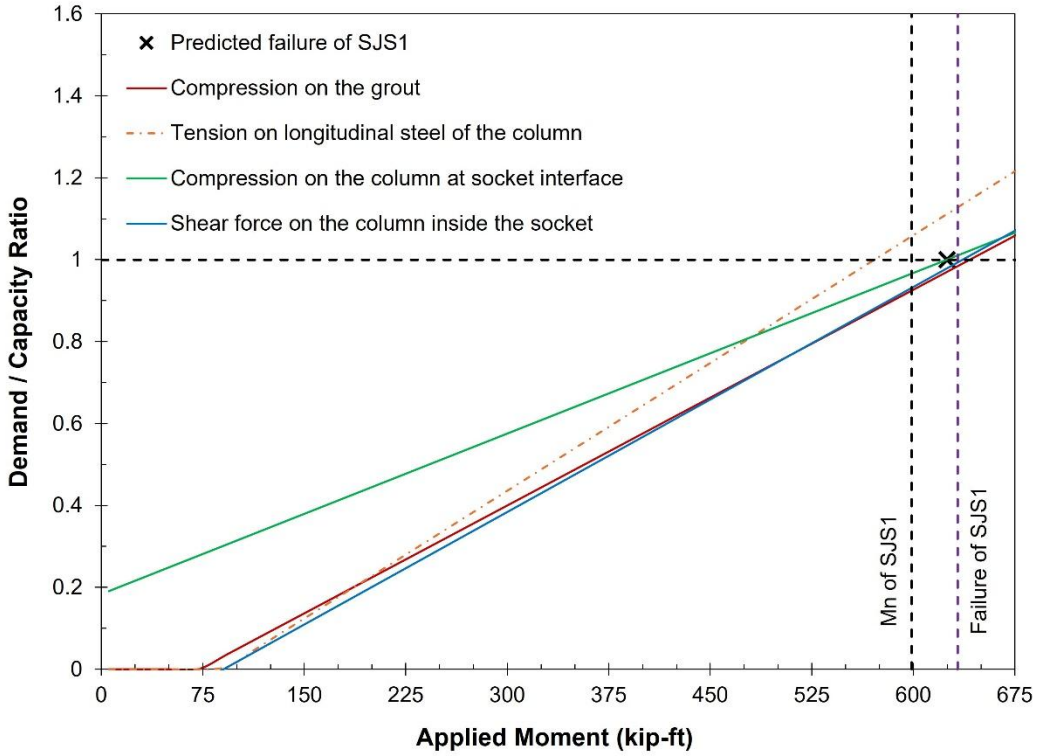


Figure 6-27. Demand-capacity vs. Applied moment for SJS1

Figure 6-29 presents the demand-capacity ratio versus the applied moment for SJS3. The first component to reach the capacity is the grout in compression, indicating that the grout will experience crushing before the column reaches its nominal capacity. The STM results also predict that the longitudinal steel of the column will reach yield stress, and the concrete will not experience crushing or shear failure. The predicted failure moment was 2% higher than the actual failure moment observed in the experiment, and the predicted failure mode matched the observed failure mode of SJS3. Notably, the longitudinal steel of the column reached the yield stress at the three extreme bars, which matches closely to what was predicted by the analytical model.

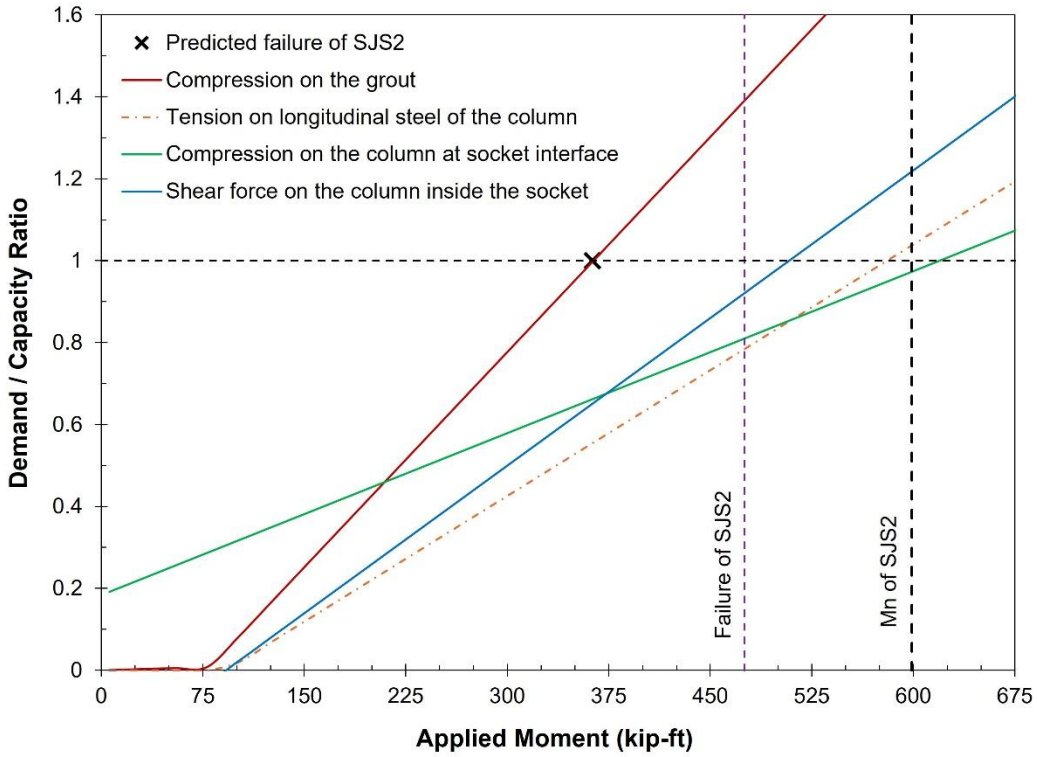


Figure 6-28. Demand-capacity vs. Applied moment for SJS2

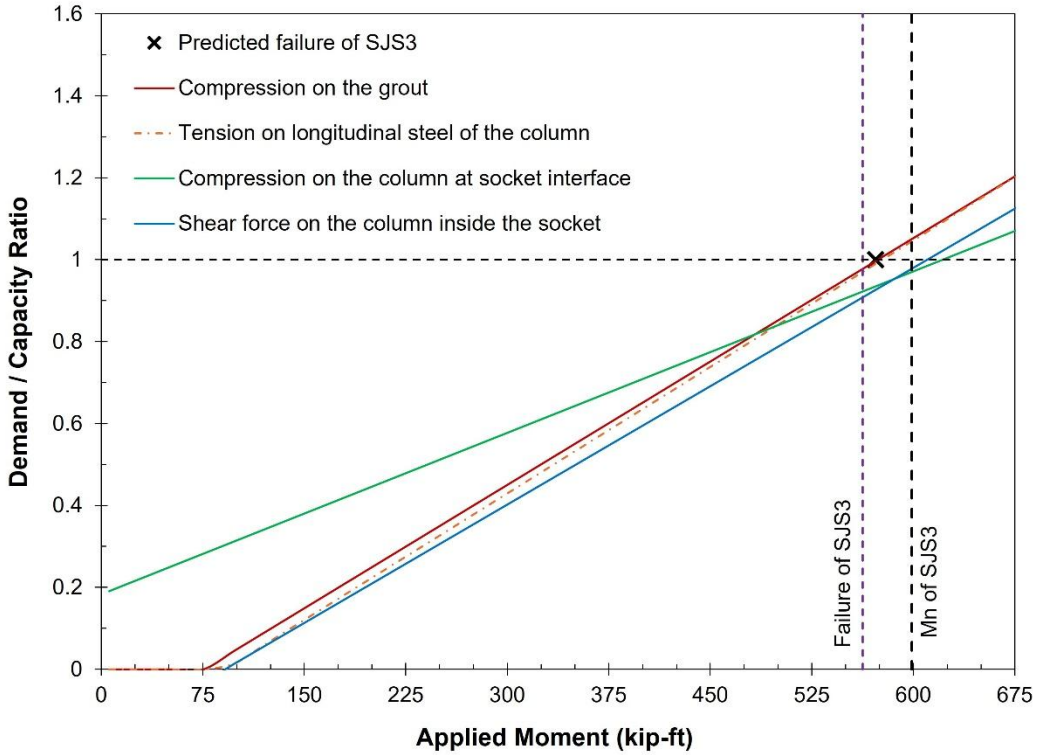


Figure 6-29. Demand-capacity vs. Applied moment for SJS3

Figure 6-30 presents the demand-capacity ratio versus the applied moment for SJS4 and shows that the tension in the longitudinal steel reaches its yield point, as expected during the formation of a plastic hinge. The next component to reach the capacity was the shear force on the column, followed by the failure of the grout. The predicted failure moment was 93% of the actual failure moment observed in the experiment. The observed failure mode for SJS4 was grout crushing, followed by shear failure within the column inside the socket. While the STM accurately predicted the combination of these two failure modes, it did not predict the correct sequence in which they occurred.

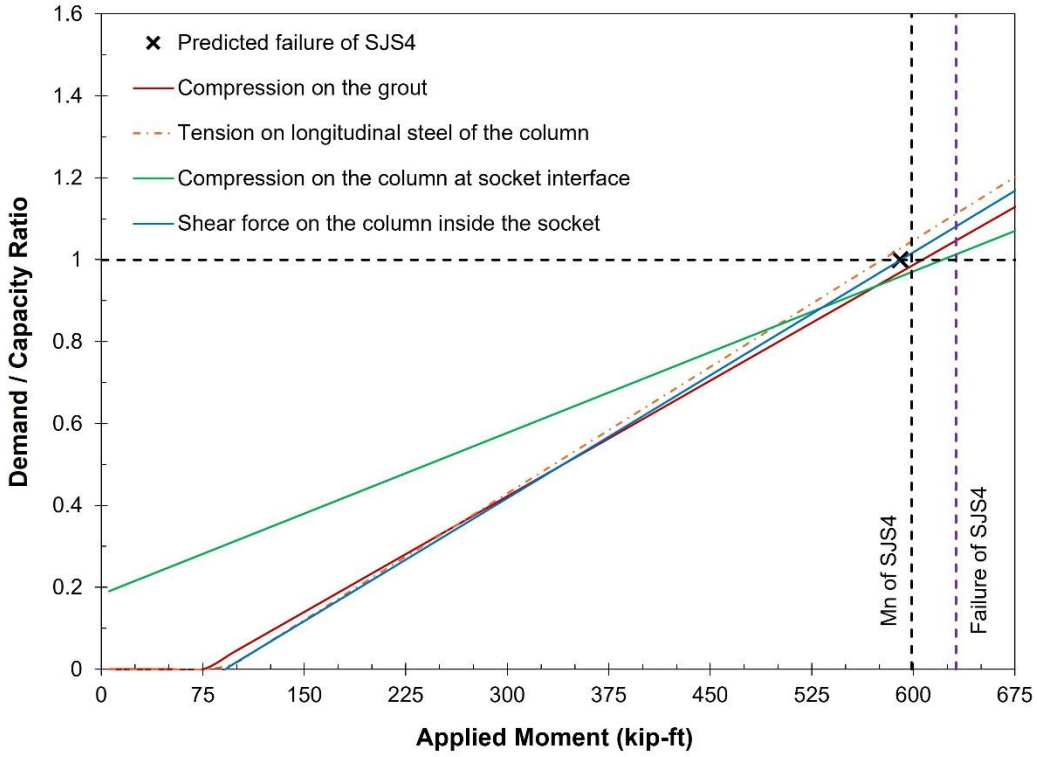


Figure 6-30. Demand-capacity vs. Applied moment for SJS4

Figure 6-31 presents the demand-capacity ratio versus the applied moment for SJS5. It shows that the tension in the longitudinal steel reaches its yield point, as expected during the formation of a plastic hinge. The next component to reach the capacity was the shear force on the column within the socket connection. The predicted failure moment was 3% higher than the actual failure moment observed in the experiment, and the predicted failure mode matched the observed failure mode of SJS5.

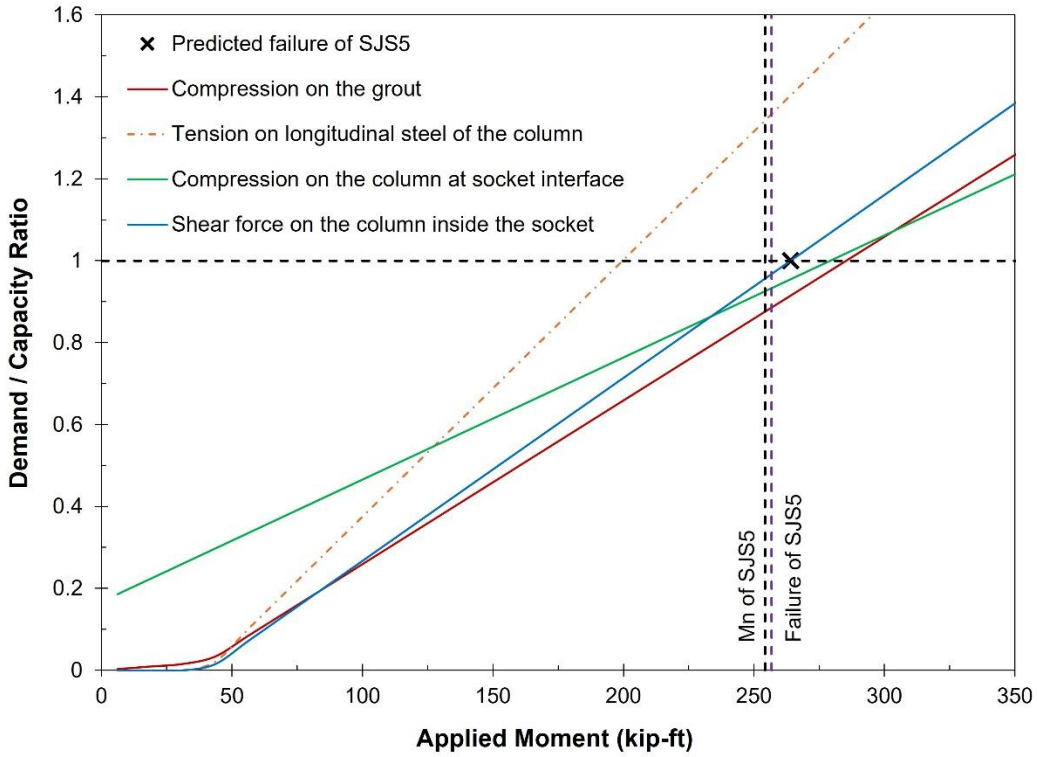


Figure 6-31. Demand-capacity vs. Applied moment for SJS5

Figure 6-32 presents the demand-capacity ratio versus the applied moment for SJS6. It shows that the tension in the longitudinal steel reaches its yield point, which is expected during the formation of a plastic hinge. The next component to reach the capacity is the compression in the column at the socket interface, indicating that the concrete will experience crushing. This suggests the failure mode will follow a flexural behavior similar to a CIP column. The predicted failure moment was 2% higher than the actual failure moment observed in the experiment, and the predicted failure mode matched the observed failure mode of SJS6.

Figure 6-33 presents the demand-capacity ratio versus the applied moment for SJS7. It shows that the tension in the longitudinal steel reaches its yield point, as expected during the formation of a plastic hinge. The next component to reach the capacity is the compression in the column at the socket interface, indicating that the concrete will experience crushing, suggesting a flexural failure mode. The predicted failure moment was 88% of the actual failure moment observed in the experiment. The observed failure mode for SJS7 was grout crushing, followed by shear failure in the column within the external socket. While the STM accurately predicted

concrete crushing, the presence of the steel tube in the column provided additional confinement, making it more difficult for the reinforcing bars to buckle and fracture. This led to shear failure, which the STM also predicted at the failure moment of SJS7.

Figure 6-34 presents the demand-capacity ratio versus the applied moment for SJS8 and shows that the tension in the longitudinal steel reaches its yield point, as expected during the formation of a plastic hinge. The next component to reach the capacity is the compression in the column at the socket interface, indicating that the concrete will experience crushing, suggesting a flexural failure mode. The predicted failure moment was 91% of the actual failure moment observed in the experiment, and the predicted failure mode matched the observed failure mode of SJS8. In this test, reinforcing bar fracture occurred because the other connection components were not near their capacity, allowing the plastic hinge to fully develop outside the external socket connection.

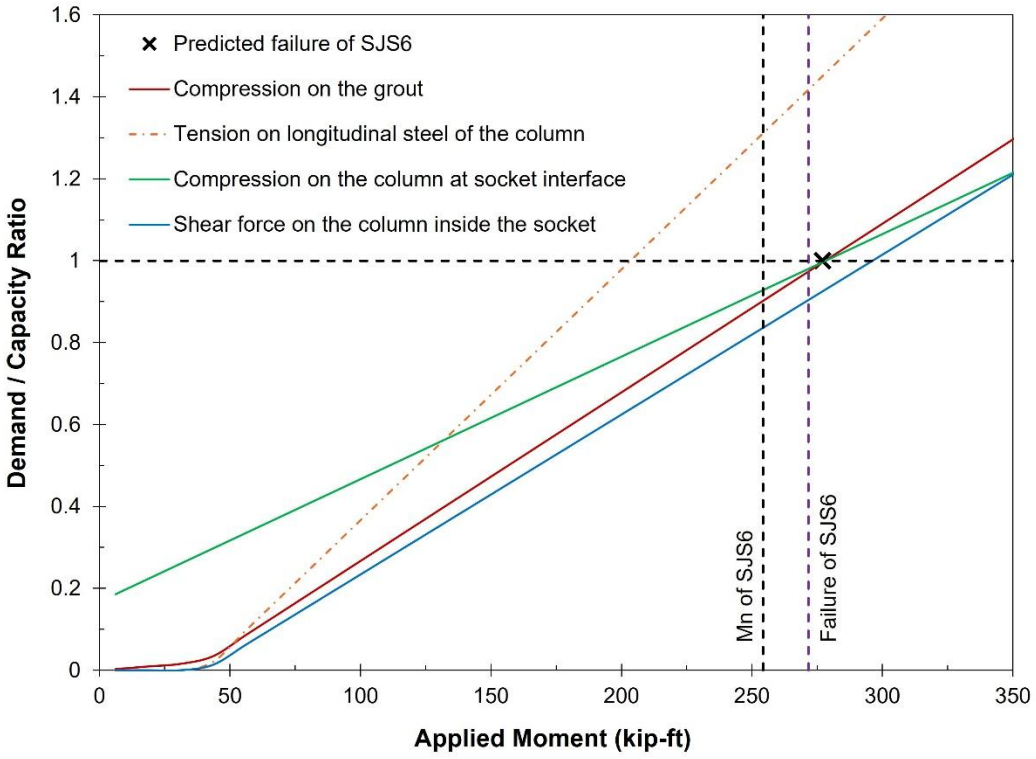


Figure 6-32. Demand-capacity vs. Applied moment for SJS6

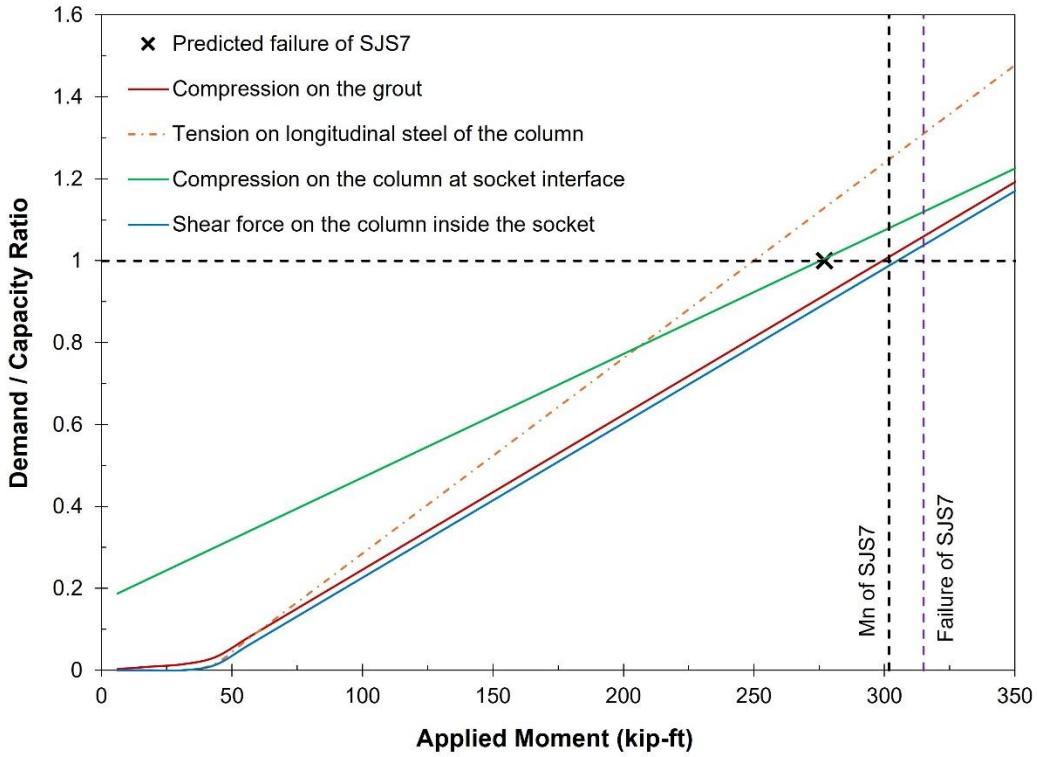


Figure 6-33. Demand-capacity vs. Applied moment for SJS7

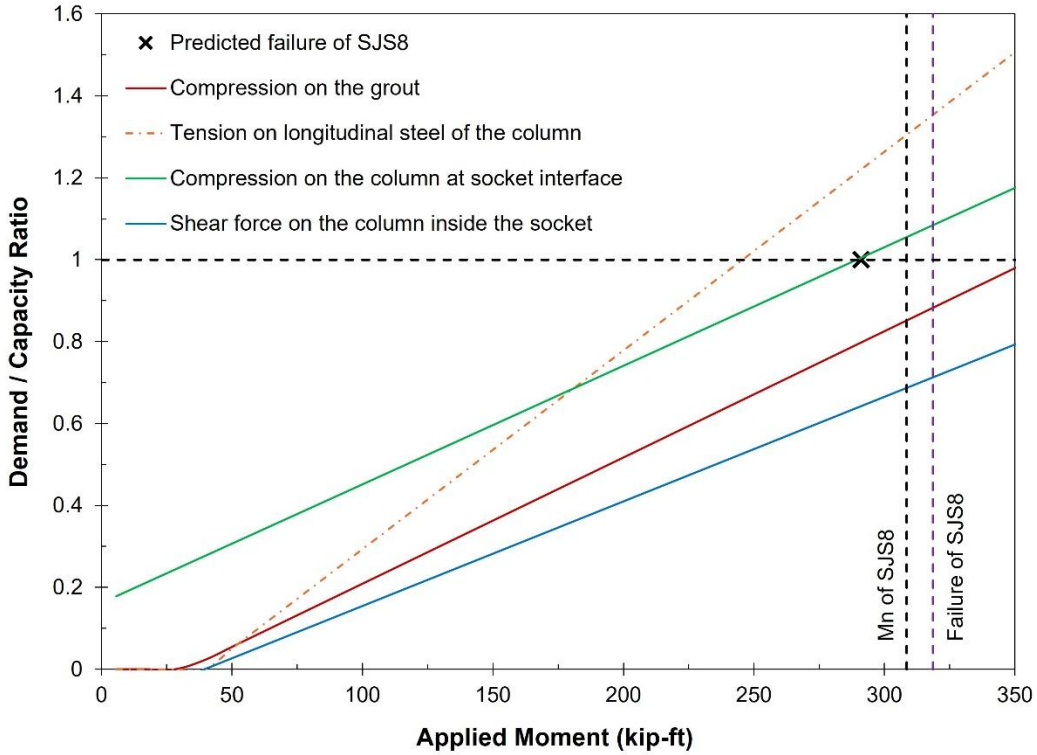


Figure 6-34. Demand-capacity vs. Applied moment for SJS8

Figure 6-35 presents the ratio of the predicted moment to the actual failure moment for each experimental test. In four of the experimental tests, the STM predictions are conservative, underestimating the failure moment with an error of less than 12%. For three of the tests, the STM slightly overpredicted the failure moment, with an error of approximately 3%. The only test with an error exceeding 12% is SJS2, which could be attributed to the strut angle, measured at around 20 degrees, while the minimum recommended angle for struts is 25 degrees.

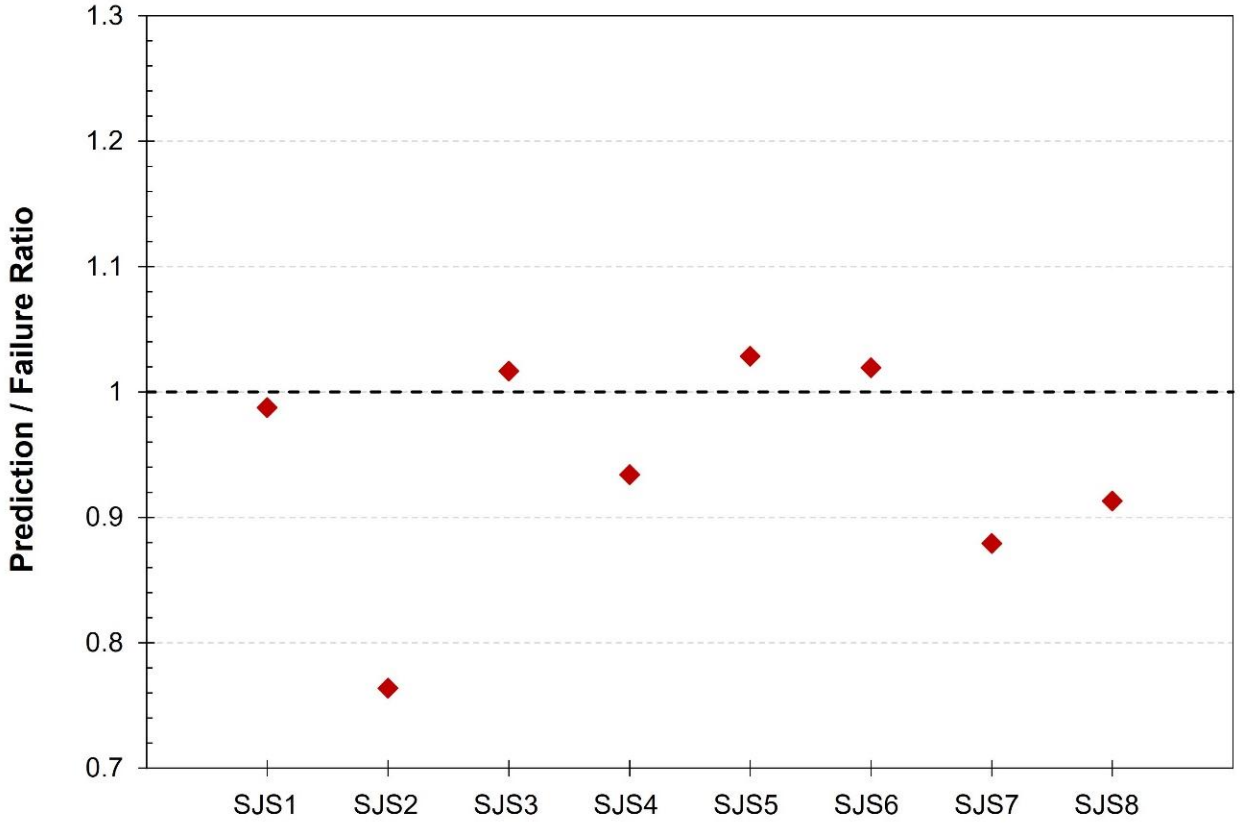


Figure 6-35. Prediction-failure ratio of the STM for the eight experimental tests

Chapter 7: Design of External Socket Connections

This chapter presents a comprehensive design methodology for external socket connections, developed from the Strut-and-Tie Model (STM) and validated through the experimental program discussed in earlier chapters. It provides the essential equations and guidelines needed for designing external socket connections, covering critical parameters such as socket height, grout strength, and reinforcement requirements.

The equations presented in this chapter are grounded in the theoretical framework established in Chapter 6, which details the development and formulation of the STM. For readers interested in understanding the model's underlying mechanics, as well as the validation process, a thorough explanation of the STM is provided in Chapter 6. Additionally, the experimental program that informed and confirmed the design equations, including test setups, instrumentation, and data analysis, is detailed in Chapter 5.

To ensure this chapter stands alone as a practical guide, it includes a step-by-step design example of an external socket connection. This example demonstrates how to apply the derived equations in real-world scenarios, aiding practitioners in incorporating external socket connections into Accelerated Bridge Construction (ABC). Readers who wish to dive deeper into the theoretical and experimental foundations are encouraged to refer to Chapter 5, Chapter 6 and the appendix for a more comprehensive understanding.

7.1. Design Equations and Recommendations

Based on the equilibrium of forces within the STMs, this section outlines the equations necessary for solving the static equilibrium of the truss system and determining the area required to calculate stresses on various components of the column and external socket connection. These equations provide a comprehensive framework for evaluating the forces acting on critical elements, including the longitudinal reinforcement, external concrete walls, and grout. By following these design equations, engineers can ensure that the connection can develop a plastic hinge on the column at the socket interface, having a similar behavior to a CIP column.

Additionally, practical recommendations are provided to assist practitioners in applying these equations effectively in real-world design scenarios. First, the nomenclature used in the design equations is outlined below to ensure clarity in the calculation process.

P = Axial force
Mn = Nominal moment capacity
Mne = Nominal moment capacity using expected properties
Dc = Diameter of the column
f'cd = Design concrete compressive strength
f'cgd = Design grout compressive strength (Cylinder)
f_{yd} = Design yield stress
Hs = Socket height
χ = Ratio between socket height and diameter of the column (Hs/Dc)

The forces acting on the critical components of the connection, as identified through the STM and experimental program, are presented in Equation 7-1 to Equation 7-7. These equations represent the forces in the struts and ties of the STM and are essential for designing the external socket connection.

1) Vertical compressive force acting on the column at the socket interface

Equation 7-1 $$F_{VCC} = 0.6 \cdot P + \frac{M_{ne}}{D_c}$$

2) Inclined compressive force acting on the column within the socket connection

Equation 7-2 $$F_{ICC} = \frac{1.15 \cdot M_{ne} \cdot \sqrt{\chi^2 + 0.8}}{\chi \cdot D_c}$$

3) Shear force acting on the column within the socket connection

Equation 7-3 $$V = \frac{M_{ne}}{\chi \cdot D_c}$$

4) Compressive force acting on the grout

Equation 7-4 $$F_{CG} = \frac{1.5 \cdot M_{ne}}{\chi \cdot D_c}$$

5) Tension force acting on the socket sleeves

Equation 7-5 $$F_{TSS} = \frac{1.5 \cdot M_{ne}}{\chi \cdot D_c}$$

6) Tension force acting on the longitudinal reinforcement of the external socket wall

Equation 7-6 $$F_{TSW} = \frac{M_{ne}}{D_c}$$

7) Inclined compressive force acting on the external socket wall

Equation 7-7 $$F_{ICW} = \frac{M_{ne} \cdot \sqrt{\chi^2 + 2.25}}{\chi \cdot D_c}$$

As shown in Equation 7-1 through Equation 7-7, the relationship between socket height and column diameter is crucial for calculating the forces acting on the various components of the connection. The forces associated with failure modes, as identified through the STM and experimental program, were considered to determine the minimum socket height.

Equation 7-8 to Equation 7-12 outline the calculations that establish the minimum socket height, selecting the highest value obtained. The areas to calculate stresses for the relevant struts and ties, along with their respective capacities, were described in Chapter 6.1 of this report. The detailed derivation of these equations can be found in the appendix for further reference.

Although the STM results demonstrate accuracy, with most predictions being on the conservative side, it is recommended to apply reduction factors for material strengths to ensure safety and reliability. Based on the STM and the experimental program results, a reduction factor of $\varphi = 0.9$ is suggested for steel components, and a reduction factor of $\varphi = 0.7$ is advised for the concrete and grout in the external socket connection components.

No material reduction factor is necessary for the column components, as the column would have already been designed as a CIP element. Using these equations and reduction factors, the connection is designed to remain elastic as well as the adjacent member such as cam beam or foundation, eliminating the need for overstrength factor applied to the column.

1) Compression on the column outside the socket connection

Equation 7-8 $$\chi \geq \frac{0.6 \cdot P \cdot D_c + 1.2 \cdot M_{ne}}{0.1 \cdot f'_{cd} \cdot {D_c}^3}$$

2) Inclined compression on the column within the socket connection

Equation 7-9 $$\chi \geq 1.75 \cdot \sqrt{\frac{M_{ne}}{f'_{cd} \cdot {D_c}^3 - 3.8 \cdot M_{ne}}}$$

3) Compression on the grout

Equation 7-10 $$\chi \geq 3.7 \cdot \sqrt{\frac{M_{ne}}{\phi \cdot f'_{cgd} \cdot {D_c}^3}}$$

4) Shear force on the column within the socket connection

Equation 7-11 $$\chi \geq \frac{M_{ne}}{1.3 \cdot \left(2.0 \cdot \frac{A_{sp} \cdot f_{yd}}{S} \cdot {D_c}^2 + 0.212 \cdot {D_c}^3 \cdot \sqrt{f'_{cd}}\right)} \; [MPa]$$

Equation 7-12 $$\chi \geq \frac{M_{ne}}{1.3 \cdot \left(2.0 \cdot \frac{A_{sp} \cdot f_{yd}}{S} \cdot {D_c}^2 + 0.081 \cdot {D_c}^3 \cdot \sqrt{f'_{cd}}\right)} \; [ksi]$$

Once the minimum ratio between socket height and column diameter (χ) is established, the external socket parameters, including the thickness of the socket wall, the thickness of the steel sleeves, and the reinforcement of the socket wall, can be determined using Equation 7-13 to Equation 7-15.

1) Thickness of socket wall

Equation 7-13 $$Th_{SW} \geq \frac{M_{ne} \cdot \sqrt{\chi^2 + 2.25}}{(\chi \cdot D_c)^2 \cdot \phi \cdot f'_{cd}}$$

2) Longitudinal reinforcement of socket wall

Equation 7-14 $$A_s \geq \frac{M_{ne}}{\phi \cdot f_{yd} \cdot D_c}$$

The steel area obtained by using Equation 7-14 should be distributed across the compressive region of the socket wall, as illustrated in Figure 6-16, which considers an arc length of 1.0 Dc.

3) Thickness of socket sleeve

Equation 7-15 $$Th_{SS} \geq \frac{1.15 \cdot M_{ne}}{(\chi \cdot D_c)^2 \cdot \phi \cdot f_{yd}}$$

Although the size of the gap, which corresponds to the grout thickness, does not have a specific equation for calculation, it is necessary to account for construction tolerances. A gap size between 1 inch and 4 inches is recommended to ensure proper fit of the column and to have a good distribution of the forces between the column and the socket wall.

7.2. Design Example

To demonstrate the application of the design methodology for external socket connections, this section will present a detailed example using a real-world bridge project: Bridge 547 at Hicks Creek. The design information for this bridge was provided by the Department of Transportation and Public Facilities, State of Alaska. The parameters from the original column design needed to design the external socket connection include the column diameter, nominal moment, concrete strength, axial force, transverse reinforcement bar size, and spacing of transverse reinforcement. These parameters are listed below.

ALR = Axial load ratio

P = 650 kips (considered as 5% ALR)

Mne = 104376 kip-in

Dc = 60 in

f'cd = 4.0 ksi

Asp = 0.44 in^2 (spiral #6)

Spacing of spiral = 3 in

f_{yd} = 60 ksi

Using the parameters of the CIP column, the required socket height can be calculated following Equation 7-8 to Equation 7-12. The results of these equations are presented below.

1) Compression on the column outside the socket connection

$$\chi \geq \frac{0.6 \cdot P \cdot D_c + 1.2 \cdot M_{ne}}{0.1 \cdot f'_{cd} \cdot {D_c}^3} = \frac{0.6 \cdot 650 \cdot 60 + 1.2 \cdot 104376}{0.1 \cdot 4.0 \cdot 60^3} = 1.72$$

2) Inclined compression on the column within the socket connection

$$\chi \geq 1.75 \cdot \sqrt{\frac{M_{ne}}{f'_{cd} \cdot {D_c}^3 - 3.8 \cdot M_{ne}}} = 1.75 \cdot \sqrt{\frac{104376}{4.0 \cdot 60^3 - 3.8 \cdot 104376}} = 0.83$$

3) Compression on the grout, Considering a *f'cgd* = 8ksi and a φ = 0.7

$$\chi \geq 3.7 \cdot \sqrt{\frac{M_{ne}}{\phi \cdot f'_{cgd} \cdot {D_c}^3}} = 3.7 \cdot \sqrt{\frac{104376}{0.7 \cdot 8.0 \cdot 60^3}} = 1.09$$

4) Shear force on the column within the socket connection

$$\chi \geq \frac{M_{ne}}{1.3 \cdot \left(2.0 \cdot \frac{A_{sp} \cdot f_{yd}}{S} \cdot {D_c}^2 + 0.081 \cdot {D_c}^3 \cdot \sqrt{f'_{cd}}\right)} \; [ksi]$$

$$\chi \geq \frac{104376}{1.3 \cdot \left(2.0 \cdot \frac{0.44 \cdot 60}{3} \cdot 60^2 + 0.081 \cdot 60^3 \cdot \sqrt{4}\right)} = 0.82$$

The governing equation for this example was the compression on the column outside the socket. It is possible to reduce the socket height by increasing the concrete strength of the original design. For example, if the concrete strength is increased to 5.5 ksi, the value of $\chi = 1.26$. Thus, as the designer, the column strength will be increased to 5.5 ksi, and a $\chi = 1.3$ will be used.

With the relationship between socket height and column diameter established, the next step is to calculate the parameters of the external socket connection using Equation 7-13 to Equation 7-15.

1) Thickness of socket wall, Considering a *f'cd* = 6.5 ksi and a φ = 0.7

$$Th_{SW} \geq \frac{M_{ne} \cdot \sqrt{\chi^2 + 2.25}}{(\chi \cdot D_c)^2 \cdot \phi \cdot f'_{cd}} = \frac{104376 \cdot \sqrt{1.3^2 + 2.25}}{(1.3 \cdot 60)^2 \cdot 0.7 \cdot 6.5} = 7.48 \; in$$

2) Longitudinal reinforcement of socket wall, Considering a fyd = 60 ksi and a φ = 0.9

$$A_s \geq \frac{M_{ne}}{\phi \cdot f_{yd} \cdot D_c} = \frac{104376}{0.9 \cdot 60 \cdot 60} = 32.2 \; in^2$$

3) Thickness of socket sleeve, Considering a fyd = 50 ksi and a φ = 0.9

$$Th_{SS} \geq \frac{1.15 \cdot M_{ne}}{(\chi \cdot D_c)^2 \cdot \phi \cdot f_{yd}} = \frac{1.15 \cdot 104376}{(1.3 \cdot 60)^2 \cdot 0.9 \cdot 50} = 0.44 \; in$$

After determining the design parameters of the external socket connection, it is essential to verify the geometry of the adjacent members, such as the cap beam or foundation. This ensures that the external socket connection fits within the width of the adjacent member and that the development length of the reinforcing bars of the external socket wall is sufficient to fully develop the bars within the height of the adjacent member.

A summary of the results of the design of the external socket connection is presented in Table 7-1. Figure 7-1 and Figure 7-2 illustrate the details of the external socket connection for this column.

Table 7-1. Design parameters for external socket connection

χ	1.3
Socket Height	78 in
Thickness of the wall	7.5 in
Area of steel on the compression region	36 in^2 (9 #18)
Thickness of the sleeves	0.5 in
Gap thickness	2 in
***f'cd* (Portion of the column inside the connection)**	5.5 ksi
f'cgd	8 ksi
f_{yd}	60 ksi

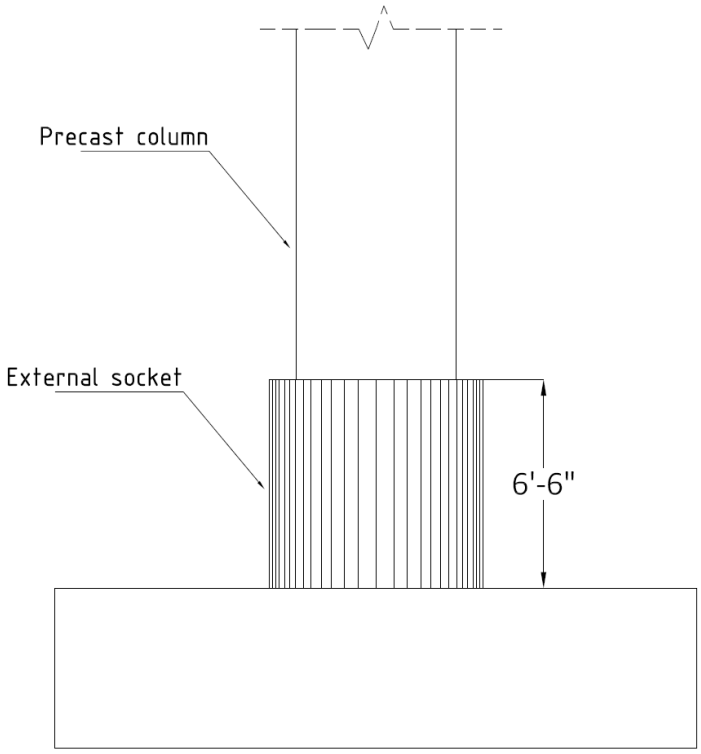


Figure 7-1. Lateral view of the designed external socket connection example

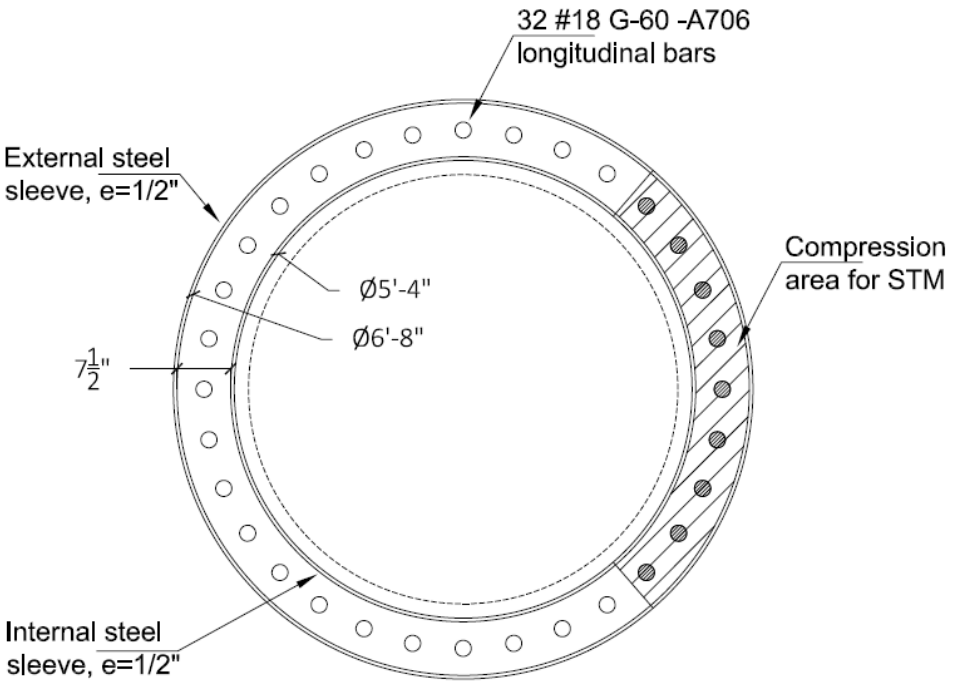


Figure 7-2. Plan view of the designed external socket connection example

Chapter 8: Conclusions and Future Work

The primary objective of this research was to gain a comprehensive understanding of the behavior of external socket connections under seismic actions and to develop a robust design methodology for their implementation in bridge construction. To achieve this, eight experimental tests were performed, varying socket heights and material strengths, to explore the different failure modes that these connections could experience. By integrating the proposed analytical model with data from the experimental program, we were able to establish clear correlations between socket height, applied moment, and critical stresses within the connection.

The findings from the proposed model, along with the outcomes of the large-scale tests, represent a critical advancement in understanding the mechanics of external socket connections. Additionally, design equations were developed, providing practical guidance for engineers in designing external socket connections. This research established a systematic framework for designing socket connections while deepening our understanding of the seismic behavior associated with these critical components in ABC connections.

The following sections will present the key conclusions drawn from the experimental program and the analytical model, highlighting their significance in understanding the behavior of external socket connections. Additionally, recommendations for future work will be provided, offering directions for further research to refine and expand upon the findings of this study.

8.1. Experimental Program

The experimental program has provided valuable insights into the performance of external socket connections, highlighting the critical role of socket height in influencing the overall behavior and design of these connections. Socket height emerged as a key design variable, significantly impacting the ability of the connection to develop the full plastic moment in the column at the socket interface.

One important finding from the experimental tests was the inverse relationship between socket height, grout strength, and the shear force acting on the column within the socket connection. Shorter socket heights required both higher grout strengths and increased consideration of shear forces to prevent a non-desired failure mode, while longer socket heights allowed for lower grout strengths and reduced shear forces without compromising the performance of the connection. This inverse relationship is a critical design consideration for engineers seeking to optimize socket connections based on material properties and forces acting on the structural components.

Furthermore, the experimental results demonstrated that regardless of the socket height, the goal of reducing plastic strain demands from the column into the footing or cap beam was consistently achieved. This indicates that external socket connections effectively protect the adjoining structural members while allowing the column to accommodate inelastic deformations.

Through the combination of experimental data and the analytical model, we established clear correlations between socket height, applied moment, and the critical stresses acting on the connection components. The experimental program successfully delineated the practical limits of external socket connections and provided a deeper understanding of the failure modes associated with different socket heights and material strengths. These failure modes included grout crushing, shear failure within the column, and reinforcing bar fracture, depending on the specific combination of design parameters. In summary, the experimental program not only validated the proposed analytical model but also offered critical insights into the structural performance and design optimization of external socket connections.

8.2. Analytical Model

The application of the Strut-and-Tie Model (STM) in this research provided a comprehensive framework for understanding the relationship between socket height, applied moment, and the critical stresses within the external socket connection. The proposed STM effectively captured the stresses in different components of the connection, including the

longitudinal reinforcing steel, the external concrete walls, and the grout between the column and socket wall for various socket heights.

The STMs developed in this research played an important role in designing the columns and external socket connection components for the experimental program. The large-scale experimental tests verified and validated the model accuracy, showing that the STM's predictions were conservative, with less than a 10 percent error compared to the actual failures observed in the experiments. The model accurately predicted the failure modes and components most susceptible to damage with a specific socket height, demonstrating its reliability in guiding the design and evaluating the structural behavior of external socket connections.

The STM analysis highlighted the critical role of grout strength in determining the maximum applied moment that the connection can experience. The model demonstrated that shorter socket heights require higher grout strengths to develop the plastic hinge on the column at the socket interface, highlighting the grout as a crucial factor in socket connection design. This inverse relationship between socket height and grout strength provides practical design guidelines for ensuring optimal performance under applied loads, particularly in seismic regions.

By correlating socket height, applied moment, and critical stresses, the STM has proven to be a practical tool in identifying the feasible boundaries of external socket connections. Specifically, the model has helped define the vulnerability of these connections to shear failures and grout crushing in the external socket connection. By understanding these boundaries, engineers can better optimize socket connections for improved performance, particularly in Accelerated Bridge Construction (ABC) and in seismic regions.

From the application of the STM, a set of design equations and recommendations were developed to guide practitioner engineers in designing external socket connections. These equations provide a reliable method for calculating important parameters, such as required grout strength, socket height, concrete strength, and reinforcement detailing, to ensure optimal performance under seismic actions.

In conclusion, the development and application of the STM have significantly contributed to advancing the understanding of external socket connections. By combining the model outputs with experimental data, this research has established a solid foundation for more effective and reliable design methodologies. This advancement will not only enhance the performance of bridge connections but also contribute to the broader adoption of external socket connections in ABC practices.

8.3. Future Work

Although this research has established a foundation for understanding the seismic behavior of external socket connections, certain parameters require further investigation to refine and expand upon the findings. The eight experimental tests conducted in this study explored different socket heights and column diameters. Still, additional parameters such as axial load ratio and column slenderness need to be evaluated for a more comprehensive understanding of these connections under different conditions. Additionally, analyzing the performance of double-bent caps will be important to assess the potential impact of tensile forces within the socket connection.

Further investigation is also needed to understand the effects of adding shear reinforcement, particularly in cases with lower socket heights. This could provide valuable insights into improving shear capacity and preventing shear failure before reaching the column nominal capacity. The role of grout thickness should also be examined to determine the maximum thickness that can effectively transmit compression forces to the external socket wall without compromising structural integrity.

For the analytical model (STM), future research could explore the potential for incorporating the effects of friction at the interface between the grout and the column within the socket. Additionally, considering the hoop effect could quantify its contribution to the overall compressive force acting perpendicular to the loading direction. This could significantly impact the shear capacity of the column, providing a more accurate assessment of the forces acting on the column within the socket connection.

Finally, while this research was conducted under quasi-static conditions, it is crucial to extend the study to dynamic actions. Shake table tests could provide valuable insights into the performance of external socket connections under dynamic loading, including strain rates, cyclic behavior at specific limit states, and the cumulative effects of multiple cycles. Understanding the behavior of these connections in seismic regions under real-world dynamic conditions will further validate the design methodologies and improve their reliability.

REFERENCES

[1] M. P. Culmo, "Accelerated Bridge Construction: Experience in Design, Fabrication and Erection of Prefabricated Bridge Elements and Systems," Final manual FHWA-HIF-12-013, Nov. 2011.

[2] M. S. Saiidi *et al.*, *Proposed AASHTO Seismic Specifications for ABC Column Connections*. Washington, D.C.: Transportation Research Board, 2020, p. 25803. doi: 10.17226/25803.

[3] J. I. Restrepo, E. E. Matsumoto, M. J. Tobolski, Transportation Research Board, National Cooperative Highway Research Program, and Transportation Research Board, *Development of a Precast Bent Cap System for Seismic Regions*. Washington, D.C.: National Academies Press, 2011, p. 14484. doi: 10.17226/14484.

[4] A. Mehrsoroush and M. S. Saiidi, "Cyclic Response of Precast Bridge Piers with Novel Column-Base Pipe Pins and Pocket Cap Beam Connections," *J. Bridge Eng.*, vol. 21, no. 4, p. 04015080, Apr. 2016, doi: 10.1061/(ASCE)BE.1943-5592.0000833.

[5] S. Motaref, M. S. Saiidi, and D. H. Sanders, "Seismic Response of Precast Bridge Columns with Energy Dissipating Joints," University of Nevada, Reno, 2011.

[6] A. Mohebbi, M. S. Saiidi, and A. M. Itani, "Shake Table Studies and Analysis of a Precast Two-Column Bent with Advanced Materials and Pocket Connections," *J. Bridge Eng.*, vol. 23, no. 7, p. 04018046, Jul. 2018, doi: 10.1061/(ASCE)BE.1943-5592.0001247.

[7] S. J. Fulmer, M. J. Kowalsky, and J. M. Nau, "Grouted shear stud connection for steel bridge substructures," *Journal of Constructional Steel Research*, vol. 109, pp. 72–86, Jun. 2015, doi: 10.1016/j.jcsr.2015.02.009.

[8] M. L. Marsh *et al.*, *Application of Accelerated Bridge Construction Connections in Moderate-to-High Seismic Regions*. Washington, D.C.: National Academies Press, 2011, p. 14571. doi: 10.17226/14571.

[9] M. P. Culmo, "Connection Details for Prefabricated Bridge Elements and Systems," Final document FHWA-IF-09-010, Mar. 2009.

[10] R. M. F. Canha, E. B. Ebeling, A. L. H. De Cresce El Debs, and M. K. El Debs, “Analysing the base of precast column in socket foundations with smooth interfaces,” *Mater Struct*, vol. 42, no. 6, pp. 725–737, Jul. 2009, doi: 10.1617/s11527-008-9416-4.

[11] M. Tazarv and M. S. Saiidi, “DESIGN AND CONSTRUCTION OF PRECAST BENT CAPS WITH POCKET CONNECTIONS FOR HIGH SEISMIC REGIONS,” University of Nevada, Reno, CCEER 15-06, Aug. 2015.

[12] O. S. Haraldsson, T. M. Janes, M. O. Eberhard, and J. F. Stanton, “Seismic Resistance of Socket Connection between Footing and Precast Column,” *J. Bridge Eng.*, vol. 18, no. 9, pp. 910–919, Sep. 2013, doi: 10.1061/(ASCE)BE.1943-5592.0000413.

[13] O. S. Haraldsson, T. M. Janes, M. O. Eberhard, and J. F. Stanton, “PRECAST BENT SYSTEM FOR HIGH SEISMIC REGIONS – LABORATORY TESTS OF COLUMN-TO-FOOTING SOCKET CONNECTIONS,” University of Washington, Seattle, WA, Final report FHWA-HIF-13-039, Jun. 2013.

[14] Z. Wang, T. Li, H. Qu, H. Wei, and Y. Li, “Seismic Performance of Precast Bridge Columns with Socket and Pocket Connections Based on Quasi-Static Cyclic Tests: Experimental and Numerical Study,” *J. Bridge Eng.*, vol. 24, no. 11, p. 04019105, Nov. 2019, doi: 10.1061/(ASCE)BE.1943-5592.0001463.

[15] Y. Hose, P. Silva, and F. Seible, “Development of a performance evaluation database for concrete bridge components and systems under simulated seismic loads,” *Earthquake Spectra*, vol. 16, no. 2, May 2000.

[16] G. Zhang, Q. Han, K. Xu, X. Du, and W. He, “Experimental investigation of seismic behavior of UHPC-filled socket precast bridge column-foundation connection with shear keys,” *Engineering Structures*, vol. 228, p. 111527, Feb. 2021, doi: 10.1016/j.engstruct.2020.111527.

[17] F. Kavianipour and M. S. Saiidi, “EXPERIMENTAL AND ANALYTICAL SEISMIC STUDIES OF A FOUR-SPAN BRIDGE SYSTEM WITH COMPOSITE PIERS,” University of Nevada, Reno, CCEER 13-17, Oct. 2013.

[18] T. Thonstad, I. M. Mantawy, J. F. Stanton, M. O. Eberhard, and D. H. Sanders, "Shaking Table Performance of a New Bridge System with Pretensioned Rocking Columns," *J. Bridge Eng.*, vol. 21, no. 4, p. 04015079, Apr. 2016, doi: 10.1061/(ASCE)BE.1943-5592.0000867.

[19] Z. Cheng and S. Sritharan, "Side Shear Strength of Preformed Socket Connections Suitable for Vertical Precast Members," *J. Bridge Eng.*, vol. 24, no. 5, p. 04019025, May 2019, doi: 10.1061/(ASCE)BE.1943-5592.0001391.

[20] Y. Osanai, F. Watanabe, and S. Okamoto, "Stress Transfer Mechanism of Socket Base Connections with Precast Concrete Columns," *SJ*, vol. 93, no. 3, 1996, doi: 10.14359/9686.

[21] ASTM C39/C39M, *Standard Test Method for Compressive Strength of Cylindrical Concrete Specimens*, Jun. 2024. doi: 10.1520/C0039_C0039M-24.

[22] ASTM A370, *Standard Test Methods and Definitions for Mechanical Testing of Steel Products*, Apr. 2024. doi: 10.1520/A0370-24.

[23] L. S. Jacobsen, "Damping in composite structures," presented at the Second World Conference on Earthquake Engineering, Tokyo and Kyoto, 1960.

[24] M. J. N. Priestley, G. M. Calvi, and M. J. Kowalsky, *Displacement-Based Seismic Design of Structures*, 2nd ed. Pavia, Italy: IUSS Press, 2007.

[25] David Michael Volpe Ruggiero, "The Behaviour of Reinforced Concrete Subjected to Reversed Cyclic Shear," University of Toronto, Toronto, Canada, 2015.

[26] C. Williams, D. Deschenes, and O. Bayrak, "Strut-and-Tie Model Design Examples for Bridges: Final Report," Technical Report FHWA/TX-12/5-5253-01-1, Jun. 2012.

[27] J. Schlaich and K. Schäfer, "Design and detailing of structural concrete using strut-and-tie models." The Structural Engineer, Volume 69, No 6, Mar. 19, 1991.

[28] M. J. Kowalsky and M. J. N. Priestley, "Improved Analytical Model for Shear Strength of Circular Reinforced Concrete Columns in Seismic Regions," *SJ*, vol. 97, no. 3, 2000, doi: 10.14359/4633.

APPENDIX

Derivation of the equation for compression in the column outside the external socket connection.

L = Lateral force

D_c = Diameter of the column

H_c = Height of the column

H_s = Height of the external socket

P = Axial force on the column

M_{ne} = Nominal moment capacity with expected properties

V_r = Vertical load on the right side of the STM of the column

A_{fr} = Vertical load on the right side of the model due to the moment of lateral force

d_1 = Distance that makes the strut and ties of the column not to be in a symmetric position

d_2 = Distance between vertical tie and vertical strut of the column

d_5 = Distance from the top of the column to the node before the socket connection

F_{VCC} = Vertical compressive force acting on the column at the socket interface

Initial equations

$$H_s = \chi \cdot D_c$$

$$d_1 = \frac{D_c}{18}$$

$$d_2 = \frac{13\ D_c}{18} \rightarrow 0.75\ D_c$$

$$d_5 = H_c - \frac{5\ H_s}{6} - \frac{13\ D_c}{6} \rightarrow H_c - 0.85\ H_s - 2\ D_c$$

$$V_r = \frac{7\ P}{13} \rightarrow 0.6\ P$$

$$L = \frac{M_{ne}}{H_c - H_s}$$

$$A_{fr} = L \times \frac{d_5}{d_2}$$

$$F_{VCC} = V_r + A_{fr} + 2\,L$$

Substituting variables on initial equations

$$L = \frac{M_{ne}}{H_c - \chi \cdot D_c}$$

$$A_{fr} = \frac{M_{ne}}{H_c - \chi \cdot D_c} \times \frac{H_c - 0.85\,H_s - 2\,D_c}{0.75\,D_c}$$

$$A_{fr} = \frac{1.1333\,M_{ne}\left(\chi \cdot D_c + 1.1765\,(2\,D_c - H_c)\right)}{D_c\,(\chi \cdot D_c - H_c)} \rightarrow \frac{1.2\,M_{ne}\left(\chi \cdot D_c + 1.0\,(2\,D_c - H_c)\right)}{D_c\,(\chi \cdot D_c - H_c)}$$

$$A_{fr} = \frac{1.2\,M_{ne}\,(\chi \cdot D_c + 2\,D_c - H_c)}{D_c\,(\chi \cdot D_c - H_c)}$$

$$F_{VCC} = 0.6\,P + \frac{1.2\,M_{ne}\,(\chi \cdot D_c + 2\,D_c - H_c)}{D_c\,(\chi \cdot D_c - H_c)} + \frac{2\,M_{ne}}{H_c - \chi \cdot D_c}$$

$$F_{VCC} = 0.6\,P + \frac{1.2\,M_{ne}[\chi \cdot D_c + 0.18182\,(D_c - 5.5\,H_c)]}{D_c\,(\chi \cdot D_c - H_c)}$$

$$0.18182\,(D_c - 5.5\,H_c) \rightarrow -0.95\,H_c$$

$$F_{VCC} = 0.6\,P + \frac{1.2\,M_{ne}[\chi \cdot D_c - 0.95\,H_c]}{D_c\,(\chi \cdot D_c - H_c)} \rightarrow 0.6\,P + \frac{1.2\,M_{ne}}{D_c}$$

$$F_{VCC} \leq Capacity\ of\ the\ strut$$

$$F_{VCC} \leq 0.1\ {f_{cd}}' \cdot D_c \cdot H_s$$

$$0.6\ P + \frac{1.2\ M_{ne}}{D_c} \leq 0.1\ {f_{cd}}' \cdot \chi \cdot {D_c}^2$$

$$\chi \geq \frac{0.6\ P \cdot\ D_c + \ 1.2\ M_{ne}}{0.1\ {f_{cd}}' \cdot\ {D_c}^3}$$

Derivation of the equation for inclined compression in the column inside the external socket connection.

L = Lateral force

D_c = Diameter of the column

H_c = Height of the column

H_s = Height of the external socket

P = Axial force on the column

M_{ne} = Nominal moment capacity with expected properties

V_l = Vertical load on the left side of the STM of the column

A_{fl} = Vertical load on the left side of the model due to the moment of lateral force

F_{ICC} = Inclined compressive force acting on the column within the socket connection

β = Angle of the inclined strut of the STM of the column inside the external socket

Initial equations

$$V_l = \frac{6\ P}{23} \rightarrow 0.25\ P$$

$$\sin\beta = \frac{0.85\ \chi \cdot D_c}{\sqrt{(0.85\ \chi \cdot D_c)^2 + \ (0.75\ D_c)^2}} \rightarrow \frac{0.85\ \chi \cdot D_c}{0.85\ D_c \cdot \sqrt{\chi^2 + 0.8}} \rightarrow \frac{\chi}{\sqrt{\chi^2 + 0.8}}$$

$$A_{fl} = A_{fr} = \frac{1.2\, M_{ne}\, (\chi \cdot D_c + 2\, D_c - H_c)}{D_c\, (\chi \cdot D_c - H_c)}$$

$$L = \frac{M_{ne}}{H_c - \chi \cdot D_c}$$

$$F_{ICC} = \frac{A_{fl} - V_l + 3\, L}{\sin \beta}$$

Substituting variables on the initial equation for F_{ICC}

$$A_{fl} + 3\, L = \frac{1.2\, M_{ne}\, (\chi \cdot D_c + 2\, D_c - H_c)}{D_c\, (\chi \cdot D_c - H_c)} + \frac{3\, M_{ne}}{H_c - \chi \cdot D_c}$$

$$A_{fl} + 3\, L = \frac{1.2\, M_{ne}\, [\, \chi \cdot D_c - 0.5\, (D_c + 2\, H_c)]}{D_c\, (\chi \cdot D_c - H_c)}$$

$$\frac{[\, \chi \cdot D_c - 0.5\, (D_c + 2\, H_c)]}{(\chi \cdot D_c - H_c)} \rightarrow \frac{[\, \chi \cdot D_c - H_c - 0.5\, D_c]}{(\chi \cdot D_c - H_c)} \rightarrow \frac{1.05\, (\chi \cdot D_c - H_c)}{(\chi \cdot D_c - H_c)}$$

$$A_{fl} + 3\, L = \frac{1.2\, M_{ne}\, [\, 1.05\, (\chi \cdot D_c - H_c)]}{D_c\, (\chi \cdot D_c - H_c)} \rightarrow \frac{1.25\, M_{ne}}{D_c}$$

$$F_{ICC} = \frac{\frac{1.25\, M_{ne}}{D_c} - 0.25\, P}{\frac{\chi}{\sqrt{\chi^2 + 0.8}}} \rightarrow \frac{-0.25\, (D_c \cdot P - 5\, M_{ne}) \cdot \sqrt{\chi^2 + 0.8}}{\chi \cdot D_c}$$

$$F_{ICC} = \frac{(1.25\, M_{ne} - 0.25\, D_c \cdot P) \cdot \sqrt{\chi^2 + 0.8}}{\chi \cdot D_c} \rightarrow \frac{(1.15\, M_{ne}) \cdot \sqrt{\chi^2 + 0.8}}{\chi \cdot D_c}$$

$$F_{ICC} \leq Capacity\ of\ the\ strut$$

$$F_{ICC} \leq f_{cd}' \cdot 0.4\, D_c \cdot \sin\beta \cdot 0.7 D_c$$

$$F_{ICC} \leq f_{cd}' \cdot 0.4\, D_c \cdot \frac{\chi}{\sqrt{\chi^2 + 0.8}} \cdot 0.7 D_c$$

$$F_{ICC} \leq \frac{0.3\, f_c' \cdot \chi \cdot {D_c}^2}{\sqrt{\chi^2 + 0.8}}$$

$$\frac{(1.15\, M_{ne}) \cdot \sqrt{\chi^2 + 0.8}}{\chi \cdot D_c} \leq \frac{0.3\, f_{cd}' \cdot \chi \cdot {D_c}^2}{\sqrt{\chi^2 + 0.8}}$$

$$1.15\, M_{ne} \cdot (\chi^2 + 0.8) \leq 0.3\, f_{cd}' \cdot \chi^2 \cdot {D_c}^3$$

Solving for χ , and choosing the feasible solution

$$\chi \geq 1.75 \sqrt{\frac{M_{ne}}{f_{cd}' \cdot {D_c}^3 - 3.8\, M_{ne}}}$$

Derivation of the equation for shear in the column inside the external socket connection.

D_c = Diameter of the column

M_{ne} = Nominal moment capacity with expected properties

V = Shear force acting on the column inside the external socket connection

F_{ICC} = Inclined compressive force acting on the column within the socket connection

β = Angle of the inclined strut of the STM of the column inside the external socket

Initial equations

$$V = F_{ICC} \times \cos\beta$$

$$\cos\beta = \frac{0.75\ D_c}{0.85\ D_c \cdot \sqrt{\chi^2 + 0.8}} \rightarrow \frac{0.9}{\sqrt{\chi^2 + 0.8}}$$

Substituting variables on the initial equation for V

$$V = \frac{(1.15\ M_{ne}) \cdot \sqrt{\chi^2 + 0.8}}{\chi \cdot D_c} \times \cos\beta$$

$$V = \frac{(1.15\ M_{ne}) \cdot \sqrt{\chi^2 + 0.8}}{\chi \cdot D_c} \times \frac{0.9}{\sqrt{\chi^2 + 0.8}}$$

$$V = \frac{(1.15\ M_{ne}) \cdot\ 0.9}{\chi \cdot D_c} \rightarrow \frac{1.03\ M_{ne}}{\chi \cdot D_c} \rightarrow \frac{M_{ne}}{\chi \cdot D_c}$$

$$V\ \leq\ V_A\ (Shear\ capacity\ )$$

The shear capacity was considered using the revised UCSD model

$$V\ \leq \frac{\pi}{2} \cdot\ A_{sp} \cdot f_{yd} \cdot \frac{D - c - cover}{S} \cdot \cot\theta +\ \alpha\beta\gamma \cdot \sqrt{f_{cd}{}'} \cdot \left(0.8\ A_g\right)$$

$$V\ \leq \frac{\pi}{2} \cdot\ A_{sp} \cdot f_{yd} \cdot \frac{D - c - cover}{S} \cdot \cot 30° +\ (1.5)(0.9)(0.25) \cdot \sqrt{f_{cd}{}'} \cdot \left(0.8\ A_g\right)\ [MPa]$$

$$\frac{M_{ne}}{\chi \cdot D_c}\ \leq \frac{\pi}{2} \cdot\ A_{sp} \cdot f_{yd} \cdot \frac{D_c - 0.2\ D_c - 0.05\ D_c}{S} \cdot \cot 30° +\ 0.27 \cdot \frac{\pi \cdot {D_c}^2}{4} \cdot \sqrt{f_{cd}{}'}\ [MPa]$$

$$\frac{M_{ne}}{\chi \cdot D_c}\ \leq \frac{\pi}{2} \cdot\ A_{sp} \cdot f_{yd} \cdot \frac{0.75\ D_c}{S} \cdot (1.75) +\ 0.27 \cdot \frac{\pi \cdot {D_c}^2}{4} \cdot \sqrt{f_{cd}{}'}\ [MPa]$$

$$\frac{M_{ne}}{\chi \cdot D_c} \leq 2.06 \cdot \frac{A_{sp} \cdot f_{yd}}{S} \cdot D_c + 0.21 \cdot {D_c}^2 \cdot \sqrt{{f_{cd}}'}$$

$$\rightarrow \frac{2 \cdot A_{sp} \cdot f_{yd} \cdot D_c}{S} + 0.21 \cdot {D_c}^2 \cdot \sqrt{{f_{cd}}'} \; [MPa]$$

$$\chi \geq \frac{M_{ne}}{1.3 \cdot \left(\frac{2 \cdot A_{sp} \cdot f_{yd} \cdot {D_c}^2}{S} + 0.21 \cdot \sqrt{{f_{cd}}'} \cdot {D_c}^3 \right)} \; [MPa]$$

$$\chi \geq \frac{M_{ne}}{1.3 \cdot \left(\frac{2 \cdot A_{sp} \cdot f_{yd} \cdot {D_c}^2}{S} + 0.081 \cdot \sqrt{{f_{cd}}'} \cdot {D_c}^3 \right)} \; [ksi]$$

An increase of shear capacity is considered with the 1.3 factor. This is explained in Chapter 6.3

Derivation of the equation for compression in the grout of the external socket connection.

L = Lateral force

D_c = Diameter of the column

H_c = Height of the column

M_{ne} = Nominal moment capacity with expected properties

V = Shear force acting on the column inside the external socket connection

F_{ICC} = Inclined compressive force acting on the column within the socket connection

β = Angle of the inclined strut of the STM of the column inside the external socket

F_{CG}= Force in the grout of the external socket connection

Initial equations

$$L = \frac{M_{ne}}{H_c - \chi \cdot D_c}$$

$$F_{CG} = L + F_{ICC} \times \cos\beta \rightarrow L + V$$

Substituting variables on the initial equation for F_{CG}

$$F_{CG} = \frac{M_{ne}}{H_c - \chi \cdot D_c} + \frac{M_{ne}}{\chi \cdot D_c}$$

The variable L was evaluated under different conditions and is conservative to consider that the maximum value that could be considered is 1/3 of V. Knowing how critical the grout is for the connection, a value of 0.5 V was considered for L.

$$F_{CG} = \frac{1.5\, M_{ne}}{\chi \cdot D_c}$$

$$F_{CG} \leq Capacity\ of\ the\ grout$$

$$F_{CG} \leq f_{cgd}{}' \cdot \left(0.11 \cdot \chi \cdot D_c{}^2\right)$$

$$\frac{1.5\, M_{ne}}{\chi \cdot D_c} \leq f_{cgd}{}' \cdot \left(0.11 \cdot \chi \cdot D_c{}^2\right)$$

Solving for χ , and choosing the feasible solution

$$\chi \geq 3.7 \cdot \sqrt{\frac{M_{ne}}{f_{cgd}{}' \cdot D_c{}^3}}$$